

Steel Shear Connections in Composite Frames Subject to Progressive Collapse

by

Amirhoushang Jamshidi

A thesis submitted in partial fulfillment of the requirements for the degree of

Doctor of Philosophy

in

Structural Engineering

Department of Civil and Environmental Engineering  
University of Alberta

© Amirhoushang Jamshidi, 2016

## **ABSTRACT**

The susceptibility of structures to extensive collapse when subjected to a localised failure due to an extreme loading event has in recent years gained considerable research attention. The scenario most often used to assess such performance, either experimentally or through finite element simulation, is the loss of a column, requiring the floor system to bridge across two building bays with the aid of arching and catenary actions. When a column is abruptly disengaged by an abnormal load, the resulting double-span beam must bridge over the removed column by developing a new equilibrium path to redistribute the load to the adjacent elements. This severe damage in a steel gravity frame, which is designed to carry primarily gravity loads, creates significant demands on shear connections.

The response of steel shear connections as a component of steel gravity composite frame systems under the column removal scenario is still largely unknown due to the complex interaction between the slab and the steel framework at large deflections. While the slab itself can participate in maintaining the integrity of the overall floor system, its presence amplifies the demand on the steel connections after experiencing initial flexural action.

This research investigated the behaviour of steel shear connections in composite frames under a simulated progressive collapse scenario. The research objectives, experimental protocols, and the most significant conclusions drawn from test observations are discussed. The present study describes the details of a comprehensive experimental and numerical program that has been completed to

assess the behaviour of connections in composite floor construction by evaluating the failure mode, load carrying mechanisms, strength, and ductility of the connections. An experimental program consisting of 17 full-scale physical tests was performed on connections that included shear tabs and double angles. A variety of parameters were considered, including the connection type, connection depth, connection material thickness, and notional beam span. A testing procedure based on the proposed loading protocols was developed and executed on connections to simulate demands and deformations expected in a composite floor system under a column removal scenario.

The second part of this research consisted of comprehensive finite element modelling and analysis techniques. Models were validated using the test results. They were also expanded to investigate the effects of critical parameters on the performance of shear connections in composite frames. Detailed three-dimensional prototype simulations were evaluated and compared with the simplified finite element models and physical tests. The overall capacity of the prototype systems was evaluated and compared with the integrity requirements stipulated in current Canadian and US building codes and design guidelines.

Design recommendations based on the experiments and finite element models are proposed for calculating the capacity and ductility of shear connections in composite frames when subject to central column removal.

*Dedicated with love to*  
*my family and my grandmother*  
*who will always have a special place in my heart*

## ACKNOWLEDGMENT

I would like to take this opportunity to express my sincere gratitude to everyone whose support, encouragement, help or remarks has contributed to the fulfilment of this work.

First and foremost, I wish to express my deep gratitude to my supervisor Professor Robert G. Driver for his consistent support, patience, motivation, and immense knowledge. His guidance in all aspects of research and writing was highly appreciated and his advice on academia, as well as my career have been invaluable. It has been an honor working with him as I've learned more from him, not only academically, but also professionally and personally.

The assistance of the technicians in the I.F. Morrison Laboratory of the University of Alberta—Greg, Cameron, and Rizaldy—who contributed to the success of the physical tests is acknowledged. Many thanks also to Shane Delorey for his help on welding the base plates of the test set-up. The assistance of my friends and fellow graduate students—Pouya, Montazar, Meisam, Hafez, Mohammad Reza, Sadegh N., Nabi, Hadi, Seyed, Parisa, and Tyler—in building formworks, casting concrete, and testing is highly appreciated.

My sincere thanks go to Dr. Scott Alexander for our lively discussions related to this project and the practical outlook he openly provided through the design process of formworks, concrete floor slab, and on the modular concept of assembling components of the composite system. Also, my gratitude goes to Dr. Samer Adeeb for his gracious support on my finite element modellings.

Funding for this research was provided by the Natural Sciences and Engineering Research Council of Canada (NSERC). All required concrete for the slabs was

donated and delivered to the lab from Lafarge North America. Numerical finite element analysis in this research required substantial computational resources which were provided in forms of Compute Canada Resource Allocation Competition (RAC) by Westgrid network, one of the Compute Canada regional partners. All their support is greatly acknowledged.

Financial support was provided through my supervisor and scholarships from the Faculty of Graduate Studies and Research of University of Alberta (Provost Doctoral Entrance Award, Queen Elizabeth II Graduate Scholarship), Graduate Student Association (professional development award, and profiling Alberta's graduate students award), University of Alberta Career Centre (Green and Gold Student Leadership and Professional Development Grant), Canadian Transportation Research Forum (Transport Canada Scholarship in Safety and Security), Canadian Institute of Steel Construction (G.L. Kulak Scholarship), Engineers Canada (Manulife Scholarship), and Golden Key International Honour Society (Golden Key Research Award) are greatly appreciated.

In addition, many thanks to friends and relatives here and back home who supported me mentally. I would like to extend a cordial thank you to my family in Iran, specially my father. His vision and dedication to provide me with nothing but the best education has been and will be truly the base of all my accomplishments. I will be eternally grateful for all the opportunities that have been provided for me.

Last but not least, I would like to express my sincere gratitude and love to my dear wife, Farnaz, for her love, kindness, selfless support, and for sharing all the ups and downs of my journey to this achievement. Her understanding, patience and companionship made this research possible. She has sacrificed so much to help me fulfill my ambitions and I thank and love her for it...

## TABLE OF CONTENTS

<b>1. Introduction.....</b>	<b>1</b>
1.1 Background .....	1
1.1.1 Overview.....	1
1.1.2 Definition of Disproportionate and Progressive Collapse .....	1
1.1.3 Steel Gravity Frames in Progressive Collapse Scenario.....	2
1.1.4 Arching Action and Catenary Action .....	3
1.2 Problem Statement and Research Motivation .....	4
1.3 Objectives and Scope .....	6
1.4 Research Methodology.....	7
1.5 Outline.....	7
<b>2. Literature Review .....</b>	<b>12</b>
2.1 Introduction .....	12
2.2 Current Design Codes, Standards, and Guidelines .....	12
2.2.1 USA.....	13
2.2.1.1 New York City Building Code (NYCBC).....	13
2.2.1.2 International Building Code (IBC).....	14
2.2.1.3 American Society of Civil Engineers (ASCE) .....	15
2.2.1.4 American Institute of Steel Construction (AISC).....	15
2.2.1.5 General Services Administration (GSA).....	16
2.2.1.6 Unified Facilities Criteria (UFC).....	17
2.2.2 Canada.....	19
2.2.2.1 National Building Code of Canada (NBCC).....	19
2.2.2.2 Canadian Standards Association (CSA S16-14) .....	20
2.2.2.3 Canadian Standards Association (CSA S850-12) .....	20
2.2.3 Europe.....	21
2.2.3.1 U.K. Standards.....	21
2.2.3.2 Eurocode.....	21

2.3	Previous Research on Robustness of Steel Shear Connections.....	22
2.3.1	Astaneh (2007).....	23
2.3.1.1	Astaneh et al. (2002).....	24
2.3.1.2	Tan and Astaneh (2003) .....	25
2.3.1.3	Liu and Astaneh (2000).....	26
2.3.2	Izzuddin et al. (2008).....	27
2.3.3	Sadek et al. (2008) .....	27
2.3.4	Thompson (2009).....	29
2.3.5	Alashker et al. (2010).....	29
2.3.6	Main and Sadek (2012, with corrections dated 2013) .....	30
2.3.7	Yang and Tan.....	31
2.3.7.1	Yang and Tan (2012).....	31
2.3.7.2	Yang and Tan (2013a, 2013b).....	32
2.3.7.3	Yang and Tan (2013c).....	32
2.3.7.4	Yang and Tan (2014).....	33
2.3.7.5	Yang and Tan (2015).....	34
2.3.8	Oosterhof and Driver (2015; 2016).....	35
2.3.9	Weigand and Berman (2014).....	36
2.4	Conclusion.....	37
<b>3.</b>	<b>Experimental Program.....</b>	<b>46</b>
3.1	Introduction .....	46
3.2	Prototype Composite Steel Frame.....	46
3.3	Test Specimens.....	47
3.3.1	Shear Connections .....	48
3.3.2	Concrete Slabs .....	49
3.3.3	Test Beams.....	51
3.3.4	Slab Anchorage Beams.....	51
3.3.5	Stub Columns.....	52
3.4	Test Set-up.....	52
3.5	Instrumentation.....	53
3.6	Loading Regime .....	56



3.6.1	Equilibrium of Forces .....	57
3.6.1.1	Point of Inflection (PoI).....	58
3.6.2	Geometric Compatibility of Displacements.....	61
3.7	Test Procedure.....	64
3.7.1	Procedure for Pilot Test and ST36A Specimens.....	64
3.7.2	Procedure for Testing Rest of Specimens.....	65
3.8	Ancillary Tests to Determine Material Properties.....	68
3.8.1	Tension Coupon Tests.....	68
3.8.2	Rebar Tension Tests.....	69
3.8.3	Concrete Cylinder Tests.....	70
<b>4.</b>	<b>Experimental Results And Discussion .....</b>	<b>99</b>
4.1	Introduction .....	99
4.2	Pilot Test .....	99
4.3	Test Results .....	101
4.3.1	Deformations and Failure Modes of Connections .....	101
4.3.1.1	Shear Tabs .....	101
4.3.1.2	Double Angles .....	102
4.3.2	Failure Modes of Concrete Slab .....	103
4.3.3	Characteristics of Load Development.....	104
4.3.3.1	Shear Tabs .....	104
4.3.3.2	Double Angles .....	106
4.3.4	Calculation of Horizontal Load Developed in Connections .....	107
4.4	Accuracy of Loading Regime: Axial Elongation and Vertical Deflection.....	109
<b>5.</b>	<b>Finite Element Modellings .....</b>	<b>123</b>
5.1	Introduction .....	123
5.2	Model Development.....	123
5.3	Model Overview.....	123
5.4	Modelling of Components.....	124
5.4.1	Steel Connections.....	124
5.4.2	Bolts .....	124

5.4.3	Concrete Slab .....	125
5.4.4	Reinforcing Steel .....	125
5.4.5	Beam .....	126
5.4.6	Column.....	126
5.5	Element Selection and Meshing Technique .....	127
5.5.1	Element Type .....	127
5.5.2	Element Hourglassing and Locking.....	128
5.5.3	Element Selection .....	129
5.5.4	Meshing Technique.....	130
5.6	Material Properties and Verification .....	132
5.6.1	Material Model for Concrete .....	132
5.6.2	Material Model for Steel Components.....	134
5.6.3	Progressive Damage and Material Failure .....	135
5.6.3.1	Damage Initiation Constitutive Model .....	136
5.6.3.2	Damage Evolution Law .....	137
5.6.3.3	Element Removal .....	139
5.6.4	Material Model for Steel Rebars.....	140
5.6.5	Material Model for High Strength Bolts.....	141
5.7	Contact Modelling.....	141
5.8	Constraints.....	142
5.9	Loading.....	142
5.10	Boundary Conditions.....	143
5.11	Analysis Solution and Procedures .....	144
5.11.1	Quasi-Static Simulation .....	145
5.12	Derivation of Results .....	146
<b>6.</b>	<b>Finite Element Results, Verifications and Discussion .....</b>	<b>162</b>
6.1	Introduction .....	162
6.2	Finite Element Results .....	162
6.3	Model Verification .....	163
6.3.1	Comparison with Oosterhof and Driver (2016) .....	163
6.3.2	Comparison of FEA with Tests Conducted in This Research .....	164

6.3.3	Comparison of Axial Elongation of Attached Connection and Vertical Deflection of Removed Column with Loading Regime and Experiments .....	165
6.3.4	Axial Deformation of Remote Connections and Comparison with the Target Loading Regime .....	166
6.4	Behaviour of Shear Tabs .....	167
6.4.1	Deformation and Failure Mode.....	167
6.4.2	Load Development and Effects of Composite Section .....	168
6.4.3	Capacity Prediction .....	170
6.4.3.1	Bolt Bearing and Tear-out Limit State .....	170
6.4.3.2	Bolt Shear Limit State .....	173
6.4.4	Ductility Prediction .....	174
6.4.4.1	First Method .....	175
6.4.4.2	Second Method .....	176
6.5	Behaviour of Double Angles.....	177
6.5.1	Deformation and Failure Mode.....	177
6.5.2	Load Development and Effects of Composite Section .....	178
6.5.3	Capacity Prediction .....	180
6.5.3.1	Gross-section Failure Limit State .....	181
6.5.3.2	Bolt Shear Limit State .....	183
6.5.4	Ductility Prediction .....	184
6.6	Simplified Design Recommendations .....	186
6.7	Detailed Finite Element Model of Prototype System.....	186
6.7.1	Axial Deformation and Accuracy of the Proposed Loading Regime .....	187
6.7.2	Behaviour of Connections in Prototype Models.....	189
6.7.3	Load–Displacement Response .....	190
6.7.4	Load Combination and Structural Integrity Requirements .....	192
6.7.5	Comparison with the Existing Research Models .....	193
<b>7.</b>	<b>Summary, Conclusions and Recommendations .....</b>	<b>241</b>
7.1	Summary .....	241
7.2	Conclusions .....	242
7.2.1	Loading Protocols .....	242

7.2.2	Concrete Slab .....	243
7.2.3	Shear Tab Connections .....	244
7.2.4	Double Angle Connections .....	245
7.2.5	Finite Element Modelling Technique .....	247
7.2.6	Detailed Prototype Models .....	247
7.3	Recommendations .....	249
7.3.1	Design Recommendations .....	249
7.3.2	Recommendations for Future Research .....	250
<b>References .....</b>		<b>251</b>
<b>APPENDIX A. Computations on Geometric Compatibilities of Displacements .....</b>		<b>258</b>
A.1	Introduction .....	258
A.2	Deflection of Removed Column ( $\Delta$ ) .....	260
A.3	Axial Deformation of Near-End Connection ( $\delta_1$ ) .....	260
A.4	Axial Deformation of Far-End Connection ( $\delta_2$ ) .....	262
A.5	Total Axial Deformation .....	264
A.5.1	Arching Action Phase .....	264
A.5.2	Catenary Action Phase .....	265
A.6	Parametric Study on the Axial Deformation of Connections .....	266
<b>APPENDIX B. Shop Drawings .....</b>		<b>275</b>
<b>APPENDIX C. Material Data .....</b>		<b>296</b>

## LIST OF TABLES

Table 2-1: Modelling Parameters and Components Capacities .....	38
Table 2-2: Acceptance Criteria for LSP of Steel Connections (m-factor).....	38
Table 2-3: Acceptance Criteria for Nonlinear Analysis Procedures of Steel Connections.....	39
Table 3-1: Experimental Test Matrix.....	72
Table 3-2: Specifications of Shear Tab Specimens* .....	72
Table 3-3: Specifications of Double Angle Specimens* .....	72
Table 3-4: Initial Angle of Arching Action ( $\alpha$ )* .....	73
Table 3-5: Idealized Model of Axial Load Development in Connections of a Composite Floor Frame under Column Removal Scenario .....	73
Table 3-6: Material Properties of Steel Coupons, Rebars, Test Beam, and Column.....	74
Table 3-7: Material Properties of Concrete Cylinders.....	74
Table 4-1: Test Results of Shear Tabs .....	111
Table 4-2: Test Results of Double Angles.....	112
Table 5-1: Parameters Used in the Damage Initiation Constitutive Model .....	147
Table 6-1: Comparison of Finite Element Model and Experiment Results Reported by Oosterhof and Driver (2016).....	196
Table 6-2: Finite Element Results of Shear Tabs (Attached Connections) in Composite Frame .....	197
Table 6-3: Finite Element Results of Shear Tabs (Remote Connections) in Composite Frame .....	198
Table 6-4: Finite Element Results of Shear Tabs in Bare Frame .....	199

Table 6-5: Effect of Concrete Slab on Shear Tabs (Attached Connections) .....	200
Table 6-6 : Comparison of Bolt Tear-out Capacity .....	200
Table 6-7: Test-to-Predicted Ratio: Bolt Tear-out Capacity with the Consideration of Inclined Shear Planes.....	201
Table 6-8: Bearing at Bolt Holes (Remote Shear Tabs).....	201
Table 6-9: Rotational Capacity Corresponding to the Ultimate Horizontal Load of Attached Shear Tabs and Comparisson with the Current Guidelines.....	202
Table 6-10: Rotational Capacity of Shear Tabs Derived based on the Proposed Emprical Methods, and Comparison with the FEA .....	203
Table 6-11: Finite Element Results of Double Angles (Attached Connections) in Composite Frame .....	204
Table 6-12: Finite Element Results of Double Angles (Remote Connections) in Composite Frame .....	205
Table 6-13: Finite Element Results of Double Angles in Bare Frame .....	206
Table 6-14: Effect of Concrete Slab on Double Angles (Attached Connections).....	207
Table 6-15 : Comparison of Double Angles Capacity: Gross-sectional Failure	207
Table 6-16: Bearing at Bolt Holes (Remote Double Angles).....	208
Table 6-17: Rotational Capacity of Double Angles Derived based on the Proposed Emprical Method, and Comparison with the FEA and Guidelines .....	208
Table 6-18: Comparison of Beam Rotations and Ultimate Strength of Shear Tabs.....	209
Table 6-19: Uniform Dead and Specified Live Loads for Various Occupancies	209
Table 6-20: Gravity Loads and Load Combination for Extraordinary Events ...	209

## LIST OF FIGURES

Figure 1-1: Shear (Simple) Connections: Bolted Double Angle, and Shear Tab ..	9
Figure 1-2: Column Loss Scenario and Bridging for Alternative Path .....	9
Figure 1-3: Arresting Collapse through Bending Action.....	9
Figure 1-4: Arresting Collapse through Vierendeel Mechanism due to Bending Moment Capacity of Beam-to-Column Connections .....	10
Figure 1-5: Compressive Arching and Tensile Catenary Actions at (a) the Beginning of Loading; (b) the Later Stages of Loading.....	10
Figure 1-6: Formation of Tensile Membrane and Compressive Ring under Central Column Removal .....	11
Figure 2-1: Generalized Component Load–Deformation Relations for Modelling Parametrs and Acceptance Criteria.....	40
Figure 2-2: Eurocode Accidental Design Strategy (EN 1991-1-7 (CEN 2006)).	40
Figure 2-3: Three-Hinge Beam Analogy with End-Support Conditions (Astaneh 2007).....	41
Figure 2-4: Plan and Elevation of Test Specimen (Astaneh 2007).....	41
Figure 2-5: Moment-Rotation Response of Shear Tab Connections Including Slab (Astaneh 2005).....	42
Figure 2-6: (a) Plan Layout and Floor Area Considered; (b) Load–Displacement of Floor System Components (Sadek et al. 2008) .....	42
Figure 2-7: Test Set-up (Yang and Tan 2014).....	43
Figure 2-8: Effect of Composite Slab on Bolted Double-Angle Connections (Yang and Tan 2014) .....	43
Figure 2-9: Parameters of (a) Shear-Tab Specimens; (b) Bolted Double-Angle Specimens (Oosterhof and Driver 2015) .....	44
Figure 2-10: Test Set-up (Oosterhof and Driver 2015) .....	44
Figure 2-11: Geometric Relationship Between Beam Rotation, Axial Extension, and Interior Column Deflection (Weigand and Berman 2014) .....	45
Figure 3-1: Plan Layout of 4×4 Bay Frame Building with Clear Span of 6.0 m..	75
Figure 3-2: Plan Layout of 4×4 Bay Frame Building with Clear Span of 9.0 m..	76
Figure 3-3: Elevation: (a) Prototype Frame Building; (b) Floor Area Considered	77

Figure 3-4: Convention for Specimen Designations.....	77
Figure 3-5: Details of Shear Tab Connections.....	78
Figure 3-6: Details of Double Angle Connections .....	79
Figure 3-7: Details of Reinforced Concrete Slabs .....	80
Figure 3-8: Elevation of Test Set-up for: (a) Pilot Test, ST36A, and ST36B; (b) Rest of Specimens.....	81
Figure 3-9: Schematic of Test Set-up .....	82
Figure 3-10: Assembly of Test Set-up and Position of Test Specimen Segments	83
Figure 3-11: Instrumentation Layout .....	83
Figure 3-12: (a) 3D Digital Camera System; (b) Speckle Pattern on an Angle; (c) Calibration Prior to Test .....	84
Figure 3-13: Double-span Frame: (a) Before Collapse; (b) After Column Removal; (c) Free Body Diagram.....	85
Figure 3-14: Moment Distribution and Point of Inflection (PoI) .....	85
Figure 3-15: Cross-sectional Properties of ST59B Specimen .....	86
Figure 3-16: Moment–Curvature Diagram for Cross-section of ST59B Specimen.....	86
Figure 3-17: Migration of Neutral Axis from Initial Elastic Position versus Curvature (Cross-section of ST59B Specimen).....	87
Figure 3-18: Moment Amplification Factor ( $f_m$ ) versus Beam Chord Rotation for ST36A Specimen based on Finite Element Analysis .....	87
Figure 3-19: Strut and Tie Model (Truss Analogy) .....	88
Figure 3-20: Geometric Compatibilities of Displacements (From Appendix A) .	89
Figure 3-21: Development of Axial Load in Connections of a Composite Floor Frame under Column-Removal Scenario (For Details Refer to Table 3-5).....	90
Figure 3-22: Axial Deformation of Connections with Span of 9.0 m (From Appendix A).....	91
Figure 3-23: Axial Deformation of Near-End Connection (From Appendix A) ..	91
Figure 3-24: Force Components of Actuators in the Test Set-up for Calculation of Internal Forces Applied at the Column Face .....	92
Figure 3-25: Loading Regime Flowchart used for Pilot Test and Specimen ST36A.....	92



Figure 3-26: Position of Testing Zone Subassemblage within the Span .....	93
Figure 3-27: Flowchart of Loading Regime used for Remaining Specimens .....	93
Figure 3-28: Position of Arching Line and Actuators 3 at Different Stages of Loading .....	94
Figure 3-29: Connection Axial Deformation: Specimen DA59B.....	95
Figure 3-30: Vertical Deflection of Removed Column: Specimen DA59B.....	95
Figure 3-31: Location and Details of Tension Coupons.....	96
Figure 3-32: Section of a Tension Coupon Test (6.3 mm Plate) at Various Stages of Formation During Development of a Cup–Cone Fracture .....	96
Figure 3-33: Stress–Strain Curves for Tension Coupons of 9.7 mm Angle .....	97
Figure 3-34: Stress–Strain Curves for Tension Coupons of 6.3 mm Plate.....	97
Figure 3-35: Stress–Strain Curves for Tension Tests of 10M Rebars .....	98
Figure 3-36: Stress–Strain Curves of Cylindrical Concrete Specimens (DA59B)98	
Figure 4-1: Load versus Beam Rotation of Pilot Test .....	113
Figure 4-2: Deformation and Failure Mode of Connection at: (a) Undeformed; (b) 0.04 radians (peak moment); (c) 0.056 radians; (d) 0.114 radians (peak horizontal).....	113
Figure 4-3: Failure Modes of Shear Tab: (a) Tensile Splitting Tear; (b) Shear Tear .....	114
Figure 4-4: Shear Tab Successive Bolt Tear-out: (a) Five Bolts; (b) Three Bolts .....	114
Figure 4-5: Unfolding of Double Angle Connections .....	115
Figure 4-6: Failure Modes of Double Angles: (a) Tearing of Gross Section Near the Heel; (b) Fracture Near Bolt Line Attached to the Stub Column .....	115
Figure 4-7: Deformation of Angle's Hole at the Bolt Line Attached to the Column: (a) Punching; (b) Bearing; (c) Punching, Bearing, and Tearing.....	116
Figure 4-8: Failure Mode of Concrete Slab: (a) Crack Distribution on the Soffit of the Slab, (b) Front View of the Concrete Slab (Opening to the Stub Column) ..	116
Figure 4-9: Load versus Beam Rotation of Shear Tab (ST59A) .....	117
Figure 4-10: Vertical Load versus Vertical Displacement and Beam Rotation of Shear Tab (ST59A).....	117
Figure 4-11: Specimen ST59A at: (a) Beginning; (b) 0.041 radians (Bolt 5 Bulge-out); (c) 0.074 radians (Bolt 5 Tear-out); (d) 0.118 radians (Failure) .....	118

Figure 4-12: Load versus Beam Rotation of Double Angle (DA59A).....	118
Figure 4-13: Vertical Load versus Vertical Displacement and Beam Rotation of Double Angle (DA59A).....	119
Figure 4-14: Specimen DA59A at: (a) Beginning; (b) 0.057 radians (Tear Initiation at Left Angle Heel); (c) 0.071 radians (Tear Initiation at Right Angle Heel); (d) 0.11 radians (Failure) .....	119
Figure 4-15: (a) Free Body Diagram; (b) Resultant Internal Forces Developed at Column Face; (c) Equivalent Force System of Tension and Compression in the Cross-section (Compression in Concrete and Tension in Steel Connection) .....	120
Figure 4-16: Variation of Eccentricity versus Beam Chord Rotation for Model ST59B (Extracted from Finite Element Analysis).....	120
Figure 4-17: Horizontal Load Developed in the Steel Connection of Model ST59B: from Finite Element Analysis (FEA); and from Equation (4-1) with Different Eccentricities of $e = 337$ mm (C.G.), $e = 378$ mm (P.N.A.), $e = 390$ mm .....	121
Figure 4-18: Horizontal Tensile Force Developed in Steel Connection of Specimen ST59B: Directly from the DLCs, and Indirect Method .....	121
Figure 4-19: Target and Experimental Axial Deformation of Connection Attached to the Removed Column versus Beam Rotation (Specimen ST59B) .....	122
Figure 4-20: Target and Experimental Vertical Deflection of the Removed Column versus Beam Rotation (Specimen ST59B).....	122
Figure 5-1: (a) Two-span Assembly; (b) One-span Assembly under Pushdown Displacement with Proper Boundary Condition at Unsupported Removed Column.....	148
Figure 5-2: Typical Finite Element Model of Shear Tab: (a) Isometric View; (b) Side View; (c) Cross-section View.....	148
Figure 5-3: Typical Finite Element Model of Double Angle: (a) Isometric View; (b) Cross-section View; (c) End View .....	149
Figure 5-4: Typical Finite Element Model of Bolt .....	150
Figure 5-5: Typical Finite Element Model of Concrete Slab .....	150
Figure 5-6: Typical Finite Element Model of Reinforcing Steel Layer.....	150
Figure 5-7: Typical Finite Element Model of Beam: (a) Assembly; (b) Solid Elements; (c) Shell Elements .....	151

Figure 5-8: Typical Finite Element Model of Column: (a) Isometric View; (b) Cross-section.....	151
Figure 5-9: Commonly Used Element Families from Abaqus Manual (Dassault Systèmes 2013).....	152
Figure 5-10: Element Type Selection in Abaqus/CAE.....	152
Figure 5-11: Plate Generated with Two Different Meshing Algorithms: (a) Medial Axis; and (b) Advancing Front.....	153
Figure 5-12: Bolt Generated with Two Distinct Meshing Techniques: (a) Free with Tetrahedral Elements (Number of Elements: about 14,000); (b) Sweep with Hexahedral Elements (Number of Elements: about 3,000).....	153
Figure 5-13: Idealized Response of Concrete to Uniaxial Loading in: (a) Compression; (b) Tension (Dassault Systèmes 2013).....	154
Figure 5-14: Concrete Uniaxial Stress–Strain Curves: 28-day Concrete Cylinder Test and Corresponding Abaqus Concrete Damage Plasticity Material Model Derived from the Concrete Cylinder Test.....	154
Figure 5-15: (a) Modelling of Concrete Cylinder in Abaqus; (b) Results in Terms of Compressive Equivalent Plastic Strain (PEEQ).....	155
Figure 5-16: Force–Displacement Response: 28-day Concrete Cylinder Test and Abaqus Finite Element Model.....	155
Figure 5-17: True and Engineering Stress–Strain Curves of One of the Coupons.....	156
Figure 5-18: Typical Uniaxial Stress–Strain Response of a Metal Specimen....	156
Figure 5-19: Stress–Strain with Damage Degradation (Dassault Systèmes 2013).....	157
Figure 5-20: (a) Force–Displacement of 6 mm Plate Coupon Test versus Results of Abaqus Modelling; (b) Coupon Test at Fracture; (c) Abaqus Model at Fracture.....	157
Figure 5-21: Force–Displacement of 6 mm Angle Coupon Test.....	158
Figure 5-22: Failure Mode of Tension Coupon Tests: (a) Angle 6 mm; (b) Angle 9 mm; (c) Plate 6 mm; (d) Plate 9 mm.....	158
Figure 5-23: Failure Mode of Double Angles: (a) Non-calibrated Progressive Damage Model; (b) Calibrated Progressive Damage Model; (c) Experimental Test.....	159
Figure 5-24: Force–Displacement of Rebar Tensile Test versus Abaqus Model	160

Figure 5-25: True Stress–Strain Curve for A325 High-Strength Bolt Material used in Abaqus Modelling.....	160
Figure 5-26: Energy Balance of DA59A Model in Quasi-Static Analysis.....	161
Figure 5-27: Boundary Conditions Imposed on the Finite Element Model.....	161
Figure 6-1: Simplified Finite Element Model and Definition of Attached and Remote Connections .....	210
Figure 6-2: Comparison of the Finite Element and Test Results for Specimen ST3A-1 of Oosterhof and Driver (2015) .....	210
Figure 6-3: Comparison of the Failure Mode with Specimen ST3A-1 of Oosterhof and Driver (2016; 2015).....	211
Figure 6-4: Failure Mode of Selected Finite Element Models for Comparison with the Experiments’ Results of Oosterhof and Driver (2016).....	211
Figure 6-5: Comparison of Finite Element and Test Results for Specimen ST59B .....	212
Figure 6-6: Comparison of Finite Element and Experimental Test on Deformation of Shear Tab Connection (Specimen ST59B) at Several Characteristic Beam Rotations: 0.0 radians; Maximum Arching Action (0.02 radians); Maximum Tensile Force in Shear Tab (0.04 radians); Failure.....	213
Figure 6-7: Comparison of the Failure Modes of Several Tested Connections with the Corresponding Finite Element Models .....	214
Figure 6-8: (a) Axial Deformation and (b) Vertical Deflection versus Beam Rotation of Attached Connection in Composite Frame (Specimen ST59B) .....	214
Figure 6-9: (a) Axial Deformation; and (b) Vertical Deflection versus Beam Rotation of Attached Connection in Bare Frame (Specimen ST59B).....	215
Figure 6-10: Calculated Target and FEA Axial Deformation versus Beam Rotation of Remote Connection in Composite Frame (Specimen DA56A).....	215
Figure 6-11: Specimen ST39A in Composite Frame at Failure .....	216
Figure 6-12: Deformation and Failure Evolution of Specimen ST39A in both Composite and Bare Frames: Connections at Several Characteristic Beam Rotations .....	217
Figure 6-13: Deformation Evolution of Remote Connection of Specimen ST39A in Composite Frame: Connection at Several Characteristic Beam Rotations.....	218
Figure 6-14: Deformation and Failure Evolution of Specimen ST59B at Several Characteristic Beam Rotations.....	219

Figure 6-15: Load versus Beam Rotation: Attached Connection of ST39A in Bare Frame .....	220
Figure 6-16: Load versus Beam Rotation: Attached Connection of ST39A in Composite Frame .....	220
Figure 6-17: Load versus Beam Rotation of Remote Connection of Specimen ST39A in Composite Frame .....	221
Figure 6-18: Effect of Concrete Slab (Composite Section) on Ductility and Horizontal Load Development in Shear Tab Connections of Specimen ST59B	221
Figure 6-19: Deformation of Shear Tab (Bolt Tear-out Failure).....	222
Figure 6-20: Bolt Tear-out Failure in Various Experimental Tests and Finite Element Models .....	222
Figure 6-21: Bolt Tear-out Capacity: Comparison of the Experimental Tests and FEA Results with the AISC Capacity Prediction, Equation (6-1).....	223
Figure 6-22: Geometry of Connections, Span, and the Arching Action Variables .....	223
Figure 6-23: Generalized Bilinear Force–Deformation Relationship.....	224
Figure 6-24: Comparison of the Rotational Capacities between the Existing Data and the Proposed Methods .....	224
Figure 6-25: Specimen DA56B in Composite Frame at Failure.....	225
Figure 6-26: Deformation and Failure Evolution of Specimen DA59A in both Composite and Bare Frames: Connections at Several Characteristic Rotations.	226
Figure 6-27: Horizontal Loads versus Beam Rotation of Angles in Bare Frame	227
Figure 6-28: Effect of Concrete Slab (Composite Section) on Ductility and Horizontal Load Development in Double Angles of Specimen DA59B .....	227
Figure 6-29: (a) Evolution of von Mises Strain over the Depth of DA59B Angle; (b) Deformation Evolution of DA59B Angle in the Horizontal Direction of Tensile Force; (c) von Mises Strain Obtained from the Experimental Test Corresponding to the Fracture Initiation; (d) Horizontal Displacement Obtained from the Experimental Test Corresponding to the Fracture Initiation; (e) Equivalent Plastic Strain Obtained from the FEA Corresponding to the Fracture Initiation.....	228
Figure 6-30: Deformation of Angle (Gross-sectional Failure at Heel).....	229
Figure 6-31: Double Angles Capacity: Comparison of the Experimental Tests and FEA Results with the Predicted Values, Equation (6-7).....	229

Figure 6-32: Simplified Proposed Method and Comparison with the FEA Results for: (a) ST36A; (b) ST56B; (c) DA39B; (d) DA59A .....	230
Figure 6-33: Finite Element Prototype Detailed Model .....	231
Figure 6-34: (a) Axial Deformation, and (b) Vertical Displacement of Attached Shear Tab (Specimen ST59B) in Composite Frame .....	232
Figure 6-35: Vertical Deflection (mm) Contours of ST59B Models with Slab Edges of (a) Horizontally Restrained, and (b) Horizontally Unrestrained .....	232
Figure 6-36: Formation of Tensile Membrane and Compressive Ring under Central Column Removal in an Unrestrained Axial Condition of Slab's Edges	233
Figure 6-37: Equivalent Tensile Plastic Strain (PEEQT) Developed in Concrete Slab of Specimen ST59B for Two Boundary Conditions of Slab Edges under Central Column Removal: Formation of Tensile Membrane (Soffit) and Compressive Ring (Top) in an Unrestrained Condition.....	234
Figure 6-38: Deformation and Failure Mode of Shear Tabs, Rebars, and Concrete Slab in the Detailed ST39B Model (Unrestrained).....	235
Figure 6-39: Deformation and Failure Mode of Shear Tabs, Rebars, and Concrete Slab in the Detailed ST59B Model (Restrained) .....	236
Figure 6-40: Horizontal Load versus Beam Rotation of Connections of Specimen ST59B Extracted From Simplified and Detailed Finite Element Models .....	237
Figure 6-41: Horizontal Load versus Beam Rotation of Connections of Specimen ST39B Extracted From Simplified and Detailed Finite Element Models .....	237
Figure 6-42: Comparison of Load–Displacement Curves of Detailed Models ..	238
Figure 6-43: Vertical Load–Displacement Curves of Specimen ST39B.....	238
Figure 6-44: Quasi-static (DIF=1.0) and Dynamic (DIF=1.5) Load–Displacement Curves of Detailed Specimen ST39B (Unrestrained) and Comparison with the Structural Integrity Load Combination of ASCE/SEI 7-10 and CSA S850-12..	239
Figure 6-45: Quasi-static Vertical Load-Displacement Curves of Detailed Finite Element Models and Comparison with the Structural Integrity Load Combination of ASCE/SEI 7-10 and CSA S850-12 .....	239
Figure 6-46: Dynamic (DIF=1.5) Load–Displacement Curves of Detailed Specimens and Comparison with the Structural Integrity Load Combination of ASCE/SEI 7-10 and CSA S850-12.....	240
Figure 6-47: Load–Displacement Curves of Detailed Finite Element Models and Comparison with Main and Sadek (2012b) and Francisco and Liu (2016).....	240

## LIST OF SYMBOLS

### *Latin Symbols*

$a$	Rotation angle corresponding to the tensile strength (initial failure) of connection, Half of crack length
$A_b$	Bolt area
$A_g$	Gross-sectional area of the double angles under tension
$A_{gv}$	Gross shear area along the horizontal shear planes (bolt tear-out)
$b$	Rotation angle corresponding to post-damage capacity at final failure
$b_1$	Width of concrete slab
$d$	Bolt diameter
$d_{bg}$	Depth of bolt group
$D$	Weld size, Overall damage variable, Dead load
$D_{max}$	Maximum degradation (element removal)
$e, e'$	Eccentricities
$E$	Modulus of elasticity of steel
$E_c$	Modulus of elasticity of concrete
$f, c, d_0$	Material parameters used for damage initiation constitutive model
$f_{arch}$	Unitless “arching factor”
$f'_c$	Compressive strength of concrete
$f_t$	Tensile strength of concrete
$f_m$	Moment amplification factor
$F_u$	Static ultimate strength
$F_{vm}$	Effective stress state at the tensile end of the angles developed from the von Mises criterion
$F_y$	Static yield strength
$g$	Distance from bolt line of connection to the column face (flange)
$G_I$	First mode fracture energy

H	Horizontal load
$K_I$	Stress intensity factor
$k_s$	Empirical material parameter used for damage modeling
$L'_c, L'_e$	Inclined edge distances (bolt tear-out)
L	Span length defined as the centre-to-centre of columns, Live load
$L_c$	Clear distance between bolt hole and edge of the material
$L_e$	Edge distance (bolt tear-out)
$l_p$	Plate/angle length
$L_r$	Reduced span defined as the original distance between centres of bolt groups of two end connections
$L_s$	Clear span defined as the original distance between the columns
$L_{survey}$	Survey live load
$M^-$	Sagging moment
$M^+$	Hogging moment
M	Bending moment
n	Total number of rows of bolts
$n_{eff}$	Number of effective bolts at bearing
P	Point load on removed column
$R_n$	Nominal strength
t	Thickness of connected component (shears tab/single angle or beam web)
T	Tensile force developed in steel connection only
$t_p$	Plate/angle thickness
V	Vertical load
$w_p$	Plate/angle width



## ***Greek Symbols***

$\delta_1$	Axial deformation of connection attached to the removed column
$\delta_1^{\text{arching}}$	Axial deformation of near-end (attached) connection at the end of arching action
$\delta_2$	Axial deformation of connection away from the removed column
$\delta_2^{\text{arching}}$	Axial deformation of far-end (remote) connection at the end of arching action
$\delta_{\text{axial}}$	Total axial deformation
$\delta_{\text{beam}}$	Axial deformation of beam
$\delta_{\text{connections}}$	Axial deformations of connections
$\delta_{\text{frame}}$	Axial deformation of the surrounding frames
$\delta_u$	Ultimate displacement
$\varepsilon_0^{\text{pl}}$	Effective plastic strain at the onset of ductile damage
$\varepsilon_{\text{eq}}^{\text{pl}}$	Equivalent plastic strain
$\varepsilon_f^{\text{pl}}$	Equivalent plastic strain at fracture
$\varepsilon_{\text{nom}}$	Nominal strain
$\varepsilon_u$	Ultimate plastic strain
$\theta^{\text{arching}}$	Beam chord rotation at the end of arching action
$\sigma_{\text{eff}}$	Effective stress
$\sigma_i$	Principal stresses
$\sigma_{\text{ln}}^{\text{pl}}$	Logarithmic plastic strain
$\sigma_{\text{mean}}$	Mean stress
$\sigma_{\text{nom}}$	Nominal stress
$\sigma^{\text{pl}}$	Stress corresponding to the effective plastic strain at the onset of damage (crack initiation)
$\sigma_{\text{true}}$	True stress
$\sigma_u$	Ultimate stress
$\tau_{\text{max}}$	Maximum shear stress

$\Delta$	Deflection of the central removed column
$\beta$	Fracture shear plane angle from horizontal (bolt tear-out)
$\gamma_c$	Density of concrete
$\delta$	Centreline axial deformation of connection at corresponding loading level
$\varepsilon_c$	Strain corresponding to the compressive strength of concrete
$\eta$	Stress triaxiality
$\theta$	Beam chord rotation
$\lambda$	Shear stress ratio
$\phi$	Ratio of maximum shear stress to effective stress
$\alpha$	Initial angle of arching action
$\mu$	Poisson's ratio

## LIST OF ABBREVIATIONS

AISC	American Institute of Steel Construction
ALP	Alternative Load Path (GSA)
ANSI	American National Standards Institute
AP	Alternative Path (UFC)
ASCE	American Society of Civil Engineers
ASTM	American Society for Testing and Materials
BSTP	Building Security Technology Program (GSA)
C.G.	Center of Geometry
CP	Collapse Prevention
CSA	Canadian Standards Association
DAQ	Data Acquisition System
DBT	Design Basis Threat
DCR	Demand–Capacity Ratio
DIF	Dynamic Increase Factor
DL	Dead Load
DLC	Donut Load Cell
DoD	Department of Defense
E.N.A.	Elastic Neutral Axis
ELR	Enhanced Local Resistance
FBD	Free Body Diagram
FEA	Finite Element Analysis
FEMA	Federal Emergency Management Agency
FSL	Facility Security Level
GSA	U.S. General Services Administration
HMB	Hottinger Baldwin Messtechnik
HPC	High Performance Computing
IBC	International Building Code

ICC	International Code Council
ISC	Interagency Security Committee
LIF	Load Increase Factor
LL	Live Load
LRFD	Load and Resistance Factor Design
LSP	Linear Static Procedure
LVDT	Linear Variable Displacement Transducer
MTRs	Mill Test Reports
N.A.	Neutral Axis
NBCC	National Building Code of Canada
NDP	Nonlinear Dynamic Procedure
NIST	National Institute of Standards and Technology
NRC	National Research Council Canada
NSP	Nonlinear Static Procedure
NYCBC	New York City Building Code
OC	Occupancy Category
P.N.A.	Plastic Neutral Axis
PBS	Portable Batch System
PC	Progressive Collapse
PEEQ	Equivalent Plastic Strain
PEEQT	Equivalent Plastic Tensile Strain
PoI	Point of Inflection
SLR	Specific Local Resistance
SSEC	Structural Steel Educational Council
TFs	Tie Forces
U.K.	United Kingdom
UFC	Unified Facilities Criteria

# **1. INTRODUCTION**

## **1.1 Background**

### **1.1.1 Overview**

Design and construction building codes do not usually account for unusual, but extreme, loading scenarios. In the event of a localised failure due to abnormal loads, “progressive collapse” can occur, where the ultimate extent of collapse is grossly disproportionate to the event that initiated it. There are prominent examples of progressive collapse all around the world. The most well-known one is the World Trade Center incident (9/11 impacts).

Structural integrity and robustness have always been one of the main goals for structural engineers in design and also for technical committees addressing safety in building codes. Buildings that have failed by progressive collapse were designed using building codes and design standards that were not able to prevent these problems. Failures such as local collapse of the Ronan Point apartment building (Great Britain, Ministry of Housing and Local Government 1968) and the World Trade Center incident revealed a major gap in understanding of disproportionate collapse in the structural engineering realms.

### **1.1.2 Definition of Disproportionate and Progressive Collapse**

Progressive or disproportionate collapse can be triggered by many events such as vehicular collision, aircraft impact, construction error, fire, or explosions. Structures that lack adequate continuity, ductility, and redundancy to resist the spread of damage are vulnerable to collapse, and significant casualties and major economic consequences can result when collapse occurs. It should be noted that there is no distinctive definition of disproportionate or progressive collapse (Starossek and Haberland 2009; 2010; 2011) to differentiate them. However, the

concept of cause and effect can be used to distinguish these two definitions, as summarized bellows.

Progressive collapse develops in a gradual manner similar to the collapse of a house of cards or collapse of a row of dominos. In structures, a progressive collapse may be horizontally from one bay to adjacent ones, or may also be vertically such as the collapse of columns supporting floor slabs. The latter one is often characterized as “pancaking” collapse. A disproportionate collapse, on the other hand, is one that is disproportionate to its initial cause. If there is a distinct disproportion between the initial event and the subsequent of a structure, this is called disproportionate collapse.

Collapse can be progressive in nature, but not essentially disproportionate in its extent. A disproportionate collapse can be progressive or non-progressive (immediate). Despite different meanings, both terms—progressive and disproportionate collapse—are often used interchangeably because disproportionate collapse often occurs in a progressive fashion and thus the term disproportionate collapse is more suitable in the design context (Starossek and Haberland 2010).

### **1.1.3 Steel Gravity Frames in Progressive Collapse Scenario**

Gravity frames typically comprise beams connected to columns through simple connections, in conjunction with a concrete floor system that may or may not act compositely with the associated beams. Two types of commonly-used shear connections that were used in this research are shown schematically in Figure 1-1, namely double angle and shear tab connections.

When a column is abruptly disengaged by an abnormal load, the resulting double span beam (Figure 1-2) must bridge over the removed column by developing a new equilibrium path (called an “alternative load path”) to redistribute the load to the adjacent elements. This severe damage in a steel gravity frame, which is designed to carry primarily gravity loads, creates significant demands on simple shear connections. Adding the large displacement of a removed column to the

double-span effect results in the development of catenary action, which alters the nature of the loading transferred to the connections. Although most recognize that there is some degree of continuity in the floor system, the effect of the floor slabs has generally been neglected when assessing the progressive collapse behaviour of steel structures. Thus, composite frames can play an essential part in the ability of a structure to resist collapse.

Amongst few numbers of analysis and design approaches that can be pursued, alternative path (AP) analysis is one of the most accepted methods used to assess the vulnerability of a structure to disproportionate collapse. Alternative load path is an analytical assessment of the structure under loss of a load-bearing component such as column, to measure whether the alternative paths are capable of effectively redistributing the additional loads imposed by the occurrence of the damage. The floor systems, in this regard, help to redistribute the vertical loads via catenary or arching action to the undamaged members.

#### **1.1.4 Arching Action and Catenary Action**

In order for structural frames to arrests progressive collapse, the load should be transferred through one or a combination of several load path mechanisms, namely bending action (Figure 1-3), Vierendeel action (Figure 1-4), catenary or membrane action, and arching action (Figure 1-5 and Figure 1-6). Each of these mechanisms is important to the robustness of structures since the redistribution of load relies mainly on the effective mobilization of these mechanisms.

The results of early studies on the collapse of reinforced concrete structures showed that membrane forces developed in a slab play an important role in collapse resistance. Flexural cracking first occurs at the early stages of loading which causes the neutral axis to rise, forcing the edges of the slabs to expand slightly outwards. The tensile membrane force, as a load-resisting mechanism, forms within the slab regardless of whether it is anchored or horizontally unrestrained at its boundaries. The development of compressive in-plane membrane force, on the other hand, is strongly dependent upon the boundary

conditions of the slab edges. If the edges of the slab are horizontally restrained, the compressive membrane forces form at early stages of loading, shown in Figure 1-5a. At higher deformation levels, they will switch to the tensile force as the slab gradually shifts away from the flexural action as depicted in Figure 1-5b.

For a slab unrestrained around its edges, the changes in slab geometry lead to the formation of a compressive ring within the depth of the slab around its perimeter, which in fact is beneficial to the in-plane tensile resistance of the slab. It should be noted that the compressive ring develops only if the vertical displacements of the perimeter edges remain small under increasing load. The tensile membrane forces are mainly carried by the steel reinforcements that are either anchored within the compressive ring or at the edges if they are horizontally restrained. Tensile membrane and compressive ring actions are shown schematically in Figure 1-6.

Mitchell and Cook (1984) developed three analytical models for predicting the post-failure tensile membrane response of flat slabs with fully restrained edges. They showed that a properly detailed slab would develop the membrane action effectively, and the importance of continuity of bottom steel reinforcement to fully achieve the post-failure response was addressed.

## **1.2 Problem Statement and Research Motivation**

Strength and stiffness of the floor slabs are often considered for the design of simply supported members under gravity loads through the engagement of composite action. In this case, the members are assumed to be pin-pin connected, and the effective width of the slab is approximated by simple rules. For typical floor beam sizes, shear connections without slabs tested cyclically, have shown low initial stiffness and moment capacity but higher ductility. In reality where the floor slab exists, it contributes to the force transfer to the connections if there is any reinforcement around the column, which implicitly can affect the ductility of shear connections.



Although most structural engineers recognize some degree of continuity in the floor system, this effect is considered difficult to quantify and thus is often ignored in design. The effect of the concrete floor slabs has also been neglected in gravity frames subjected to lateral loads, as it has been assumed that neglecting the effect results in a conservative design. However, results from research programs on gravity frames subjected to earthquake-type loading (Liu and Astaneh-Asl 2000) and progressive collapse loading (Izzuddin et al. 2008; Alashker et al. 2010; Main and Sadek 2012; Sadek et al. 2008) have shown that there is a need to reevaluate the effect of composite action in gravity frames in progressive collapse scenarios.

Recent attention has shifted away from the catenary ability of connections to sustain significant rotations, towards the contribution of the floor slab to resistance against collapse. This in fact reflects that connections, particularly in structural steel frames, may not possess adequate rotational ductility to resist collapse through catenary action alone; rather, compressive arching may be substantial.

For the progressive collapse analysis of typical steel building structures, consideration of the slab–connection interaction becomes extremely important when the slab experiences large displacement. During collapse, interaction between the connection and the slab causes the slab and connection response to differ significantly from what is expected in conventional design philosophy.

In fact, most researchers have focused on the benefits of the slab in mitigating progressive collapse, whereas this research shows that the presence of a concrete slab (composite action) can actually be severely detrimental to the survival of the steel frame connections (Jamshidi and Driver 2014; 2013; 2012).

The key in abating progressive collapse may be found by designing connections such that they are able to sustain a load-carrying mechanism after initial failure of the slab. The interactions between the connection and the slab substantially change the response of the structure from that of a bare steel frame. Therefore,

consideration of the slab remains a key aspect of investigating the real behaviour of structures under unexpected loading events.

The primary focus of the research is a comprehensive experimental and analytical investigation of the progressive collapse resistance of shear connections in steel gravity frames with composite floor systems.

### **1.3 Objectives and Scope**

The main purpose of this research program is to develop a comprehensive understanding of how the presence of a composite floor system can change the load-carrying mechanism and the resulting demands transferred to the shear connections in steel gravity frames. This consideration is providing insight into the real behaviour of connections, from which the failure hierarchy, strength and ductility can be obtained.

To assess the strength and ductility demands and performance of shear connections in composite floor systems under progressive collapse scenarios, an experimental program along with a comprehensive finite element analysis are defined. The experimental program consists of 17 full-scale physical tests of shear tab and bolted double angle connections, each with two different thicknesses and depths, in a composite frame system.

The overarching objective of this research program is to investigate the connection response in composite floor construction following a column loss. Specific objectives are summarized as follows:

- Proposing and developing loading regimes and connection load history for establishment of experimental tests;
- Carrying out detailed component-level experimental tests to investigate the effects of the concrete slab on strength, ductility and stiffness of connections;
- Developing high-fidelity finite element models to mimic the behaviour of prototypes under notional column removal;
- Characterizing connections' failure modes, ductility, and strength;

- Modelling and analyzing a full-scale three dimensional finite element prototype to compare with the results of associated component-level tests;
- Evaluating connections in both hogging and sagging moments due to the presence of arching and catenary actions; and
- Developing simple, practical design recommendations to assess the ductility and capacity of shear connections in a composite construction frame.

#### **1.4 Research Methodology**

This research consists of both an experimental program and comprehensive numerical investigations. Experimental tests were conducted in the I.F. Morrison structural engineering laboratory at the University of Alberta using the set-up designed to test steel connections. Numerical analysis was carried out by means of Abaqus (Dassault Systèmes 2013) and implementation of high performance computing (HPC) resources using an explicit solver. Behaviour of steel connections in both skeleton and composite frames was examined so as to acquire a better understanding of the influence of the floor system. Since significant effects of the slab on the overall progressive collapse capacity have been proven, different connections and parameters contributing to the overall behaviour of frames were tested and simulated to capture and reveal these recondit capacity effects.

#### **1.5 Outline**

This document consists of seven chapters and three appendices following the main body. An overview of the ensuing chapters follows:

In Chapter 2, an overview of the current design codes and guidelines in Canada, USA, and Europe pertaining to progressive collapse mitigation is presented. Previous studies on robustness of steel shear connections are briefly reviewed in chronological order. Various numerical simulations and experimental programs

on the behaviour of simple connections in bare steel frames and composite construction frames are explained.

Chapter 3 describes the details of the experimental program, including the geometry of the prototype steel frames, test specimens, test set-up, instrumentation, proposed loading regimes, and test procedure. Moreover, this chapter provides the results of ancillary tests to determine the material properties of the test specimens.

Chapter 4 reports the observations made during the physical tests and from the test data, including discussions on the observed failure modes, deformation, and load-development histories.

Chapter 5 presents details on the comprehensive numerical finite element models developed to mimic the experimental tests. Modelling of components, along with the element selections and optimized meshing techniques are explained. Material properties of the tested components and the constitutive model for the steel material, including plasticity, hardening, material failure, and damage initiation and evolution, are introduced. Results of material verifications based on the coupon tests, concrete cylinder tests, and observed failure modes of connections during the main tests are presented. Numerical challenges encountered in solving the highly nonlinear aspects of the modelling and solver techniques are explained.

Chapter 6 contains the main results of the finite element modellings of both shear tabs and double angles in composite and non-composite frames. Comparison of the numerical results with experimental tests, and a detailed discussion and proposed design method, are presented. Comparison of the component-level experimental tests with both the simplified and detailed three dimensional prototype finite element models is shown.

Chapter 7 provides a summary of the research program, conclusions, and a discussion of the design recommendations. Areas for further research work are highlighted at the end of this chapter.

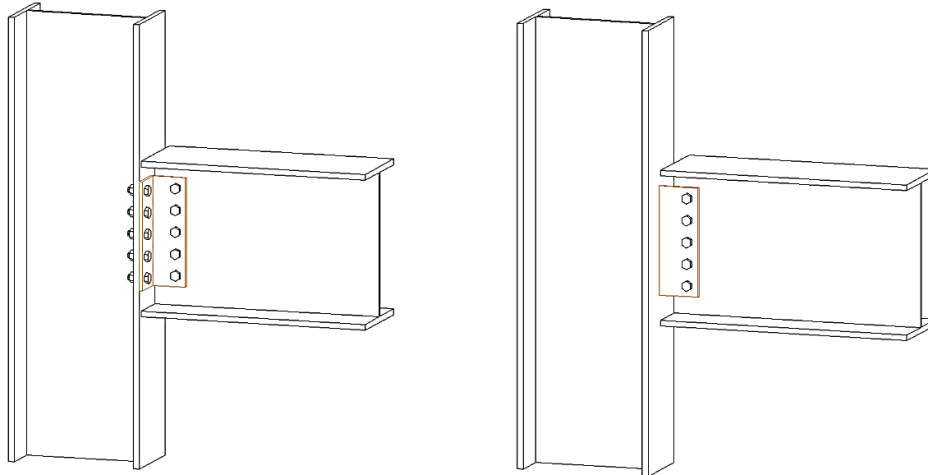


Figure 1-1: Shear (Simple) Connections: Bolted Double Angle, and Shear Tab

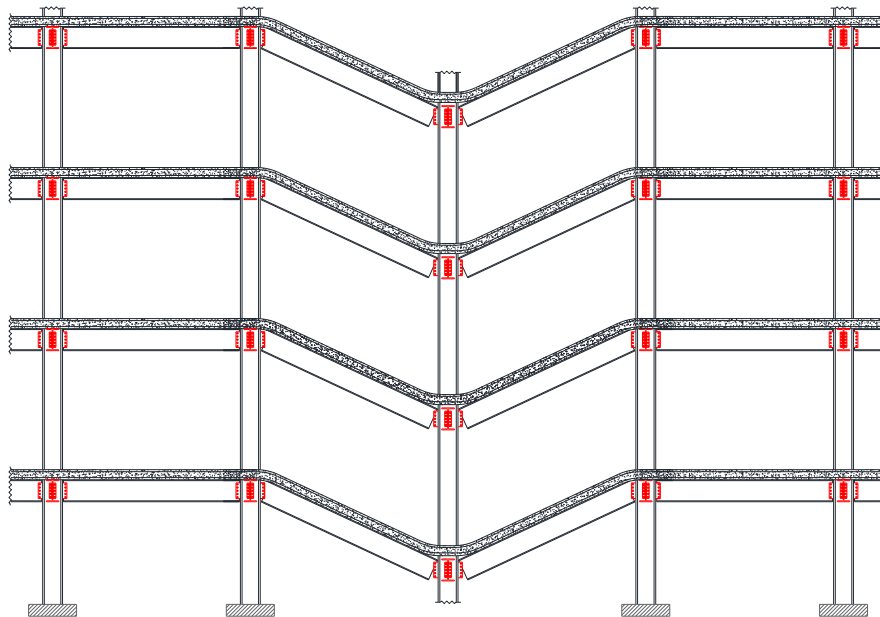


Figure 1-2: Column Loss Scenario and Bridging for Alternative Path

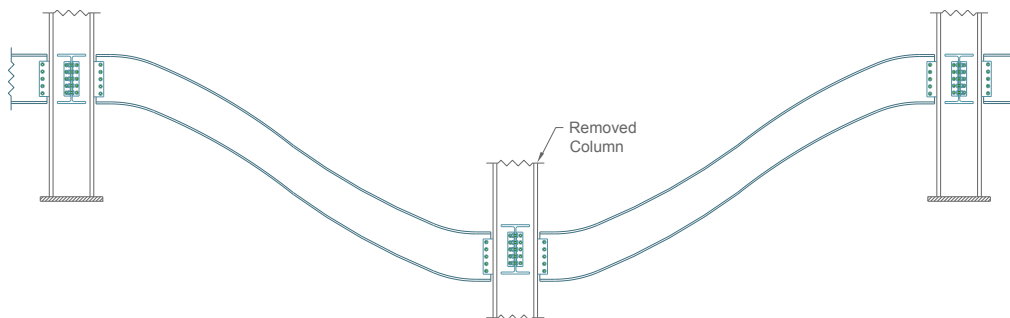


Figure 1-3: Arresting Collapse through Bending Action

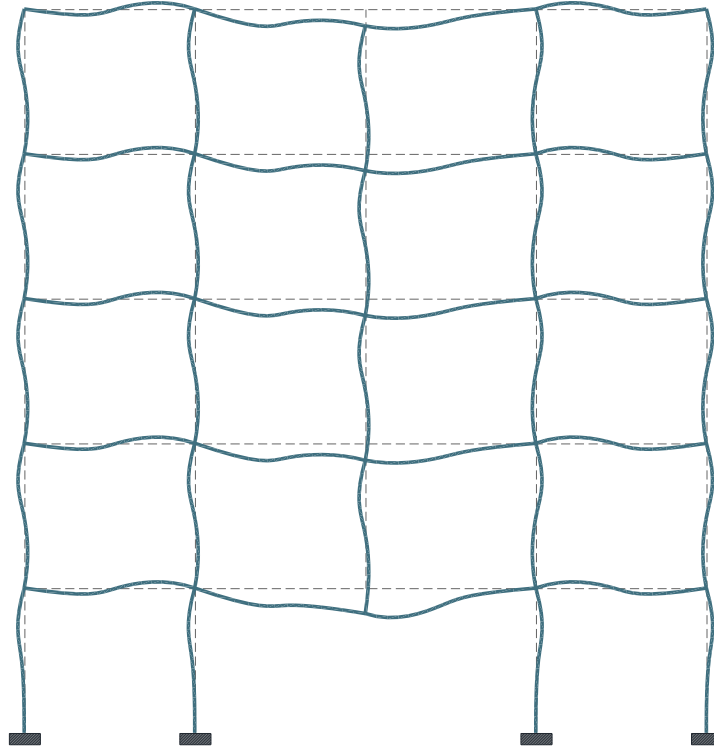


Figure 1-4: Arresting Collapse through Vierendeel Mechanism due to Bending Moment Capacity of Beam-to-Column Connections

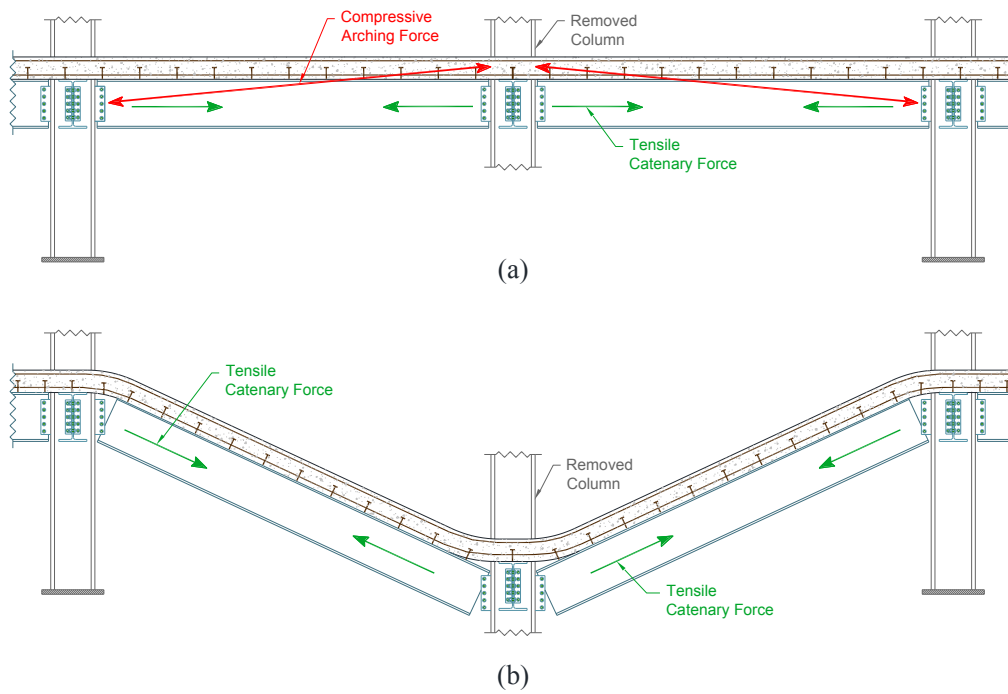


Figure 1-5: Compressive Arching and Tensile Catenary Actions at (a) the Beginning of Loading; (b) the Later Stages of Loading

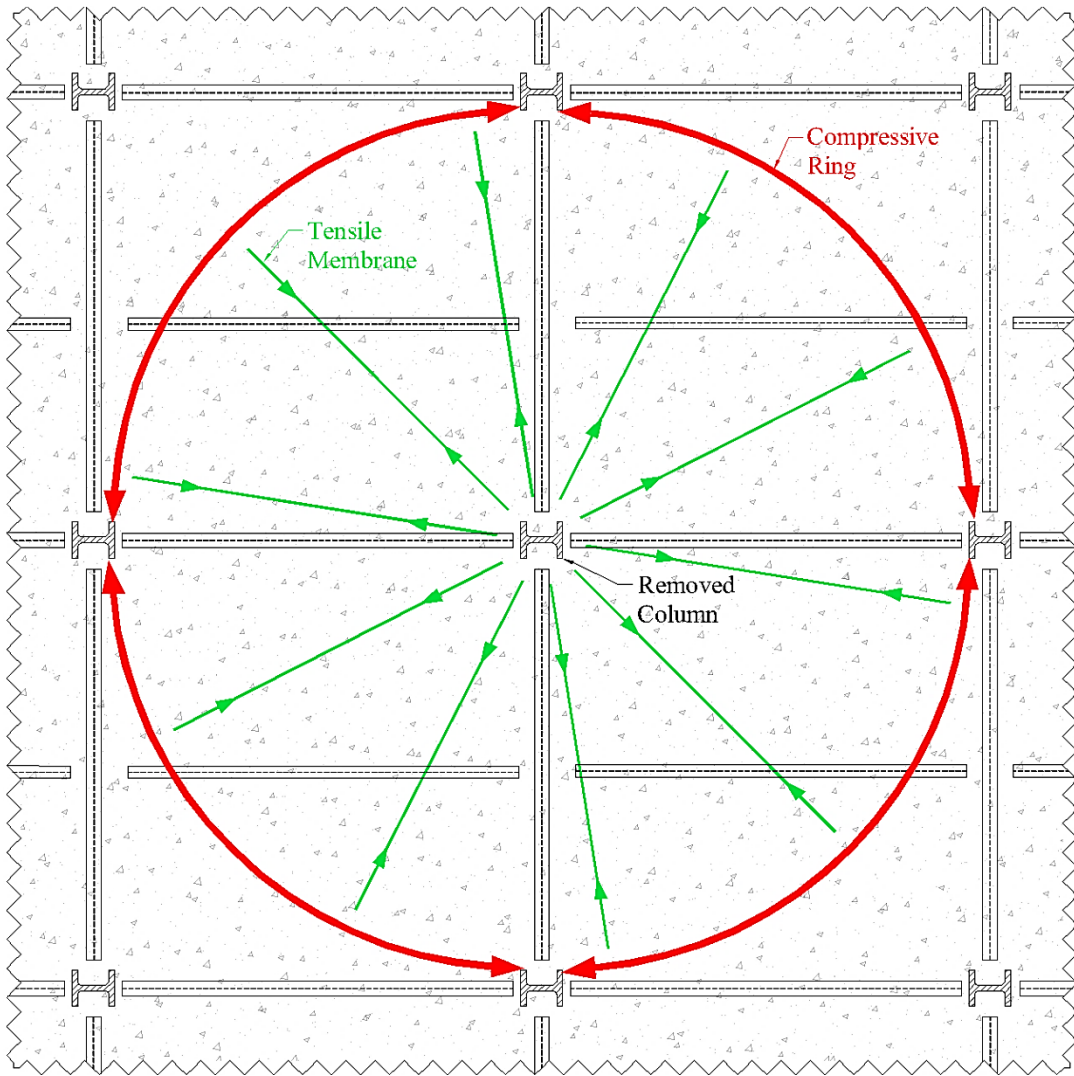


Figure 1-6: Formation of Tensile Membrane and Compressive Ring under Central Column Removal

## **2. LITERATURE REVIEW**

### **2.1 Introduction**

This chapter reviews the literature pertinent to this research program, which focuses mainly on the behaviour of simple (shear) connections in a composite/non-composite frame system under a progressive collapse loading scenario. It is divided into two sections. First, a summary of current design codes and guidelines addressing progressive collapse hazard and mitigation is presented. Second, previous research on the robustness of shear connections and the importance of the floor slab in a so-called “column-removal” scenario is discussed.

### **2.2 Current Design Codes, Standards, and Guidelines**

This section provides a summary and insight into the current codes and guidelines employed to date in the USA, Canada and Europe that address progressive collapse (disproportionate collapse) mitigation, while emphasizing design criteria pertaining specifically to steel shear connections. It should be noted that the terms “progressive collapse” and “disproportionate collapse” are used interchangeably throughout this chapter because of their general reference to the degree of structural collapse, in spite of different specific meanings. The distinction between the terms is addressed in Chapter 1.

There are three general approaches in building codes and guidelines for reducing the likelihood of disproportionate collapse, namely, event control, indirect and direct design methods. Event control involves taking actions to minimize the likelihood of the hazards, such as changes in the building site, or use of perimeter barriers. This is often the most cost-effective approach and generally does not require professional structural engineering services. Indirect design methods provide prescriptive requirements typically in the form of tie forces (TFs) by specifying minimum tensile forces in vertical and horizontal members and joints.



This method is intended to incorporate a minimum level of integrity and robustness between various structural components. The direct design methods, on the other hand, rely on structural analysis given a prescribed initial state of damage. This method explicitly considers the resistance to progressive collapse of key structural elements under postulated abnormal loads through one of two techniques: (1) Alternative Path (AP) method, in which the structure is assessed for its ability to bridge over the local failure zone; and (2) Specific Local Resistance (SLR) technique, or structural hardening, which requires structural elements to possess sufficient strength to resist a specific load or a quantified threat.

Owing to the public safety implications and rising interest from the structural engineering community, significant advances in the design of structures to resist progressive collapse are actively underway in universities and research facilities, resulting in ongoing advancements in the development of building codes and design standards.

## **2.2.1 USA**

### **2.2.1.1 New York City Building Code (NYCBC)**

The New York City Building Code (NYC 2008) was the first building code in the USA to incorporate structural integrity requirements. Sections BC1605.6, 1605.7BC, and BC1614 to BC1616 of the latest edition of the NYCBC (NYC 2014) contain load combinations and general analysis requirements for structural integrity using both direct and indirect approaches, namely, prescriptive requirements and key element analysis.

Specific design requirements on steel and composite structures are provided in Section BC2212. Requirements in this section are waived for one-storey structures with floor plans of less than 465 m<sup>2</sup> and structures in Group R-3 occupancy (less than three storeys in height). Subsection BC2212.2 requires that all bolted connections have a minimum of two bolts. It states that “End

connections of all beams and girders shall have a minimum available tensile strength equal to the larger of the available vertical shear strength of the connections at either end, but not less than 45 kN (10 kips).”

Tensile strength of single-plate shear connections is determined only for the limit state of bolt bearing on the plate and the beam web. For single and double angle shear connections, the tensile strength is determined for the limit states of bolt bearing on the angles and beam web and for tension yielding on the gross area of the angles. For other connections, the tensile force capacity is calculated in accordance with the provisions of AISC 360 (AISC 2010). For steel framing members acting compositely with a concrete slab, requirements are provided on details of shear studs, side lap connections of steel decking, and welded wire reinforcement. However, no provision on the end connections of beams and girders in composite construction is provided.

#### **2.2.1.2 International Building Code (IBC)**

Structural integrity requirements were added as a new section to the 2009 edition of the International Building Code (IBC), shortly after the 2008 edition of the NYCBC. Section 1615 of the IBC (ICC 2015) introduces indirect tie-force requirements that are applicable to high-rise buildings in Risk Category III or IV (buildings with substantial hazard to human life in the event of collapse). Section 1615.3.2 addresses two types of connections (column splices and beam end connections) for steel and composite frame structures.

For beam end connections, the provision (Section 1615.3.2.2) includes a minimum level of axial tensile strength equal to two-thirds of the required shear strength for load and resistance factor design (LRFD), but not less than 45 kN (10 kips). For composite construction where beams and girders support a concrete slab with or without steel deck, the nominal axial tensile strength of the end connections is permitted to be taken as one-third of the required shear strength for LRFD, with a minimum of 45 kN (10 kips).

### **2.2.1.3 American Society of Civil Engineers (ASCE)**

Shortly after the partial collapse of the Ronan Point building in the UK, ANSI A58.1-72 of the American National Standards Institute (ANSI 1972) included a brief statement to address the issue, but it did not contain any requirements or commentary. However, in the 1982 edition ANSI A58.1-82 (ANSI 1982) elaborated by addressing general structural integrity definitions and requirements in the appendix. ANSI A58.1 is now withdrawn and is superseded by ASCE/SEI 7.

ASCE/SEI 7-10 (ASCE 2010), *Minimum Design Loads for Buildings and Other Structures*, does not contain any specific criteria for resistance to progressive collapse beyond general structural integrity guidance. However, the commentary of ASCE/SEI 7-10 (C1.4) explains direct and indirect design approaches. It provides guidelines on design concepts and details such as good plan layout, redundant structural systems, providing an integrated system of ties and so on. Developed with a probabilistic basis, Section 2.5 of ASCE/SEI 7-10 also provides load combinations for extraordinary events to evaluate the residual capacity and stability requirements following notional removal of key structural elements.

### **2.2.1.4 American Institute of Steel Construction (AISC)**

The American Institute of Steel Construction (AISC 2015) defines structural integrity as “a performance characteristic of a structure indicating resistance to catastrophic failure”. ANSI/AISC 360 (AISC 2010) comments briefly on general structural integrity requirements (Clause 4.2.4.1) that have been addressed in the various building codes. Requirements are consistent with the clauses appearing in ASCE/SEI 7-10 (ASCE 2010).

To calculate the nominal capacity to satisfy strength requirements defined for structural integrity, AISC allows employing the full ductile load–deformation (stress–strain) response of steel. Limiting deformations of connections is not necessary for the structural integrity checks; rather, it is the case for traditional load combinations (Comm. B3.2). For the design of single-plate shear

connections, AISC (2010) refers to the work by Geschwindner and Gustafson (2010). However, the latest draft version of AISC 360 (2015) provides similar requirements as those in the New York City Building Code (NYC 2014).

### **2.2.1.5 General Services Administration (GSA)**

The U.S. General Services Administration (2003; 2013) introduced a set of guidelines by GSA's Building Security Technology Program (BSTP) team, formerly titled *Progressive Collapse Analysis and Design Guidelines for New Federal Office Buildings and Major Modernization Projects*, and recently titled *Alternate Path Analysis and Design Guidelines for Progressive Collapse Resistance*. The focus of this document is to reduce the risk of progressive collapse and provide guidelines on upgrading existing federal buildings. The 2013 edition of the GSA guidelines replaced the previous document (GSA 2003) to bring into alignment security standards with the provisions of the Interagency Security Committee (ISC) regarding progressive collapse and to reduce the discrepancies between the DoD and GSA provisions. GSA documents take threat-dependent and risk-based approaches, which are reliant on the required level of protection as determined by the Facility Security Level (FSL). The significant modification to the 2013 version of GSA guidelines includes the elimination of TFs and SLR clauses in all chapters. Hence, the design procedures outlined in GSA (2013) bear only upon the AP method and redundancy requirements. The AP method utilizes procedures presented in UFC 4-023-03 (2013) and ASCE/SEI 41-06 (ASCE 2006) and the redundancy requirements aim to distribute resistance up the height of the building without any explicit need to consider a column removal scenario at each level.

The AP method outlined in the GSA guidelines follows the ASCE/SEI 7-10 (ASCE 2010) load combination for extraordinary events and the general approach in ASCE/SEI 41-06 (ASCE 2006). It employs three analysis procedures: Linear Static (LSP), Nonlinear Static (NSP), and Nonlinear Dynamic (NDP). However, material-specific criteria and deformation and strength criteria in ASCE/SEI 41-06 (ASCE 2006) have been modified in the GSA guidelines to

accommodate the specific issues related to progressive collapse. For each of these analysis techniques, GSA mandates acceptance criteria for evaluation. Evaluation of structural components using the LSP is mainly based on the Demand–Capacity Ratios (DCRs), while in the nonlinear procedures the assessment is mostly based upon plastic rotation angle. For structural steel components, the GSA guidelines adopt the Collapse Prevention (CP) Structural Performance Level (S-5) acceptance criteria (shown in Figure 2-1) in accordance with ASCE/SEI 41-06 (ASCE 2006). It should be noted that the acceptance criteria in the GSA guidelines for structural steel components are adopted, with modifications, from Chapter 5 of the UFC 4-023-03 (2013).

A Load Increase Factor (LIF) is considered for load combinations in static procedures to account, in a simplified way, for the dynamic effect of loading. Modelling parameters and component capacities for deformation- and force-controlled elements are summarized in Table 2-1. Acceptance criteria for linear (m-factor) and nonlinear analysis procedures for the connection types in this research are presented in Table 2-2 and Table 2-3, respectively.

Previous GSA guidelines (2003) used an amplification factor of 2.0 for both LSP and NSP. One of the significant differences in the newer edition of the GSA guidelines is the modifications to the dynamic factor, which are now based on the allowable plastic rotation and element yield rotation. The NDP in the GSA guidelines is essentially the same as in UFC 4-023-03 (2013).

#### **2.2.1.6 Unified Facilities Criteria (UFC)**

The United States Department of Defense (DoD) introduced the Unified Facilities Criteria (UFC) 4-023-03 (2013) to address the vulnerability of structures to progressive collapse and provide design guidelines to protect its new and existing facilities. DoD released Change 2 of UFC in June 2013 after years of application of the 2009 version with a number of significant improvements and modifications such as the tie forces method, and acceptance criteria. Contrary to GSA (2013), which uses only the direct design approach (AP and SLR), UFC (2013)

incorporates both the direct and indirect approaches: AP and SLR methods, and TFs, respectively. According to the UFC, the level of progressive collapse design is based upon the Occupancy Category (OC) of the structure, which is considered a measure of the collapse consequences and building function. Based on the OC, the UFC employ various combinations of the AP method, SLR, and TF requirements.

The indirect design approach is accomplished through the TF requirements, which require transferring the load from damaged components to the rest of the structure. TFs are intended to mechanically tie structural members together to enhance continuity and develop alternative load paths. Vertical ties for columns and three horizontal ties, including longitudinal, transverse, and peripheral, must be provided. The required tie strength for various components and structures are given based on the floor load, and plan layout and geometry. The 2005 edition of the UFC adopted its TF approach directly from the UK building codes, as developed after the Ronan Point building incident (1968). However, edition 2009 revamped the TF criteria owing to the fact that steel and concrete connections were unable to sustain large rotations. According to UFC (2013), beams, girders, spandrels and their connections must be able to sustain the specified tie forces at a rotation of 0.2 rad, unless these forces can be carried by the floor deck and roof deck systems. Although the simplified tie forces approach applies only to the general integrity and continuity of the structural system, evaluation of the performance of connections from local damage due to a column removal is not considered.

The UFC use ASCE/SEI 7-10 (ASCE 2010) load factor combinations by employing various analysis procedures based on the general approach in ASCE/SEI 41-06 (ASCE 2006), with modifications to take into account issues related to progressive collapse. Three analysis procedures mentioned in UFC are: LSP, NSP, and NDP. To define modelling parameters and acceptance criteria required for the analysis procedures, the UFC refer to ASCE/SEI 41-06 (ASCE 2006). These criteria are mainly stipulated based on seismic loads, which are, in nature, horizontal and transient while the loads for collapse situations are

vertical and permanent. The criteria are considered conservative for progressive collapse as they have been established for cyclic loads (backbone curves), whereas in a progressive collapse scenario only a half load cycle is applied. Thus, modifications and changes have been made to the values of the acceptance criteria in UFC 4-023-03. It should be noted that the requirements and criteria in UFC 4-023-03 and the GSA guidelines are principally similar for all three analysis procedures. Acceptance criteria and modelling parameters for both GSA Guidelines (2013) and UFC 4-023-03 (2013) are shown in Table 2-1 to Table 2-3.

Although acceptance criteria and modelling parameters for shear connections with and without the presence of a slab are provided in ASCE/SEI 41-06 (ASCE 2006), no criteria for connections with a slab are mentioned in either GSA or UFC. The acceptance values of these connections from ASCE/SEI 41-06 (Table 5.5 and Table 5.6) are shown in Table 2-2 and Table 2-3. As shown, there is no difference between the shear connections with and without a slab for both linear and nonlinear acceptance criteria, indicating that explicit accounting for the influence of the slab that has not been considered.

## **2.2.2 Canada**

### **2.2.2.1 National Building Code of Canada (NBCC)**

The National Building Code of Canada (NBCC) (NRC 2010) is one of the building codes that has addressed progressive collapse for decades. However, provisions have changed and evolved to various levels of detail over the years. In 1975, the issue was addressed in Article 4.1.1.8, Structural Integrity, which pointed to Supplement No. 4 of Commentary C. The Commentary provided information on abnormal loads and general design considerations. In the 1980 edition, the commentary was rather short and had no design details compared to the preceding 1975 edition due to the assumption of having a low probability of failure. The NBCC after 1995 expanded again from the brevity in 1980. Currently, Commentary B of the latest NBCC (NRC 2010) contains requirements

on structural integrity to resist progressive collapse. It is stated that adequate integrity is achieved for structures designed in accordance with CSA standards through detailing requirements for the connections, although for those structures not conforming with CSA standards, Commentary B provides general guidance but no procedures for implementation are provided. The guidance is provided through safety measures such as control of accidental events, local resistance, tie forces, and alternative load paths.

#### **2.2.2.2 Canadian Standards Association (CSA S16-14)**

Clause 6.1.2 (Structural Integrity) of the latest Canadian steel design standard, *Design of Steel Structures*, CSA Standard S16-14 (2014), addresses general requirements regarding disproportionate collapse. It simply states that “The requirements of this standard generally provide a satisfactory level of structural integrity for steel structures.”, and provides no details on the subject. However, the Commentary to CSA S16-14 (CISC 2010) states that although being inherently ductile, details of steel connections are important and should be prudently evaluated for such events. CSA S16-14 refers to the User’s Guide of NBCC for further guidance.

#### **2.2.2.3 Canadian Standards Association (CSA S850-12)**

Clause 10 of CSA S850-12 (CSA 2012), *Design and Assessment of Buildings Subjected to Blast Loads*, addresses structural integrity and mitigation of disproportionate collapse for buildings after incurring blast damage. To mitigate the risk of progressive collapse, CSA S850-12 requires implementing one of the methods: SLR or AP. If the structural components do not satisfy the SLR limit stipulated in Clause 4 for the design basis threat, one of the three analysis techniques (LSP, NSP, NDP) of the AP procedure shall be performed. However, the load combination and procedure for element removal in CSA S850-12 is different than in the UFC guidelines (4-023-03). Acceptance criteria and modelling parameters are adopted directly from UFC 4-023-03, as listed in Table 2-2 and Table 2-3.



## **2.2.3 Europe**

### **2.2.3.1 U.K. Standards**

The phenomenon of progressive collapse was first identified after the 1968 partial collapse of the Ronan Point 22-storey precast concrete building (Great Britain, Ministry of Housing and Local Government 1968). Six months after the incident, the U.K. Ministry of Housing issued regulations to address the issues of progressive collapse by providing two methods, namely, alternative path of support and stiffness and continuity criteria of construction.

These provisions became part of the Fifth Amendment of the 1970 Building Regulations and later in the 1974 edition, provisions of structural ties came into effect. In the 1976 edition, buildings were required to be designed to prevent progressive collapse after a localized failure. The indirect approach was used first in the U.K. standards and has been adopted in part by other guidelines and standards in Canada and the USA.

Methods for preventing progressive collapse (tying, bridging, and key element removal) have been addressed in various British Standards such as BS5950 (BSI 2010), which was superseded by Eurocode Standard, EN 1993 (CEN 2005). The Eurocode contains more design details for accidental actions than the British Standards.

### **2.2.3.2 Eurocode**

Part 1-7 of the Eurocode (CEN 2006) provides general design guidelines and procedures to resist disproportionate collapse. Strategies used in the Eurocode for accidental actions are shown in Figure 2-2. It provides both direct and indirect approaches based on the building consequences class. Buildings are categorized in four safety classes (from low to severe risk) based on the type and occupancy. The lowest categories (Class 1 and Class 2a) require no consideration for accidents except that Class 2a requires robustness and stability provisions, such as effective horizontal ties or effective anchorage of suspended floors. Two other

classes (Class 2b and Class 3) require consideration of progressive collapse analysis techniques such as notional removal of “key elements”, members upon which the stability of the structure depends.

Annex A, *Design for consequences of localised failure in buildings from an unspecified cause*, provides more details and methods of preventing localized failure. It includes information on the categorization of buildings’ classes, provisions of horizontal and vertical ties, and design of “key elements”. The tie forces method in Annex A is similar to that in UFC 4-023-03, except that the minimum of 75 kN is required for a horizontal tie force.

### **2.3 Previous Research on Robustness of Steel Shear Connections**

Beam-to-column connections are typically the most critical components in steel structures and their response under cyclic or extreme loading conditions has a direct impact on the performance of structures. Shear connections, which are commonly used in the gravity frame systems, have been brought more into attention due to the relatively unknown behaviour under a column-removal demand. Shear connections are generally designed to sustain shear forces only, but under an abnormal condition they experience different load combinations.

The nature of loading transferred to the connections from a column-removal scenario is mostly axial load resulting from catenary actions, while gravity loads impose mostly vertical demands to the connections. In seismic loading applications, moment–rotation relationships are of principal importance. Most of the standards and guidelines underline the performance of connections generally based on the moment–rotation response with no axial load effect. This section discusses previous experimental and numerical research programs conducted on steel shear connections in composite and bare steel framing systems under progressive collapse loading scenarios.

### 2.3.1 Astaneh (2007)

Astaneh (2007) presented a summary of his research on progressive collapse through the SSEC (Structural Steel Educational Council) Steel TIPS report based on research conducted at the University of California at Berkeley. He discussed general information on progressive collapse and provided numerical and experimental test results along with an example. He first summarized the three-hinge beam analogy developed by Timoshenko (1955) and then extended the analogy to consider the inelastic behaviour of a typical shear connection shown in Figure 2-3. He extended the three-hinge model by adding axial springs to consider the connections' end-support conditions, as shown in Figure 2-3. One of the assumptions he made was that the stiffness of the support is much larger than that of the connections and thus the elongation of the connection was the only source of axial deformation.

Since information on the axial stiffness and elongation of shear connections was limited at the time, Astaneh and his research team conducted several experiments (Astaneh et al. 2002a; 2002b; Tan and Astaneh 2003; 2003b), summarized in this section, to investigate the behaviour of shear connections. Their results showed that the shear tabs elongate in the axial direction at least 19 mm ( $\frac{3}{4}$  in.) prior to fracture. In addition, previous tests in the 1990s (De Stefano and Astaneh 1991; Ho and Astaneh 1993) on bolted double-angle connections under shear and axial load showed similar results of a minimum axial elongation of 19 mm ( $\frac{3}{4}$  in.). Based on the results, Astaneh suggested a conservative value of 16 mm ( $\frac{5}{8}$  in.) to be used for the axial elongation of shear connections, which results in an ultimate rotation of 0.10 and 0.08 radians for spans of 6.1 m and 12.2 m, respectively.

Astaneh concluded that bending of the material behind the bolt, bearing deformation, and slippage are the main causes of axial elongation of bolted shear connections, while in welded shear connections yielding of the steel in tension is considered to be the primary cause of axial elongation. As such, he stated that the axial deformation of 16 mm ( $\frac{5}{8}$  in.) is used only if yielding is the governing failure mode. Otherwise, appropriate values of ultimate rotation should be

established for failure modes such as net section fracture, edge distance, and block shear failure.

#### **2.3.1.1 Astaneh et al. (2002)**

Astaneh et al. (2002a; 2002b) conducted two full-scale column-removal tests on a single-floor composite frame with steel shear connections. The dimensions and geometries of the specimens were identical except that a so-called “catenary” cable was added to the slab in the second test to measure the retrofit capability of the structural system in a column-removal scenario (Astaneh et al. 2002b). The geometry of the test specimens is shown in Figure 2-4.

The size of the specimens was 18.3 m (60 ft.) × 6.1 m (20 ft.), four bays long with the main span of 6.1 m (20 ft.), and one bay wide with the span of 5.5 m (18 ft.). The composite floor was composed of an 89 mm (3.5 in.) thick normal-weight concrete slab with WWF 6×6 wire mesh over 76 mm (3 in.) deep 20 gauge corrugated steel deck. The steel decks were oriented in the E-W direction parallel to the W18×35 girders. The 19 mm ( $\frac{3}{4}$  in.) diameter Nelson studs were welded at 203 mm (8 in.) centres along the longitudinal beams. All steel materials of beams, columns, and connections were specified as A36 steel. The shear connections used for both tests were shear tabs and bolted seat angles combined with a single angle on the web. In the N-S direction, five-bolt shear tabs were connected to the beam with long slotted holes on both ends to allow more rotational flexibility before failure of the connections. The three-bolt single angle connections were bolted to the beams and column webs and the bottom seat angles were connected to the flanges of beams and column. All bolts were ASTM A325X with 22 mm ( $\frac{7}{8}$  in.) diameter.

Middle columns were terminated 914 mm (36 in.) above the strong floor to accommodate the hydraulic actuators to impose a downward force. The column was pushed down at a rate of 6.35 mm/s (0.25 in./s). Successive tests were performed on the specimens with column drop displacements between 483 mm (19 in.) and 889 mm (35 in.). Results of both tests showed that the

capacity of the structure was limited by the connections' capacity. However, the cable-reinforced system had significantly higher capacity than the conventional system. The steel deck was able to develop catenary action and redistribute the vertical load. The study showed that the capacity was limited to the fracture of bolts of the seat angles. The web single angle fractured through the fillet, while the shear tabs with slotted holes reached a rotation of 0.14 radians without substantial damage. In both cases, the concrete slab experienced significant crushing and cracking around the columns. After failure of the connections, the reserve capacity was attributed to the longitudinal rebars, since the concrete itself cannot tolerate any significant catenary action. It was stated that further research is required to establish parameters that affect resistance of the structural system.

#### **2.3.1.2 Tan and Astaneh (2003)**

Tan and Astaneh (2003) conducted three tests similar to the previous research (Astaneh et al. 2002a) with the aim of understanding the behaviour of frames with shear connections, and to develop a cable-based retrofit mechanism to prevent progressive collapse of typical steel structures. Two of the specimens were retrofitted by placing steel cables within the depth of the web of the exterior girders. The size of the single-storey frame specimens was 18.3 m (60 ft.)  $\times$  6.1 m (20 ft.), four bays long with a system of steel deck and concrete slab. The shear tab connections in the area close to the drop column were all ASTM A36 steel. Bolts at connections were ASTM A325X with 22 mm ( $\frac{7}{8}$  in.) diameter. Load was applied to the drop columns by actuators pushing downward in a displacement-control condition with a rate of 6.35 mm/s (0.25 in./s). Maximum displacements of 559 mm (22 in.) for the first two tests (with and without cable) and 813 mm (32 in.) for the last one (with cable) were applied to the drop columns.

Results of the first test (no retrofit cable) showed that the fracture of the weld on one of the shear tabs, at the early stages of loading, was the main failure of the connection, which resulted in the partial development of catenary forces. However, they attributed the fracture to the low quality of an atypical welding detail (only one fillet weld) of that specific shear tab. Even though fracture

occurred at the weld, the connection was able to reach catenary forces up to a rotation of about 0.07 radians. For the other two tests (retrofitted with cable), block shear failure of the edge and end distances of the shear tabs was observed.

It was found that the floor slab contributed about 30% of the total resistance to collapse. Since only a small ratio of steel reinforcement was provided in the slab, resistance of the slab system was reported to be mainly due to the steel deck. The results of the strain gauges on the steel deck affirmed the participation and resistance to the catenary forces. However, local buckling and yielding of the steel deck were reported near the beam's top flange. It was recommended that cellular decks with a flat plate at the bottom be used to develop catenary action independent of the rib direction. It was also reported that the floor system was able to sustain the in-plane compressive forces due to the tension in the cables.

### **2.3.1.3 Liu and Astaneh (2000)**

To quantify the importance and contribution of the floor slab to the behaviour of simple connections, Liu and Astaneh (2000) conducted 16 full-size tests under combined gravity and cyclic loading (four tests without a slab and 12 with a typical floor slab). The results showed that the composite action was lost at 0.04 radians due to the crushing of concrete in front of the column. It was observed that the connections experienced a large moment and rotation, which resulted in substantial tensile forces.

It was found that the rotational capacity of the shear tabs was reduced by an increase in connection depth, which accelerated closure of the gap between the beam and column face. Although beneficial to seismic performance, one of the damaging effects of such a high rotational stiffness was reported to be panel zone yielding, which was not usually considered in typical design. A simplified moment–rotation model was proposed (Astaneh 2005) for typical shear tab connections in composite construction frames, as shown in Figure 2-5.

### **2.3.2 Izzuddin et al. (2008)**

Izzuddin et al. (2008) proposed a simplified energy-based approach to assess the progressive collapse resistance of structures. In the companion paper (Vlassis et al. 2008), the proposed procedure was implemented to assess the behaviour of steel-frame composite systems following column removal. The results showed that composite steel-framed buildings with typical details and configurations have a tendency to collapse under a column-removal scenario due to the impact from upper floors. The study showed that the use of shear tabs (fin plates) should be cautiously reviewed, especially for long spans. Having additional rebars in the negative moment regions was found to be beneficial to the system capacity. An excessive reinforcement ratio, however, in the hogging (negative) moment zones can result in an adverse brittle failure mode accompanied by local buckling in the steel beams. The authors recommended further experimental study on the behaviour of connections and the ductility demand under combined bending and axial loading.

### **2.3.3 Sadek et al. (2008)**

Sadek et al. (2008) performed computational finite element analysis to evaluate the behaviour of composite floor systems with simple shear connections under a column removal scenario. Two different models were investigated: in the first model, a bare frame without any floor slab components was investigated, and in the second one, all components of the composite floor system were considered. The prototype building used in the study was designed for the purpose of evaluating the robustness of steel frame structures under a removed column scenario. As shown in Figure 2-6, the floor bays considered were 6.1 m × 9.14 m. The composite floor system consisted of 76.2 mm (3 in.) deep 20 gauge steel deck with 82.5 mm thick lightweight concrete topping, reinforced with W1.4×1.4 wire mesh. All shear tab connections in the models were 9.5 mm thick with three bolts of 22.2 mm ( $\frac{7}{8}$  in.) diameter.

Since no experimental data were available to verify the finite element responses of the frames, several component verifications were utilized. Three different reduced and detailed finite element component models of shear tab connections were investigated. The result of the detailed model showed that tear out of the beam web was the failure mode. Although the shear tab and bolts underwent significant plastic strain, neither exhibited fracture. The reduced simulations of connections were modelled using nonlinear springs based on the force–displacement response stipulated in FEMA 355D (FEMA 2000). Results of the three models showed that the connection reached the ultimate capacity at a rotation of 0.088 rad.

It was noted that the GSA acceptance criteria (GSA 2013) on connection rotational capacity was relatively conservative (less than 0.035 rad). In order to investigate the behaviour of shear connections in the composite floor system, springs were added to the reduced model to simulate the response of the floor slab, and the results were compared against the cyclic test data by Liu and Astanteh (2000). Although the results agreed well in the positive moment region, the model underestimated the negative moment capacity. It was noted that the difference is attributed to the lack of detailing the fully-composite system, since the steel deck, reinforced wire mesh, and concrete tension softening were not modelled.

The results of pushdown analysis of different components of a floor system, from frame-only to detailed-floor models, are shown in Figure 2-6. The detailed floor model showed higher capacity (more than twice) than the frame-only model through two mechanisms: by preventing peripheral columns from being pulled in toward the removed central column, and by membrane action of the floor slab. The results revealed that even though the addition of floor components enhanced the capacity of the system significantly, the model cannot withstand the uniform vertical load (Dead Load + 25% of Live Load) specified by the GSA Guidelines even if the dynamic amplification factor is 1.0. It was suggested that more research is needed to investigate the robustness of composite floor systems.



#### **2.3.4 Thompson (2009)**

Thompson (2009) conducted nine tests on shear tab connections under column-removal loading. Shear tabs had only a single row of bolts ranging from three to five bolts. The two-span test set-up comprised shear tabs connecting each beam to the central stub column. The inflection point was assumed to be about 2 m away from the central column and the end of the beams connected to the reaction frame was a true pin. Specimens were loaded under displacement control using a single actuator by pulling down the stub column.

The internal forces were determined based on simple beam calculations using data from strain gauges attached to the beams. Three failure modes were observed: bolt shear, shear plate tension rupture, and shear rupture of the bottom hole. The beam end rotation at failure was found to be 0.133 and 0.076 rad for the three-bolt and five-bolt shear tab connections, respectively. The study suggested that further research is necessary to investigate the effect of composite action including a concrete slab and steel deck. In addition, finite element modelling was suggested to be developed to evaluate the key parameters affecting the behaviour of connections under combined loading.

#### **2.3.5 Alashker et al. (2010)**

Alashker et al. (2010) investigated the progressive collapse capacity of composite floor systems with shear tab connections using finite element modelling. The simulation models were verified through comparing the behaviour of composite slab components with discrete experimental test data. The purpose of the research was to examine the effects of key parameters on the behaviour of composite frames built upon previous work by Sadek et al. (2008). These parameters were deemed to be steel deck thickness, steel rebar area, and number of shear tab bolts. Two different methods of loading on the central removed column were employed: point load–displacement control; and uniform load–force control.

The results showed that the steel deck is the most significant component contributing to the floor's strength, and was as much as 60% of the total. It should be noted that their model assumed continuity of the metal deck between panels and did not consider capacity of puddle welds or shear stud welds of the metal deck to the steel beams. While doubling the steel deck's thickness promotes the capacity by 37%, adding more bolts to the shear tab connections has a minimal effect on the overall collapse capacity. It was because the connections failed before the floor's full capacity was reached, meaning that adding more bolts to the connections was not essentially additive to the capacity. The simulation results also showed that the uniform loading method captures more accurately the collapse resistance, but was difficult to accomplish numerically. The point load method, on the other hand, was found to be much simpler but less accurate due to the fact that the failure of connections close to the removed column limits the loads transferred to the floor system.

### **2.3.6 Main and Sadek (2012, with corrections dated 2013)**

Main and Sadek (2012) presented a technical report on the performance of steel framing systems with shear tab connections in composite floor slabs under a column-removal scenario. The investigation under both quasi-static and dynamic loading was a computational assessment using a reduced modelling approach. The components of the reduced model were verified against experimental data (Thompson 2009; Rex and Samuel Easterling 2003). This approach was used to examine the effects of different parameters such as bay size, slab, and mode of connection failure on the behaviour of the system. An energy-based method built on the work by Izzuddin et al. (2008) and the direct dynamic method presented by Alshaker et al. (2010; 2011) were also considered to evaluate the structural capacity under sudden column loss. One of the prototype gravity framing systems used was similar to the one by Sadek et al. (2008), as illustrated in Figure 2-6.

Results showed that fracture of the shear tab connections reduced the ultimate capacity of the gravity floor system under static loading by about 23% for bare

steel frames and about 13% for composite floor systems. It was reported that the rotational capacity of the shear tabs due to the presence of axial load was significantly smaller than the acceptance criteria stipulated based on the seismic data. The rotational ductility was about half and one-fourth of the acceptance criteria for bare frame and composite frame systems, respectively. It was mentioned that axial compression was developed in the far-end connections, imposing a substantial tensile force on the connections attached to the removed column. The effect of considering adjacent bays was found to be substantial to the ultimate capacity. Based on the numerical results, the authors proposed an empirical equation for calculating tie forces.

### **2.3.7 Yang and Tan**

Yang and Tan utilized several approaches (numerical, experimental, component-based model, and mechanical model) to investigate the behaviour of steel beam-to-column joints under a central column-removal scenario.

#### **2.3.7.1 Yang and Tan (2012)**

A numerical finite element approach on six different types of connections was presented (Yang and Tan 2012) employing both static and explicit dynamic solvers with fracture simulation using Abaqus software. The finite element analysis results were verified with the results of tests conducted by the authors. The results of the static and explicit dynamic method were compared and difficulties pertaining to each numerical method were addressed. It was concluded that the depth of connections has a substantial effect on the behaviour of joints subjected to catenary action.

It was noted that the current acceptance criteria on rotational ductility are very conservative. Thus, based on the conducted parametric studies they proposed four acceptance criteria on rotational capacity considering catenary action.

### **2.3.7.2 Yang and Tan (2013a, 2013b)**

Yang and Tan (2013a; 2013b) presented a series of experimental tests of common types of simple and semi-rigid bolted connections, such as bolted–bolted double angle and shear tab, under column-removal loading conditions. Even though it was assumed that the internal forces and deformations of connections at opposite ends are different, the inflection point was assumed to be located at the middle of the beam span. Therefore, only half of the beam span from each side of the removed column was used for the tests. The beam was connected at the end away from the stub column by a pin connection and a point load was applied to the central column using an actuator. Although the study focused only on the behaviour of connections in a bare frame, the authors acknowledged that the contribution of the floor slab would alter the deformations and internal forces at both end connections.

The results of the tests showed that the behaviour of shear tab and double angle connections was mainly governed by catenary action. Bolted double angles failed by tearing and fracture near the angle heels, while the shear tab connections failed by bolt shear failure with substantial bearing deformation. It was mentioned that due to the limited rotational capacity of shear tabs compared to double angles, the vertical shear load capacity was lower. Based on the results, bolted double angles were deemed to provide better performance in developing catenary action and resistance at higher rotational demand. It was reported that the rotational capacity of connections was much higher than criteria in both ASCE 41-06 (ASCE 2006) and DoD (UFC 2013). Based on results of the bolted angle connections, Yang and Tan (2013b) concluded that an increase to the angle thickness reduced the deformation capacity and changed the failure mode from fracture at the angle heel to bolt fracture along with angle yielding.

### **2.3.7.3 Yang and Tan (2013c)**

Yang and Tan (2013c) developed a mechanical model for bolted-angle connections based on 14 experimental tests subjected to a monotonic tensile force.

The parameters varied in the tests were angle thickness, bolt size and material properties. The proposed mechanical model agreed well with the experimental tests results. The load–displacement behaviour of the connections was governed mainly by the response at the later stages of loading, rather than at the early loading stage. Five different failure modes were observed and were dependent on the strength ratio between bolts and angles. The deformation capacity and failure mode were also governed by the angle thickness. Deformation capacity was lower as the thickness of angle increased.

#### **2.3.7.4 Yang and Tan (2014)**

Yang and Tan (2014) conducted a series of column-removal experimental tests on composite beam-to-column joints to investigate the failure modes and behaviour of connections in a composite frame under sagging and hogging moments. Two types of connections were considered: bolted double angle, and flush end plate.

Even though the authors acknowledged the presence of a slab would change the anti-symmetric nature of the loading and deformation, similar to the previous work (Yang and Tan 2013a), the inflection point was assumed to be located at the middle of the span as illustrated in Figure 2-7. However, they mentioned that the location of the inflection point may change due to the different rotational stiffness at positive and negative moments. Since one of the objectives of the study was to compare various types of connections with the same boundary and loading conditions, similar beam spans and inflection points were considered for the both positive and negative moment tests.

The prototype composite frame was designed according to the Eurocode. Test specimens were scaled to two-thirds of the original design. Test beams had a total length of about 3.0 m and the distance between pin supports was 4.85 m. The length of the concrete slab was kept same as the beam span, the width of slab was 587 mm, and the slab thickness was 110 mm. Two specimens had similar configurations to the previous work on bare frames (Yang and Tan 2013a).

Comparisons between the results of bare and composite frames revealed that the presence of a concrete slab significantly affects the behaviour and response of the system, as shown in Figure 2-8. Concrete crushed severely around the stub column and one of the angles fractured at the early stages of loading, resulting in a considerable drop in the vertical applied load. The failure mode of the bolted double-angle connection in the composite frame was fracture at the heel for both specimens under hogging and sagging moment conditions. Local buckling of the beam top flange under hogging moment was also reported.

It was shown that for the side joints while the slab was in tension, the steel connections were in compression. Thus, they acknowledged the development of compressive forces (arching action) in the composite slab system, as was also observed by Sadek et al. (2011). No failure of shear studs was observed and thus fully-composite action was assumed to be developed.

#### **2.3.7.5 Yang and Tan (2015)**

Based on the five tests on composite frame connections conducted by (Yang and Tan 2014), component-based models were developed to examine the behaviour of connections under simulated progressive collapse loading. A parametric investigation of the effects of rebars, steel deck, and concrete slab on the performance of connections and the overall structural system were carried out. The results showed that adding steel rebars would increase the system capacity, while the steel deck can only increase the capacity at flexural stage and has less effect at large deformations.

It was found that the beam span-to-depth ratio has a substantial impact on the frame behaviour. Increasing the ratio from 13 to 25 decreases the ultimate resistance and it results in a small increase in the beam axial force and a significant reduction in the rotational angle.

### **2.3.8 Oosterhof and Driver (2015; 2016)**

Oosterhof (2015; 2016) conducted a comprehensive series of experiments consisting of 45 full-scale tests, in addition to developing mechanical models, to investigate the performance of various steel shear connections under column-removal loading. Types of connections included shear tab, bolted double angle, single angle, and combined top and bottom angles. Several geometric parameters of connections under different loading regimes were included in the investigation. Specifications and details of the shear-tab and double-angle connections are illustrated in Figure 2-9, because of their relevance to the current research.

A test set-up, as shown in Figure 2-10, was designed in order to load the specimen in a pre-defined column-removal scenario. Three independent hydraulic actuators were used to be able to impose an appropriate progressive collapse load history to the connections attached to a cantilever stub beam.

The load history procedure was derived based on the equilibrium of forces and compatibilities of displacements of a symmetric three-hinged beam under point or uniformly distributed load. It was assumed that half of the total span elongation is attributed to each end connection by ignoring the elastic elongation of the beam as being very small compared to the elongation of connections. Both equilibrium of forces and compatibilities of displacements required an assumed span length for which a span range of 6 m to 12 m for connections with three and five bolts was selected.

The results showed that bolt tear-out was the main failure mode for all shear-tab connections and no bolt failure and shear deformation was observed. The failure mode of the double angle connections was tearing of the net section near the column bolt line or at the angle heel. Compressive arching action was found to exist at the early stage of loading and it was reported to have a negligible effect on the performance of the shear connections. It was found that bolted angle connections have a lower stiffness, but greater ductility, compared to the shear-tab ones. Based on the range of shear connections tested, it was concluded that the connection bending moment at the ultimate limit state was small and need not be

considered as a strength parameter in progressive collapse cases. Even though the concrete floor slab was not considered in the mechanical model, it was acknowledged that the floor slab would change the demand and resistance of the system. It was recommended that “The effects of a concrete floor slab on the collapse resistance of a steel gravity frame should be studied. ...”.

### **2.3.9 Weigand and Berman (2014)**

As a part of collaborative research program with University of Illinois and Purdue University, Weigand and Berman (2014) experimentally evaluated the capacity of single plate shear connections in column removal loading at the University of Washington. Two beam spans (9.1m and 14.6m) and connection parameters including plate thickness, number of bolts, bolt grade, hole type (standard versus short slotted), and edge distance were considered. Shear plates were made of ASTM A36 steel and bolt grades were A325 and A490. Beams and stub columns were A992 steel.

The test set-up included three actuators attached to the load beam to deliver a combination of shear, tension and flexural action. Rotation and axial demands were applied quasi-statically to the connection in a displacement control. The demand applied to the connection was based on geometric compatibility among the stub column deflection, beam rotation, and axial extension, as illustrated in Figure 2-11. The authors acknowledged that a relatively high shear force was developed at the connections due to the length of the specimen beam stub within the reaction frame.

The results showed that the primary failure modes of connections were shearing of the bolts or plate tear-out. Shear connections provided only 15% to 25% of the LRFD specified design shear strength. Thus, they concluded that the capacity of the composite slab components may be important to arresting system collapse. The short-slotted holes showed higher ductility and load-carrying capacity by reducing the bearing deformation. It is reported that binding adversely affected the strength and ductility of the connection by about 15% compared to the



benchmark specimen. A rigid-body fiber displacement approach was proposed to predict the ductility and capacity of the connections. The authors acknowledged that more research is needed to comprehensively understand the behaviour of connections in composite floor systems.

## **2.4 Conclusion**

Most of the recent building codes, standards, and design guidelines provide several approaches to evaluate the integrity of structures against progressive collapse. Amongst those approaches, alternative load path is recognized to be an acceptable method to assess the vulnerability of structures to disproportionate collapse. The assessment is based on acceptance criteria that are mostly stipulated based upon the research derived from seismic and cyclic loading conditions. Since the loading nature of progressive collapse is, in effect, different than seismic loads, new measures need to be introduced or current criteria need to be modified. Steel connections, in this regard, are found to play an important role in capturing the true behaviour of steel structures. Although several researchers have investigated the behaviour of shear connections in frame-only systems under a column-removal scenario, there is a lack of understanding when it comes to composite frames, as has been acknowledged in the literature.

It has been proclaimed that there is a need to investigate the response of shear connections in composite floor systems due to the complex interaction of connections and slab. There is, however, limited research that examined the effect of composite slab components on the overall behaviour of the system. These works are mostly numerically or partially-scaled experimental tests and there are no full-scale tests that fully examine the behaviour of shear connections in composite construction frames. Therefore, the objective and scope of this research is to understand the response of steel shear connections in composite floor construction following a column loss.

Table 2-1: Modelling Parameters and Components Capacities

Parameter	Force-Controlled	Deformation-Controlled
Linear Static Procedure (LSP)		
Strength Capacity	$\phi Q_{CL}$	$\phi m Q_{CE}$
LIF	2.0	$0.9 m_{LIF} + 1.1$
Allowable DCR	1.0	m
Nonlinear Static Procedure (NSP) & Nonlinear Dynamic Procedure (NDP)		
Strength Capacity	N/A	$\phi Q_{CL}$
Deformation Capacity	Limit (Table 2-3)	N/A
Dynamic Increase Factor (NSP only)	$\Omega_N = 1.08 + 0.76/(\theta_{pra}/\theta_y + 0.83)$	

$\phi$ : Strength Reduction Factor.

$Q_{CL}$ : Lower-bound Strength.

$Q_{CE}$ : Expected Strength.

$\theta_{pra}$ : Plastic Rotation Angle Given in ASCE/SEI 41.

$\theta_y$ : Yield Rotation Angle Given in ASCE/SEI 41.

m: Component or Element Demand Modifier as Defined in Table 2-2.

$m_{LIF}$ : Smallest m-factor of Primary Element Connected to the Column.

Table 2-2: Acceptance Criteria for LSP of Steel Connections (m-factor)

Connection Type	Primary *	Secondary *
GSA Guidelines, UFC 4-023-03, and CSA S850-12		
Double Angles		
Shear in Bolt	$5.8 - 0.107 d_{bg}$	$8.7 - 0.161 d_{bg}$
Tension in Bolt	1.5	4.0
Flexure in Angles	$8.9 - 0.193 d_{bg}$	$13.0 - 0.290 d_{bg}$
Shear Tab	$5.8 - 0.107 d_{bg}$	$8.7 - 0.161 d_{bg}$
ASCE/SEI 41-06		
Shear Connection with Slab	---	$17.0 - 0.387 d_{bg}$
Shear Connection without Slab	---	$17.0 - 0.387 d_{bg}$

\* Refers to Section 3.2.4 of GSA and UFC, and Clause 3.1 of CSA S850 for Primary & Secondary Classification.

$d_{bg}$ : Depth of Bolt Group, in.

Table 2-3: Acceptance Criteria for Nonlinear Analysis Procedures of Steel Connections

Connection Type	Nonlinear Modeling Parameters **			Acceptance Criteria (Plastic Rotation Angle)	
	a	b	c	Primary *	Secondary *
GSA Guidelines, UFC 4-023-03, and CSA S850-12					
Double Angles					
Shear in Bolt	$0.0502 - 0.0015d_{bg}$	$0.072 - 0.0022d_{bg}$	0.2	$0.0502 - 0.0015d_{bg}$	$0.0503 - 0.0011d_{bg}$
Tension in Bolt	$0.0502 - 0.0015d_{bg}$	$0.072 - 0.0022d_{bg}$	0.2	$0.0502 - 0.0015d_{bg}$	$0.0503 - 0.0011d_{bg}$
Flexure in Angles	$0.1125 - 0.0027d_{bg}$	$0.150 - 0.0036d_{bg}$	0.4	$0.1125 - 0.0027d_{bg}$	$0.150 - 0.0036d_{bg}$
Shear Tab	$0.0502 - 0.0015d_{bg}$	$0.1125 - 0.0027d_{bg}$	0.2	$0.0502 - 0.0015d_{bg}$	$0.1125 - 0.0027d_{bg}$
ASCE/SEI 41-06					
Shear Connection with Slab	$0.029 - 0.0002d_{bg}$	$0.150 - 0.0036d_{bg}$	0.4	---	$0.150 - 0.0036d_{bg}$
Shear Connection without Slab	$0.150 - 0.0036d_{bg}$	$0.150 - 0.0036d_{bg}$	0.4	---	$0.150 - 0.0036d_{bg}$

\* Refers to Section 3.2.4 of GSA and UFC, and Clause 3.1 of CSA S850 for Primary & Secondary Classification.

\*\* Refers to Figure 2-1 for Definition of Parameters a, b, and c.

$d_{bg}$ : Depth of Bolt Group, in.

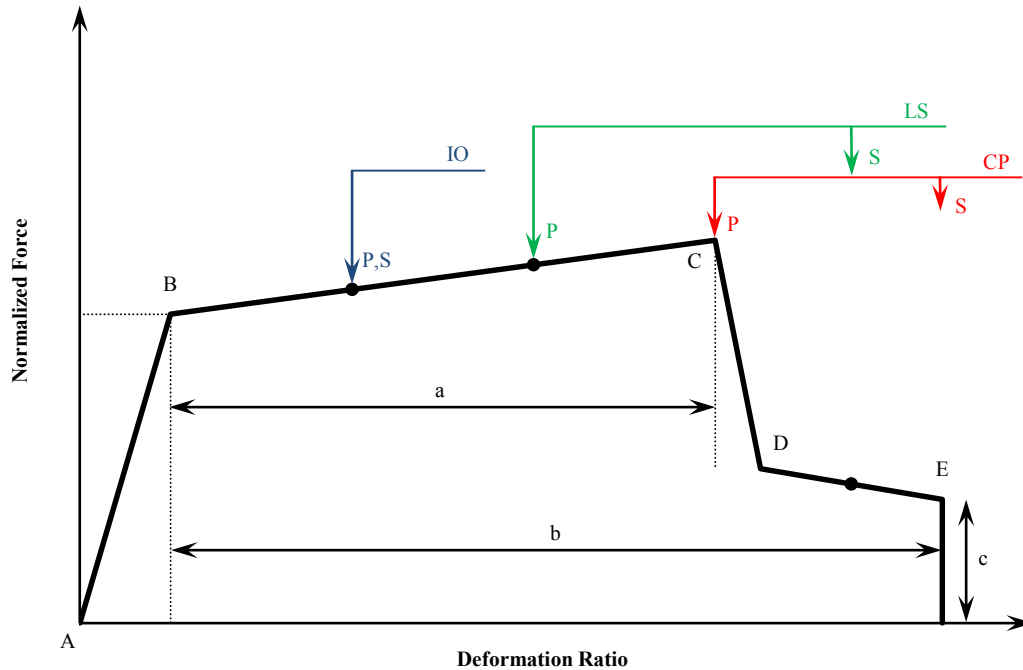


Figure 2-1: Generalized Component Load–Deformation Relations for Modelling Parameters and Acceptance Criteria

IO: Immediate Occupancy; LS: Life Safety; CP: Collapse Prevention

P: Primary Component; S: Secondary Component; A: Unloaded Point; B: Effective Yield; C: Peak Strength; D: Residual Strength; E: Ultimate Deformation

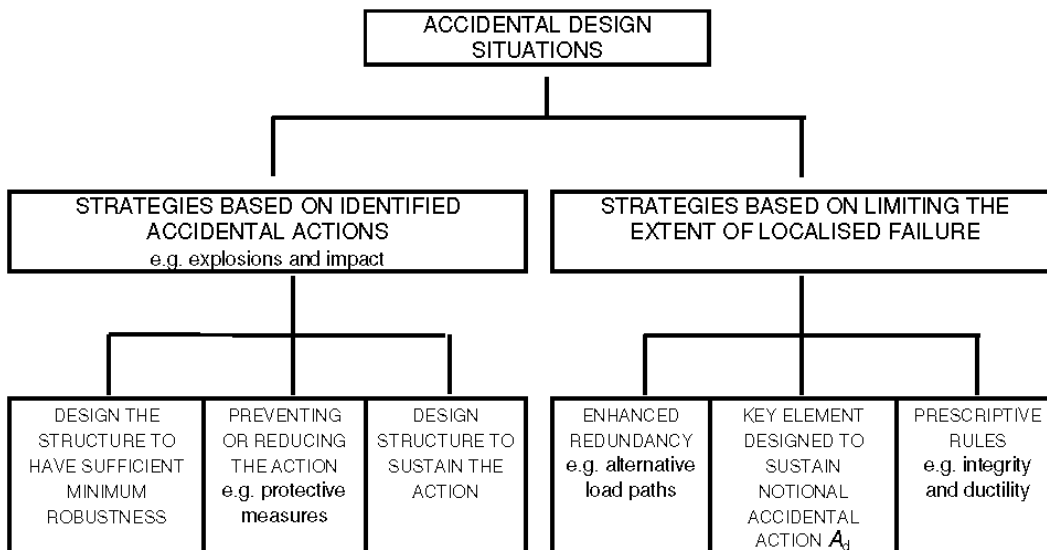


Figure 2-2: Eurocode Accidental Design Strategy (EN 1991-1-7 (CEN 2006))

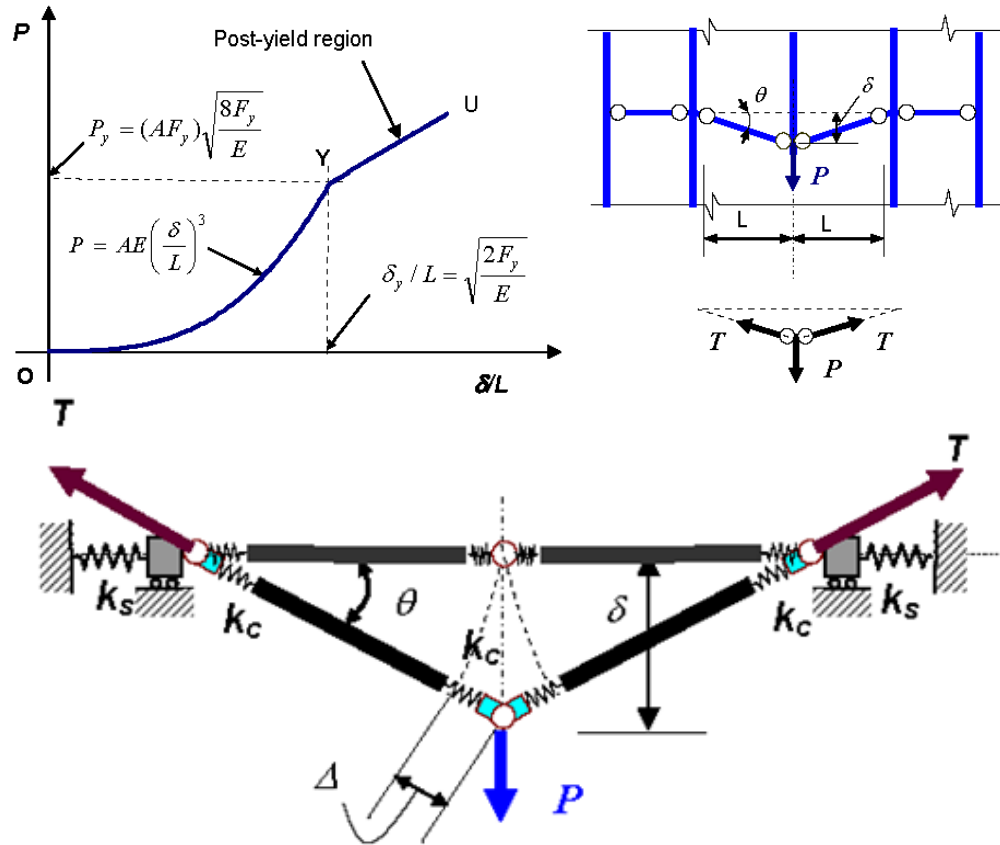


Figure 2-3: Three-Hinge Beam Analogy with End-Support Conditions (Astaneh 2007)

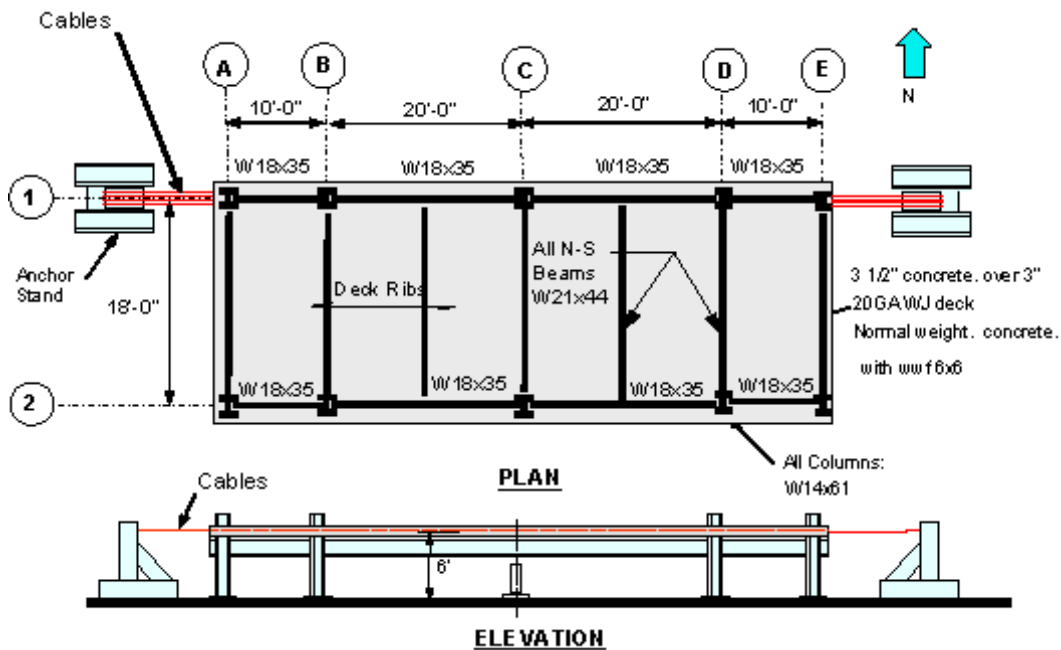


Figure 2-4: Plan and Elevation of Test Specimen (Astaneh 2007)

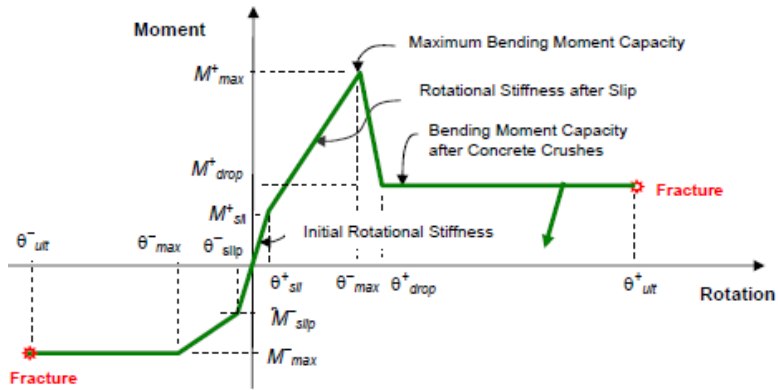


Figure 2-5: Moment-Rotation Response of Shear Tab Connections Including Slab (Astaneh 2005)

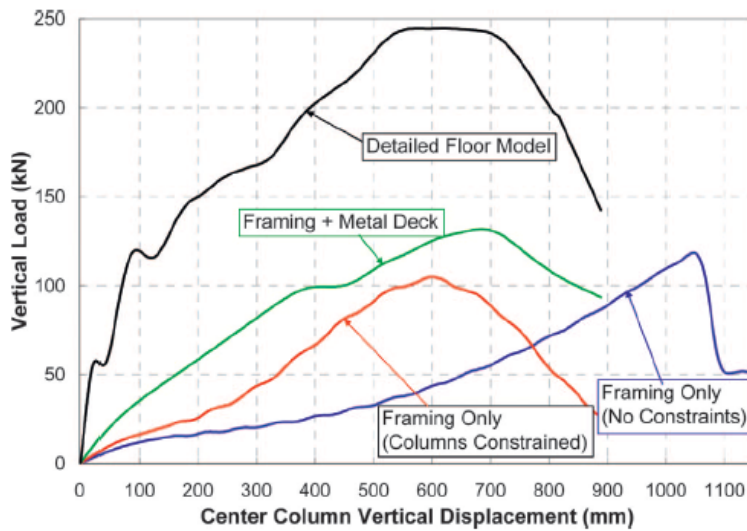
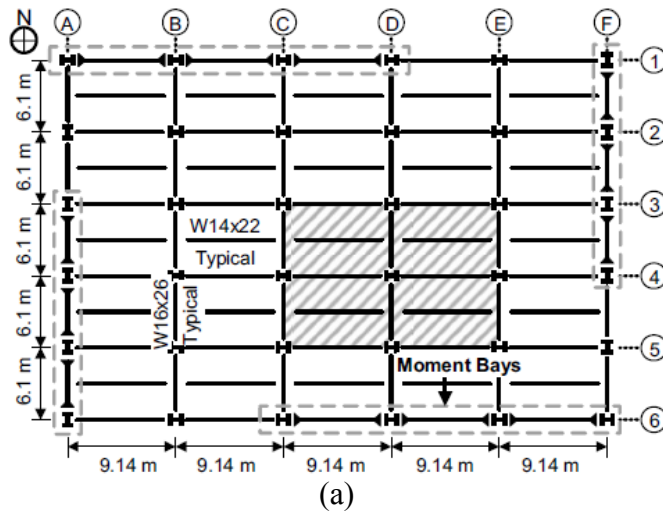


Figure 2-6: (a) Plan Layout and Floor Area Considered; (b) Load-Displacement of Floor System Components (Sadek et al. 2008)

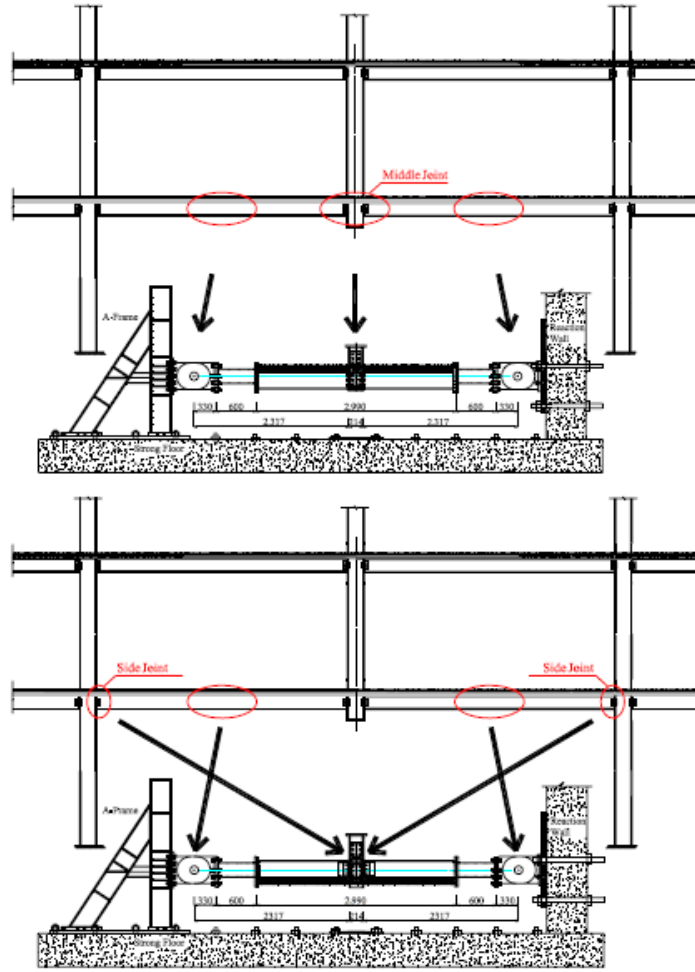


Figure 2-7: Test Set-up (Yang and Tan 2014)

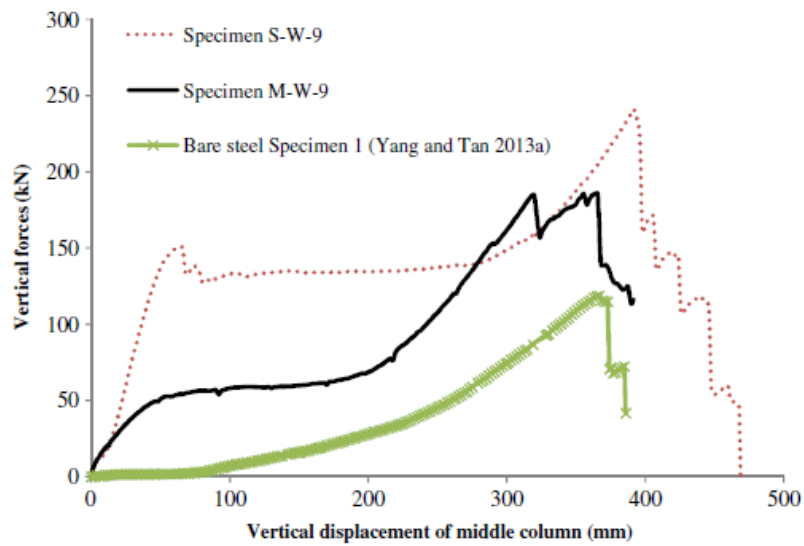


Figure 2-8: Effect of Composite Slab on Bolted Double-Angle Connections (Yang and Tan 2014)

Specimen ID	Specimen Geometry <sup>†</sup>				Load History Parameters <sup>††</sup>	
	Rows of Bolts	Plate Thickness t (mm)	Bolt Diameter d (mm)	Weld Size S (mm)	Load Arrangement P or $\omega$	Span Length L (m)
ST3A-1	3	9.5	22	6	P	6.0
ST3A-2	3	9.5	22	6	$\omega$	6.0
ST3A-3	3	9.5	22	6	$\omega$	9.0
ST3B-1	3	6.4	19	5	$\omega$	6.0
ST3B-2	3	6.4	19	5	$\omega$	9.0
ST5A-1	5	9.5	22	6	$\omega$	8.0
ST5A-2	5	9.5	22	6	$\omega$	12.0
ST5B-1	5	6.4	19	5	$\omega$	8.0
ST5B-2	5	6.4	19	5	$\omega$	12.0

(a)

Specimen ID	Specimen Geometry <sup>†</sup>				Load History Parameters <sup>††</sup>	
	Rows of Bolts	Angle Thickness t (mm)	Bolt Diameter d (mm)	Stiffened Column	Load Arrangement P or $\omega$	Span Length L (m)
DA3B-1	3	6.4	19	Yes	$\omega$	6.0
DA3B-2	3	6.4	19	Yes	$\omega$	9.0
DA3B-3	3	6.4	19	No	$\omega$	9.0
DA5B-1	5	6.4	19	Yes	$\omega$	8.0
DA5B-2	5	6.4	19	Yes	$\omega$	12.0
DA5B-3	5	6.4	19	No	$\omega$	8.0

(b)

Figure 2-9: Parameters of (a) Shear-Tab Specimens; (b) Bolted Double-Angle Specimens (Oosterhof and Driver 2015)

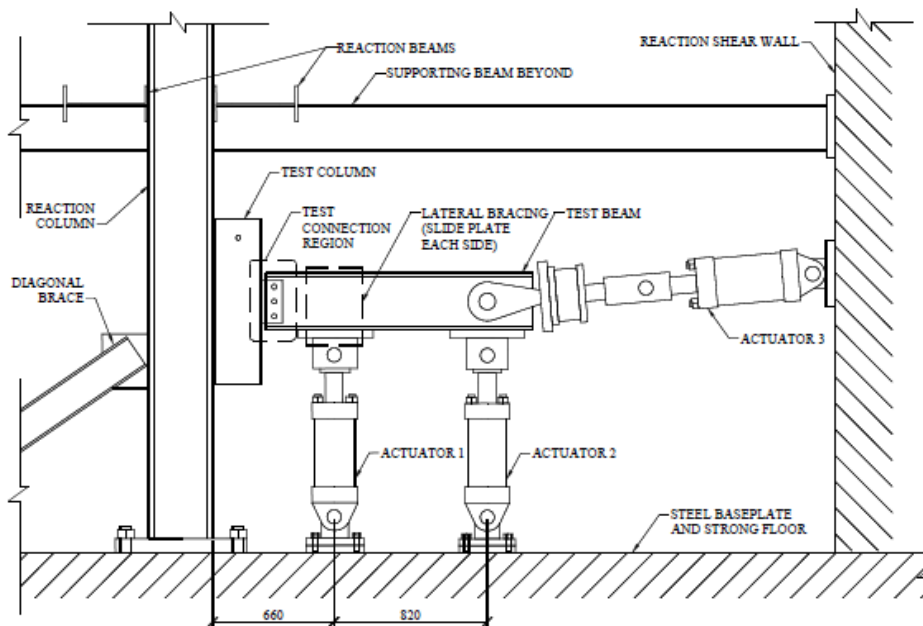


Figure 2-10: Test Set-up (Oosterhof and Driver 2015)



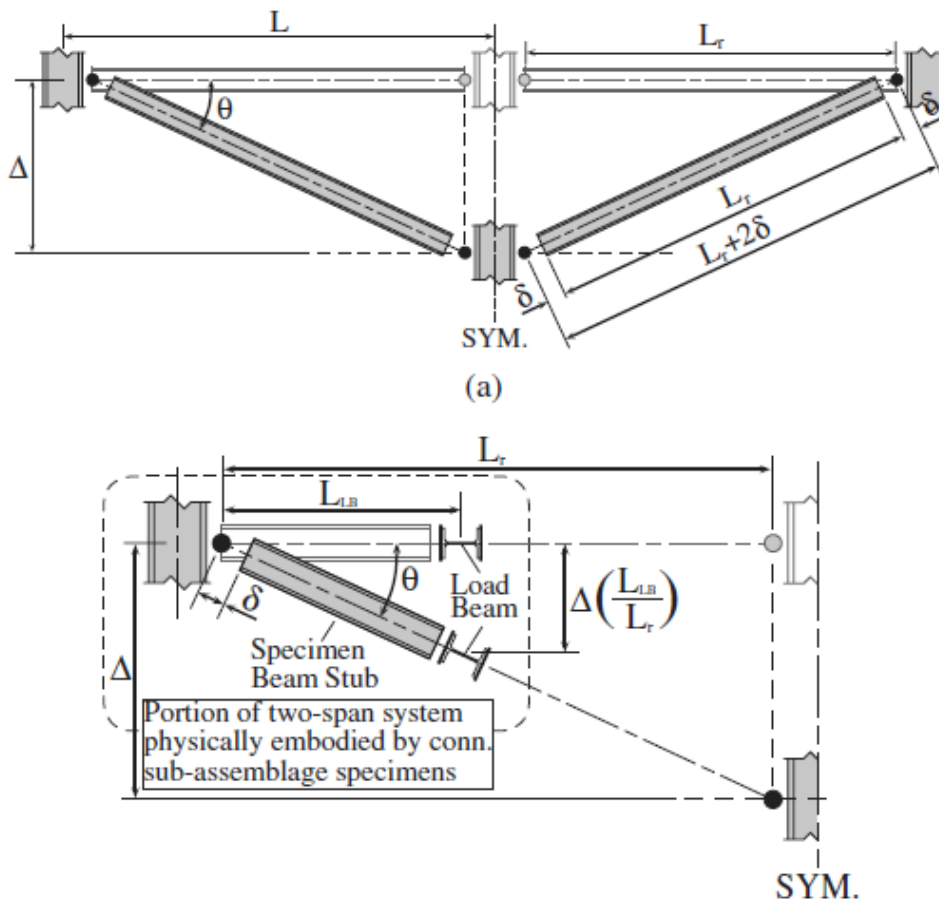


Figure 2-11: Geometric Relationship Between Beam Rotation, Axial Extension, and Interior Column Deflection (Weigand and Berman 2014)

### **3. EXPERIMENTAL PROGRAM**

#### **3.1 Introduction**

This chapter describes comprehensive details of the experimental program consisting of 17 full-scale physical tests conducted in the I.F. Morrison Structural Engineering Laboratory at the University of Alberta. The objective of the experimental program is to investigate the behaviour of shear tab and bolted double-angle connections in composite floor construction under a simulated progressive collapse scenario. For this purpose, a range of parameters was varied, including the connection depth, connection thickness, concrete slab width, and assumed beam span. Details of test specimens, test set-up, loading regime, and material properties are presented in this chapter and the results of the experiments are described in Chapter 4.

#### **3.2 Prototype Composite Steel Frame**

In gravity frames, steel beams are connected to the column using shear connections. Two prototype steel gravity framing systems with a rectangular plan and clear spans of 6.0 m and 9.0 m were designed, as shown in Figure 3-1 to Figure 3-3. These dimensions and beam spans are typical for steel gravity framing systems with shear connections. Two types of shear connections with two different material thicknesses (6.4 mm and 9.5 mm) were considered in this research: shear tab welded to the column and bolted to the beam; and double-angle bolted to both the column and beam. Geometry and details of two of the connections were selected similar to those used in the experimental program of Oosterhof and Driver (2015), wherein connections of beams without a floor slab were tested, to be able to compare the results directly.

The flooring system considered includes a 127 mm (5 in.) thick flat concrete slab connected to the beams by shear studs designed for fully-composite action. The floor area considered in this research is a 2 bay  $\times$  2 bay portion of the prototype

system (hatched area in the plan layouts of Figure 3-1 and Figure 3-2). The central column in the examined area is assumed to be disengaged, so as to represent the removed column under a column-loss scenario. Only connections attached to the removed column are considered in this experimental program, with the testing zone depicted in Figure 3-1 to Figure 3-3.

### **3.3 Test Specimens**

In order to examine the effect of the composite slab on steel connections, a total of 17 (16, plus a pilot test) full-scale steel shear connections with concrete slab were designed to test under a column removal condition. Table 3-1 summarizes the matrix of the experimental program. The specimens vary in type and depth of connection (and number of bolts), plate/angle thickness, and assumed span length (with associated concrete slab width). In general, the matrix is classified into two connection types: shear tab and double angle.

Specimens are named to provide information on the connection type and geometry, and beam span. Each specimen's designation contains both letters and numbers. The first and second letters represent the connection type: ST for Shear Tab and DA for Double Angle. The third character indicates the number of bolts per single vertical line (either 3 or 5). The fourth shows the thickness of the shear tab plate or angle in millimeters, rounded down to the nearest integer (either 6 or 9). Finally, the last letter represents the clear span length: specimens ending in "A" have the clear span length of 6.0 m, and specimens with ending in "B" have the clear span length of 9.0 m. As an example, specimen DA59B is a 9.7 mm thick double angle with 5 horizontal bolt rows, having an assumed clear span length of 9.0 m. Figure 3-4 describes the naming convention of specimens.

In this test program, a modular concept for assembling components of the composite frame was implemented, allowing for rapid assembly and beam reuse. Since only a small portion of the two-span frame was considered in the test program (testing zone shown in Figure 3-3), proper boundary conditions needed

to be imposed on the concrete slab to represent the symmetry and continuity of the slab at the location of the removed column.

### **3.3.1 Shear Connections**

Shear-tab connections with a single plate were welded to the column flange and bolted to the beam web. The vertical pitch of 80 mm and end/edge distance of 35 mm from the centre of bolt holes to the edges were used for all shear tabs. Both pitch and edge/end distances comply with Clause 22.3 of CSA-S16 (CSA 2014). Shear tabs were welded using fillet welds to the column flange, with a weld size of 5 mm and 6 mm for the 6.4 mm and 9.5 mm thick plates, respectively. Plates were welded to the stub columns' flanges with a 7 mm offset from the column web centreline to align it with the test beam centreline. The specifications and details of the shear tabs are tabulated in Table 3-2 and shown in Figure 3-5.

Double-angle connections comprising two similar angles were bolted to both the column flange and beam web in a single vertical line at each leg. The vertical pitch of 80 mm and vertical edge distance of 35 mm were used for all connections. Bolt lines were placed at a distance of 60 mm from the heel of the angles, resulting in an end distance (for tension in the connection) to the angle toe of 29 mm. Although the minimum pitch and edge distance of the angles satisfy Clause 22.3 of CSA-S16 (CSA 2014), the end distance was less than the limit in order to provide a standard gauge distance for the angle size. Details of the double angles are reported in Table 3-3 and shown in Figure 3-6.

The nominal diameter of the holes was specified to be 2 mm greater than the bolt diameter: 21 mm holes for 19 mm ( $\frac{3}{4}$  in.) bolts and 24 mm holes for 22 mm ( $\frac{7}{8}$  in.) bolts. Plates and angles were specified to be manufactured as Grade 300W in accordance with standard G40.20-13/G40.21-13 (CSA 2013). The measured material properties are reported in Section 3.8.1.

All connections were bolted to the web of the test beams, and the angles were also bolted to the support column stub, using ASTM A325 high strength bolts with

threads excluded from the shear planes. Since none of the bolts were designed to be either in tension or in cyclic loading (designed as typical shear connections), they were installed to the snug-tight condition where the component parts are brought into firm contact with one another. Heavy hex structural nuts with washers were used for all connections. Washers were only placed on the nut side of the grip.

### **3.3.2 Concrete Slabs**

Since two clear span lengths were considered (6.0 m and 9.0 m) for connections, concrete slabs were constructed with two different widths (1.50 m and 2.04 m). The width was considered to be an effective width of the concrete slab according to Clause 17.4 of CSA-S16 (CSA 2014), which was taken as the lesser of 0.25 times the composite beam span and the average distance between beam centrelines. Due to the space limitation in the test set-up, the effective width of 2.04 m was constructed for the 9.0 m span instead of the 2.25 m width required by Clause 17.4. The effect of concrete slab widths on the behaviour of connections is numerically investigated in Chapter 6.

As the purpose of this study is to understand the effects of concrete slabs on the behaviour of steel connections, a 127 mm (5.0 in.) thick solid concrete slab with two layers of rebar in two directions (10M top and bottom @ 250 mm) was used. Rebars used in the concrete slab were specified as CSA G30.18-M09 (CSA 2009) Grade 400. The concrete slab was designed to have a minimum compressive strength of 25 MPa and a maximum of 35 MPa at 28 days. The material properties of the concrete and rebars are reported later in this chapter. The details and geometry of the concrete slabs are shown in Figure 3-7. All required concrete for the slabs was delivered to the lab by a ready-mix truck. The formwork fabrication and concrete casting were done in the lab.

Headed shear studs (connectors) used in the slab were mild steel specified according to ASTM A108-13 (ASTM 2013a) and AWS D1.1 (AWS 2010). They were 19 mm ( $\frac{3}{4}$  in.) in diameter and had an embedded length of 115 mm, which

satisfies the minimum length-to-diameter ratio of Clause 17.7 of CSA-S16 (CSA 2014). The studs were not welded to the beam, as it is usually the case in composite construction. Instead, they were end-threaded and cast into the slab to protrude from the bottom by 50 mm for modular assembly purposes.

The studs were placed for the concrete pour with the aid of a plywood template that was fabricated to match the as-built test beam flange holes in order to ensure proper fit-up upon assembly. Washers tack welded to the studs were used to ensure vertical alignment and stability of the studs within the formwork during concrete pouring. In addition, the washers provided partial constraint to the studs during assembly to avoid any rotational slip within the concrete. Fourteen shear studs were used in two rows in each slab with a spacing of 200 mm in the longitudinal and 135 mm in the transverse directions, which are within the limits of Clause 17.7.

20M CSA G30.18-M09 (CSA 2009) Grade 400 reinforcing bars with threaded ends were placed horizontally at mid-depth of the slab close to the column opening, as shown in Figure 3-7. The threaded ends protruded 80 mm out of the slab to be secured within the end-supporting anchor beams and the bars were spaced 130 mm apart. The embedment length of the bars was long enough to develop their yield capacity.

In order to have a flush and clean surface at the end of the slabs, C130×13 channel sections were cut, drilled and placed inside the formwork at the column end. An individual segment of channel was placed each side of the slab opening. Another purpose of using channels was to secure the threaded reinforcing bars within the formwork during concrete pouring. The bars were secured by means of nuts attached to the inside and outside of the formwork. The completed precast concrete slabs with protruding threaded-end studs were placed on the test beam top flange. The studs passed through pre-drilled holes in the flange and were fastened with matching nuts to induce composite action. Details on the formwork and construction procedure are provided in Appendix B.

### 3.3.3 Test Beams

A W310×143 test beam was used for the pilot test and two of the three-bolt shear tabs with 6.4 mm thickness (ST36A and ST36B). A W530×165 beam with five holes was used for the rest of the specimens to accommodate connections with either three and five rows of bolts. The holes in the web were 24 mm ( $1^{5/16}$  in.) in diameter to accommodate both connection bolt sizes and provide tolerance for alignment of components.

Fourteen 22 mm ( $7/8$  in.) diameter holes were drilled in the top flange to accommodate the protruding studs. In addition, eight 28 mm ( $1^{1/8}$  in.) diameter holes were placed in the bottom flange for attaching the test beam to the vertical actuators. A 50 mm (2 in.) thick end plate was welded using a 12 mm fillet weld all around to the end of the W530×165 beam. Holes with 32 mm ( $1^{1/4}$  in.) diameter were drilled in the end plate to attach the horizontal actuators that applied the principal axial forces to the beam. Details and geometry of test beams are provided in Appendix B.

### 3.3.4 Slab Anchorage Beams

In order to simulate the symmetry and continuity of the slab at the location of the removed column, the concrete slabs were anchored using partially-embedded reinforcing bars by passing them through the web of stiff anchorage beams to simulate a fixed-end support condition. Thus, two W530×165 sections were fabricated and were drilled (slotted holes) to accommodate the two different connection bolt sizes. Five stiffeners were fitted and welded to one side of the web using fillet welds to ensure no failure of these anchorage members would occur during the tests. Finite element analyses using Abaqus (Dassault Systèmes 2013) were implemented to check any potential local deformation and deflection that might arise during the tests. Details and geometry of the slab anchorage beams (identified there as “end-supporting” beams) are provided in Appendix B.

### 3.3.5 Stub Columns

To focus the study on the strength and ductility of the connections, test stub columns (W250×89 sections) were designed to ensure no failure would occur during the tests. All shear tab connections were welded to the flange of the columns using fillet welds. For double angle connections, two stiffened columns (two different sizes of hole: 21 mm and 24 mm) were fabricated and used to limit any deformation arising from bending of the column flange during the tests. All columns were extended 300 mm beyond the top and bottom of the welded shear-tab plates or double angles. All columns were also drilled on the opposite flange to be able to attach them to the heavy reaction column. To fasten the stub columns to the reaction frame, 25 mm (1 in.) diameter ASTM A490 bolts were used. All bolts were pre-tensioned by the turn-of-nut method to ensure no slip would occur. Details and geometry of test columns are shown in Figure 3-5 and Figure 3-6.

### 3.4 Test Set-up

The tests were conducted in the I.F. Morrison structural engineering lab at the University of Alberta using the set-up afore-designed to test steel connections. This test set-up was conceptually introduced by Astaneh (1989) and modified to meet the research needs. Figure 3-8 and Figure 3-9 show the schematic of the test set-up. Four hydraulic actuators (two vertical and two horizontal) at three locations were placed to load the specimens. Actuators were pin-connected to the test beam to be able to rotate freely. Capacities of actuators 1 and 2 were each 1354 kN in compression and 1098 kN in tension, with 255 mm (10 in.) stroke. Two hydraulic actuators were combined in parallel, acting together as actuators 3 to axially load the specimens, each with capacity of 677 kN in compression and 549 kN in tension and 406 mm (16 in.) stroke. Since the specimens were mostly in axial compression due to the arching action, modifications were made to actuators 3 to ensure no buckling or instability would occur. Instead of three pins between the test beam and reaction wall, as was the case in the previous progressive collapse testing program (Oosterhof and Driver 2015) where axial



loads were tensile, pins were present only at the ends of the actuator assembly. After Assembly (Side View)

Figure 3-9 illustrates the configuration of pins within the actuator assemblies. Actuators 1 and 2 were mainly used to apply rotation and vertical deflection of the two-span system, while actuators 3 were exercised to apply axial force (compression or tension) by controlling the axial deformation of the shear connections. The actuators were all operated in displacement control.

To develop axial compression due to the arching action, actuators 3 were installed initially inclined with respect to the test beam axis at a rotation corresponding to that expected at the maximum applied axial load. Ideally, a testing set-up mechanism would allow actuators 3 to follow arching action at each loading stage. However, for practical reasons, only at the peak axial load did the arching line and the axis of actuators 3 become aligned.

Reaction frames and a rigid shear wall were provided adjacent to the stub column and actuators 3, respectively, to provide the required stiff reaction points for the applied loads. They were both connected rigidly to the lab strong floor using pre-tensioned anchor rods. Although the reaction frames were diagonally cross-braced to limit in-plane displacement, after completion of half of the tests another support beam was added to the back of the reaction frame close to the stub column at the elevation of the concrete slab to further limit the in-plane deformation observed in the previous tests. Figure 3-10 depicts the overall configuration of the test set-up and one of the test specimens.

### **3.5 Instrumentation**

Several measuring instruments and devices were implemented in the test set-up to capture desired information and data. Figure 3-11 shows the instrumentation layout used for the test specimens.

Load cells were installed on each actuator to measure the applied force. Pressure transducers were also connected to the hydraulic hoses of the actuators to allow a

redundant computation of each applied tensile and compressive force. The force was calculated based on the imposed pressure and the engaged piston's area. The capacity of each actuator was about 5000 psi (34.5 MPa). All load cells and pressure transducers were calibrated prior to the first test. However, the load cells were again checked and recalibrated after completion of half of the tests due to discrepancies observed between the pressure transducer and load cell readings.

Cable transducers were placed to measure each actuator stroke to track the location of applied forces with respect to the stub column at each loading stage. This allowed calculating the instantaneous projection of applied forces and their corresponding moment arms to the reference point (stub column flange surface) for determining axial and shear forces and bending moments imposed at the cross-section (stub column face). Three cable transducers were also placed between the strong shear wall and the front reaction frame at the elevation close to the centre of the concrete slab to monitor the in-plane displacements. A cable transducer was also installed under the test beam in line with the connection bolt line to measure the vertical deformation of connections.

Eight "donut" load cells (DLCs) with 20 mm inner diameter and a capacity of 220 kN each were used to measure the axial force transferring to the concrete slab. DLCs were placed between the end supporting beams and concrete slab edge channel sections, with the threaded 20M reinforcing bars passing through. All DLCs were calibrated prior to the first test and two more times afterward.

The purpose of using DLCs was to explicitly determine the net axial force transferred to the connection by subtracting the summation of horizontal components of actuator forces from DLC forces. Some of the DLCs were damaged during the tests due to the uneven distribution of forces caused at the concrete slab end. One of the reasons of uneven load distribution was an unavoidable gap between the channels cast into the slab and the slab anchorage beams, which caused some of the DLCs to carry more load. Even a small gap (2 mm) disengaged the DLCs from load sharing. Unfortunately, the DLCs did not perform well and in general the data was not used to measure the axial demand on

the connections. However, the data from those tests immediately after the DLCs were recalibrated and verified is used as a benchmark for an indirect method that computes the axial force on the connection based on the value of bending moment and position of the neutral axis with respect to the centreline of test beam. The method is explained in Chapter 4.

Since the deformation of the test specimens was mainly concentrated within the connection region, a linear variable displacement transducer (LVDT) was placed on the web of the test beam to directly measure the axial elongation of the connection along the centreline of the beam. Initially, a cable transducer was used to measure the axial elongation of connections, but due to the presence of white noise in the data acquisition system, after five tests the cable transducer was replaced with an accurate LVDT.

Two more LVDTs were mounted on the unstiffened stub columns and concrete slab. The LVDT mounted on the stub columns (shear tabs only) was used to monitor column flange deformation due to the axial demand on the connections. Another LVDT was placed underneath the concrete slab away from the connection to monitor any potential interfacial slip of the slab with respect to the test beam top flange.

A clinometer was mounted on each actuator to measure its rotation. Rotation of the test beam was also measured using a clinometer attached to the web along the centreline of the beam. As a redundant measurement, beam rotation was also calculated using the extensions and inclination angles of the actuators. The rotation was compared with the clinometer mounted on the beam web.

All instruments were processed using an HBM MGCplus data acquisition system (DAQ) with the capacity of 36 channels (24 channels of low-level voltage and 12 channels of high-level voltage). Load cells and pressure transducers were connected to the low-level channels, while cable transducers, clinometers, and LVDTs were linked to the high-level ones.

A total of up to 35 channels of data were recorded at the interval of two seconds (0.5 Hz) and about 70 additional parameters were calculated in real time by the

HBM catmanEasy software (V3.4.1). The catman software was used to simplify the acquisition, and to visualize and analyze the measurement data. It helped to monitor the data concurrently, which allowed checking the target parameters at each stage of loading to ensure the accuracy of the applied loading regime. Prior to each test, the initial geometry and position of the actuators with respect to the stub column were measured and recorded, as it was required for the data processing in the catman software during each test.

A Correlated Solutions system, as shown in Figure 3-12, was used to measure the surface strains in the region of interest close to the connection area. The monitored area was mill-scale ground, brushed, cleaned, and painted in white, and then was speckled with a pattern of black dots to provide the contrast for mapping surfaces. The system includes a set of two cameras located at two different angles, both taking high resolution images focused on the speckled area.

Commercial software Vic-3D (Version 2009) was used for post-processing the images by comparing the relative position of speckle points to the reference image (usually the first), to calculate strains, displacements, and rotations. The camera system was set to take images every four seconds. Prior to each test, calibration images using a calibration grid were taken to ensure quality and resolution of images based on the cameras' angle, distance from the speckle pattern area, and lighting. Figure 3-12 shows a set of cameras with two images of the speckle pattern and calibration.

### **3.6 Loading Regime**

It is widely accepted that in order to study progressive collapse behaviour of connections, consideration may be given to the affected spans by imposing appropriate boundary conditions to represent the surrounding structure. In the absence of a predefined loading protocol for testing specimens in a progressive collapse scenario, column removal has been adopted by guidelines and codes as a useful method by which the robustness of structural components is assessed by bridging a two-span frame over the local failure of the middle column. A loading

regime based on the column removal approach is believed to provide a gauge of capacity and ductility demands of components such as connections.

It is not always feasible to test a full frame, owing to the high associated costs and structural lab limitations. One method to carry out the test, while maintaining full scale, is to isolate the area of interest of the structure (usually connections) and define the load history due to the progressive collapse scenario in advance. Two such methods are presented below based on the equilibrium of forces and geometrical compatibility of displacements.

### 3.6.1 Equilibrium of Forces

The equilibrium of forces method outlines a basis for proportioning shear and axial forces and bending moment at each loading stage. Figure 3-13 shows a symmetrical double-span frame before and after column removal with a central point load and corresponding internal forces in one of the spans.

It was shown by Oosterhof and Driver (2015) and Astaneh (2007) that the moment resistance of shear connections is typically small and could be ignored in a progressive collapse scenario. Even though the moment resistance of shear connections is insignificant, once employed in a composite frame, the presence of the concrete slab adds a significant moment to the cross-section that could affect the behaviour of connections due to the shift of the neutral axis. Thus, the loading regime applied to the connections can be derived from the free body diagram shown in Figure 3-13, where the horizontal, vertical forces ( $H$ ,  $V$ ) and bending moments ( $M^+$ ,  $M^-$ ) are considered and are assumed to be centred on the steel connections. The resulting vertical force carried by each end section,  $V$ , in terms of horizontal force, bending moments, and the beam chord rotation angle,  $\theta$ , is given by:

$$V = H \tan \theta + \frac{M^+ + M^-}{L_s} \quad (3-1)$$

Equation (3-1) is the general form of the approach Oosterhof and Driver (2015) used for the loading history. They assumed equal bending moments would develop at the ends and thus the second term in Equation (3-1) was simplified to  $2M/L_s$ , which resulted in the inflection point (Figure 3-14) being located at the middle of span. However, this assumption is valid only if the two connections behave similar and are both placed at the centreline of the beam.

### **3.6.1.1 Point of Inflection (PoI)**

In the case of asymmetrical connections, such as those in composite construction, owing to the nature of the concrete slab being in tension at one end and compression at the other, the assumption of similar moments is no longer valid and the location of the inflection point (Figure 3-14) won't be located at the middle of span. In this case, the location of the PoI is highly dependent on the magnitude of positive and negative bending moments developed at the ends of the span during the various loading stages. Generally speaking, having identical cross-sections at both ends (shear connection plus concrete slab, as shown in Figure 3-15), the positive moment is usually larger than the negative moment due to the different flexural capacities and thus the inflection point is closer to the negative moment ( $M^-$ ) end.

Bending moment and migration of the PoI versus curvature for hogging and sagging moments ( $M^+$ ,  $M^-$ ) of one of the specimens (ST59B), with and without rebars, is shown in Figure 3-16. The graphs are merely based on the cross-sectional analysis without considering axial load. True stress-strain curves from the material testing were considered in the calculations.

As shown in Figure 3-16, the effect of rebars on the positive bending moment is insignificant, while the behaviour changes drastically for the hogging moment when rebars are added (increase of cross-sectional strength by nearly 300%). Thus, the location of the PoI varies between about 0.55 and 0.85 of the span length for the two extreme cases of slab with and without rebars. The detailing of

the cross-section at the hogging moment, including appropriate anchorage of the rebar, clearly plays an important role in pinpointing the point of inflection.

Figure 3-17 illustrates the migration of the neutral axis from its initial elastic position versus curvature for hogging and sagging moments of the specimen with and without rebars. For positive moment, the neutral axis shifts up dramatically as curvature increases, while except for very small curvatures prior to concrete cracking it remains nearly constant for the negative moment. Rebars change the migration of the neutral axis slightly for both moments. Intuitively, the neutral axis for negative moment remains at the centroid of the connection for slabs without rebars, meaning that no migration of the neutral axis is expected.

Due to the different rotational stiffnesses and evolutionary behaviours in composite beams under positive and negative bending moments, the behaviour of the hogging moment ( $M^-$ ) cannot be taken equal to that of the sagging moment ( $M^+$ ). Therefore, assuming that the inflection point is located at the middle of the span, as was considered by researchers investigating both bare and composite steel frames (Thompson 2009; Yang and Tan 2013a; Weigand and Berman 2014; Oosterhof and Driver 2015) would not be an accurate premise.

As explained earlier, once the concrete cracks in tension the inflection point migrates toward the negative moment end. Therefore, it is imperative to properly incorporate the inter-relationship of the end moments during the loading history, while only isolating and focusing on the connection at one end (“Testing Zone” in Figure 3-13). However, this is not a simple approach for determining the loading regime for the isolated connection without having knowledge of the projected behaviour of the other connection during each loading stage of progressive collapse simulation. Therefore, the unknown parameter in Equation (3-1) is the bending moment at the remote end ( $M^-$ ) when isolating the connection attached to the removed column. As such, high-fidelity models using the finite element software Abaqus (Dassault Systèmes 2013) were developed to capture the behaviour and failure of the remote connection (Jamshidi and Driver 2012; 2013; 2014). The numerical models confirmed that the two ends of the composite

beam exhibit markedly dissimilar behaviour. Chapter 6 discusses the finite element analysis results in detail.

To simplify Equation (3-1) for use during the tests, “M<sup>-</sup>” was taken as a fraction of “M<sup>+</sup>”, shown as a moment amplification factor ( $f_m$ ) in Equation (3-2). One complexity that makes this step very difficult to incorporate is that the neutral axes tend to migrate as the downward deflection is applied (as shown in Figure 3-17). The variation of the amplification factor versus beam chord rotation based on the finite element analysis for specimen ST36A is illustrated in Figure 3-18. The factor was found to have a relatively constant value of about 1.7 for the majority of steps after initial rotation.

$$V = H \tan \theta + \frac{M^+ + M^-}{L_s} = H \tan \theta + \frac{f_m M^+}{L_s} \quad (3-2)$$

Having the load combination history (Equation (3-2)) a priori, the test could be achieved by applying loads at three locations on a short cantilever beam, as shown in Figure 3-9. By adjusting the three actuator loads, a unique combination of shear force, bending moment, and axial compressive or tensile force can be achieved. The test procedure is explained in Section 3.7.

Equation (3-2) was only applied to the pilot test and specimen ST36A due to the limitation in predicting the true and instantaneous magnitude of the hogging moment. Even though the amplification factor ( $f_m$ ) was introduced to take into account the effect of hogging moment, numerical analysis based on the true day-of-testing material properties was essential prior to each test to extract the moment amplification factor.

Since one of the intents of the experimental program was to validate the numerical model, running a finite element analysis prior to each test to extract input for the load history put the equation in a closed loop, a condition that might call into question the rationality of the results. Therefore, an approach based on the compatibility of displacements was introduced to overcome the limitations encountered in the abovementioned method.



### 3.6.2 Geometric Compatibility of Displacements

Due to the limitation explained in the preceding section, a new approach relying on the geometric compatibility of the central removed-column deflection and the connections' deformation was developed. This technique correlates vertical deflection of the central column, axial deformation of the connections, and beam rotation based on simple trigonometry, as shown in Figure 3-19 and Figure 3-20.

Since only the portion of the span close to the removed column was considered as the testing zone, a mechanism is defined to capture the development of arching action in the span. Arching action develops as a result of unsymmetrical neutral axes at the two ends and axial restraint provided by the surrounding frames at both ends of the span. Thus, deformations are computed based on a simple strut and tie model (truss analogy), shown in Figure 3-19, to capture the arching/catenary action.

The line of arching action (strut line) is taken from the centroid of the concrete slab (located between, and close to, both the elastic and plastic neutral axes of the entire cross-section) above the bolt group near the removed column, to the centroid of bolt group at the other end. A tie member is drawn between the centroids of the shear connections at the ends. The angle developed between the strut and tie members is called the initial angle of arching action ( $\alpha$ ), which is the key parameter in developing the required axial force in the test. This parameter is calculated based on the original distance between the centre of the bolt groups of the two connections at the ends, and the eccentricity at the connection near the removed column (distance from the centre of the bolt group to the centroid of the concrete slab), as tabulated in Table 3-4.

A short span with a large eccentricity has a large initial arching angle, which significantly amplifies the resulting axial force. It is clear that in the absence of such an eccentricity, no arching action is established and catenary action develops immediately upon removal of the central column.

Based on the truss analogy illustrated in Figure 3-19, throughout the phase of arching action, connections attached to the removed column remain constantly in tension, while the far-end connections experience compressive force. Once arching action terminates, i.e., at the beginning of catenary action, both connections undergo tensile axial force. However, once arching action ends the connection attached to the removed column might already have failed and partial failure of the far-end connections might have occurred.

An idealized model that depicts the various phases of axial force development during arching/catenary action phases is graphically exemplified by Figure 3-21 and is tabulated in Table 3-5. The total axial elongation of the connections is assumed to be entirely attributed to the connection close to the removed column as long as the arching action exists. Once the arching action switches to the catenary phase, the elongation is attributed to both connections.

For a symmetric double-span frame, the central removed column is restrained to deflect downward. Thus, if the deformations of the surrounding frames and the elongation of the beams are neglected as being much smaller than the axial deformation of the shear connections, the deformation of the connections along the axis of the rotated beam prior to and after catenary action is summarized below. Full details of the computations are provided in Appendix A.

*Arching action:*

$$\delta_1 = \left( \frac{1}{\cos \theta} - 1 \right) L_r \quad (3-3)$$

$$\delta_2 = \left[ \frac{\cos \alpha - \cos(\alpha - \theta)}{\cos \theta} \right] \sqrt{L_r^2 + e^2} = \left[ \frac{\cos \alpha - \cos(\alpha - \theta)}{\cos \alpha \cos \theta} \right] L_r \quad (3-4)$$

$$\delta_{\text{axial}} = |\delta_1| + |\delta_2| = e \tan \theta \quad (3-5)$$

$$\Delta = L_r \tan \theta \quad (3-6)$$

*Catenary action:*

$$\delta_1 = \left( \frac{1}{\cos \theta} + \frac{1}{\cos \theta^{\text{arching}}} - 2 \right) \frac{L_r}{2} \quad (3-7)$$

$$\delta_2 = \left[ \frac{1}{\cos \theta} + \frac{1}{\cos \theta^{\text{arching}}} - \frac{2 \cos(\alpha - \theta^{\text{arching}})}{\cos \alpha \cos \theta^{\text{arching}}} \right] \frac{L_r}{2} \quad (3-8)$$

$$\begin{aligned} \delta_{\text{axial}} &= \delta_1 + \delta_2 \\ &= \left( \frac{1}{\cos \theta} - 1 \right) L_r + \left( \frac{1}{\cos \theta^{\text{arching}}} - 1 \right) L_r - e \tan \theta^{\text{arching}} \end{aligned} \quad (3-9)$$

$$\Delta = L_r \tan \theta \quad (3-6)$$

where  $\delta$  = connection axial deformation;  $\theta$  = beam chord rotation;  $\alpha$  = angle of original arching line;  $L_r$  = reduced span defined as the original distance between centre of bolt groups of two connections at the end;  $e$  = eccentricity;  $\Delta$  = vertical deflection of the central removed column;  $\delta_{\text{axial}}$  = total axial deformation of connections measured between the location of original column faces;  $\theta^{\text{arching}}$  = beam chord rotation at the end of arching action. Definitions of the aforementioned parameters are illustrated in Figure 3-20.

The local axial deformation of connections, as an example, for a span of 9.0 m is plotted in Figure 3-22. Appendix A provides more details on the results of local axial demands of connections generated by the above equations and plots are presented for a range of typical spans. Connections of beams with varying length undergo substantially different axial demand, as shown in Figure 3-23.

By increasing the span length, while keeping the eccentricity constant, arching action drops markedly. Therefore, connections in longer spans shift to catenary action more rapidly than those in shorter spans.

### 3.7 Test Procedure

The proposed loading regimes outlined in Section 3.6 were used to establish the testing procedures. The first approach, Section 3.6.1, was implemented to the pilot test and ST36A specimens, while the second method, Section 3.6.2, was used for the rest of the specimens.

The test was performed by successively applying incremental load steps to each of the actuators. Loading was applied to all tests until failure, a point at which the connection was damaged severely and no further residual capacity was gained.

#### 3.7.1 Procedure for Pilot Test and ST36A Specimens

Having three actuators provides liberty to produce a unique combination of horizontal force, vertical force, and bending moment at the connection. This allows the connection to undergo a loading profile, Equation (3-2) that is compatible with a column-removal scenario, without demanding construction of a two-span frame. Figure 3-24 illustrates the component of forces of each actuator with respect to the reference point (column face).

The loading procedure is controlled by three actuators at each finite load step, as shown in Figure 3-8. First, a small incremental rotation is applied using actuator 2. Having rotated the beam, the axial deformation in the connection is measured and then adjusted using actuator 3 based on the target deformation, which is the total elongation of each span solved geometrically by Equation (3-3) or Equation (3-7), depending on the phase of loading (arching or catenary). The target deformation requires the selection of a span length that is suitable based on the geometry of the connection being tested.

The iterative process to achieving the desired load history is summarised below and is illustrated in Figure 3-25 using a self-explanatory flowchart:

- Apply a small incremental rotation ( $\theta$ ) using actuator 2;
- Measure horizontal load at column face located at centroid of connection:

Horizontal Load:  $H = \sum H_i$

- Calculate the target required axial elongation ( $\delta_1$ ) based on the rotation and assumed span length (Equations (3-3) and (3-7)):

$$\delta_1 = \left( \frac{1}{\cos \theta} - 1 \right) L_r \quad \text{If } H < 0 \quad (\text{arching phase})$$

$$\delta_1 = \left( \frac{1}{\cos \theta} + \frac{1}{\cos \theta_{\text{arching}}} - 2 \right) \frac{L_r}{2} \quad \text{If } H > 0 \quad (\text{catenary phase})$$

- Adjust  $\delta_1$  using actuator 3;
- Measure loads at column face located at centroid of connection:

Bending Moment:  $M^+ = \sum (V_i d_{V_i} + H_i d_{H_i})$

Vertical Load:  $V = \sum V_i$

Horizontal Load:  $H = \sum H_i$

- Apply load using actuator 1 to approach the target shear force ( $V_{\text{target}}$ ) based on Equation (3-2). Moment amplification factor ( $f_m$ ) was taken to be 1.7.

$$V_{\text{target}} = H \tan \theta + \frac{f_m M^+}{L_s}$$

- Record loads ( $M^+$ ,  $V$ ,  $H$ ) and axial deformation ( $\delta_1$ );
- Iterate to failure.

Calculation of bending moment and vertical/horizontal loads at each stage of testing is illustratively shown in Figure 3-24. The projected arms of the actuators' force components for calculating moment were measured by using updated values from the cable transducers and clinometers at each stage of loading.

### 3.7.2 Procedure for Testing Rest of Specimens

Having the target displacements a priori, Equations (3-4) to (3-9), the test could be achieved by applying loads on a short cantilever test beam, as shown in Figure 3-9.

Rotation and axial deformation were applied quasi-statically to the specimens through the load beam using three actuators, as shown in Figure 3-28. The displacements were computed based on the planar geometry explained in Section 3.6.2.

The axial deformation is attributed entirely to the near-end connection up to the catenary action or connection's failure (whichever occurs first) and is divided equally between the two end connections afterward. Thus, Equations (3-3), (3-6), and (3-7) were used to test the specimens.

Since only a portion of the span was considered for testing ("Testing Zone" shown in Figure 3-26), to approximate the arching mechanism developed in the span, the initial position of actuators 3 was selected such that it would align closely with the arching line in the range of beam rotation angles corresponding to the expected maximum arching force.

Figure 3-28 illustrates the position of actuators 3 with respect to the lines of arching action at various loading stages.

The iterative process to achieving the desired loading protocol is summarised below and is shown in Figure 3-27 using a self-explanatory flowchart:

- Apply a small incremental rotation,  $\theta$ , by using actuator 2;
- For the applied rotation and assumed reduced span length ( $L_r$ ), calculate required vertical deflection, Equation (3-6):  $\Delta = L_r \tan \theta$
- Measure vertical displacement of actuator 2 ( $\Delta_2$ ) and calculate corresponding target deflection:  $\Delta_{\text{target}} = \left(\frac{L_r}{L_2}\right) \Delta_2$

where  $L_2$  is the horizontal distance from actuator 2 to the centroid of bolt group (shown in Figure 3-26)

- Adjust to  $\Delta_{\text{target}}$  using actuators 1 and 2;
- Measure horizontal load at centroid of connection located at stub column face:

Horizontal Load:  $H = \sum H_i$

- Calculate the target required axial elongation ( $\delta_1$ ) based on the rotation and assumed reduced span length (Equations (3-3) and (3-7)) :

$$\delta_1 = \left( \frac{1}{\cos \theta} - 1 \right) L_r \quad \text{If } H < 0 \text{ (arching phase)}$$

$$\delta_1 = \left( \frac{1}{\cos \theta} + \frac{1}{\cos \theta_{\text{arching}}} - 2 \right) \frac{L_r}{2} \quad \text{If } H > 0 \text{ (catenary phase)}$$

- Adjust  $\delta_1$  using actuator 3;
- Measure loads at column face located at centroid of connection:

$$\text{Bending Moment: } M^+ = \sum (V_i d_{V_i} + H_i d_{H_i})$$

$$\text{Vertical Load: } V = \sum V_i$$

$$\text{Horizontal Load: } H = \sum H_i$$

- Record loads ( $M^+$ ,  $V$ ,  $H$ ), axial deformation ( $\delta_1$ ), and vertical deflection ( $\Delta$ );
- Iterate to failure.

Figure 3-29 shows the connection axial deformation of one of the test specimens (DA59B). As seen, the connection axial deformation followed well with the required extension. However, arching action terminated slightly earlier than expected, which could be due to concrete slip and in-plane movement of the reaction frame.

It should be noted that the equations in Section 3.6.2 were derived simply based on the planar geometry compatibilities with no proper definition of composite section stiffness (connection + concrete slab) at both ends.

Figure 3-30 also depicts the required and measured vertical deflection for the same specimen (DA59B). It is acknowledged that the shear load developed in the simulated system for all specimens was relatively high because approaching the required vertical deflection forced actuator 1 to produce an artificially high vertical load. To partially compensate for this, the vertical deflection deviated intentionally from the target value slightly.

### **3.8 Ancillary Tests to Determine Material Properties**

To determine properties of the concrete and steel materials used in the testing program, a series of ancillary tests—including compressive concrete cylinder and steel tension tests—was conducted. Tests were performed in the I.F. Morrison Structural Engineering Lab at the University of Alberta.

#### **3.8.1 Tension Coupon Tests**

Plates and angles were specified as Grade 300W and test beams and stub columns as Grade 350W in accordance with G40.21-13 (CSA 2013). To precisely quantify the mechanical properties of the connections' material, i.e., shear-tabs and angles, a total of 20 tension coupon tests were performed. All plates and angles of the same thickness were fabricated from the same piece of material in order to minimize the number of coupon tests required. Extra material was provided by the fabricator from the same materials used in the specimens. Locations and details of coupons for both plates and angles are shown in Figure 3-31.

A total of six tension coupons were water-jet cut from each shear-tab plate. Three of them were cut parallel to the longitudinal direction and the other three were extracted from the transverse direction. Four coupons in the rolling direction were extracted using water-jet from each angle, i.e., two from each leg. No tension test was performed on the beams and columns as they were designed to remain elastic.

Tension tests were conducted in accordance with ASTM Standard A370-12a (ASTM 2012b). Tests were performed using an MTS 1000 universal testing machine. Load was measured by an internal load cell in the machine and the elongation measurement was taken by an extensometer with a gauge length of 50 mm. The loading rate was 0.125 mm/min up to the onset of strain-hardening, 1.25 mm/min until ultimate, and 2.5 mm/min afterwards until fracture. To obtain the static values of yield and ultimate strengths, loading was halted five times with 45 sec pauses at stresses on the yield plateau (three times), at ultimate, and prior to necking. As expected, the typical cup-cone fracture occurred for all



coupons as a result of considerable plastic deformation, which is a characteristic of a ductile fracture. Figure 3-32 shows the formation of a cup-cone fracture for one of the tension coupon tests.

Figure 3-33 and Figure 3-34 show the engineering stress–strain curves for the coupons cut from the 9.7 mm angles and 6.3 mm plates, respectively. The results of the tension coupons of the 6.3 mm plates exhibited only a very slight yield plateau, which is due to the rolling effects on the thin plates.

The modulus of elasticity was obtained from the slope of a linear regression curve fitted over the initial linear region of stress–strain curves. The values ranged between 190,000 MPa and 205,000 MPa. Yield and tensile strengths were found to satisfy the minima required by CSA Standard G40.21-13 (CSA 2013). For all coupons, the yield strain was about 0.17%, onset of strain hardening happened between 1.7% and 2.0% (except for the 6.3 mm plate coupons which showed no clear plateau), ultimate strain occurred in the neighbourhood of 18%, and rupture took place in a range of 31% to 37%. The mean values of the mechanical properties of the tension coupon tests are summarised and tabulated in Table 3-6. Values from the mill test reports for the beams and stub columns are also reported in the table. Further information about the results of individual coupon tests can be found in Appendix C.

### **3.8.2 Rebar Tension Tests**

Rebars (10M) were specified as Grade 400 in accordance with Standard G30.18-09 (CSA 2009). To precisely quantify the mechanical properties of rebars, a total of six tension tests were performed. All rebars were cut in a length of about 450 mm from the same pieces used in the concrete slabs. In order to measure the accurate diameter of the bars, the procedure of ASTM Standard E8/E8M-13a (ASTM 2013b) was followed. According to the ASTM method, the diameter was calculated from the cross-sectional area, which was calculated based on the mass of the specimen divided by the length and the density of the material

(7850 kg/m<sup>3</sup>). The average diameter was found to be 11.1 mm, close to the nominal value of 11.3 mm.

Tension tests were conducted in accordance with ASTM Standard A370-12a (ASTM 2012b). Tests were performed using an MTS 1000 universal testing machine. Load was measured by the machine's load cell and the elongation measurement was taken by an extensometer with a gauge length of 200 mm. The loading rate was 0.35 mm/min for the elastic zone, and 3.5 mm/min afterwards until fracture. To obtain the static values of the yield and ultimate strengths, loading was halted four times with 45 sec pauses at stresses on the yield plateau (three times), and at ultimate before necking.

Figure 3-35 shows the engineering stress–strain curves of the rebars. The modulus of elasticity was obtained in a similar manner to the coupon tests, with a mean value of about 192,000 MPa. Yield and tensile strengths were found to satisfy the minimum required values of CSA Standard G30.18-09 (CSA 2009). The static yield and ultimate stresses were close to 450 MPa and 650 MPa, respectively. For all tests, the yield strain was about 0.24%, onset of strain hardening happened between 0.85% and 1.05%, ultimate strain occurred in the neighbourhood of 14%, and rupture took place in the range of 20% to 25%. Mechanical properties of the tension tests are summarised and tabulated in Table 3-6. Further information about the results of individual tests can be found in Appendix C.

### **3.8.3 Concrete Cylinder Tests**

In order to obtain the mechanical properties of concrete specimens, 48 cylinders were cast at the time of pouring the slabs. Three samples were taken for each concrete slab (total of 15 slabs resulted in 45 samples), and three extra for the 28-day testing. (All slabs were cast from the same concrete batch.) Properties were determined at 28-days and on the date of each test. The procedure for measuring and testing the concrete cylinders followed ASTM Standards C39/C39M-12a and C469/469M-10 (ASTM 2012a; 2010).

Concrete cylinders were tested in an MTS 2600 rock mechanics testing machine. Load was measured by an internal load cell in the system and the deformation measurement was taken by an approved combined ASTM compressometer-extensometer device. Two highly accurate extensometers were installed on the compressometer: one vertically to measure the shortening (to calculate the vertical strain), and one horizontally to gauge expansion at the mid-section (to calculate the Poisson's ratio). A constant loading rate of 0.3 mm/min was applied throughout the test until crushing of the material took place. Typical fracture pattern Type 3, according to C39/C39M-12a (ASTM 2012a), was observed, which is defined as a columnar vertical cracking throughout both ends with no well-formed cones.

The mean density of concrete was found to be 2334 kg/m<sup>3</sup>. The mean value of the compressive strength of concrete ( $f'_c$ ) of all cylinders (excluding 28-day) was 29.4 MPa, which was in the centre of the range of design strengths of 25 MPa to 35 MPa. The mean strain ( $\epsilon_c$ ) corresponding to the compressive strength was about 0.22%. Modulus of elasticity and Poisson's ratio were calculated based on the procedure explained in C469/469M-10 (ASTM 2010). The mean values were found to be about 22,000 MPa and 0.15 for the modulus of elasticity ( $E_c$ ) and Poisson's ratio ( $\mu$ ), respectively. The mechanical properties of all concrete cylinder tests are summarised and tabulated in Table 3-7. Engineering stress-strain curves of concrete cylinders for one of the test specimens (DA59B) are shown in Figure 3-36. Further information about the results of individual cylinder tests can be found in Appendix C. The tensile strength of concrete is used for material modelling in the finite element analysis, which is explained in Chapter 5. In the absence of direct tension tests, the tensile strength ( $f_t$ ) was calculated in terms of compressive strength of concrete ( $f'_c$ ) as:

$$f_t = 0.33\sqrt{f'_c} \quad (3-10)$$

The tensile strength of concrete in flexure could also be taken as about 10% to 15% of the compressive strength according to Clause R10.2.5 of ACI Standard 318-11 (ACI 2011).

Table 3-1: Experimental Test Matrix

Connection Type	Number of Bolt Rows		Type of Slab* (Span Length)
	3 Bolts	5 Bolts	
Shear Tab (ST)	2 + 1 <sup>(Pilot Test)</sup>	2	A
	2	2	B
Double Angle (DA)	2	2	A
	2	2	B

\* Type A: Clear Span Length ( $L_s$ ) = 6.0 m and Slab Width ( $b_1$ ) = 1.50 m

\* Type B: Clear Span Length ( $L_s$ ) = 9.0 m and Slab Width ( $b_1$ ) = 2.04 m

Table 3-2: Specifications of Shear Tab Specimens\*

Specimen ID	Plate Thickness $t_p$ (mm)	Plate Length $l_p$ (mm)	Plate Width $w_p$ (mm)	Rows of Bolts	Bolt Dia. $d$ (mm)	Weld Size $D$ (mm)	Span Length $L_s$ (m)	Slab Width $b_1$ (m)
ST39A**	9.5	230	110	3	22	6	6.0	1.50
ST36A	6.4	230	110	3	19	5	6.0	1.50
ST36B	6.4	230	110	3	19	5	9.0	2.04
ST39A	9.5	230	110	3	22	6	6.0	1.50
ST39B	9.5	230	110	3	22	6	9.0	2.04
ST56A	6.4	390	110	5	19	5	6.0	1.50
ST56B	6.4	390	110	5	19	5	9.0	2.04
ST59A	9.5	390	110	5	22	6	6.0	1.50
ST59B	9.5	390	110	5	22	6	9.0	2.04

\* For Details Refer to Figure 3-5

\*\* Pilot Test

Table 3-3: Specifications of Double Angle Specimens\*

Specimen ID	Angle Thickness $t_p$ (mm)	Angle Length $l_p$ (mm)	Rows of Bolts	Bolt Dia. $d$ (mm)	Span Length $L_s$ (m)	Slab Width $b_1$ (m)
DA36A	6.4	230	3	19	6.0	1.50
DA36B	6.4	230	3	19	9.0	2.04
DA39A	9.5	230	3	22	6.0	1.50
DA39B	9.5	230	3	22	9.0	2.04
DA56A	6.4	390	5	19	6.0	1.50
DA56B	6.4	390	5	19	9.0	2.04
DA59A	9.5	390	5	22	6.0	1.50
DA59B	9.5	390	5	22	9.0	2.04

\* For Details Refer to Figure 3-6

Table 3-4: Initial Angle of Arching Action ( $\alpha$ )\*

Connection	$L_s$ (mm)	$g^\dagger$ (mm)	$L_r = L_s - 2g$ (mm)	$e$ (mm)	$\alpha$ (rad)	$2\alpha$ (rad)
Shear Tab (ST)	6000	75	5850	336.5	0.0575	0.1149
	9000	75	8850	336.5	0.0380	0.0760
Double Angle (DA)	6000	60	5880	336.5	0.0572	0.1143
	9000	60	8880	336.5	0.0379	0.0758

\* For Details Refer to Figure 3-19 and Figure 3-20

$\dagger$ : Distance from Bolt Line of Connection to the Column Face (Flange)

Table 3-5: Idealized Model of Axial Load Development in Connections of a Composite Floor Frame under Column Removal Scenario

Phase*	Axial Demand <sup>!!</sup>	Near-End Connection	Far-End Connection	Geometric Deformation	$\theta^\ddagger$
1 Arching	C	T <sup>†</sup>	C <sup>††</sup>	Eq. (3-3) <sup>N</sup> Eq. (3-4) <sup>F</sup>	$0 < \theta < \alpha$
	C	T	C	Eq. (3-3) <sup>N</sup> Eq. (3-4) <sup>F</sup>	$\alpha < \theta < 2\alpha$
3 Transition	0	T	C	Eq. (3-3) <sup>N</sup> Eq. (3-4) <sup>F</sup>	$\theta = 2\alpha$
4 Catenary	T	Probably Failed	T	Eq. (3-7) <sup>N</sup> Eq. (3-4) <sup>F</sup>	$\theta > 2\alpha$
	T	Failed	Failed	Eq. (3-7) <sup>N</sup> Eq. (3-4) <sup>F</sup>	$\theta > 2\alpha$

\* For Details Refer to Figure 3-21

<sup>!!</sup> Axial Demand Developed at Cross-section (Connection + Concrete Slab)

T<sup>†</sup>: in Tension

C<sup>††</sup>: in Compression

$\ddagger\alpha$ : Initial Angle of Arching Action

<sup>N</sup>: Near-End Connection (Attached Connection)

<sup>F</sup>: Far-End Connection (Remote Connection)

Table 3-6: Material Properties of Steel Coupons, Rebars, Test Beam, and Column

Type	Thickness / Diameter (mm)	Static Yield Strength $F_y$ (MPa)	Static Ultimate Strength $F_u$ (MPa)	Modulus of Elasticity $E$ (MPa)
Shear Tab	6.3	355.5	477.8	201,984
	9.5	300.1	439.5	197,227
Double Angle	6.6	346.7	498.9	192,763
	9.7	329.3	490.8	195,520
Test Beam*	---	375.2	493.3	---
Stub Column*	---	400.0	519.6	---
Rebar	11.1	454.3	656.6	192,869

\*Extracted from Mill Test Reports (MTRs)

Table 3-7: Material Properties of Concrete Cylinders

Specimen ID	Casting to Testing (Days)	Density $\gamma_c$ (kg/m <sup>3</sup> )	Compressive Strength $f'_c$ (MPa)	Strain at $f'_c$ $\epsilon_c$ (micro)	Modulus of Elasticity $E_c$ (MPa)
28-Day	29	2,299	24.2	1,858	20,412
ST36A	132	2,352	32.9	2,270	21,363
ST36B	139	2,345	31.7	2,182	22,640
DA36A	194	2,341	30.6	2,205	20,913
DA36B	200	2,309	28.0	2,496	18,941
DA56A	204	2,343	28.2	1,656	23,633
DA56B	211	2,343	29.1	1,986	22,095
ST56A	216	2,306	28.5	2,207	21,709
ST56B	231	2,337	28.9	2,244	21,093
ST39A	238	2,349	29.6	2,223	22,473
ST39B	239	2,323	27.3	2,300	20,377
ST59B	244	2,331	29.6	2,071	22,497
ST59A	246	2,353	30.9	2,122	23,528
DA39B	250	2,339	29.6	2,317	20,464
DA39A	252	2,337	30.6	2,224	23,119
DA59B	263	2,333	28.1	2,186	21,483
DA59A	264	2,310	26.6	2,263	20,443
Mean*		2,334	29.4	2,184	21,673
STD*†		15	1.7	180	1,290
CoV*††		0.6%	5.7%	8.2%	6.0%

\*Excluding 28-Day Test; †Standard Deviation; ††Coefficient of Variation

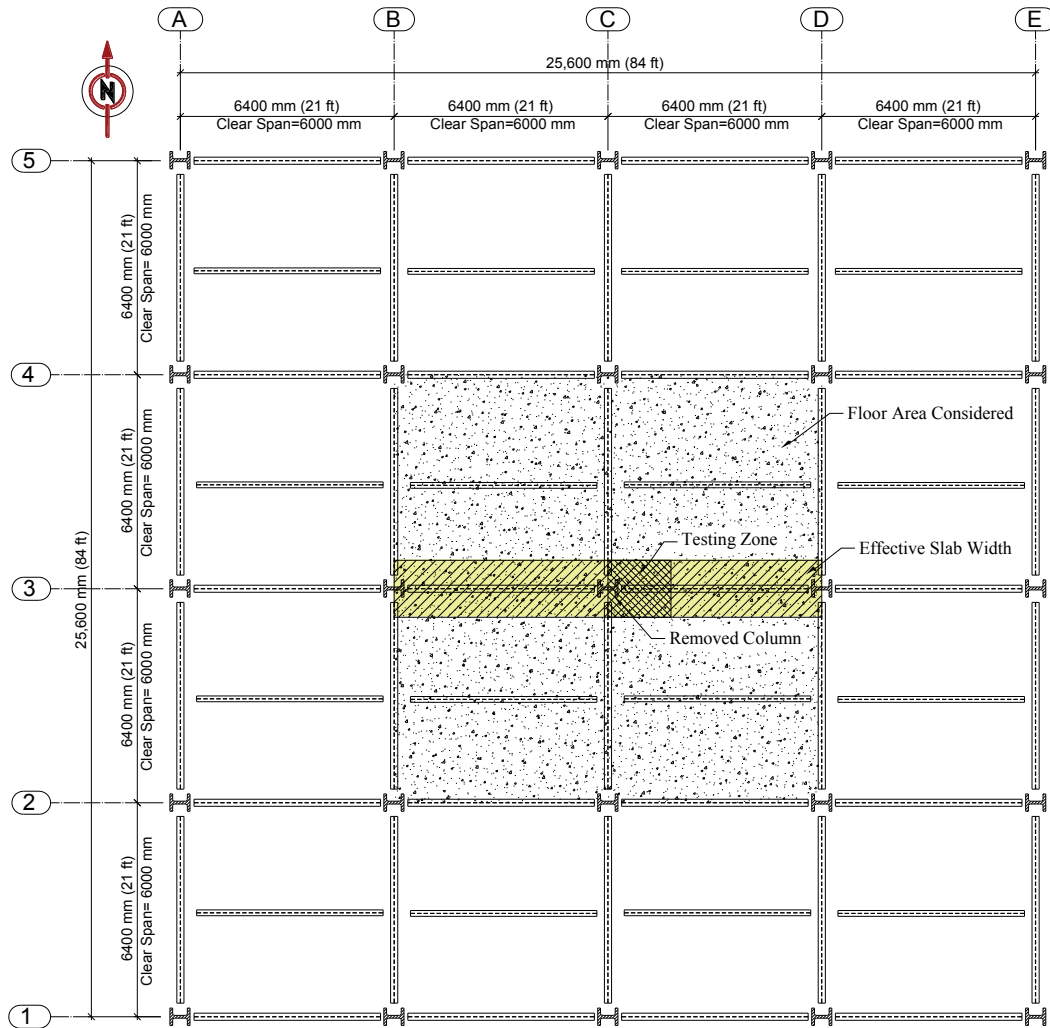


Figure 3-1: Plan Layout of 4x4 Bay Frame Building with Clear Span of 6.0 m

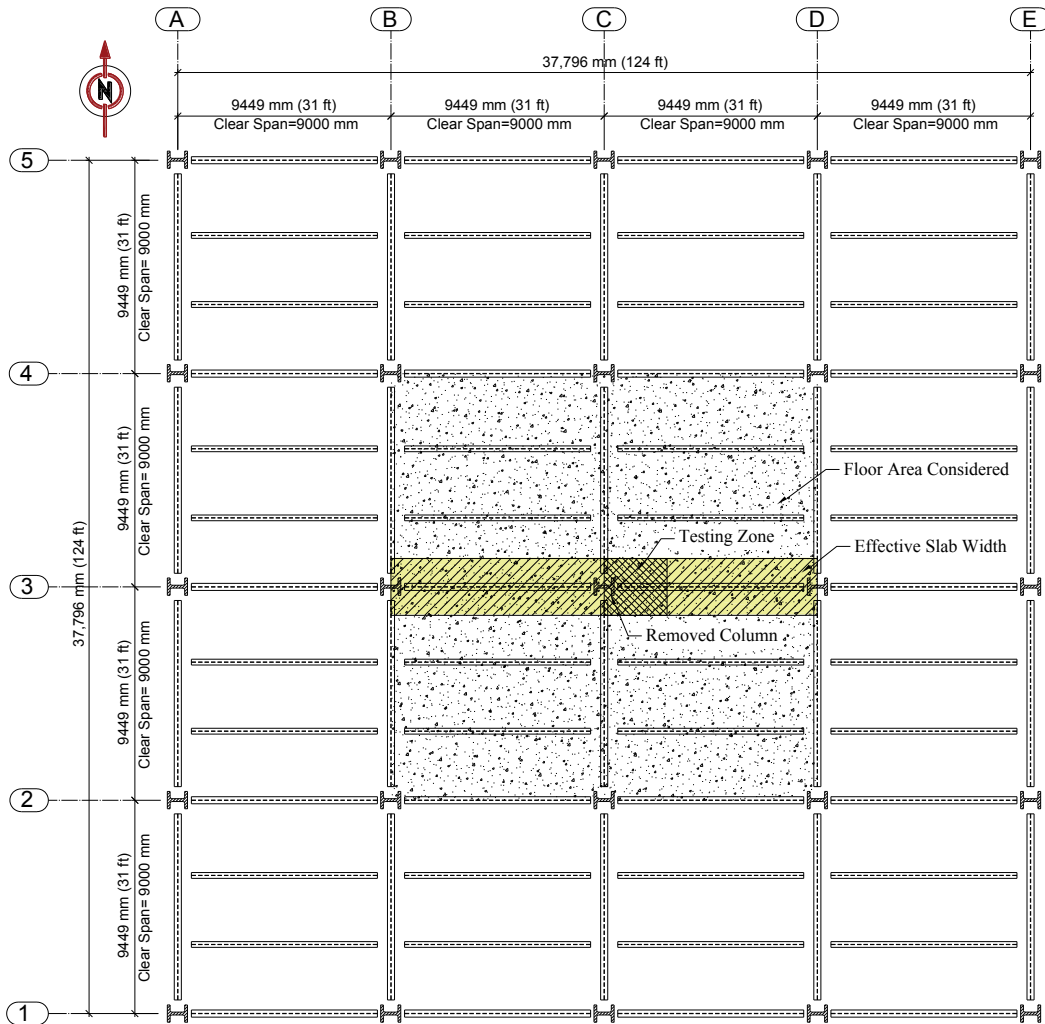


Figure 3-2: Plan Layout of 4x4 Bay Frame Building with Clear Span of 9.0 m



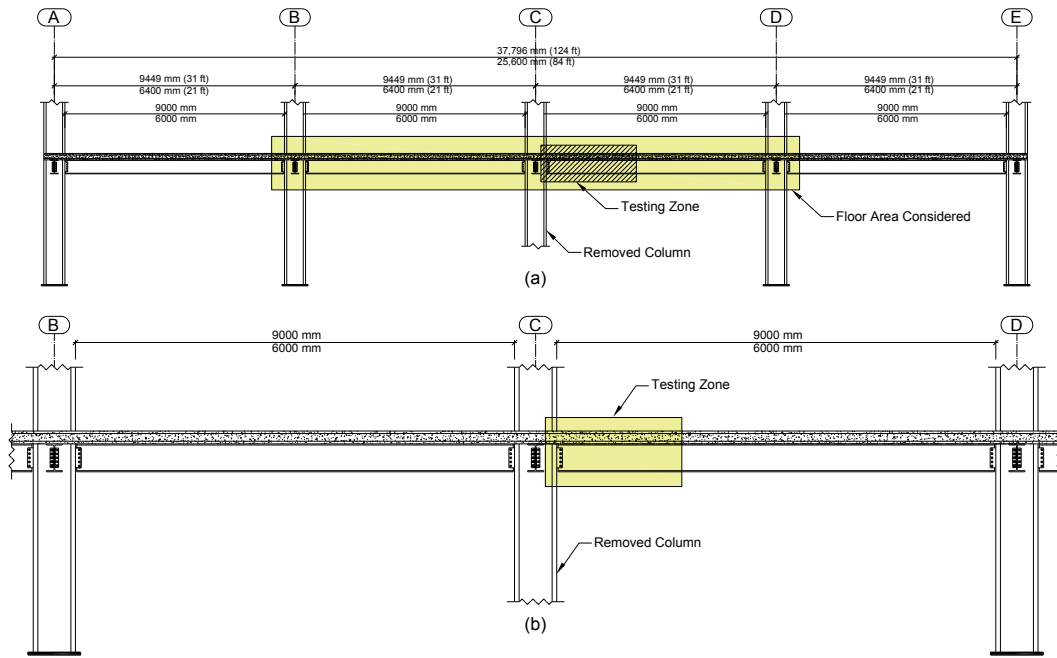


Figure 3-3: Elevation: (a) Prototype Frame Building; (b) Floor Area Considered

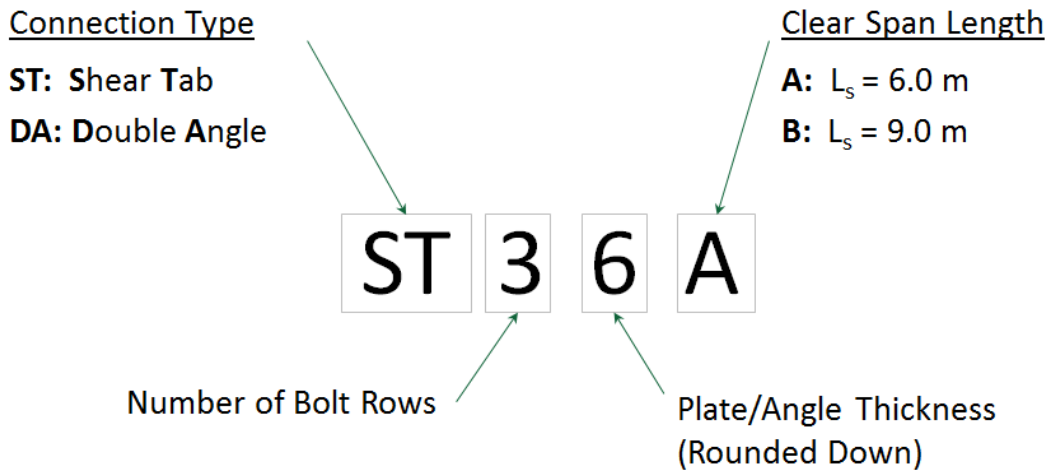


Figure 3-4: Convention for Specimen Designations

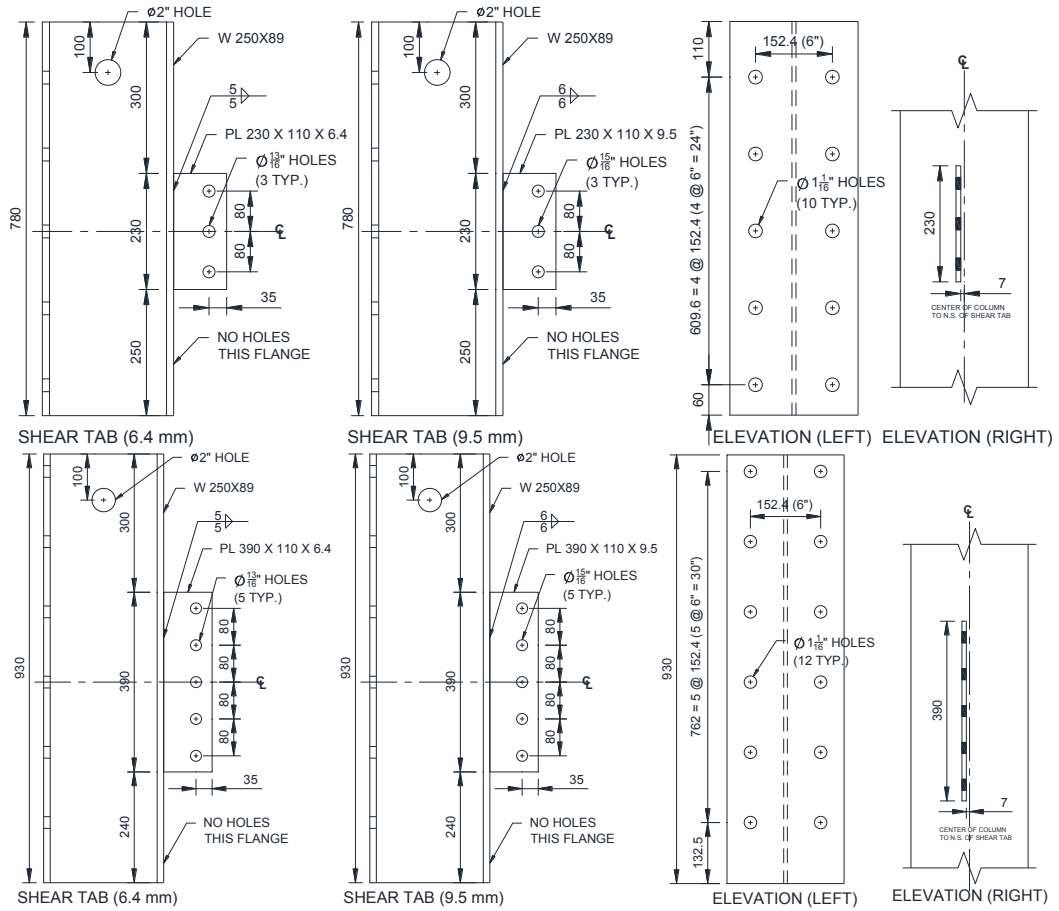


Figure 3-5: Details of Shear Tab Connections

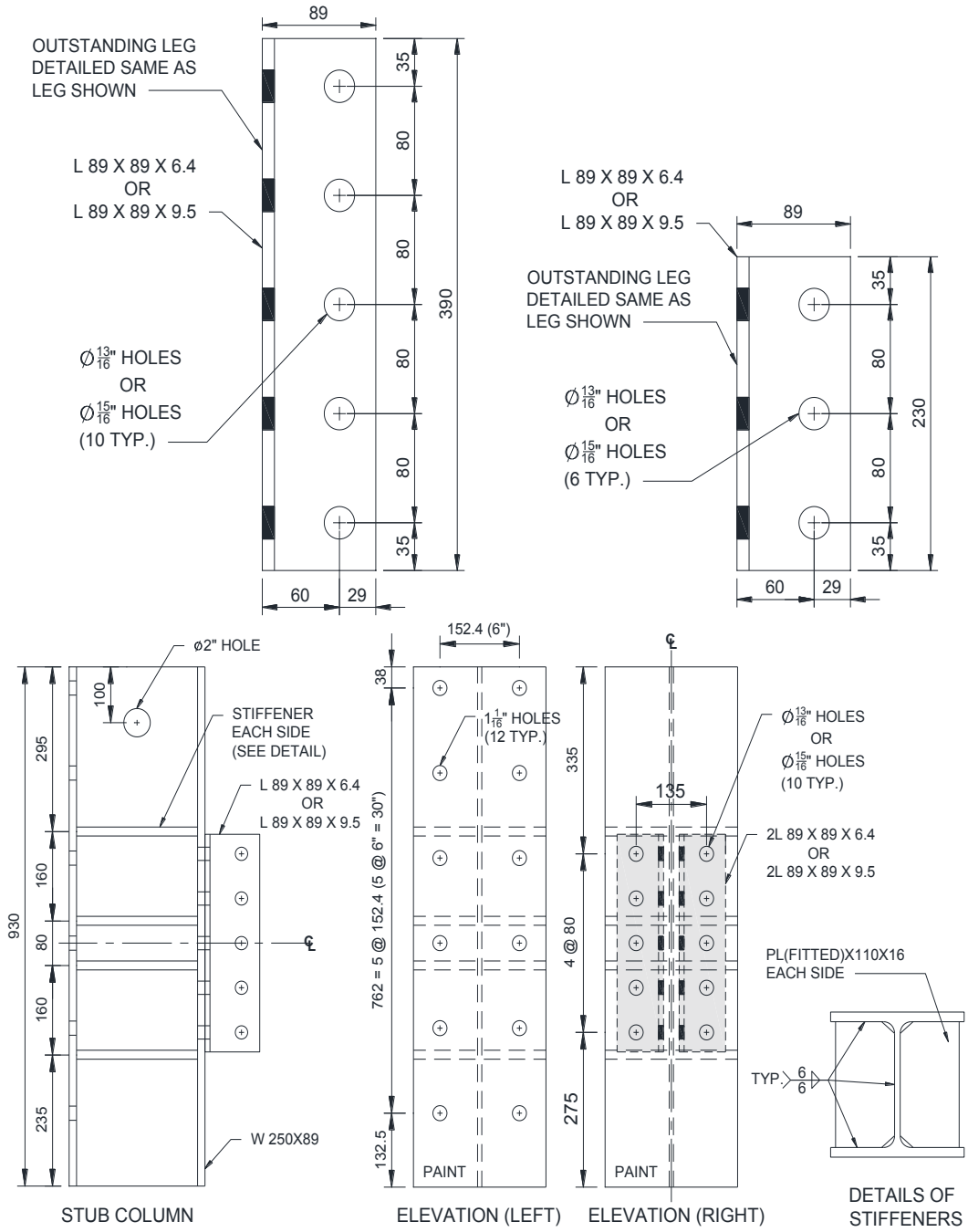


Figure 3-6: Details of Double Angle Connections

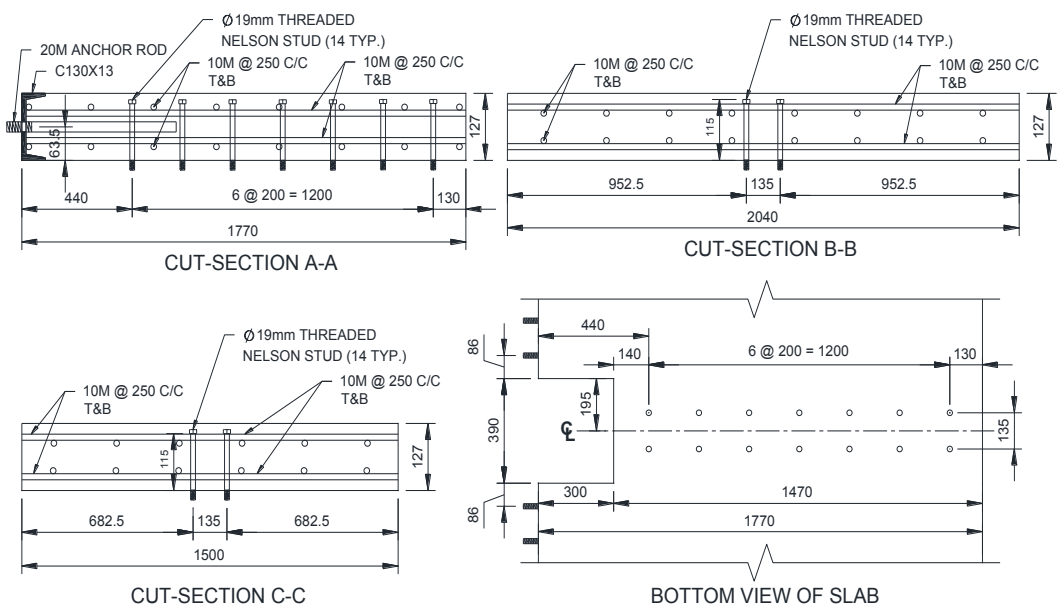
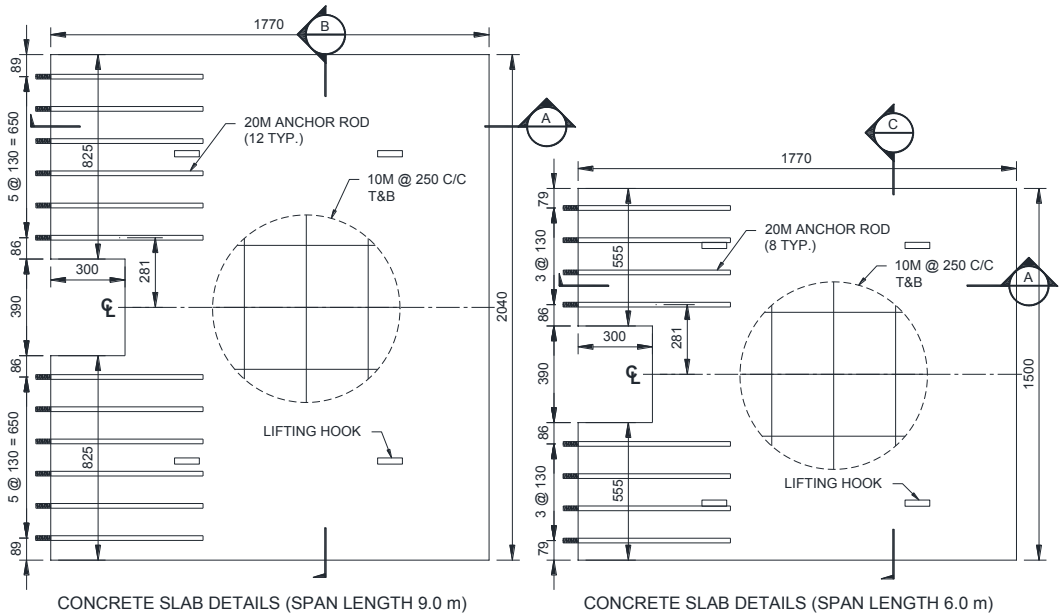
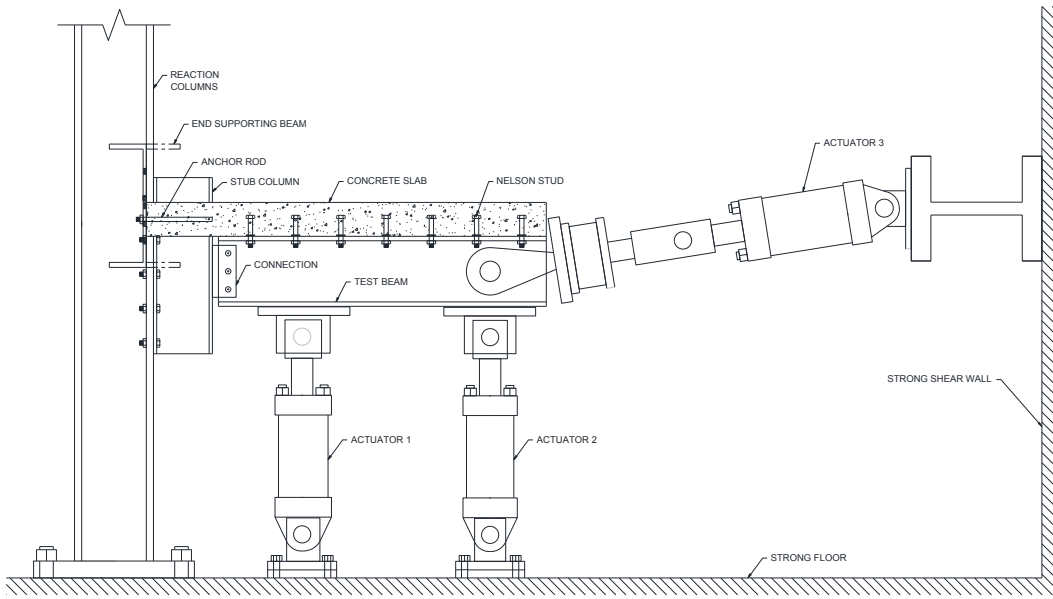
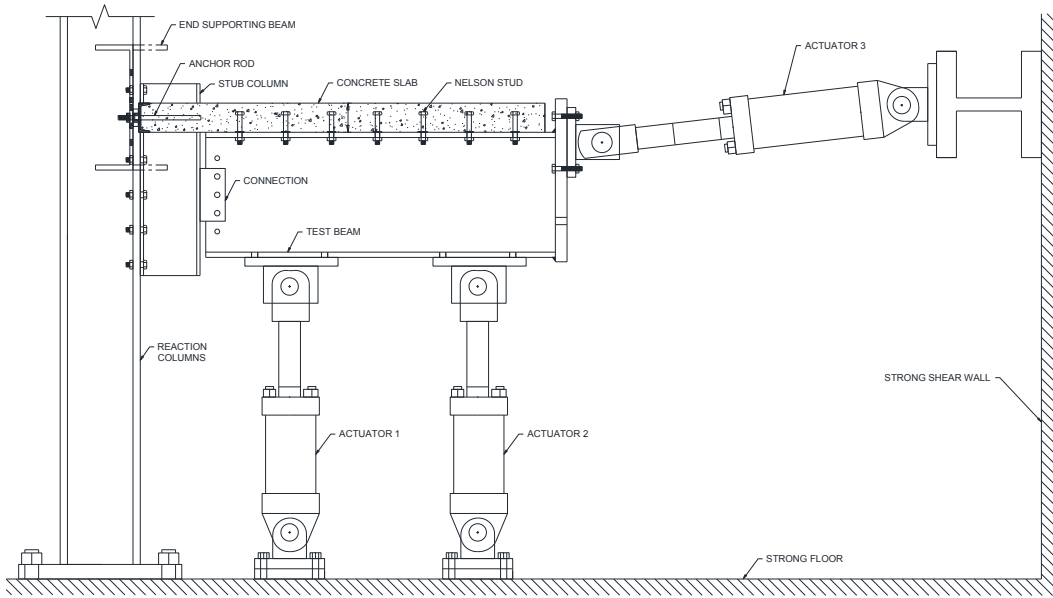


Figure 3-7: Details of Reinforced Concrete Slabs

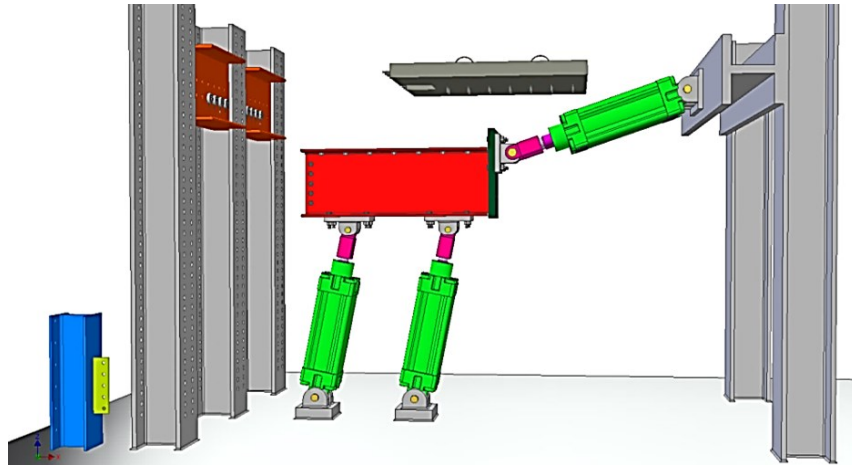


(a)

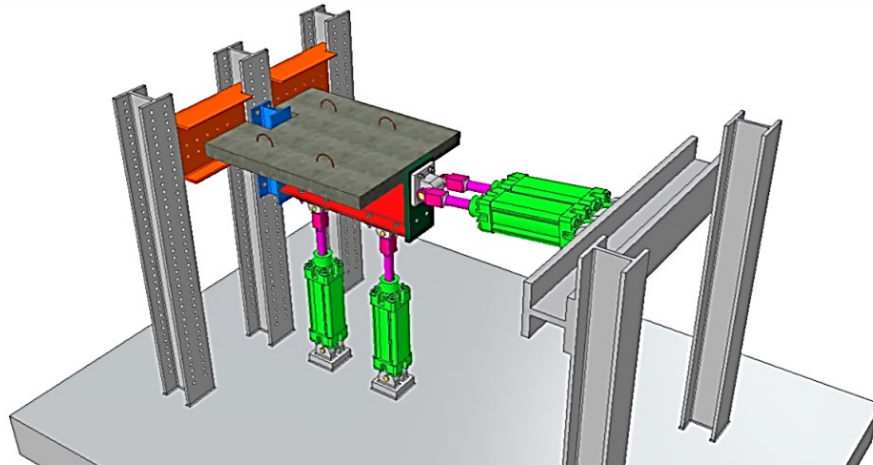


(b)

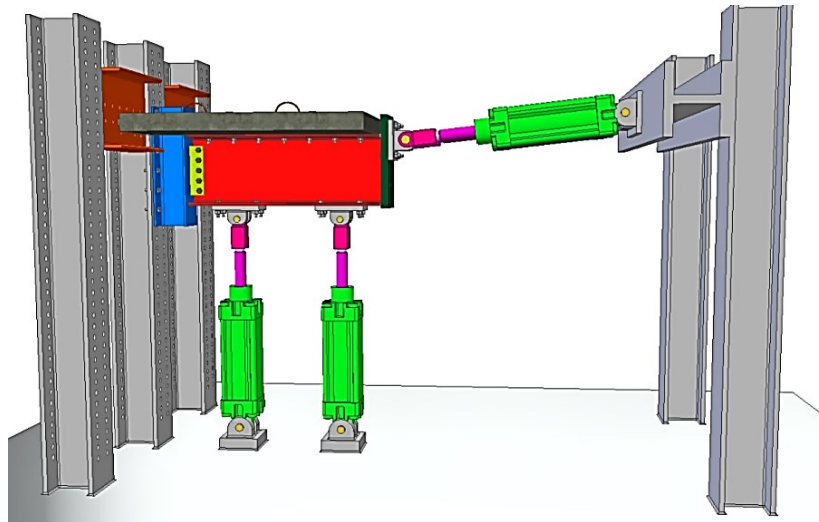
Figure 3-8: Elevation of Test Set-up for: (a) Pilot Test, ST36A, and ST36B;  
(b) Rest of Specimens



(a) Before Assembly



(b) After Assembly (Isometric View)



(c) After Assembly (Side View)

Figure 3-9: Schematic of Test Set-up

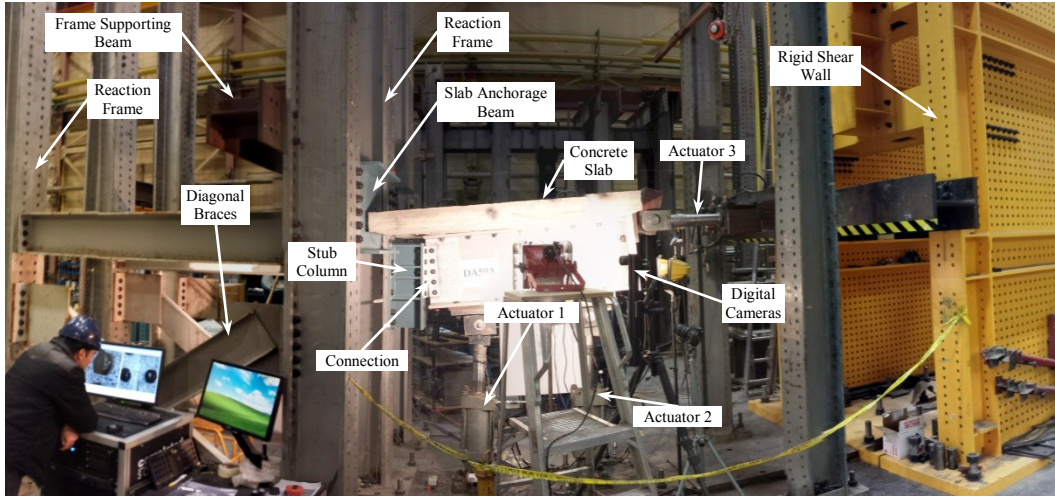


Figure 3-10: Assembly of Test Set-up and Position of Test Specimen Segments

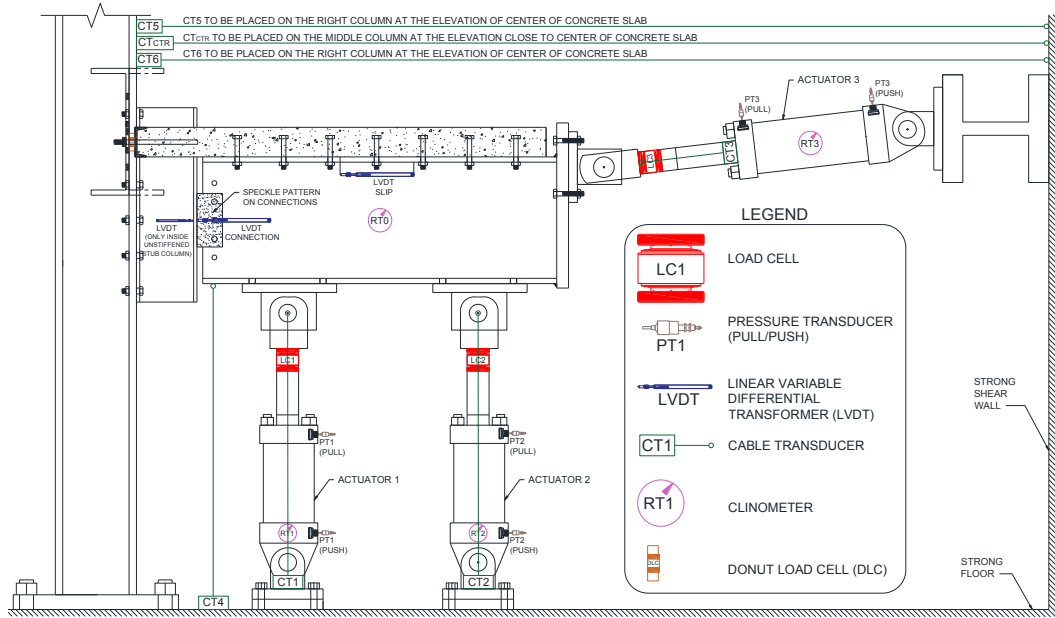
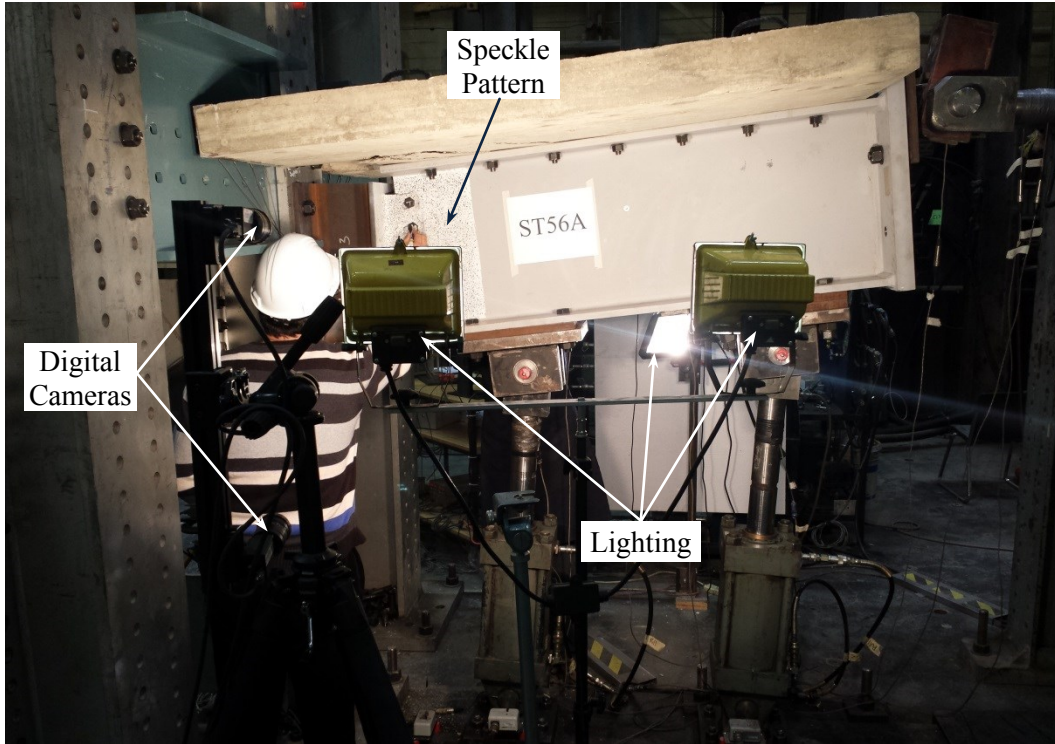


Figure 3-11: Instrumentation Layout



(a)



(b)

(c)

Figure 3-12: (a) 3D Digital Camera System; (b) Speckle Pattern on an Angle; (c) Calibration Prior to Test



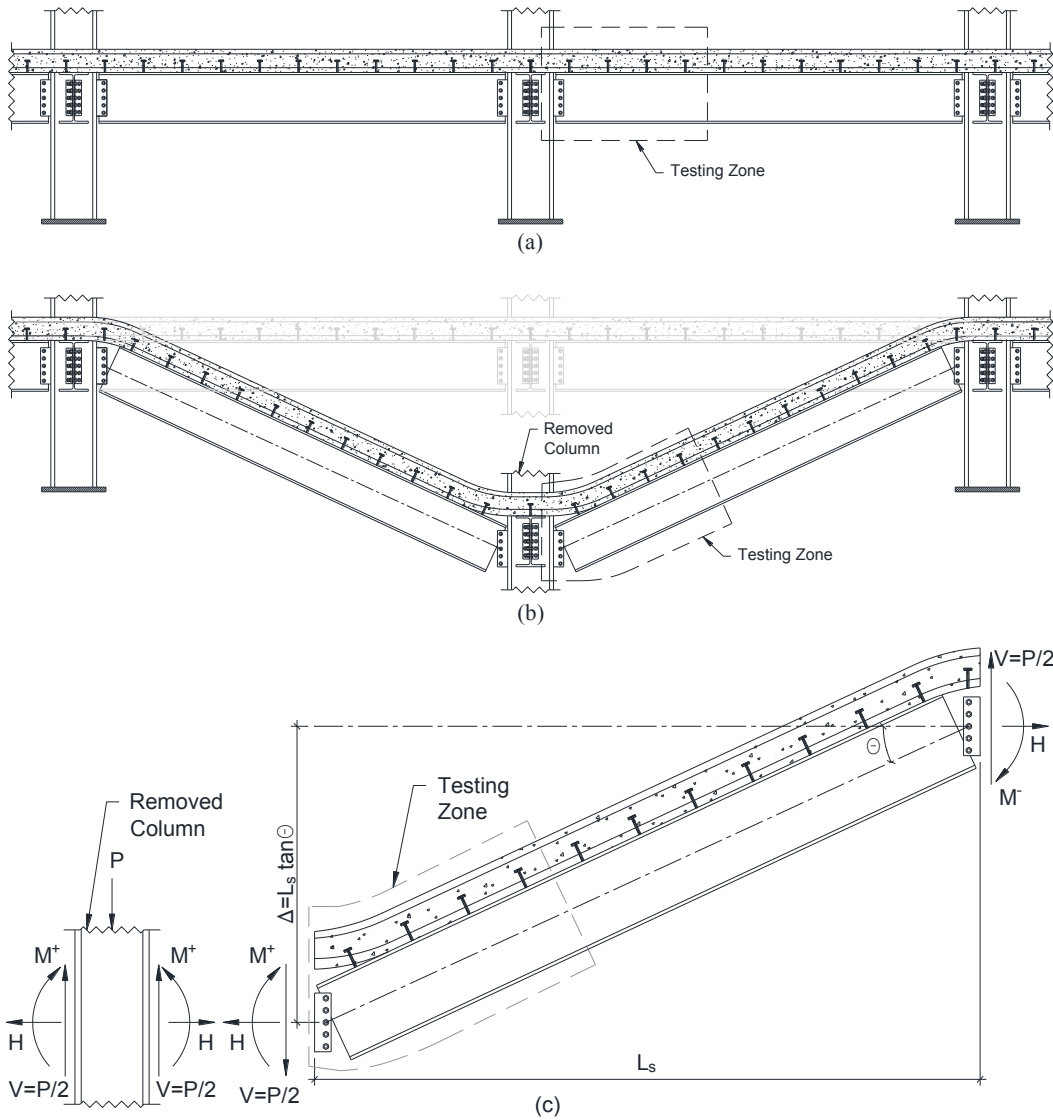


Figure 3-13: Double-span Frame: (a) Before Collapse; (b) After Column Removal; (c) Free Body Diagram

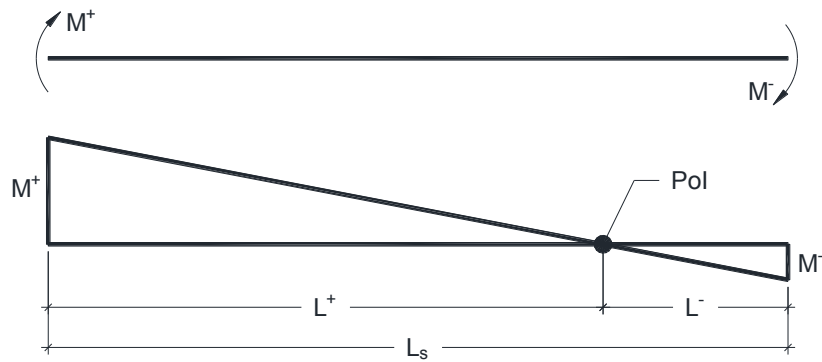


Figure 3-14: Moment Distribution and Point of Inflection (PoI)

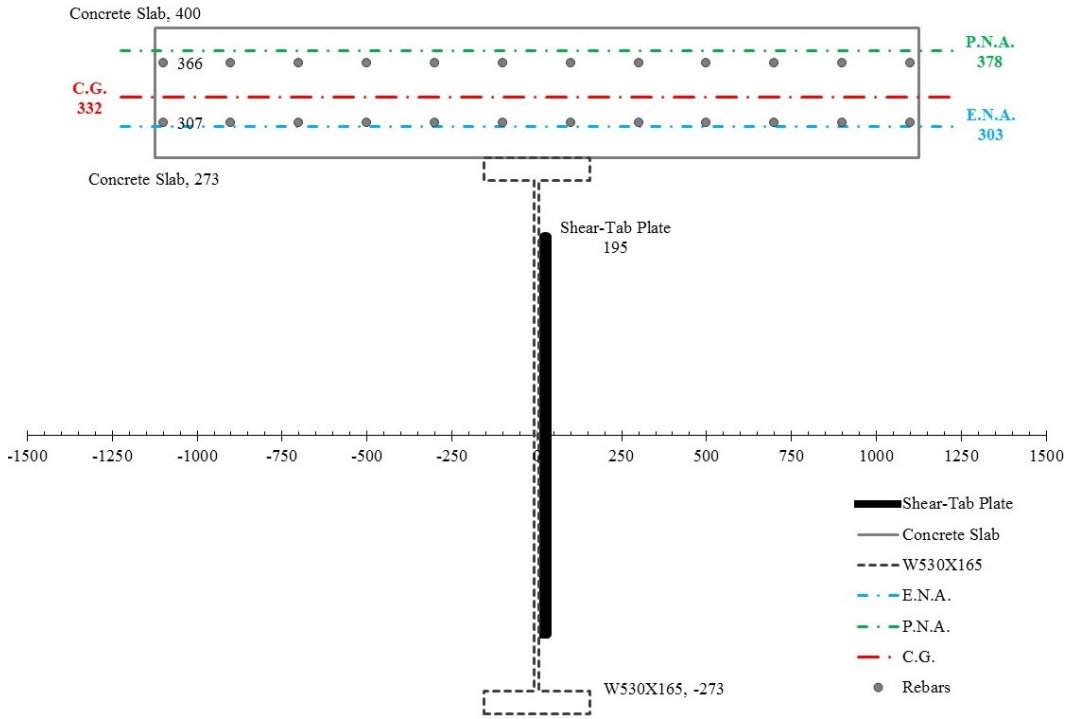


Figure 3-15: Cross-sectional Properties of ST59B Specimen

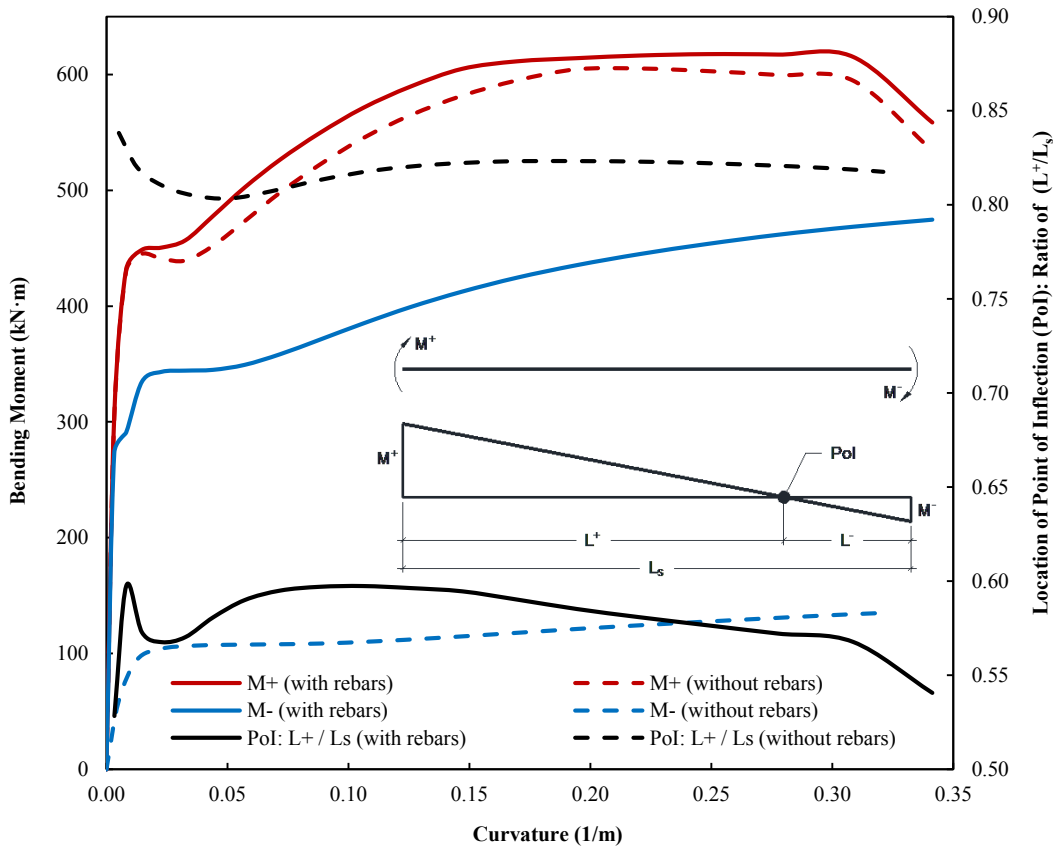


Figure 3-16: Moment-Curvature Diagram for Cross-section of ST59B Specimen

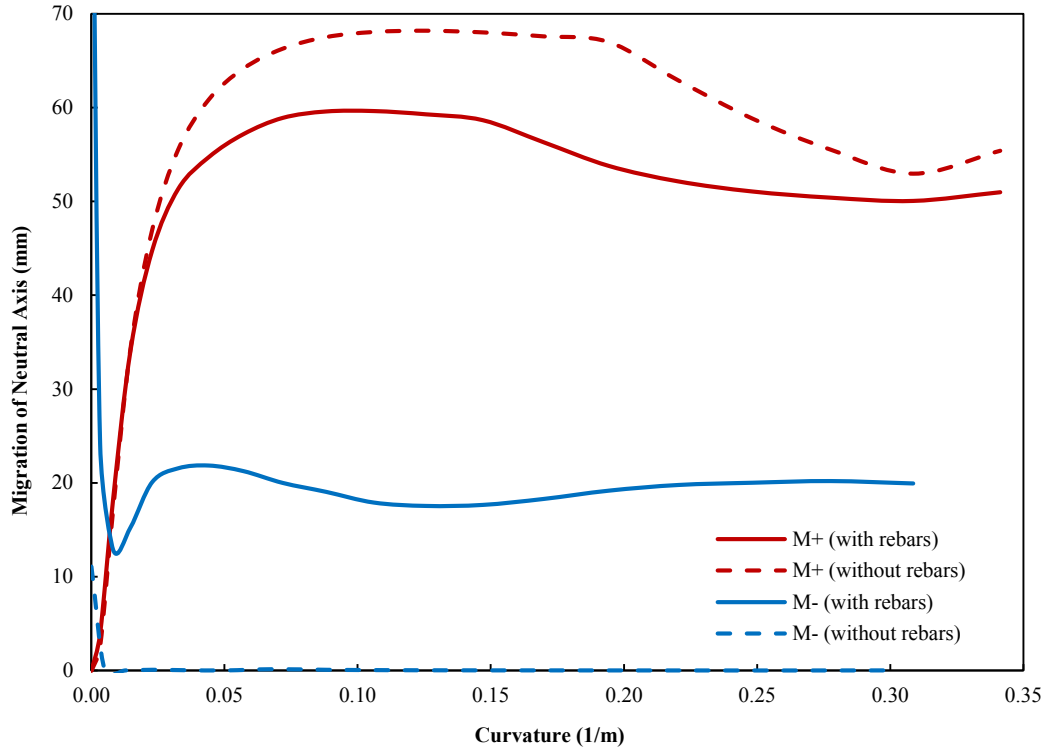


Figure 3-17: Migration of Neutral Axis from Initial Elastic Position versus Curvature (Cross-section of ST59B Specimen)

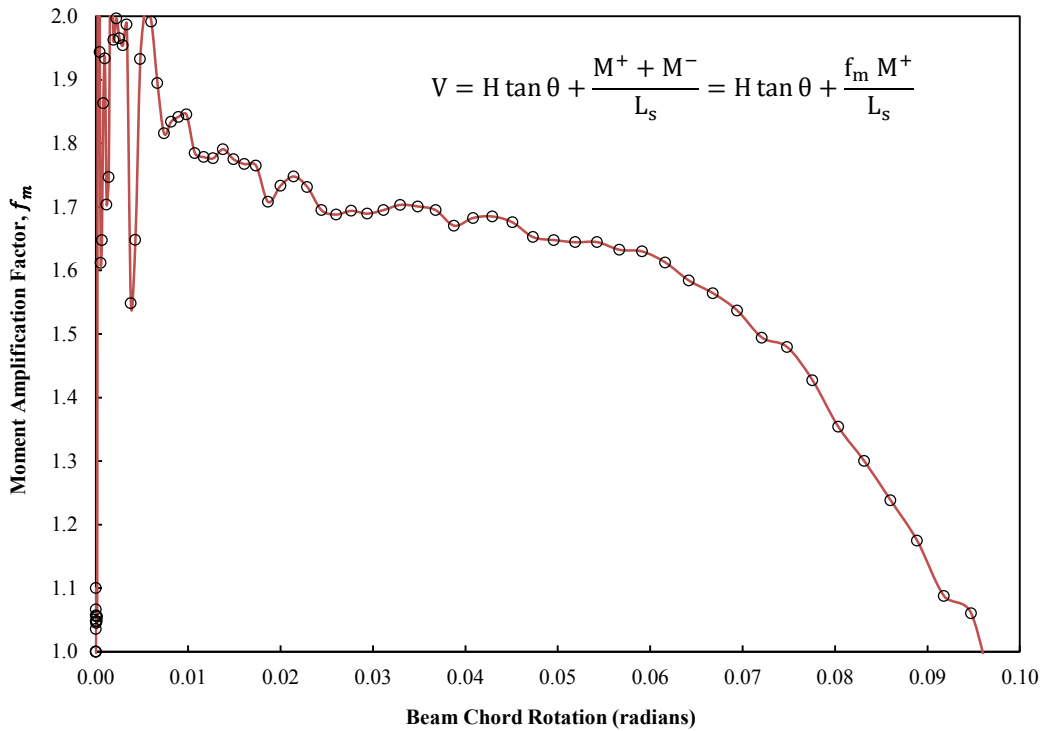


Figure 3-18: Moment Amplification Factor ( $f_m$ ) versus Beam Chord Rotation for ST36A Specimen based on Finite Element Analysis

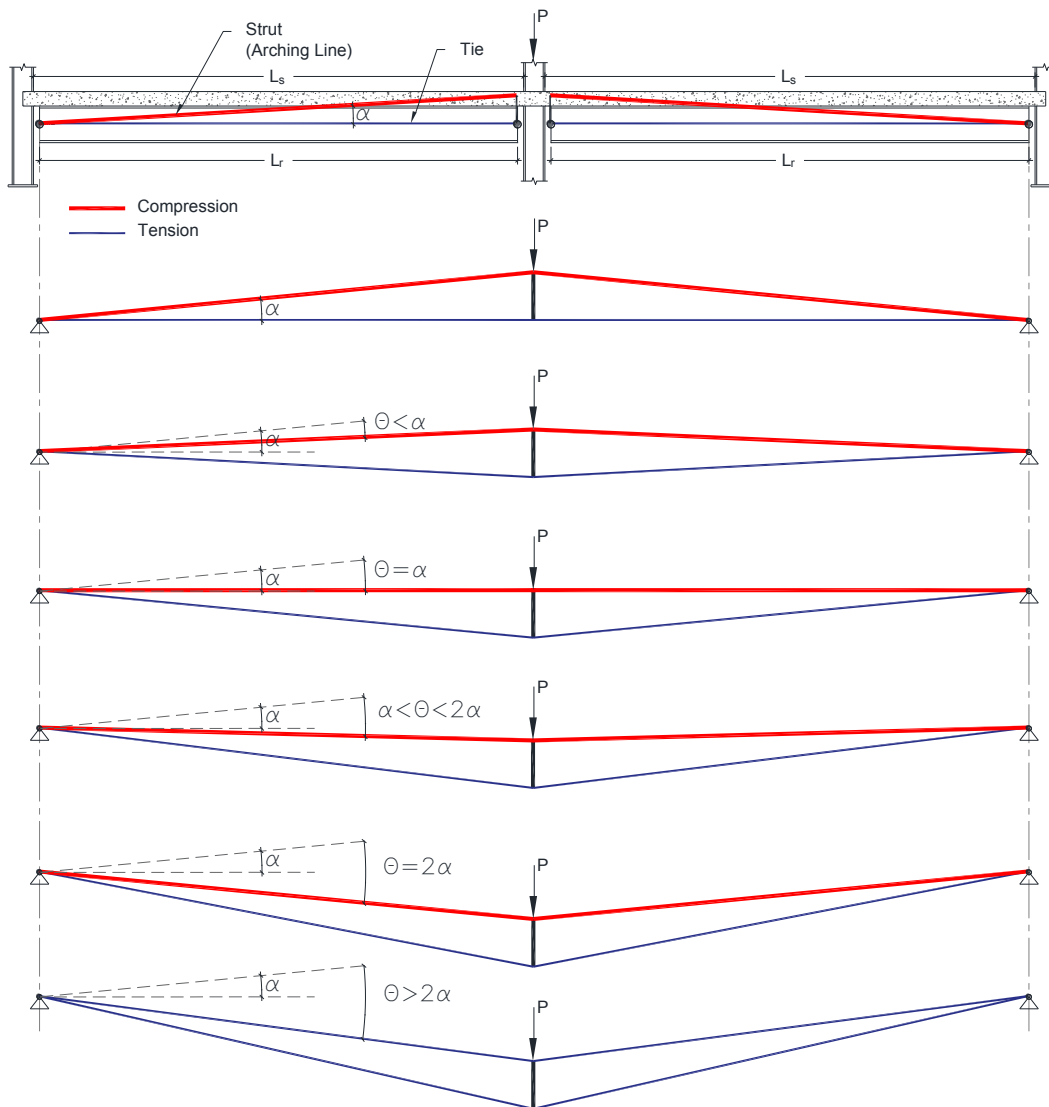
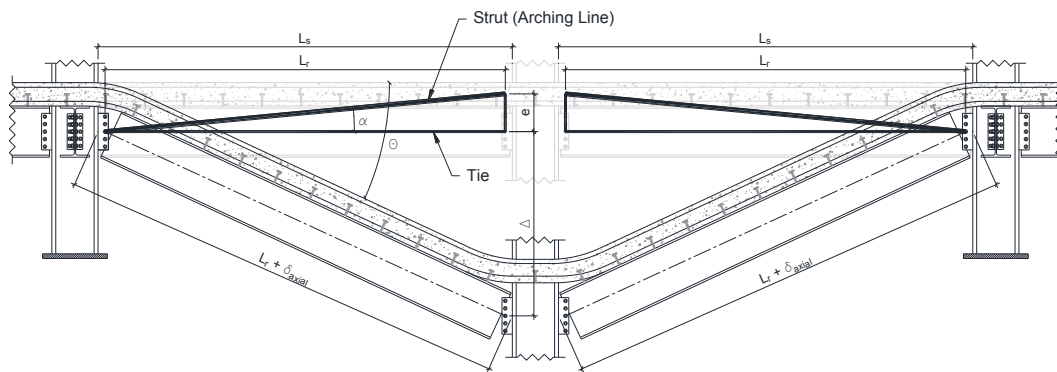


Figure 3-19: Strut and Tie Model (Truss Analogy)

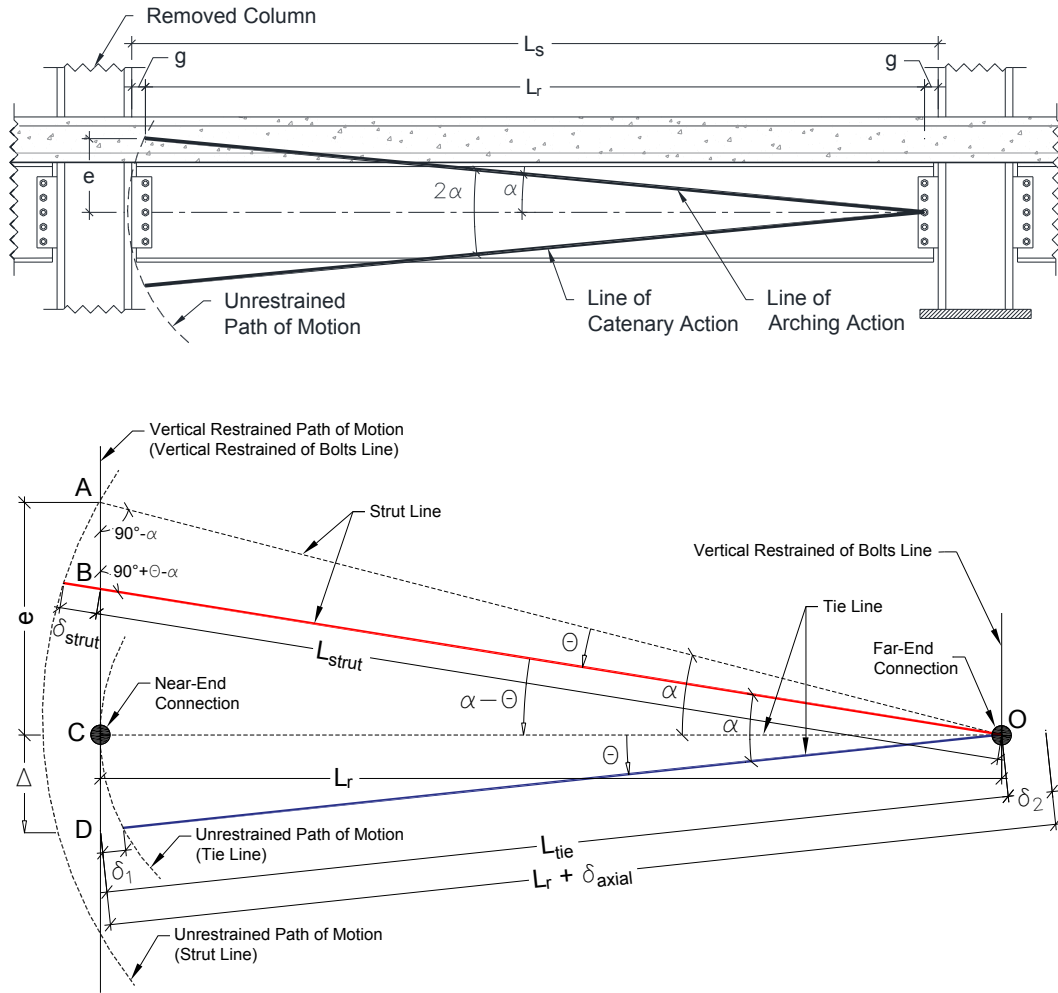


Figure 3-20: Geometric Compatibilities of Displacements (From Appendix A)

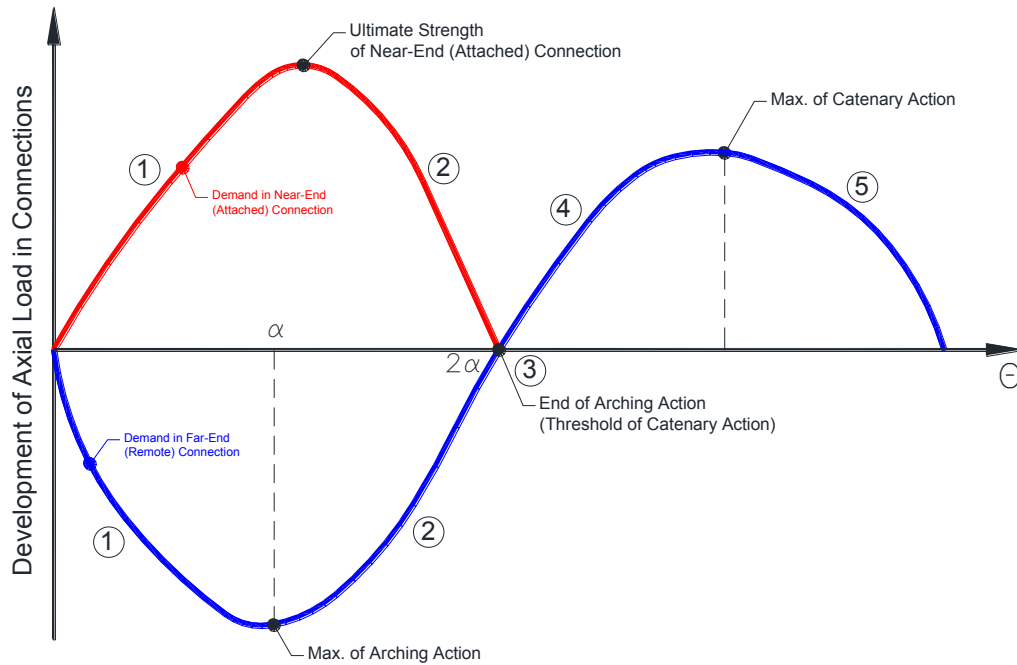
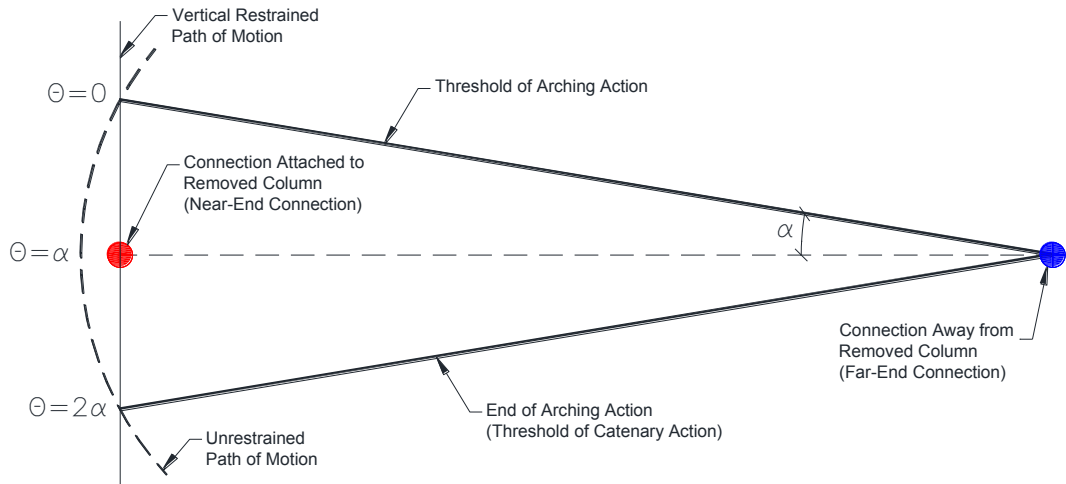


Figure 3-21: Development of Axial Load in Connections of a Composite Floor Frame under Column-Removal Scenario (For Details Refer to Table 3-5)

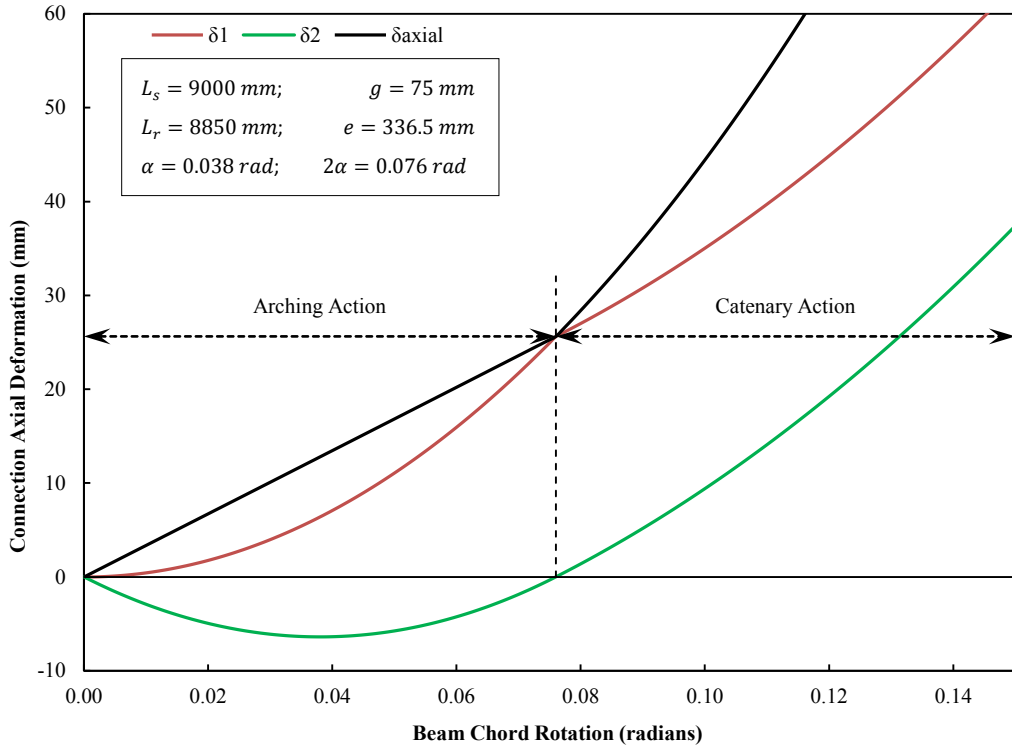


Figure 3-22: Axial Deformation of Connections with Span of 9.0 m (From Appendix A)

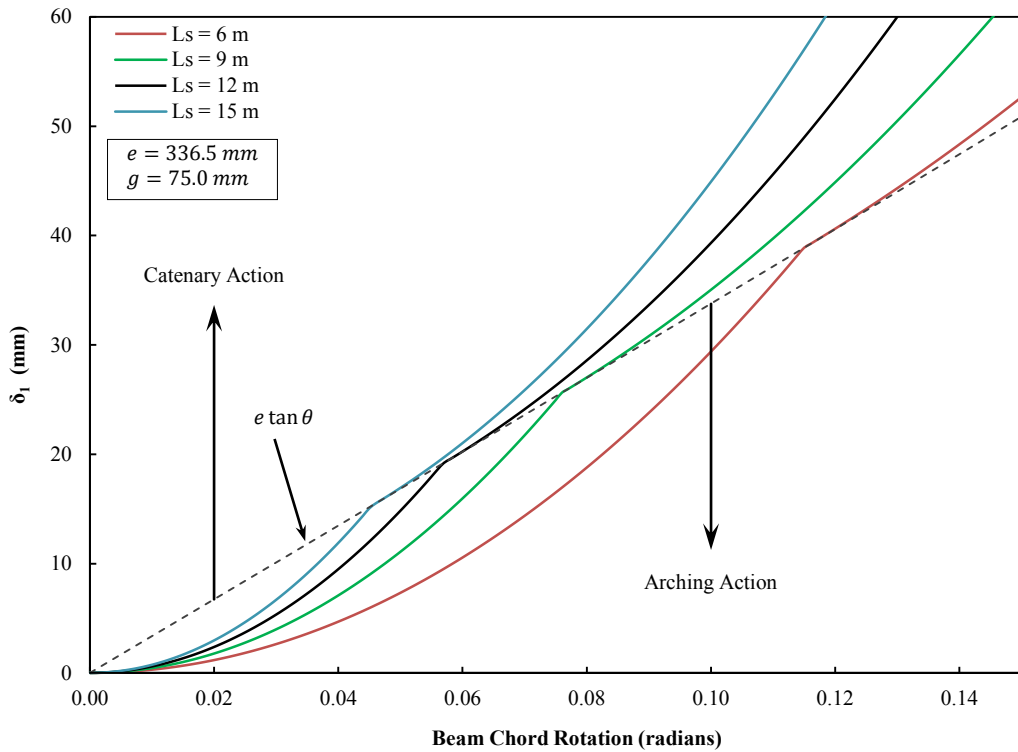


Figure 3-23: Axial Deformation of Near-End Connection (From Appendix A)

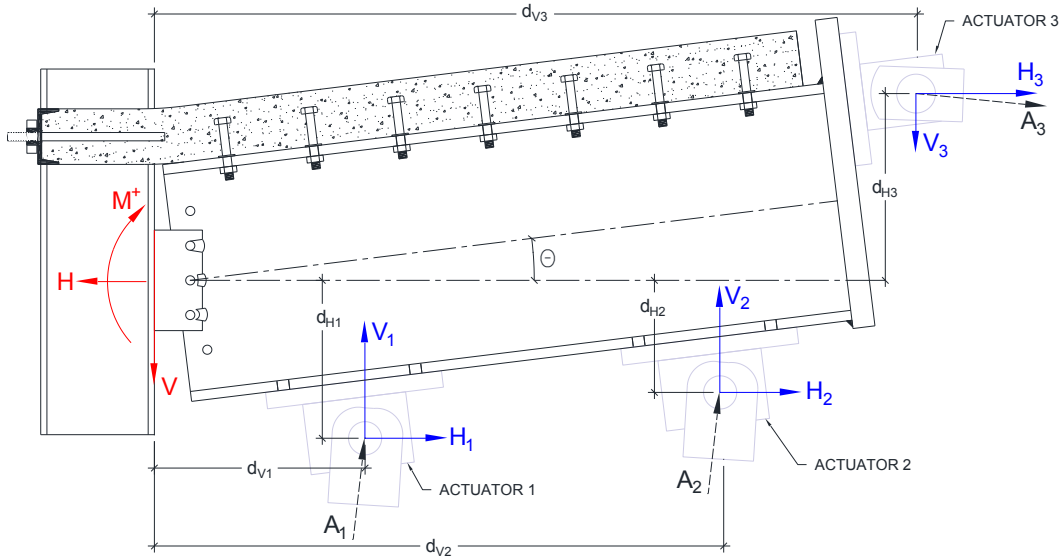


Figure 3-24: Force Components of Actuators in the Test Set-up for Calculation of Internal Forces Applied at the Column Face

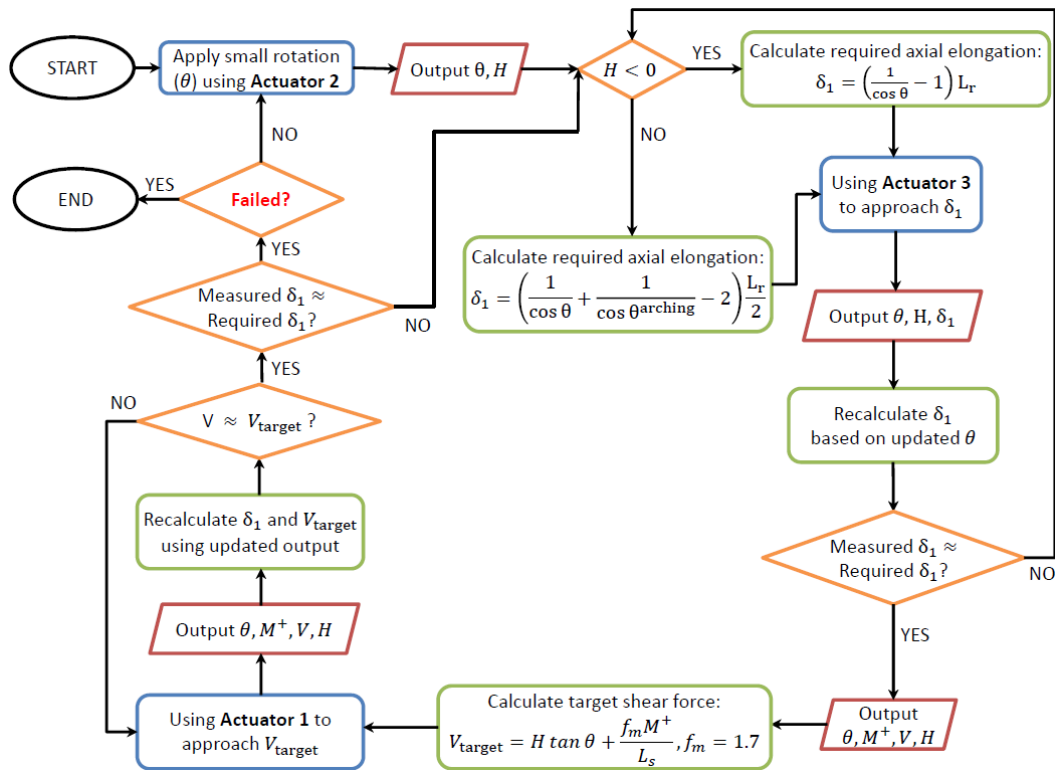


Figure 3-25: Loading Regime Flowchart used for Pilot Test and Specimen ST36A



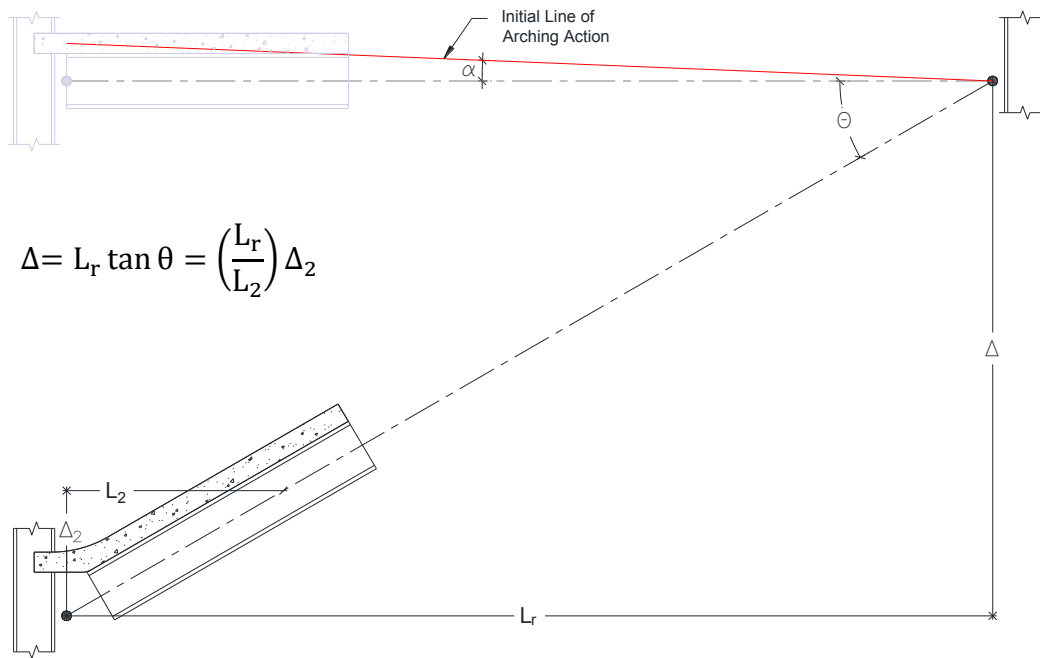


Figure 3-26: Position of Testing Zone Subassembly within the Span

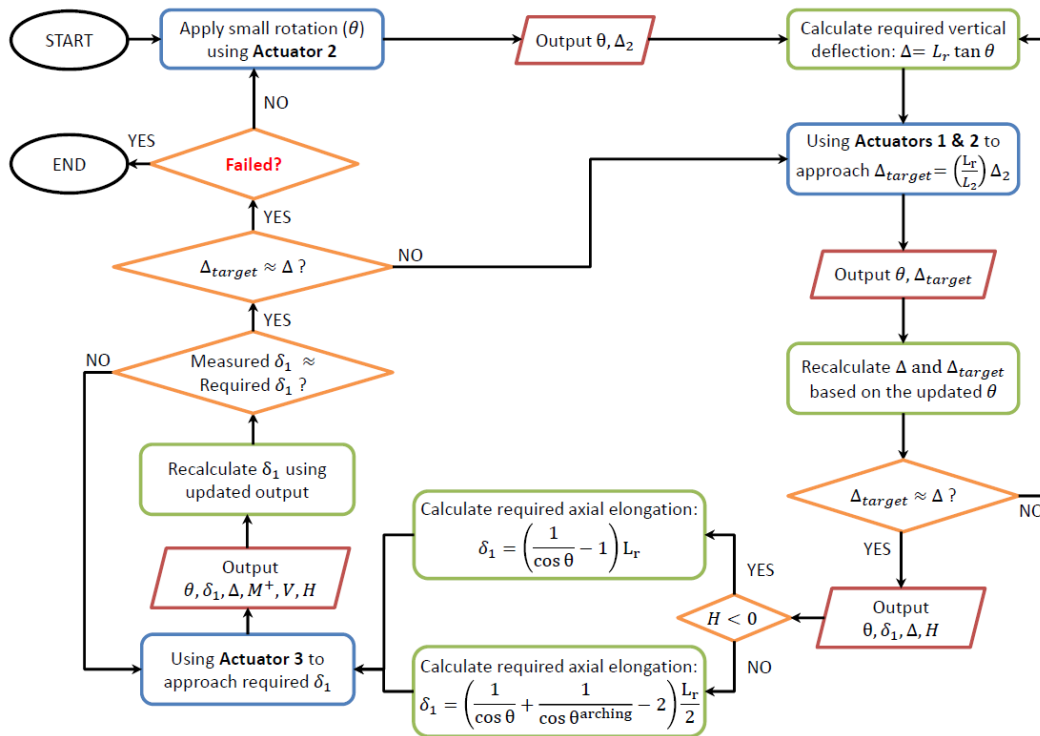


Figure 3-27: Flowchart of Loading Regime used for Remaining Specimens

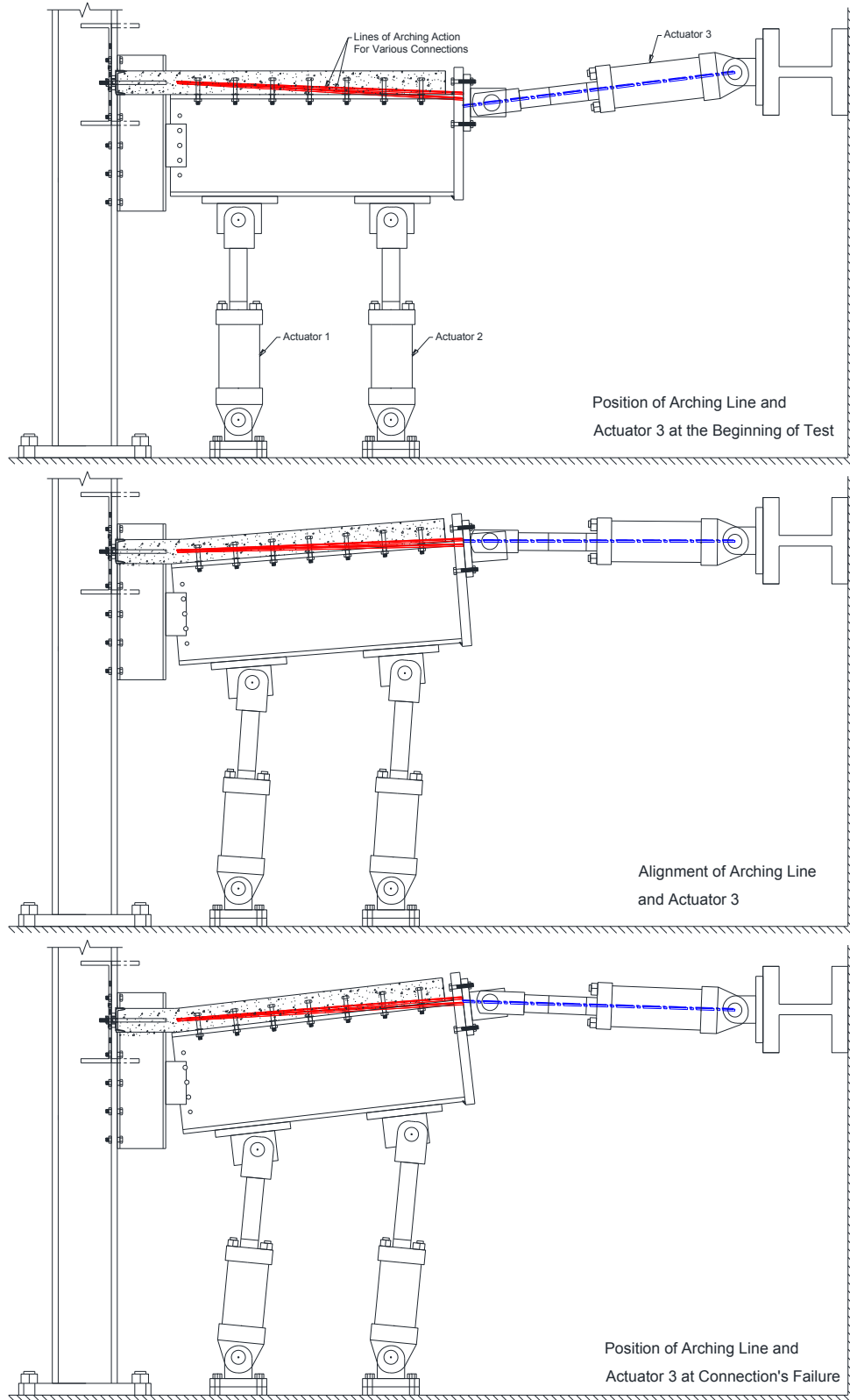


Figure 3-28: Position of Arching Line and Actuators 3 at Different Stages of Loading

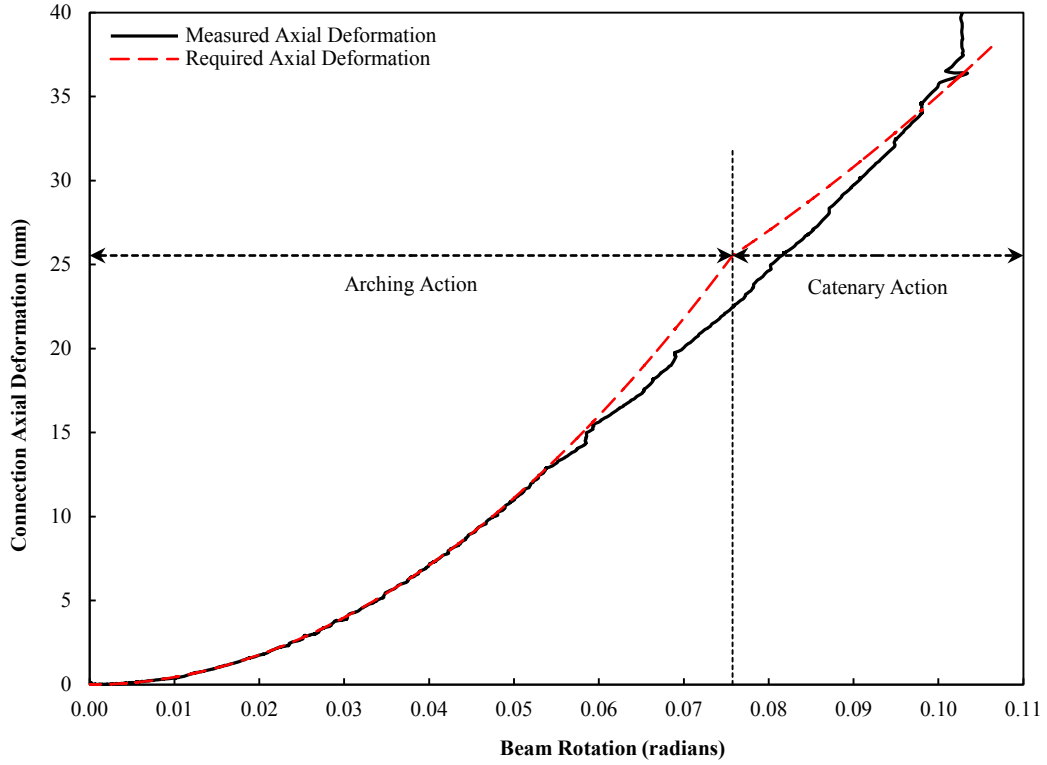


Figure 3-29: Connection Axial Deformation: Specimen DA59B

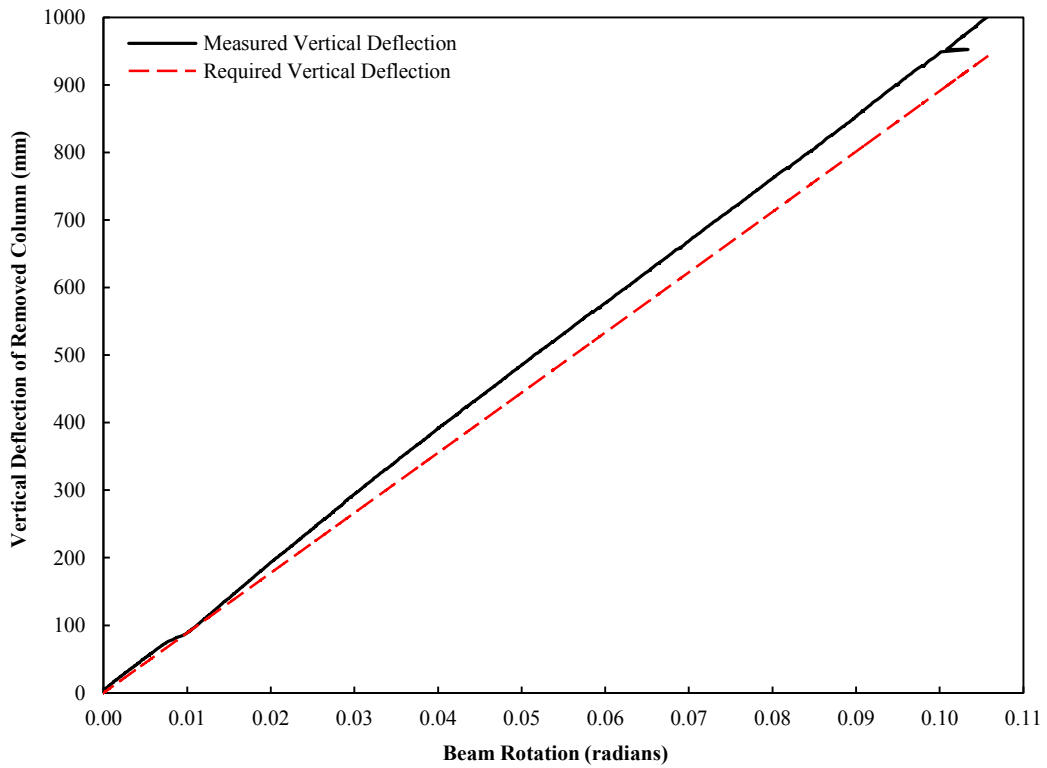


Figure 3-30: Vertical Deflection of Removed Column: Specimen DA59B

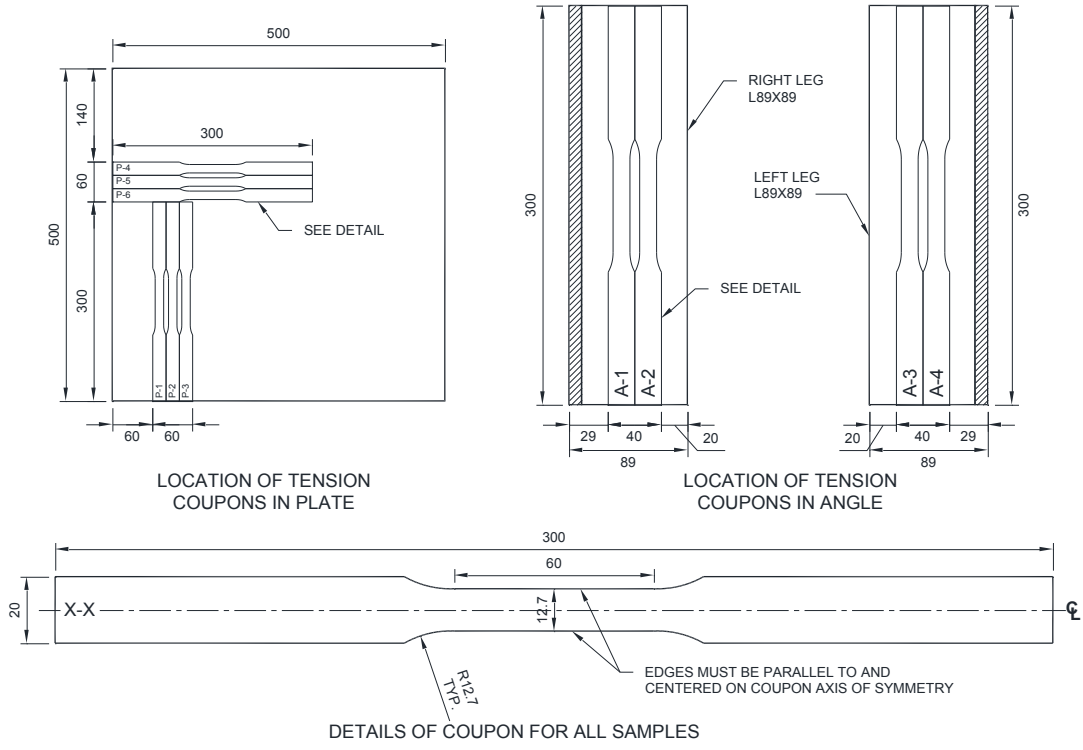


Figure 3-31: Location and Details of Tension Coupons

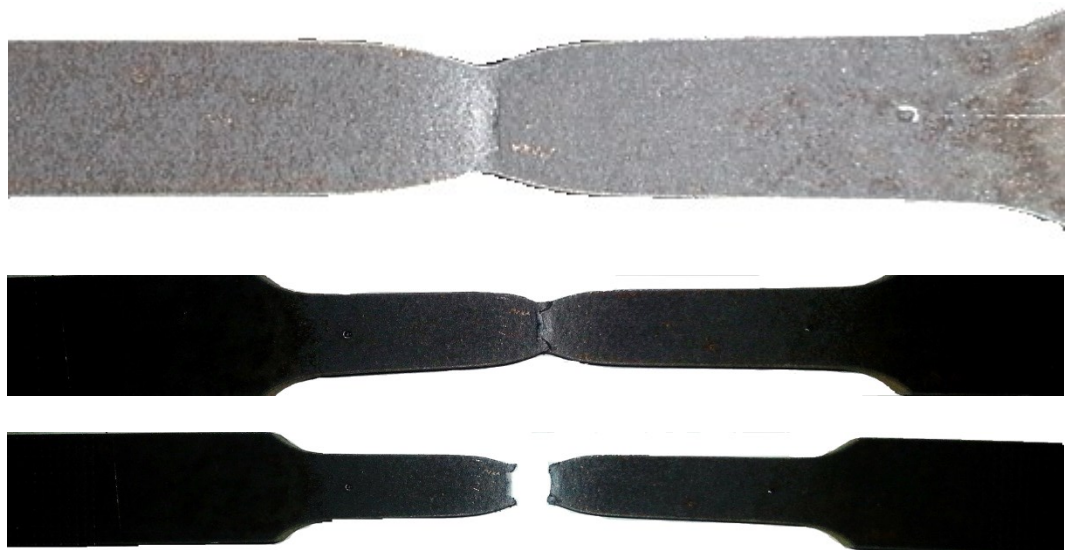


Figure 3-32: Section of a Tension Coupon Test (6.3 mm Plate) at Various Stages of Formation During Development of a Cup–Cone Fracture

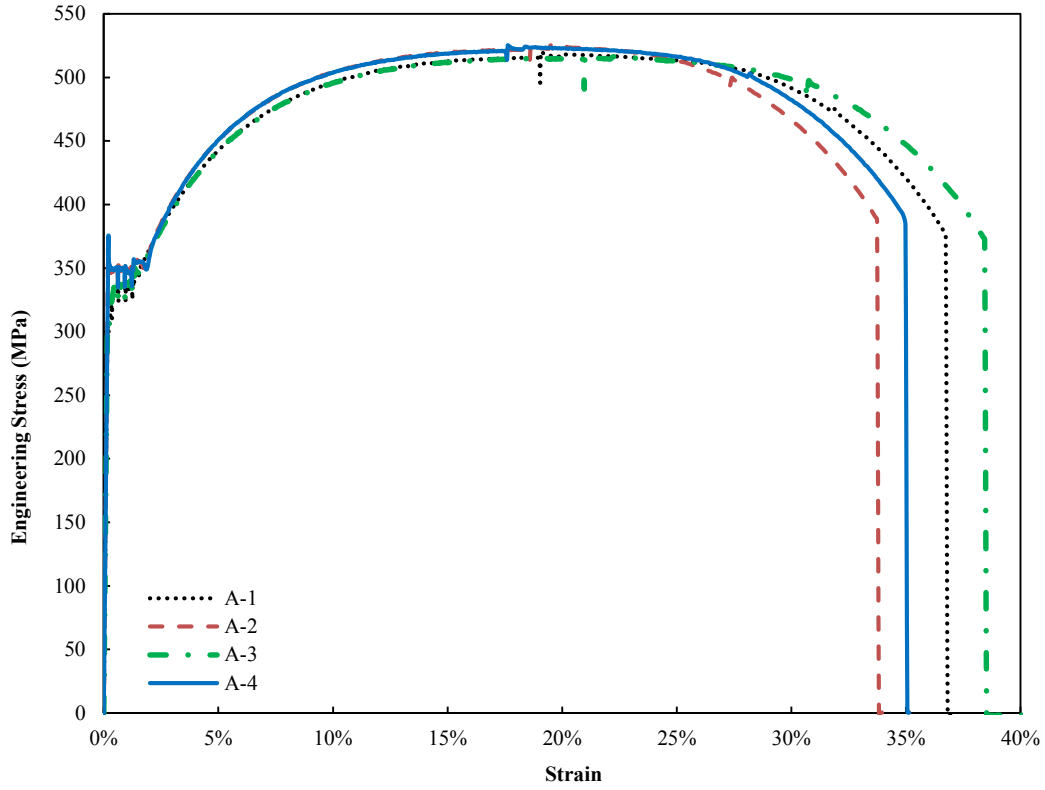


Figure 3-33: Stress–Strain Curves for Tension Coupons of 9.7 mm Angle

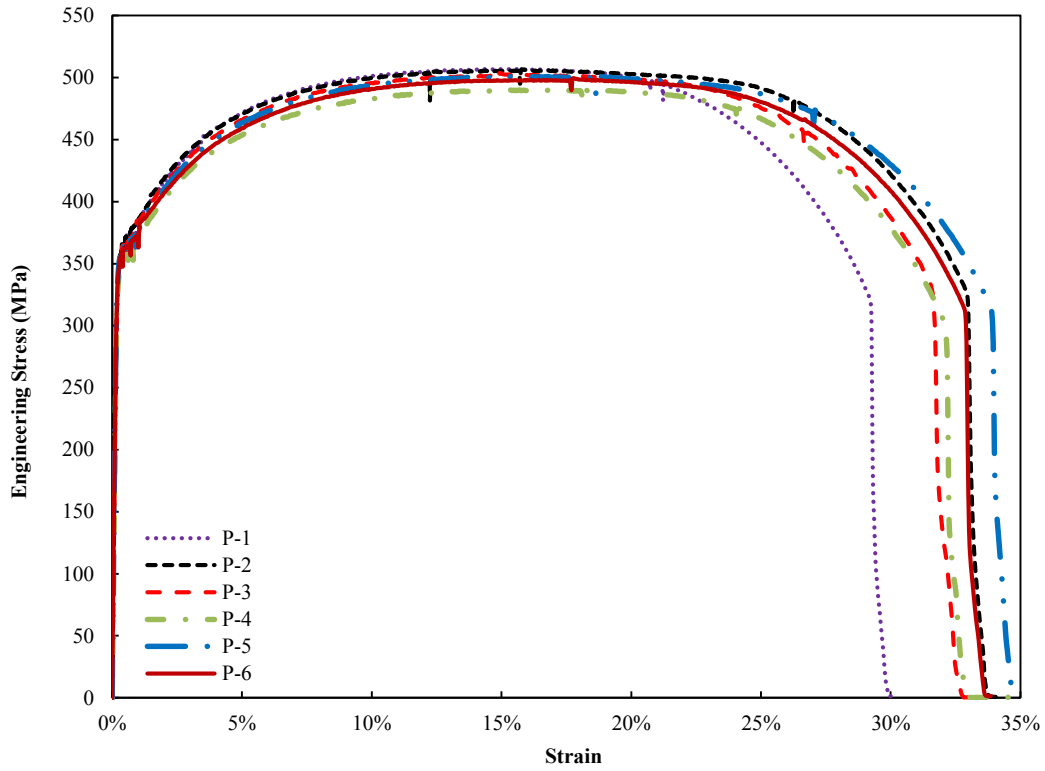


Figure 3-34: Stress–Strain Curves for Tension Coupons of 6.3 mm Plate

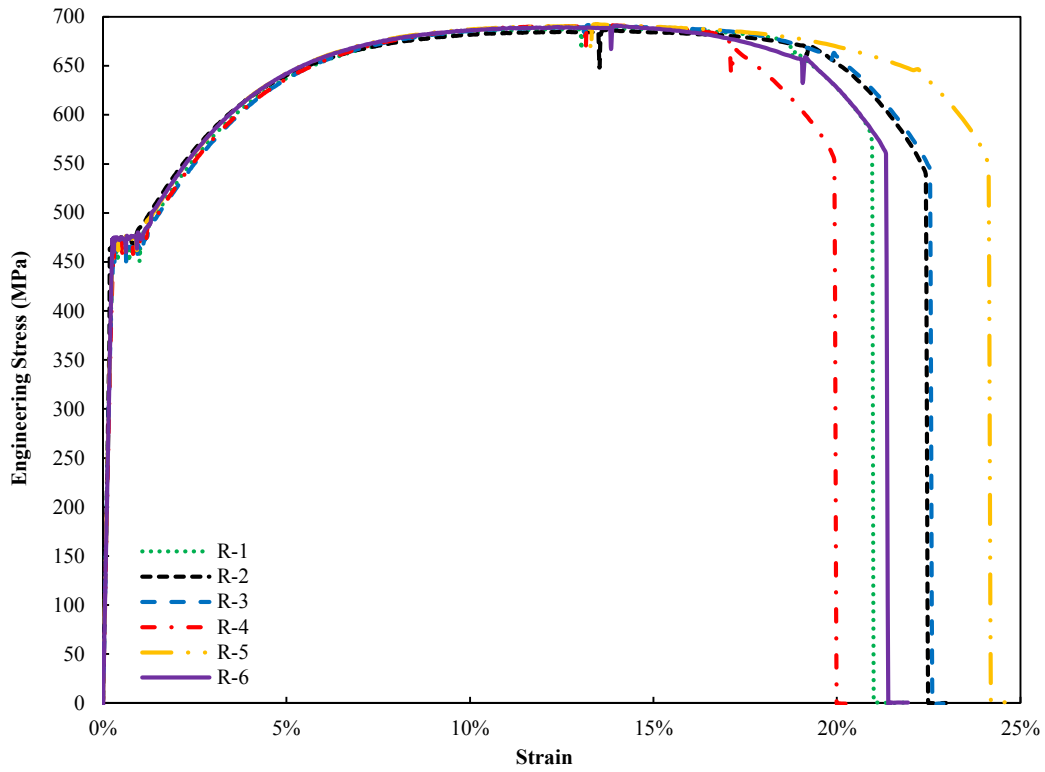


Figure 3-35: Stress–Strain Curves for Tension Tests of 10M Rebars

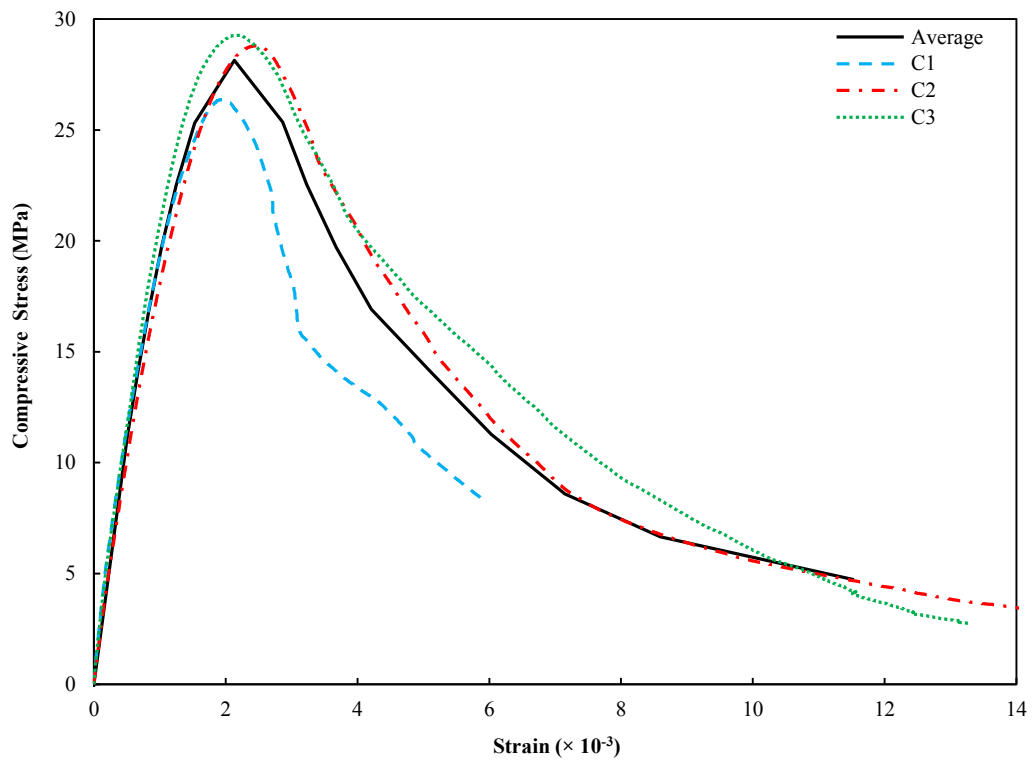


Figure 3-36: Stress–Strain Curves of Cylindrical Concrete Specimens (DA59B)

## **4. EXPERIMENTAL RESULTS AND DISCUSSION**

### **4.1 Introduction**

In this chapter, the general behaviour of specimens and observations made during the tests are discussed. Failure modes, axial deformations of connections, and internal loads versus beam rotation are presented. Detailed discussions and analyses of the test results of the pilot test, and two tested connection types are provided.

### **4.2 Pilot Test**

The purpose of the pilot test was to ensure the geometry and capacity of the test set-up for the following 16 tests. The pilot test was designed and built from existing materials (surplus materials from Oosterhof's experiments) in the I.F. Morrison structural engineering laboratory. A 9.5 mm thick shear-tab connection with three bolts and an assumed span of 6 m was considered. A concrete slab with 1.5 m width was cast and placed on top of the test beam to simulate the composite section. Average of the 28-day concrete cylinders' test for the slab of the pilot test was 38.3 MPa. Details of the test set-up and instrumentation are explained in Chapter 3. The pilot test loading procedure (method based on the equilibrium of forces) is described in Section 3.7.1.

The overall behaviour of the connection (steel shear tab and concrete slab combined) is studied by plotting the internal forces (horizontal, vertical, and bending moment) at the column face versus the beam rotation in Figure 4-1.

Photographs of the shear tab at four beam rotations are shown in Figure 4-2, which collectively display the evolution of deformation and eventual failure. Failure surfaces develop in the plate adjacent to each bolt, as shown in Figure 4-2. This indicates the importance of bolt end distance as a significant factor for shear-tab connections in structures susceptible to progressive collapse.

The compressive horizontal load (representing the arching action) dominated the behaviour from the beginning of loading. As shown in Figure 4-1, the composite connection displays relatively high rotational stiffness and reaches a peak bending moment at the beam rotation of 0.04 rad., at which time the material behind the bottom bolt starts to bulge out. At this stage, the slab concrete starts to spall and cracking develops. Partial failure of the connection occurs first at the lowest bolt, which is moving away from the removed column.

The bending moment and compressive horizontal load both decrease to near zero at the beam rotation of about 0.06 rad., at which time the material behind the middle bolt starts to bulge out. At this rotation, the arching action changes to catenary action by developing tensile force. Finally, failure of the shear-tab plate due to bolt tear-out occurs at the beam rotation of about 0.11 rad and thereafter the force is carried entirely by the steel reinforcement in the slab. The peak internal actions—horizontal/vertical loads and bending moment—did not occur concurrently, as shown in Figure 4-1. Although the peak value of moment occurred as plate deformations at the bottom bolt began to increase rapidly (at 0.04 rad.), the maximum compressive and tensile forces were reached at rotations of about 0.03 and 0.11 rad., respectively.

The concrete slab affects the behaviour of the connection mainly by shifting of the neutral axis to within the slab, placing the connection into nearly pure tension. Bolt tear-out of the shear-tab plate was the governing failure mode. The results demonstrate that the presence of a concrete slab amplifies the demand on the connections considerably and reduces the ductility. Although a higher axial load developed in the composite beam, its rotational capacity was markedly smaller than that obtained by Oosterhof and Driver (2012) for a steel beam alone due to the prying force induced at an early stage of loading. The results and discussion on the pilot test were previously presented in a paper by Jamshidi and Driver (2014). Test set-up, loading regime and material selection for the next 14 tests were modified based on the findings from the pilot test and ST36A; this method was explained in Section 3.7.



### **4.3 Test Results**

Results are provided based on the deformation and failure modes of the connection and concrete slab, load development in the overall cross-section and steel connection, and capacity and ductility. Table 4-1 and Table 4-2 summarize the maximum values of the internal forces developed in the composite section and steel connections, failure modes, and axial deformation. The means of isolating the axial force developed in the steel connection is explained in Section 4.3.4.

#### **4.3.1 Deformations and Failure Modes of Connections**

No failure or significant permanent deformation of bolts was observed in either the shear-tab or double-angle connections. Bearing of the top flange of the testing beam against the stub column was not observed for either connection type. A gap of 25 mm and 10 mm was placed initially for shear tabs and double angles, respectively. Although at higher rotations the gap increased before contact happened, after the beginning of each test the beam rotation caused the top flange to move towards the stub column's flange.

##### **4.3.1.1 Shear Tabs**

Excessive elongation of the shear tab plate holes under the bearing stress exerted by the bolts was the main factor for ductility of shear tab connections. Bolt tear-out of the shear-tab plate was the governing failure mode for all specimens. As a result of the tensile force developed in the plate, all shear-tab plates failed by bolt tear-out in the direction of the beam axis. Partial failure of the plate always occurred first at the bottom bolt by extensive bearing on the thickness of the shear tab plate holes. It happened when the bending moment in the cross-section was the greatest. Fracture was then followed and developed by successive bolt tear-out from bottom to the top by increasing beam rotation.

Two types of fractures were observed in the bolt tear-out failure mechanism, as shown in Figure 4-3: shear tearing on one or two shear planes, or tensile splitting

at the free edge adjacent to the centreline of the hole. Single shear-plane tearing occurred only in the material behind the top bolt, while double tearing occurred along two shear planes of the plate (material behind the bolt hole) for the rest of the holes. Shear failure surfaces were closely aligned with the direction of the tangent of the beam rotation. Tensile splitting tears were observed and occurred only at the material behind the top bolt and were then followed by a single-plane shear tearing, leading to a bolt tear-out. These tensile tears were a result of transverse tensile stress developed at the free edge of the arch shape of the material behind the bolt. Figure 4-4 shows the aftermath of two shear tabs with three and five bolts configurations. Successive bolt tear-out and failure progression from the bottom to the top bolt is evident from Figure 4-4.

#### **4.3.1.2 Double Angles**

The failure mechanism of double angles was different from the shear tabs mostly because of the ability of angles to unfold, as shown in Figure 4-5. Deformation was initially shaped by unfolding of both angles, at which time the angle heels were pulling away from the stub column flange. Since the top of the angles were not as free as the bottom (due to the presence of the concrete slab), the unfolding mechanism was only developed along a partial length of the angles. After unfolding, tearing initiated and propagated from the bottom of the angles where the maximum tensile stress developed. Fracture initiated in both angles symmetrically. However, one angle usually failed earlier than the other one due to the initial geometry and in-place imperfection in the test beam, and asymmetrical loading conditions.

Two types of fractures were observed in the double angle connections, as shown in Figure 4-6: tearing of the gross section near the angle heel, and/or fracture near the bolt line attached to the stub column. Tearing of the gross section was found to be more common in all specimens. This brittle failure mode developed suddenly with a rapid propagation along the depth of the angles and accompanied by a loud noise. This failure was found to be unstable as any small increase in rotation caused the propagation to develop quickly and axial load to decrease. It

should be noted that although tearing of the gross section was the main failure mode for most of the specimens, excessive deformation such as punching, and bearing around the angle's hole at the bolt line attached to the stub column was also observed, as shown in Figure 4-7.

Fracture along the column bolt line, on the other hand, was mostly observed in the thinner and deeper connections (five-bolt configurations). The fracture occurred along a zigzag pattern between bolts attached to the stub column, as shown in Figure 4-6(b). This failure was found to be more stable than the other failure mode because tears were arrested once reaching each bolt hole.

#### **4.3.2 Failure Modes of Concrete Slab**

The failure modes were similar for all specimens and were characterized by concrete cracking and crushing, typically concentrated around the slab's opening close to the stub column. The cracks always initiated at a small beam rotation (less than 0.025 rad) at the shear studs closest to the stub column and propagated circumferentially around the column, as shown in Figure 4-8(a). Cracks then developed in a similar manner at shear studs progressively farther from the column as the beam rotation increased. Cracks located at shear studs close to the connections penetrated deep through the slab, especially for the specimens with shorter notional spans (6.0 m). Near the steel connections, the length, depth and number of cracks in the bottom of the concrete slab were greater due the stress concentration. Nearly all specimens had cracks perpendicular to the test beam in the top of the concrete slab at the locations of the shear studs.

The compressive stresses in the top region of the slab, termed herein the "compressive region", caused the concrete slab to crush against the end supporting beam. Severe cracking and crushing was observed near the connections causing the concrete to spall. It was more severe for the specimens with the shorter notional span because of the higher initial angle of arching action, which resulted in more compressive force to be developed in the specimen.

Since the neutral axis was initially placed within the concrete slab (based on the composite cross-sectional geometry and configuration), cracks always occurred at the soffit of the concrete slab, which is termed the “tensile region”. Cracks continued to grow, which led to a shifting of the neutral axis within the cross-section. The cracking that propagated through the thickness of the slab, as shown in Figure 4-8(b), is evidence of shifting of the neutral axis during the different stages of loading. This also proves that the steel connections always remain in tension, since the neutral axis remains within the concrete slab above the connections. After each test, the shear studs were examined for any failure. No excessive deformation or failure was observed in the shear studs.

### **4.3.3 Characteristics of Load Development**

In this section, characteristics of internal loads developed are explained. They were recorded based on the overall cross-section of the specimens (i.e., connections plus concrete slab) during the tests in terms of horizontal load, vertical load, and bending moment. Loads were measured at the centroid of the steel connections at the face of the column (see Section 4.3.4 for further discussion on the measurements of loads in the steel section only).

#### **4.3.3.1 Shear Tabs**

General shapes of the loads path were similar for all eight shear tab tests. Figure 4-9 shows the load development in terms of vertical and horizontal loads, as well as bending moment (note that the horizontal axis for bending moments is at the bottom of the figure), of one of the specimens (ST59A). As shown, the connection exhibited a relatively high initial axial and rotational stiffness. Cracks on the bottom of the concrete slab were mostly initiated at low rotations (less than 0.011 radians) at which point the axial and rotational stiffness changed slightly, as seen in Figure 4-9 at 0.011 rad.

The horizontal component of the arching force developed in the cross-section increased rapidly at low rotations and it reached a maximum immediately prior

the extreme bolt starting to bulge out. It then decreased in a smooth manner until switching to the catenary phase. Most of the bolt tear-out and fracture failures occurred prior the onset of the catenary phase. The horizontal load was compressive for most of the test, while the bending moment was positive causing the shear tab itself to be always in tension. In fact, the combination of negative horizontal load and positive bending moment, which causes a tensile force to be developed in the connection, identifies the capacity of the connection. An indirect method to measure the horizontal load developed in connections is explained in Section 4.3.4.

The maximum bending moment was reached when the plate behind the extreme bolt bulged out, and then decreased smoothly until complete failure of shear tabs occurred. Following the tear-out of each bolt, the bending moment dropped because the moment arm within the cross-section decreased. Any change in the bending moment was associated with a drop in the vertical (shear) load. Figure 4-10 shows the vertical load versus vertical displacement of the beam (measured directly at the bolt line) and beam rotation for specimen ST59A.

Vertical load had a different path. With the applied rotation, the vertical load increased smoothly and usually reached its maximum value when tear-out ensued at the extreme bolt. It then decreased in a stepwise manner as failure in the shear tab occurred successively at bolts from bottom to top. Any partial fracture, failure, and cracks in the connection were clearly identifiable at spikes and drops in the vertical load history.

Maxima of horizontal load, vertical load and bending moment did not occur concurrently. However, the maximum of bending moment and horizontal compressive load were reached at a similar beam rotation. Figure 4-11 depicts photos of specimen ST59A at four rotations during the test: at the beginning, bulge-out at extreme bolt at maximum moment (0.041 radians), tear-out of extreme bolt (0.074 radians), and fracture (0.118 radians).

#### 4.3.3.2 Double Angles

Throughout the remainder of this chapter and thereafter, the angle with speckles located in front of the camera system is designated as the “left angle” (also by looking toward the stub column from actuators 3, the left one is labeled as the “left angle”), and the opposite one as the “right angle”. General shapes of the loads path were similar for all eight double angle connections tests. Figure 4-12 shows the load development in terms of vertical and horizontal loads, as well as bending moment, of one of the specimens (DA59A). As shown in Figure 4-12, the composite connection exhibited a relatively high initial axial and rotational stiffness. Cracks on the bottom of the concrete slab were usually initiated at low beam rotations (less than 0.02 radians) at which point the axial and rotational stiffnesses slightly changed (it is clearly shown in Figure 4-12).

Similar to the shear tabs, the horizontal component of the arching force developed in the cross-section increased rapidly at low rotations and it reached a maximum value immediately prior the tear initiation at the bottom of the angle heel. It then decreased in a smooth manner until switching to the catenary phase. Most of the tearing initiation and fracture occurred prior the catenary phase. While for most of the beam rotation the horizontal load was in compression, bending moment was positive resulting in a load combination of horizontal load and bending moment that caused the angles to be always in tension. The tear was always initiated at the front surface of the angles and then developed and propagated to a through-thickness tear as rotation increased.

The maximum bending moment was reached when tear initiation took place at the bottom of either angle, and then decreased smoothly until complete failure of the double angles occurred. However, in those cases where tearing initiated and occurred near the stub column bolt line, bending moment dropped because the moment arm within the cross-section decreased. Any change in the bending moment was usually associated with a drop in the vertical (shear) load. Figure 4-13 shows the vertical load versus vertical displacement of the beam (measured at the bolt line) and beam rotation for specimen DA59A.

Partial fracture, failure, and cracks in the connection were clearly identifiable at spikes and drops in the vertical load history. The maximum of horizontal load, vertical load and bending moment did not occur concurrently. However, the maximum bending moment and horizontal load occurred at a similar rotation. Figure 4-14 depicts specimen DA59A at four beam rotations during the test: at the beginning, tear initiation at left angle heel (0.057 radians), tear initiation at right angle heel (0.071 radians), and failure (0.11 radians).

#### 4.3.4 Calculation of Horizontal Load Developed in Connections

As explained in Section 3.5, the purpose of using “donut” load cells (DLCs) was to explicitly measure the net axial force transferred to the steel connection. Although the DLCs did not perform well, an indirect method is proposed here to extract the axial load from the existing test data. The data from the test (ST59B) immediately after the DLCs were recalibrated and verified is used as a benchmark for the indirect method.

The indirect method computes the axial force on the connection simply based on the recorded values of the horizontal component of the arching load and bending moment developed in the composite cross-section. The internal load developed at the composite cross-section is schematically shown in Figure 4-15. Implementing an equivalent force-couple system method, the internal forces in Figure 4-15(b) can be resolved into a new force system shown in Figure 4-15(c). The new system of tensile force in the steel connection (T) and compressive force in concrete slab (C) are then derived from the horizontal load (H) and bending moment (M). It should be noted that the vertical loads (V) for the two systems are equal. The calculation is derived from the free body diagrams of both systems, as summarized in Equation (4-1).

$$\begin{cases} H = T - C \\ M = C e \end{cases} \xrightarrow{\text{yields}} \begin{cases} C = \frac{M}{e} \\ T = H + \frac{M}{e} \end{cases} \quad (4-1)$$

Having both bending moment ( $M$ ) and horizontal load ( $H$ ) recorded from the test, the axial load developed in the steel connection ( $T$ ) can be derived. The only parameter in the Equation (4-1) that needs to be defined is the eccentricity ( $e$ ), which is the distance between the tensile and compressive forces shown in Figure 4-15(c). In this indirect method, the horizontal load in the steel connection is calculated based on the eccentricity, total horizontal load ( $H$ ) and bending moment ( $M$ ) obtained using the finite element model. As explained in Section 3.6, the eccentricity is not constant and it varies with the progression of the beam rotation due to the partial failure in both the concrete slab and steel connection.

In order to fully understand the variation of eccentricity and its effect on the axial load developed in the steel connection, finite element analysis was implemented using Abaqus (Dassault Systèmes 2013). Figure 4-16 shows the variation of the eccentricity versus beam chord rotation for specimen ST59B based on the finite element modelling. Eccentricity alters between centre of geometry and top of the concrete slab (for more details refer to Section 3.6). The horizontal load developed in the steel connection was directly extracted from the Abaqus model as shown by the solid line in Figure 4-17.

To evaluate the proposed indirect method of calculating the horizontal load introduced by Equation (4-1), three different values of eccentricity were considered. Eccentricity considered was at the values of: center of geometry ( $e = 337$  mm), plastic neutral axis ( $e = 378$  mm), and  $e = 390$  mm. The latter value has been selected such that it approximates the horizontal load closely to the real one (solid line in Figure 4-17). In fact, it is from the rough average of the eccentricity at the low rotations (Figure 4-16), and from the migration of the neutral axis, as previously explained and shown in Figure 3-17. As seen in Figure 4-17, the eccentricity of  $e = 390$  mm agrees very well up to the maximum horizontal load and it diverges slightly afterward.

Based on the findings from the numerical finite element analysis mentioned above, Equation (4-1) is used to extract the tensile force developed in the steel connections from the recorded test data. The tensile force developed in the steel



connection of specimen ST59B is then verified against the direct values of the recalibrated DLCs, as shown in Figure 4-18. As seen, the results of the proposed indirect method agree well with those of the test. It captured the maximum values of tensile force and its associated beam rotation compared well to the values from DLCs (less than 5% difference). Thus, this method is implemented to extract the capacity of the steel connections. It should be noted that the indirect method assumes a constant value of eccentricity. However, in reality the value varies as the connection experiences local failure, which could affect the load path and history of the tensile force developed in the connection.

#### **4.4 Accuracy of Loading Regime: Axial Elongation and Vertical Deflection**

As explained in Section 3.6.2, a new loading regime approach relying on the geometric compatibility of the central removed-column deflection and the connections' deformation was developed and implemented to test the component-level connections in a composite construction system. The iterative procedure entails that calculated target values of both axial displacement and vertical deflection be achieved simultaneously, by means of actuators, in order to impose demands and to develop arching action consistent with a column removal scenario on the connection being tested. Axial deformation was applied to the connection using Equation (3-3), and/or Equation (3-7), while satisfying Equation (3-6). Due to the high initial stiffness of the composite system, axial deformation was applied in the order of 0.01 mm during the initial phases of loading. Target values for one of the tested specimens (ST59B) are shown in Figure 4-19 and Figure 4-20.

As explained in Section 3.7, it is acknowledged that the shear load developed in the simulated system for all specimens was relatively high because approaching the required vertical deflection forced actuator 1 to produce an artificially high vertical load. To partially compensate for this, the vertical deflection deviated intentionally from the target value slightly (Figure 4-20). The accuracy of this method was dictated by the limitation on the increment displacement and sudden changes in the connection capacity due to the damage incidents caused during

testing. These incidents produced deviation and discontinuity in the calculated target and measured displacements. Deviation was mostly after initial damage and remained within about 4 mm for all specimens. Nonetheless, as shown in Figure 4-19 for one of the specimens (ST59B), the target axial deformation was followed accurately for the majority of the testing until failure of connection happened.

Table 4-1: Test Results of Shear Tabs

Specimen ID	Composite Section					Steel Connection		
	Maximum Bending Moment			Maximum Force of Arching Action*		Maximum Vertical Load (kN)	Maximum Tensile Load (kN)**	Failure Mode of Steel Connection†
	Value (kN·m)	Beam Rotation (radians)	Axial Deformation‡ (mm)	Value (kN)	Beam Rotation (radians)			
ST39A	398.2	0.050	7.3	-767.2	0.037	147.5	484.5	Bolt Tear-out
ST39B	382.3	0.048	9.7	-699.8	0.032	161.8	512.7	Bolt Tear-out
ST56A	419.8	0.044	5.8	-828.6	0.031	185.2	602.3	Bolt Tear-out
ST56B	402.3	0.041	9.6	-765.3	0.027	189.2	612.6	Bolt Tear-out
ST59A	443.0	0.043	5.5	-803.4	0.028	229.8	740.2	Bolt Tear-out
ST59B	424.4	0.042	7.9	-622.7	0.023	248.5	835.7	Bolt Tear-out

\* Equal to Minimum Horizontal Load (Maximum Horizontal Compressive Force)

‡ Centreline Axial Deformation of Connection at Maximum Bending Moment

\*\* Refer to Section 4.3.4

† Refer to Section 4.3.1.1

Table 4-2: Test Results of Double Angles

Specimen ID	Composite Section						Steel Connection	
	Maximum Bending Moment			Maximum Force of Arching Action*		Maximum Vertical Load (kN)	Maximum Tensile Load (kN)**	Failure Mode of Steel Connection†
	Value (kN·m)	Beam Rotation (radians)	Axial Deformation‡ (mm)	Value (kN)	Beam Rotation (radians)			
DA36A	332.8	0.045	6.8	-635.4	0.023	43.5	318.2	TG
DA36B	275.3	0.034	5.0	-565.9	0.030	64.0	305.3	TG
DA39A	368.3	0.049	7.1	-827.1	0.036	123.6	511.6	TG
DA39B	303.0	0.034	5.1	-601.2	0.027	130.3	508.4	TG
DA56A	371.0	0.053	8.0	-763.9	0.040	162.7	595.9	TG, TN
DA56B	254.8	0.039	6.5	-527.3	0.023	143.9	541.6	TG, TN
DA59A	413.3	0.056	9.2	-680.9	0.038	193.6	729.3	TG, TN
DA59B	341.0	0.037	6.1	-574.4	0.029	231.3	799.3	TG, TN

\* Equal to Minimum Horizontal Load (Maximum Horizontal Compressive Force)

‡ Centerline Axial Deformation of Connection at Maximum Bending

\*\* Refer to Section 4.3.4

† Failure Mode (Refer to Section 4.3.1.1 and Section 4.3.1.2):

TG: Tearing of Gross Section Near Angle Heel

TN: Tearing of Net Section Near Bolt Line Attached to Stub Column

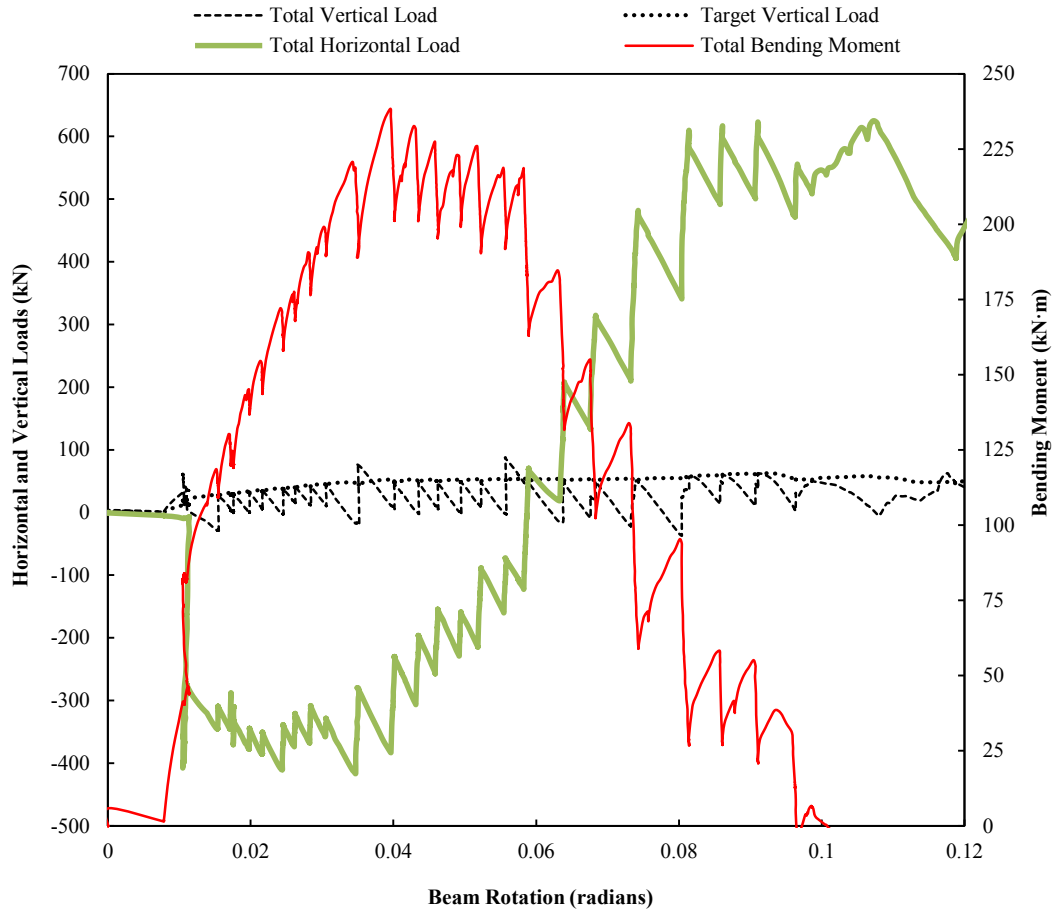


Figure 4-1: Load versus Beam Rotation of Pilot Test

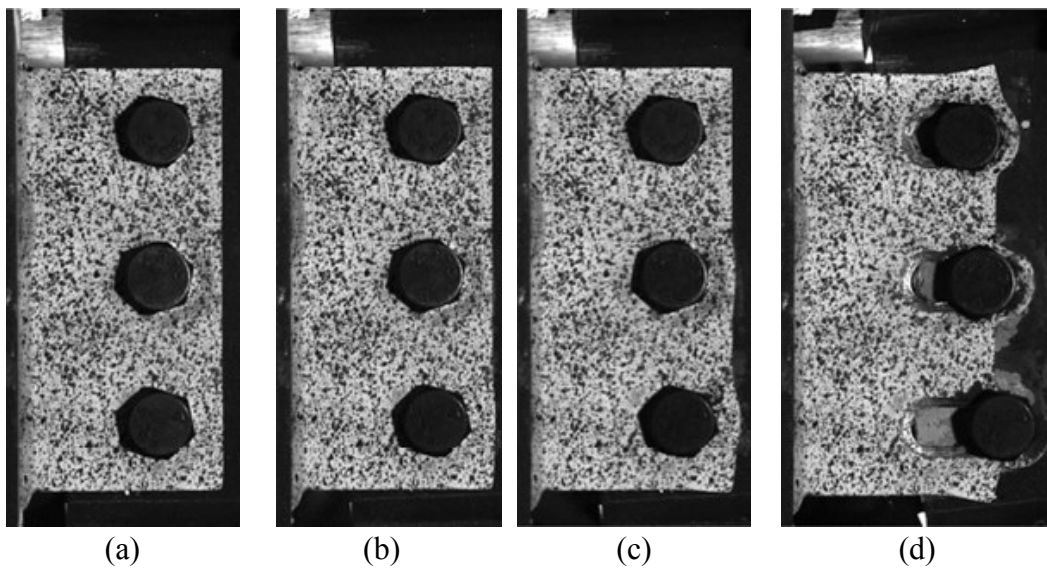
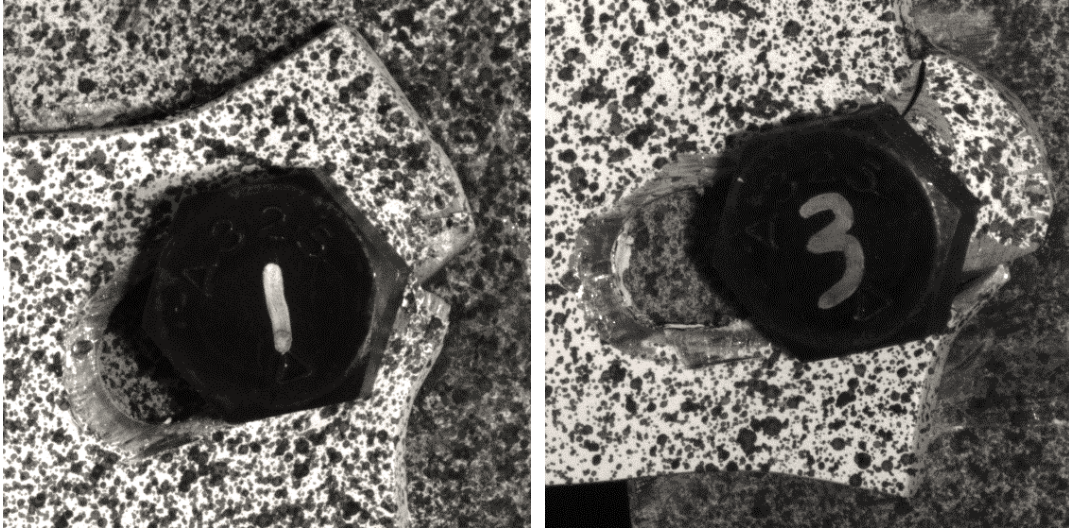


Figure 4-2: Deformation and Failure Mode of Connection at: (a) Undeformed; (b) 0.04 radians (peak moment); (c) 0.056 radians; (d) 0.114 radians (peak horizontal)



(a)

(b)

Figure 4-3: Failure Modes of Shear Tab: (a) Tensile Splitting Tear; (b) Shear Tear



(a)



(b)

Figure 4-4: Shear Tab Successive Bolt Tear-out: (a) Five Bolts; (b) Three Bolts

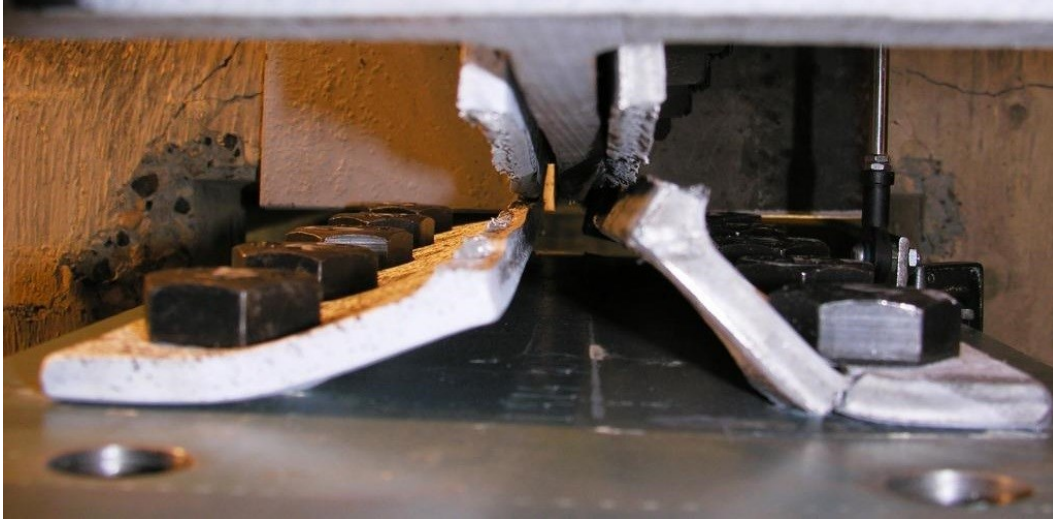


Figure 4-5: Unfolding of Double Angle Connections

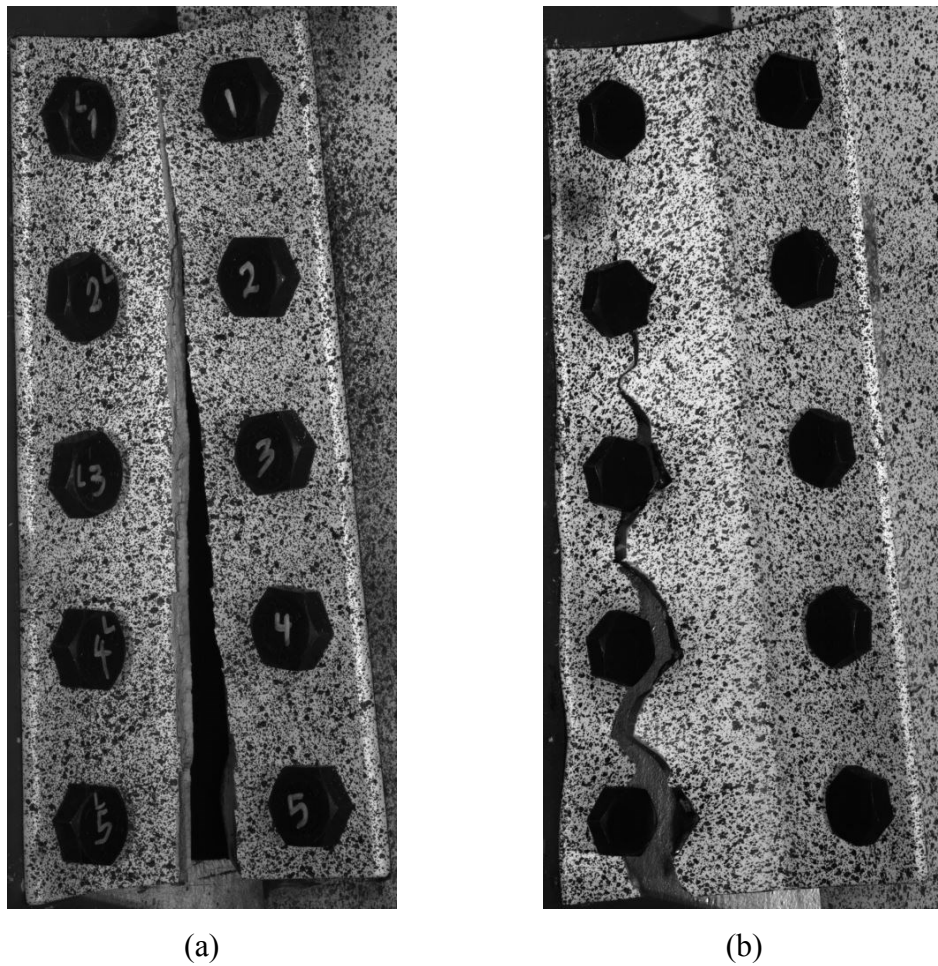


Figure 4-6: Failure Modes of Double Angles: (a) Tearing of Gross Section Near the Heel; (b) Fracture Near Bolt Line Attached to the Stub Column

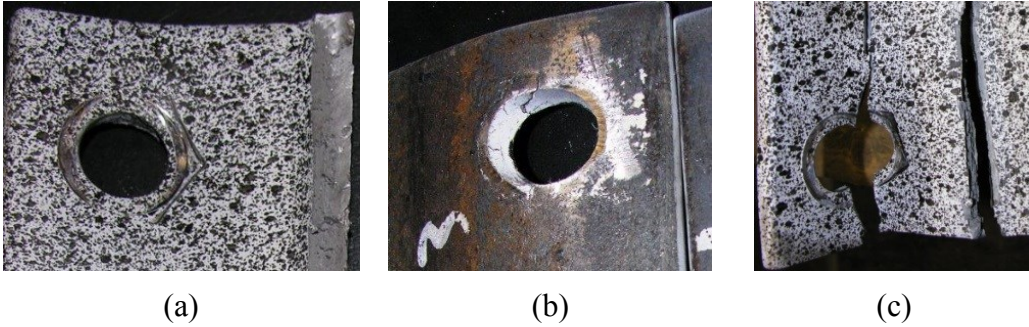


Figure 4-7: Deformation of Angle's Hole at the Bolt Line Attached to the Column:  
 (a) Punching; (b) Bearing; (c) Punching, Bearing, and Tearing



(a)



(b)

Figure 4-8: Failure Mode of Concrete Slab: (a) Crack Distribution on the Soffit of the Slab, (b) Front View of the Concrete Slab (Opening to the Stub Column)



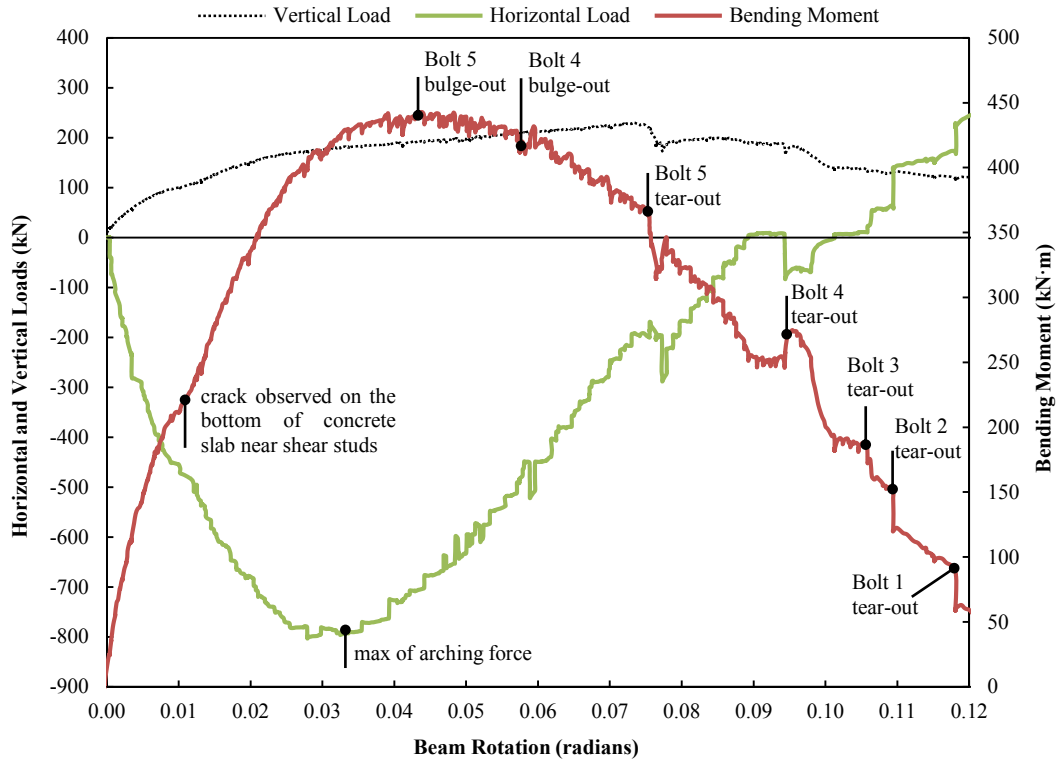


Figure 4-9: Load versus Beam Rotation of Shear Tab (ST59A)

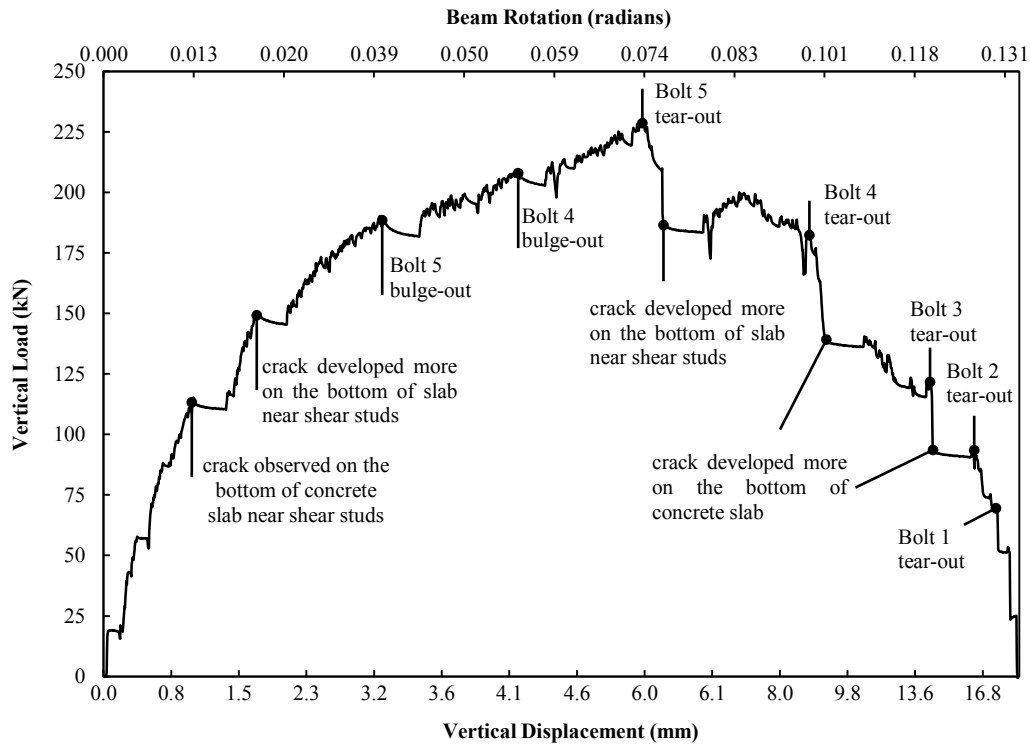


Figure 4-10: Vertical Load versus Vertical Displacement and Beam Rotation of Shear Tab (ST59A)

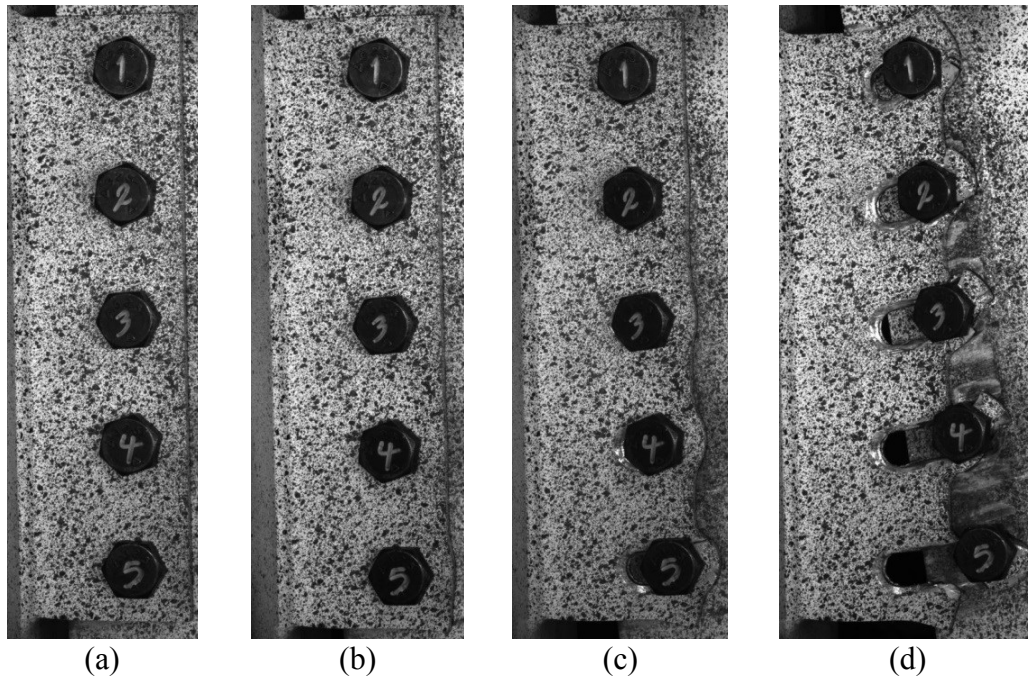


Figure 4-11: Specimen ST59A at: (a) Beginning; (b) 0.041 radians (Bolt 5 Bulge-out); (c) 0.074 radians (Bolt 5 Tear-out); (d) 0.118 radians (Failure)

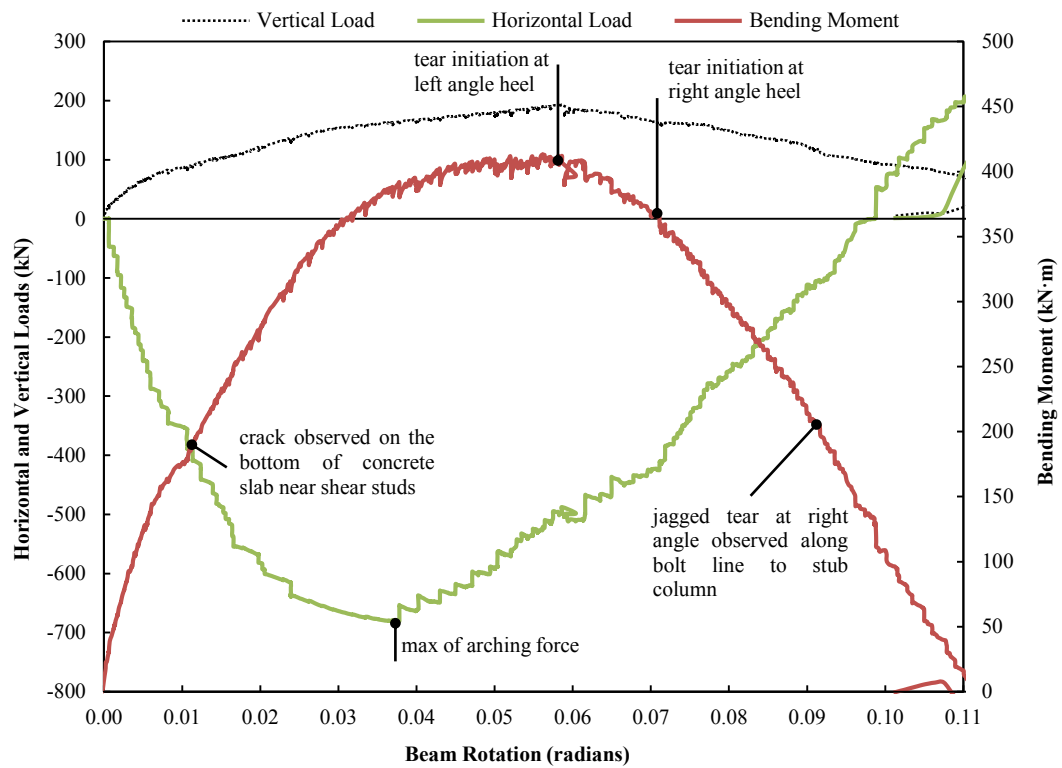


Figure 4-12: Load versus Beam Rotation of Double Angle (DA59A)

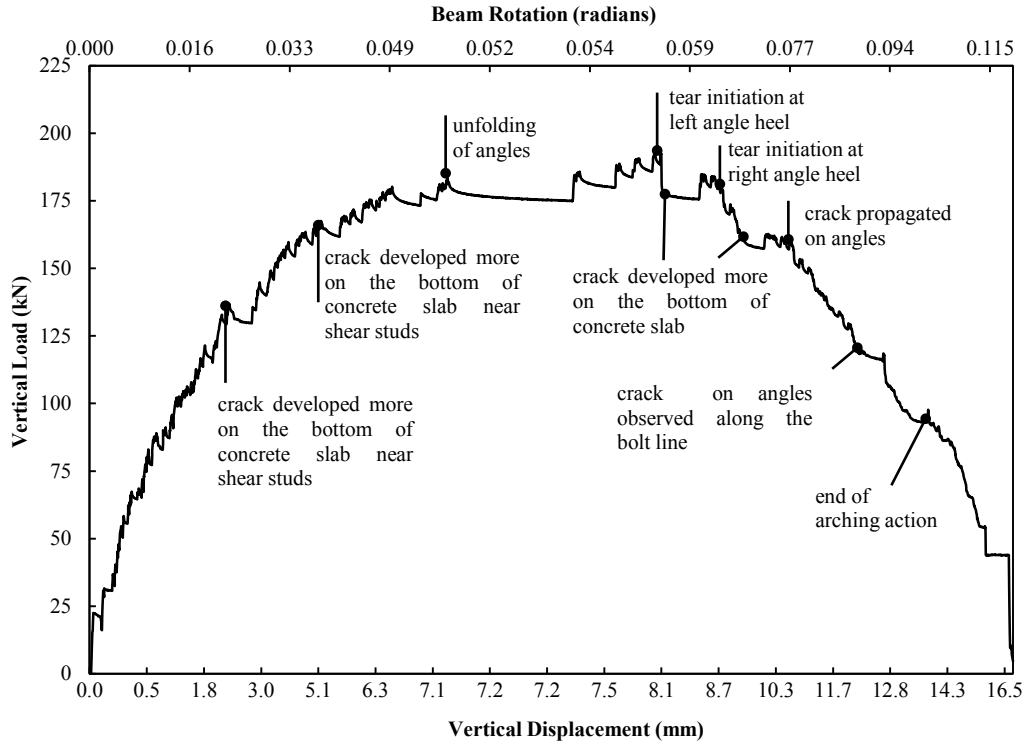


Figure 4-13: Vertical Load versus Vertical Displacement and Beam Rotation of Double Angle (DA59A)

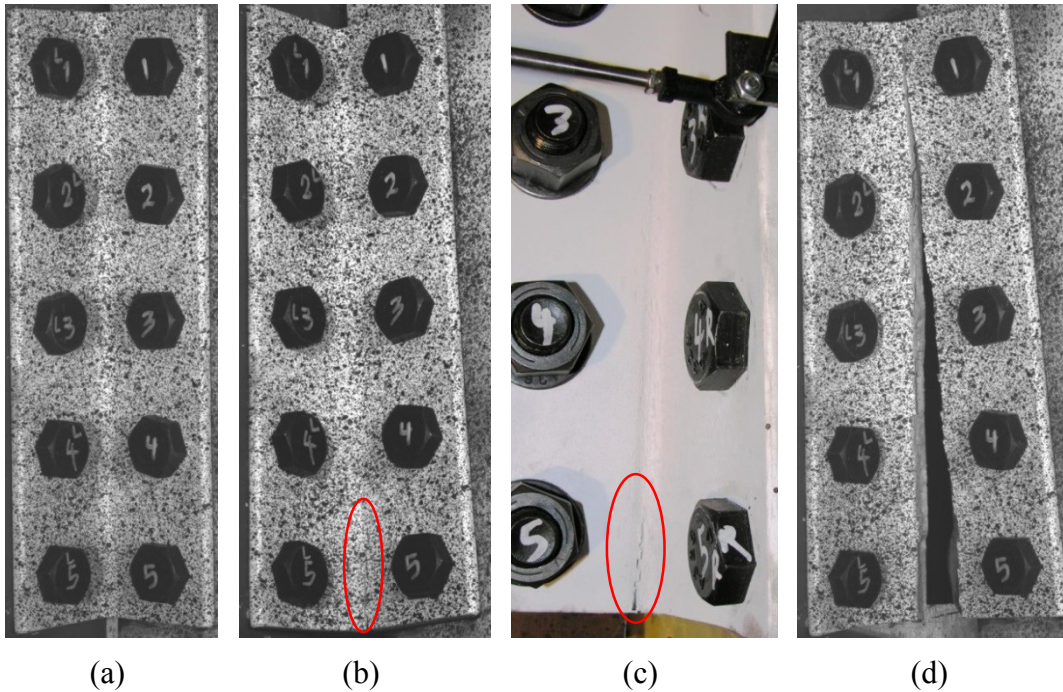


Figure 4-14: Specimen DA59A at: (a) Beginning; (b) 0.057 radians (Tear Initiation at Left Angle Heel); (c) 0.071 radians (Tear Initiation at Right Angle Heel); (d) 0.11 radians (Failure)

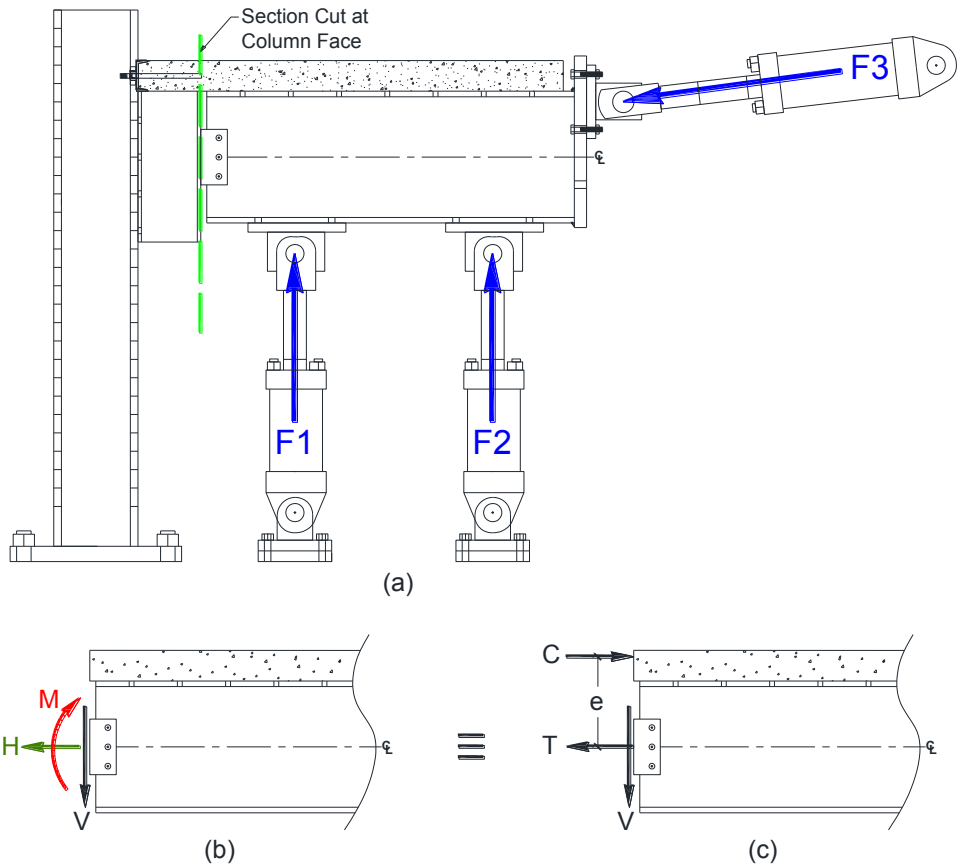


Figure 4-15: (a) Free Body Diagram; (b) Resultant Internal Forces Developed at Column Face; (c) Equivalent Force System of Tension and Compression in the Cross-section (Compression in Concrete and Tension in Steel Connection)

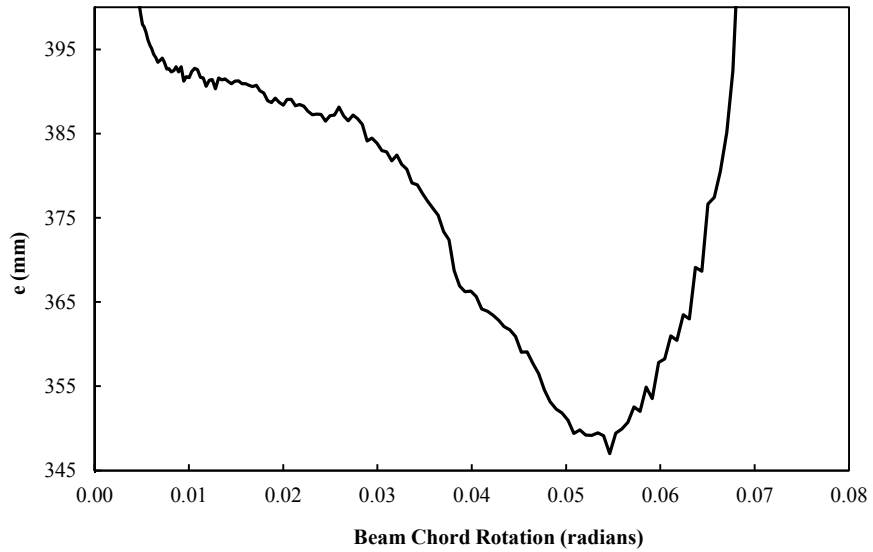


Figure 4-16: Variation of Eccentricity versus Beam Chord Rotation for Model ST59B (Extracted from Finite Element Analysis)

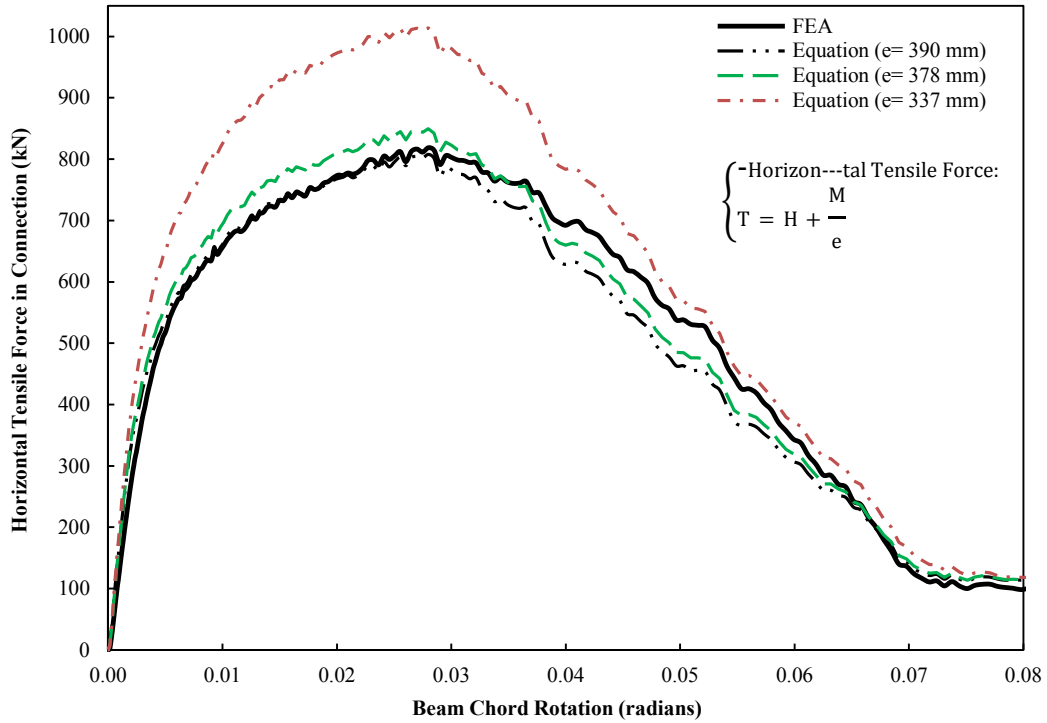


Figure 4-17: Horizontal Load Developed in the Steel Connection of Model ST59B: from Finite Element Analysis (FEA); and from Equation (4-1) with Different Eccentricities of:  $e = 337$  mm (C.G.),  $e = 378$  mm (P.N.A.),  $e = 390$  mm

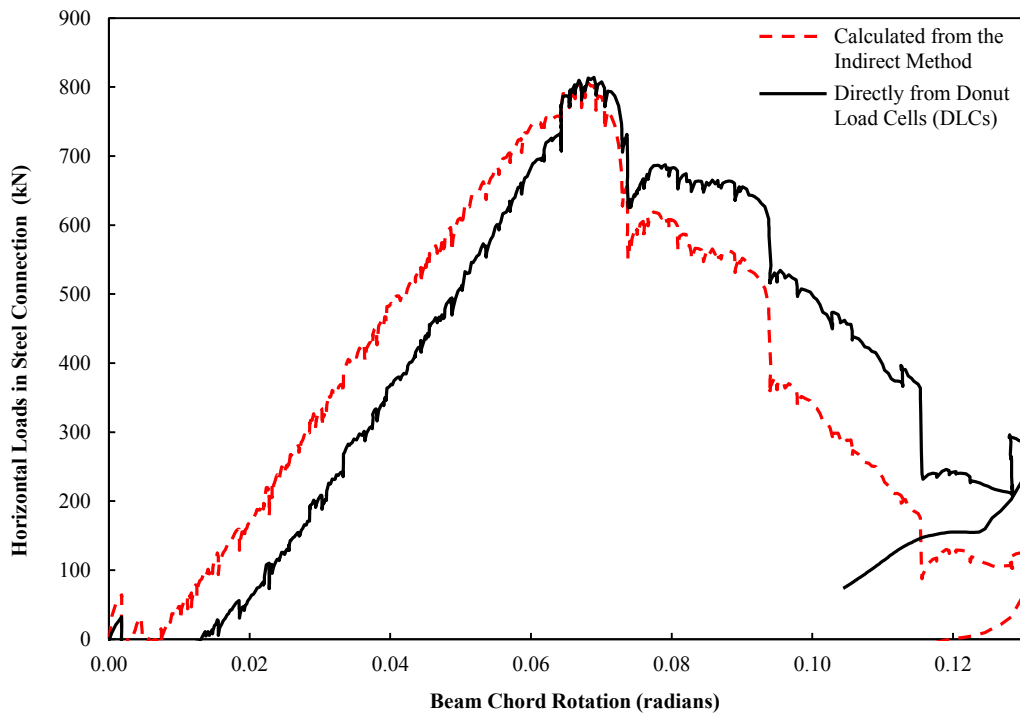


Figure 4-18: Horizontal Tensile Force Developed in Steel Connection of Specimen ST59B: Directly from the DLCs, and Indirect Method

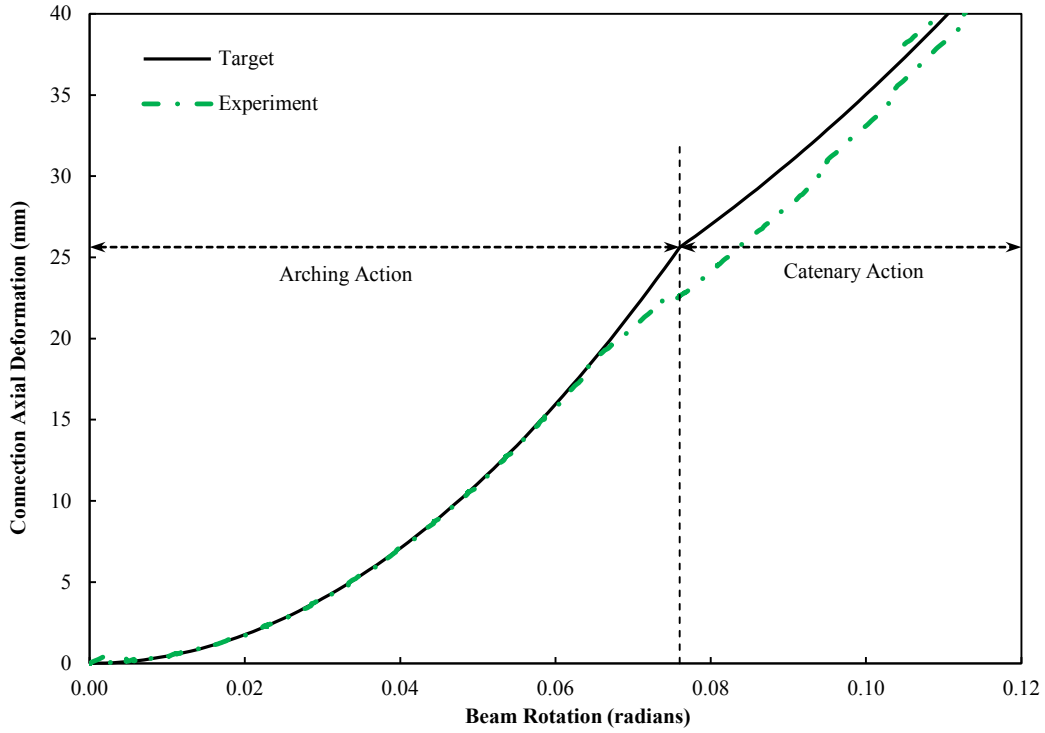


Figure 4-19: Target and Experimental Axial Deformation of Connection Attached to the Removed Column versus Beam Rotation (Specimen ST59B)

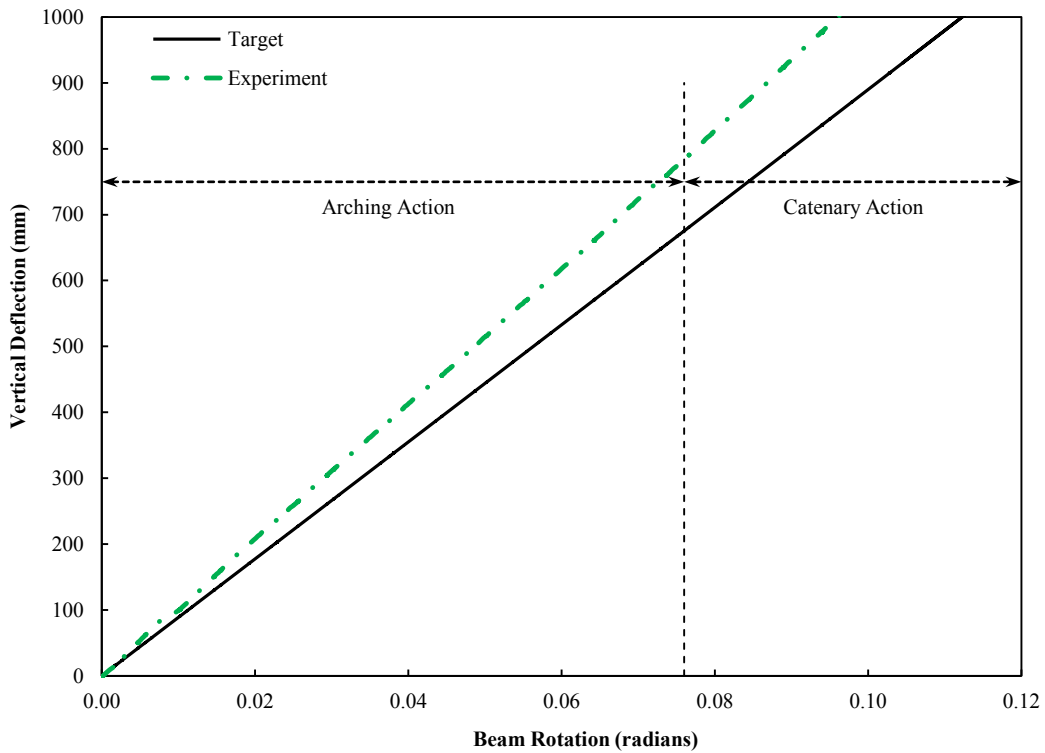


Figure 4-20: Target and Experimental Vertical Deflection of the Removed Column versus Beam Rotation (Specimen ST59B)

## **5. FINITE ELEMENT MODELLINGS**

### **5.1 Introduction**

This chapter describes a detailed finite element modelling and analysis technique for composite floor framing systems including concrete slab under column loss scenarios. Modelling techniques include part creation, meshing, modelling of plasticity and fracture of material, progressive damage and material failure, nonlinear interaction. The accuracy and efficiency of the material models was validated by comparing the finite element results with the experimental test data.

### **5.2 Model Development**

A reliable high-fidelity finite element model to accurately capture the behaviour of the composite structure was developed. It required various numerical details and application of appropriate features to the models. Development of the numerical finite element model for various components of the structure, including connection, bolt, concrete slab, and beam, is discussed. The model was created, developed and analyzed using the Abaqus finite element software (Dassault Systèmes 2013) with the means of explicit time integration technique.

### **5.3 Model Overview**

As explained in Chapter 3, two prototype steel gravity framing systems with a rectangular plan and clear spans of 6.0 m and 9.0 m were designed, as shown in Figure 3-1 to Figure 3-3. Two different types of shear connections with different material thicknesses were considered in the modelling: shear tab welded to the column and bolted to the beam; and double-angle bolted to both column and beam. A two-span composite frame assembly under push-down loading with an unsupported centre column was considered, as shown in Figure 5-1(a). However, due to the capability of finite element software to simulate the symmetry, only

one span was modelled and proper boundary conditions were imposed to the plane of symmetry, as illustrated in Figure 5-1(b).

## **5.4 Modelling of Components**

Components were each created as an individual part in Abaqus using the “Part Module” tools. Instances of the parts were then assembled using the “Assembly Module”. All features including type of parts (deformable, rigid), shape (solid, shell, or wire), geometry of cross-section, section extrusion, creating hole and cut were defined in the “Part Module”.

### **5.4.1 Steel Connections**

Both connections (shear tabs and double angles) were created as a three-dimensional deformable part. Each connection was generated by sketching the angle/plate cross-section and then extruding to the depth of the section (230 mm or 390 mm). The sketch and the extrusion depth were the modifiable parameters that defined the base feature. It allowed generating a part with the ability to tweak the section dimensions easily, since various thicknesses were modelled. The bolt holes were cut through the plate and angle thickness based on the defined hole’s profile. A two-dimensional profile was sketched for the geometry and position of the holes, and then the profile was extruded through the plates. Typical finite element models of the connection components are shown in Figure 5-2 and Figure 5-3.

### **5.4.2 Bolts**

Two diameters of bolt (19 mm or 22 mm) were used. The dimensions and geometrical properties of the bolts, including head, shank, and nut, were extracted from part six of the CISC Handbook of Steel Construction (CISC 2012). To avoid unnecessary complexity and a highly-time-consuming process, since in none of the experiments were bolts either failed or substantially deformed, threads were



not modelled. Similar to the steel connections, bolts were created as a three-dimensional deformable part.

All three segments of the bolt (head, shank, and nut) were generated and added in one part using the “Shape Module” feature. To model a bolt, a hexagonal section of the head was first sketched and then extruded to the length of the head. Second, the shank was added to the end of the bolt head by sketching a circular section and then extruding it to the length of the grip, which is the summation of beam web thickness and plate thicknesses (either shear tab or double angle). At the end, the nut was added to the end of the bolt shank similar to the procedure used for creating the bolt head. A typical model of bolt is illustrated in Figure 5-4.

### **5.4.3 Concrete Slab**

The concrete slab was created as a three-dimensional deformable part. The slab was generated by sketching a rectangular section (cross-section of slab) and then extruding the section to the length of span from centre to centre of columns (9260 mm or 6260 mm). Similar to the steel connections, the sketch and the extrusion length were modifiable, which facilitated generating slabs with two different widths (1500 mm width for 6.0 m clear span, and 2250 mm width for 9.0 m clear span). A typical model of the concrete slab is shown in Figure 5-5.

### **5.4.4 Reinforcing Steel**

Since rebars are usually assumed to be either in tension or compression, they were created as a three-dimensional deformable wire part. Two layers of rebars in two directions (longitudinal and transverse) were generated. Initially, one wire was sketched and then it was replicated by using the linear pattern feature to create a layer of rebars (spacing of 200 mm). Rebars in the longitudinal and transverse direction were similar in length and width to the corresponding concrete slab. Longitudinal rebars were either 9260 mm or 6260 mm long and transverse rebars were either 1500 mm or 2250 mm. A typical part of rebars is shown in Figure 5-6.

#### **5.4.5 Beam**

The beam was created as a three-dimensional deformable part. Two different types of part (solid and shell) were used to model the beam with the same cross-section. A partial length of beam close to the connection on both ends was modelled by solid elements, as this is the region with the most complex stress field and the potential for inelasticity. The beam portion between these end zones, where stresses remained in the elastic range, was modelled using shell elements. Proper constraint was applied to the solid/shell interface to connect the two segments of beam together. Details of interaction are explained in Sections 5.8.

To create the beam part (either solid or shell), the I-shaped section was drawn and extruded to the required beam length. The bolt holes using a two-dimensional profile were then cut through the web thickness on the solid element (part attached to the connections). For the shell part of the beam, since web and flanges had different thicknesses, different thicknesses were applied to the shell surfaces individually. For a homogeneous section like steel shell beam, five integration points were specified through the thickness of each layer. A typical model of a beam created in both shell and solid parts is shown in Figure 5-7.

#### **5.4.6 Column**

Since no deformation or failure was expected from the central removed column in a progressive collapse scenario, the column was created as a three-dimensional discrete rigid part. No section or material properties can be applied to the rigid part. However, the motion of the part is controlled by selecting a rigid body reference point for constraining its motion.

The main purpose of using a rigid column was to avoid any local stress concentration and to apply load and symmetry boundary conditions to the reference point. A typical model of a column is illustrated in Figure 5-8.

## **5.5 Element Selection and Meshing Technique**

Mesh generation and element type selection for the parts are assigned in the “Mesh Module” within Abaqus/CAE. Similar to creating parts, the process of assigning a mesh to the parts—such as seeds, mesh techniques and element types—is a feature based. Since different types of parts were created, appropriate forms of elements were selected and assigned to the individual parts. In the following sections, the type of elements, meshing techniques and kernel of the modelling techniques are explained.

### **5.5.1 Element Type**

Behaviour of an element in Abaqus is characterized by five aspects: family; degrees of freedom (directly related to the element family); number of nodes; formulation; and integration. Element families that were used include continuum elements (solid/brick elements), shell elements, rigid elements, and truss elements. The commonly used Abaqus element families are shown in Figure 5-9. The first letter of an element’s name indicates to which family the element belongs. For example, the C3D8R element, which was used for the connections and concrete slab, is a continuum element.

The degrees of freedom are the fundamental variables calculated during the analysis. For a stress/displacement simulation the degrees of freedom are mostly translations and, for shell and beam elements, the rotations at each node as well.

Displacements and other degrees of freedom are calculated at the element nodes. At any other point in the element, the displacements are obtained by interpolating from the nodal displacements. Elements such as the 8-node brick that have nodes only at their corners use linear interpolation in each direction and are often called linear elements or first-order elements.

An element's formulation refers to the mathematical theory used to define the element's behaviour (Lagrangian or Eulerian). In Abaqus, all stress/displacement elements are based on the Lagrangian formulation.

Abaqus uses numerical techniques to integrate quantities over the volume of each element, thus allowing broad generality in material behaviour. Using Gaussian quadrature for most elements, Abaqus evaluates the material response at each integration point. Continuum elements in Abaqus can utilize full integration or reduced integration (only one integration point per element), a choice that has a significant effect on the accuracy of the element for a given problem. Abaqus uses the letter R at the end of the element name to label reduced-integration elements. For example, C3D8R is the 8-node linear brick, reduced integration element.

Due to the dynamic nature of the progressive collapse analysis (quasi-static analysis), elements were selected from the explicit library (shown in Figure 5-10) with a wide range of spatial dimensionality. Like other explicit codes, Abaqus/Explicit uses the lumped mass formulation and primarily reduced-integration method for the elements. Reduced integration uses a lower-order integration to form element stiffness, but the mass matrix and distributed loadings use full integration. Although Abaqus offers fully integrated elements, reduced-integration elements are more efficient and computationally inexpensive.

### **5.5.2 Element Hourglassing and Locking**

The use of the reduced-integration scheme has a drawback that can result in mesh instability, commonly referred to as “hourglassing”. It performs in a manner similar to that of a rigid body mode, which does not cause any strain and, hence, no contribution to the internal energy.

There are several common reasons of excessive hourglassing: boundary condition, contact and concentrated load at a single node; and bending with too few elements. For the latter one, hourglassing would not be a problem if multiple elements are used through the thickness (at least four). By preventing the aforementioned causes and by activating the “enhanced hourglass control” in Abaqus (shown in Figure 5-10), the hourglass no longer would be a problem.

Another method to avoid hourglassing is simply to implement full integration or incompatible-modes elements. The problem with the use of full-integration

elements is their susceptibility to shear and volumetric locking. Shear locking causes the element to behave too stiffly in bending and volumetric locking occurs when the material is nearly incompressible, which causes no volume change.

The first-order incompatible-modes element is a special form of full-integration element, which is very helpful in modelling bending with only one element through the thickness, provided the element is well shaped. It models shear behaviour correctly and does not have any hourglass modes (because full integration is used). It does not lock for approximately incompressible materials.

The drawback of incompatible-modes elements is that they are more expensive than the regular elements and accuracy degrades significantly when the mesh is distorted. Since progressive damage and ductile fracture of connections, which involves a heavily element distortion, is modelled in this study, the incompatible-modes element was not an appropriate choice. Thus, reduced-integration elements were used for all types of elements.

### **5.5.3 Element Selection**

Due to the complex nature of connections and being the region of interest to this study, the need for three-dimensional elements (brick elements) was dictated. Thus, the connections and the solid parts of the beam were selected from the “3D Stress” element family known as the C3D8R element with reduced-integration. Since modelling progressive damage and failure of materials was considered, element deletion and stiffness degradation was activated in the element controls, as shown in Figure 5-10. In Abaqus/Explicit, this capability is available for solid elements with progressive damage behaviour.

Element controls are provided to specify the value of the maximum stiffness degradation, and whether element deletion occurs when the degradation reaches this level. The choice of element deletion also affects how the damage is applied. Details on progressive damage and ductile fracture are provided in Section 5.6.3. Similar to the connections, eight-node reduced-integration solid elements were assigned to the bolts and concrete slab (shown in Figure 5-4 and Figure 5-5).

Four-node reduced-integration shell elements (S4R) were assigned to the non-solid part of the beam, as shown in Figure 5-7. Since this portion remains mainly in the elastic phase, no progressive damage behaviour was considered.

Four-node 3D bilinear discrete rigid quadrilateral elements (R3D4) were assigned to the column, as shown in Figure 5-8. A discrete rigid part is assumed to be rigid and is used in the analyses to model bodies that cannot deform. Thus, by default no applicable element controls are available for rigid elements.

Two-node linear 3D truss elements (T3D2) were used to model the reinforcing steel bars. Trusses are modelled as line-like structures that support loading only along the axis or the centreline of the element. No moments or forces perpendicular to the centreline are supported. Since no cross-sectional geometry of rebars was created in the Part module, the cross-sectional area of the rebars was defined in the Property module.

#### **5.5.4 Meshing Technique**

To create an acceptable mesh in Abaqus, the “Mesh Module” provides a range of tools that allow specifying different mesh characteristics, such as mesh control, mesh density, and element type. A variety of mesh controls, such as an element shape meshing technique and meshing algorithm, were used. The density or size of elements for each component was dictated by a comparison between the results of material testing and material modelling, such as the force—displacement graph. Details of the results of these comparisons are shown in Section 5.6.

In general, there are two meshing methodologies in Abaqus/CAE: top-down and bottom-up. Top-down meshing generates a mesh by working down from the geometry of a part, while the bottom-up meshing produces a mesh by working up from two-dimensional shapes to create a three-dimensional mesh.

The top-down meshing technique was used to generate meshes, since all parts were created individually in the Part module. The top-down mesh usually matches the geometry of the parts. However, for complex shapes some techniques such as

partitioning or selecting a proper mesh algorithm can be implemented to generate a high-quality mesh. This was mostly the case for the geometry of connections with holes, and bolts. Figure 5-2 to Figure 5-8 show the mesh density and element shape of all components used in the model.

As a part of the optimization, several meshing techniques and mesh algorithms were tried to reach a high-quality mesh that was not computationally expensive. As an example, Figure 5-11 shows meshing of a shear tab plate generated with two different mesh algorithms with similar element sizes. Figure 5-11(a) shows meshing with the “Advancing front” algorithm that generated about 36,000 elements, while Figure 5-11(b) displays meshing with the “Medial axis” technique that generated about 29,000 elements.

Another example is shown in Figure 5-12 (two distinct meshing techniques on a bolt), which self-explains the importance of applying a proper meshing technique to the parts. Not only is the number of elements significantly reduced, which directly influences the analysis running time, the element shape in the second technique also had a structured pattern which was very important, especially in the progressive damage and failure modelling.

Paying attention to the shape and density of the elements is the key to achieving reliable results. Most of the modelling and analysis issues stem from implementation of poor meshing techniques. Although Abaqus provides the “Verify Mesh” feature for verifying mesh quality such as shape factor and aspect ratio of elements, it may not necessarily be adequate for achieving an optimized model. Having fine meshes may also not provide accurate and reliable output, while well-defined and structured-pattern meshes establish a consistent result.

Numerous geometry creation methods and meshing techniques, such as those shown in Figure 5-11 and Figure 5-12 were undertaken to reach reliable results yet having a less-expensive running time.

## 5.6 Material Properties and Verification

Material properties are defined in the Property module in Abaqus. Material definition specifies all the property data relevant to a material. In the following sections, material properties of the components used in the models are explained. Results in terms of failure mode and force—displacement graphs are presented. In addition, progressive damage and material failure definition, which was used only for the steel connections, is explained.

### 5.6.1 Material Model for Concrete

Abaqus offers three concrete material models: concrete smeared cracking; brittle cracking; and concrete damaged plasticity. Due to the limitations existing in the first two models, the “concrete damaged plasticity” was used to model the concrete properties.

“Concrete damaged plasticity” is a continuum, plasticity-based damage model assuming two main failure mechanisms: tensile cracking and compressive crushing. The model assumes that the uniaxial tensile and compressive responses are characterized by damaged plasticity, as shown by an idealized model in Figure 5-13. The concrete damaged plasticity model assumes that the reduction of the elastic modulus is given in terms of a scalar degradation variable and initial modulus of elasticity, as illustrated in Figure 5-13.

The stress–strain response under a uniaxial tension follows a linear elastic relationship up to the tensile strength (the onset of micro-cracking in the concrete material). As mentioned in Section 3.8.3, in the absence of concrete tensile test the tensile strength of concrete was calculated in terms of its compressive strength ( $f'_c$ ) as  $0.33\sqrt{f'_c}$ . Beyond that, formation of micro-cracks is characterized by a softening stress–strain response, which prompts strain localization in concrete. Since reinforcement embedded in the concrete was provided by means of one-dimensional truss rebars, the concrete behaviour was considered independently of the rebars.



Effects of reinforcement interaction with the concrete slab, such as bond slip and dowel action, were accounted for by introducing a “tension stiffening” mechanism into the concrete modelling to simulate load transfer across cracks through the rebars. Tension stiffening was specified by means of a post-failure stress–strain curve, as shown in Figure 5-13(b).

Under uniaxial compression, the response was assumed linear until 40% of the compressive strength of concrete ( $f'_c$ ). In the plastic region, the response was typically characterized by stress hardening followed by strain softening beyond the ultimate stress ( $f'_c$ ). This representation, although somewhat simplified, captures the main features of the response of concrete. The stress–strain curve was defined beyond the compressive strength into the strain-softening regime as shown in Figure 5-13(a). Figure 5-14 shows material stress–strain curves of one of the 28-day concrete cylinder tests along with the corresponding Abaqus material model, and the tension softening region was drawn based on the recommendation provided in the Abaqus manual.

Figure 5-15(a) shows modelling of the concrete cylinder similar to the one tested in the structural laboratory. Mechanical properties (Figure 5-14) were assigned to the three-dimensional eight-node element cylinder part. Explicit analysis was performed with the loading rate similar to the tested one. The concrete cylinder was tied to the top and bottom rigid element caps, analogous to the test. The results of the analysis in terms of compressive equivalent plastic strain (PEEQ) are shown in Figure 5-15(b).

In addition, the force–displacement responses of both the experimental and Abaqus tests are illustrated in Figure 5-16. As shown, there is excellent agreement between the results. The results demonstrate significantly the validity and reliability of the concrete damaged plasticity model. It captured the response of the concrete cylinder well in terms of maximum force, corresponding displacement, and post-failure response.

### 5.6.2 Material Model for Steel Components

Steel material initially responds elastically and then exhibits considerable plastic deformation. Since the steel connections experienced significant plastic deformation, proper constitutive plasticity and hardening material models were considered for achieving reliable and acceptable results. Plasticity models the material's mechanical response as it undergoes non-recoverable deformation in a ductile manner. Materials like steel that display ductile behaviour (large inelastic strains) yield at stress levels lower than that defined by the elastic modulus. This implies that the stress and strain are in fact “true” stress (Cauchy stress) and logarithmic strain. Consequently, material data in Abaqus was defined in terms of true stress and strain (Dassault Systèmes 2013).

Having engineering stress–strain data obtained from the uniaxial tests, true stress ( $\sigma_{\text{true}}$ ) and logarithmic plastic strain ( $\sigma_{\text{ln}}^{\text{pl}}$ ) of an isotropic material can be obtained from nominal stress and strain ( $\sigma_{\text{nom}}, \epsilon_{\text{nom}}$ ) by implementing the conversion formula shown in Equation (5-1):

$$\begin{aligned}\sigma_{\text{true}} &= \sigma_{\text{nom}}(1 + \epsilon_{\text{nom}}) \\ \sigma_{\text{ln}}^{\text{pl}} &= \ln(1 + \epsilon_{\text{nom}}) - \frac{\sigma_{\text{true}}}{E}\end{aligned}\tag{5-1}$$

where E is the modulus of elasticity (Young's modulus).

Figure 5-17 shows engineering and true stress–strain curves of one of the tested coupons. A simplified piecewise form of the true static curve up to the maximum stress was used in Abaqus to represent the material behaviour of the component in the detailed modelling approach. The post-necking behaviour and material failure is explained in Section 5.6.3.

Figure 5-17 illustrates two pairs of curves: dynamic, and static. The static curve was constructed from the dynamic one obtained during the tension coupon tests. Since only up to six static points were recorded during the tensile tests, the static curve was developed parallel to the dynamic one by passing through the recorded static points. As the purpose of the numerical finite element modelling was to

evaluate the behaviour under a quasi-static loading condition (similar to the physical test). It should be noted that no tension coupon tests were performed on the testing beam and stub column members. As such, calibrated and scaled material properties of tested coupon plates were considered for testing beam. Since the column in the finite element modelling was simulated as a rigid element, no material properties were required to be assigned to the column.

### **5.6.3 Progressive Damage and Material Failure**

Abaqus offers a capability of modelling progressive damage and material failure in ductile metals in conjunction with a piecewise-linear plasticity model. Material failure refers to the complete loss of load-carrying capacity, which results from progressive degradation of the material stiffness.

The degradation process is modelled using damage mechanics. Figure 5-18 shows stress–strain response of a typical metal specimen during a tensile coupon test. The response is initially linear elastic (o-a), followed by yielding and strain hardening (a-b). Beyond point b, curve (b-d) is the damaged response during which the deformation is localized in a necking region. Point b identifies the onset of damage, which is referred to the damage initiation criterion. Beyond this point, the stress–strain response (b-d) is governed by the degradation of the stiffness in the region of strain localization (Dassault Systèmes 2013). In the context of damage mechanics, curve (b-d) can be viewed as the degraded response of the curve (b-c) that the material would have followed in the absence of damage. Thus, in Abaqus the definition of the material failure mechanism consists of four distinct parts:

- definition of the effective (or undamaged) material response (curve o-a-b-c) as explained in Section 5.6.2;
- damage initiation criterion (point b);
- damage evolution law (curve b-d); and
- choice of element removal whereby elements can be removed once the material stiffness is fully degraded (point d).

### 5.6.3.1 Damage Initiation Constitutive Model

There are several constitutive models that predict the damage initiation of the material. However, the model proposed by Hooputra et al. (2004) was used in this study. They suggested that sheets and thin-walled extrusions made of aluminum may fail due to one or a combination of the different failure mechanisms: ductile failure (based on initiation, growth and coalescence of voids), shear fracture (based on shear band localization), and instability due to localized necking. In tests conducted as part of that research, the main fracture modes were found to be shear and ductile failure, while instability failure did not govern.

Most of the phenomenological fracture models are based on a fracture diagram that gives the equivalent plastic strain at fracture as a function of the stress state (i.e. stress triaxiality). Theoretical and experimental studies have shown that the stress state is the key parameter controlling the magnitude of the fracture strain (Bai et al. 2009). In Hooputra et al. (2004) model, it is assumed that there is no interaction between the ductile and shear fracture mechanisms.

The ductile damage criterion assumes that the equivalent plastic strain ( $\epsilon_{eq}^{pl}$ ) is a function of stress triaxiality ( $\eta$ ) and strain rate. For a given strain rate, assumed to be small, effective plastic strain at the onset of ductile damage ( $\epsilon_0^{pl}$ ), as shown in Equation (5-2), is defined as a monotonically decreasing function of the stress triaxiality. The model considers the effect of a hydrostatic stress condition on material damage by introducing a stress triaxiality parameter, which is the ratio of mean stress ( $\sigma_{mean}$ ) to effective stress ( $\sigma_{eff}$ ).

$$\begin{aligned} \epsilon_0^{pl} &= d_0 e^{-c\eta} \\ \eta &= \frac{\sigma_{mean}}{\sigma_{eff}} = \frac{\sigma_1 + \sigma_2 + \sigma_3}{\sqrt{\sigma_1^2 + \sigma_2^2 + \sigma_3^2 - \sigma_1\sigma_2 - \sigma_2\sigma_3 - \sigma_3\sigma_1}} \end{aligned} \quad (5-2)$$

where  $c$  and  $d_0$  are directionally-dependent material parameters; and  $\sigma_i$  are principal stresses.

Assuming homogeneous material properties for steel, the parameter  $c$  becomes scalar and the value suggested by Hooputra et al. (2004) was used ( $c = 5.4$ ). The

parameter  $\eta$  was selected so that the stress–strain curves obtained from finite element models would correspond closely to coupon test results. Substituting the parameter  $\eta$  for the uniaxial coupon test into Equation (5-2) gives  $d_0 = e^{5.4\eta} \varepsilon_u$ , where  $\varepsilon_u$  is the uniaxial plastic strain of the material at which the failure was initiated. The ultimate plastic strain of the materials from the tension coupon tests was used as  $\varepsilon_u$ . The shear damage criterion assumes that the equivalent plastic strain at the onset of damage is a function of shear stress ratio ( $\lambda$ ) and strain rate.

$$\begin{aligned}\varepsilon_0^{pl} &= d_0 e^{f\lambda} \\ \lambda &= \frac{1 - k_s \eta}{\phi} \\ \phi &= \frac{\tau_{\max}}{\sigma_{\text{eff}}}\end{aligned}\tag{5-3}$$

where  $k_s$  is an empirical material parameter ( $k_s = 0.3$  was selected as proposed by Hooputra et al. (2004));  $\phi$  is the ratio of maximum shear stress ( $\tau_{\max}$ ) to effective stress ( $\sigma_{\text{eff}}$ ); and  $f, d_0$  are scalar material parameters.

The value for the parameter  $f$  suggested by Hooputra et al. (2004) for quasi-static analysis was used ( $f = 4.04$ ). Similar to the ductile criterion, the same approach was used to calculate parameter  $d_0$ . Substituting the parameter  $\lambda$  for the uniaxial coupon test into the Equation (5-3) yields  $d_0 = e^{-4.04\lambda} \varepsilon_u$ . Table 5-1 summarises the parameters used for both the ductile and shear criteria, in this research.

### 5.6.3.2 Damage Evolution Law

After plastic strain in the material reaches the onset of damage (damage initiation), the material enters the damage phase. From this point onward, the plasticity model cannot accurately denote the material behaviour since it introduces a mesh dependency due to strain localization. Thus, a damage evolution law for ductile metals was added to the material response, which assumes that damage is defined by the progressive degradation of the material stiffness. Moreover, it eventually results in complete material failure at the plastic strain equal to the effective plastic strain at the end of the failure evolution phase.

It describes the rate of stiffness degradation once the initiation criterion is satisfied. Figure 5-19 shows a typical stress–strain curve of a ductile material undergoing damage. The solid curve illustrates the damaged response, while the dashed curve is the response in the absence of a damage definition. The overall damage variable,  $D$ , captures the combined effect of all active damage mechanisms. The damage variable starts from 0 at the onset of damage and ends to 1 at the complete loss of capacity. The equivalent plastic strain at failure ( $\epsilon_f^{pl}$ ) occurs once the overall damage variable reaches the value  $D = 1$ .

For an elastic–plastic material with isotropic hardening like structural steel, the damage manifests itself in two forms: softening of the post-damage stress–strain curve and degradation of the elasticity. Since the stress–strain relationship does not accurately represent the material's behaviour due to the strong mesh dependency, Abaqus uses Hillerborg's approach (Hillerborg et al. 1976) based on the fracture energy to follow the strain-softening branch of the stress–strain curve. This approach is based on creating a stress–displacement response after damage is initiated. So, Abaqus formulates the damage evolution law based on stress–displacement response by introducing either fracture energy dissipation or the effective plastic displacement at failure. The implementation of this stress–displacement concept requires the definition of a characteristic length of the element, which depends on the element geometry and formulation: it is a typical length of a line across an element for a first-order element, and it is half of the same typical length for a second-order element. Characteristic length is used because the direction in which fracture occurs is not known in advance. Therefore, elements with large aspect ratios will have rather different behaviour in the two principal directions. Thus, mesh sensitivity remains because of this effect, and elements that have aspect ratios close to unity are recommended.

Linear evolution softening was used for the material stiffness degradation evolution from the plastic strain at the onset of fracture to the effective plastic strain at failure. Displacement at failure (effective plastic displacement,  $\delta_u$ ) was estimated based on the material and mechanical properties of the coupon tests by

implementing the classical fracture mechanics theories. Based on fracture mechanics, first mode fracture energy ( $G_I$ ) per unit area required for a crack to be opened is calculated by Equation (5-4). Fracture energy dissipation can also be defined based on the ultimate stress ( $\sigma_u$ ) and displacement ( $\delta_u$ ).

$$G_I = \frac{K_I^2}{E}$$

$$K_I = \sigma \sqrt{\pi a}$$

$$G_I = \frac{\sigma_u \delta_u}{2}$$
(5-4)

where  $E$  is the modulus of elasticity;  $K_I$  is the stress intensity factor of the first mode of crack opening;  $\sigma^{pl}$  is the stress corresponding to the effective plastic strain at the onset of damage (crack initiation); and  $2a$  is the crack length. The ultimate stress ( $\sigma_u$ ) was considered as the stress corresponding to the effective plastic strain. By simplifying the equations above, the plastic displacement at failure can be estimated by Equation (5-5):

$$\delta_u = \frac{2\sigma_u \pi a}{E}$$
(5-5)

From coupon tests, assuming the average crack length of 12 mm, ultimate stress of 490 MPa, modulus of elasticity of 194 GPa, the effective plastic displacement at failure is  $\delta_u = 0.095$  mm. It should be noted that by changing the crack length from 12 mm to 24 mm, the global response of the structure did not change significantly. It affects the post-peak response only slightly.

### 5.6.3.3 Element Removal

Abaqus offers a choice to remove the element from the mesh once the material stiffness is fully degraded. An element is said to have failed when all section points at any integration points have lost their load-carrying capacity. Elements are deleted by default upon reaching maximum degradation ( $D_{max} = 0.99$ ), as shown in Figure 5-19. The maximum degradation was considered to be 0.95 ( $D_{max} = 0.95$ ), since reaching 0.99 is not always attainable. Figure 5-20 and Figure

5-21 show the force–displacement curves of coupon tests for 6 mm thickness of plate and angle, respectively, versus results of Abaqus models. As seen, the progressive damage and material failure parameters selected caused the models to predict accurately the ultimate capacity and ductility of the coupons. Figure 5-22 also shows the failure mode of four different materials of plates and angles used in the experimental tests. It can easily be seen that the failure mode is similar to the one of the tension coupon tests.

Other than the finite element simulations of coupons, the shear tabs and double angles were each individually modelled and investigated to ensure the failure modes were similar to those observed in the physical tests. Failures of one of the double angles with two different damage parameters are illustrated in Figure 5-23 and are compared against the result of the corresponding physical test. As illustrated in Figure 5-23(a), introducing a non-calibrated progressive damage mechanism into the finite element material models would result in an incorrect failure mode, as compared to the calibrated model displayed in Figure 5-23(b).

#### **5.6.4 Material Model for Steel Rebars**

Similar to the above-mentioned steel materials, true stress was obtained from the engineering stresses and strains from the tensile tests on rebars by implementing the conversion formulae shown in Equation (5-1). Figure 5-24 illustrates the force–displacement curves of one of the rebars from both the tensile physical test and Abaqus numerical modelling. As explained in Section 5.4.4, as a part of the optimization process rebars were considered as a truss element with the ability of carrying only tensile/compressive forces. Thus, steel rebars for the purpose of simulating the tensile test were modelled as truss elements to be consistent with the combined structural models. Clearly, necking would not be observed in the model and as a result the post-ultimate segment of the force-displacement curve, as shown in Figure 5-24, did not follow the tensile test pattern. However, results agreed very well in terms of stiffness, ultimate capacity, and ductility.



### **5.6.5 Material Model for High Strength Bolts**

Material properties of A325 high-strength bolts were used. They were obtained from the bolt tests on ASTM A325 high-strength bolts conducted at the University of Alberta (Salem and Driver 2014). It should be noted that during the experiments none of the bolts experienced significant damage or deformation, and since the failure and deformation of the connections were mostly concentrated in the plates/angles, progressive damage and detailed material models were not required for the bolts. Thus, material properties used by Salem and Driver (2014) were used. Figure 5-25 shows the true stress–strain relationship for the bolt material used in the Abaqus modelling.

## **5.7 Contact Modelling**

Contact is an extremely discontinuous form of nonlinearity. Most of the non-convergence difficulties in Abaqus stem from the contact definition between parts. It is possible to solve complicated contact problems with deformable bodies if proper contact is defined. Abaqus/Explicit provides two algorithms for modelling contact: general contact and contact pairs.

The general contact algorithm is faster than the “contact pairs” and is geared toward models with complex topology and interactions, as was the case in this study. In this algorithm, all members interact with one another and with themselves. However, in the “contact pairs” algorithm, contact between every two potential surfaces must have been defined separately. General contact was used to define contact between all regions with a single interaction property. Appropriate properties should be defined and assigned to the contact interaction to mimic the actual behaviour of components, so normal and tangential contacts were introduced to the interaction properties. Normal behaviour was modelled using the “Hard Contact” pressure-overclosure method and the “Penalty” friction formulation method was used for the definition of tangential contact. Taken from the ASM Handbook Volume 18 (ASM International 1992), the coefficient of friction in the tangential contact was considered to be 0.3.

## 5.8 Constraints

The individual meshed parts were assembled and constrained to construct the finite element model. The surface-based “tie” constraint was implemented to tie two surfaces together to make the translational/rotational motion equal. Shear tabs were attached to the rigid stub columns at both ends by means of tie constraints in Abaqus. Since no rupture was observed at the location of welds (this was also verified later by the results of finite element analysis), welds were not modelled in any of the finite element models and instead the tie constraint was used to connect two surfaces.

The tie constraint technique was also used to attach the solid and shell parts of the beam, as shown in Figure 5-7. This ensured the integrity of the beam pieces (two solid segments and the middle shell segment) together and eliminating local stress concentrations at the interface.

The “embedded element” kinematic constraint was used to model the set of truss-element-based rebars that lie embedded in the concrete slab element. Abaqus searches for the geometric relationships between the nodes on rebars and the concrete host elements. If nodes on the rebars lie within a host element, the translational degrees of freedom of the node are constrained to the interpolated values of the corresponding ones of the concrete element. The layers of rebars were embedded into the concrete slab using truss elements and assuming they were fully bonded into the concrete slab.

## 5.9 Loading

The loading rate was selected so that the simulation is conducted as quickly as possible, while ensuring that the dynamic effects are minimal. A general recommendation is to limit the velocity to less than 1% of the material wave speed (the wave speed in steel is approximately 5000 m/sec). Thus, rate of 50 m/sec for steel would be the maximum value.

To load the prototype model, the middle stub column was pushed down in displacement control at a rate of 65 mm/sec. To ensure that the rate was proper and corresponded to the low-speed physical problem, the kinetic energy was compared against the internal energy to ensure the simulation reflects a quasi-static solution. The kinetic energy of the deforming material should not exceed 5% of its internal energy throughout the majority of the analysis. Figure 5-26 shows the energy balance of one of the finite element models (DA59B). It is seen that the kinetic energy is a small fraction of the internal energy.

The 65 mm/sec rate was selected based on running a series of simulations in the order from the fastest to the lowest rate. The results in terms of energy, failure mode, stress and plastic strain were examined to get an understanding of the effect of varying rates. Excessive loading rates resulted in a steep initial slope of the load–displacement curve and different failure modes, inconsistent with what was observed in the experimental tests.

Since instantaneous loading may induce the wave propagation through the model, which produces inaccurate results, loading was applied gradually to the model to promote the quasi-static solution. As such, the “smooth step” amplitude curve was implemented to ramp up the loading gradually from zero to the end. This curve is a fifth-order polynomial transition between two amplitudes such that the first and the second derivatives are zero at the beginning and the end of transition.

## **5.10 Boundary Conditions**

The boundary condition is deemed to be of significant importance in attaining reliable response for structures subjected to an extreme loading such as the column removal scenario. Several boundary conditions were applied to the model, as shown in Figure 5-27. The central stub column was only free to move in the vertical direction, while the other column was fully restrained against translation and rotation. Since only half of the span was modelled due to the symmetry, the proper boundary condition was imposed on both ends of the slabs. Similar conditions were also applied to the sides of the concrete slab.

In the slab-free finite element models (frames only), since no concrete slab existed to secure the beam, the top and bottom edges of the beam flanges were restrained against out-of-plane displacement.

### **5.11 Analysis Solution and Procedures**

Abaqus offers two unique methods to solve finite element problems: implicit and explicit. The implicit method solves both static and dynamic problems. Explicit method, on the other hand, solves only dynamic models by utilizing a direct-integration method to solve the dynamic equilibrium. The fundamental difference between implicit and explicit methods stems from the algorithm each method uses to solve the structure.

In the implicit method, the global mass and stiffness matrices of the structure have to be assembled and inverted, and a large set of nonlinear equations must be solved at each increment. In this method, since the solution at each step is unconditionally stable, there is no limit on the increment size. However, iteration and convergence checking are required. The out-of-balance force is used to check equilibrium; the equation has to be solved repeatedly.

The explicit dynamic method is a mathematical technique for integrating the equations of motion through time. It is also known as the forward Euler or central difference algorithm. In the explicit method, neither iteration nor convergence checking is required. The time increment has to be small enough in order to lie on the curve. The explicit dynamic procedure solves every problem as a wave propagation problem. Out-of-balance forces are propagated as stress waves between neighbouring elements. Thus, great attention should be paid when the explicit dynamic method is used by evaluating the energy balance to ensure the explicit simulation is yielding an appropriate response. Excessive artificial strain energy, which is an indicator of hourglassing, should be limited to less than 2% of internal energy. Excessive kinetic energy in a quasi-static simulation should be limited to a maximum of 5% of the internal energy. Figure 5-26 shows the energy balance of one of the finite element models (DA59B).

Since the nature of loading was quasi-static and due to the highly nonlinear and discontinuous nature of the analysis (such as large deformation, fracture and material damage and failure), implementing an explicit approach was an appropriate choice. One of the benefits of the explicit algorithm is that it does not require as much disk space as implicit for large problems, and it often provides a more efficient solution. However, since loading was applied very slowly to the structure (quasi-static), it required a significant total running time, which created the need for a high performance computing (HPC) system to obtain a reasonable processing time. Since the explicit solver required substantial computational resources, analyses were carried out on the Westgrid network, one of the Compute Canada regional partners. Portable batch system (PBS) jobs in conjunction with a Linux cluster environment were used to allocate computation tasks to the Abaqus input files placed on the Westgrid machines.

### **5.11.1 Quasi-Static Simulation**

Application of explicit dynamics to model quasi-static events requires special consideration. It is computationally impractical to model the process in its natural time period. Literally millions of time increments would be required. Artificially speeding up the process in the simulation is necessary to obtain an economical solution. Abaqus offers two approaches to obtaining economical quasi-static solutions with an explicit dynamics solver: increased load rates and mass scaling.

The time scale of the process artificially reduces if the loading rate increases. In this method, material strain rates calculated are artificially high by the same factor applied to the loading rate. The issue with this method is the kinetic energy balance. As the speed of the loading is increased, a state of static equilibrium evolves into a state of dynamic equilibrium, and thus inertia forces become more dominant. The selection of loading rate was explained in Section 5.9.

Mass scaling, on the other hand, allows the analyst to model in a natural time scale when considering rate-sensitive materials. Artificially increasing the material density by a factor of  $f^2$  increases the stable time increment by factor  $f$ .

By artificially increasing the stable time through mass scaling, the model can be analyzed in its natural time period. Variable mass scaling was applied to the whole model throughout the time steps. It was selected such that the inertial effects remained minimal enough to avoid an erroneous solution.

## **5.12 Derivation of Results**

Abaqus/viewer post-processing software was used to extract the results of the finite element analyses. Energy balances, internal forces and bending moment at different cross-sections, connection axial deformation, and failure modes were the most important results that were extracted. The most significant result achieved from the numerical studies was the connection capacity and ductility.

As explained in Section 5.11, energy balance was checked at the beginning of the post-processing step to ensure the quasi-static solution was achieved appropriately. Energy—in terms of internal, kinetic, artificial strain, and whole mode—was obtained and the components were compared against each other.

The internal forces developed in the cross-section of interest were derived directly from Abaqus by means of the “free body cut” feature. This feature creates a section cut at the user defined location and calculates the internal forces and moments acting on the section using the nodal forces.

Visual inspection of the model was an important tool in defining the failure mode and development of plasticity in the model. To track the plasticity development in the model, development of strains needed to be monitored closely. The equivalent plastic strain (PEEQ) was selected as an appropriate indication of the yielded areas of the connection.

Table 5-1: Parameters Used in the Damage Initiation Constitutive Model

Plate Thickness	Ductile Fracture			Shear Fracture		
	c	d <sub>0</sub> *	η	f	d <sub>0</sub> **	λ
9.5 mm	5.4	6.152	0.58	4.04	0.000339	1.652
6.5 mm	5.4	5.123	0.60	4.04	0.000266	1.640

\*  $d_0 = e^{5.4\eta} \epsilon_u$

\*\*  $d_0 = e^{-4.04\lambda} \epsilon_u$

$\epsilon_u$ : Ultimate Plastic Strain of the Material from the Tension Coupon Test

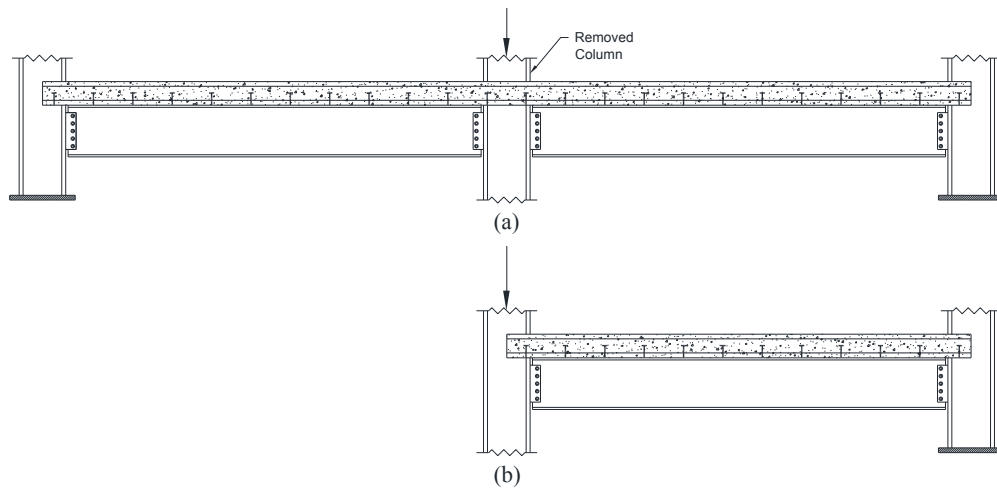


Figure 5-1: (a) Two-span Assembly; (b) One-span Assembly under Pushdown Displacement with Proper Boundary Condition at Unsupported Removed Column

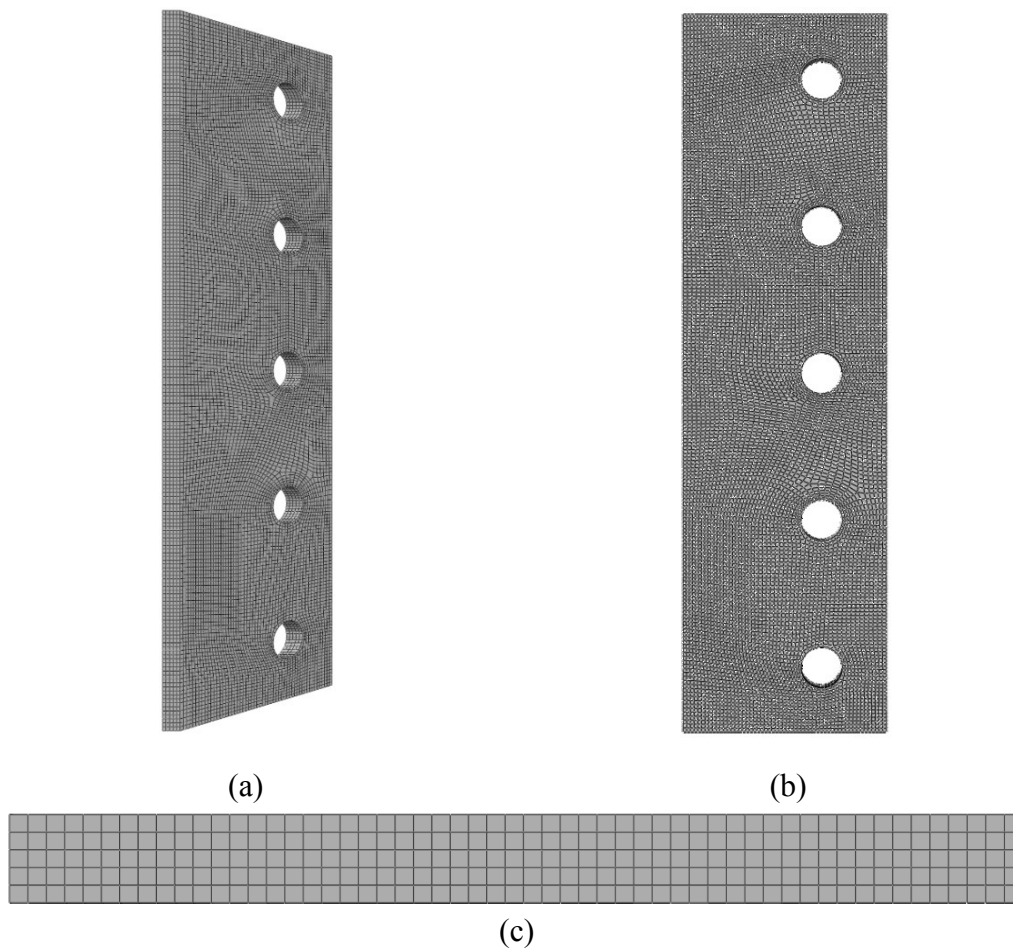
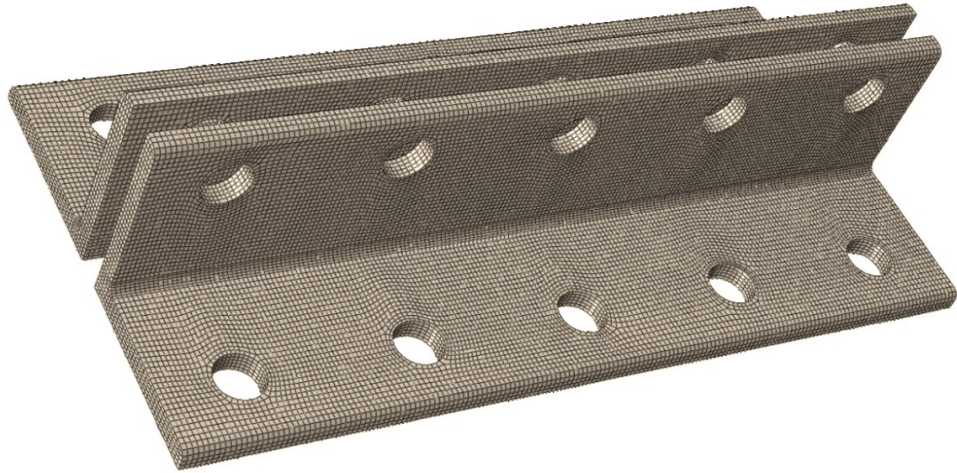
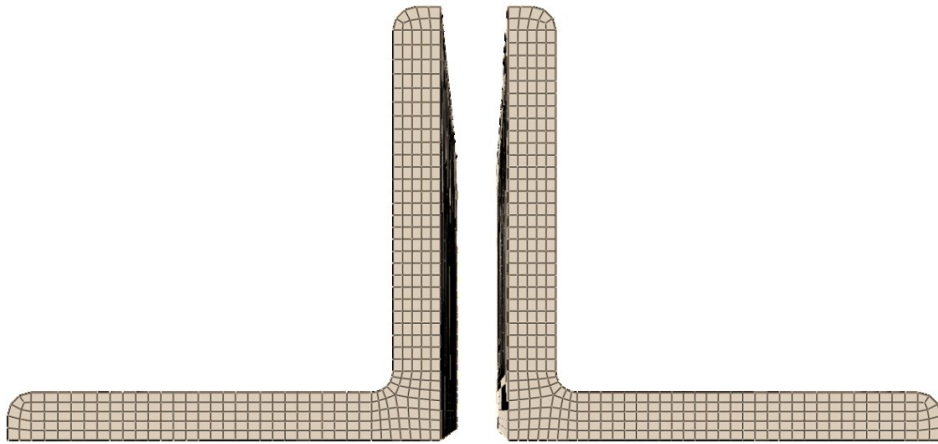


Figure 5-2: Typical Finite Element Model of Shear Tab: (a) Isometric View; (b) Side View; (c) Cross-section View





(a)



(b)



(c)

Figure 5-3: Typical Finite Element Model of Double Angle: (a) Isometric View; (b) Cross-section View; (c) End View

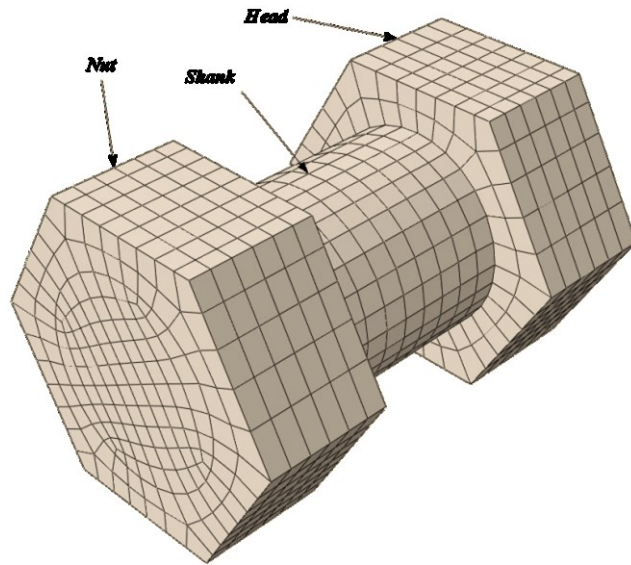


Figure 5-4: Typical Finite Element Model of Bolt

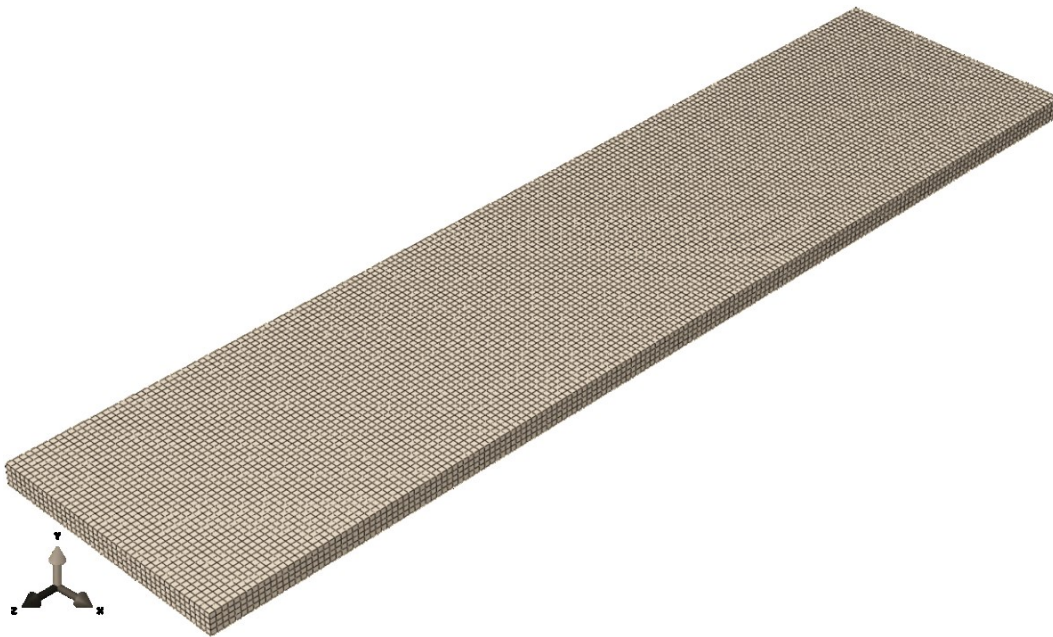


Figure 5-5: Typical Finite Element Model of Concrete Slab

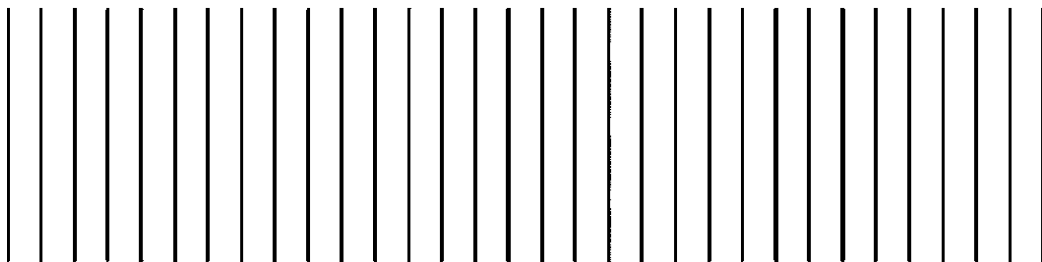
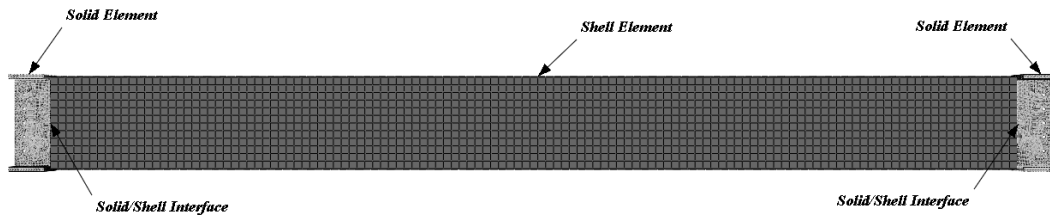
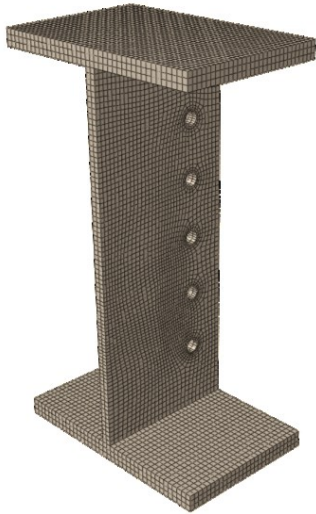


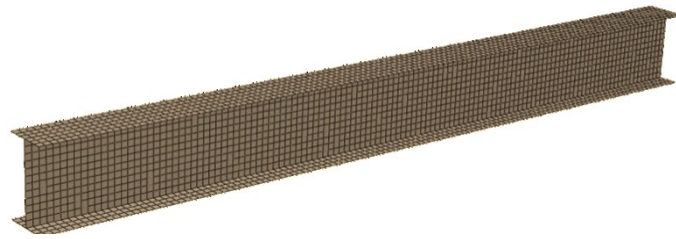
Figure 5-6: Typical Finite Element Model of Reinforcing Steel Layer



(a)

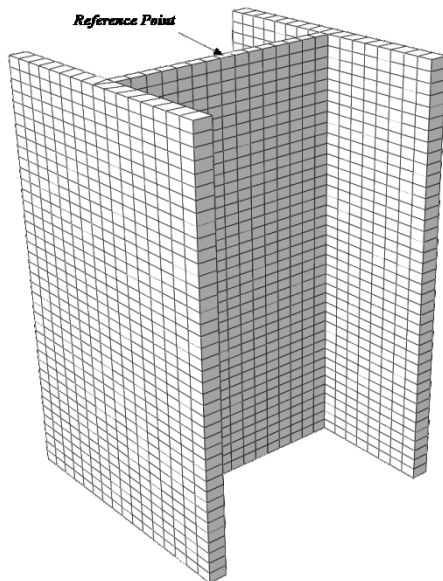


(b)

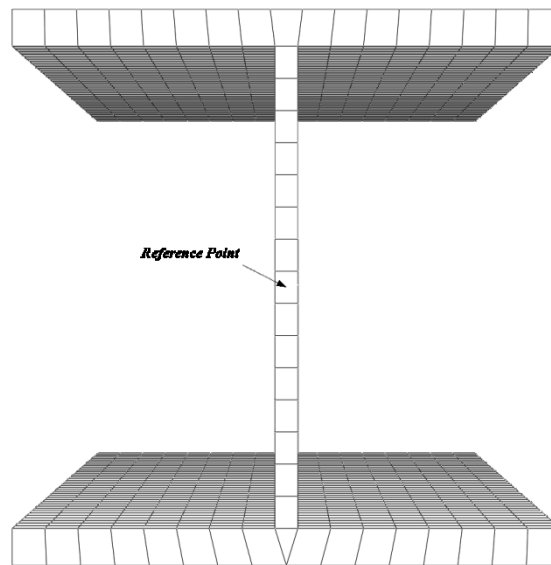


(c)

Figure 5-7: Typical Finite Element Model of Beam: (a) Assembly; (b) Solid Elements; (c) Shell Elements



(a)



(b)

Figure 5-8: Typical Finite Element Model of Column: (a) Isometric View; (b) Cross-section

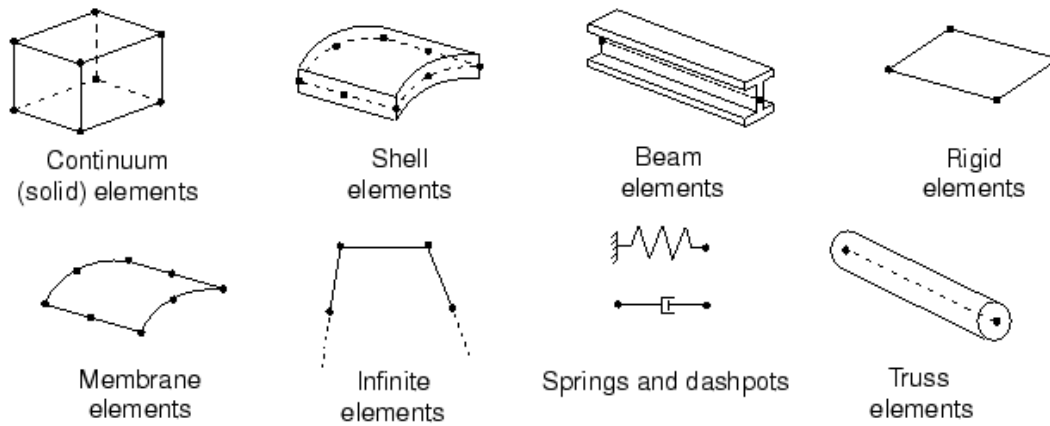


Figure 5-9: Commonly Used Element Families from Abaqus Manual (Dassault Systèmes 2013)

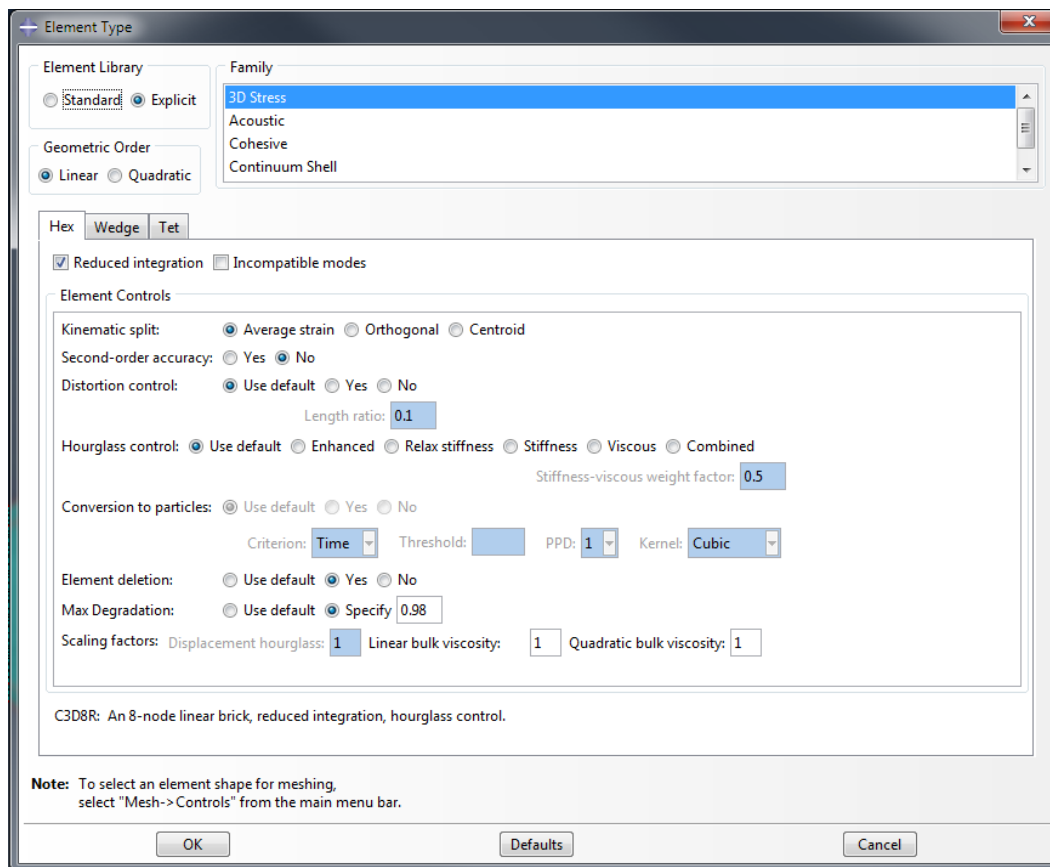


Figure 5-10: Element Type Selection in Abaqus/CAE

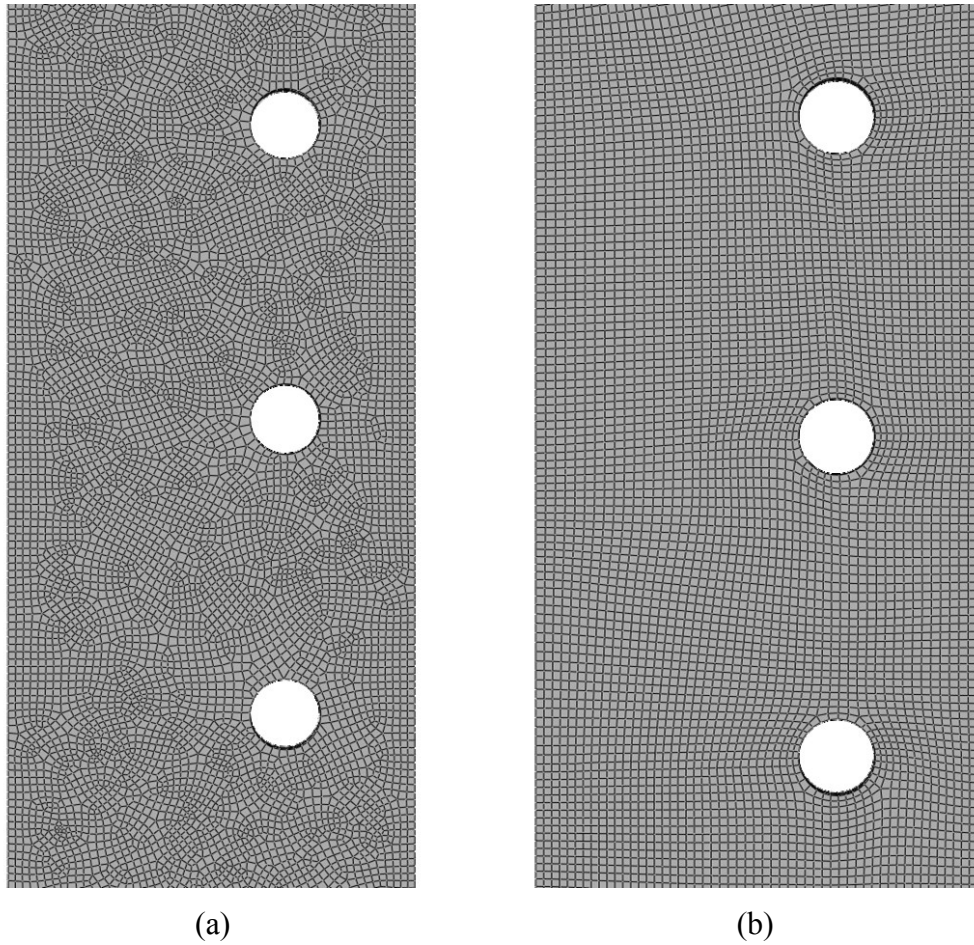


Figure 5-11: Plate Generated with Two Different Meshing Algorithms: (a) Medial Axis; and (b) Advancing Front

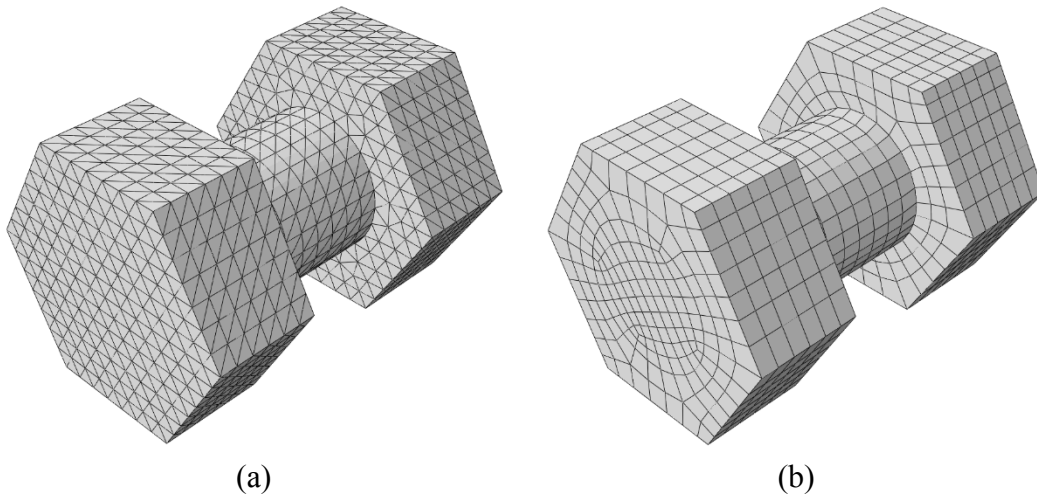


Figure 5-12: Bolt Generated with Two Distinct Meshing Techniques: (a) Free with Tetrahedral Elements (Number of Elements: about 14,000); (b) Sweep with Hexahedral Elements (Number of Elements: about 3,000)

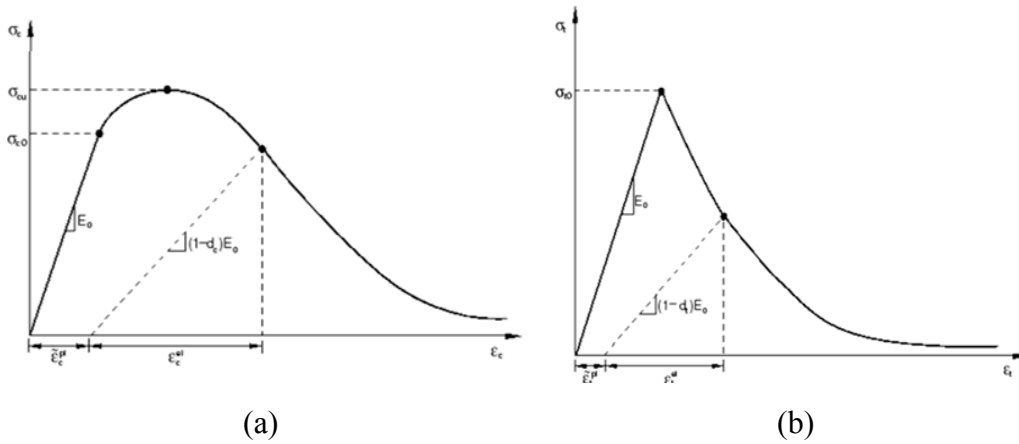


Figure 5-13: Idealized Response of Concrete to Uniaxial Loading in: (a) Compression; (b) Tension (Dassault Systèmes 2013)

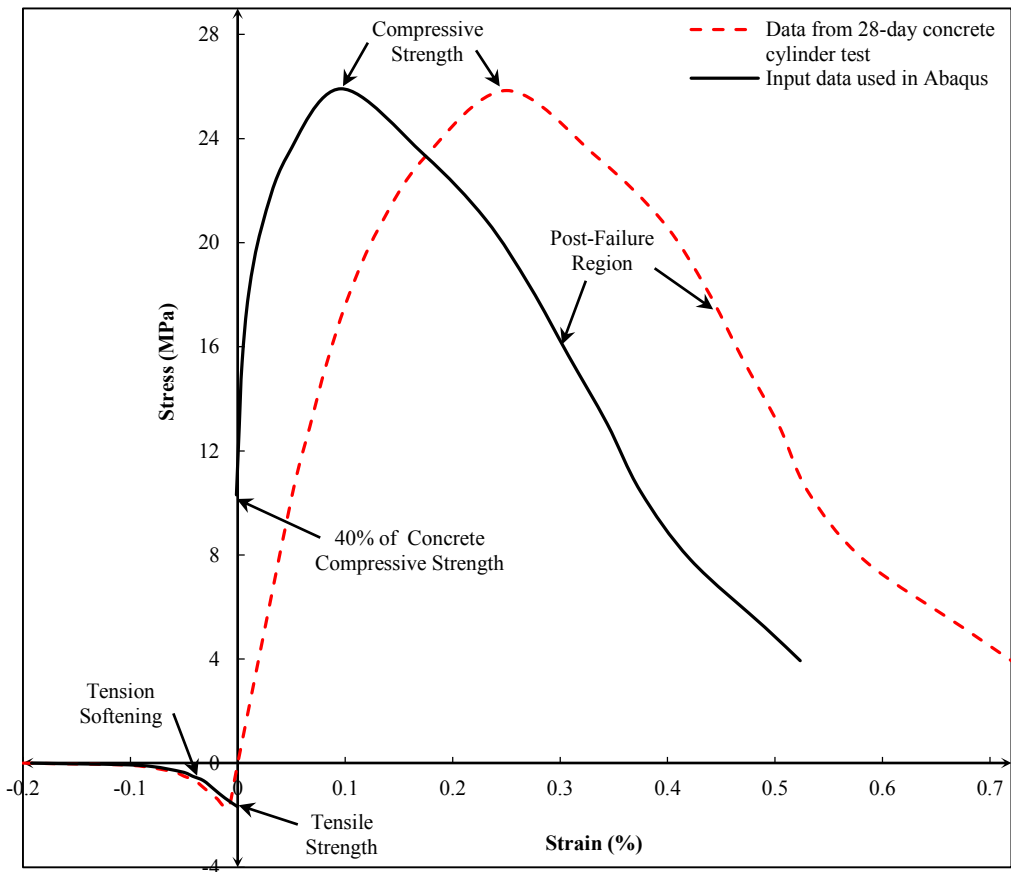


Figure 5-14: Concrete Uniaxial Stress–Strain Curves: 28-day Concrete Cylinder Test and Corresponding Abaqus Concrete Damage Plasticity Material Model Derived from the Concrete Cylinder Test

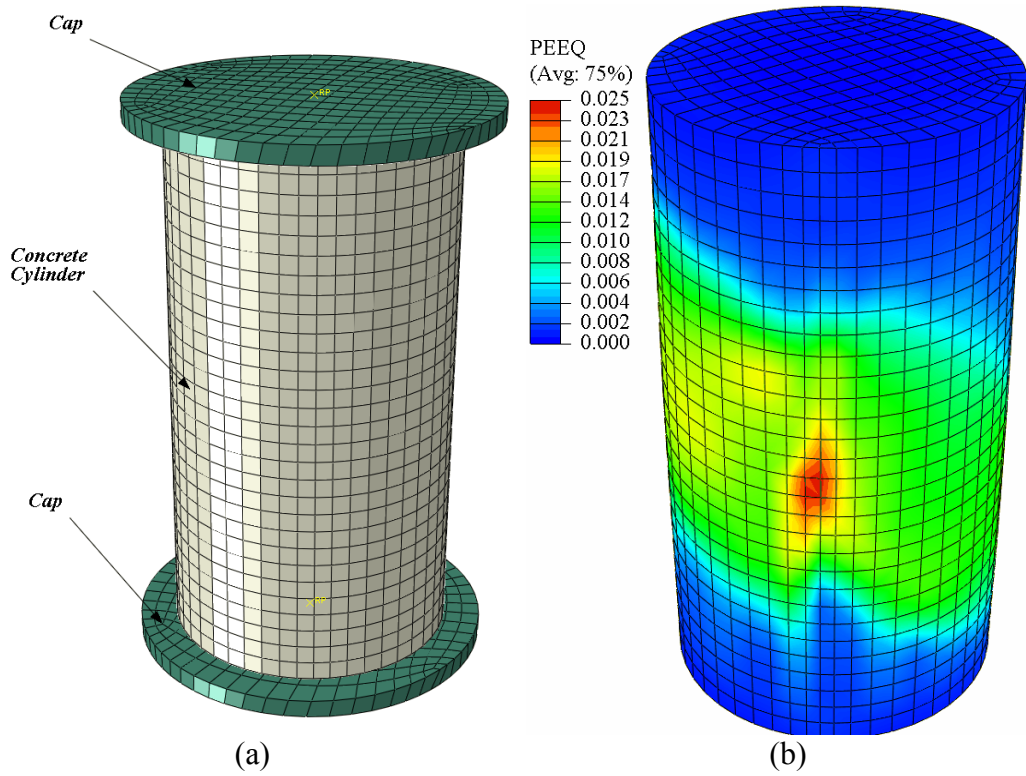


Figure 5-15: (a) Modelling of Concrete Cylinder in Abaqus; (b) Results in Terms of Compressive Equivalent Plastic Strain (PEEQ)

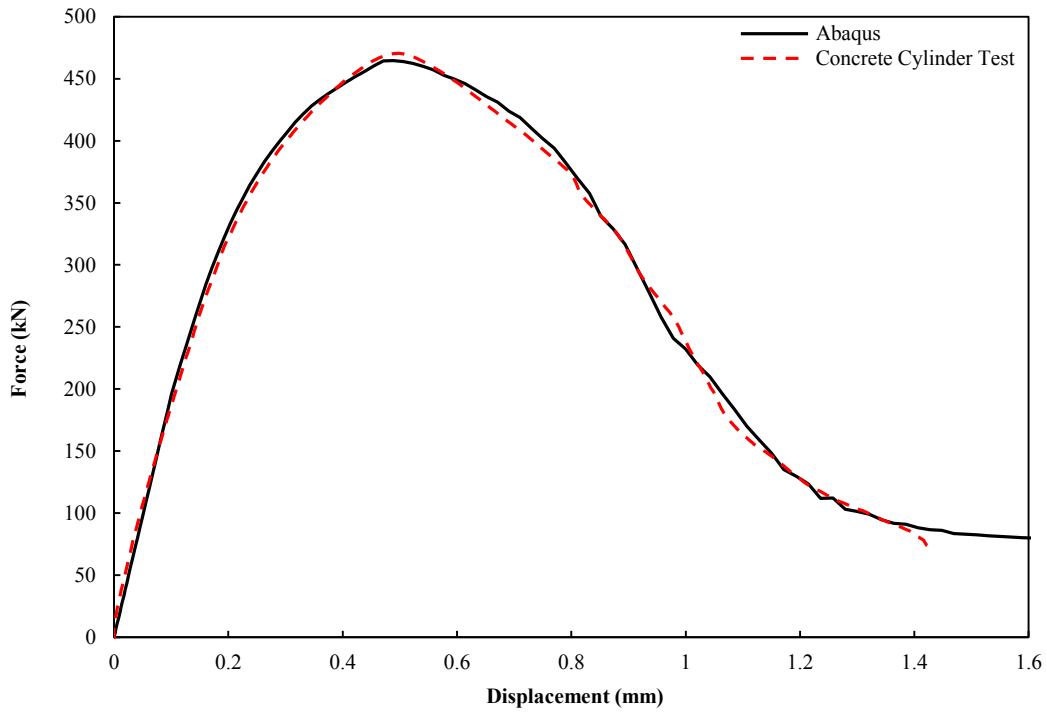


Figure 5-16: Force–Displacement Response: 28-day Concrete Cylinder Test and Abaqus Finite Element Model

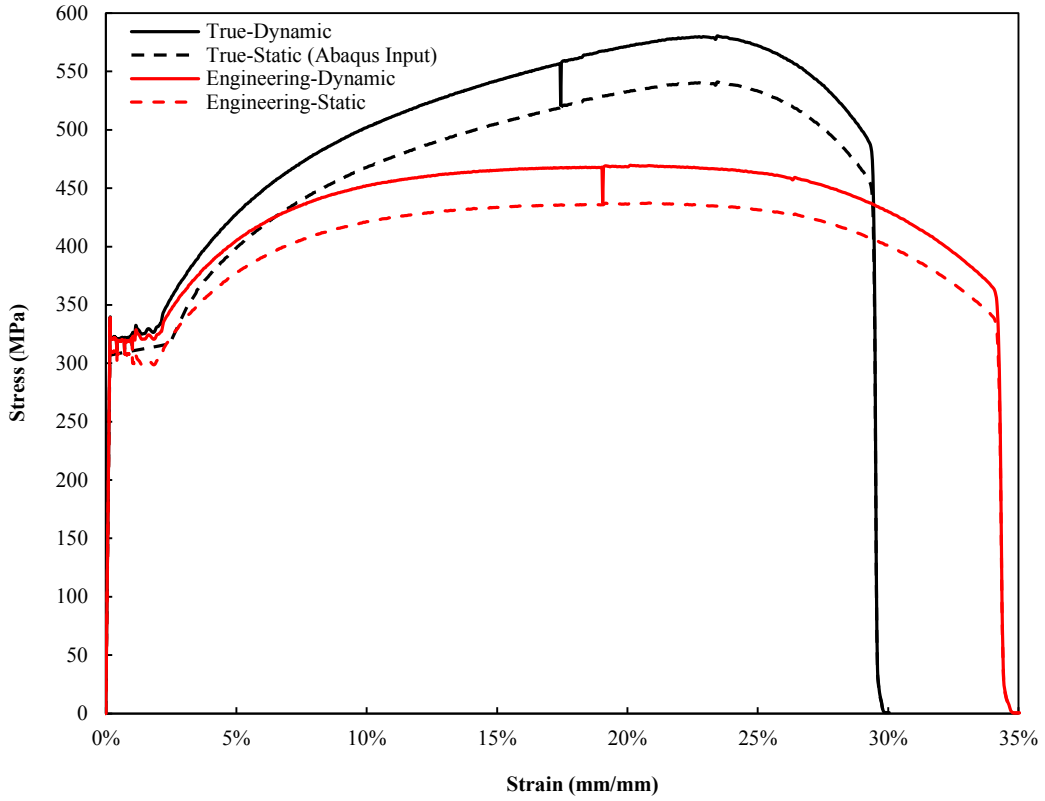


Figure 5-17: True and Engineering Stress–Strain Curves of One of the Coupons

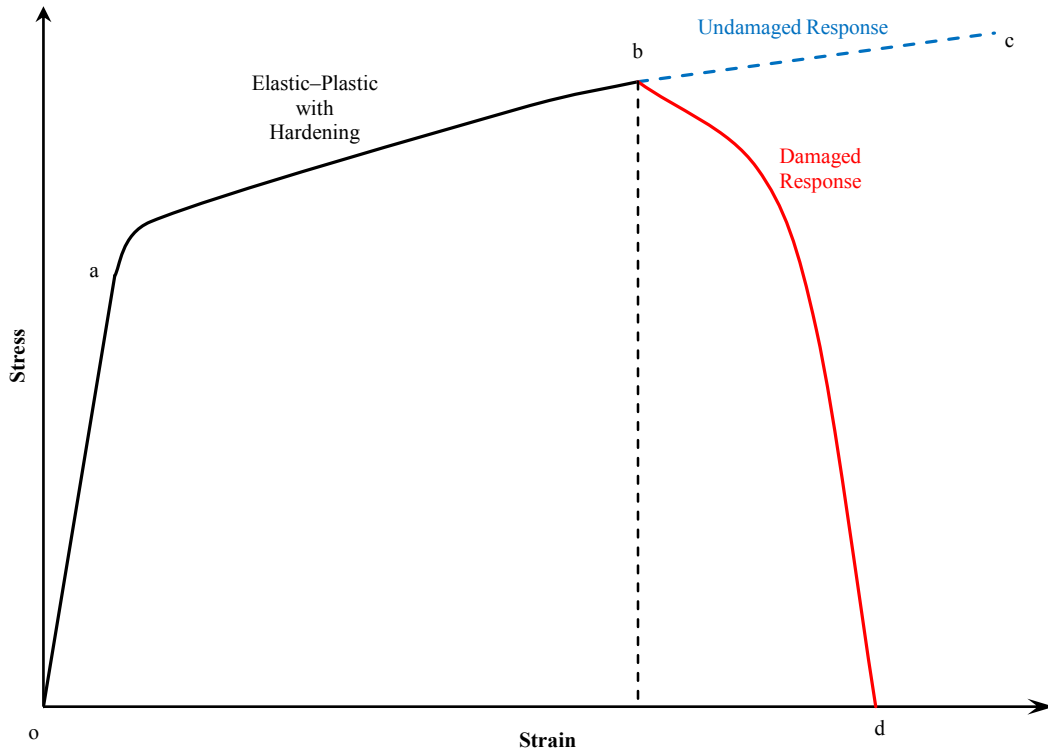


Figure 5-18: Typical Uniaxial Stress–Strain Response of a Metal Specimen



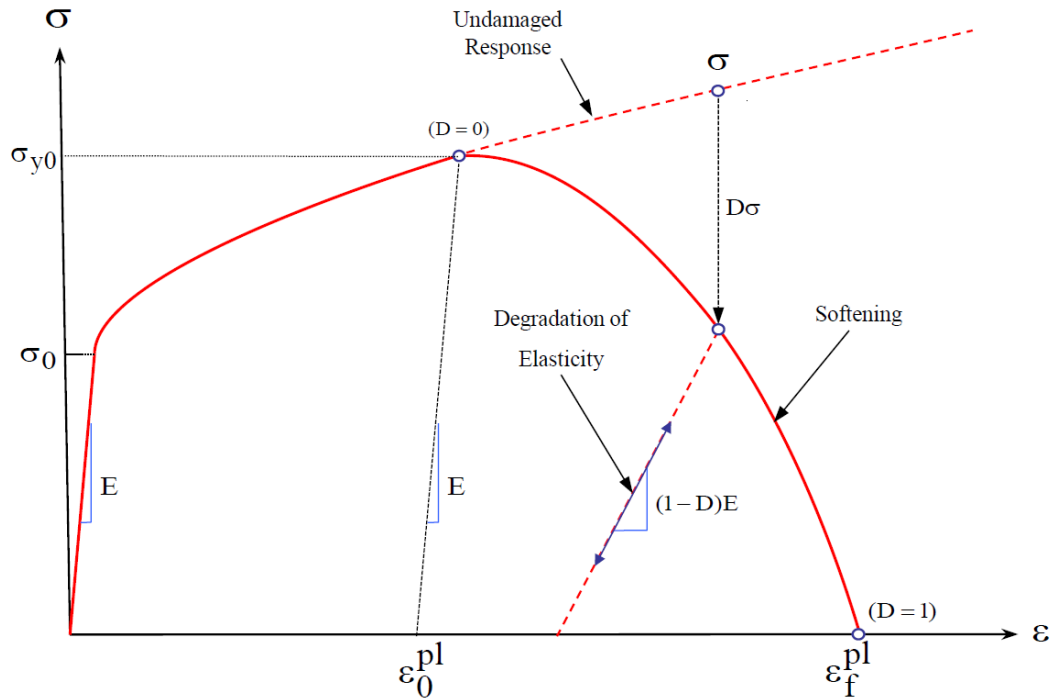


Figure 5-19: Stress–Strain with Damage Degradation (Dassault Systèmes 2013)

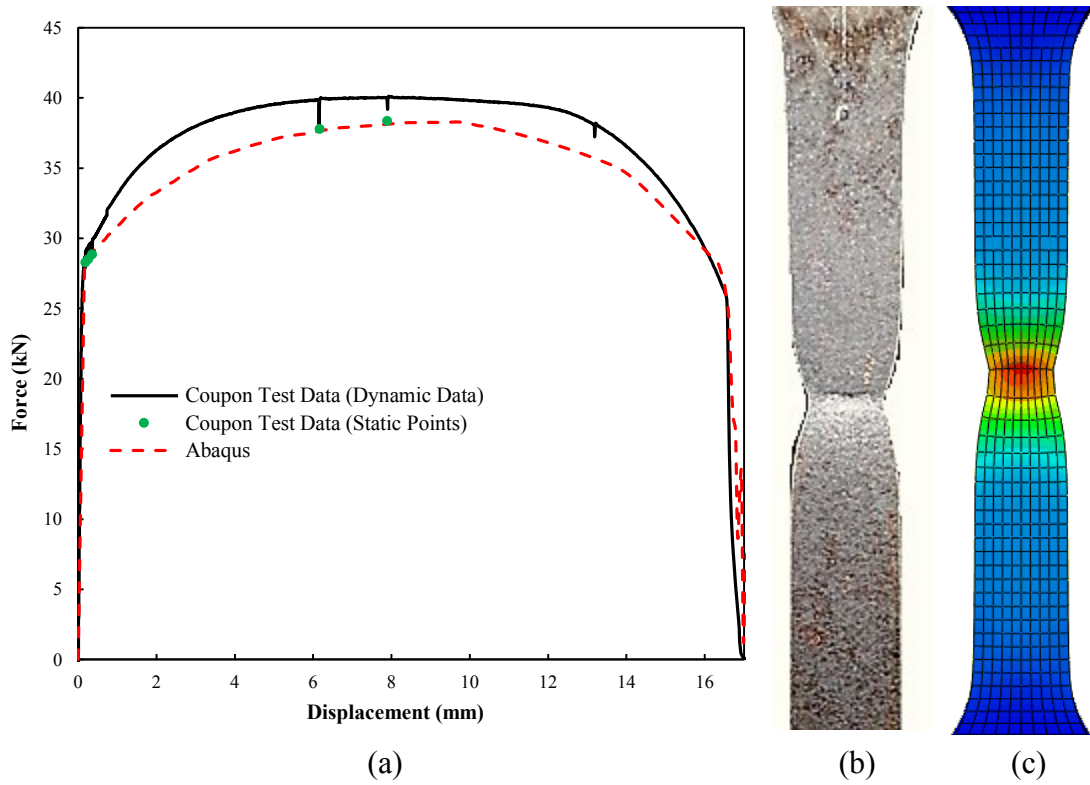


Figure 5-20: (a) Force–Displacement of 6 mm Plate Coupon Test versus Results of Abaqus Modelling; (b) Coupon Test at Fracture; (c) Abaqus Model at Fracture

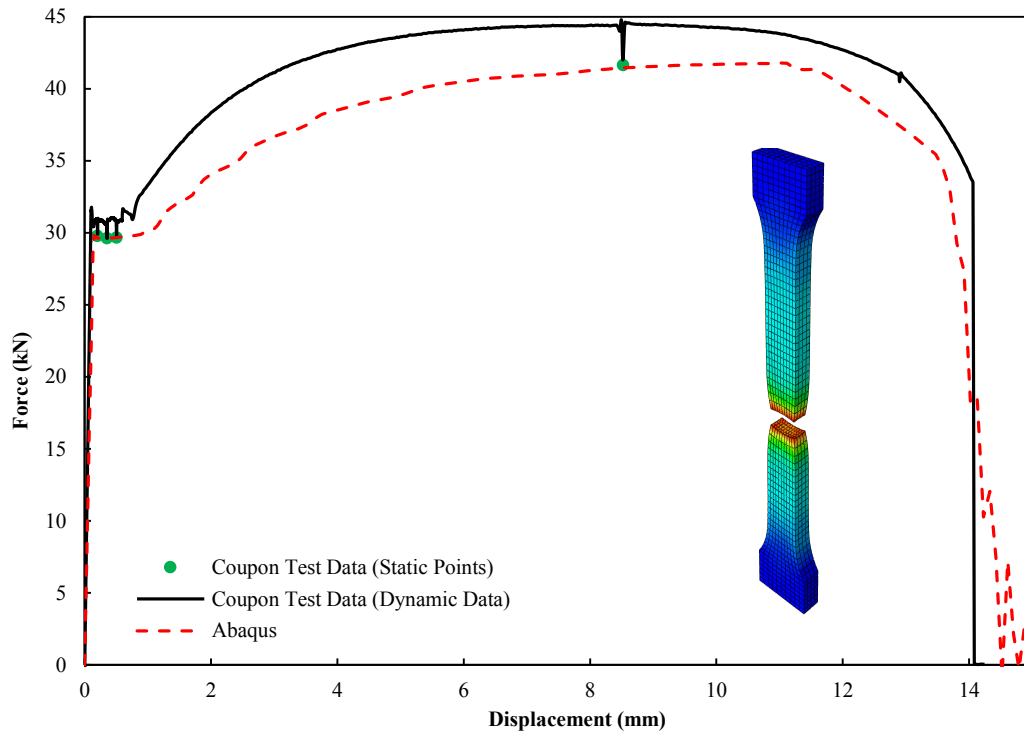


Figure 5-21: Force–Displacement of 6 mm Angle Coupon Test

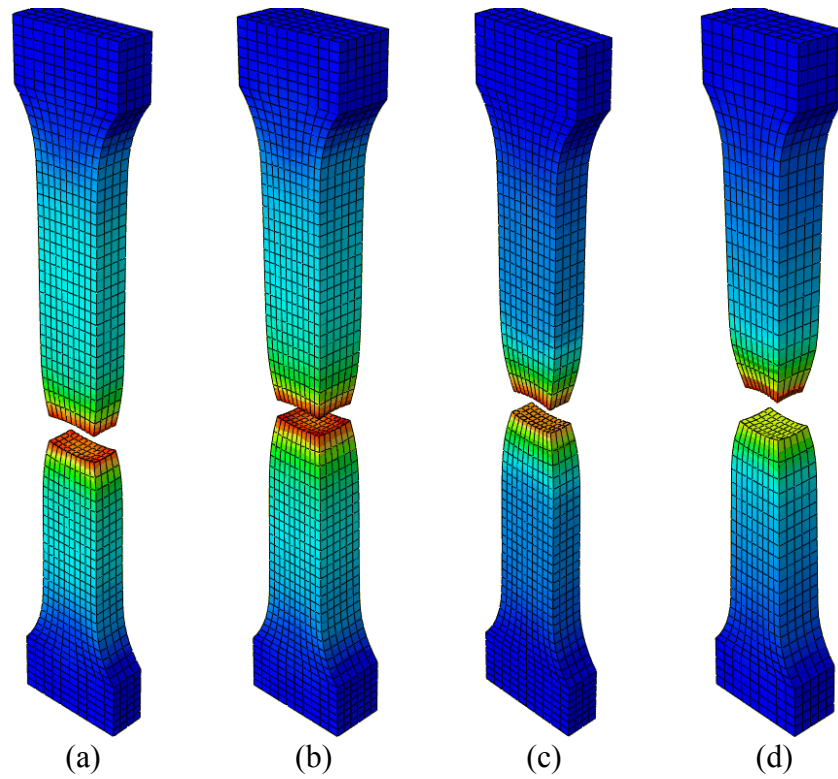


Figure 5-22: Failure Mode of Tension Coupon Tests: (a) Angle 6 mm; (b) Angle 9 mm; (c) Plate 6 mm; (d) Plate 9 mm

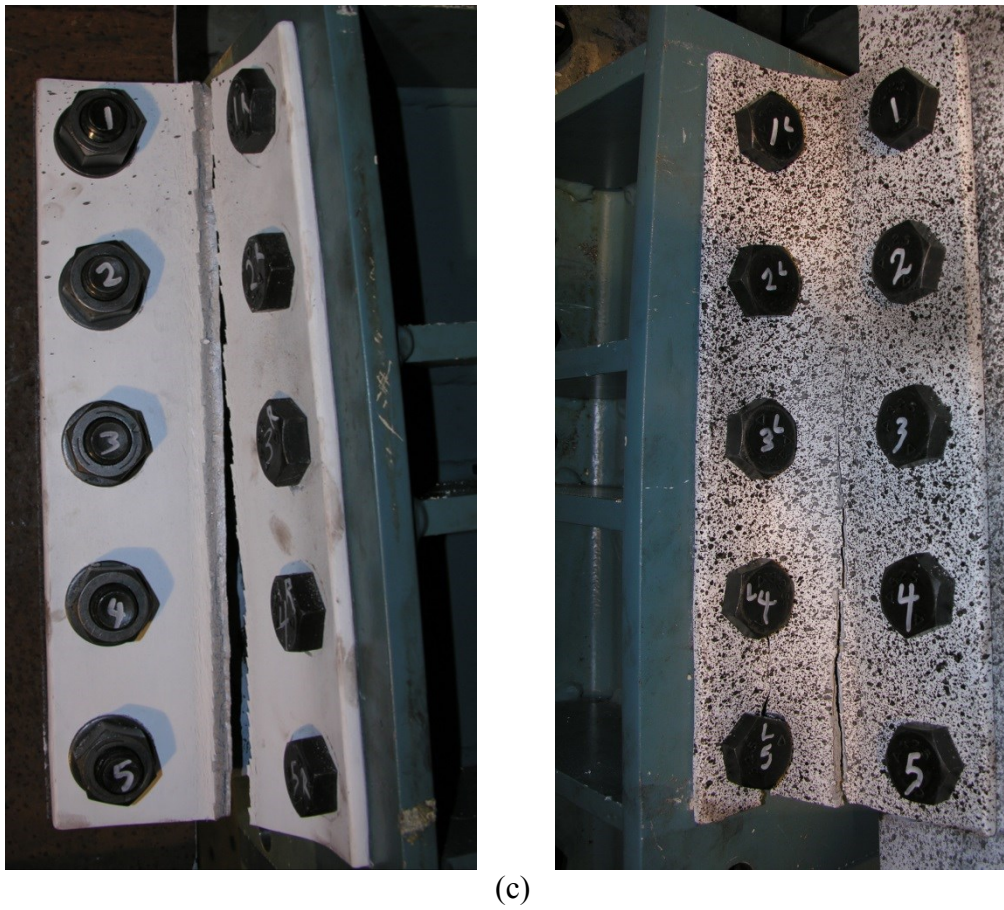
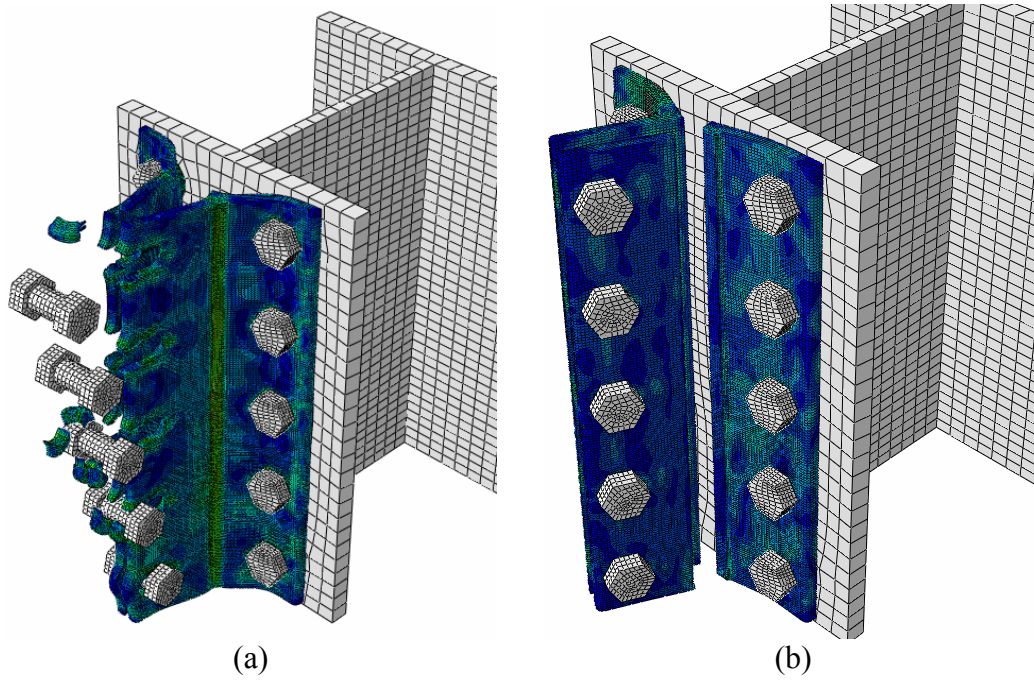


Figure 5-23: Failure Mode of Double Angles: (a) Non-calibrated Progressive Damage Model; (b) Calibrated Progressive Damage Model; (c) Experimental Test

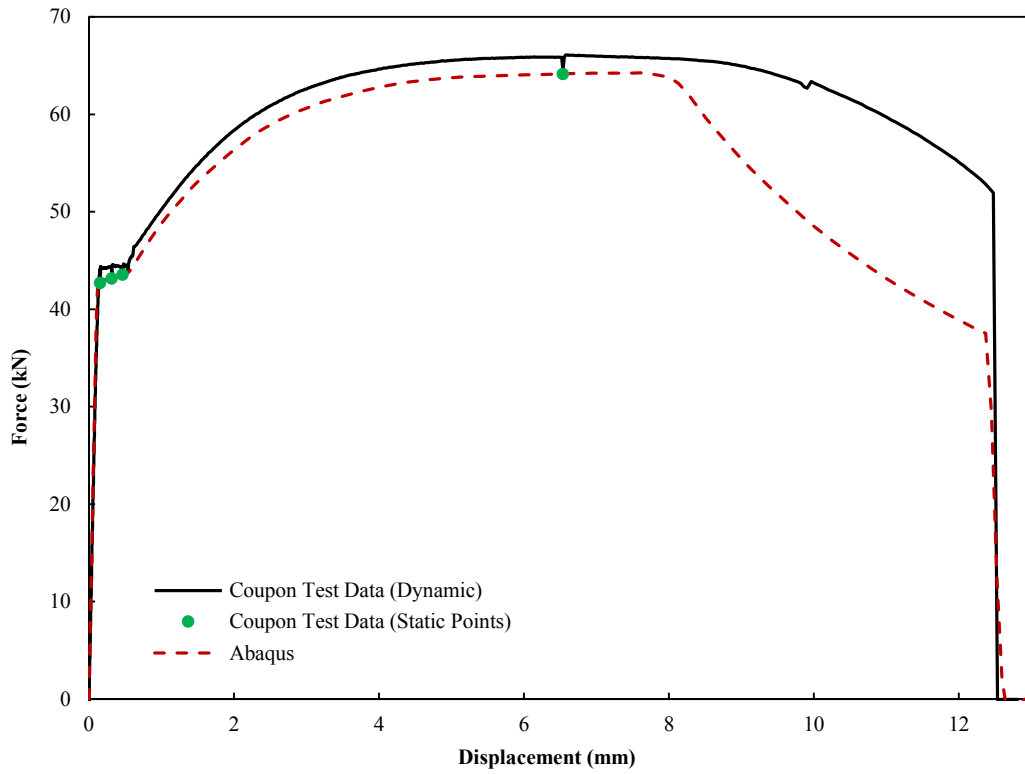


Figure 5-24: Force–Displacement of Rebar Tensile Test versus Abaqus Model

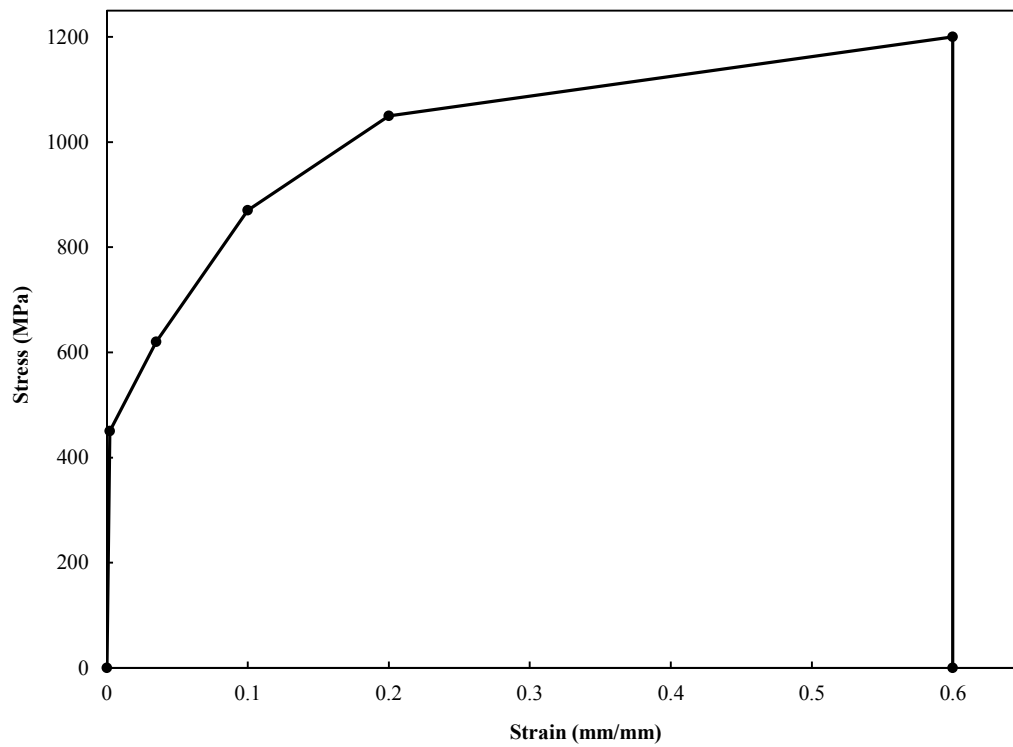


Figure 5-25: True Stress–Strain Curve for A325 High-Strength Bolt Material used in Abaqus Modelling

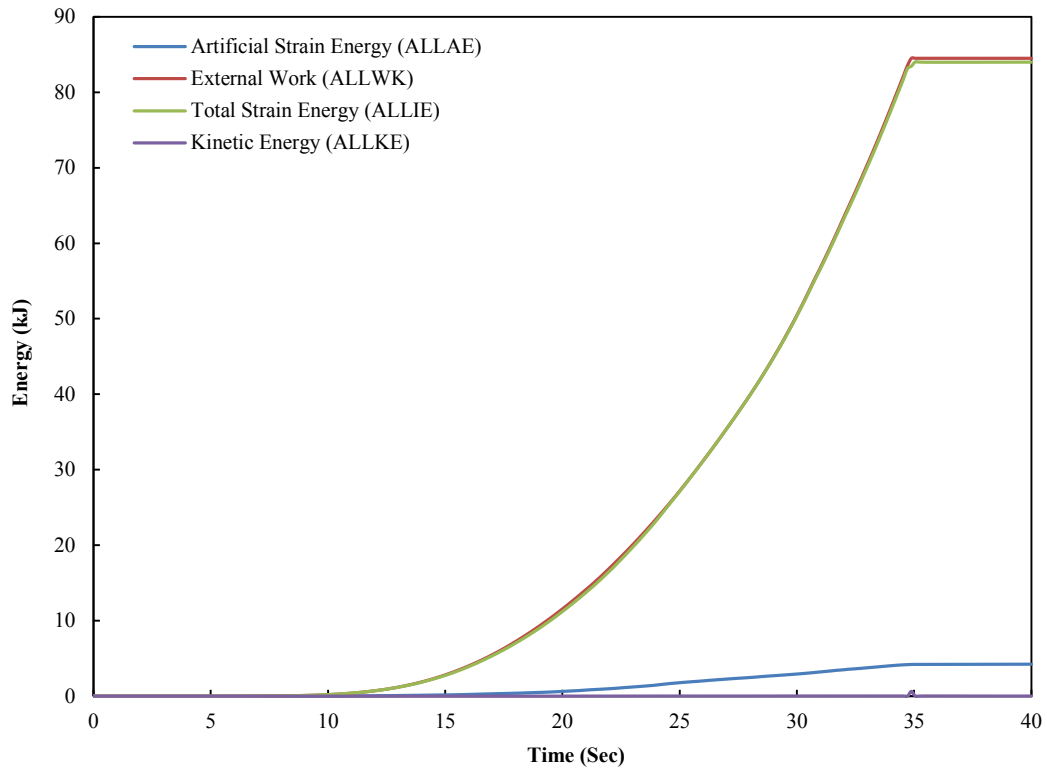


Figure 5-26: Energy Balance of DA59A Model in Quasi-Static Analysis

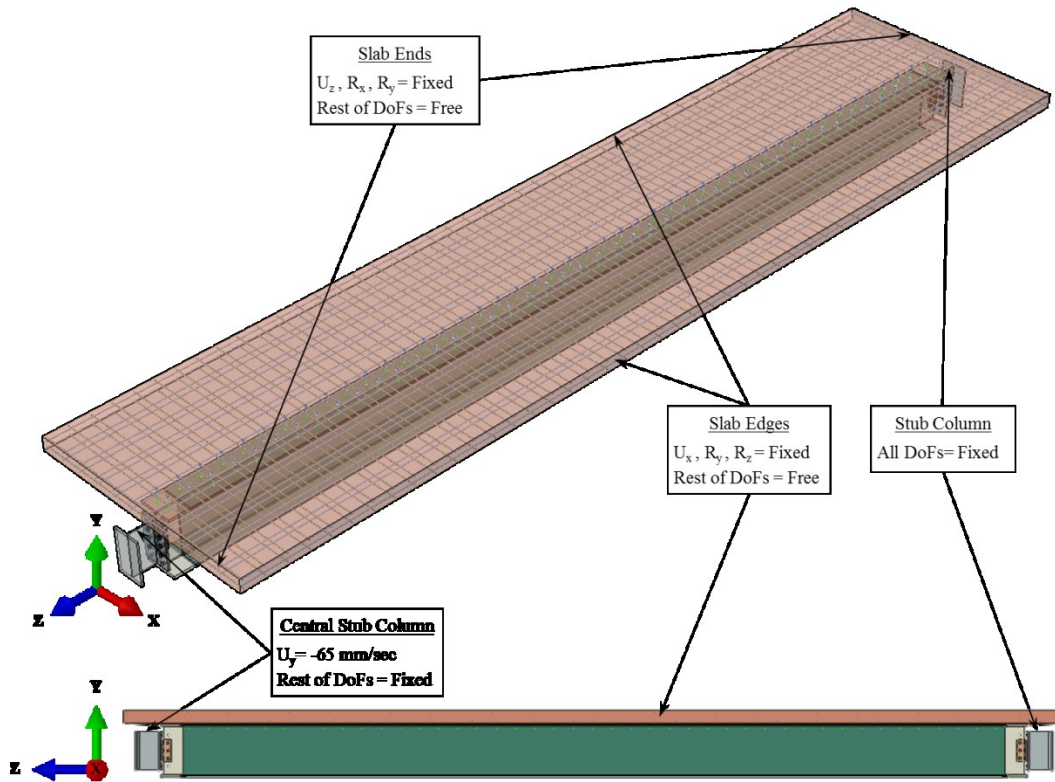


Figure 5-27: Boundary Conditions Imposed on the Finite Element Model

## **6. FINITE ELEMENT RESULTS, VERIFICATIONS AND DISCUSSION**

### **6.1 Introduction**

This chapter describes the results of the finite element modelling of the experimental tests. The accuracy and efficiency of the models were validated by comparing the finite element results with the test data. The behaviour of both shear tab and double angle connections at both ends of a beam in a structure undergoing a collapse in that bay based on the finite element results are explained and compared to the physical tests. Detailed three-dimensional prototype simulations were evaluated and compared with the simplified finite element models. Design recommendations based on the results of the experiments and finite element models are proposed to calculate the capacity and ductility of the connections.

### **6.2 Finite Element Results**

The connection capacity and ductility, as the most significant results of the study, were investigated for each model. Failure modes and deformations observed in the models are discussed.

Internal forces of connections at both ends of the beam undergoing a collapse in that bay were derived and discussed as a measure of plasticity development in the connections. Throughout this chapter, the connection attached to the removed column is called the “attached connection” and the one at the other end is named the “remote connection”, as shown in Figure 6-1. Forty-four models with shear tabs and double angles (28 composite frames and 16 associated bare frames) were modelled to investigate and compare the effect of the composite section on the behaviour of connections.

In addition, detailed three-dimensional finite element prototypes of two of the shear tab models (ST39B and ST59B) are compared with the results of associated component-level physical tests and the simplified finite element models.

### **6.3 Model Verification**

The developed finite element models were validated versus the available test data to assure the reliability and accuracy of the models. The verification was performed by comparing the results of bare frame models with those of the tests by Oosterhof and Driver (2016; 2015), and results of the composite frame models with the tests conducted as part of this research program (Chapter 4). In addition, consistency between the measured and target axial deformation and vertical deflection, which were the basis for the proposed loading regime, are shown and are compared with the results of the finite element models.

#### **6.3.1 Comparison with Oosterhof and Driver (2016)**

As discussed in Section 2.3.82.3.8, Oosterhof and Driver (2016) conducted a series of full-scale tests on simple connections in a bare frame system. The specimens varied in type of connection, assumed span lengths, and plate thicknesses. For the purpose of verification, only connections from the Oosterhof and Driver (2015) experiments that matched the geometry, assumed span length, and material properties were selected. To ensure the reliability of the finite element models, two independent series of simulations were developed: in the first series, one of the specimens (ST3A-1) with the corresponding material and geometric properties was selected, while in the second series only details and geometry of the connections were considered. The second series of bare frame specimens included: ST3B-2 (similar to ST36B) and DA3B-2 (similar to DA36B).

The comparison of specimen ST3A-1 with the finite element analysis and associated failure modes is shown in Figure 6-2 and Figure 6-3 in terms of internal forces developed at the column face of the shear tab. As noticed from Figure 6-2, excellent level of agreement was achieved. The pattern of the load development versus beam rotation clearly demonstrates the overall consistency with the experiment, and thus yields confidence in the validity and versatility of the finite element models to accurately predict the behaviour of connection,

failure mode, deformation and capacity based on the loading scenario and imposed boundary conditions. Quantitative comparisons of the second series in terms of connection geometry, material properties, load arrangement, and capacity are reported in Table 6-1. Although negligible, the differences between the experiments and selected finite element models results from the slightly different material properties. Nonetheless, the capacities of the selected connections are within 10% of those predicted by the finite element models. Connections of the second series at failure are shown in Figure 6-4. As observed from Table 6-1 and Figure 6-2 to Figure 6-4, the failure mode and the developed internal forces from finite element analyses accurately mimicked the actual observed behaviour in the testing program. It is concluded that the numerical finite element models developed are capable of modelling the bare frame structures accurately.

### **6.3.2 Comparison of FEA with Tests Conducted in This Research**

The comparison of the results is shown based on the failure mode and the internal horizontal force developed at the column face of the attached connection. The horizontal load developed in the cross-section (ST59B) is shown in Figure 6-5. The response serves to verify acceptable agreement with the associated experimental results. The capacity and ductility in terms of beam rotation and the trend of post-peak response were accurately captured.

Deformation mechanism and failure of the ST59B connection at several characteristic beam rotations are shown in Figure 6-6, and are compared with the experiment. As seen, deformations are noticeably localised at bolt bearing locations similar to the experiments and are relatively small elsewhere. Thus, the development of tear-out from the bottom to top bolts was clearly captured by the numerical models as compared to the experiments. This allows the behaviour of connection to be accurately simulated by finite element modelling.

All other specimens showed the similar trends of loading and development of failure modes. As a validation of the numerical models, failure of several specimens is also compared against the experiments in Figure 6-7.



### **6.3.3 Comparison of Axial Elongation of Attached Connection and Vertical Deflection of Removed Column with Loading Regime and Experiments**

As explained in Section 3.6.2, a revised loading approach relying on the geometric compatibility of the central removed-column deflection and the connections' deformation was developed and implemented to test the component-level connections in a composite construction system. The loading regime was developed based on the premises that the total axial elongation (Equation (3-3)) is entirely attributed to the attached connection (in a composite frame) as long as the arching action exists. Once the arching action switches to the catenary phase, the elongation is then attributed to both connections. This assumption can be verified by comparing the axial deformation and vertical deflection of the finite element models with the associated component-level physical tests.

The comparison is shown in Figure 6-8 for one of the composite specimens (ST59B) tested. As seen, not only does the comparison show good agreement between the results, but also the assumption of total axial elongation being entirely attributable to the connection is an accurate premise. Thus, this assures the precision of the proposed loading regime, which was developed and implemented for testing the connections in composite construction systems. Assuming that the inflection point is located at the middle of the span, as was considered by researchers investigating shear connections in composite frames (Yang and Tan 2014; 2013a; 2013b; 2013c) would not be a precise assumption. Thus, the proposed approach can be implemented as a loading protocol to test connections in composite frame systems under a removed-column scenario.

To validate the finite element modelling of connections in bare frame systems, a comparison of deformation histories was also made with the results of experiments by Oosterhof and Driver (2015) and the calculated target value, as shown in Figure 6-9.

Despite the span length difference, the comparison shows a good agreement between the physical test, calculated target value, and the finite element model. This validates the accuracy and reliability of the simulations in this research. It

should be noted that the calculated target value in bare frames is based on the assumption that the axial elongation is attributed evenly to both connections (Weigand and Berman 2014; Oosterhof and Driver 2011; Thompson 2009; Astaneh-Asl et al. 2002), dissimilar with the composite systems.

#### **6.3.4 Axial Deformation of Remote Connections and Comparison with the Target Loading Regime**

Due to the presence of arching action at the early stages of loading, remote connections are often in compression and experience a substantial amount of axial deformation (Figure 6-12 and Figure 6-13). To test remote connections at the component level of a composite frame, a loading regime was proposed to address the axial deformation that these connections would experience. The details of the proposed loading regime are explained in Appendix A.

Since in this research program no physical tests were carried out on the remote connections, the validation of the numerical models, as was explained in the previous section, gave confidence on the proposed loading regime for testing remote connections.

The axial deformation of one of the remote connections from both the verified finite element analysis and the proposed target value are shown in Figure 6-10. As seen, good agreement is reached between the target and the numerical simulation. Thus, the proposed method can be used as a loading protocol for testing the remote connections in a composite system under column-loss scenario.

Finally, based on the aforementioned verifications (Sections 6.3.1 to 6.3.4) on the failure modes, developed internal forces, and loading regimes, it can be concluded that the finite element analysis closely mimicked the observed response in the testing program. Thus, the numerical simulations are capable of modelling the actual behaviour in the real structure quite accurately.

## **6.4 Behaviour of Shear Tabs**

Twenty-eight finite element models of shear tabs—14 in composite frames and 14 in associated bare frames—were considered to investigate and compare the effect of the concrete slab on the behaviour of connections under a column removal.

### **6.4.1 Deformation and Failure Mode**

The failure mode was similar for all shear tabs attached to the removed column in both bare and composite frames. The failure was mainly governed by bolt tear-out, similar to those of experiments. Remote connections, however, experienced initially a substantial compressive bearing stress due to the presence of arching action. Once the arching action diminished and the catenary phase began, bearing stresses developed in the opposite direction when the connections were experiencing tensile forces. The deformation and failure evolution of two of the finite element models (ST39A and ST59B), are shown in Figure 6-11 to Figure 6-14. As seen, strains were noticeably localised at bolt bearing locations and were relatively small elsewhere. It is evident that the deformation of connections in a bare frame is different once placed in a composite frame.

It should be noted that at the beginning of catenary action, the attached connections almost failed, after which no further load was applied to the system. The finite element models developed in this study were not capable of capturing the capacity of the system in the post-damage phase because once the attached connection failed, the removed column becomes disengaged and no load could be transferred to the system.

It was shown by Oosterhof and Driver (2016) that efficiency of the bolt group in catenary tension at failure is dependent on the ratio of the number of effective bolts at failure to the total number of bolts in the connection. If the number of bolts increases, the efficiency was found to be quickly decreased. The efficiency can be justified by the fact that the centre of rotation is usually within the depth of the connection in a bare frame system. However, this may not be valid for

connections in composite frames, where the centre of rotation is usually within the slab (outside of the connection). This is illustrated in Figure 6-12 and Figure 6-14. As seen, all bolts in the attached shear tab were engaged in bearing and in development of tear-out planes in the tensile direction, while the bolts in the remote connection were engaged in bearing in the compressive direction.

#### **6.4.2 Load Development and Effects of Composite Section**

The internal forces versus beam rotation (vertical and horizontal forces, and bending moment) developed at the column face were extracted from numerical modellings. Table 6-2 to Table 6-4 summarize the finite element analysis results of the internal forces, along with the associated beam rotations and connection axial deformations for connections in both bare and composite frames. It can be seen that the magnitude of bending moments on the connection (steel section only) in composite frames are negligible the ultimate capacity. Thus, no discussions on the bending moments of steel sections will be given hereafter.

Figure 6-15 to Figure 6-17 show the load versus beam rotation of both attached and remote connections for a 3-bolt shear tab specimen (ST39A), and Figure 6-18 illustrates the response for a 5-bolt specimen (ST59B). Figure 6-15 shows the load development of connections (specimen ST39) in a bare frame system. The maximum value of horizontal and vertical loads reached almost simultaneously. From the early stages of loading, the connection was purely in tension, meaning that the compressive arching action was not developed for shear tabs. Daneshvar (2013), and Oosterhof and Driver (2016) presented similar conclusions on shear tabs in bare frames. Figure 6-16 and Figure 6-17 show the load development of attached and remote connections in the composite frame system. The behaviour of the attached connection is different from the remote one. While the attached connection is purely in tension, the remote connection experiences substantial compressive force up to the beginning of catenary action. This is due to the positions of the neutral axes with respect to the centroid of the connections during the vertical push down of the removed column, as explained in Chapter 3.

Compressive arching action becomes more noticeable for short span lengths, as the compressive strut line, shown in Figure 3-23, develops steeper in proportion to the horizontal tie component (high initial angle of arching action,  $\alpha$ ). The results reported in Table 6-2 and Table 6-3 prove the importance of the initial angle of arching action on the performance of connection. Specimens with a designation ending in “A” (span of 6 m) have higher compressive arching forces compared to those of the longer spans.

The effect of the concrete floor slab on the horizontal load developed in one of the shear tabs (ST59B) is shown in Figure 6-18, where the connections in a composite system are compared with those in the bare frame. As illustrated, the ultimate capacity of the attached connection is about the same for two frame types. However, the stiffnesses and ductilities are significantly different. While the composite frame added a substantial stiffness to the steel connection, the beam rotation at the ultimate capacity is about 40% of that in the bare frame. The comparison based on the finite element results between the horizontal tensile load, beam rotation, and axial deformation for attached shear tabs are listed in Table 6-5. The average composite-to-bare frame ratios for the horizontal tensile load, beam rotation, and axial deformation are 0.98, 0.32, and 0.36, respectively. The corresponding coefficients of variation are 0.1, 0.28, and 0.15, respectively. The reported statistics suggest that the horizontal ultimate load of the shear tabs is independent of the presence of the concrete slab. However, the concrete slab affects the axial deformation and rotation substantially.

The considerably smaller rotations at failure are, in fact, a consequence of the composite action between the beam and the concrete floor slab. Due to the formation of arching action, the slab places the attached beam-to-column connections in tension and carries compression along the perimeter, with the neutral axis of the composite section being located approximately within the slab. Rather than equal extension occurring at both connections of the beam span, as is the case for the bare frame, the remote connection thus indeed experiences compressive deformation, which imposes a significantly larger extension on the connection to the unsupported removed column.

### 6.4.3 Capacity Prediction

Limit states are considered as the mechanisms contributing to the failure of the connection. They are calculated based on the governing failure mode of the connection under axial loading, with no resistance reduction factor. Calculations are based on the values of yield and ultimate strengths for each connection obtained from the tension coupon tests, reported in Chapter 3.

While bolt tear-out was the only observed governing failure mode, other modes such as bearing failure at bolt holes, and bolt shear failure are considered in this section for the sake of discussion and analysis. However, bearing at bolts in compression was the case for the remote connections where they experienced a substantial axial compressive force. Although bolt shear failure—a brittle load-controlled failure mode—was not observed in any of the numerical and physical tests, it is a potential failure for shear tabs loaded under tension. Thus, the three aforementioned limit states are explained below.

#### 6.4.3.1 Bolt Bearing and Tear-out Limit State

When a bolt is placed close to the end of the plate, bolt tear-out failure is likely to occur. However, as the bolt gets farther away from the end, excessive bearing deformation (bearing failure at bolt hole) happens. Thus, bearing failure is an upper limit to the tear-out capacity, meaning that increasing the end distance further does not effectively increase the strength.

The most common capacity model for bolt tear-out prediction was developed by Fisher and Struik (1974) based on a simple plate shearing model. Figure 6-19 shows bolt tear-out model for a shear tab connection. The strength is presumed to be developed by two shear planes radiating from the edges of the hole to the end of the plate at an angle of  $\beta$ . Although a lower bound is obtained by assuming the angle  $\beta$  to be zero (shortest horizontal shear planes), it was observed from both the experiments and the numerical analysis that the shear planes are not horizontal, as was also addressed by other researchers (Oosterhof and Driver 2016; Daneshvar 2013; Thompson 2009).

It should be noted that Fisher and Struik (1974) studied bolt tear-out capacity in pure tension, whereas connections in this study were in tension and twist, yielding a substantial difference in the lower of the two shear planes. Based on the recorded data in this research, it was found that the angle of shear planes varies between 15 to 25 degrees. Figure 6-20 illustrates the bolt tear-out failure of some of the tested and finite element models representing the inclined shear planes.

The bolt tear-out capacity,  $R_n$ , is calculated based on the provisions of AISC 360-15 (2015)—shown in Equation (6-1)—and clauses of CSA S16 14 (2014)—reproduced in Equation (6-2). Variables in these equations are shown in Figure 6-19, where  $F_y$  and  $F_u$  are static yield and static ultimate strengths of the tested material,  $t$  is the thickness of the connected component (shear tab plate or beam web),  $L_c$  is the clear distance between the bolt hole and edge of the connected material,  $d$  is diameter of the bolt,  $A_{gv}$  is the gross shear area (based on parallel shear planes),  $L_e$  is the edge distance,  $L'_c$  and  $L'_e$  are the inclined edge distances, and  $\beta$  is the shear plane angle from horizontal.

Tear-out capacity is multiplied by the number of bolts to obtain the capacity corresponding to the shear-tab connection. While the capacity defined in AISC and CSA is calculated based on the parallel shear planes ( $\beta = 0$ ), Equation (6-3) was introduced to take into consideration the effect of inclined shear planes.

$$R_n = 1.5L_c t F_y \leq 3dtF_u \quad (6-1)$$

$$L_c = L_e - \frac{d}{2}$$

$$R_n = 0.6 A_{gv} \frac{F_y + F_u}{2} \leq 3dtF_u \quad (6-2)$$

$$A_{gv} = 2L_e t$$

$$L'_c = \frac{L_c}{\cos \beta} \quad (6-3)$$

$$L'_e = \frac{L_e}{\cos \beta}$$

A summary of the predicted capacities is provided in Table 6-6 and Figure 6-21. Comparisons were made based on the ratios of test-to-FEA, test-to-AISC, and test-to-CSA. The mean test-to-FEA ratio is 0.99 with a coefficient of variation of 0.05, which demonstrates the reliability of the finite element modelling in predicting the capacity. Equation (6-1) produces a mean ratio of test-to-AISC of 1.07 with a coefficient of variation of 0.05, and Equation (6-2) gives a mean ratio of test-to-CSA of 1.10 with a coefficient of variation of 0.1.

In order to examine the effect of the inclined shear planes on the bolt tear-out capacity, three shear plane angles (15, 20, and 25 degrees) were considered and used in both Equations (6-1) and (6-2). Results of the test-to-predicted ratios are summarized in Table 6-7. As seen, the ratios vary between 0.97 to 1.03 for AISC and between 1.0 to 1.06 for CSA, with a coefficient of variation of 0.05. Although assuming failure along the inclined shear plane (between 15 and 25 degrees) leads to an error of less than 5%, it is recommended the shear plane inclination be included in the capacity calculations since bolt tear-out is considered as an ultimate limit state. Ignoring such would result in a lower capacity prediction.

It should be noted that in this research, since the beam used in the physical tests and numerical modellings had a significantly higher tear-out capacity (compared to the shear tabs), the focus was shifted only toward the shear tabs. The ratio of the tear-out resistance of the beam web to shear tabs was an average of 3.4, which indicates the considerably higher capacity of the beam web. In reality, however, the beam web might become more susceptible to tear-out, and thus the capacity of the beam web should also be checked.

The ultimate capacity of the remote connection was calculated by using the upper limit of Equation (6-1) because they were mainly in compression during the arching action. A summary of the ultimate bearing capacity in compression is given in Table 6-8 for all the finite element models. It was found that the average of 70 % of the bearing capacity was engaged in the load development, meaning that these connections had about 30 % reserve capacity while they underwent compressive arching forces. After arching action diminished and the catenary



phase began, the direction of horizontal force shifted and as a result the connections experienced bearing deformation in tension. The capacity of the connection at this stage is believed to be similar to the strength of the attached connections while in tension (bolt tear-out capacity). In fact, the arching action is beneficial to the overall capacity of the system, since the failure of connections does not occur at the same time. The attached connection fails initially in tension, while the remote connection is in compression, and afterward the remote connection contributes to the capacity of the system in the catenary phase.

#### 6.4.3.2 Bolt Shear Limit State

Although no bolt failure was observed during the physical tests or the finite element analyses, for the sake of discussion the capacity of the bolt in shear is calculated here to compare with the bolt bearing capacity. Bolts used for all connections in the current testing program had threads excluded from the shear plane. The unfactored nominal bolt shear resistance ( $R_n$ ) in bearing-type connection is calculated according to the provisions of AISC 360-15 (2015) and CSA S16-14 (2014)—presented in Equation (6-4).

$$R_n = 0.60A_bF_u$$
$$A_b = \frac{\pi}{4}d^2 \tag{6-4}$$

In the absence of bolt testing, the specified minimum tensile strength of the bolt ( $F_u$ ) was considered in the calculations. For the ASTM A325 bolts used in the experiments, an ultimate strength of 830 MPa (nominal) was considered. Only two sizes of bolts were used in the testing program: 19 mm ( $\frac{3}{4}$  in.) and 22 mm ( $\frac{7}{8}$  in.) bolts. The shear resistance of each bolt in single shear is 141.9 kN and 193.2 kN, respectively. The resistance was calculated based on the nominal area based on the imperial values. By comparing the bolt shear resistance with the bolt tear-out capacity (ratio of 1.24 for  $\frac{3}{4}$  in. bolt, and ratio of 1.29 for  $\frac{7}{8}$  in. bolt), it can be concluded that the bolt shear failure is not the governing limit state. Similar results were yielded by Oosterhof and Driver (2016), whereas Thompson (2009) and Weigand and Berman (2014) did observe bolt failure in their tests.

#### 6.4.4 Ductility Prediction

The existing moment–rotation relationships are adopted from seismic design recommendations, whereas in the column-loss scenario the development of catenary action introduces large tensile forces, which substantially affects the rotational capacity. While the moment–rotation behaviour of connections is an essential characteristic of plastic hinges in the seismic design concept, the axial force–deformation relationship is significant to the shear connections to arrest collapse following column loss since the magnitude of bending moment developed in the connections is small.

The rotational capacities corresponding to the ultimate tensile horizontal strength developed in the attached connections are listed in Table 6-9 and are compared with the values of current guidelines mentioned in Chapter 2, namely GSA, UFC 4-023-03, CSA S850-12, and ASCE/SEI 41-06. For comparison, an elastic rotation of 0.02 radians (Main and Sadek 2012a) was added to the values of Table 2-3 to calculate the total rotational capacity.

As reported in Table 6-9, rotational capacities were found to be 68% of GSA, 83% of ASCE/SEI 41-06 (with slab consideration), and 33% of ASCE/SEI 41-06 (without slab consideration), with all having the coefficient of variation of 14%. This is an indication that the characteristics of the seismic-oriented formulation are not representative of the actual behaviour for which the introduction of arching and catenary action reduces the rotational capacity.

Moreover, the results are in contrast with the numerical and experimental data obtained for simple connections in bare frames under a column-removal scenario (Oosterhof and Driver 2016; Weigand and Berman 2014; Thompson 2009; Sadek et al. 2011a), for which the rotational capacities were found to be about quadruple that of similar connections in composite construction. Main and Sadek (2012a) showed that the rotational capacity of shear tabs in composite floor system was approximately one-fourth of those predicted based on seismic test data, similar to the results this research program concluded.

A parametric study based on the existing experiments and numerical data was developed and carried out to correlate the rotational capacity of the shear tabs with respect to the parameters influencing the connection's ductility. Two empirical methods were derived and are presented here to measure the rotational capacities of shear tabs corresponding to characteristic points of horizontal strength: one signifying the maximum tensile force, and the second one representing the final rotation corresponding to complete failure (zero force).

#### 6.4.4.1 First Method

An empirical equation—Equation (6-5)—is proposed as a function of a unitless “arching factor” ( $f_{\text{arch}}$ ), which encompasses only the effective factors. These factors include: eccentricity ( $e$ ), reduced span length between bolt lines ( $L_r$ ), and depth of bolt group ( $d_{bg}$ ), as illustrated graphically in Figure 6-22.

The proposed equation yielded good agreement with the existing data, summarised in Table 6-10. As seen, the ratios of the data to the corresponding values from the proposed method produce an average of 1.01 with a coefficient of variation of 5%.

$$a = 0.075 (1 - f_{\text{arch}})$$

$$f_{\text{arch}} = e \left( \sqrt[12]{d_{bg} L_r^3} \right) \quad , \quad (\text{parameters on RHS in meters}) \quad (6-5)$$

$$b = \alpha = \frac{e}{L_r}$$

Equation (6-5) proposes rotation angles corresponding to the tensile strength (initial failure) of connection, denoted "a", and post-damage capacity at final failure, labelled "b". The generalized form of the proposed bilinear force–deformation relation is illustrated schematically in Figure 6-23. Having the rotations along with the predicted capacity, as explained in Section 6.4.3, the bilinear force–deformation relation can be established.

#### 6.4.4.2 Second Method

Although not as accurate as the first one, the second proposed method provides also a simple calculation to estimate the rotational capacity of the shear tabs based on the measured axial deformation and eccentricities of the connections ( $e'$  and  $e$ ). Based on the limited data available (reported in Table 6-10), axial deformation ( $\delta_1$ ) corresponding to the ultimate horizontal strength can be approximated as 20 % of the edge distance,  $L_e$  (35 mm), providing that bolt tear-out is the governing failure mode. This approximation yields an axial elongation of 7 mm, which is about half of the value (16 mm) suggested by Astaneh (2007). Moreover, Oosterhof (2013) proposed an average total deformation between 27 mm to 35 mm, which is about 4 to 5 times the average value observed in this testing program. This is because of the presence of concrete slab which accelerates the development of tensile force resulting in a lower axial elongation.

The second proposed method is given in Equation (6-6). The equation is derived based on the loading regime proposed in Chapter 3. It was developed from the expansion of Equation (3-3) using the mathematical Maclaurin series to simplify the equation. Since only the first term of the Maclaurin series was considered in the expansion, a constant factor of 2.0 was replaced with 1.7 in order to compensate for the elimination of the ensuing mathematical terms. The equation yielded relatively good agreement with the existing data, summarised in Table 6-10. As seen, the ratio of FEA-to-proposed method produces an average of 0.99 with a coefficient of variation of 12%. Comparison between the proposed methods and existing data on rotational capacities is plotted in Figure 6-24.

$$\theta_1 = \sqrt{\frac{1.7\delta_1}{L_r}} = \sqrt{\frac{0.34L_e}{L_r}} \cong 0.6 \sqrt{\frac{L_e}{L_r}} \quad \text{where} \quad \delta_1 = 0.2L_e$$

$$\theta_2 = \frac{e' - e}{L_r} \tag{6-6}$$

$$a = \theta_1 + \theta_2$$

$$b = \alpha = \frac{e}{L_r}$$

## **6.5 Behaviour of Double Angles**

Sixteen finite element models of double angles—eight in composite frames and eight in associated bare frames—were also considered to investigate and compare the effect of the concrete floor slab on the behaviour of these simple connections under a column-loss scenario.

### **6.5.1 Deformation and Failure Mode**

The failure mechanism of the double angle connections was different from the shear tabs mostly because of the ability of angles to unfold. Due to the presence of the concrete slab, unfolding of angles was mostly concentrated on the bottom side, after which fracture initiated and propagated from the bottom of the angles where the maximum tensile stress developed. Similar to the experiments, two types of fractures were observed in the double angle connections, as shown in Figure 6-25 and Figure 6-26: tearing of the gross section near the angle heel, and/or fracture near the bolt line attached to the stub column. Tearing of the gross section was found to be more common in all specimens, while fracture near the bolt line was mostly observed in deep and thin angles (5-bolt connections with 6.3 mm thickness). In fact, localized deformations around the column's bolts were less severe for thicker plates.

The deformation and failure evolution of two of the finite element models (DA56B and DA59A), as an example, are shown in both composite and bare frames in Figure 6-25 and Figure 6-26. As seen, strains were noticeably localised at the bottom of angles near the heels and the column bolt line where the fracture initiation occurs. Remote connections experienced initially a substantial compressive bearing stress due to the presence of arching action where bolts were engaged in bearing in the compressive direction. Once the arching action diminished and the catenary phase began, bearing stresses developed in the opposite direction where the connections experienced tensile forces. It can be seen in Figure 6-25 and Figure 6-26 that the deformation of the connections in a bare frame is different once placed in a composite frame.

Fractures that developed near the angle heels are in good agreement with the results of the angles tested in composite frames by Yang and Tan (2013c; 2013b; 2012) and with some of the bolted angles tested in a bare frame system by Weigand and Berman (2016). However, based on the experimental results of Oosterhof and Driver (2016), it was concluded that plastic hinges near the angle heel are less critical than at the column bolt line, primarily because of the higher net cross-sectional area. Although tearing at the column bolt line was also observed in thinner and deeper angles tested in this research program, fracture did not propagate in a straight line of the net cross-sectional area; rather, a zigzag pattern was observed. This fracture pattern from both experiments and numerical analysis is illustrated in Figure 6-7, Figure 6-25, and Figure 6-26.

### **6.5.2 Load Development and Effects of Composite Section**

The internal forces (vertical and horizontal forces, and bending moment) versus beam rotation developed at the column face were extracted from the numerical modellings. Table 6-11 to Table 6-13 summarize the finite element analysis results of the internal forces along with the associated beam rotations and connection axial deformations in both bare and composite frames. It can be seen that the magnitude of bending moments on the connections (steel section only) in composite frames have a negligible effect on the ultimate capacity. Thus, no discussions on the bending moments of steel sections will be given hereafter.

Figure 6-27 depicts the horizontal loads versus beam rotation of three attached connections in a bare frame system. As seen, the compressive arching action developed during the initial stages of the loading in the 9.5 mm angles. Other than the bolt slippage and the surrounding horizontal restraints, the unequal stiffness of the double angles in tension and compression, in fact, is the key factor in the development of the compressive arching action. Because angles are considerably stiffer in compression than in tension, the instantaneous point of rotation is not located at the centroid of the connection, which is the source of arching action development. In connections such as shear tabs, where the compressive and

tensile stiffnesses are nearly equal, arching action may not develop and instead catenary tension initiates at very low rotations.

Arching action was only observed in the thicker double angles in the bare frames and was even more severe when the connection was deeper. It was observed in the 9.5 mm thick angles and more evidently in the five-bolt thicker double angles. Other researchers also addressed the development of the compressive arching action in angle connections at the early stages of loading (Sadek et al. 2011b; Yang and Tan 2012; Daneshvar 2013; Oosterhof and Driver 2016). Once angles are placed in the composite frames, however, the attached connections undergo pure tension similar to those of shear tabs. This is due to the initial position of the neutral axes with respect to the centroid of connections during the vertical push down of the removed column, which places the angles in tension from early stages of loading. While the attached connection is purely in tension, the remote connection experiences substantial compressive force up to the beginning of the catenary action.

The effect of the concrete floor slab on the horizontal loads developed in one of the double angles (DA59B) is shown in Figure 6-28. The horizontal loads are compared in both the composite system and bare frame. As illustrated, the ultimate capacity of the attached connection is about the same as the bare frame. However, stiffness and ductility are significantly different. While the concrete floor slab adds substantial stiffness to the steel connection, the beam rotation at the ultimate capacity is reached at about 25% that of the bare frame.

The comparison based on the finite element results between the horizontal tensile loads, beam rotations, and axial deformations for attached double angles are listed in Table 6-14. The average composite-to-bare frame ratios for the horizontal tensile load, beam rotation, and axial deformation are 1.03, 0.60, and 0.36, respectively. The corresponding coefficients of variation are 0.02, 0.36, and 0.34, respectively. The reported statistics suggest that although about 3 % higher, the ultimate strength of the double angles is independent of the presence of the

concrete floor slab. However, the concrete slab affects the axial deformations and rotations substantially.

Since it was found that the thickness of angles plays an important role in the behaviour of connections, another comparison was made based on the thicknesses of angles, as tabulated in Table 6-14. The average axial elongations of 6.3 mm angles were about 14 mm and 18 mm for composite and bare frames, respectively, while for 9.5 mm angles elongations were about 8 mm and 19 mm for composite and bare frames, respectively. It clearly demonstrates that even though no compressive force was developed in the composite attached connections, the thicker angles (9.5 mm) had an axial elongation of about half that of the 6.3 mm ones. Similar results were also examined for the rotational capacity of angles. While the average beam rotation of 0.044 radians was observed for the 6.3 mm angles, it was about 0.027 radians for the 9.5 mm angles. Consequently, the concrete floor slab dropped the rotational capacity of angles by about 50 % and 75 % for 6.3 mm and 9.5 mm angles, respectively.

### **6.5.3 Capacity Prediction**

Limit states are considered as the mechanisms contributing to the failure of the connection. They are calculated based on the governing failure mode of the connection under axial loading, with no resistance reduction factor. Calculations are based on the static values of yield and ultimate strengths of angles obtained from the tension coupon tests, reported in Chapter 3.

While tearing of the gross section near the angle heel, and/or fracture near the column bolt line was the only observed governing failure mode, other modes such as bearing failure at bolt holes, and bolt shear failure are considered in this section for the sake of discussion and analysis. For remote connections, bearing at bolts in compression was the case where they were experiencing a substantial axial compressive force. Although bolt shear failure was not observed in any of the numerical and physical tests, it is a potential failure for angles loaded under tension. Thus, the aforementioned limit states are explained in the sections below.



### 6.5.3.1 Gross-section Failure Limit State

As explained in Section 6.5.1, double angles failed mostly by rupture of the gross section near the angle heel. Although tearing near the column bolt line was also observed in the thin deep angles, it is believed that assuming the net section area as the critical cross-section is not an accurate premise, since a zigzag pattern was developed rather than a straight line along the column bolt line. In order to predict the ultimate capacity of the double angles under column-loss scenario, the procedure developed by Gong (2013) and used by Oosterhof and Driver (2016) is implemented here. The method predicts the strength based on the von Mises yield criterion at the tearing point once it exceeds the ultimate tensile strength of the material. By calculating the effective stress state from the material properties and critical cross-section, the capacity of the angle can easily be obtained.

The formulation used by Gong (2009; 2013) and Oosterhof and Driver (2016) was based on the constant measured effective stress state along the depth of the connection. However, based on the results of the experiments and the finite element numerical analysis, as shown in Figure 6-29 for specimen DA59B, it was found that the stress state is not constant over the depth of connection simply due to the effect of the concrete slab, which shifts the neutral axis above the angles. Rather, it was almost linear from the top of the angle to the maximum value of the stress state at the bottom of angle where the tearing initiates.

Figure 6-29 illustrates the evolution of the von Mises strain and horizontal displacement of the DA59B connection along the applied force over the depth of the angle. Figure 6-29(c)(d)(e) shows the strain and deformation developed in the angle corresponding to the failure initiation (red lines in Figure 6-29(a)(b)). Similar results were also yielded for the rest of the double angles. Thus, a simple linear von Mises stress distribution was assumed over the depth of the angle, as illustrated in Figure 6-30.

It should be noted that although Oosterhof and Driver (2016) concluded that considering the critical stress state at the net section provides a failure criterion that underestimates the ultimate capacity of the connection when tearing at the

gross section occurs, considering a linear stress distribution could justify the ultimate capacity at the gross section. However, the linear distribution was developed based on the fact that the concrete floor slab exists, which brings the connection into a nearly pure tension mechanism.

The nominal horizontal tensile resistance,  $R_n$ , of the double-angle connection can be calculated from Equation (6-7), where  $F_y$  and  $F_u$  are the static yield and static ultimate strengths of the tested material,  $F_{vm}$  is the effective stress state at the tensile end of the angles developed from the von Mises criterion,  $A_g$  is the gross-sectional area of the double angles under tension,  $t_p$  is thickness of one angle, and  $l_p$  is the depth of the angle. It should be noted that the gross-sectional area,  $A_g$  is the cross-sectional area of the double angles ( $2l_p t_p$ ) perpendicular to the direction of horizontal load.

$$\begin{aligned}
 R_n &= \frac{1}{2} A_g F_{vm} \\
 A_g &= 2l_p t_p \\
 F_{vm} &= \sqrt{\frac{F_u^2 - F_y^2}{3}}
 \end{aligned} \tag{6-7}$$

Based on the average ratio of static yield to static ultimate strengths of the tested material (ratio of 1.4), the effective stress,  $F_{vm}$ , in Equation (6-7) is simplified into Equation (6-8). As a result, the nominal horizontal tensile strength of a double-angle connection,  $R_n$ , can be calculated using the equation below:

$$\begin{aligned}
 F_{vm} &\approx \frac{F_y + F_u}{4} = 0.6 F_y \\
 R_n &= \frac{1}{2} A_g \frac{F_y + F_u}{4} = 0.3 A_g F_y
 \end{aligned} \tag{6-8}$$

A summary of the predicted capacities is tabulated in Table 6-15 and plotted in Figure 6-31. Comparisons were made based on the ratios of test-to-FEA, test-to-predicted of Equation (6-7), and test-to-predicted of Equation (6-8). Ratio of test-to-FEA is an average of 0.99 with a coefficient of variation of 0.06, which proves the reliability of the finite element modelling in predicting the capacity of

double-angle connections. Equation (6-7) produces a ratio of test-to-predicted of 1.03 with a coefficient of variation of 0.06, and Equation (6-8) gives a ratio of 1.03 with a coefficient of variation of 0.07. Thus, both equations calculate the nominal horizontal tensile resistance of double-angle connection accurately and closely to experimental tests with a relatively low standard deviation of 7 %.

Similar to the shear tabs, the ultimate capacity of the remote double angles was calculated by using the upper limit of Equation (6-1) because they were mainly in compression during the arching action. The summary of the ultimate bearing capacity in compression is listed in Table 6-16. It was found that the average of 55 % of the bearing capacity was engaged in the load development, meaning that these connections had about 45 % reserve capacity while they underwent compressive arching forces.

After arching action diminished and catenary phase began, the direction of horizontal force shifted and as a result the connections experienced bearing deformation in tension. The capacity of the connection at this stage is believed to be similar to the strength of the attached connections while in tension (gross-sectional capacity).

#### **6.5.3.2 Bolt Shear Limit State**

Although no bolt failure was observed during the physical tests and finite element modellings, for the sake of discussion the capacity of the bolt in shear is calculated here to compare with the bolt bearing capacity. Similar to the shear tabs, bolts used for all connections had their threads excluded from the shear plane. The unfactored nominal bolt shear resistance ( $R_n$ ) in bearing-type connections is calculated according to Equation (6-4).

For the ASTM A325 bolts used in the experiments, the nominal ultimate strength of 830 MPa was considered. Only two sizes of bolts were used in the testing program: 19 mm ( $\frac{3}{4}$  in.) and 22 mm ( $\frac{7}{8}$  in.) bolts. The shear resistance of each bolt in double shear is 284 kN, and 386 kN, respectively. The resistance was calculated based on the nominal area based on the imperial values.

By comparing the bolt shear resistance with the gross-sectional failure capacity (ratio of 2.5), it can be concluded that bolt shear failure is not the governing limit state. Similar results were also yielded by Oosterhof and Driver (2016), whereas some of the bolted angle specimens tested by Weigand and Berman (2016) exhibited bolt shear failure.

#### **6.5.4 Ductility Prediction**

The existing moment–rotation relationships are adopted from seismic design recommendations, whereas in the column-loss scenario development of the catenary action introduces large tensile forces, which substantially affects the rotational capacity. While the moment–rotation behaviour of connections is an essential characteristic of plastic hinges in the seismic design concept, the axial force–deformation relationship is significant to the shear connections to arrest collapse following column loss.

The rotational capacity corresponding to the ultimate tensile horizontal strength developed in the attached connections is listed in Table 6-17 and is compared with the values of current guidelines mentioned in Chapter 2, namely GSA, UFC 4-023-03, and CSA S850-12. For comparison, an elastic rotation of 0.02 radians (Main and Sadek 2012a) was added to the values of Table 2-3 to calculate the total rotational capacity.

As reported in Table 6-17, rotational capacities were found to be an average of 33 % of those predicted using the methods of the GSA Guidelines when flexure in the angles governs, with a coefficient of variation of 27 %. This is an indication that the characteristics of the seismic-oriented formulation are not representative of the actual behaviour for which the introduction of arching and catenary action underestimates the rotational capacity. Moreover, the results are in contrast with the numerical and experimental data obtained for simple connections in bare frames under a column-removal scenario (Oosterhof and Driver 2016; Weigand and Berman 2016), for which the rotational capacities were found to be double.

A parametric study based on the existing experiments and numerical data was developed and carried out to correlate the rotational capacity of the shear tabs with respect to the parameters influencing the connection's ductility. An empirical method was derived and is presented here to predict the rotational capacities of double angles corresponding to the characteristic points of tensile strength of connections: one signifying the point of maximum tensile force, and the second one representing the final rotation corresponding to the complete failure.

Similar to shear tabs, an empirical equation—Equation (6-5)—was proposed as a function of a so-called “arching factor” ( $f_{\text{arch}}$ ) which encompasses only the effective factors. These factors include: eccentricity ( $e$ ), thickness of angle ( $t$ ), and depth of the bolt group ( $d_{bg}$ ), as illustrated graphically in Figure 6-22.

The proposed equation yielded good agreement with the existing data, summarised in Table 6-17. As seen, the ratio of the FEA to the proposed method produces an average of 1.01, with a coefficient of variation of 5 %.

$$a = 0.075 (1 - f_{\text{arch}})$$

$$f_{\text{arch}} = 225 e t d_{bg}^{0.1} \quad , \quad (\text{parameters on RHS in meters}) \quad (6-9)$$

$$b = \alpha = \frac{e}{L_r}$$

Equation (6-9) proposes rotations corresponding to the tensile strength (initial failure) of the connection, denoted "a", and post-damage capacity at final failure, labeled "b". The generalized form of the proposed bilinear force–deformation relation is illustrated in Figure 6-23.

Having the rotations along with the predicted capacity, the bilinear force–deformation relation can be established. Comparisons between the proposed methods and existing data on rotational capacities for both shear tabs and double angles are plotted in Figure 6-24.

## 6.6 Simplified Design Recommendations

Based on the procedures described in the previous sections, a simplified approach is proposed to calculate the nominal tensile resistances versus corresponding beam rotations using a single bilinear force–rotation relationship, shown in Figure 6-23. The simplified hand-calculations method eliminates the need for a detailed numerical model in order to predict connection’s strength and ductility.

For shear tabs, nominal strength is calculated using Equation (6-1) or (6-2), and rotational capacity is estimated by either Equation (6-5) or (6-6). For double angles, nominal strength is derived by using either Equation (6-7) or (6-8), and Equation (6-9) provides the corresponding rotations.

For comparison, the load–development curves generated by applying the proposed approach are reproduced for four of the specimens—shear tabs and double angles—as illustrated in Figure 6-32, and are compared to the finite element results. The proposed method yields good general agreement with the results; however, the accuracy is limited by the governing failure mode which was bolt tear-out for the shear tabs, and rupture of gross section near the heel for the double angles. As seen in Figure 6-32, the nominal strengths of the shear tabs are slightly less than those from the test results. This is because the nominal strength was calculated based on the parallel shear failure plane, which underestimates the capacity of the connection slightly.

## 6.7 Detailed Finite Element Model of Prototype System

In order to examine the degree of accuracy of the proposed loading regime and also to validate the physical component experimental tests, a detailed three-dimensional finite element model of two of the prototype systems was considered, namely ST39B and ST59B, as shown in Figure 6-33. The results are compared with the corresponding experiment and the simplified finite element model. The finite element models consist of a 2 bay  $\times$  2 bay portion (span of 9.0 m) of the prototype building, as defined in Section 3.2 (Figure 3-2).

To evaluate the effect of horizontal-restrained boundary conditions on the performance of the composite system, two different scenarios were considered for each model: in the first one edges of the concrete slab were fully restrained against horizontal movement, while in the second one the slab edges were horizontally free, hereafter called “restrained” and “unrestrained” models, respectively.

The concrete floor slab was assumed to be connected to the beams by shear studs designed for fully-composite action. Shear studs were considered to be embedded in the concrete slab and attached to the beams. They shared common nodes with the solid elements of the concrete slab and the shell elements of steel beams.

The removed column was considered unsupported vertically, and loads were applied gradually. The unsupported centre column was pushed down under displacement-controlled loading to simulate a quasi-static column loss, as described in Chapter 5.

To ensure that the simulation was performed in a quasi-static manner, first the internal and kinetic energies were compared. Second, the applied vertical force was checked against the summation of shear forces developed in the steel composite sections attached to the removed column. In a static solution, the total vertical force should always be equal to the summation of shear forces of attached components. However, the static solution might get compromised if the dynamic effects are high due to the high acceleration that usually develops in the failed and damaged elements at large deflections.

### **6.7.1 Axial Deformation and Accuracy of the Proposed Loading Regime**

As explained in Section 3.6.2, in order to test the component-level connections in a composite construction system, a new loading regime was developed based on the assumption that the total axial elongation (Equation (3-3)) is entirely attributed to the attached connection (in a composite frame) as long as arching action exists. Once the arching action switches to the catenary phase, the elongation is then attributed to both connections.

The loading protocol was established upon the geometric compatibility of the central removed-column deflection and the connections' axial deformation. This assumption will now be verified by comparing the axial deformation and vertical deflection of the detailed and simplified finite element models with the component-level physical tests. The accuracy of the loading regime was previously verified by results of the simplified finite element model, in which the concrete slab was considered partially, as shown in Figure 6-1. While proper boundary conditions on the slab edges were imposed to the simplified finite element models to mimic the actual slab, the transverse contribution of the slab can be now evaluated by comparing the results with the detailed three-dimensional models. Comparisons between the test and finite element results are shown in Figure 6-34 for specimen ST59B. As seen, not only is there good agreement between the results obtained from the experiment and the finite element analysis, but also the assumption of axial elongation being entirely attributed to the attached connection is an accurate premise. This assures the accuracy of the proposed loading regime, which was developed and implemented for testing steel connections in composite frames.

The comparison reveals that for cases of both horizontally restrained and unrestrained models, the developed axial deformations are similar and are entirely attributed to the attached connection. This means that the axial deformation of the attached connection is independent of the horizontal boundary conditions of the edges of the concrete slab. This is by virtue of the compressive ring and tensile membrane that develops in the slab with horizontally unrestrained conditions around its edges. As the composite slab experiences large deflection, the edges will be pulled inward resulting in the formation of a compressive ring.

The vertical deflections of both models are shown in Figure 6-35. As perceived, the horizontal restraint affects the distribution of the vertical displacement within the slab. Figure 6-36 and Figure 6-37 illustrate the Equivalent Tensile Plastic Strain (PEEQT) developed in the concrete slab for specimens ST39B and ST59B. Figure 6-36 shows the formation of compressive ring for both specimens when the slab edges are horizontally unrestrained, while Figure 6-37 compares the



effect of the slab edge conditions on the formation of compressive ring and tensile membrane on specimen ST59B.

The tension that is developed in the tensile membrane due to the column loss equilibrates the compressive ring formed around the edges. In a horizontally unrestrained slab, the change in the geometry leads to the formation of compressive ring around slab's perimeter, providing that the vertical displacements of the perimeter edges remain small under increasing load at large deflections. Otherwise, the internal horizontal edge restraint would not form.

### **6.7.2 Behaviour of Connections in Prototype Models**

As expected, the governing failure mode, bolt tear-out, and deformation of shear tabs were similar to those of the physical tests and simplified finite element models, as shown in Figure 6-38 and Figure 6-39. While the attached connections were all in pure tension starting at the early stages of loading up to the failure or ultimate capacity of the system, the remote connections performed differently as they were subjected to the axial restrained conditions imposed on the concrete edges. For models with horizontally unrestrained edges, neither axial compressive demands nor substantial axial deformation were imposed on the remote connections despite the formation of a compressive ring, as shown in Figure 6-38 for model ST39B. For models with restrained edges, however, significant compressive demands were imposed on remote connections, as shown in Figure 6-39 for specimen ST59B.

Horizontal loads developed in both the attached and remote connections for specimens ST39B and ST59B are shown in Figure 6-40 and Figure 6-41. Good correlation is observed between the simplified and detailed models. The trend of load development and ultimate strength and rotational capacities of the attached connections are similar and are independent of the horizontal axial conditions of the slab. However, the remote connections undergo substantial compressive forces once the slab edges are arrested against horizontal movement. Table 6-18

summarizes beam chord rotations and ultimate strengths for the initial failure of the attached shear tabs of the prototype models.

For comparison, the results presented in Sections 6.4 and 6.5 are also shown in Table 6-18. The results demonstrate excellent agreement with the experiments and proposed method values (Sections 6.4.3 and 6.4.4), with differences being 10 % or less. Moreover, Figure 6-40 and Figure 6-41 show the region of arching and catenary actions based on the theoretical value of initial angle of arching action ( $\alpha = 0.076$ ). As seen from the figures, the idealized model, introduced in Section 3.6.2 and shown in Figure 3-21, depicts precisely the various phases of axial force development during arching and/or catenary actions in connections.

For the results shown in Figure 6-40 and Figure 6-41, initial connection failures (corresponding to the ultimate strength of the shear tabs) occurred at removed-column displacements between 300 mm and 400 mm, shown by dot points on the curves in Figure 6-42. This shows that the initial failure of the attached connections occurred prior the failure of the composite system, which is an indication that membrane action in the slab has developed and subsequently carried the ultimate capacity of the floor system after failure of the attached beam-to-column connections. Similar results were also drawn by Main and Sadek (2012b), concluding that "...connection failures occurring before tie forces were able to significantly enhance the structural capacity."

### **6.7.3 Load–Displacement Response**

Figure 6-42 shows the load–displacement curves for all of the detailed models. In all cases, connections attached to the removed column completely failed at deflections between 300 mm and 400 mm, before the system reaches its ultimate strength. The initial failure of attached connections had a direct influence on the response of the system where the slope of the connection post-ultimate response reduces significantly. This is more noticeable by comparing the plateau-like response of the unrestrained models after initial failure of the connections.

The ultimate capacity of the unrestrained systems is about 56% of that of the restrained ones. The ultimate capacity of the unrestrained systems reached about 1.5 times the total shear forces developed in the four attached connections once at their ultimate strength, while the ratio was about 2.1 for the restrained models. In fact, the reserve capacity of the structural system after the connections' post-ultimate response is higher in restrained systems. This is certainly due to the formation of arching action in the restrained systems, which provide rigid axial constraints to the edges of slab. Although the compressive ring developed in the unrestrained models is beneficial to the structural capacity compared to the bare frame systems, the results show that it is not as effective as the restrained system in which the slab edges are axially arrested. However, providing full horizontal restrained conditions to the perimeter of slab may not be feasible.

The effect of the concrete slab on the vertical load–displacement response and ultimate capacity of specimen ST39B is illustrated in Figure 6-43. The comparison shows the response of the model ST39B in four different cases: bare frame, simplified composite frame, detailed restrained composite frame, and detailed unrestrained composite frame. The results indicate that in the bare frame system, the structural system attains its capacity at the initial failure of the connections (corresponds to the ultimate strength of the connection). However, regardless of the boundary conditions, once placed in the composite frames the response is different and the structural system attains a higher capacity and noticeably gains a reserve capacity after connections' initial failure.

It should be noted that in the simplified FEA models, the slab edges were fully restrained against horizontal displacements, and also the effective width of the concrete slab over the steel beam was considered, as shown in Figure 6-1. However, the results of the simplified FEA model are comparable with the unrestrained detailed model. The difference between the simplified and unrestrained detailed models is due to the formation of a compressive ring, which develops fully in the detailed models. However, once the slab is considered fully (three-dimensional model) with a restrained boundary conditions on the perimeter, the ultimate capacity of the structural system increases significantly, as

illustrated in Figure 6-43. Thus, the effects of the concrete slab and perimeter boundary conditions of the slab are very significant on the overall capacity of the structural system.

As explained previously, remote connections experience a prominent compressive force in restrained models, while in an unrestrained system no axial demand is imposed on them. Therefore, remote connections become an important component in restrained or partially restrained systems in order to arrest the system against collapse.

#### **6.7.4 Load Combination and Structural Integrity Requirements**

In this section, a comparison is made between the results of the detailed finite element analysis and possible required loads defined by the building codes and standards. Several loading levels were considered based on the load combinations for extraordinary events specified in Section 10.3.3 of CSA S850-12 (CSA 2012), and Section 2.5 of ASCE/SEI 7-10 (ASCE 2010).

The design loads on the prototype buildings were determined from Part 4/Division B of National Building Code of Canada (NBCC) (NRC 2010), and from Section 2.5 of ASCE/SEI 7-10. For typical floors, a total expected dead load of  $3.6 \text{ kN/m}^2$  was considered, which includes the self-weight of the concrete floor slab and superimposed dead load. Minimum specified live loads were considered for two different occupancies of residential and office buildings. For simplicity, the reduction in live loads was not considered. In addition, mean values of the live load based on the survey data from Table C4-2 of ASCE/SEI 7-10 was extracted for the sake of comparison. Other loads such as wind and snow are omitted since the investigation is focused on the intermediate floor of the prototype. Table 6-19 and Table 6-20 summarize the specified uniform gravity loads and expected load combinations, respectively.

Values of the load intensity calculated by dividing the applied load of the unsupported removed column by the tributary area of  $81.0 \text{ m}^2$  ( $9.0 \text{ m} \times 9.0 \text{ m}$ ) are plotted in Figure 6-44 to Figure 6-46. Although in this approach a concentrated

load was applied to the central removed column, it was shown by Alashker et al. (2010) that the capacity of the system in terms of load intensity is comparable if uniform loading was applied instead.

The collapse resistances of the prototype systems were assessed by comparing the capacities under both quasi-static and dynamic loading. In some cases, the capacity was found to be inadequate to sustain even the lower level of load combination. Since no direct dynamic analysis was performed, the dynamic response was generated by dividing the quasi-static curve by a Dynamic Increase Factor, denoted as “DIF”. The DIF of 1.5 was considered for the prototype models in this research based on the report by Main and Sadek (2012b).

Figure 6-44 shows the quasi-static and dynamic load–displacement responses of detailed unrestrained model of specimen ST39B, and are compared with the structural integrity load combinations tabulated in Table 6-20. As seen in Figure 6-44, while the quasi-static capacity barely satisfies the expected load combinations, the approximate dynamic capacity accomplished none of the expected gravity loadings. Figure 6-45 and Figure 6-46 illustrate quasi-static and dynamic load–displacement responses for all of the detailed models. As shown, while the quasi-static response of the unrestrained systems barely satisfies the expected load combinations, the dynamic capacity did not reach the expected gravity loadings. However, for the restrained models the quasi-static and dynamic capacities were both higher than the expected gravity loadings.

### **6.7.5 Comparison with the Existing Research Models**

The load–displacement curves are compared with the results of Main and Sadek (2012b) and Francisco and Liu (2016) in Figure 6-47. Although the span lengths are not identical (9.1 m by 6.1 m) to the current prototype models (9.0 m by 9.0 m) and also the material properties are slightly different (A36 compare to 300W), the comparison was made here since the results are shown based on the uniform load intensity.

The evaluation was based on the 3 bay  $\times$  4 bay Building Type B of Main and Sadek (2012b) with two different reinforcement details of concrete slab, namely S20-1.4 and S16-14. Model S20-1.4 includes 20 gauge steel deck with 152 mm  $\times$  152 mm grid spacing wire mesh having a cross-sectional area of 9.03 mm<sup>2</sup>, while Model S16-14 includes 16 gauge steel deck with 152 mm  $\times$  152 mm grid spacing wire mesh having a cross-sectional area of 90.3 mm<sup>2</sup>. In terms of reinforcement density, Model S16-14 is analogous to the current prototype models (no steel decks were considered in this research).

The 2 bay  $\times$  2 bay reduced model developed by Francisco and Liu (2016) was replicated based on the structure with a 6.1  $\times$  9.1 m bay size used in Main and Sadek (2012b). Their finite element model was developed based on a reduced two-shell model, representing a metal-deck reinforced concrete slab.

As seen in Figure 6-47, generally good agreement was attained between different models despite the variances in the model geometry and material properties. Results of the unrestrained model are consistent with the conclusion made by Main and Sadek (2012b) and Francisco and Liu (2016) that the structure (Model S20-1.4 versus ST39B and ST59B) was not able to sustain the expected dynamic gravity loadings and to meet the ASCE/SEI 7-10 load combination requirement. However, for the restrained models and enhanced slab model of S16-14 by Main and Sadek (2012b), the floor system sustained higher gravity loading. It can be concluded that by increasing the reinforcement area and/or imposing proper horizontal axial constraints, the capacity of the composite system can be increased substantially to sustain the expected gravity loads under column removal.

As explained previously, attention should be paid to the interpretation of the results of the restrained models, since attaining fully axially restrained conditions at the edges of a slab might bring into question the validity of the results. More research is needed to investigate the effects of axial stiffness on the overall structural capacity and performance. Nonetheless, the results of the current prototype models are upper bound and lower bound values, since two extreme horizontal boundary conditions were considered.

The main outcome drawn from this section is that the modelled prototype structures can be made adequately robust, provided due allowance is taken of compressive arching action that develops under axial restraint. Since the rotational ductility and ultimate strength of the connections were inadequate for the development of full tensile catenary action, reliance should be placed primarily on bending and compressive arching resistance for the establishment of robustness under column-loss scenarios.

Table 6-1: Comparison of Finite Element Model and Experiment Results  
Reported by Oosterhof and Driver (2016)

Property	Shear Tab		Double Angle	
	Test	FEA	Test	FEA
<b>Geometry and Material Properties</b>				
Specimen ID	ST3B-2	ST36B	DA3B-2	DA36B
Number of Bolts	3	3	3	3
Plate/Angle Thickness (mm)	6.4	6.3	6.4	6.6
Load Arrangement *	w	P	w	P
Span Length (m)	9.0	9.0	9.0	9.0
Yield Strength (MPa)	323	356	344	347
Ultimate Strength (MPa)	458	478	499	499
<b>Results</b>				
Failure Mode †	TS, TO	TS, TO	TG	TG
Ultimate Horizontal Load (kN)	335	373	308	323
Beam Rotation at Ultimate Load (radians)	0.086	0.094	0.123	0.108
Axial Displacement at Ultimate Load (mm)	16.7	19.0	34.3	26.5

\* “P” Refers to Central-Column Point Load, and

“w” Refers to Uniformly Distributed Load

† Failure Mode (Refer to Section 4.3.1.1 and Section 4.3.1.2):

TS: Tensile Splitting Tear

TO: Bolt Tear-out

TG: Tearing of Gross Section Near Angle Heel



Table 6-2: Finite Element Results of Shear Tabs (Attached Connections) in Composite Frame

Specimen ID	Composite Section									Steel Section								
	H <sub>min</sub> (kN)	θ <sub>Hmin</sub> (rad.)	δ <sub>Hmin</sub> (mm)	M <sub>max</sub> (kN·m)	θ <sub>Mmax</sub> (rad.)	δ <sub>Mmax</sub> (mm)	V <sub>max</sub> (kN)	θ <sub>Vmax</sub> (rad.)	δ <sub>Vmax</sub> (mm)	H <sub>max</sub> (kN)	θ <sub>Hmax</sub> (rad.)	δ <sub>Hmax</sub> (mm)	M <sub>max</sub> (kN·m)	θ <sub>Mmax</sub> (rad.)	δ <sub>Mmax</sub> (mm)	V <sub>max</sub> (kN)	θ <sub>Vmax</sub> (rad.)	δ <sub>Vmax</sub> (mm)
<b>ST36A</b>	-472.7	0.017	1.9	292.8	0.019	2.2	82.5	0.114	40.4	386.4	0.040	8.2	8.4	0.010	0.9	97.2	0.115	41.5
<b>ST36B</b>	-407.2	0.012	1.0	251.3	0.015	1.5	94.2	0.092	39.0	373.0	0.035	7.1	8.0	0.010	0.9	99.4	0.092	39.0
<b>ST39A</b>	-544.4	0.025	3.4	388.5	0.030	4.6	81.4	0.114	39.8	492.3	0.041	7.2	8.6	0.006	0.7	96.4	0.114	39.8
<b>ST39B</b>	-384.1	0.019	2.4	313.7	0.025	3.8	100.4	0.096	40.5	489.3	0.036	6.2	8.2	0.006	0.7	103.9	0.096	40.5
<b>ST56A</b>	-457.6	0.027	3.7	398.5	0.031	4.9	106.1	0.129	48.2	603.2	0.037	6.4	25.5	0.013	1.1	115.8	0.129	48.2
<b>ST56B</b>	-370.6	0.011	0.9	354.5	0.028	4.4	117.2	0.104	44.7	618.2	0.037	7.0	24.6	0.011	0.9	119.4	0.104	44.7
<b>ST59A</b>	-615.7	0.021	2.0	527.2	0.036	4.5	114.8	0.126	45.2	825.3	0.038	4.8	28.0	0.008	0.8	123.6	0.126	45.2
<b>ST59B</b>	-497.1	0.019	1.9	473.3	0.028	3.3	124.0	0.105	45.2	831.1	0.039	5.2	27.2	0.008	0.7	125.8	0.105	45.2

δ Refers to Centreline Axial Deformation of Connection at Corresponding Loading Level

θ Refers to Beam Chord Rotation at Corresponding Loading Level

Table 6-3: Finite Element Results of Shear Tabs (Remote Connections) in Composite Frame

Specimen ID	Composite Section									Steel Section								
	H <sub>min</sub> (kN)	θ <sub>Hmin</sub> (rad.)	δ <sub>Hmin</sub> (mm)	M <sub>min</sub> (kN·m)	θ <sub>Mmin</sub> (rad.)	δ <sub>Mmin</sub> (mm)	V <sub>max</sub> (kN)	θ <sub>Vmax</sub> (rad.)	δ <sub>Vmax</sub> (mm)	H <sub>min</sub> (kN)	θ <sub>Hmin</sub> (rad.)	δ <sub>Hmin</sub> (mm)	M <sub>min</sub> (kN·m)	θ <sub>Mmin</sub> (rad.)	δ <sub>Mmin</sub> (mm)	V <sub>max</sub> (kN)	θ <sub>Vmax</sub> (rad.)	δ <sub>Vmax</sub> (mm)
<b>ST36A</b>	-566.3	0.017	-1.3	-23.4	0.073	-4.5	170.4*	0.115	-3.8	-464.8	0.051	-3.9	-22.1	0.079	-4.5	173.1*	0.115	-3.8
<b>ST36B</b>	-488.0	0.013	-1.0	-31.8	0.037	-2.4	97.3	0.092	-3.1	-397.7	0.041	-2.5	-20.2	0.074	-3.1	98.5	0.092	-3.1
<b>ST39A</b>	-708.1	0.025	-1.2	-30.0	0.080	-1.2	204.8*	0.115	-0.8	-602.2	0.041	-1.1	-28.9	0.083	-1.2	208.1*	0.115	-0.8
<b>ST39B</b>	-521.7	0.012	-0.8	-31.3	0.095	-1.8	106.8	0.097	-1.8	-534.3	0.030	-1.2	-29.2	0.097	-1.8	109.2	0.097	-1.8
<b>ST56A</b>	-607.2	0.030	-2.1	-61.9	0.124	-3.8	241.8*	0.129	-3.4	-636.2	0.039	-2.5	-61.7	0.129	-3.4	242.8*	0.129	-3.4
<b>ST56B</b>	-512.9	0.022	-1.3	-74.4	0.100	-1.0	118.8	0.104	-0.9	-547.8	0.037	-1.8	-72.2	0.104	-0.9	120.4	0.104	-0.9
<b>ST59A</b>	-793.4	0.021	-0.7	-82.0	0.112	0.7	223.9*	0.126	1.8	-816.8	0.032	-0.4	-79.8	0.111	0.6	224.4*	0.126	1.8
<b>ST59B</b>	-708.0	0.024	-0.7	-101.3	0.107	0.7	131.9	0.108	0.7	-744.2	0.026	-0.6	-98.4	0.107	0.7	134.1	0.108	0.7

δ Refers to Centreline Axial Deformation of Connection at Corresponding Loading Level

θ Refers to Beam Chord Rotation at Corresponding Loading Level

\* Exceeded by Binding Effects and at Post-Damage Vertical Load

Table 6-4: Finite Element Results of Shear Tabs in Bare Frame

Specimen ID	Attached Connection									Remote Connection								
	H <sub>max</sub> (kN)	θ <sub>Hmax</sub> (rad.)	δ <sub>Hmax</sub> (mm)	M <sub>max</sub> (kN·m)	θ <sub>Mmax</sub> (rad.)	δ <sub>Mmax</sub> (mm)	V <sub>max</sub> (kN)	θ <sub>Vmax</sub> (rad.)	δ <sub>Vmax</sub> (mm)	H <sub>max</sub> (kN)	θ <sub>Hmax</sub> (rad.)	δ <sub>Hmax</sub> (mm)	M <sub>min</sub> (kN·m)	θ <sub>Mmin</sub> (rad.)	δ <sub>Mmin</sub> (mm)	V <sub>max</sub> (kN)	θ <sub>Vmax</sub> (rad.)	δ <sub>Vmax</sub> (mm)
<b>ST36A</b>	410.1	0.112	20.4	13.3	0.084	10.5	46.0	0.112	20.4	411.8	0.106	16.2	-13.2	0.082	10.4	46.6	0.107	16.4
<b>ST36B</b>	426.2	0.094	20.3	12.1	0.061	7.8	40.5	0.092	19.0	427.0	0.093	18.3	-12.1	0.060	7.8	40.4	0.094	18.4
<b>ST39A</b>	537.2	0.105	15.5	16.2	0.069	6.6	60.5	0.107	15.9	535.9	0.106	17.0	-16.3	0.070	7.1	60.6	0.110	19.3
<b>ST39B</b>	556.2	0.090	16.9	14.7	0.051	5.3	52.7	0.090	16.9	556.4	0.091	18.6	-14.4	0.050	5.3	54.0	0.094	21.0
<b>ST56A</b>	565.2	0.133	26.7	46.5	0.055	4.4	76.2	0.140	29.4	562.7	0.133	25.8	-47.0	0.057	4.5	76.5	0.142	30.7
<b>ST56B</b>	632.5	0.107	25.4	36.6	0.058	6.9	70.8	0.114	28.1	635.0	0.113	28.5	-37.0	0.061	7.6	69.7	0.113	28.5
<b>ST59A</b>	706.6	0.134	25.2	71.0	0.053	4.1	90.9	0.134	25.2	710.0	0.128	26.3	-71.1	0.05	3.1	93.1	0.135	30.7
<b>ST59B</b>	807.8	0.091	18.7	62.7	0.040	3.2	80.8	0.109	23.1	808.8	0.092	18.1	-62.2	0.036	3.1	81.7	0.109	21.9

δ Refers to Centreline Axial Deformation of Connection at Corresponding Loading Level

θ Refers to Beam Chord Rotation at Corresponding Loading Level

Table 6-5: Effect of Concrete Slab on Shear Tabs (Attached Connections)

Specimen ID	$H_{Comp.}$	$H_{Bare}$	$\delta_{Comp.}$	$\delta_{Bare}$	$\theta_{Comp.}$	$\theta_{Bare}$	$H_{Comp.}$	$\delta_{Comp.}$	$\theta_{Comp.}$
	kN	kN	mm	mm	radians	radians	to $H_{Bare}$	to $\delta_{Bare}$	to $\theta_{Bare}$
<b>ST36A</b>	386	410.1	8.2	20.4	0.040	0.112	0.94	0.40	0.36
<b>ST36B</b>	373	426.2	7.1	20.3	0.035	0.094	0.88	0.35	0.37
<b>ST39A</b>	492	537.2	7.2	15.5	0.041	0.105	0.92	0.46	0.39
<b>ST39B</b>	489	556.2	6.2	16.9	0.036	0.090	0.88	0.37	0.40
<b>ST56A</b>	603	565.2	6.4	26.7	0.037	0.133	1.07	0.24	0.28
<b>ST56B</b>	618	632.5	7.0	25.4	0.037	0.107	0.98	0.27	0.34
<b>ST59A</b>	825	706.6	4.8	25.2	0.038	0.134	1.17	0.19	0.28
<b>ST59B</b>	831	807.8	5.2	18.7	0.039	0.091	1.03	0.28	0.43
Average			6.5	21.1	0.038	0.108	0.98	0.32	0.36
Standard Deviation			1.1	4.2	0.002	0.02	0.10	0.09	0.05
Coefficient of Variation			0.17	0.20	0.05	0.16	0.10	0.28	0.15

Table 6-6 : Comparison of Bolt Tear-out Capacity

Specimen ID	$R_{Test}$	$R_{FEA}$	$R_{AISC}$	$R_{CSA}$	$R_{Test}$	$R_{Test}$	$R_{Test}$
	kN	kN	kN	kN	to $R_{FEA}$	to $R_{AISC}$	to $R_{CSA}$
<b>ST36A</b>	N/A	386.4	345.4	330.7	N/A	N/A	N/A
<b>ST36B</b>	N/A	373.0	345.4	330.7	N/A	N/A	N/A
<b>ST39A</b>	484.5	492.3	450.9	442.7	0.98	1.07	1.09
<b>ST39B</b>	512.7	489.3	450.9	442.7	1.05	1.14	1.16
<b>ST56A</b>	602.3	603.2	575.7	551.2	1.00	1.05	1.09
<b>ST56B</b>	612.6	618.2	575.7	551.2	0.99	1.06	1.11
<b>ST59A</b>	740.2	825.3	751.5	737.8	0.90	0.98	1.00
<b>ST59B</b>	835.7	831.1	751.5	737.8	1.01	1.11	1.13
Average					0.99	1.07	1.10
Standard Deviation					0.05	0.05	0.05
Coefficient of Variation					0.05	0.05	0.05

Table 6-7: Test-to-Predicted Ratio: Bolt Tear-out Capacity with the Consideration of Inclined Shear Planes

Specimen ID	R <sub>Test</sub> to R <sub>AISC</sub>			R <sub>Test</sub> to R <sub>CSA</sub>		
	$\beta = 15$	$\beta = 20$	$\beta = 25$	$\beta = 15$	$\beta = 20$	$\beta = 25$
ST39A	1.04	1.01	0.97	1.06	1.03	0.99
ST39B	1.10	1.07	1.03	1.12	1.09	1.05
ST56A	1.01	0.98	0.95	1.06	1.03	0.99
ST56B	1.03	1.00	0.96	1.07	1.04	1.01
ST59A	0.95	0.93	0.89	0.97	0.94	0.91
ST59B	1.07	1.04	1.01	1.09	1.06	1.03
Average	1.03	1.01	0.97	1.06	1.03	1.00
Standard Deviation	0.05	0.05	0.05	0.05	0.05	0.05
Coefficient of Variation	0.05	0.05	0.05	0.05	0.05	0.05

Table 6-8: Bearing at Bolt Holes (Remote Shear Tabs)

Specimen ID	R <sub>FEA</sub>	R <sub>AISC</sub> <sup>*</sup>	n	n <sub>eff</sub> <sup>†</sup>	n <sub>eff</sub> to n
	kN	kN			
ST36A	464.8	514.7	3	2.71	0.90
ST36B	397.7	514.7	3	2.32	0.77
ST39A	602.2	826.7	3	2.19	0.73
ST39B	534.3	826.7	3	1.94	0.65
ST56A	636.2	857.9	5	3.71	0.74
ST56B	547.8	857.9	5	3.19	0.64
ST59A	816.8	1377.8	5	2.96	0.59
ST59B	744.2	1377.8	5	2.70	0.54
Average				2.71	0.70
Standard Deviation				0.58	0.11
Coefficient of Variation				0.21	0.17

\* R<sub>AISC</sub> = n(3dtF<sub>u</sub>)

n Refers to the Number of Bolts

† n<sub>eff</sub> = R<sub>FEA</sub> / (3dtF<sub>u</sub>)

Table 6-9: Rotational Capacity Corresponding to the Ultimate Horizontal Load of Attached Shear Tabs and Comparison with the Current Guidelines

Specimen ID	$d_{bg}^*$	$e^*$	FEA	GSA <sup>‡</sup>	ASCE <sup>†</sup> (rad.)		FEA	FEA to ASCE	
	mm	mm	rad.	rad.	with Slab	without Slab	to GSA	with Slab	without Slab
<b>ST36A</b>	160	336	0.04	0.061	0.048	0.127	0.66	0.83	0.31
<b>ST36B</b>	160	336	0.035	0.061	0.048	0.127	0.58	0.74	0.28
<b>ST39A-1</b>	160	336	0.041	0.061	0.048	0.127	0.67	0.85	0.32
<b>ST39A-2</b>	160	256	0.051	0.061	0.048	0.127	0.84	1.07	0.40
<b>ST39A-3</b>	160	416	0.035	0.061	0.048	0.127	0.57	0.73	0.27
<b>ST39B-1</b>	160	336	0.036	0.061	0.048	0.127	0.59	0.75	0.28
<b>ST39B-2</b>	160	416	0.032	0.061	0.048	0.127	0.52	0.66	0.25
<b>ST39B-3</b>	160	256	0.048	0.061	0.048	0.127	0.78	1.00	0.37
<b>ST39B-4</b>	160	336	0.037	0.061	0.048	0.127	0.60	0.77	0.29
<b>ST39B-5</b>	160	256	0.046	0.061	0.048	0.127	0.76	0.96	0.36
<b>ST56A</b>	320	336	0.037	0.051	0.046	0.105	0.72	0.80	0.35
<b>ST56B</b>	320	336	0.037	0.051	0.046	0.105	0.71	0.79	0.35
<b>ST59A</b>	320	336	0.038	0.051	0.046	0.105	0.74	0.82	0.36
<b>ST59B</b>	320	336	0.039	0.051	0.046	0.105	0.76	0.84	0.37
Average			0.039	0.058	0.047	0.121	0.68	0.83	0.33
Standard Deviation			0.005	0.004	0.001	0.011	0.09	0.11	0.05
Coefficient of Variation			0.14	0.08	0.01	0.09	0.14	0.14	0.14

\* For Details Refer to Figure 6-22 ( $d_{bg}$ : Depth of Bolts Group,  $e$ : Eccentricity)

‡ Refers to Section 3.2.4 of GSA Guidelines (Similar to UFC 4-023-03, and Clause 3.1 of CSA S850)

† Refers to ASCE/SEI 41-06

Table 6-10: Rotational Capacity of Shear Tabs Derived based on the Proposed Empirical Methods, and Comparison with the FEA

Specimen ID	$d_{bg}^*$	$e^*$	$e'^*$	$\alpha^*$	Rot. ‡	Axial Deformation‡	Proposed Method (rad.)		Ratio to Proposed	
	mm	mm	mm	rad.	rad.	mm	(1)	(2)	(1)	(2)
<b>ST36A</b>	160	336	336	0.057	0.040	8.2	0.041	0.045	0.97	0.88
<b>ST36B</b>	160	336	336	0.038	0.035	7.1	0.037	0.037	0.94	0.96
<b>ST39A-1</b>	160	336	336	0.057	0.041	7.2	0.041	0.045	0.99	0.90
<b>ST39A-2</b>	160	256	336	0.057	0.051	7.3	0.049	0.059	1.04	0.87
<b>ST39A-3</b>	160	416	336	0.057	0.035	7.1	0.033	0.031	1.05	1.11
<b>ST39B-1</b>	160	336	336	0.038	0.036	6.2	0.037	0.037	0.96	0.98
<b>ST39B-2</b>	160	416	336	0.038	0.032	6.6	0.029	0.028	1.11	1.15
<b>ST39B-3</b>	160	256	336	0.038	0.048	7.0	0.046	0.046	1.02	1.04
<b>ST39B-4</b>	160	336	416	0.038	0.037	6.3	0.037	0.037	0.98	1.00
<b>ST39B-5</b>	160	256	256	0.029	0.046	6.6	0.046	0.037	0.99	1.25
<b>ST56A</b>	320	336	336	0.057	0.037	6.4	0.039	0.045	0.95	0.82
<b>ST56B</b>	320	336	336	0.038	0.037	7.0	0.035	0.037	1.04	1.00
<b>ST59A</b>	320	336	336	0.057	0.038	4.8	0.039	0.045	0.97	0.84
<b>ST59B</b>	320	336	336	0.038	0.039	5.2	0.035	0.037	1.10	1.06
Average					0.039	6.7	0.039	0.040	1.01	0.99
Standard Deviation					0.005	0.9	0.006	0.008	0.05	0.12
Coefficient of Variation					0.14	0.13	0.14	0.19	0.05	0.12

\* For Details Refer to Figure 6-22

‡ Rotation at Corresponding Horizontal Tensile Strength of Shear Tabs based on the Finite Element Analysis Results

Table 6-11: Finite Element Results of Double Angles (Attached Connections) in Composite Frame

Specimen ID	Composite Section									Steel Section								
	H <sub>min</sub> (kN)	θ <sub>Hmin</sub> (rad.)	δ <sub>Hmin</sub> (mm)	M <sub>max</sub> (kN·m)	θ <sub>Mmax</sub> (rad.)	δ <sub>Mmax</sub> (mm)	V <sub>max</sub> (kN)	θ <sub>Vmax</sub> (rad.)	δ <sub>Vmax</sub> (mm)	H <sub>max</sub> (kN)	θ <sub>Hmax</sub> (rad.)	δ <sub>Hmax</sub> (mm)	M <sub>max</sub> (kN·m)	θ <sub>Mmax</sub> (rad.)	δ <sub>Mmax</sub> (mm)	V <sub>max</sub> (kN)	θ <sub>Vmax</sub> (rad.)	δ <sub>Vmax</sub> (mm)
<b>DA36A</b>	-1390	0.054	16.7	623	0.054	16.7	92.6	0.043	13.0	354	0.046	14.1	2.8	0.109	36.8	110.5	0.120	41.7
<b>DA36B</b>	-807	0.041	15.1	417	0.041	15.1	115.0	0.111	50.6	332	0.045	16.3	5.2	0.085	33.7	120.8	0.109	49.0
<b>DA39A</b>	-1535	0.046	15.1	684	0.047	15.5	101.6	0.045	14.7	497	0.027	7.9	6.6	0.009	2.2	108.1	0.057	19.4
<b>DA39B</b>	-1117	0.046	16.2	530	0.036	12.0	157.0	0.096	40.1	503	0.029	9.2	5.7	0.008	2.1	168.0	0.096	40.1
<b>DA56A</b>	-1494	0.047	14.0	690	0.047	14.0	96.5	0.044	13.0	561	0.043	12.6	23.0	0.040	11.6	123.5	0.101	31.3
<b>DA56B</b>	-1038	0.051	17.0	516	0.050	16.3	199.5	0.091	35.0	531	0.043	13.7	19.0	0.036	11.0	169.4	0.121	56.1
<b>DA59A</b>	-1422	0.030	8.3	711	0.027	7.4	146.4	0.062	18.7	806	0.027	7.4	20.8	0.011	2.4	146.4	0.062	18.7
<b>DA59B</b>	-1324	0.048	16.4	642	0.037	12.1	163.2	0.090	35.0	782	0.025	7.2	20.6	0.010	2.3	163.2	0.090	35.0

δ Refers to Centreline Axial Deformation of Connection at Corresponding Loading Level

θ Refers to Beam Chord Rotation at Corresponding Loading Level



Table 6-12: Finite Element Results of Double Angles (Remote Connections) in Composite Frame

Specimen ID	Composite Section									Steel Section								
	H <sub>min</sub> (kN)	θ <sub>Hmin</sub> (rad.)	δ <sub>Hmin</sub> (mm)	M <sub>min</sub> (kN·m)	θ <sub>Mmin</sub> (rad.)	δ <sub>Mmin</sub> (mm)	V <sub>max</sub> (kN)	θ <sub>Vmax</sub> (rad.)	δ <sub>Vmax</sub> (mm)	H <sub>min</sub> (kN)	θ <sub>Hmin</sub> (rad.)	δ <sub>Hmin</sub> (mm)	M <sub>min</sub> (kN·m)	θ <sub>Mmin</sub> (rad.)	δ <sub>Mmin</sub> (mm)	V <sub>max</sub> (kN)	θ <sub>Vmax</sub> (rad.)	δ <sub>Vmax</sub> (mm)
<b>DA36A</b>	-745	0.020	-1.5	-33.4	0.035	-2.0	182.7*	0.053	-2.5	-700	0.036	-2.1	-30.2	0.062	-2.5	182.5*	0.053	-2.5
<b>DA36B</b>	-610	0.023	-1.2	-44.0	0.034	-1.5	117.5	0.040	-1.7	-607	0.032	-1.5	-29.6	0.045	-1.8	120.0	0.040	-1.7
<b>DA39A</b>	-1011	0.045	-1.2	-186.2	0.075	-1.2	144.9*	0.032	-1.0	-1029	0.045	-1.2	-184.3	0.075	-1.2	144.1*	0.032	-1.0
<b>DA39B</b>	-1007	0.024	-0.7	-49.9	0.050	-1.0	158.5	0.050	-1.0	-1039	0.024	-0.7	-42.8	0.049	-1.0	159.3	0.050	-1.0
<b>DA56A</b>	-989	0.042	-2.0	-85.4	0.049	-1.9	192.6*	0.052	-1.9	-1011	0.042	-2.0	-80.1	0.049	-1.9	191.9*	0.052	-1.9
<b>DA56B</b>	-1326	0.045	-1.7	-193.6	0.048	-1.6	86.8	0.032	-1.6	-1351	0.041	-1.7	-187.5	0.052	-1.5	85.4	0.032	-1.6
<b>DA59A</b>	-1481	0.027	-0.7	-131.5	0.066	-0.4	212.1*	0.046	-0.9	-1487	0.029	-0.7	-130.8	0.077	0.2	211.7*	0.056	-0.8
<b>DA59B</b>	-1625	0.039	-0.7	-228.9	0.059	-0.2	149.1	0.050	-0.7	-1450	0.027	-0.7	-130.0	0.058	-0.3	149.1	0.050	-0.7

δ Refers to Centreline Axial Deformation of Connection at Corresponding Loading Level

θ Refers to Beam Chord Rotation at Corresponding Loading Level

\* Exceeded by Binding Effects and at Post-Damage Vertical Load

Table 6-13: Finite Element Results of Double Angles in Bare Frame

Specimen ID	Attached Connection									Remote Connection								
	H <sub>max</sub> (kN)	θ <sub>Hmax</sub> (rad.)	δ <sub>Hmax</sub> (mm)	M <sub>max</sub> (kN·m)	θ <sub>Mmax</sub> (rad.)	δ <sub>Mmax</sub> (mm)	V <sub>max</sub> (kN)	θ <sub>Vmax</sub> (rad.)	δ <sub>Vmax</sub> (mm)	H <sub>max</sub> (kN)	θ <sub>Hmax</sub> (rad.)	δ <sub>Hmax</sub> (mm)	M <sub>min</sub> (kN·m)	θ <sub>Mmin</sub> (rad.)	δ <sub>Mmin</sub> (mm)	V <sub>max</sub> (kN)	θ <sub>Vmax</sub> (rad.)	δ <sub>Vmax</sub> (mm)
<b>DA36A</b>	344.1	0.091	17.3	12.8	0.088	8.5	30.5	0.095	9.7	352.1	0.107	17.300	-9.7	0.078	6.3	26.8	0.144	40.5
<b>DA36B</b>	322.9	0.083	18.7	9.2	0.079	13.5	26.2	0.080	13.9	297.2	0.108	25.0	-10.5	0.074	11.9	25.0	0.071	10.7
<b>DA39A</b>	496.3	0.121	20.4	26.4	0.035	1.8	26.5	0.065	5.4	488.7	0.121	20.7	-25.7	0.035	1.8	32.5	0.071	6.0
<b>DA39B</b>	493.5	0.099	21.9	17.7	0.024	1.2	29.1	0.048	4.2	471.8	0.105	22.7	-18.2	0.143	18.5	37.6	0.143	18.5
<b>DA56A</b>	539.4	0.109	14.9	47.8	0.061	5.3	25.4	0.168	24.7	547.8	0.109	15.1	-47.2	0.061	5.5	27.5	0.157	21.2
<b>DA56B</b>	510.0	0.104	21.5	31.3	0.069	8.5	34.2	0.094	16.8	506.3	0.105	21.4	-29.3	0.071	8.8	40.0	0.106	21.2
<b>DA59A</b>	749.8	0.109	16.1	104.5	0.047	3.0	125.4	0.158	25.0	738.6	0.110	16.5	-106	0.05	3.3	108.6	0.118	18.5
<b>DA59B</b>	749.6	0.096	18.9	84.9	0.038	3.1	64.0	0.117	17.8	734.6	0.096	19.0	-90.3	0.036	2.8	44.7	0.119	23.2

δ Refers to Centreline Axial Deformation of Connection at Corresponding Loading Level

θ Refers to Beam Chord Rotation at Corresponding Loading Level

Table 6-14: Effect of Concrete Slab on Double Angles (Attached Connections)

Specimen ID	$H_{Comp.}$	$H_{Bare}$	$\delta_{Comp.}$	$\delta_{Bare}$	$\theta_{Comp.}$	$\theta_{Bare}$	$H_{Comp.}$	$\delta_{Comp.}$	$\theta_{Comp.}$
	kN	kN	mm	mm	rad.	rad.	to $H_{Bare}$	to $\delta_{Bare}$	to $\theta_{Bare}$
<b>DA36A</b>	354	344	14.1	17.3	0.046	0.091	1.03	0.81	0.51
<b>DA36B</b>	332	323	16.3	18.7	0.045	0.083	1.03	0.87	0.54
<b>DA39A</b>	497	496	7.9	20.4	0.027	0.121	1.00	0.39	0.22
<b>DA39B</b>	503	494	9.2	21.9	0.029	0.099	1.02	0.42	0.29
<b>DA56A</b>	561	539	12.6	14.9	0.043	0.109	1.04	0.84	0.40
<b>DA56B</b>	531	510	13.7	21.5	0.043	0.104	1.04	0.64	0.41
<b>DA59A</b>	806	750	7.4	16.1	0.027	0.109	1.07	0.46	0.25
<b>DA59B</b>	782	750	7.2	18.9	0.025	0.096	1.04	0.38	0.26
Average			11.0	18.7	0.036	0.101	1.03	0.60	0.36
Standard Deviation			3.5	2.5	0.009	0.012	0.02	0.22	0.12
Coefficient of Variation			0.32	0.13	0.26	0.12	0.02	0.36	0.34
Average (6.3 mm Angles)			14.2	18.1	0.044	0.097	1.03	0.79	0.46
Standard Deviation (6.3 mm Angles)			1.6	2.7	0.002	0.012	0.01	0.11	0.07
Coefficient of Variation (6.3 mm Angles)			0.11	0.15	0.03	0.12	0.01	0.13	0.15
Average (9.5 mm Angles)			7.9	19.3	0.027	0.106	1.03	0.41	0.26
Standard Deviation (9.5 mm Angles)			0.9	2.5	0.002	0.011	0.03	0.04	0.03
Coefficient of Variation (9.5 mm Angles)			0.11	0.13	0.06	0.11	0.03	0.09	0.11

Table 6-15 : Comparison of Double Angles Capacity: Gross-sectional Failure

Specimen ID	$R_{Test}$	$R_{FEA}$	$R_n^*$	$R_n^\dagger$	$R_{Test}$	$R_{Test}$	$R_{Test}$
	kN	kN	kN	kN	to $R_{FEA}$	to $R_n^*$	to $R_n^\dagger$
<b>DA36A</b>	318.2	354.3	314.4	320.9	0.90	1.01	0.99
<b>DA36B</b>	305.3	331.8	314.4	320.9	0.92	0.97	0.95
<b>DA39A</b>	511.6	497.1	468.9	457.5	1.03	1.09	1.12
<b>DA39B</b>	508.4	502.7	468.9	457.5	1.01	1.08	1.11
<b>DA56A</b>	595.9	561.4	533.1	544.1	1.06	1.12	1.10
<b>DA56B</b>	541.6	530.5	533.1	544.1	1.02	1.02	1.00
<b>DA59A</b>	745.9	806.0	795.2	775.7	0.93	0.94	0.96
<b>DA59B</b>	799.3	781.8	795.2	775.7	1.02	1.01	1.03
Average					0.99	1.03	1.03
Standard Deviation					0.06	0.06	0.07
Coefficient of Variation					0.06	0.06	0.07

\* Equation (6-7)

† Equation (6-8)

Table 6-16: Bearing at Bolt Holes (Remote Double Angles)

Specimen ID	R <sub>FEA</sub> (kN)	R <sub>AISC</sub> <sup>*</sup> (kN)	n	n <sub>eff</sub> <sup>†</sup>	n <sub>eff</sub> to n
<b>DA36A</b>	699.9	1126.1	3	1.86	0.62
<b>DA36B</b>	607.4	1126.1	3	1.62	0.54
<b>DA39A</b>	1028.8	1885.6	3	1.64	0.55
<b>DA39B</b>	1039.5	1885.6	3	1.65	0.55
<b>DA56A</b>	1010.6	1876.9	5	2.69	0.54
<b>DA56B</b>	1351.0	1876.9	5	3.60	0.72
<b>DA59A</b>	1486.6	3142.7	5	2.37	0.47
<b>DA59B</b>	1450.2	3142.7	5	2.31	0.46
Average				2.38	0.55
Standard Deviation				0.73	0.09
Coefficient of Variation				0.31	0.17

\* R<sub>AISC</sub> = n(3dtF<sub>u</sub>) where “n” Refers to the Number of Bolts

† n<sub>eff</sub> = R<sub>FEA</sub> / (3dtF<sub>u</sub>)

Table 6-17: Rotational Capacity of Double Angles Derived based on the Proposed Empirical Method, and Comparison with the FEA and Guidelines

Specimen ID	d <sub>bg</sub> <sup>*</sup>	e <sup>*</sup>	t <sup>*</sup>	α <sup>*</sup>	Axial Elong. <sup>‡</sup>	FEA	GSA <sup>†</sup>	Proposed Method	Ratio of FEA to	
	mm	mm	mm	rad.	mm	rad.	rad.	rad.	GSA	Proposed
<b>DA36A</b>	160	336	6.6	0.057	14.1	0.046	0.115	0.044	0.40	1.05
<b>DA36B</b>	160	336	6.6	0.038	16.3	0.045	0.115	0.044	0.39	1.02
<b>DA39A</b>	160	336	6.6	0.057	7.9	0.027	0.115	0.029	0.23	0.91
<b>DA39B</b>	160	256	6.6	0.038	9.2	0.029	0.115	0.029	0.25	0.98
<b>DA56A</b>	320	336	9.7	0.057	12.6	0.043	0.098	0.042	0.44	1.04
<b>DA56B</b>	320	336	9.7	0.038	13.7	0.043	0.098	0.042	0.44	1.03
<b>DA59A</b>	320	336	9.7	0.057	7.4	0.027	0.098	0.026	0.28	1.05
<b>DA59B</b>	320	336	9.7	0.038	7.2	0.025	0.098	0.026	0.25	0.96
Average					11.0	0.036	0.107	0.035	0.33	1.01
Standard Deviation					3.5	0.009	0.009	0.008	0.09	0.05
Coefficient of Variation					0.32	0.26	0.08	0.23	0.27	0.05

\* For Details Refer to Figure 6-22

\* d<sub>bg</sub>: Depth of Bolts Group, e: Eccentricity)

‡ Values at Corresponding Horizontal Tensile Strength of Double Angles

† Refers to Section 3.2.4 of GSA Guidelines (Similar to UFC 4-023-03, and Clause 3.1 of CSA S850)

Table 6-18: Comparison of Beam Rotations and Ultimate Strength of Shear Tabs

Specimen ID	Beam Rotation (rad.) *			Ultimate Strength of Connection (kN)			
	Detailed FEA	Simplified FEA	Proposed Method	Detailed FEA	Physical Test	Simplified FEA	Proposed Method ‡
<b>ST39B (Restrained)</b>	0.039	0.036	0.041	512	513	489	451
<b>ST39B (Unrestrained)</b>	0.038	0.036	0.041	513	513	489	451
<b>ST59B (Restrained)</b>	0.034	0.039	0.035	832	836	831	752
<b>ST59B (Unrestrained)</b>	0.034	0.039	0.035	831	836	831	752

\* Corresponding to the Ultimate Strength of Shear Tabs (Initial Failure)

‡ Calculated Based on the Parallel Shear Failure Planes

Table 6-19: Uniform Dead and Specified Live Loads for Various Occupancies

Type of Load	Uniform Load (kN/m <sup>2</sup> )	
	Residential	Office
Dead Load (D)	3.60	3.60
Live Load (L)	1.90 ‡ (1.92 *)	2.40 **
Survey Live Load (L <sub>survey</sub> ) †	0.29 †	0.52 †

‡ From Table 4.1.5.3 of Part 4/Division B of NBCC (NRC 2010)

\* From Table 4-1 of ASCE/SEI 7-10

† From Table C4-2 of ASCE/SEI 7-10

Table 6-20: Gravity Loads and Load Combination for Extraordinary Events

Load Combination	Value (kN/m <sup>2</sup> )	
<b>CSA-1</b> *	1.0D + 0.5L <sub>off.</sub>	4.80
<b>CSA-2</b>	1.0D + 0.5L <sub>res.</sub>	4.55
<b>ASCE-1</b> †	1.2D + 0.5L <sub>off.</sub>	5.52
<b>ASCE-2</b>	1.2D + 0.5L <sub>res.</sub>	5.28
<b>ASCE-3</b>	1.05D + L <sub>survey-off.</sub>	4.30
<b>ASCE-4</b>	1.05D + L <sub>survey-res.</sub>	4.07

\* From Section 10.3.3 of CSA S850-12

† From Section 2.5 of ASCE/SEI 7-10

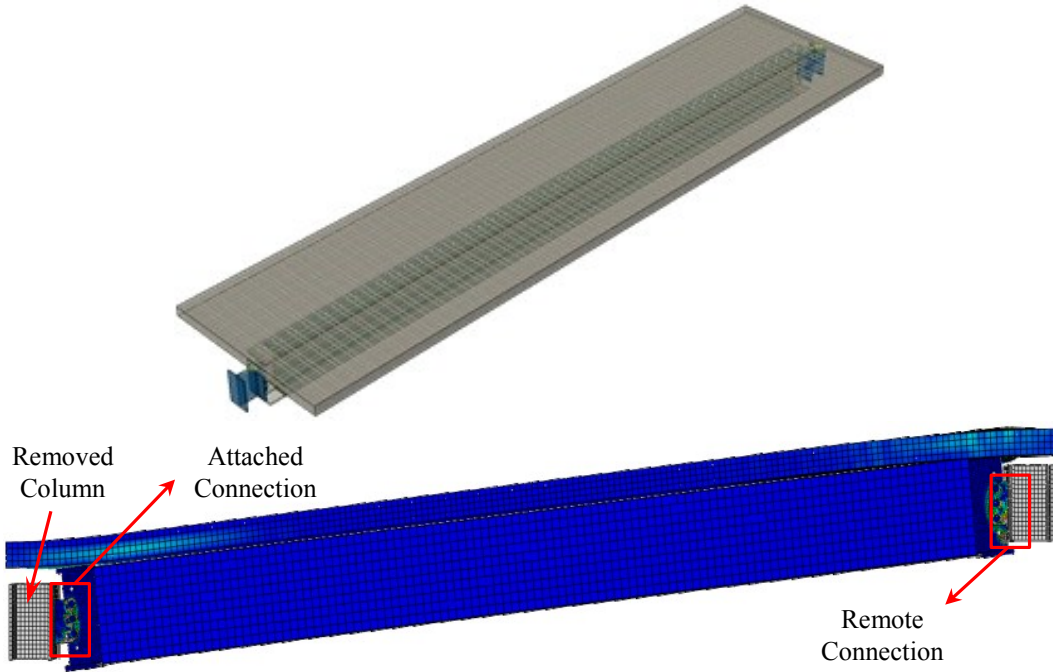


Figure 6-1: Simplified Finite Element Model and Definition of Attached and Remote Connections

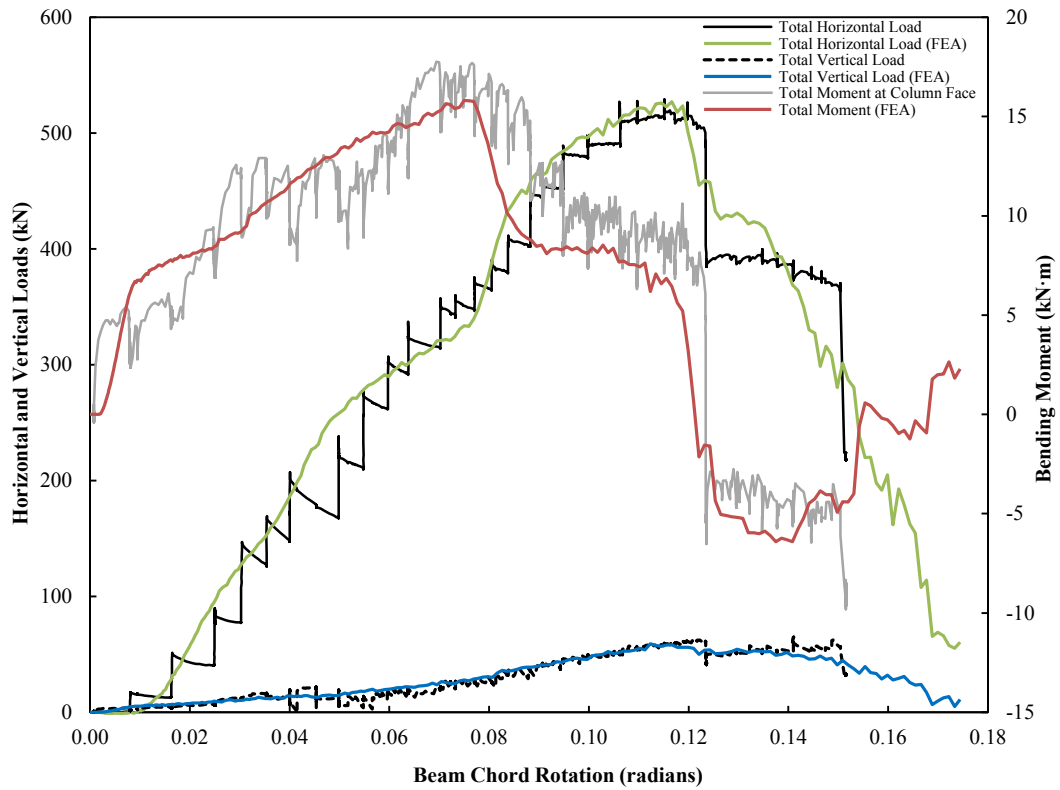


Figure 6-2: Comparison of the Finite Element and Test Results for Specimen ST3A-1 of Oosterhof and Driver (2015)

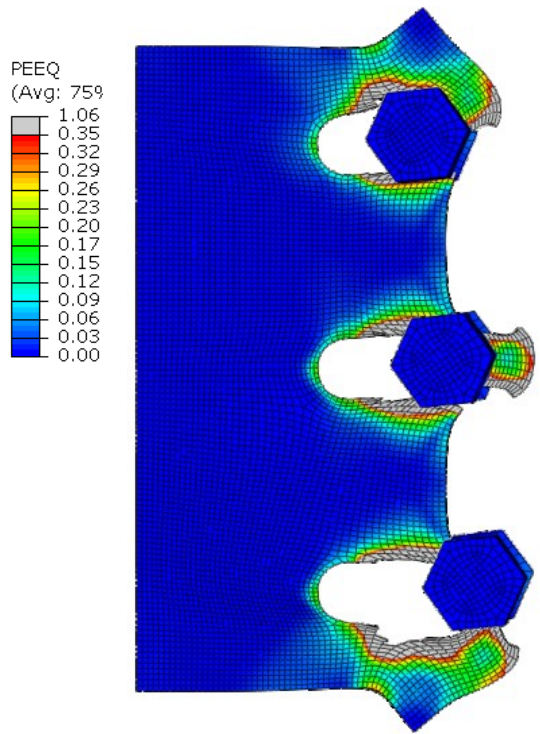


Figure 6-3: Comparison of the Failure Mode with Specimen ST3A-1 of Oosterhof and Driver (2016; 2015)

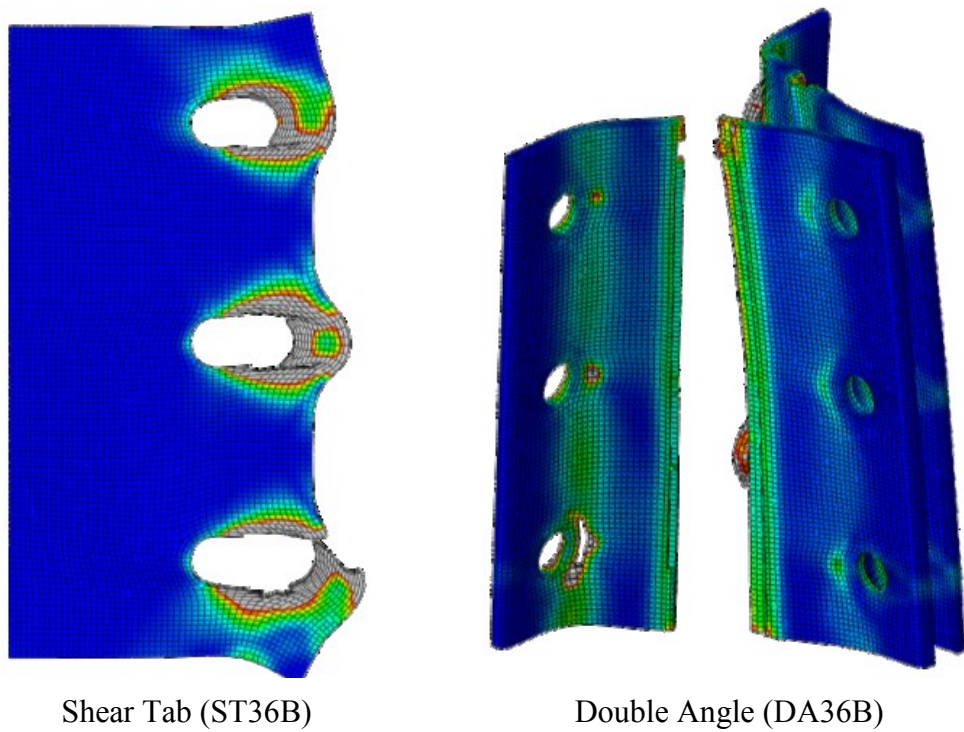


Figure 6-4: Failure Mode of Selected Finite Element Models for Comparison with the Experiments' Results of Oosterhof and Driver (2016)

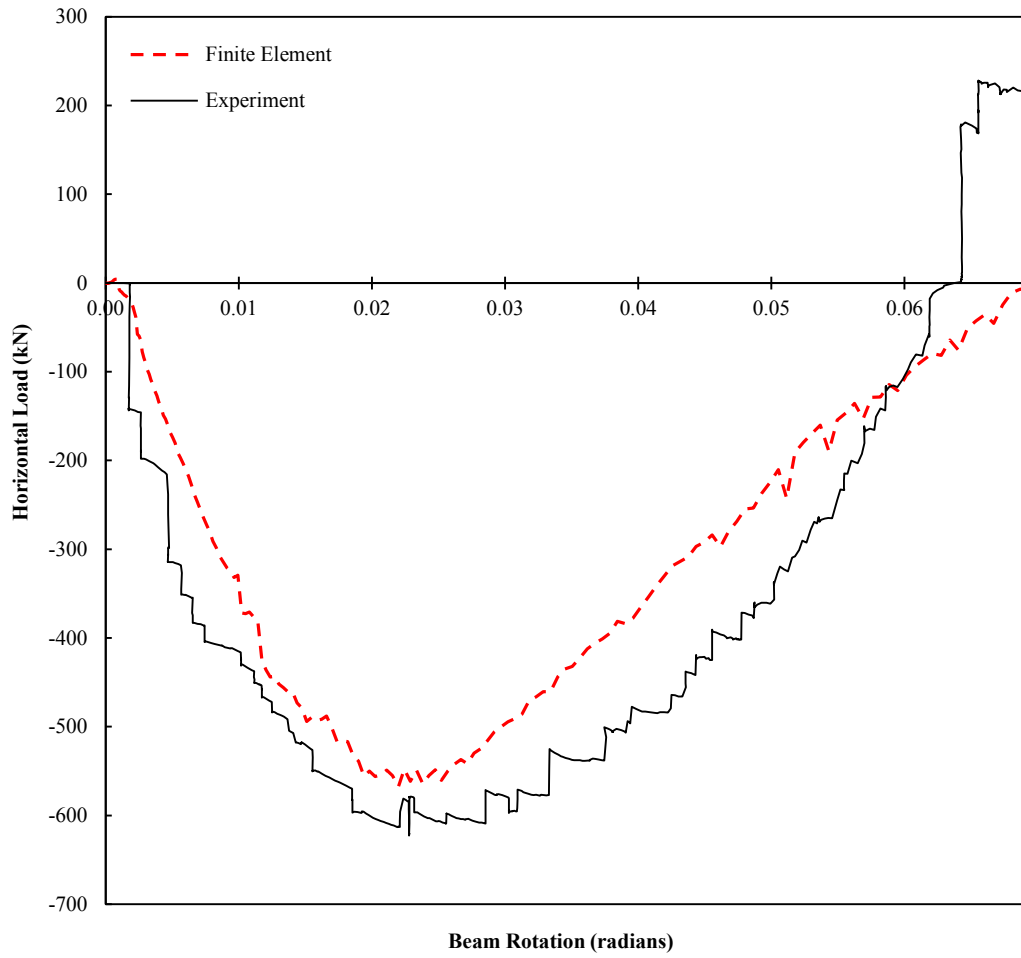


Figure 6-5: Comparison of Finite Element and Test Results for Specimen ST59B



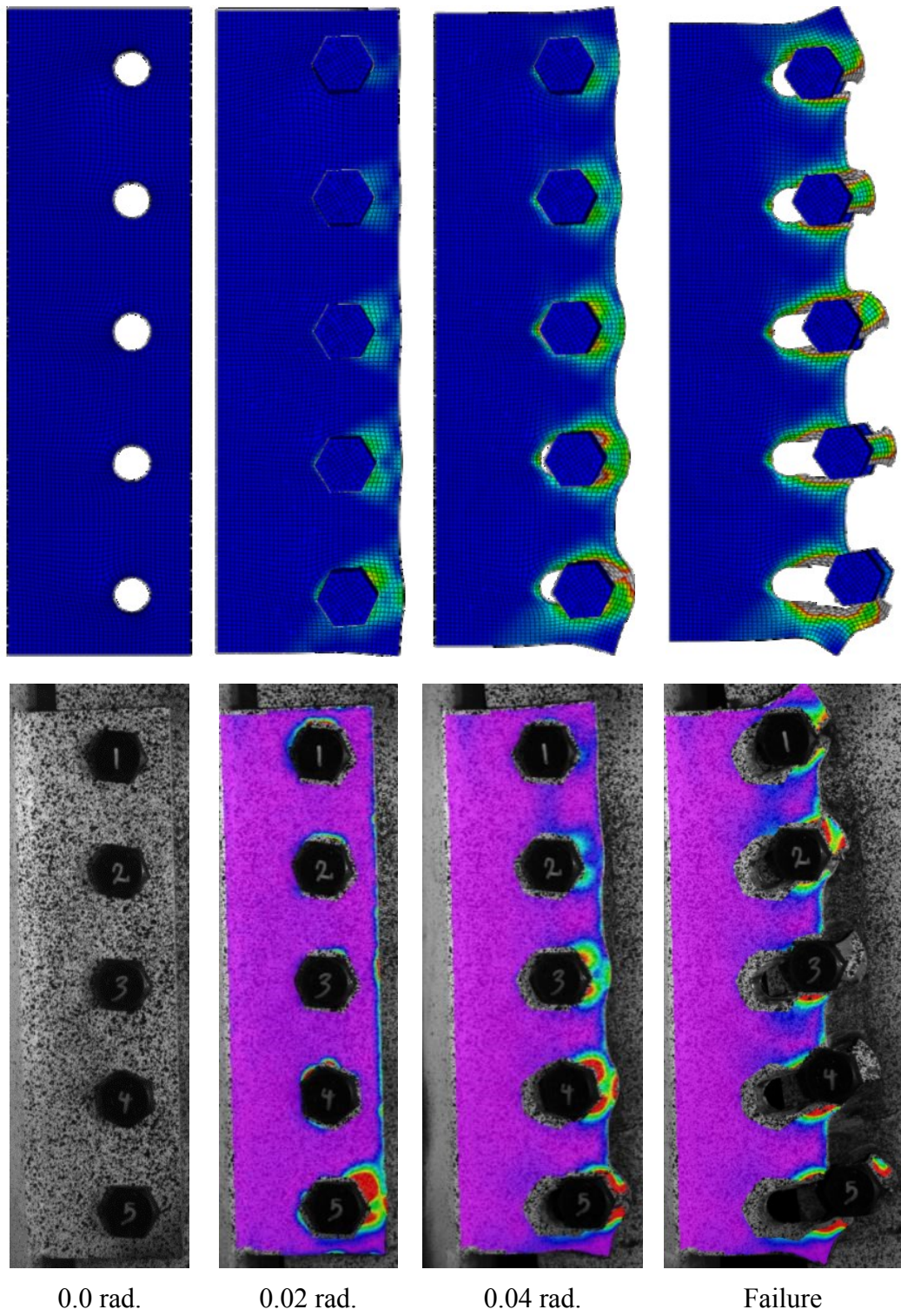


Figure 6-6: Comparison of Finite Element and Experimental Test on Deformation of Shear Tab Connection (Specimen ST59B) at Several Characteristic Beam Rotations: 0.0 radians; Maximum Arching Action (0.02 radians); Maximum Tensile Force in Shear Tab (0.04 radians); Failure

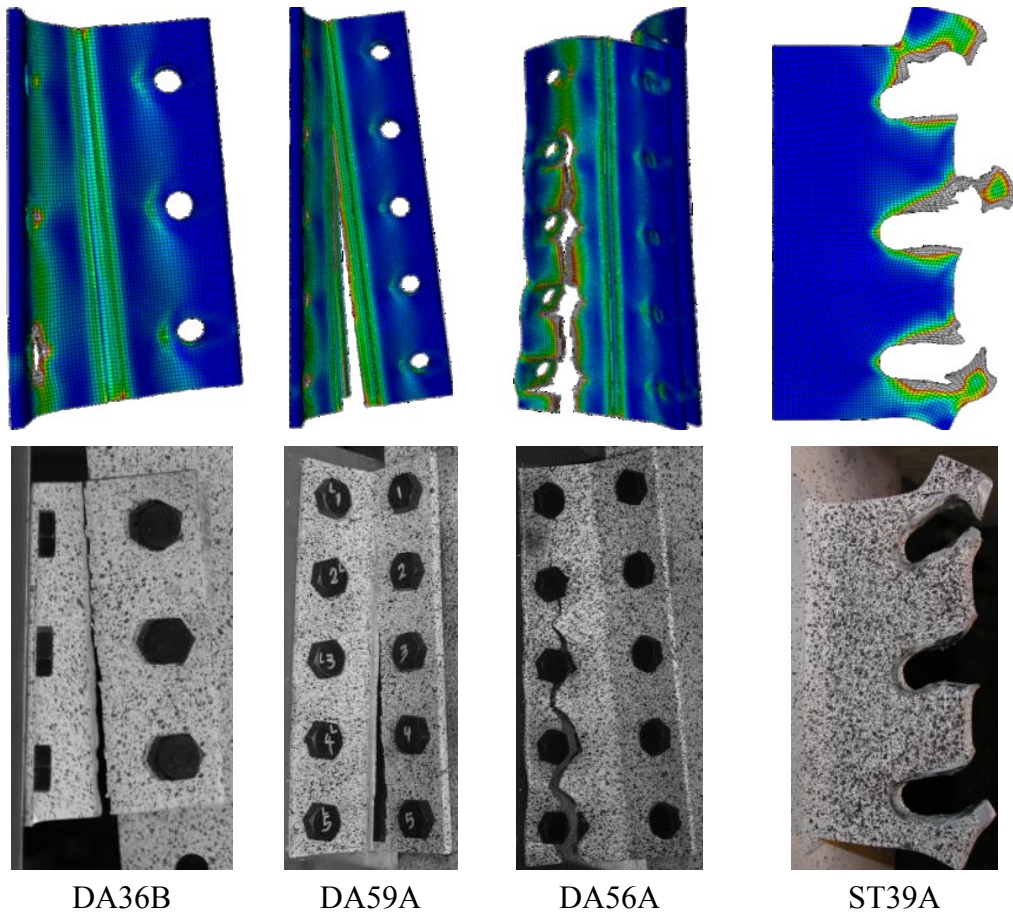


Figure 6-7: Comparison of the Failure Modes of Several Tested Connections with the Corresponding Finite Element Models

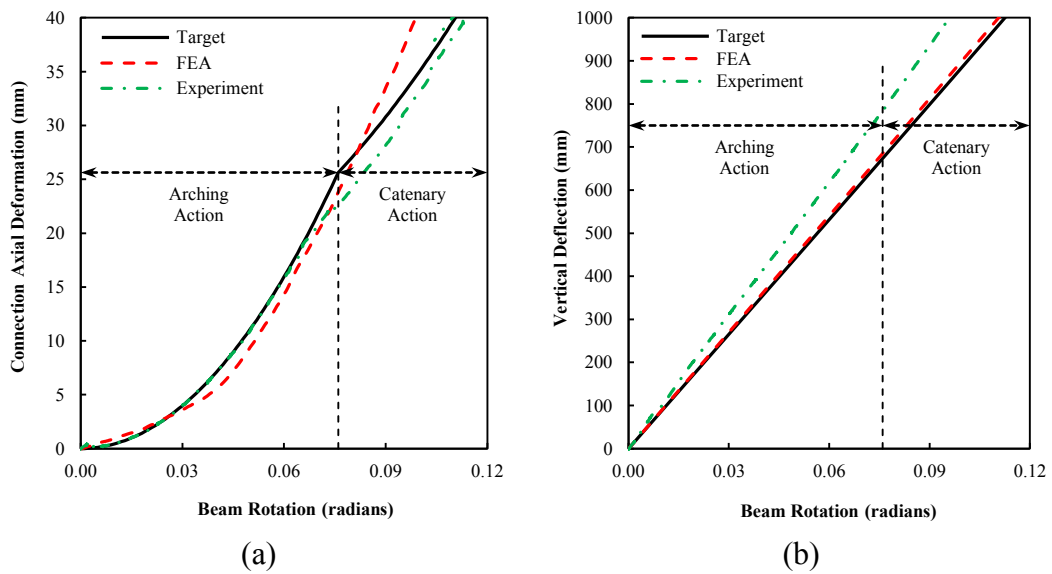


Figure 6-8: (a) Axial Deformation and (b) Vertical Deflection versus Beam Rotation of Attached Connection in Composite Frame (Specimen ST59B)

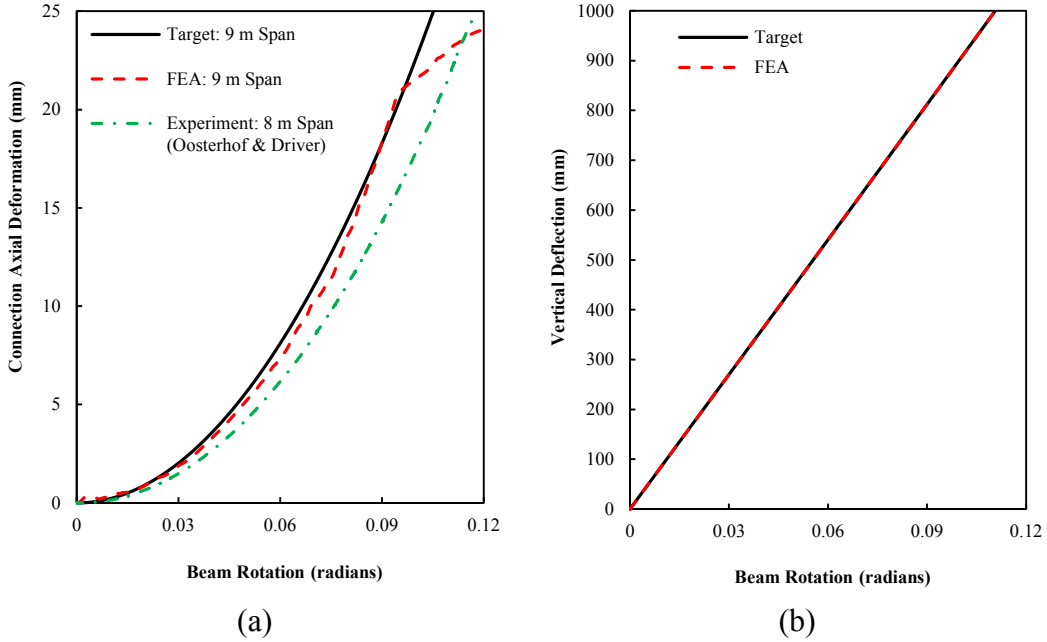


Figure 6-9: (a) Axial Deformation; and (b) Vertical Deflection versus Beam Rotation of Attached Connection in Bare Frame (Specimen ST59B)

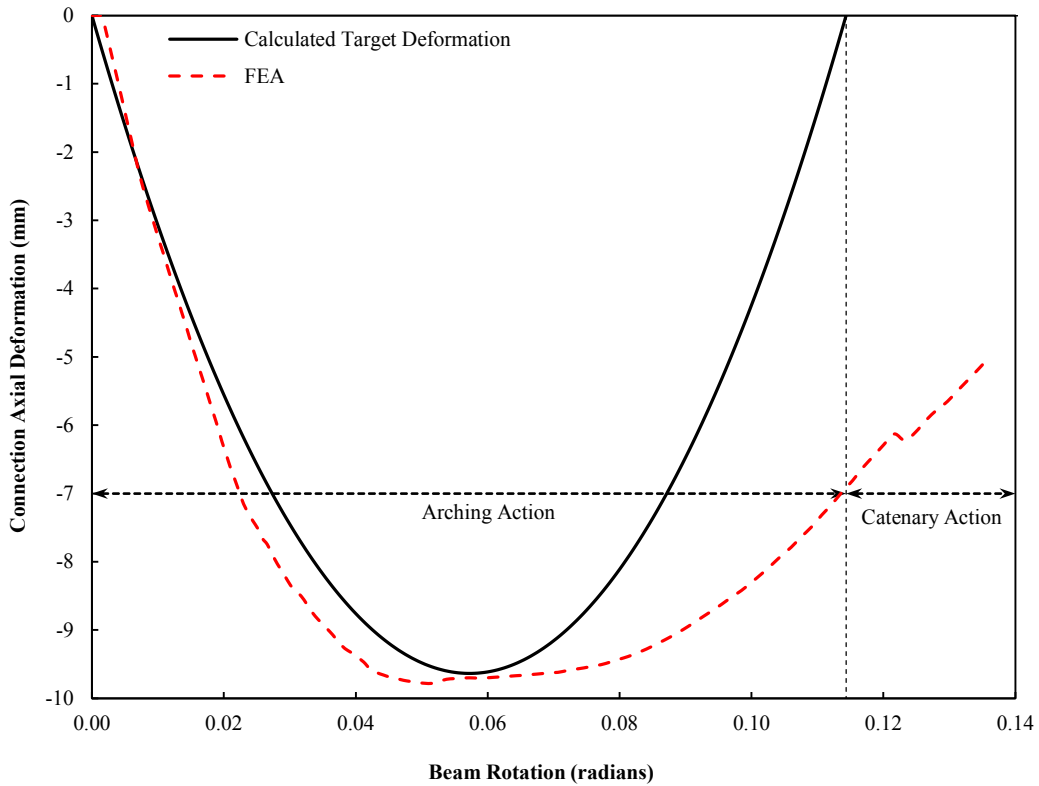
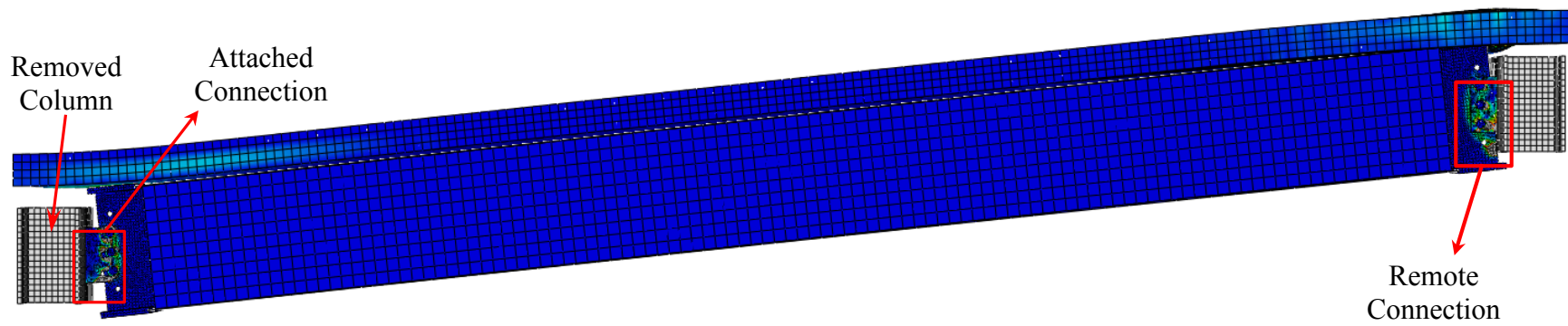
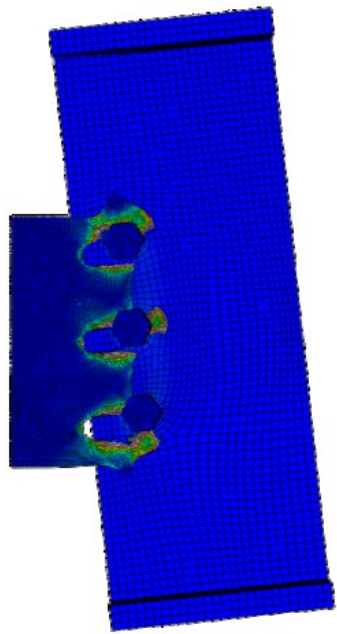


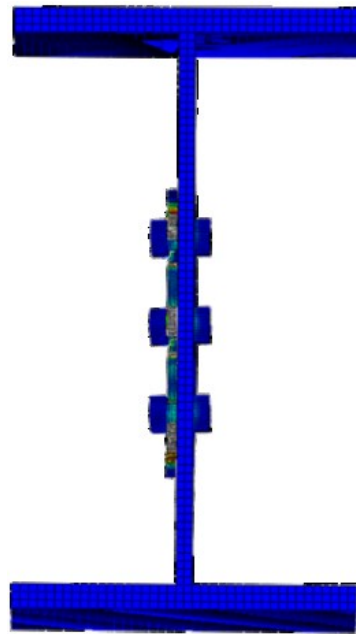
Figure 6-10: Calculated Target and FEA Axial Deformation versus Beam Rotation of Remote Connection in Composite Frame (Specimen DA56A)



Side View



Attached Connection



Remote Connection

Figure 6-11: Specimen ST39A in Composite Frame at Failure

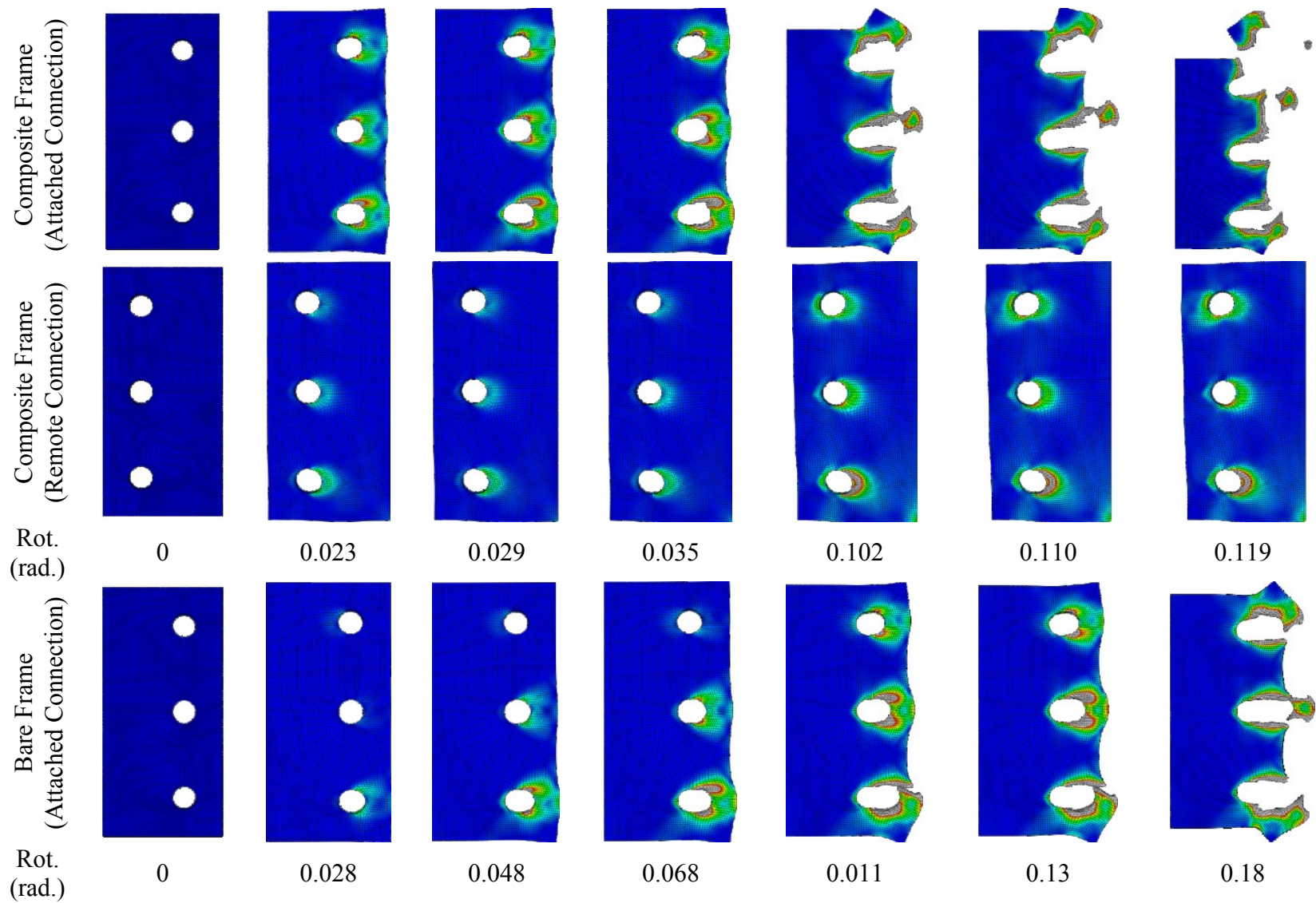


Figure 6-12: Deformation and Failure Evolution of Specimen ST39A in both Composite and Bare Frames: Connections at Several Characteristic Beam Rotations

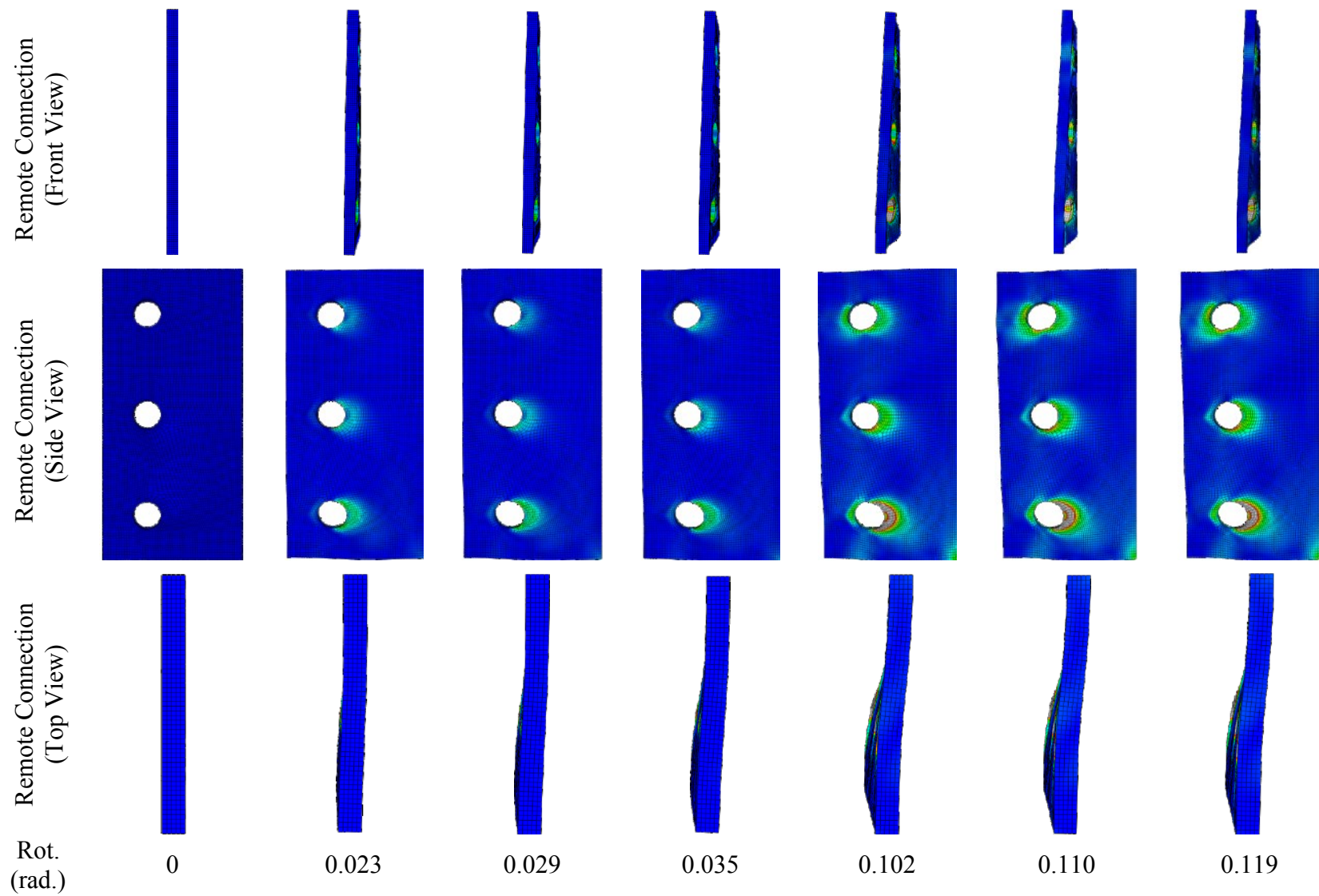


Figure 6-13: Deformation Evolution of Remote Connection of Specimen ST39A in Composite Frame: Connection at Several Characteristic Beam Rotations

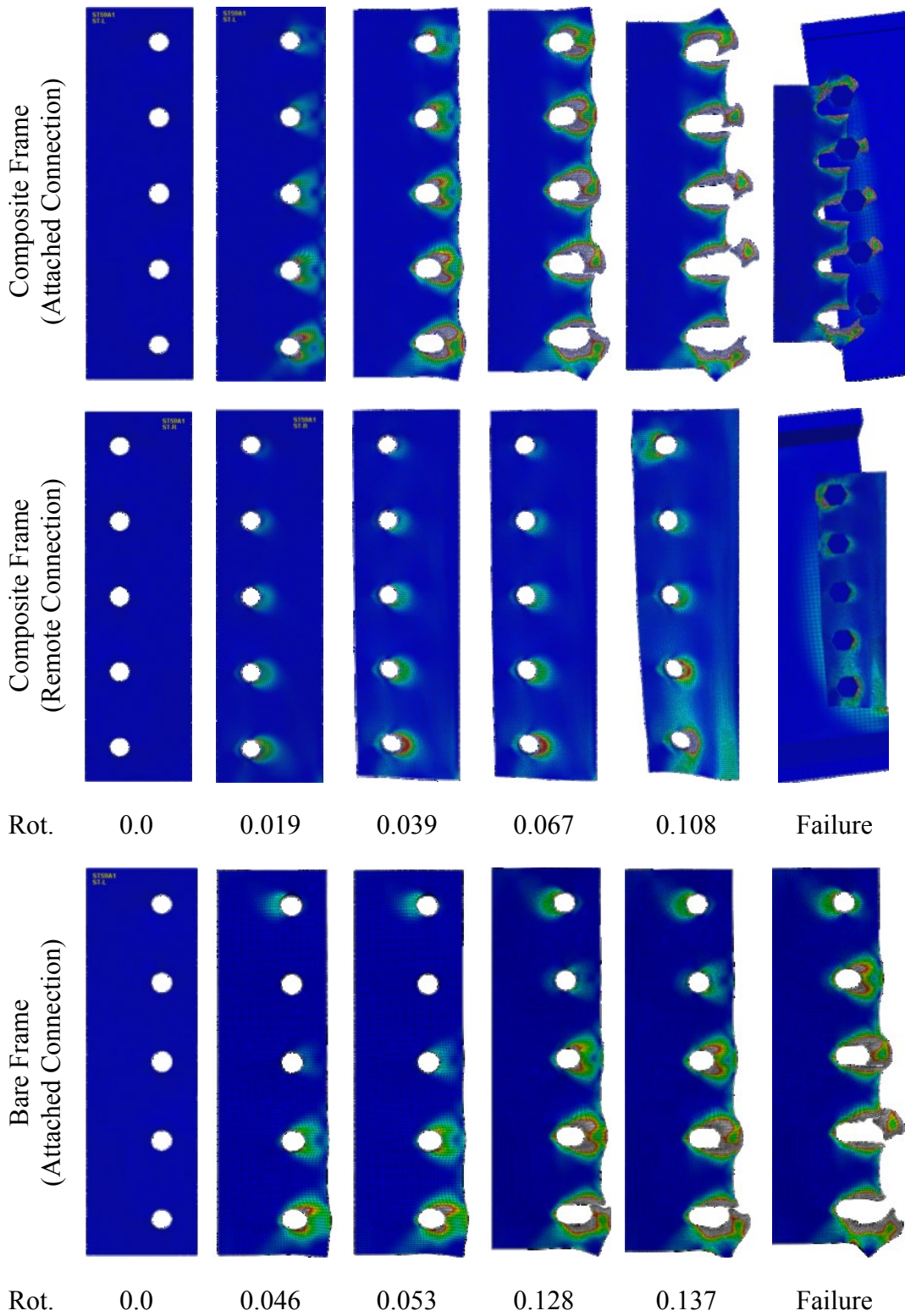


Figure 6-14: Deformation and Failure Evolution of Specimen ST59B at Several Characteristic Beam Rotations

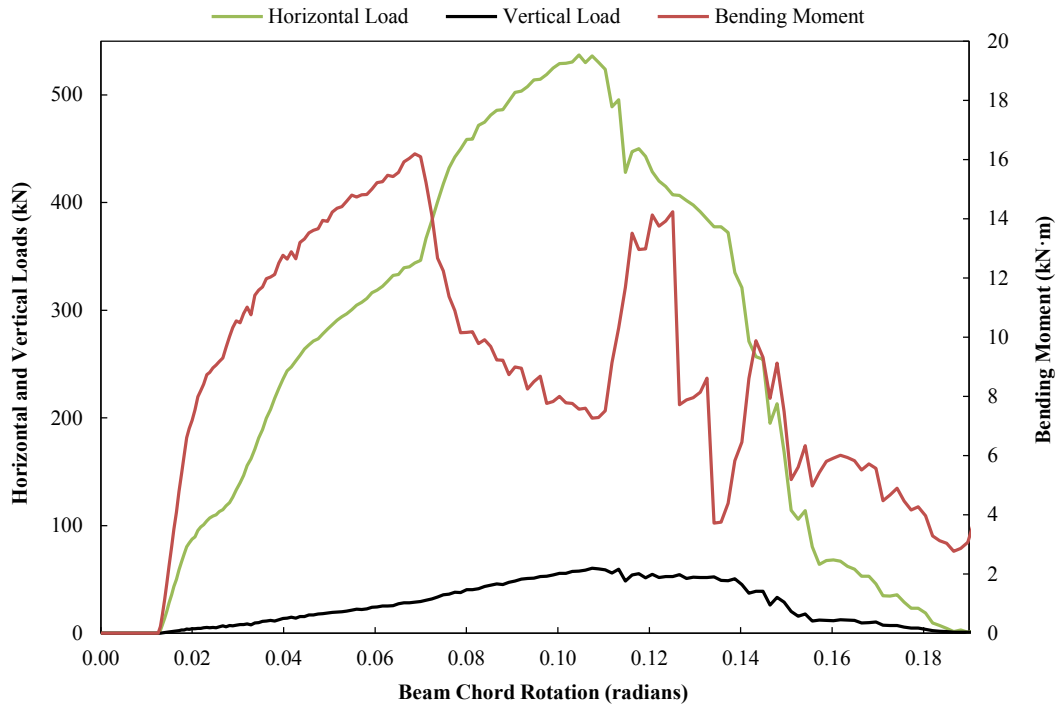


Figure 6-15: Load versus Beam Rotation: Attached Connection of ST39A in Bare Frame

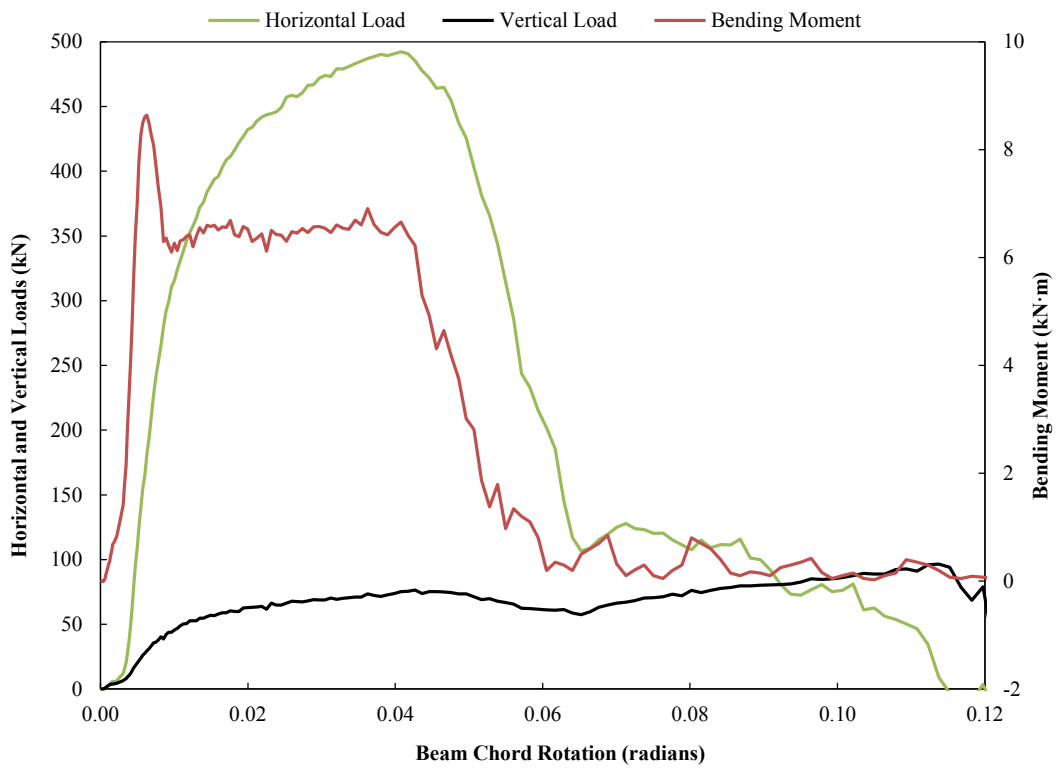


Figure 6-16: Load versus Beam Rotation: Attached Connection of ST39A in Composite Frame



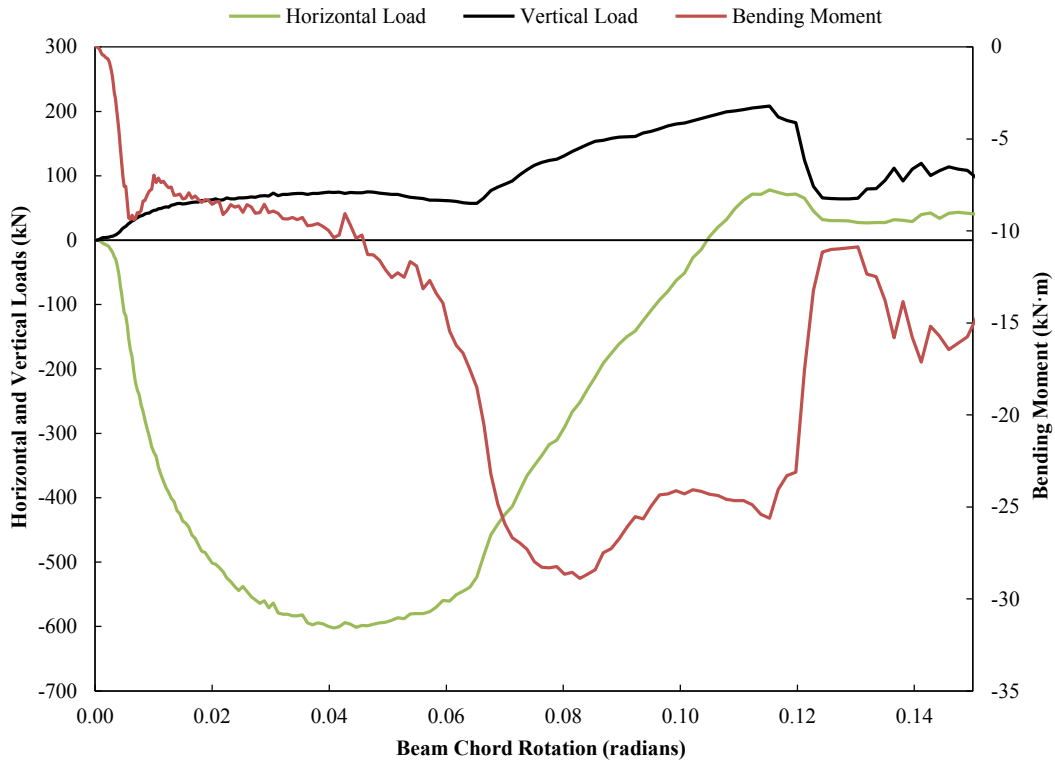


Figure 6-17: Load versus Beam Rotation of Remote Connection of Specimen ST39A in Composite Frame

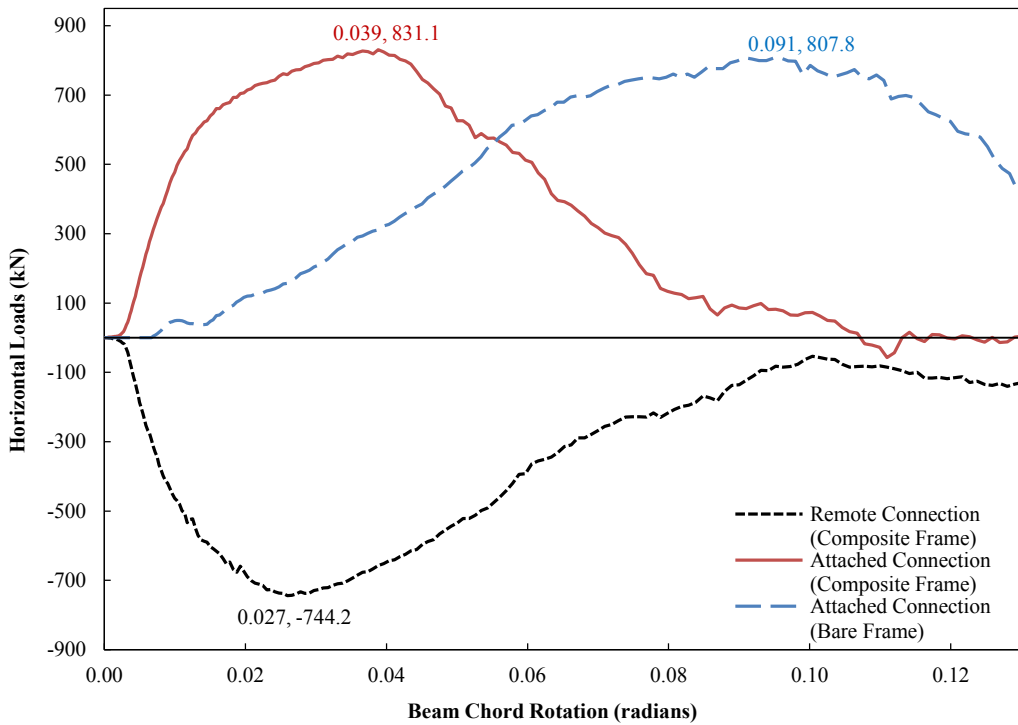


Figure 6-18: Effect of Concrete Slab (Composite Section) on Ductility and Horizontal Load Development in Shear Tab Connections of Specimen ST59B

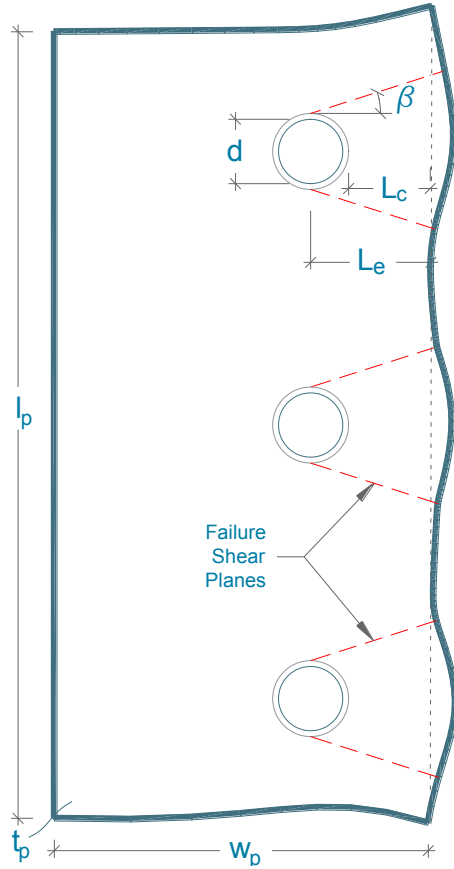
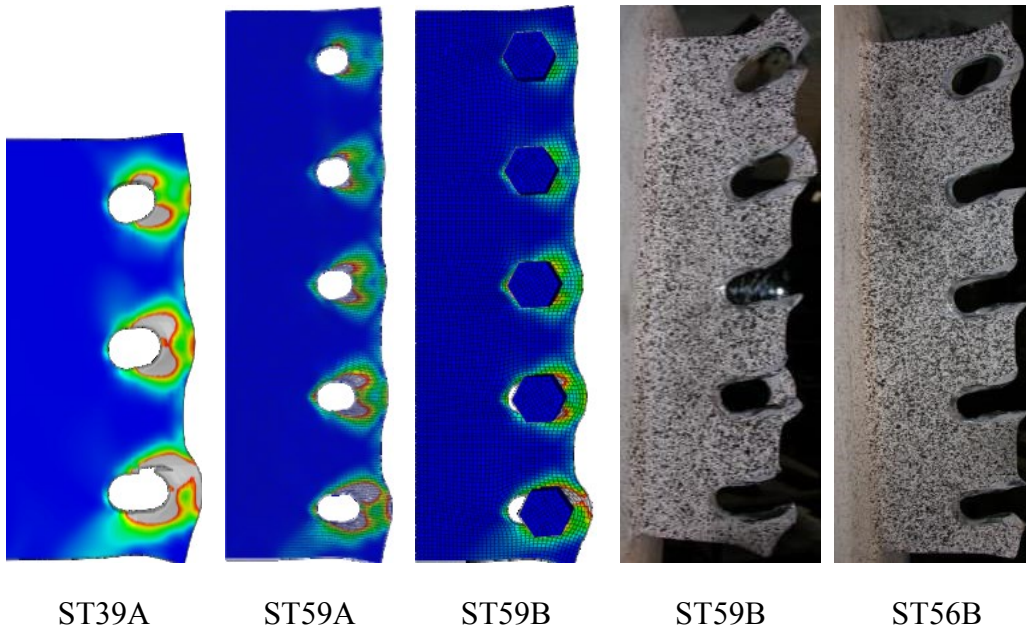


Figure 6-19: Deformation of Shear Tab (Bolt Tear-out Failure)



ST39A      ST59A      ST59B      ST59B      ST56B

Figure 6-20: Bolt Tear-out Failure in Various Experimental Tests and Finite Element Models

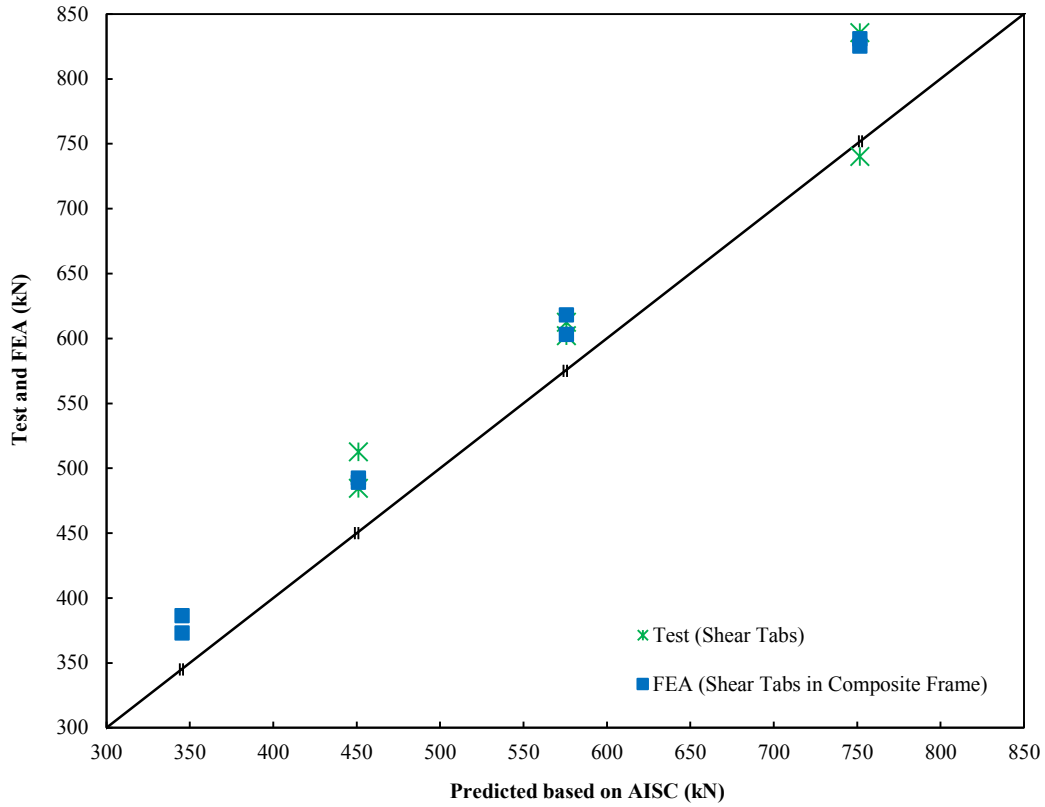


Figure 6-21: Bolt Tear-out Capacity: Comparison of the Experimental Tests and FEA Results with the AISC Capacity Prediction, Equation (6-1)

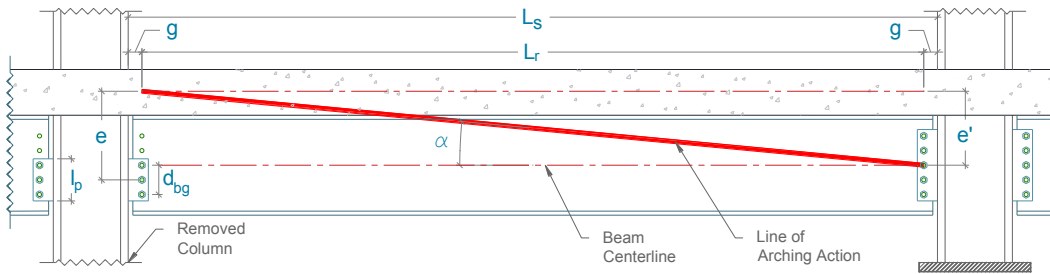


Figure 6-22: Geometry of Connections, Span, and the Arching Action Variables

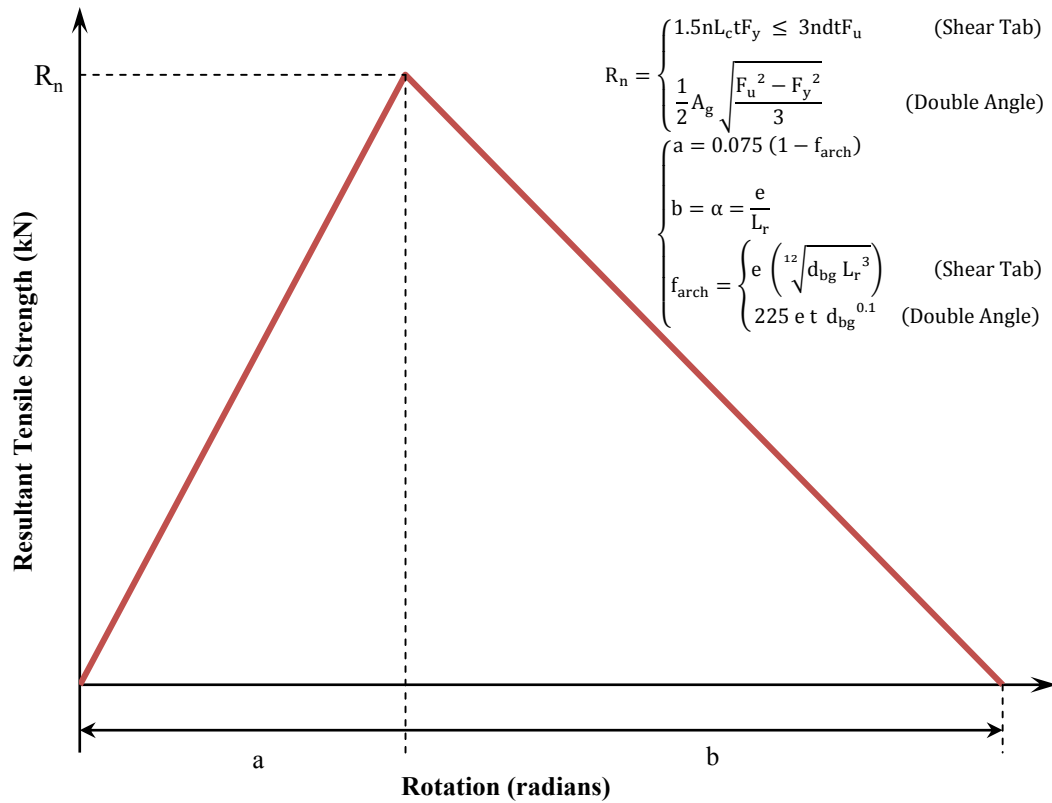


Figure 6-23: Generalized Bilinear Force–Deformation Relationship

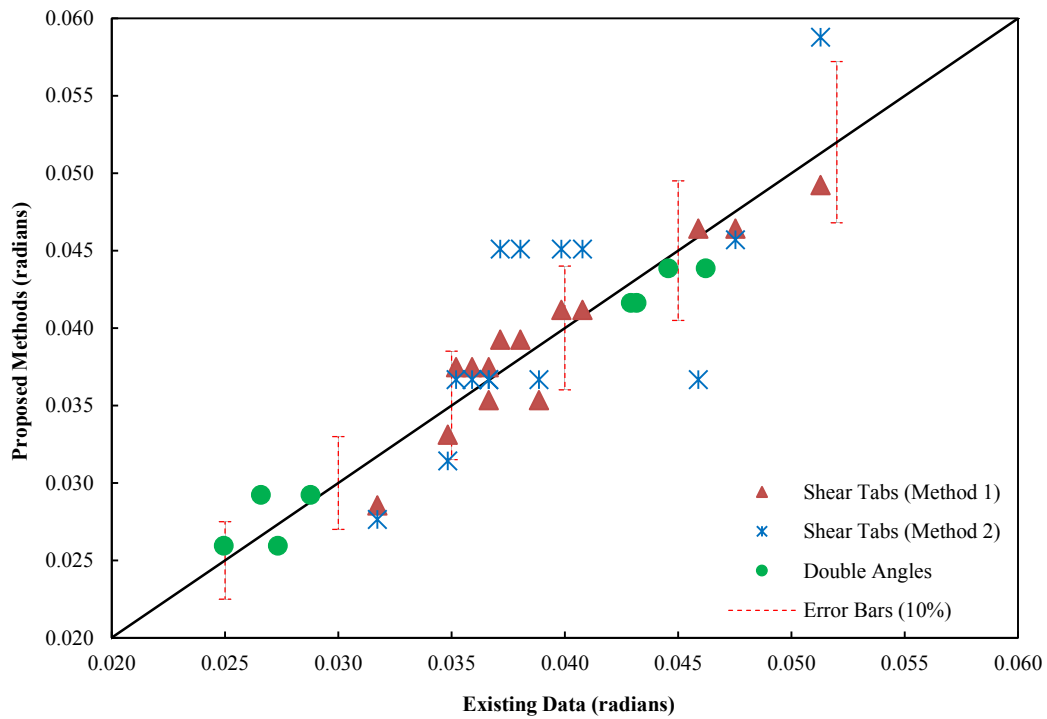
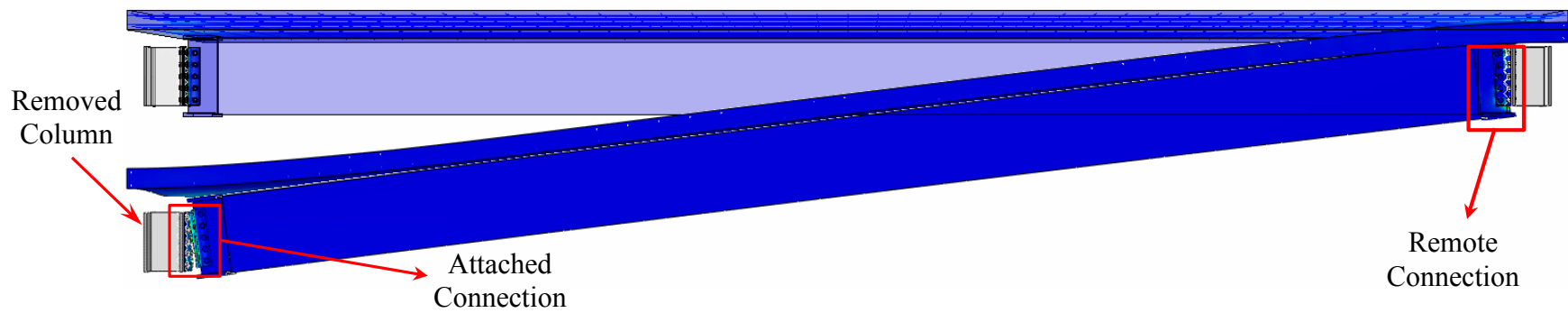
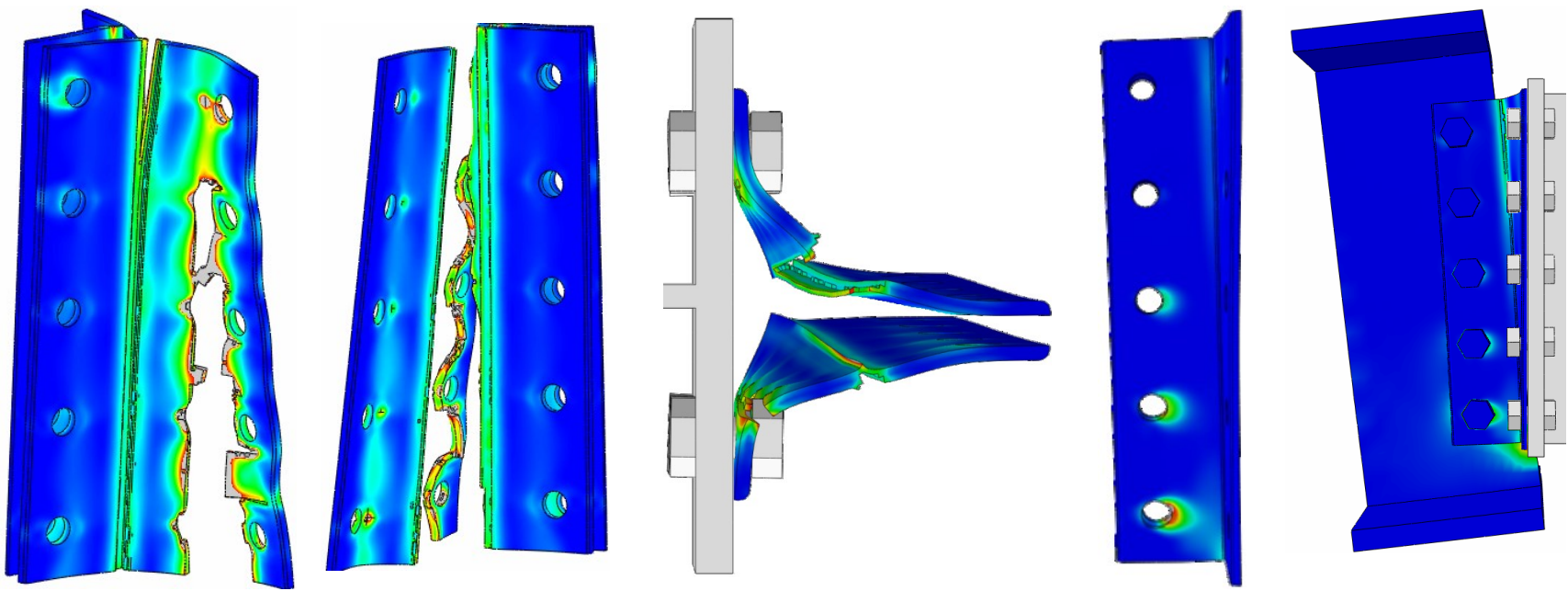


Figure 6-24: Comparison of the Rotational Capacities between the Existing Data and the Proposed Methods



Side View



Attached Connection

Remote Connection

Figure 6-25: Specimen DA56B in Composite Frame at Failure

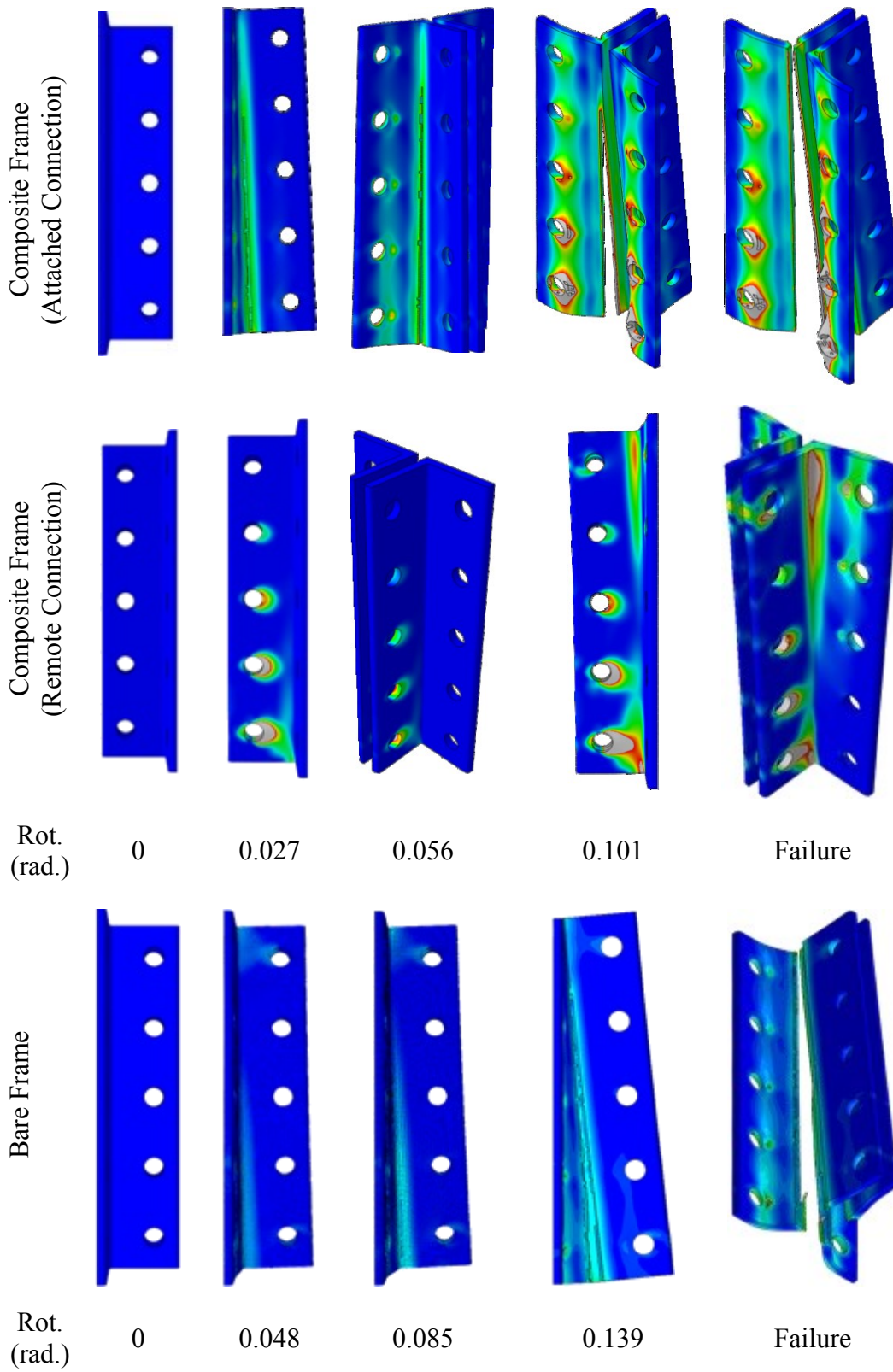


Figure 6-26: Deformation and Failure Evolution of Specimen DA59A in both Composite and Bare Frames: Connections at Several Characteristic Rotations

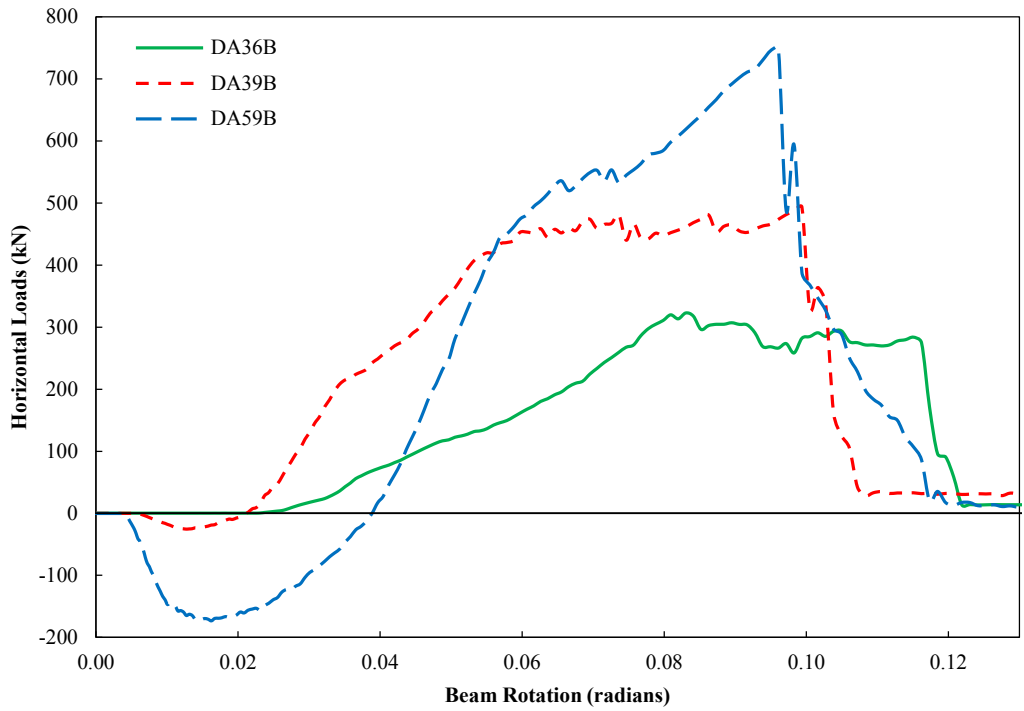


Figure 6-27: Horizontal Loads versus Beam Rotation of Angles in Bare Frame

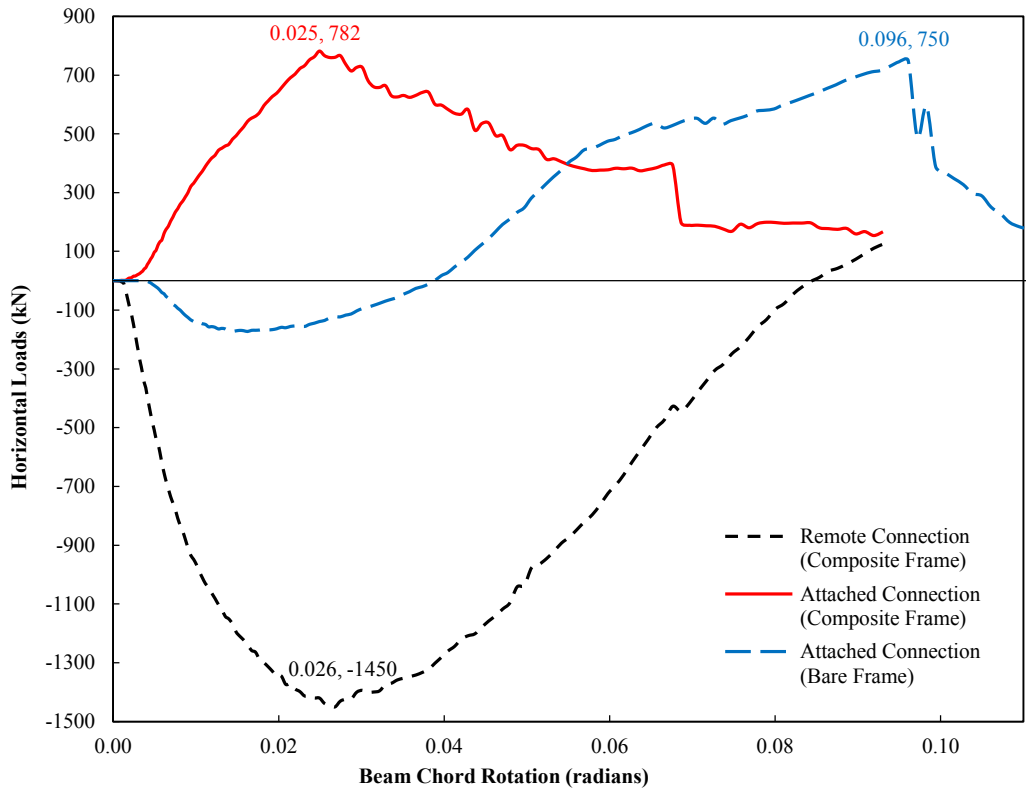
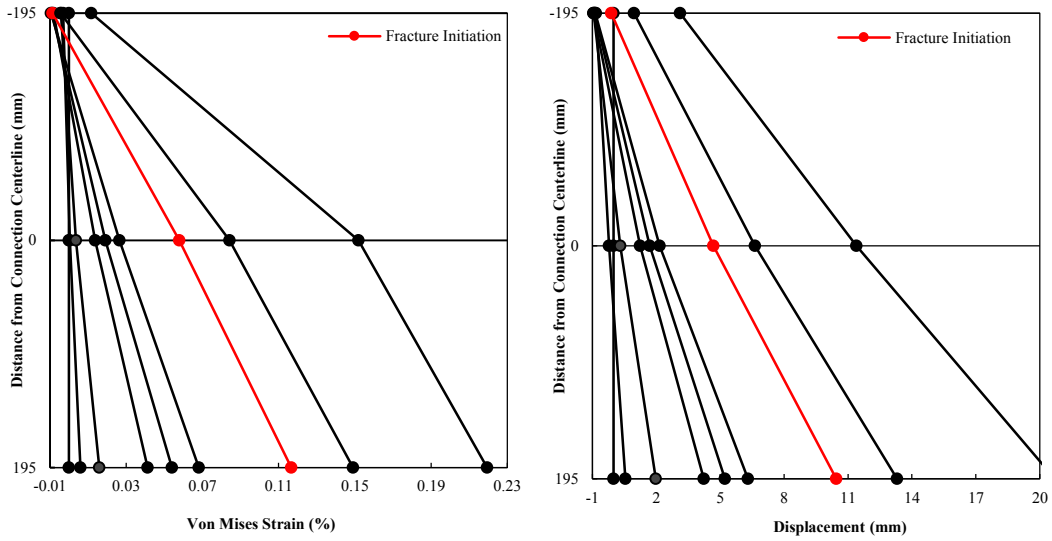
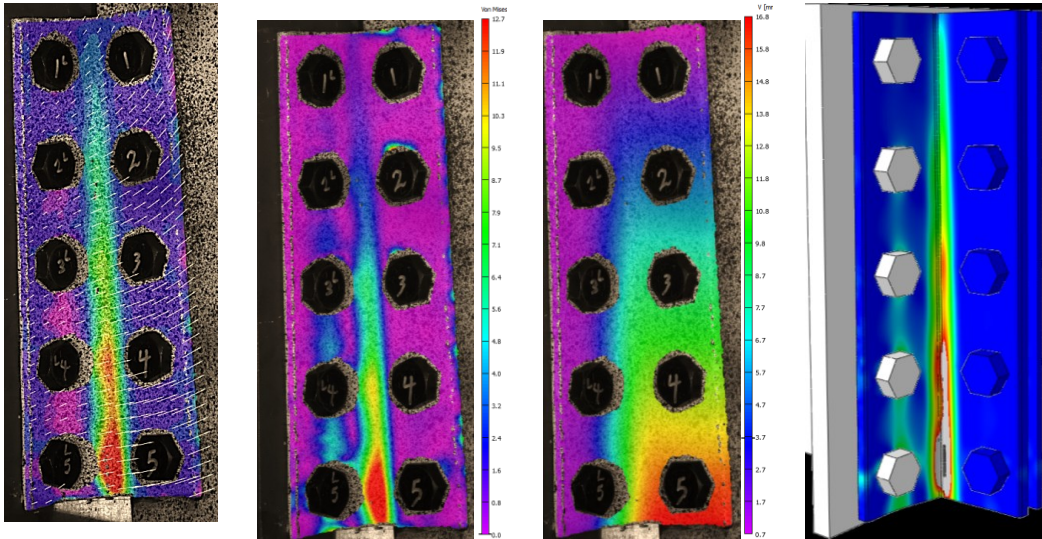


Figure 6-28: Effect of Concrete Slab (Composite Section) on Ductility and Horizontal Load Development in Double Angles of Specimen DA59B



(a)

(b)



(c)

(d)

(e)

Figure 6-29: (a) Evolution of von Mises Strain over the Depth of DA59B Angle; (b) Deformation Evolution of DA59B Angle in the Horizontal Direction of Tensile Force; (c) von Mises Strain Obtained from the Experimental Test Corresponding to the Fracture Initiation; (d) Horizontal Displacement Obtained from the Experimental Test Corresponding to the Fracture Initiation; (e) Equivalent Plastic Strain Obtained from the FEA Corresponding to the Fracture Initiation



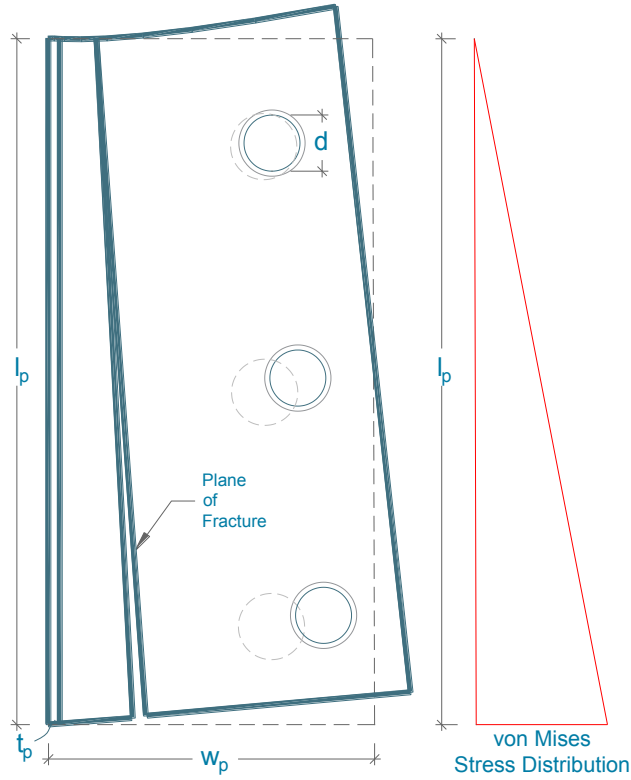


Figure 6-30: Deformation of Angle (Gross-sectional Failure at Heel)

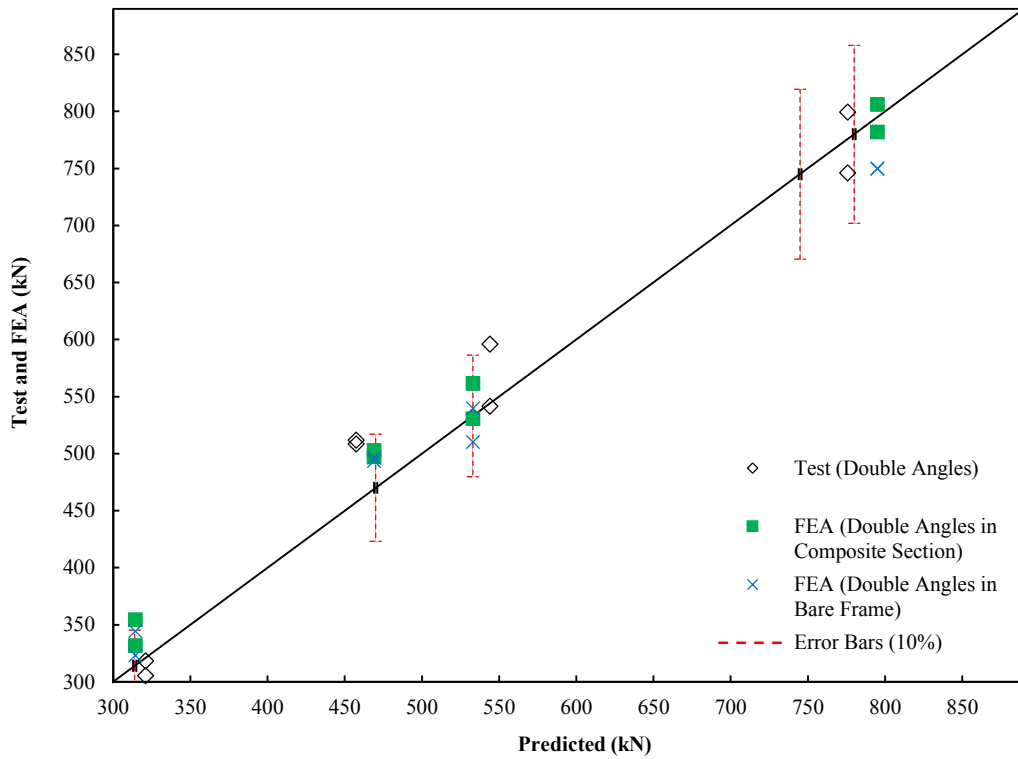


Figure 6-31: Double Angles Capacity: Comparison of the Experimental Tests and FEA Results with the Predicted Values, Equation (6-7)

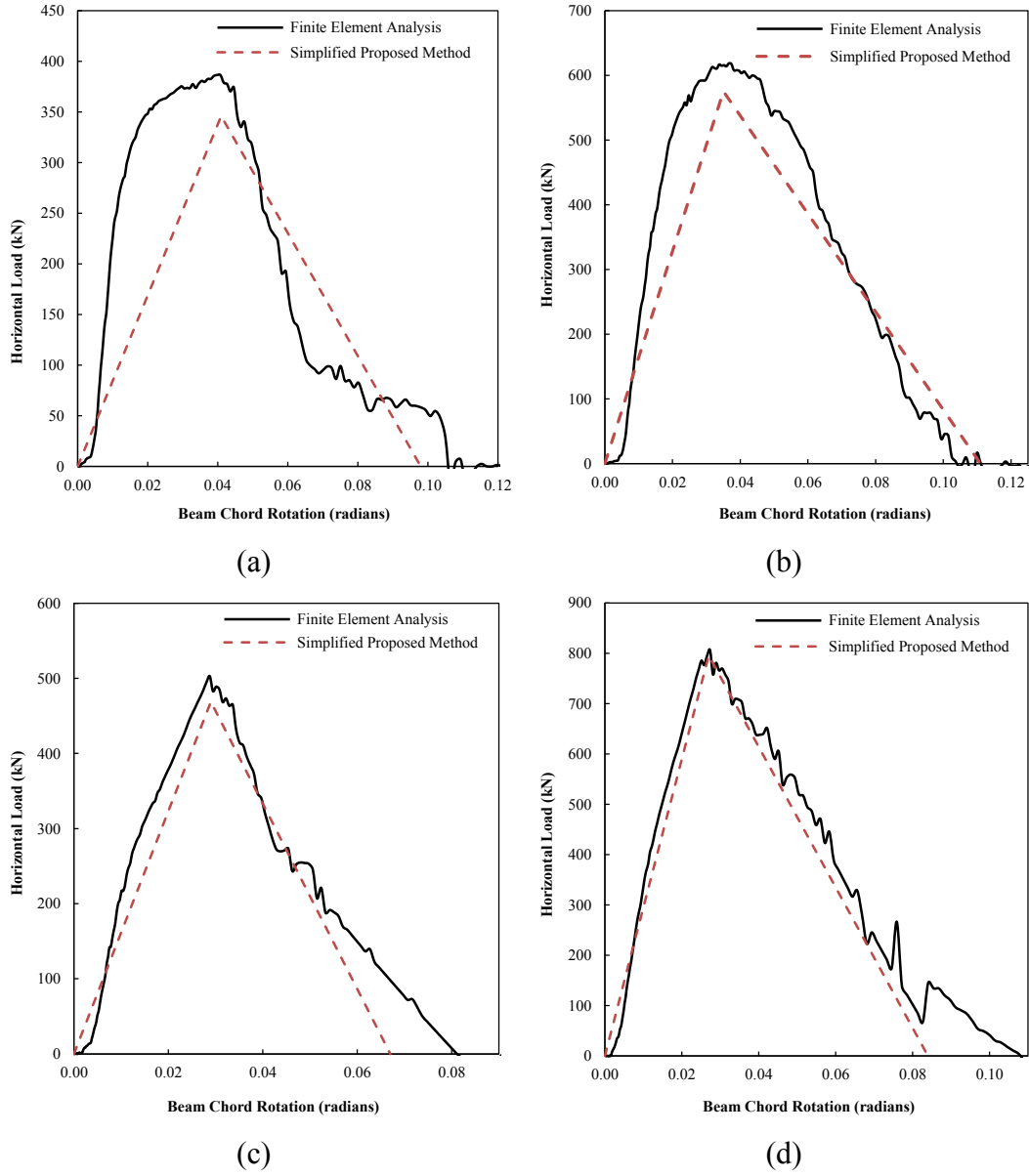
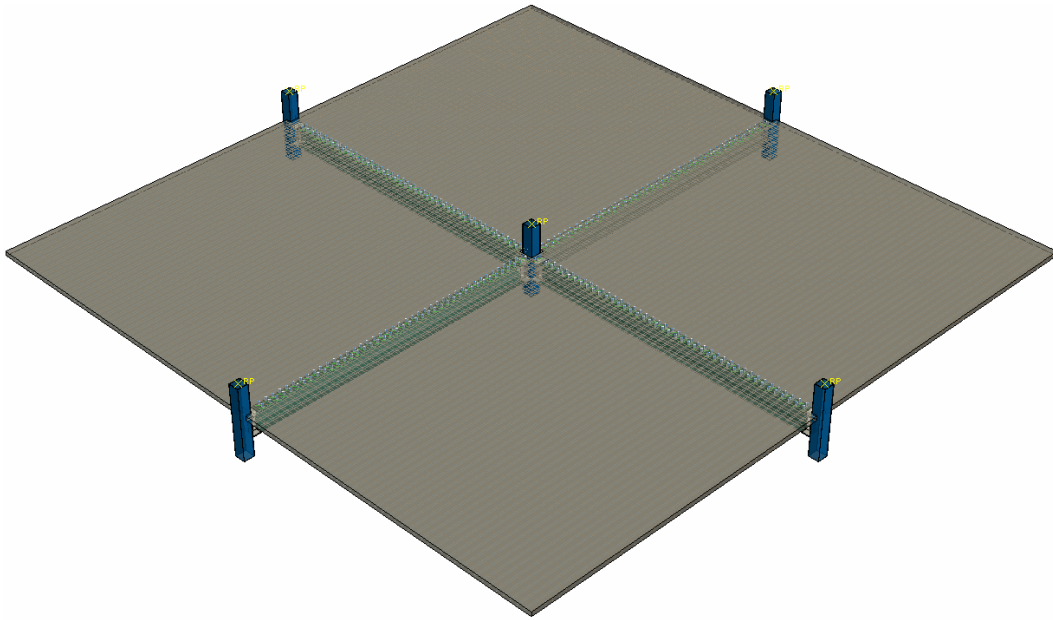
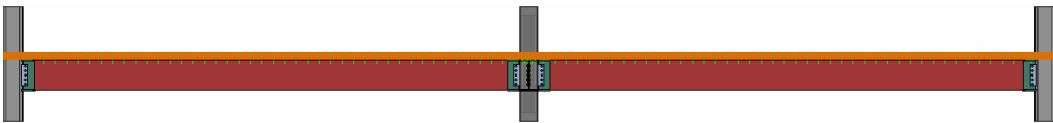


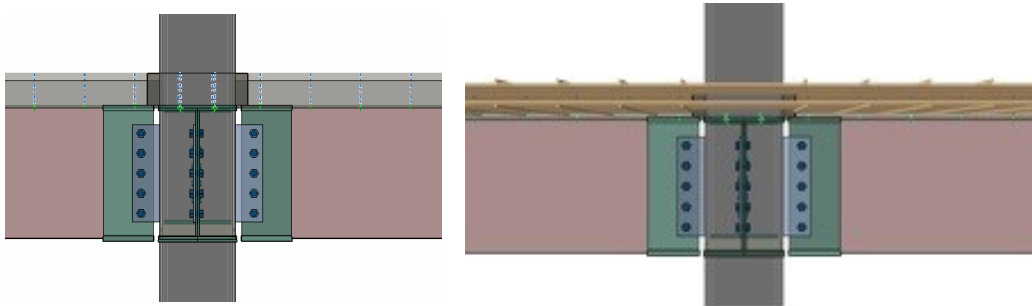
Figure 6-32: Simplified Proposed Method and Comparison with the FEA Results for: (a) ST36A; (b) ST56B; (c) DA39B; (d) DA59A



Isometric View



Side View



Details of Connections, Shear Studs, and Rebar

Figure 6-33: Finite Element Prototype Detailed Model

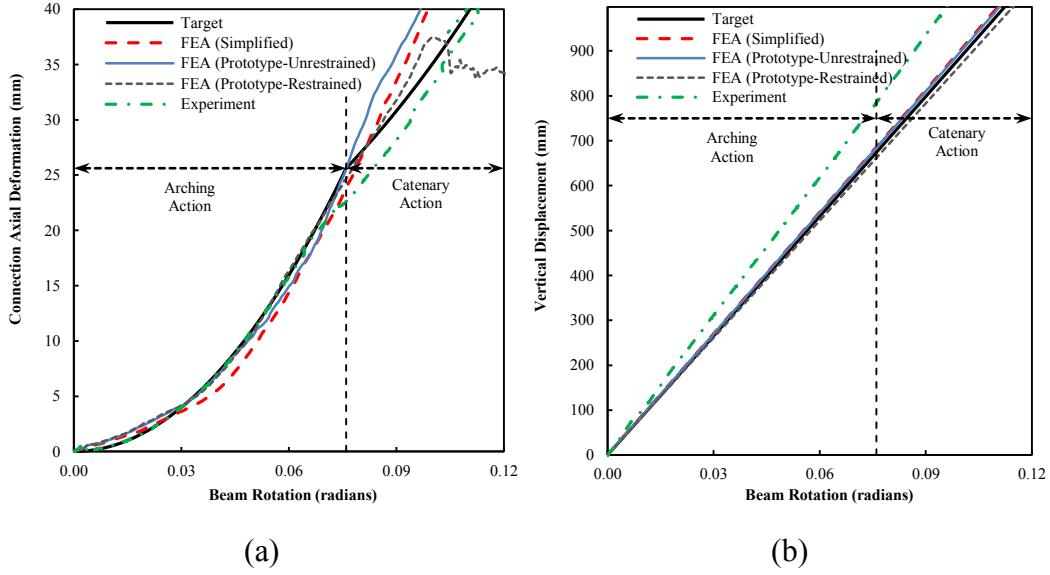


Figure 6-34: (a) Axial Deformation, and (b) Vertical Displacement of Attached Shear Tab (Specimen ST59B) in Composite Frame

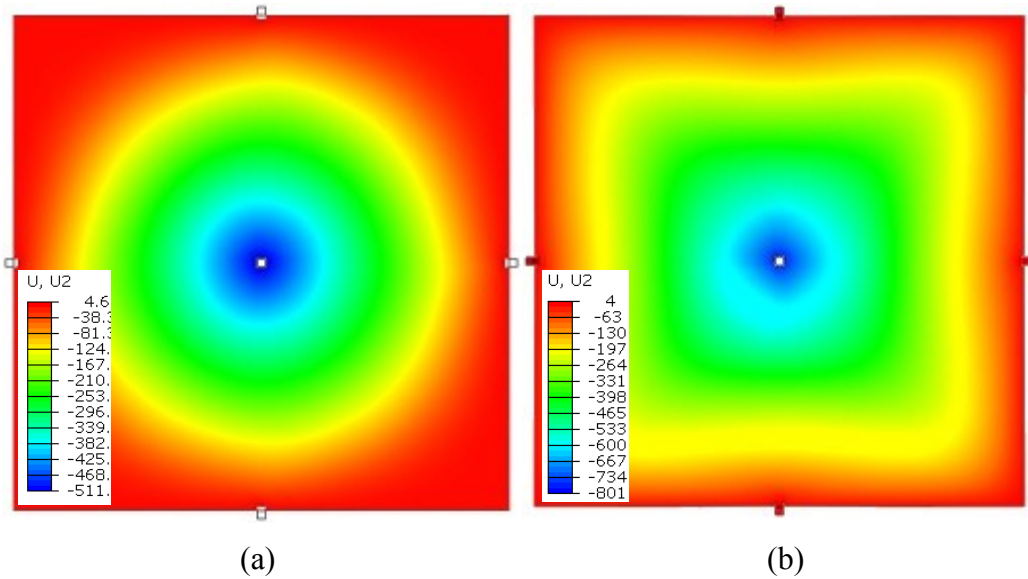
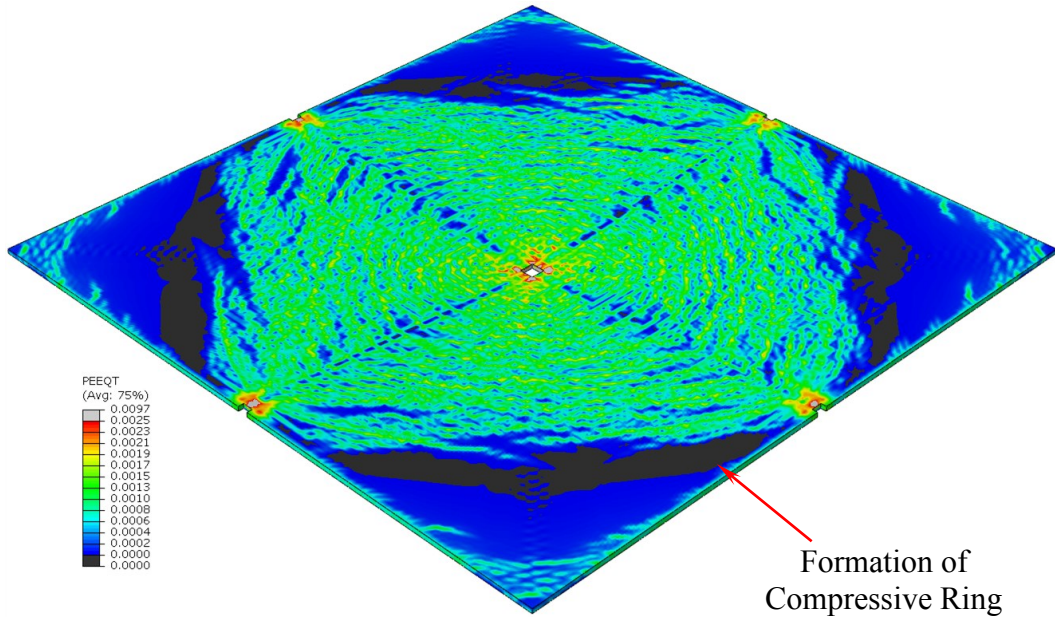
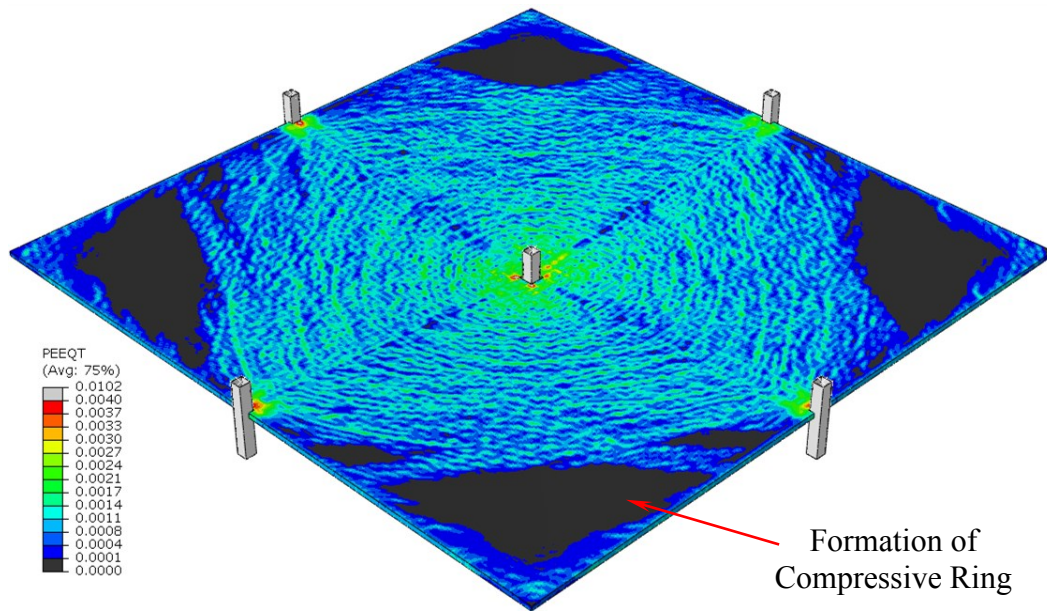


Figure 6-35: Vertical Deflection (mm) Contours of ST59B Models with Slab Edges of (a) Horizontally Restrained, and (b) Horizontally Unrestrained

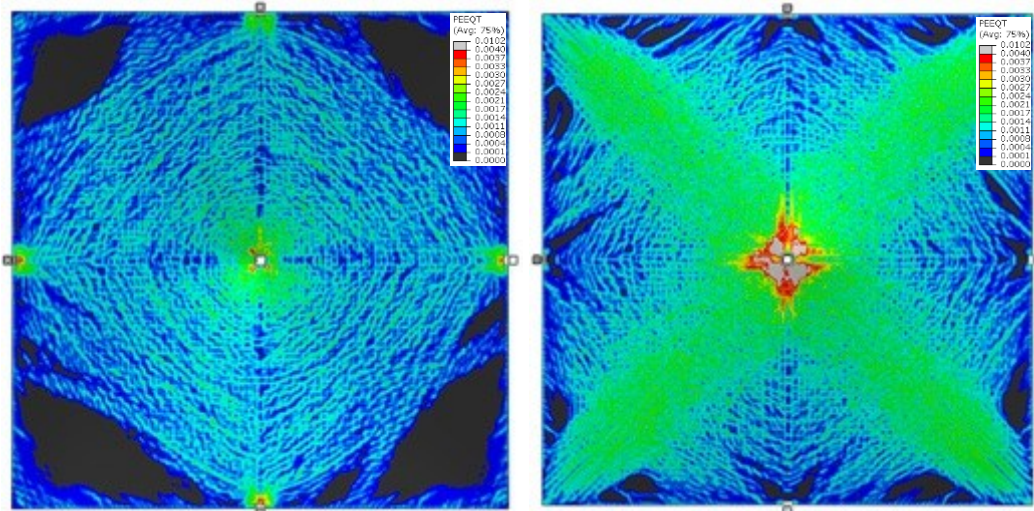


ST39B



ST59B

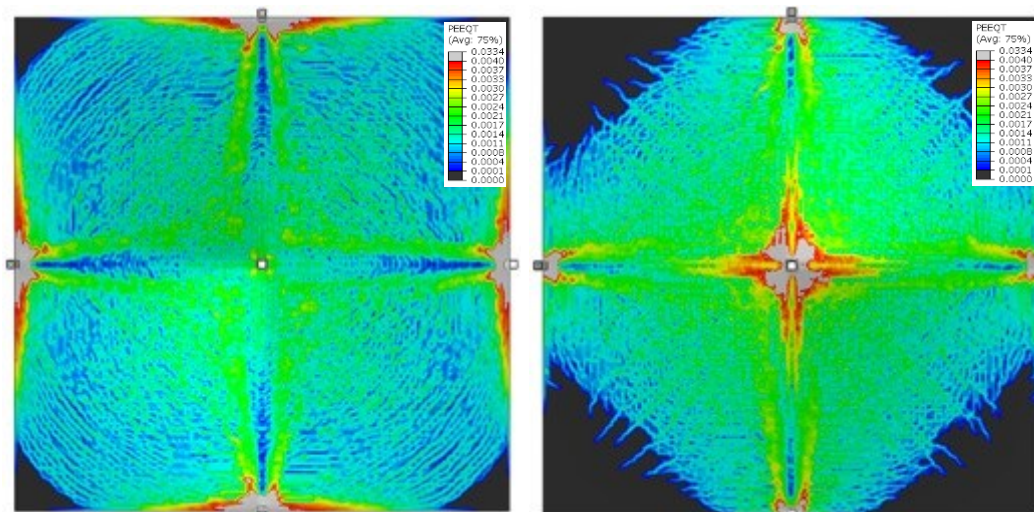
Figure 6-36: Formation of Tensile Membrane and Compressive Ring under Central Column Removal in an Unrestrained Axial Condition of Slab's Edges



Top of Slab

Slab Soffit

ST59B (Unrestrained)



Top of Slab

Slab Soffit

ST59B (Restrained)

Figure 6-37: Equivalent Tensile Plastic Strain (PEEQT) Developed in Concrete Slab of Specimen ST59B for Two Boundary Conditions of Slab Edges under Central Column Removal: Formation of Tensile Membrane (Soffit) and Compressive Ring (Top) in an Unrestrained Condition

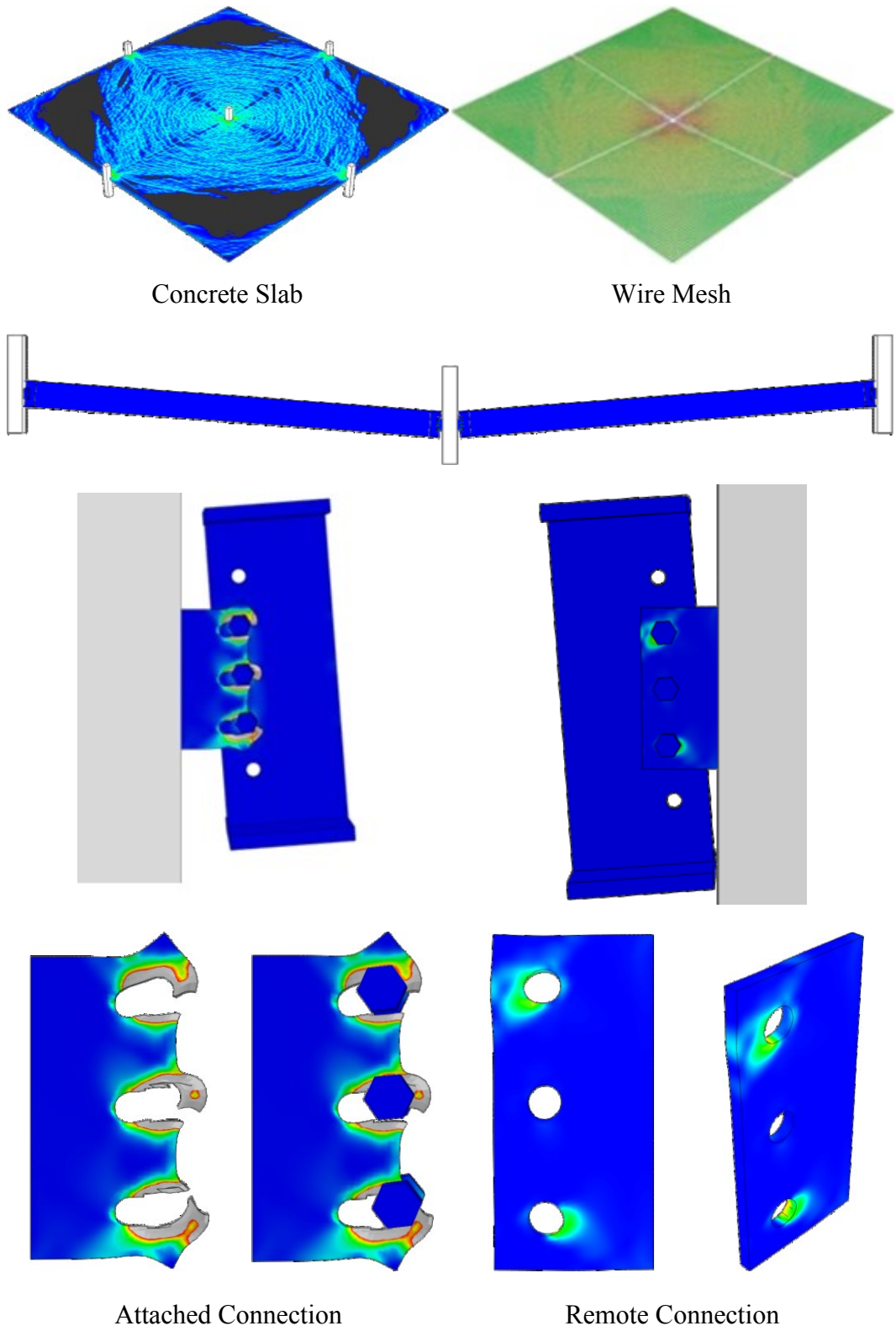


Figure 6-38: Deformation and Failure Mode of Shear Tabs, Rebars, and Concrete Slab in the Detailed ST39B Model (Unrestrained)

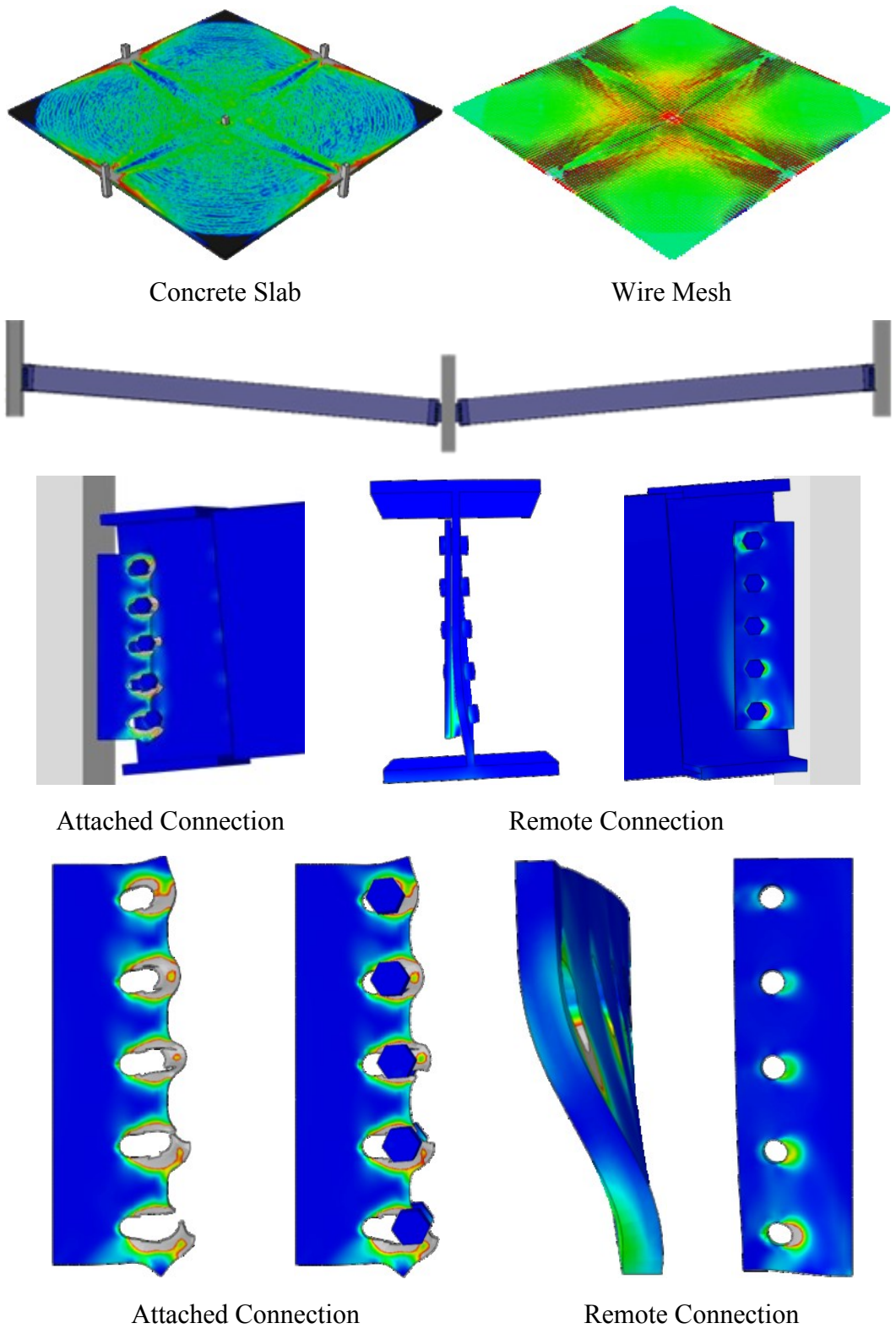


Figure 6-39: Deformation and Failure Mode of Shear Tabs, Rebars, and Concrete Slab in the Detailed ST59B Model (Restrained)



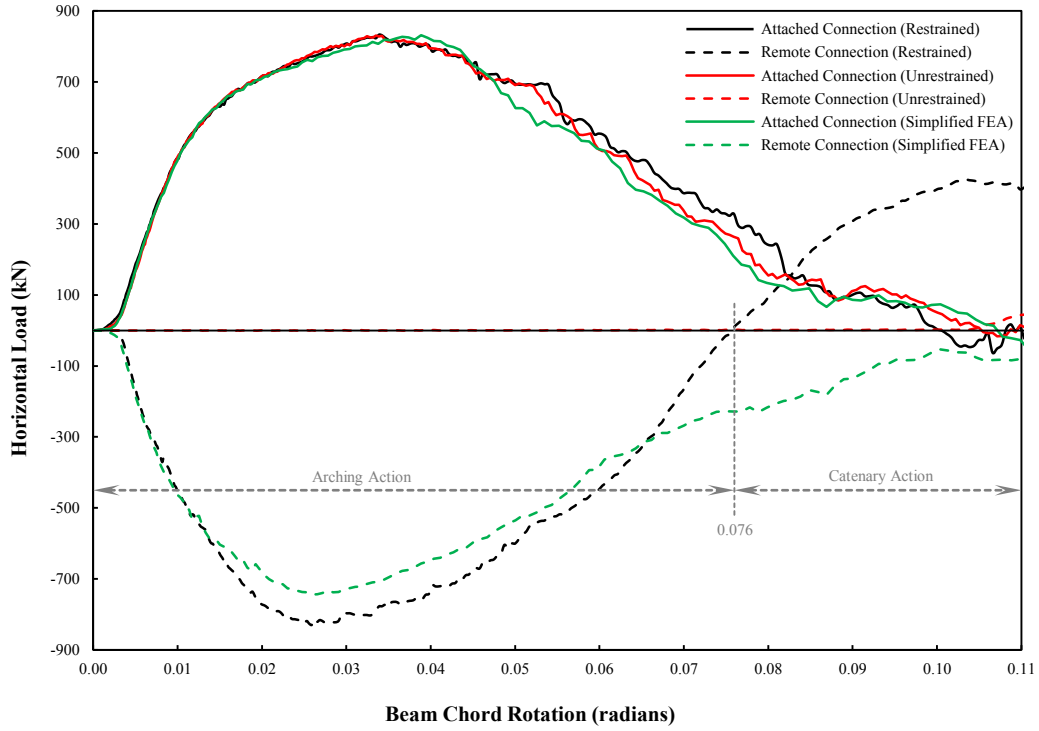


Figure 6-40: Horizontal Load versus Beam Rotation of Connections of Specimen ST59B Extracted From Simplified and Detailed Finite Element Models

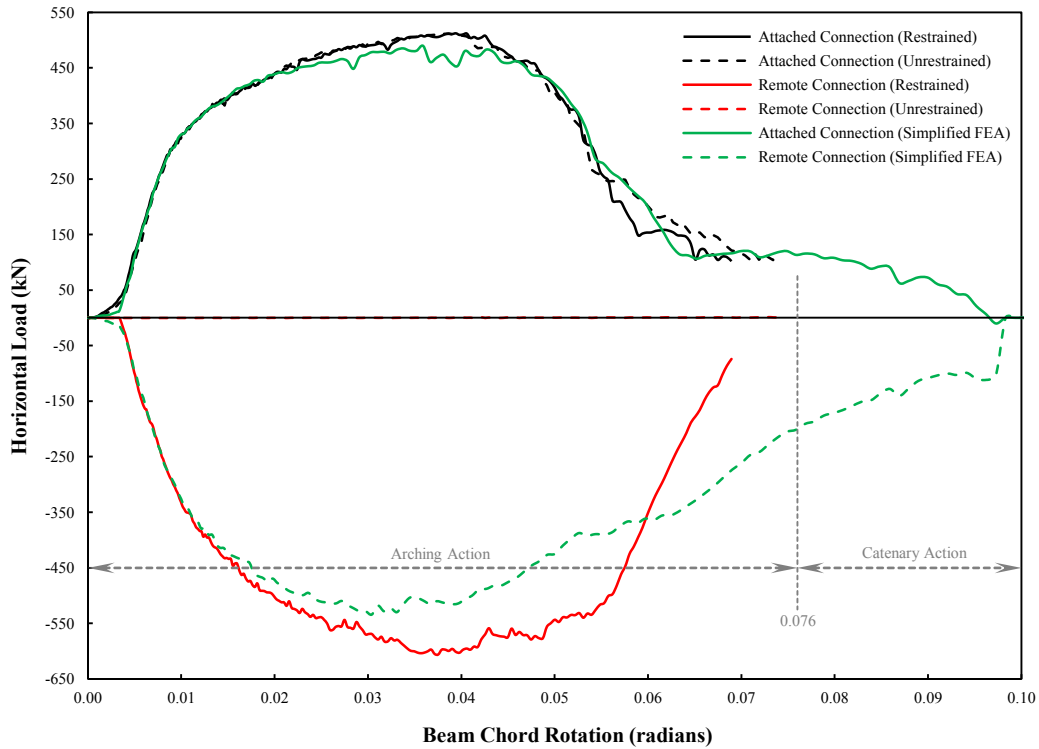


Figure 6-41: Horizontal Load versus Beam Rotation of Connections of Specimen ST39B Extracted From Simplified and Detailed Finite Element Models

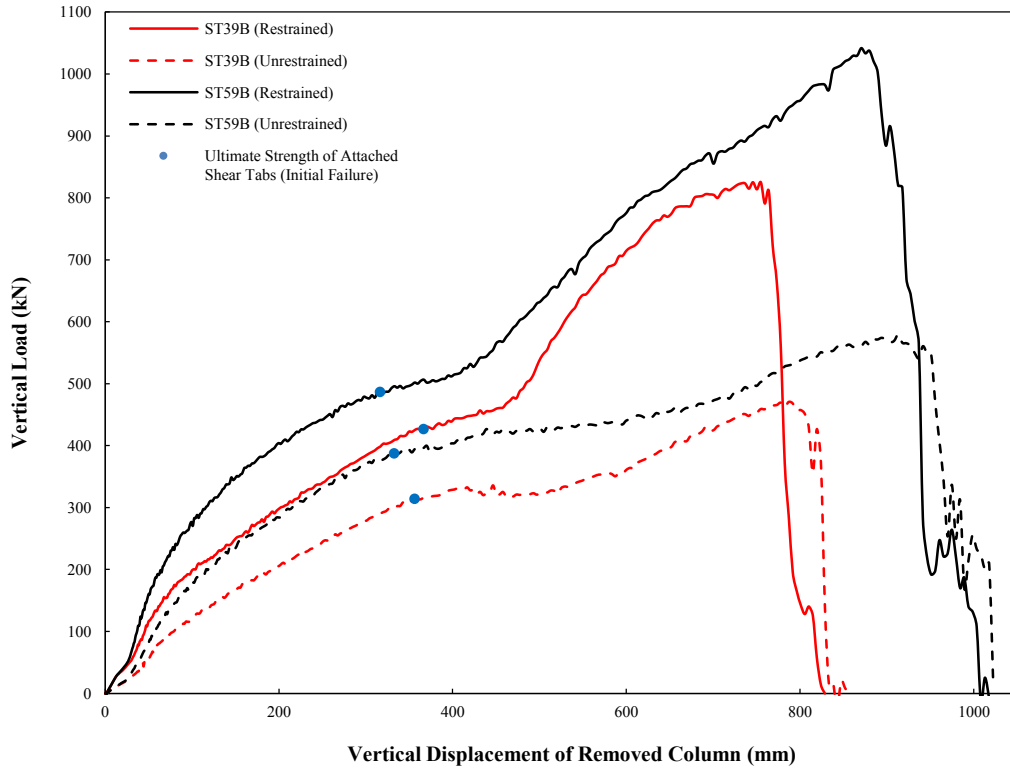


Figure 6-42: Comparison of Load–Displacement Curves of Detailed Models

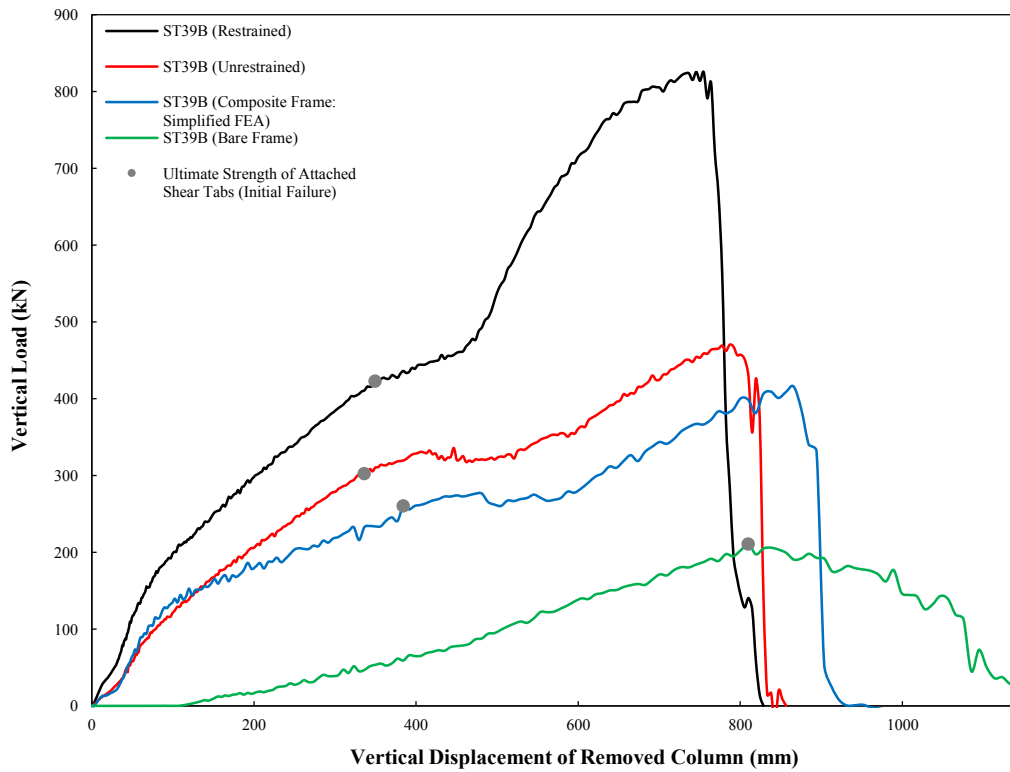


Figure 6-43: Vertical Load–Displacement Curves of Specimen ST39B

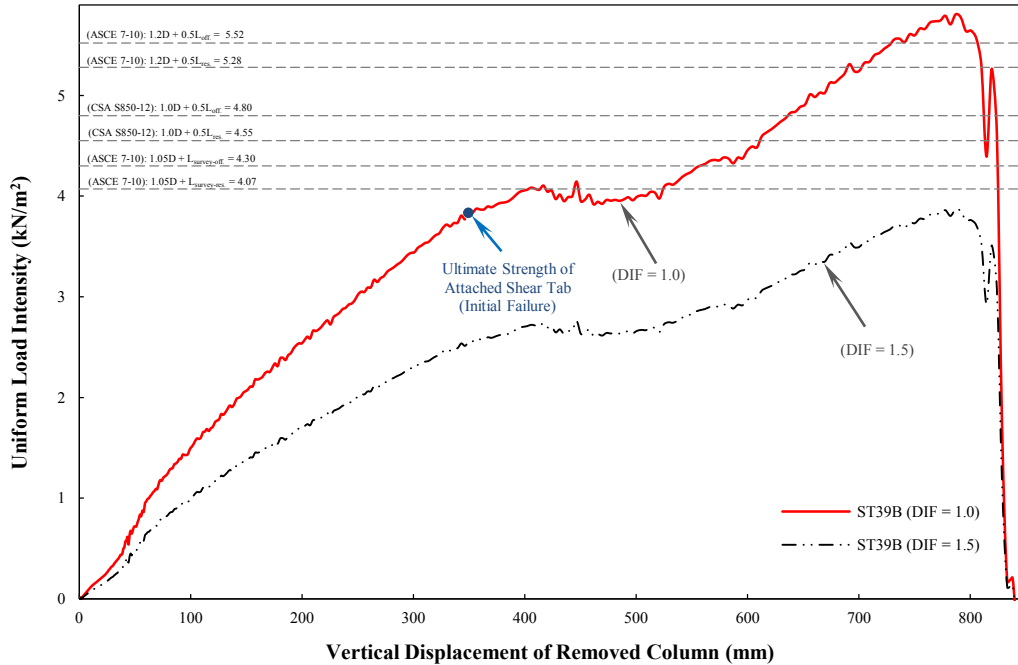


Figure 6-44: Quasi-static (DIF=1.0) and Dynamic (DIF=1.5) Load–Displacement Curves of Detailed Specimen ST39B (Unrestrained) and Comparison with the Structural Integrity Load Combination of ASCE/SEI 7-10 and CSA S850-12

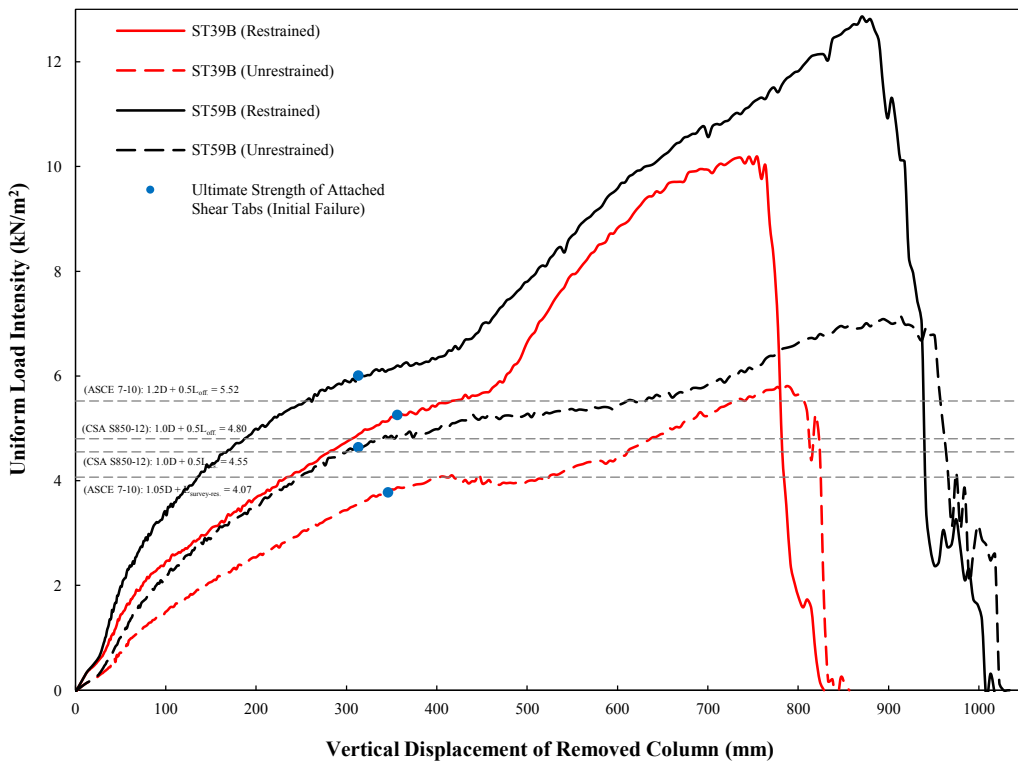


Figure 6-45: Quasi-static Vertical Load-Displacement Curves of Detailed Finite Element Models and Comparison with the Structural Integrity Load Combination of ASCE/SEI 7-10 and CSA S850-12

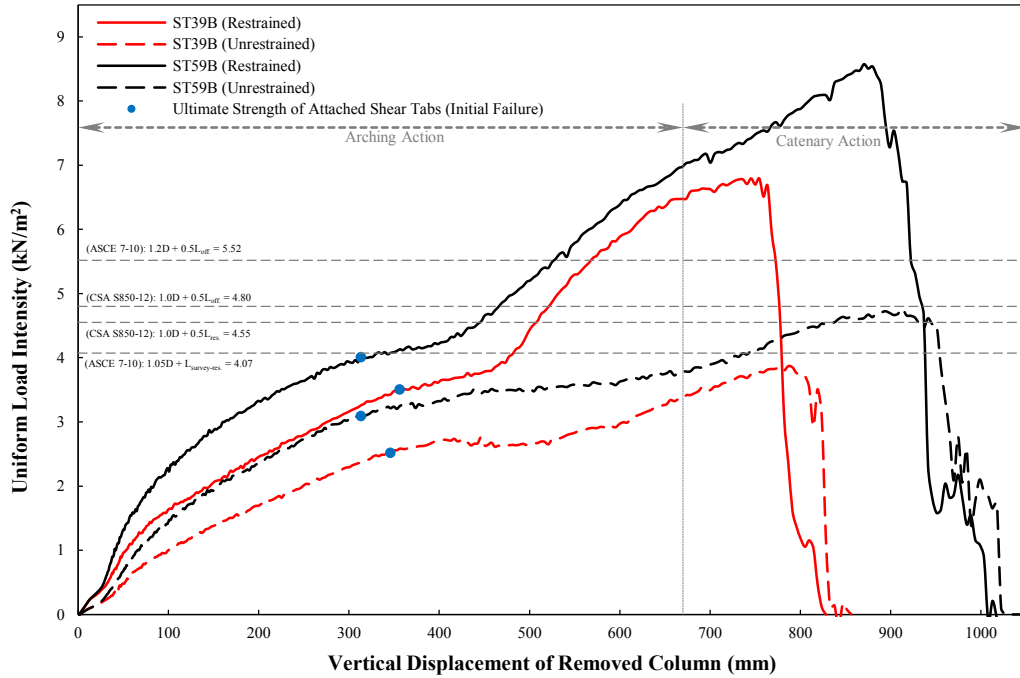


Figure 6-46: Dynamic (DIF=1.5) Load–Displacement Curves of Detailed Specimens and Comparison with the Structural Integrity Load Combination of ASCE/SEI 7-10 and CSA S850-12

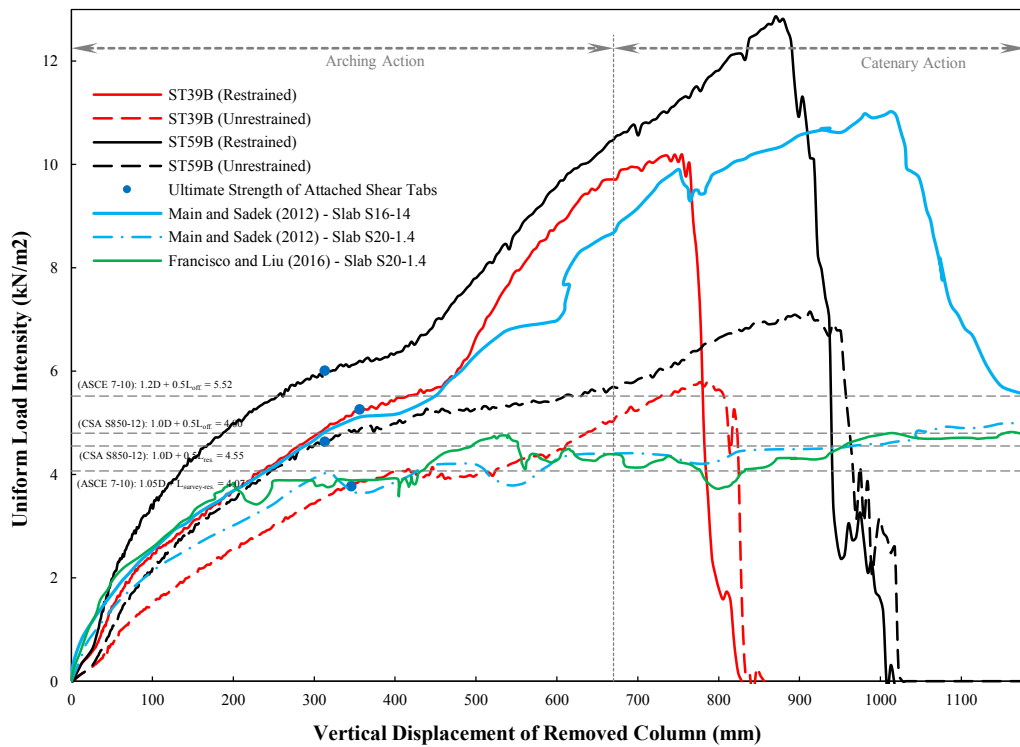


Figure 6-47: Load–Displacement Curves of Detailed Finite Element Models and Comparison with Main and Sadek (2012b) and Francisco and Liu (2016)

## **7. SUMMARY, CONCLUSIONS AND RECOMMENDATIONS**

### **7.1 Summary**

This research investigated the behaviour of steel shear connections in composite frames under a simulated progressive collapse scenario. The study consisted of two main phases. The first phase consisted of a comprehensive experimental program of 17 full-scale physical tests of two connection types in composite floor systems with flat slabs: shear tabs and double angles. For this purpose, a range of parameters was varied, including the connection depth, connection thickness, concrete slab width, and notional beam span. It should be noted that the shear studs were designed such that fully-composite action would develop.

In the absence of a predefined loading protocol for testing specimens in a progressive collapse scenario, removal of the central column has been adopted as a useful method by which the robustness of structural components is assessed by bridging a two-span frame over the local failure of the middle column. Owing to the high associated costs and structural lab limitations, it is not always feasible to test a full frame. Therefore, one method to carry out the test, while maintaining full scale, is to isolate the area of interest (composite connections) and define the load history due to the progressive collapse scenario in advance. Component-level tests were conducted focusing on the behaviour of shear connections in column loss scenarios to investigate how that behaviour was affected by the presence of the concrete composite slab. As such, two methods of determining the loading regime were presented: one based on the equilibrium of forces and the other based on the geometrical compatibility of displacements.

The second part of this research consisted of simplified and detailed finite element modelling and analysis techniques for composite floor framing systems including steel connections and a concrete slab under a column loss scenario. These models were developed to investigate the effects of critical parameters on the performance of shear connections in composite frames. The numerical study

covered various critical parameters like connection types, eccentricities, and notional beam spans. Detailed three-dimensional prototype simulations were evaluated and compared with the simplified finite element models. Design recommendations based on the experiments and finite element models are proposed to calculate the capacity and ductility of the shear connections.

## **7.2 Conclusions**

Based on the results of analytical, experimental and numerical analyses in this study, the following main conclusions were reached:

### **7.2.1 Loading Protocols**

The main findings are summarised below:

1. In the absence of a predefined method for testing specimens in a case of progressive collapse, loading protocols were developed allowing composite connections with a cantilever beam to represent a continuous beam with similar connections at each end. Based on the proposed loading regime, the progression of arching/catenary actions was observed, resulting in the composite connection attached to the column undergoing primarily tension.
2. Two loading protocols, namely equilibrium of forces and geometric compatibility of displacements, were proposed and limitations pertaining to each were addressed.
3. Most of the existing loading regimes were developed based on the assumption that the point of inflection is located at the middle of the span in a structure undergoing a collapse, meaning that equal bending moments would develop at each end of the span. However, due to the different rotational stiffnesses and evolutionary behaviours in composite connections under positive and negative bending moments, the behaviour of the hogging moment cannot be taken equal to that of the sagging moment. Therefore, assuming that the inflection point is located at the middle of the span is not an accurate premise.

4. The equilibrium of forces method outlines a basis for proportioning shear and axial forces and bending moment at each loading stage, while the second approach relies on the correlation between the geometric compatibility of the central removed-column deflection and the connections' deformation based on simple trigonometry. Axial deformation in connections was derived based on the strut and tie model (truss analogy) proposed in this study.
5. The proposed mechanism captures the development of arching action in the span as a result of unsymmetrical neutral axes at the two ends of composite frame and axial restraint provided by the surrounding frames at both ends of the span. Based on the definition of truss analogy, throughout the phase of arching action connections attached to the removed column remain constantly in tension, while the far-end connections experience a compressive force.
6. An idealized model that depicts the various phases of axial force development during arching and catenary action phases was introduced. The total axial elongation of the connections was assumed to be entirely attributed to the connection close to the removed column as long as the arching action exists. Once the arching action switches to the catenary phase, the elongation is attributed to both connections.

### **7.2.2 Concrete Slab**

The main findings are summarised below:

1. The failure modes of the concrete slabs were similar for all specimens and were characterized by concrete cracking and crushing, typically concentrated around the slab's opening close to the stub column.
2. The cracks always initiated at a small beam rotation (less than 0.025 rad) at the shear studs closest to the stub column and propagated circumferentially around the column. Cracks then developed in a similar manner at shear studs progressively farther from the column as the beam rotation increased. Cracks penetrated deep through the slab, especially for the shorter notional spans.

### 7.2.3 Shear Tab Connections

The main outcomes related to the shear tab connections are summarised below:

1. No failure or significant permanent deformation of bolts was observed in the shear tab connections.
2. Elongation of the shear tab plate holes under the bearing stress exerted by the bolts was the main factor for providing ductility in the shear tab connections. By increasing the beam rotation, successive bolt tear-out by gradual failure progression from the bottom to the top bolt was observed. Bolt tear-out of the shear tab plate was the governing failure mode for all specimens.
3. Two types of fractures were observed in the bolt tear-out failure mechanism: shear tearing on one or two shear planes, or tensile splitting at the free edge adjacent to the centreline of the hole.
4. Finite element modelling was able to predict the behaviour of shear tab connections accurately and provided excellent agreement with the physical test results.
5. Based on the finite element results, deformations of the connections at both ends of the beam in a bare frame were different once placed in a composite frame. While the attached connection is primarily in tension, the remote connection experiences substantial compressive force up to the end of arching action. This significant force can be developed at the remote connection providing that shear studs are present that can develop full composite action. Due to the formation of arching action, the slab places the attached connections in tension and carries compression along the perimeter of slab, with the neutral axis of the composite section being located within the slab.
6. The ultimate horizontal capacity of the attached connection is about the same in both bare and composite frames. However, the stiffnesses and ductilities are significantly different. Since the composite frame added a substantial stiffness to the steel connection, the beam rotation at the ultimate capacity is about 40% of that in the bare frame.



7. The average composite-to-bare frame ratios for the horizontal tensile load, beam rotation, and axial deformation are 0.98, 0.32, and 0.36, respectively. It is concluded that the horizontal ultimate load of the shear tabs is independent of the presence of the concrete slab. However, the concrete slab affects the axial deformation and rotation substantially.
8. Failure of shear tabs in a composite system was observed at rotations lower than those captured in the associated bare frames. The considerably smaller rotations at failure are, in fact, a consequence of the composite action between the beam and the concrete floor slab.
9. Based on the results, rotational capacities of shear tabs were significantly smaller than those predicted based on seismic test data, for which the introduction of arching action underestimates the rotational capacity. This is due to the axial extension imposed on the connections in addition to rotation.
10. A parametric study based on the existing experiments and numerical data was developed and carried out to correlate the rotational capacity of the shear tabs with respect to the parameters influencing the connection's ductility.

#### **7.2.4 Double Angle Connections**

The main results specific to the double angle connections are summarised below:

1. No failure or significant permanent deformation of bolts was observed in the double-angle connections.
2. Deformation was initially shaped by unfolding of the angles, at which time the angle heels pulled away from the stub column flange. After unfolding, tearing initiated and propagated from the bottom of the angles where the maximum tensile stress developed.
3. Two types of fractures were observed in the double angle connections: tearing of the gross section near the angle heel, and/or fracture near the bolt line attached to the stub column.

4. Tearing of the gross section was found to be more common in all specimens. This brittle failure mode developed suddenly with a rapid propagation along the depth of the angles. This failure was found to be unstable, as any small increase in rotation caused the propagation to develop quickly.
5. Fracture along the column bolt line was mostly observed in the thin–deep connections (five-bolt configurations). The fracture occurred along a zigzag pattern between bolts attached to the column and was found to be more stable than the other failure mode because tears were arrested at hole intercepted.
6. Finite element modelling was able to predict the behaviour of double angle connections accurately and provided good agreement with the experiments.
7. Compressive arching action was developed at low rotations of double angles in bare frames due to the unequal stiffness of the double angles in tension and compression. Arching action was only observed in the thicker double angles in the bare frames and was even more severe when the connection was deeper.
8. Based on the finite element results, deformation of double angles at both ends of the beam in a bare frame was different once placed in a composite frame. Once angles are placed in the composite frames, the attached connections undergo pure tension similar to those of shear tabs. This is due to the initial position of the neutral axes with respect to the centroid of connections during the vertical push down of the removed column, which places the angles in tension from early stages of loading. While the attached connection is predominantly in tension, the remote connection experiences substantial compressive force up to the beginning of the catenary action.
9. The average composite-to-bare frame ratios for the horizontal tensile load, beam rotation, and axial deformation are 1.03, 0.60, and 0.36, respectively. Similar to the shear tabs, the ultimate horizontal strength of the double angles was found to be independent of the presence of the concrete floor slab. However, the concrete slab affects the axial deformations and rotations substantially.

### **7.2.5 Finite Element Modelling Technique**

Due to the development of bolt tear-out of shear tab connections and the occurrence of sudden fracture of double angle connections, which were both observed in the tests, it is highly recommended that material failure and damage evolution be introduced into the finite element models. Such consideration significantly affects the ultimate capacity, rotation and post-ultimate gradual softening advancement of shear connections.

### **7.2.6 Detailed Prototype Models**

The main conclusions of the detailed prototype models are summarised below:

1. Detailed three-dimensional finite element models were developed to examine the degree of accuracy of the proposed loading regime and also to validate the physical component experimental tests. To evaluate the effect of horizontally-restrained boundary conditions on the performance of the composite system, two different boundary conditions of slab edges were considered: restrained and unrestrained models.
2. Axial deformation developed in the attached connections was similar for the two boundary conditions, meaning that the connection axial deformation is independent of the horizontal conditions of the edges of the concrete slab. This is by virtue of the compressive ring and tensile membrane that develops in the slab with horizontally unrestrained conditions around its edges.
3. Excellent agreement between the results obtained from the experiment and the finite element analysis was reached. The results assured the accuracy of the proposed loading regime, which was developed and implemented for testing steel connections in composite frames.
4. Good correlation was observed between the simplified and detailed models. The trend of load development and ultimate strength and rotational capacities of the attached connections were similar and were independent of the horizontal axial conditions of the slab.

5. While the attached connections were all predominantly in tension starting at the early stages of loading, the remote connections performed differently. For models with horizontally unrestrained edges, neither axial compressive demands nor substantial axial deformation were imposed on the remote connections despite the formation of a compressive ring. For models with restrained edges, however, significant compressive demands were imposed on the attached connections.
6. Connections attached to the removed column completely failed at vertical deflections of the removed column between 300 mm and 400 mm, before the system reaches its ultimate strength.
7. The ultimate capacity of the unrestrained systems is about 56% of that of the restrained ones. The ultimate capacity of the unrestrained systems reached about 1.5 times the total shear forces developed in the four attached connections once at their ultimate strength, while the ratio was about 2.1 for the restrained models.
8. The reserve capacity of the structural system after the connections' post-ultimate response is higher in restrained systems. This is certainly due to the formation of arching action in the restrained systems, which provided rigid axial constraints to the edges of the slab.
9. The collapse resistances of the prototype systems were assessed by comparing the capacities with the integrity requirements by current building codes. The capacity of three-bolt connections was found to be inadequate to sustain the lower level of load combination. While the quasi-static response of the unrestrained systems barely satisfied the expected load combinations, the dynamic capacity did not reach the expected gravity loadings.
10. Compressive arching action plays a significant role once axial restraint exists. This is mainly important for composite frames with simple to semi-rigid connections, where the double-span condition is associated with offset centres of rotations at the removed column and connections.

11. The main outcome drawn from this section is that the modelled prototype structures can be made adequately robust, provided due allowance is taken of compressive arching action that develops under axial restraint. Since the rotational ductility and ultimate strength of the connections were inadequate for the development of full tensile catenary action, reliance should be placed primarily on bending and compressive arching resistance for the establishment of robustness under column-loss scenarios.

### **7.3 Recommendations**

#### **7.3.1 Design Recommendations**

The main findings are summarised below:

1. A simplified approach was proposed to calculate the nominal tensile resistances versus corresponding beam rotations of simple connections using a single bilinear force–rotation relationship. The proposed method yields good general agreement with the results; however, the accuracy is limited by the governing failure mode, which was bolt tear-out for the shear tabs and rupture of the gross section near the heel for the double angles.
2. The bolt tear-out capacity in the shear tab connections was calculated based on the horizontal failure shear planes. However, it was found that the angle of shear planes varies between 15 to 25 degrees. Therefore, it is recommended the failure shear plane inclination be included in the capacity calculations, since bolt tear-out is considered as an ultimate limit state. Ignoring such would result in a lower capacity prediction.
3. Empirical methods, based on the parameters influencing the connection’s ductility, were derived and presented to measure the rotational capacities of both connections corresponding to characteristic points of horizontal strength: one signifying the maximum tensile force, and the second one representing the final rotation corresponding to complete failure.

### 7.3.2 Recommendations for Future Research

This research, numerically and experimentally, focused mainly to the behaviour and robustness of shear tab and double angle connections in composite frames under a column loss scenario. However, below are recommendations for future research to further enhance the current understanding of the topic:

1. Since this research was mainly focused on flat concrete slabs of constant thickness, it is suggested that composite systems comprising steel decks be investigated due to the orthotropic nature of the slab with metal deck.
2. Since in this research the floor slab was assumed to act fully composite, partially-composite systems should be evaluated as they are more common in practice.
3. It is recommended that other types of connections with different geometric arrangements (such as end/edge distance, and more vertical rows of bolts), notional spans, and unequal span lengths be investigated.
4. As explained previously, remote connections experience a prominent compressive force in restrained models, while in an unrestrained system no axial demand is imposed on them. Therefore, remote connections become an important component in restrained or partially restrained systems in order to arrest the system against collapse. Since in this research program no physical tests were carried out on the remote connections, it is recommended that the behaviour of these connections in composite frame systems be evaluated.
5. Dynamic analysis is recommended to evaluate the performance of shear connections in composite frames under various real-time loading conditions.
6. A full-scale three-dimensional physical testing program that examines the importance of the arching/catenary action is suggested to measure the vulnerability of steel gravity frames to disproportionate collapse.
7. More research is needed to investigate the effects of axial stiffness of surrounding structures on the performance and capacity of the connections and overall structural systems.

## REFERENCES

- ACI. (2011). "Building Code Requirements for Structural Concrete and Commentary." ACI 318-11, Farmington Hills, MI, USA.
- AISC. (2010). "Specification for Structural Steel Buildings." ANSI/AISC 360-10, Chicago, Illinois, USA.
- AISC. (2011). "Steel Construction Manual, 14th Edition." AISC 325-11, Chicago, IL, USA.
- AISC. (2015). "Specification for Structural Steel Buildings Draft Available for Public Review." ANSI/AISC 360-16, Chicago, Illinois, USA.
- Alashker, Y., El-Tawil, S., and Sadek, F. (2010). "Progressive Collapse Resistance of Steel-Concrete Composite Floors." *J.Struct.Eng.*, 136(10), 1187-1196.
- ANSI. (1972). "Building Code Requirements for Minimum Design Loads in Buildings and Other Structures." ANSI A58.1-1972, New York, NY, USA.
- ANSI. (1982). "Minimum Design Loads for Buildings and Other Structures." ANSI A58.1-1982, New York, NY, USA.
- ASCE. (2006). "Seismic Rehabilitation of Existing Buildings." ASCE 41-06, Reston, VA, USA.
- ASCE. (2010). "Minimum Design Loads for Buildings and Other Structures." ASCE/SEI 7-10, Reston, VA, USA.
- ASM International. (1992). "ASM Handbook Volume 18: Friction, Lubrication, and Wear Technology." USA.
- Astaneh, A. (2005). "Design of Shear Tab Connections for Gravity and Seismic Loads." Rep. No. Steel TIPS, Structural Steel Educational Council (SSEC), Moraga, CA, USA.
- Astaneh, A. (2007). "Progressive Collapse Prevention of Steel Frames with Shear Connections." Rep. No. Steel TIPS, Structural Steel Educational Council (SSEC), Moraga, CA, USA.
- Astaneh, A., Jones, B., Zhao, Y., and Hwa, R. (2002a). "Progressive Collapse Resistance of Steel Building Floors." Rep. No. UCB/CEE-Steel-2001/03, Department of Civil and Environmental Engineering, University of California, Berkeley, California, USA.

Astaneh, A., Madsen, E. A., Noble, C., Jung, R., McCallen, D. B., Hoehler, M. S., Li, W., and Hwa, R. (2002b). "Use of Catenary Cables to Prevent Progressive Collapse of Buildings." Rep. No. UCB/CEE-Steel-2001/02, Department of Civil and Environmental Engineering, University of California, Berkeley, California, USA.

ASTM. (2010). "Standard Test Method for Static Modulus of Elasticity and Poisson's Ratio of Concrete in Compression." C469/C469M-10, West Conshohocken, PA, USA.

ASTM. (2012). "Standard Test Method for Compressive Strength of Cylindrical Concrete Specimens." C39/C39M-12a, West Conshohocken, PA, USA.

ASTM. (2012). "Standard Test Methods and Definitions for Mechanical Testing of Steel Products." A370-12a, West Conshohocken, PA, USA.

ASTM. (2013). "Standard Specification for Steel Bar, Carbon and Alloy, Cold-Finished." A108-13, West Conshohocken, PA, USA.

ASTM. (2013). "Standard Test Methods for Tension Testing of Metallic Materials." E8/E8M-13a, West Conshohocken, PA, USA.

ASTM. (2014). A370-14: Standard Test Methods and Definitions for Mechanical Testing of Steel Products. ASTM International, West Conshohocken, PA, USA.

AWS. (2010). "Structural Welding Code-Steel." AWS D1.1, Miami, Florida, USA.

Bai, Y., Teng, X., and Wierzbicki, T. (2009). "On the Application of Stress Triaxiality Formula for Plane Strain Fracture Testing." Journal of Engineering Materials and Technology-Transactions of the ASME, 131(2), 21002.

BSI. (2010). "Structural Use of Steelwork in Building. Code of Practice for Design. Rolled and Welded Sections." BS 5950-1:2000, London, UK.

Cashell, K. A., Elghazouli, A. Y., and Izzuddin, B. A. (2011). "Failure Assessment of Lightly Reinforced Floor Slabs. II: Analytical Studies." J.Struct.Eng., 137(9 - September), 989-1001.

CEN. (2005). "Eurocode 3: Design of Steel Structures." EN 1993:2005, Brussels, Belgium.

CEN. (2006). "Eurocode 1 - Actions on Structures - Part 1-7: General Actions - Accidental Actions." EN 1991-1-7:2006, Brussels, Belgium.

CISC. (2010). "Handbook of Steel Construction, 10th Edition." CISC, Markham, ON, Canada.



- CSA. (2004). "Design of Concrete Structures." CAN/CSA-A23.3-04, Mississauga, Ontario, Canada.
- CSA. (2009). "Carbon Steel Bars for Concrete Reinforcement." CAN/CSA G30.18-09 (R2014), Mississauga, Ontario, Canada.
- CSA. (2012). "Design and Assessment of Buildings Subjected to Blast Loads." CSA-S850-12, Mississauga, Ontario, Canada.
- CSA. (2013). G40.21-13: General Requirements for Rolled or Welded Structural Quality Steel. Canadian Standards Association, Mississauga, ON, Canada.
- CSA. (2013). "Welded Steel Construction (Metal Arc Welding)." CAN/CSA-W59-13, Mississauga, Ontario, Canada.
- CSA. (2014). "Limit State Design of Steel Structures." CAN/CSA-S16-14, Mississauga, Ontario, Canada.
- Daneshvar, H. (2013). "One-sided Steel Shear Connections in Column Removal Scenario". PhD. Department of Civil and Environmental Engineering, University of Alberta, Edmonton, AB, Canada.
- Dassault Systèmes Simulia Corp. (2013). "Abaqus Analysis User's Guide." Version 6.13-4, Providence, RI, USA.
- De Stefano, M., and Astaneh, A. (1991). "Axial Force-Displacement Behavior of Steel Double Angles." *Journal of Constructional Steel Research*, 20(3), 161-181.
- Ellingwood, B., and Leyendecker, E. E. (1978). "Approaches for Design against Progressive Collapse." *Journal of the Structural Division*, 104(3), 413-423.
- Federal Emergency Management Agency. (2000). "State of the Art Report on Connection Performance." FEMA-355D, Washington, D.C., USA.
- Fisher J. W., and Struik, J. H. A. (1974). *Guide to Design Criteria for Bolted and Riveted Joints*. Wiley, New York, USA.
- Francisco, T., and Liu, J. (2016). "Application of Experimental Results to Computational Evaluation of Structural Integrity of Steel Gravity Framing Systems with Composite Slabs." *J.Struct.Eng.*, 142(3), 04015152.
- Geschwindner, L. F., and Gustafson, K. D. (2010). "Single-Plate Shear Connection Design to Meet Structural Integrity Requirements." *AISC-Engineering Journal*, 47(3), 189-202.
- Gong, Y. (2013). "Re-examination of Double-angle Knife Shear Connections." *Journal of Constructional Steel Research*, 81 44-51.

- Gong, Y. (2014). "Ultimate Tensile Deformation and Strength Capacities of Bolted-angle Connections." *Journal of Constructional Steel Research*, 100 50-59.
- Great Britain, Ministry of Housing and Local Government. (1968). *Report of the Inquiry into the Collapse of Flats at Ronan Point, Canning Town*. London, UK.
- GSA. (2003). "Progressive Collapse Analysis and Design Guidelines for New Federal Office Buildings and Major Modernization Projects." General Service Administration, Auburn, WA, USA.
- GSA. (2013). "GSA Alternate Path Analysis and Design Guidelines for Progressive Collapse Resistance." General Service Administration, Auburn, WA, USA.
- Hillerborg, A., Mod er, M., and Petersson, P. -. (1976). "Analysis of crack formation and crack growth in concrete by means of fracture mechanics and finite elements." *Cem.Concr.Res.*, 6(6), 773-781.
- Ho, I., and Astaneh, A. (1993). "Behavior of Double Angle Connections Subjected to Shear and Axial Monotonic or Cyclic Loads." Rep. No. UCB/CE-Steel-93/17, Department of Civil Engineering, University of California, Berkeley, CA, USA.
- Hooputra, H., Gese, H., Dell, H., and Werner, H. (2004). "A comprehensive failure model for crashworthiness simulation of aluminium extrusions." *International Journal of Crashworthiness*, 9(5), 449-464.
- International Code Council (ICC). (2015). "International Building Code (IBC)." Country Club Hills, IL, USA.
- Izzuddin, B. A., Vlassis, A. G., Elghazouli, A. Y., and Nethercot, D. A. (2008). "Progressive Collapse of Multi-Storey Buildings due to Sudden Column Loss - Part I: Simplified Assessment Framework." *Eng.Struct.*, 30(5), 1308-1318.
- Jamshidi, A., and Driver, R. G. (2012). "Progressive Collapse Resistance of Steel Gravity Frames Considering Floor Slab Effects." 3rd International Structural Specialty Conference, CSCE 2012, Edmonton, AB, Canada, STR-1003-1 to STR-1003-10.
- Jamshidi, A., and Driver, R. G. (2013). "Structural Integrity of Composite Steel Gravity Frame Systems." Structures Congress 2013, American Society of Civil Engineers (ASCE), Pittsburgh, PA, USA, 55-66.
- Jamshidi, A., and Driver, R. G. (2014). "Full-Scale Tests on Shear Connections of Composite Beams under a Column Removal Scenario." Structures Congress 2014, American Society of Civil Engineers (ASCE), Boston, MA, USA, 931-942.

Jamshidi, A., Koduru, S., and Driver, R. G. (2014). "Reliability Analysis of Shear Tab Connections under Progressive Collapse Scenario." Structures Congress 2014, American Society of Civil Engineers (ASCE), Boston, MA, USA, 2151-2161.

Liu, J., and Astaneh, A. (2000). "Cyclic Tests on Simple Connections, Including Effects of the Slab." Rep. No. SAC/BD-00/03, SAC Joint Venture, Berkeley, California, USA.

Main, J. A., and Sadek, F. (2012). "Robustness of Steel Gravity Frame System with Single-Plate Shear Connections." Rep. No. NIST Technical Note 1749 (corrections dated February 2013), National Institute of Standards and Technology (NIST), U.S. Department of Commerce, Gaithersburg, MD, USA.

Main, J., Weigand, J., Johnson, E., Francisco, T., Liu, J., Berman, J., and Fahnestock, L. (2015). "Analysis of a Half-Scale Composite Floor System Test under Column Loss Scenarios." American Society of Civil Engineers, 1065-1077.

Mitchell, D., and Cook, W. (1984). "Preventing Progressive Collapse of Slab Structures." J.Struct.Eng., 110(7), 1513-1532.

NRC. (2010). "National Building Code of Canada, Canadian Commission on Building and Fire Codes." National Research Council of Canada, Ottawa, Ontario, Canada.

NYC. (2008). "New York City Building Code." NYCBC, New York, NY, USA.

NYC. (2014). "New York City Building Code." NYCBC, New York, NY, USA.

Oosterhof, S. A. (2013). "Behaviour of Steel Shear Connections for Assessing Structural Vulnerability to Disproportionate Collapse". PhD. Department of Civil and Environmental Engineering, University of Alberta, Edmonton, AB, Canada.

Oosterhof, S. A., and Driver, R. (2015). "Behavior of Steel Shear Connections under Column-Removal Demands." J.Struct.Eng., 141(4), 04014126.

Oosterhof, S. A., and Driver, R. G. (2012). "Performance of Steel Shear Connections under Combined Moment, Shear, and Tension." Structures Congress 2012, American Society of Civil Engineers (ASCE), Chicago, IL, USA, 146-157.

Oosterhof, S. A., and Driver, R. G. (2016). "Shear Connection Modelling for Column Removal Analysis." Journal of Constructional Steel Research, 117 227-242.

Rex, C. O., and Samuel Easterling, W. (2003). "Behavior and Modeling of a Bolt Bearing on a Single Plate." J.Struct.Eng., 129(6), 792-800.

- Sadek, F., El-Tawil, S., and Lew, H. S. (2008). "Robustness of Composite Floor Systems with Shear Connections: Modeling, Simulation, and Evaluation." *J.Struct.Eng.*, 134(11), 1717-1725.
- Salem, P., and Driver, R. G. (2014). "Behaviour of Unstiffened Extended Shear Tabs under Shear Loading." CSCE 2014 4th International Structural Specialty Conference, Canadian Society for Civil Engineering, Halifax, NS, Canada.
- Starossek, U., and Haberland, M. (2010). "Disproportionate Collapse: Terminology and Procedures." *J.Perform.Constr.Facil.*, 24(6), 519-528.
- Tan, S., and Astaneh, A. (2003). "Cable-Based Retrofit of Steel Building Floors to Prevent Progressive Collapse." Rep. No. UCB/CEE-Steel-2003/02, Department. of Civil and Environmental Engineering, University of California, Berkeley, California, USA.
- Tan, S., and Astaneh, A. (2003b). "Use of Steel Cables to Prevent Progressive Collapse of Existing Buildings." Annual Meeting of the Los Angeles Tall Buildings Structural Design Council, Los Angeles, California, USA.
- Thompson, S. L. (2009). "Axial, Shear and Moment Interaction of Single Plate "Shear Tab" Connections". M.Sc. Milwaukee School of Engineering, Milwaukee, WI, USA.
- Timoshenko. (1955). *Strength of Materials*. Van Nostrand Company, New York, NY, USA.
- Unified Facilities Criteria (UFC). (2013). "Design of Buildings to Resist Progressive Collapse (including change 2 - June 2013)." UFC 4-023-03, Washington, DC, USA.
- Vlassis, A. G., Izzuddin, B. A., Elghazouli, A. Y., and Nethercot, D. A. (2008). "Progressive Collapse of Multi-Storey Buildings due to Sudden Column Loss-Part II: Application." *Eng.Struct.*, 30(5), 1424-1438.
- Weigand, J., and Berman, J. (2014). "Integrity of Steel Single Plate Shear Connections Subjected to Simulated Column Removal." *J.Struct.Eng.*, 140(5), 04013114.
- Weigand, J., and Berman, J. (2016). "Integrity of Bolted Angle Connections Subjected to Simulated Column Removal." *J.Struct.Eng.*, 142(3), 04015165.
- Yang, B., and Tan, K. H. (2013b). "Robustness of Bolted-Angle Connections against Progressive Collapse: Experimental Tests of Beam-Column Joints and Development of Component-Based Models." *J.Struct.Eng.*, 139(9), 1498-1514.

Yang, B., and Tan, K. H. (2014). "Behavior of Composite Beam-Column Joints in a Middle-Column-Removal Scenario: Experimental Tests." *J.Struct.Eng.*, 140(2), 04013045.

Yang, B., and Tan, K. H. (2012). "Numerical Analyses of Steel Beam–Column Joints Subjected to Catenary Action." *Journal of Constructional Steel Research*, 70(0), 1-11.

Yang, B., and Tan, K. H. (2013a). "Experimental Tests of Different Types of Bolted Steel Beam–Column Joints under a Central-Column-Removal Scenario." *Eng.Struct.*, 54(0), 112-130.

Yang, B., and Tan, K. H. (2013c). "Robustness of Bolted-Angle Connections Against Progressive Collapse: Mechanical Modelling of Bolted-Angle Connections Under Tension." *Eng.Struct.*, 57(0), 153-168.

## APPENDIX A. COMPUTATIONS ON GEOMETRIC COMPATIBILITIES OF DISPLACEMENTS

This appendix provides details on computations of geometric compatibilities of displacements and complements the information that has been addressed in Section 3.6.2.

### A.1 Introduction

In general, total axial deformation ( $\delta_{\text{axial}}$ ) along the axis of the beam (one span of the two-bay frame), shown in Figure A-1, is the summation of three components:

$$\delta_{\text{axial}} = \delta_{\text{connections}} + \delta_{\text{beam}} + \delta_{\text{frame}} \quad (\text{A-1})$$

$$\delta_{\text{connections}} = \delta_1 + \delta_2 \quad (\text{A-2})$$

where  $\delta_{\text{connections}}$  = axial deformations of both connections at the ends;  $\delta_{\text{beam}}$  = axial deformation of beam;  $\delta_{\text{frame}}$  = axial deformation of the surrounding frames;  $\delta_1$  = axial deformation of connection attached to the removed column (near-end connection);  $\delta_2$  = axial deformation of connection away from the removed column (far-end connection). Components of Equation (A-1) are shown in Figure A-2 as series of axial springs.

As explained in Chapter 3, arching action, which results in the development of axial compression, is highly dependent on the boundary conditions imposed by the surrounding structure. In theory, if the horizontal restraints at far-end connections, which represent the stiffness of the surrounding structure, are flexible enough to allow the end columns to push outward at the onset of column removal, no arching action would develop and catenary action forms immediately after removal of the central column. In reality, however, adjacent bays tend to provide stiff horizontal restraints ( $\delta_{\text{frame}} \simeq 0$ ), which prevent the end columns from moving outward (or inward) and cause the arching action to develop.

In addition, since the beams are axially much stiffer than the shear connections at both ends, they remain elastic and their axial deformation is typically much smaller than the connections. Thus, similar to the deformation of adjacent bays the contribution of beam deformation could be ignored and assumed to be zero ( $\delta_{\text{beam}} \simeq 0$ ). As a result, Equation (A-1) simplifies to Equation (A-3), which includes the deformation of the connections only.

$$\delta_{\text{axial}} = \delta_{\text{connections}} = \delta_1 + \delta_2 \quad (\text{A-3})$$

Based on the truss analogy (Figure A-3) explained in Chapter 3, in order to compute the axial deformation of connections the total axial elongation is assumed to be entirely attributed to the connection attached to the removed column as long as the arching action exists. Once the arching action switches to the catenary phase, the elongation contributes to both connections.

For a symmetric double-span frame, the central removed column is restrained to deflect downward. Thus, since the deformation of the surrounding frames and the beams are neglected—as being much smaller than the axial deformation of the shear connections—the deformation of the connections along the axis of the rotated beam can easily be computed from the geometric compatibilities illustrated in Figure A-4.

Oosterhof and Driver (2015) assumed that for bare steel frames half of the deformation is carried by each connection because of the symmetry of the two ends. However, this is not valid once a concrete slab exists, as a compressive strut develops (“arching” action) during the first stages of loading before switching to catenary action. As such, finite element analysis on a double-span composite frame was carried out to evaluate whether the assumption of total axial elongation being entirely attributed to the connection attached to the removed column is reasonable. It was shown (Jamshidi and Driver 2012; 2013) that although the compressive axial force due to arching action exists in the system, the near-end connection close to the removed column is always in tension, while the far-end is in compression. Based on this finding, the total elongation of the connections was assumed to be entirely attributed to the connection close to the removed column

as long as the arching action exists. Figure A-6 shows the finite element numerical result of near-end connection axial elongation of one of the models. The result indicates that the axial elongation is in close proximity with the target compatibility deformation given by Equation (A-5), implying that nearly the total elongation is contributed by the near-end connection, which verifies the aforementioned assumption. Calculations of the target axial deformation for each connection are explained in more detail in the next section.

## A.2 Deflection of Removed Column ( $\Delta$ )

The right triangle OCD formed by the initial reduced length ( $L_r$ ) and the beam rotation ( $\theta$ ) can be used, based on simple trigonometry, to compute the vertical deflection of the central removed column ( $\Delta$ ), as shown in Figure A-4:

$$\Delta = L_r \tan \theta \quad (\text{A-4})$$

## A.3 Axial Deformation of Near-End Connection ( $\delta_1$ )

The right triangle OCD is formed by the initial reduced (i.e., between the bolt lines) length ( $L_r$ ), the final length ( $L_{\text{tie}}$ ), and the vertical deflection of the central removed column ( $\Delta$ ) based on the beam rotation, as shown in Figure A-4. Using simple trigonometry, elongation along the axis of beam ( $\delta_1$ ), which is the change in length of the hypotenuse, can be calculated as:

$$\cos \theta = \frac{L_r}{L_{\text{tie}}} \longrightarrow L_{\text{tie}} = \frac{L_r}{\cos \theta}$$

$$\delta_1 = L_{\text{tie}} - L_r = \frac{L_r}{\cos \theta} - L_r$$

$$\delta_1 = \left( \frac{1}{\cos \theta} - 1 \right) L_r \quad (\text{A-5})$$

From Equation (A-5), it is clear that the magnitude of  $\delta_1$  is always positive since  $\frac{1}{\cos \theta}$  is greater than 1.0. Equation (A-5) is only valid as long as arching action



exists. However, at the end of the arching phase (onset of catenary action), it is assumed that the elongation thereafter distributes evenly between both ends and thus the axial deformation is calculated as:

$$\delta_1 = \delta_1^{\text{arching}} + \frac{1}{2} \left[ \left( \frac{1}{\cos \theta} - 1 \right) L_r - \delta_1^{\text{arching}} \right] = \frac{1}{2} \left[ \left( \frac{1}{\cos \theta} - 1 \right) L_r + \delta_1^{\text{arching}} \right]$$

$$\delta_1^{\text{arching}} = \left( \frac{1}{\cos \theta^{\text{arching}}} - 1 \right) L_r$$

After simplification:

$$\delta_1 = \left( \frac{1}{\cos \theta} + \frac{1}{\cos \theta^{\text{arching}}} - 2 \right) \frac{L_r}{2} \quad (\text{A-6})$$

where  $\delta_1^{\text{arching}}$  = axial deformation of near-end connection at the end of arching action;  $\theta^{\text{arching}}$  = beam chord rotation at the end of arching action.

Theoretically,  $\theta^{\text{arching}}$  is equal to  $2\alpha$  but in reality due to the relative stiffnesses of the end connections this value could be slightly different from  $2\alpha$ . By substituting  $\theta^{\text{arching}} = 2\alpha$ , Equation (A-6) simplifies to:

$$\delta_1 = \left( \frac{1}{\cos \theta} + \frac{1}{\cos(2\alpha)} - 2 \right) \frac{L_r}{2} \quad (\text{A-7})$$

It should be noted that Equation (A-7) was derived based on the assumption that axial deformations are evenly distributed between connections after the end of arching action. However, the distribution is highly dependent on the stiffness of the connections at the final stage of arching action.

For a large initial angle of the arching line (short span with large eccentricity), the near-end connection usually fails prior reaching the end of the arching phase, which is nearly at the beginning of the far-end connection elongation. For the shallower case, on the other hand, the arching action might not be significant and thus behaviour is mainly governed by the catenary action, which causes the axial deformation to distribute equally to both ends. In this case, the failure of both connections may occur concurrently or very close to each other.

#### A.4 Axial Deformation of Far-End Connection ( $\delta_2$ )

The triangle OAB is formed by the initial strut length, the final length ( $L_{\text{strut}}$ ), and the vertical deflection of the central removed column ( $\Delta$ ) based on the beam rotation and initial angle of arching action, as shown in Figure A-4. Using the law of sines, deformation along the axis of the strut ( $\delta_{\text{strut}}$ ) can be calculated as:

$$\frac{L_{\text{strut}}}{\sin(90 - \alpha)} = \frac{\sqrt{L_r^2 + e^2}}{\sin(90 + \theta - \alpha)} \xrightarrow{\text{yields}} L_{\text{strut}} = \left( \frac{\sin(90 - \alpha)}{\sin(90 + \theta - \alpha)} \right) \sqrt{L_r^2 + e^2}$$

Using trigonometric co-function identities, this equation simplifies to:

$$L_{\text{strut}} = \left( \frac{\cos \alpha}{\cos(\alpha - \theta)} \right) \sqrt{L_r^2 + e^2}$$

$$\delta_{\text{strut}} = L_{\text{strut}} - \sqrt{L_r^2 + e^2} = \left( \frac{\cos \alpha}{\cos(\alpha - \theta)} \right) \sqrt{L_r^2 + e^2} - \sqrt{L_r^2 + e^2}$$

$$\delta_{\text{strut}} = \left( \frac{\cos \alpha}{\cos(\alpha - \theta)} - 1 \right) \sqrt{L_r^2 + e^2}$$

In order to obtain the axial deformation of the far-end connection ( $\delta_2$ ) along the axis of the beam, deformation along the axis of the strut ( $\delta_{\text{strut}}$ ) should be projected on the axis of beam, as shown in Figure A-5. Two projections should be applied to get the deformation along the beam: first projecting from the current position to the horizontal axis; and then from the horizontal line to the beam axis. Calculations are summarized below:

$$\delta'_{\text{strut}} = \cos(\alpha - \theta) \delta_{\text{strut}}$$

$$\cos \theta = \frac{\delta'_{\text{strut}}}{\delta_2} \xrightarrow{\text{yields}} \delta_2 = \frac{\cos(\alpha - \theta) \delta_{\text{strut}}}{\cos \theta} = \frac{\cos(\alpha - \theta)}{\cos \theta} \delta_{\text{strut}}$$

$$\delta_2 = \frac{\cos(\alpha - \theta)}{\cos \theta} \left( \frac{\cos \alpha}{\cos(\alpha - \theta)} - 1 \right) \sqrt{L_r^2 + e^2}$$

$$\delta_2 = \left[ \frac{\cos \alpha - \cos(\alpha - \theta)}{\cos \theta} \right] \sqrt{L_r^2 + e^2} = \left[ \frac{\cos \alpha - \cos(\alpha - \theta)}{\cos \alpha \cos \theta} \right] L_r \quad (\text{A-8})$$

It should be noted that throughout the arching phase the magnitude of  $\delta_2$  is always negative since  $\cos \alpha$  is always less than  $\cos(\alpha - \theta)$ .

At the end of the arching phase (onset of catenary action), it is assumed that the elongation distributes evenly between both ends and thus the axial deformation is calculated as:

$$\begin{aligned}\delta_2 &= \delta_2^{\text{arching}} + \frac{1}{2} \left[ \left( \frac{1}{\cos \theta} - 1 \right) L_r - \delta_1^{\text{arching}} \right] \\ &= \delta_2^{\text{arching}} + \left[ \left( \frac{1}{\cos \theta} - 1 \right) - \left( \frac{1}{\cos \theta^{\text{arching}}} - 1 \right) \right] \frac{L_r}{2} \\ &= \left( \frac{\cos \alpha - \cos(\alpha - \theta^{\text{arching}})}{\cos \theta^{\text{arching}}} \right) \sqrt{L_r^2 + e^2} + \left( \frac{1}{\cos \theta} - \frac{1}{\cos \theta^{\text{arching}}} \right) \frac{L_r}{2}\end{aligned}$$

To simplify the equation,  $\sqrt{L_r^2 + e^2}$  is rewritten based on  $L_r$  and  $\cos \alpha$  from the right triangle OAC, shown in Figure A-4.

$$\cos \alpha = \frac{L_r}{\sqrt{L_r^2 + e^2}} \xrightarrow{\text{yields}} \sqrt{L_r^2 + e^2} = \frac{L_r}{\cos \alpha}$$

After substituting,  $\delta_2$  simplifies to:

$$\delta_2 = \left( \frac{\cos \alpha - \cos(\alpha - \theta^{\text{arching}})}{\cos \theta^{\text{arching}}} \right) \frac{L_r}{\cos \alpha} + \left( \frac{1}{\cos \theta} - \frac{1}{\cos \theta^{\text{arching}}} \right) \frac{L_r}{2}$$

After simplification:

$$\delta_2 = \left[ \frac{1}{\cos \theta} + \frac{1}{\cos \theta^{\text{arching}}} - \frac{2 \cos(\alpha - \theta^{\text{arching}})}{\cos \alpha \cos \theta^{\text{arching}}} \right] \frac{L_r}{2} \quad (\text{A-9})$$

where  $\delta_2^{\text{arching}}$  = axial deformation of far-end connection at the end of arching action;  $\theta^{\text{arching}}$  = beam chord rotation at the end of arching action.

By substituting  $\theta^{\text{arching}} = 2\alpha$ , Equation (A-9) simplifies to:

$$\delta_2 = \left[ \frac{1}{\cos \theta} - \frac{1}{\cos(2\alpha)} \right] \frac{L_r}{2} \quad (\text{A-10})$$

Theoretically,  $\theta^{\text{arching}}$  is equal to  $2\alpha$  but in reality due to the relative stiffnesses of the connections this value could be slightly different from  $2\alpha$ .

## A.5 Total Axial Deformation

The total axial elongation of the connections is assumed to be entirely attributed to the connection close to the removed column as long as the arching action exists. Once the arching action switches to catenary, the elongation contributes to both connections. Below summarizes the total deformation for two phases:

### A.5.1 Arching Action Phase

The total deformation is the absolute summation of both deformations. Since the signs of the near-end and far-end connections are different, the second term below is multiplied by  $-1$  to convert it to a positive value:

$$\delta_{\text{axial}} = |\delta_1| + |\delta_2| = \left( \frac{1}{\cos \theta} - 1 \right) L_r - \left( \frac{\cos \alpha - \cos(\alpha - \theta)}{\cos \theta} \right) \sqrt{L_r^2 + e^2}$$

To simplify the equation,  $L_r$  is rewritten by  $L_r = \cos \alpha \sqrt{L_r^2 + e^2}$

$$\delta_{\text{axial}} = \left( \frac{1}{\cos \theta} - 1 \right) \cos \alpha \sqrt{L_r^2 + e^2} - \left( \frac{\cos \alpha - \cos(\alpha - \theta)}{\cos \theta} \right) \sqrt{L_r^2 + e^2}$$

$$\delta_{\text{axial}} = \left( \frac{\cos \alpha - \cos \alpha \cos \theta - \cos \alpha + \cos(\alpha - \theta)}{\cos \theta} \right) \sqrt{L_r^2 + e^2}$$

Using trigonometric identities to expand  $\cos(\alpha - \theta)$ , the equation simplifies to:

$$\delta_{\text{axial}} = \left( \frac{\cos \alpha - \cos \alpha \cos \theta - \cos \alpha + \cos \alpha \cos \theta + \sin \alpha \sin \theta}{\cos \theta} \right) \sqrt{L_r^2 + e^2}$$

$$\delta_{\text{axial}} = \left( \frac{\sin \alpha \sin \theta}{\cos \theta} \right) \sqrt{L_r^2 + e^2} = \sin \alpha \tan \theta \sqrt{L_r^2 + e^2}$$

From the right triangle OAC:  $\sin \alpha = e / \sqrt{L_r^2 + e^2}$

$$\delta_{\text{axial}} = \frac{e}{\sqrt{L_r^2 + e^2}} \tan \theta \sqrt{L_r^2 + e^2}$$

After simplification:

$$\delta_{\text{axial}} = e \tan \theta \tag{A-11}$$

### A.5.2 Catenary Action Phase

Once the arching action ends, the elongation is assumed to contribute to both end connections evenly. Deformation at the end of the arching action shall be added to the new deformations. The summary of the calculations is shown below.

$$\begin{aligned}\delta_{\text{axial}} &= |\delta_1| + |\delta_2| \\ &= \left( \frac{1}{\cos \theta} + \frac{1}{\cos \theta^{\text{arching}}} - 2 \right) \frac{L_r}{2} \\ &\quad + \left[ \frac{1}{\cos \theta} + \frac{1}{\cos \theta^{\text{arching}}} - \frac{2 \cos(\alpha - \theta^{\text{arching}})}{\cos \alpha \cos \theta^{\text{arching}}} \right] \frac{L_r}{2}\end{aligned}$$

$$\delta_{\text{axial}} = \left( \frac{1}{\cos \theta} + \frac{1}{\cos \theta^{\text{arching}}} - \frac{\cos(\alpha - \theta^{\text{arching}})}{\cos \alpha \cos \theta^{\text{arching}}} - 1 \right) L_r$$

Expanding  $\cos(\alpha - \theta^{\text{arching}})$ :

$$\begin{aligned}\delta_{\text{axial}} &= \left( \frac{1}{\cos \theta} + \frac{1}{\cos \theta^{\text{arching}}} - \frac{\cos \alpha \cos \theta^{\text{arching}} + \sin \alpha \sin \theta^{\text{arching}}}{\cos \alpha \cos \theta^{\text{arching}}} - 1 \right) L_r \\ &= \left( \frac{1}{\cos \theta} + \frac{1}{\cos \theta^{\text{arching}}} - \tan \alpha \tan \theta^{\text{arching}} - 2 \right) L_r\end{aligned}$$

Substituting  $\tan \alpha = \frac{e}{L_r}$ :

$$\begin{aligned}\delta_{\text{axial}} &= \left( \frac{1}{\cos \theta} + \frac{1}{\cos \theta^{\text{arching}}} - \frac{e}{L_r} \tan \theta^{\text{arching}} - 2 \right) L_r \\ &= \left( \frac{1}{\cos \theta} + \frac{1}{\cos \theta^{\text{arching}}} - 2 \right) L_r - e \tan \theta^{\text{arching}}\end{aligned}$$

$$\delta_{\text{axial}} = \left( \frac{1}{\cos \theta} - 1 \right) L_r + \left( \frac{1}{\cos \theta^{\text{arching}}} - 1 \right) L_r - e \tan \theta^{\text{arching}} \quad (\text{A-12})$$

Substituting  $\theta^{\text{arching}} = 2\alpha$  and using trigonometric identities, Equation (A-12) simplifies to:

$$\delta_{\text{axial}} = \left[ \frac{1}{\cos \theta} - 1 \right] L_r \quad (\text{A-13})$$

Equation (A-13) shows that the total axial deformation in the catenary action phase is independent of arching action parameters such as eccentricity.

## A.6 Parametric Study on the Axial Deformation of Connections

Table A-1 summarizes the axial deformation of connections during arching and catenary phases. The local axial deformation of connections based on the equations summarized in Table A-1 for two clear spans of 9.0 m and 6.0 m are plotted in Figure A-7 and Figure A-8. As seen, the minimum axial deformation in the far-end connections, which is equivalent to the maximum arching force, occurs at the beam chord rotation equal to the initial angle of the arching line.

Local far-end, near-end, and total axial deformation of connections are plotted for various clear spans of 6.0 m to 15.0 m. In these cases, eccentricity ( $e$ ) is taken as 336.5 mm and gauge distance from the bolt group to the adjacent column face ( $g$ ) is taken as 75 mm, similar to the specifications of shear-tab connections in the experimental tests. Results are shown in Figure A-9 to Figure A-11. In all of the plots, the boundary between the arching and catenary actions is demarcated. Remarkably, the arching/catenary regions are divided by a simple locus linear equation  $e \tan \theta$  which basically emphasises that the arching action is governed by eccentricity.

The curves in Figure A-9 to Figure A-11 show that connections within spans with varying length undergo substantially different axial demand. Having constant eccentricity, increasing the span length results in markedly less arching action. Therefore, connections shift to catenary action more rapidly in shorter spans.

It can be seen from the curves in Figure A-9 to Figure A-11 that by increasing the eccentricity the rate of total axial deformation intensifies, from which it can be inferred that larger eccentricities cause connections to experience more elongation demands and earlier failure. This is one of the reasons that including the concrete slab in the evaluation of connection behaviour and performance, i.e., considering eccentricity, is an important consideration.

Table A-1: Axial Deformation of Connections During Arching Action and Catenary Action Phases

Connection	Arching	Catenary	Catenary ( $\theta^{\text{arching}} = 2\alpha$ )
Near-End* ( $\delta_1$ )	$\left[ \frac{1}{\cos \theta} - 1 \right] L_r$	$\left[ \frac{1}{\cos \theta} + \frac{1}{\cos \theta^{\text{arching}}} - 2 \right] \frac{L_r}{2}$	$\left[ \frac{1}{\cos \theta} + \frac{1}{\cos(2\alpha)} - 2 \right] \frac{L_r}{2}$
Far-End ( $\delta_2$ )	$\left[ \frac{\cos \alpha - \cos(\alpha - \theta)}{\cos \alpha \cos \theta} \right] L_r$	$\left[ \frac{1}{\cos \theta} + \frac{1}{\cos \theta^{\text{arching}}} - \frac{2 \cos(\alpha - \theta^{\text{arching}})}{\cos \alpha \cos \theta^{\text{arching}}} \right] \frac{L_r}{2}$	$\left[ \frac{1}{\cos \theta} - \frac{1}{\cos(2\alpha)} \right] \frac{L_r}{2}$
Total ( $\delta_{\text{axial}}$ )	$e \tan \theta$	$\left[ \frac{1}{\cos \theta} - 1 \right] L_r + \left[ \frac{1}{\cos \theta^{\text{arching}}} - 1 \right] L_r - e \tan \theta^{\text{arching}}$	$\left[ \frac{1}{\cos \theta} - 1 \right] L_r$

\* Refer to Figure A-1 for Details and Location of Each Connection

$\delta_1$  = Axial Deformation of Near-end Connection

$\delta_2$  = Axial Deformation of Far-end Connection

$\delta_{\text{axial}}$  = Total Axial Deformation of Connections Measured Between the Location of Original Column Faces

$\theta$  = Beam Chord Rotation

$\alpha$  = Angle of Original Arching Line

$L_r$  = Reduced Span Defined as the Original Distance Between Centres of Bolt Groups of Two End Connections

$e$  = Eccentricity

$\theta^{\text{arching}}$  = Beam Chord Rotation at the End of Arching Action

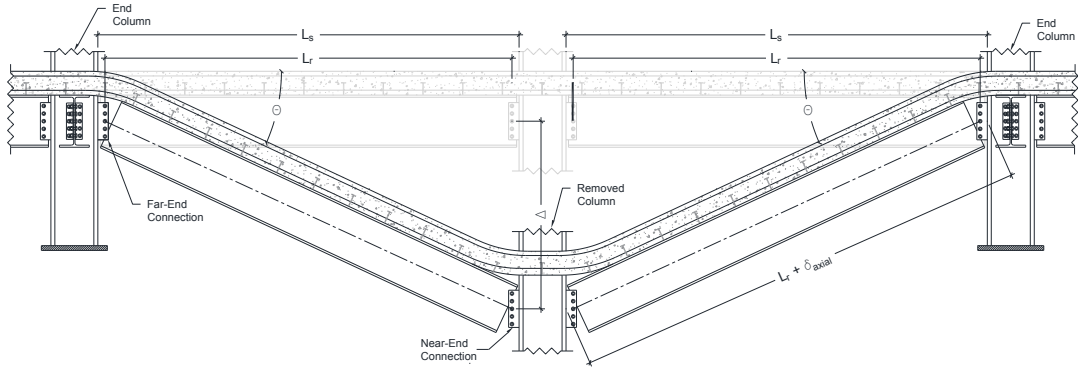


Figure A-1: Axial Deformations of Components of a Double-span Frame under a Central-column Removal Scenario

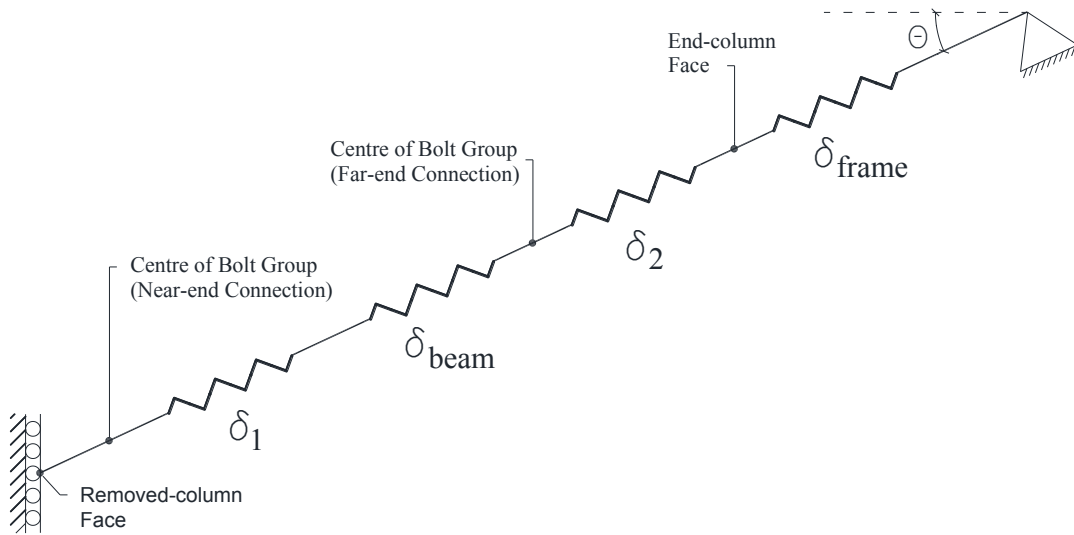


Figure A-2: Components of Total Axial Deformation Shown as Series of Springs



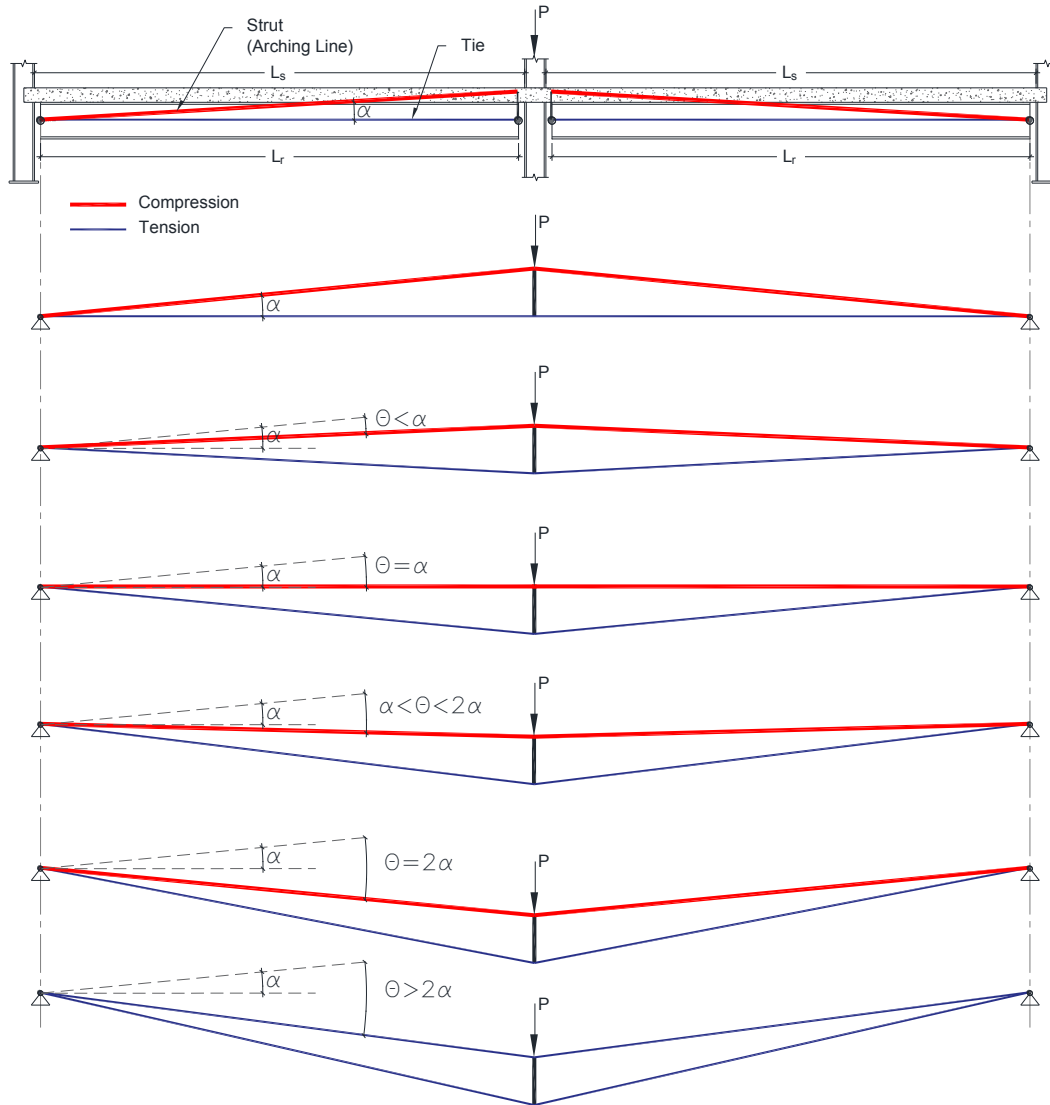


Figure A-3: Strut and Tie Model (Truss Analogy)

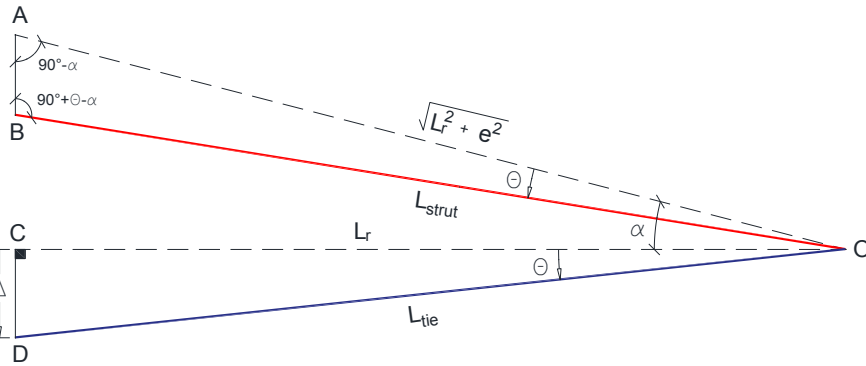
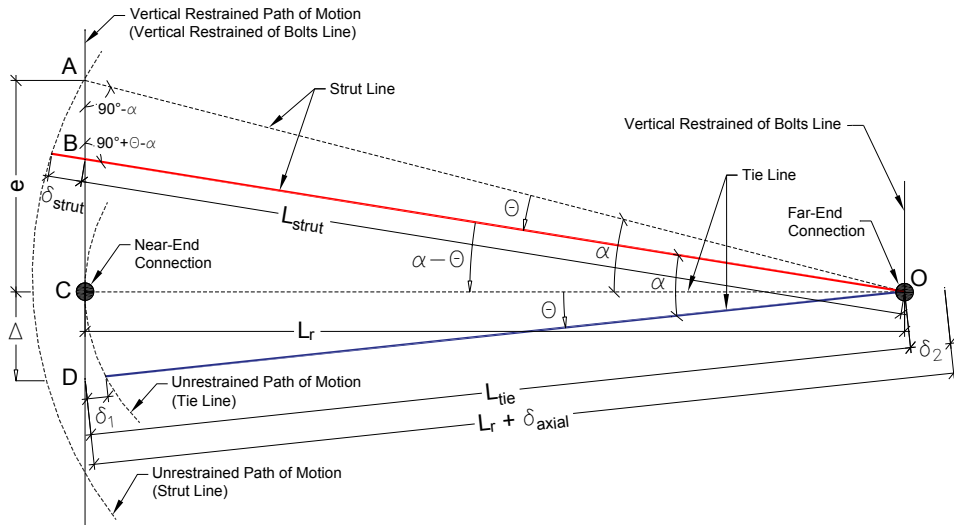
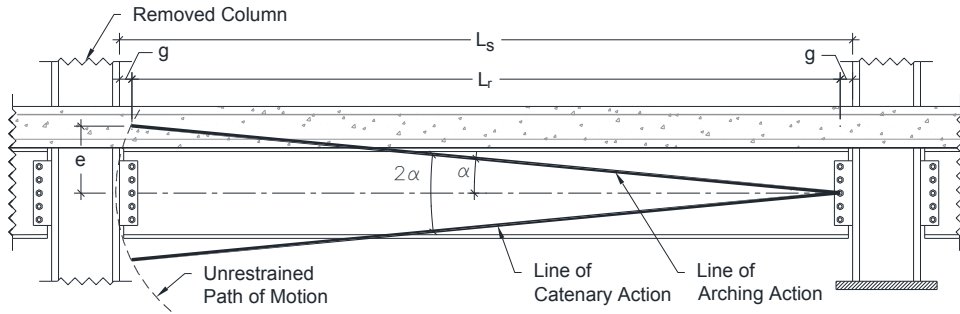


Figure A-4: Geometric Compatibilities of Displacements

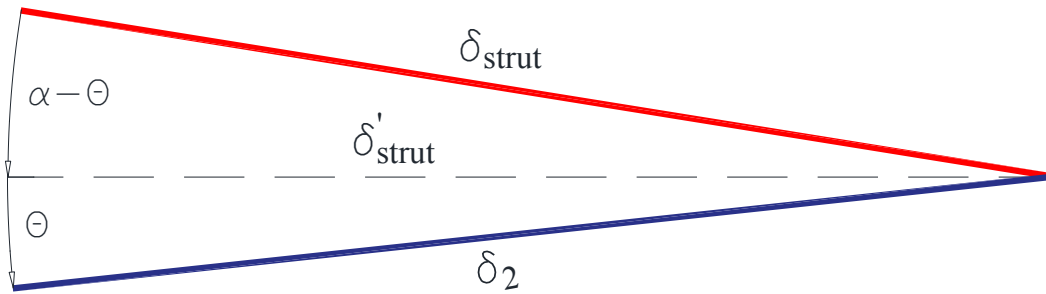


Figure A-5: Projection of Strut Deformation ( $\delta_{strut}$ ) on the Axis of Beam ( $\delta_2$ )

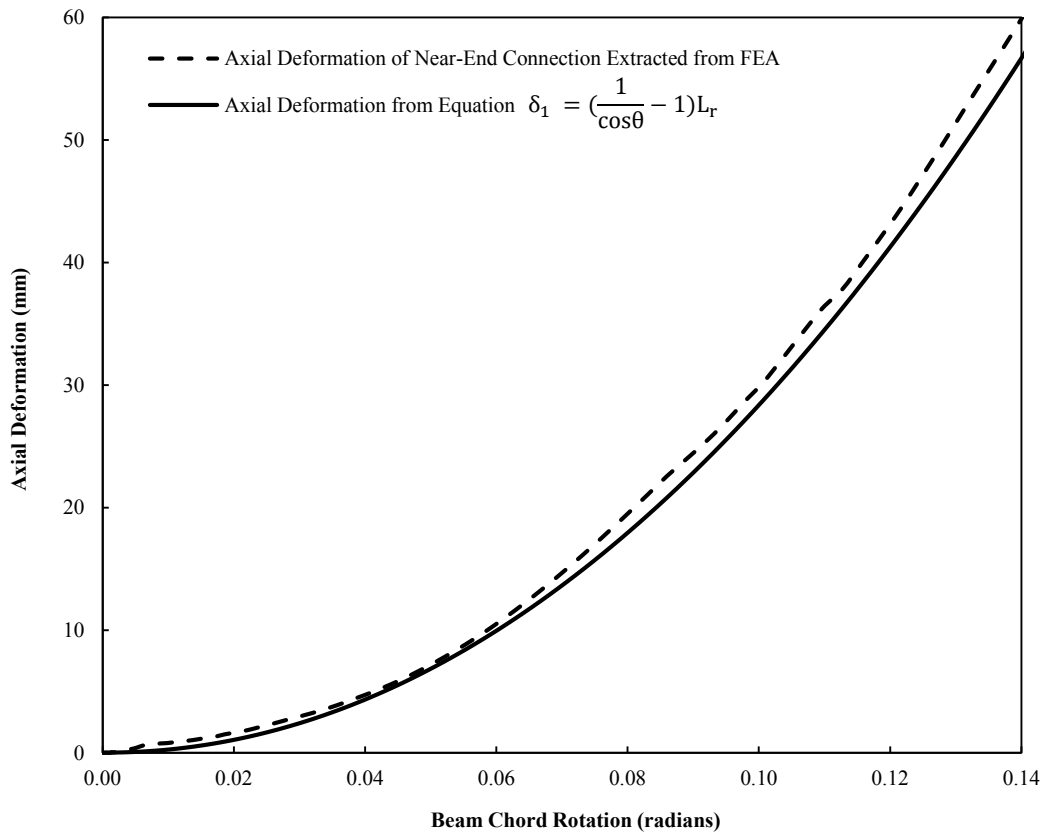
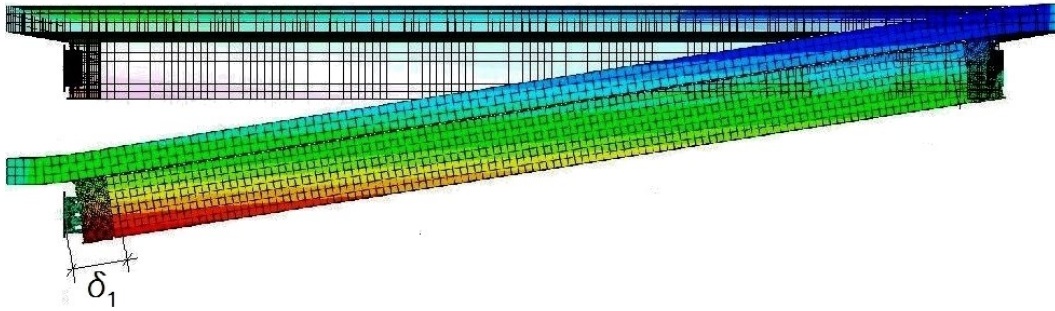
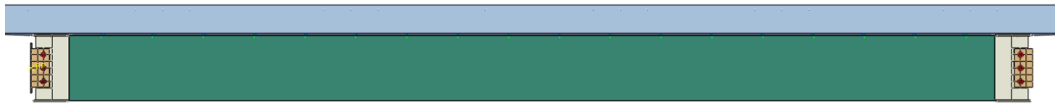


Figure A-6: (a) Undeformed FEA Model; (b) Deformed FEA Model; (c) Axial Deformation of Near-end Connection

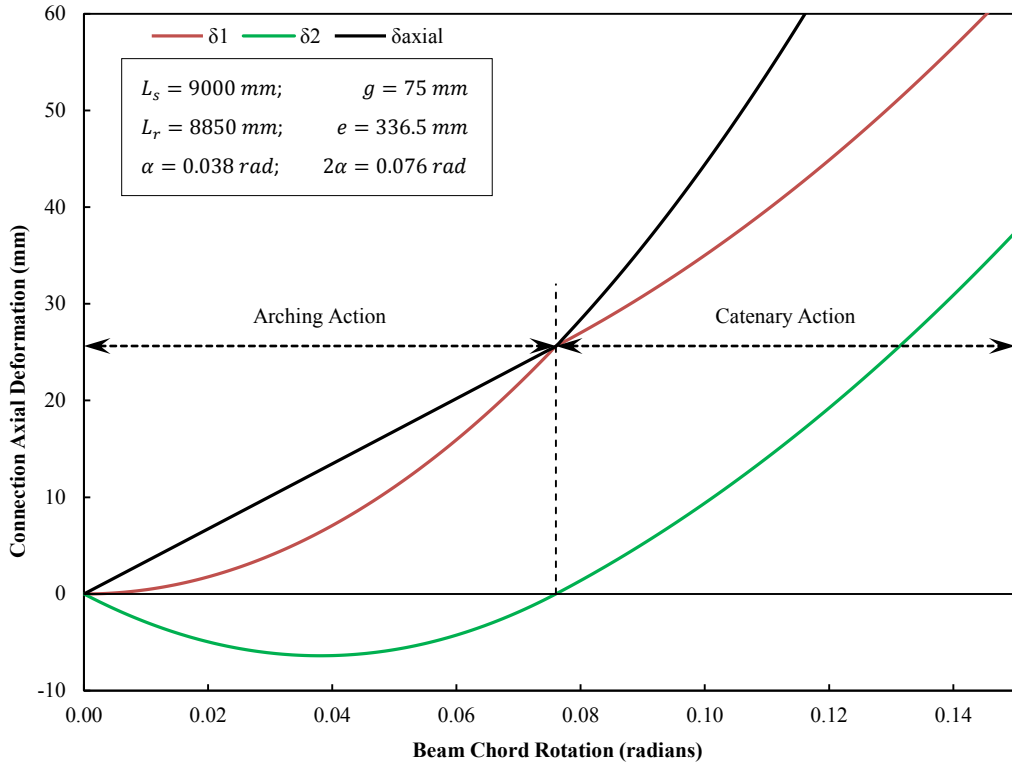


Figure A-7: Axial Deformation of Connections with Span of 9.0 m

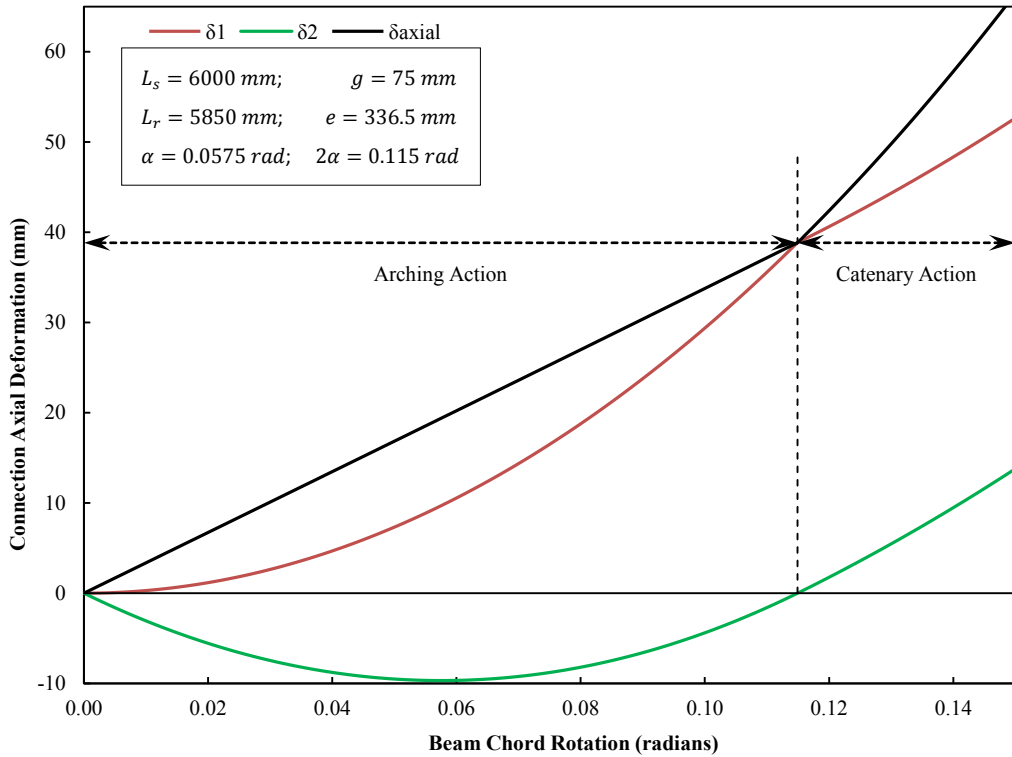


Figure A-8: Axial Deformation of Connections with Span of 6.0 m

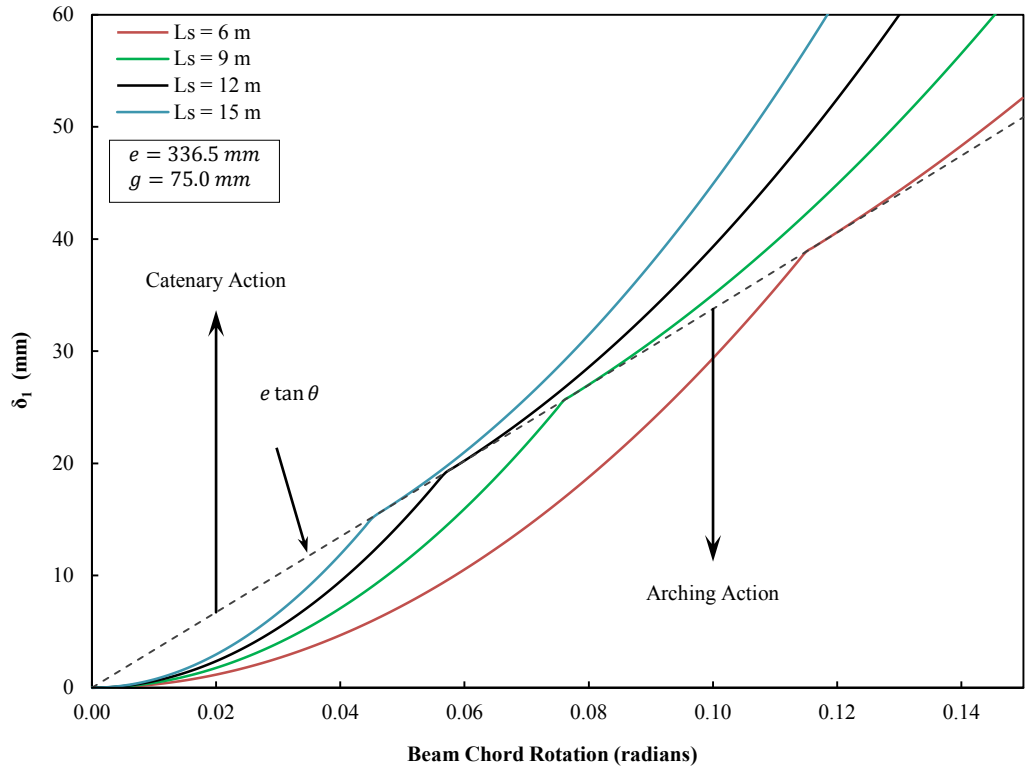


Figure A-9: Axial Deformation of Near-end Connection with Various Spans

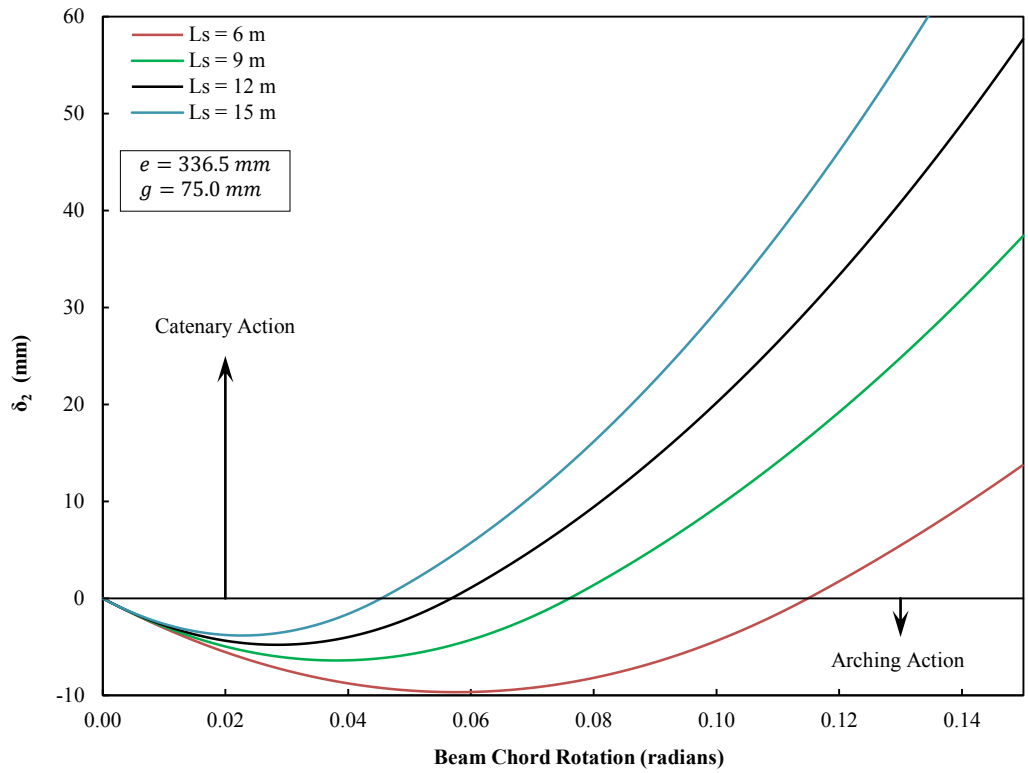


Figure A-10: Axial Deformation of Far-end Connection with Various Spans

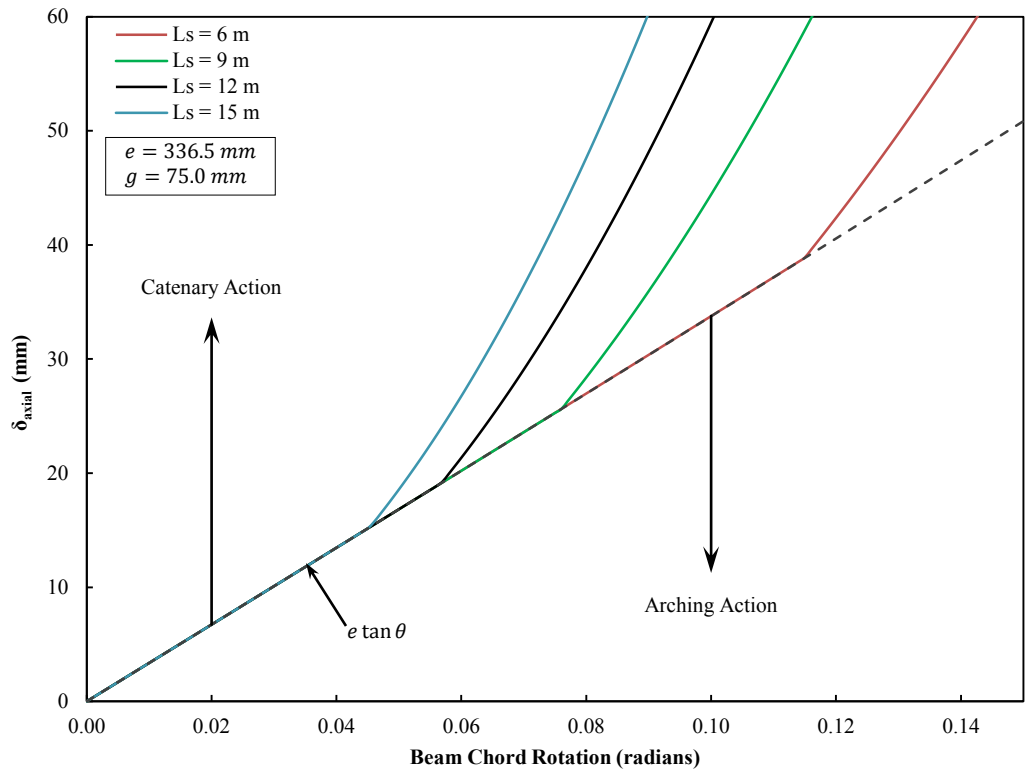


Figure A-11: Total Axial Deformation of Connections with Various Spans

## **APPENDIX B. SHOP DRAWINGS**

This appendix contains the drawing set used to build the formworks and concrete slabs and to fabricate the test specimens. It also shows the test set-up and loading fixtures and elements of the reaction frame used in the experimental program. Scaling factor of 67% has been applied here to the original drawing to accommodate the 8.5"×11" page size of this document.

1 2 3 4 5 6 7 8 9 10 11 12 13 14 15 16

A  
B  
C  
D  
E  
F  
G  
H  
I  
J

# PLANS

OF

TEST PROGRAM ON CONNECTIONS  
CONSIDERING CONCRETE SLAB

DEPARTMENT OF CIVIL & ENVIRONMENTAL ENGINEERING

## UNIVERSITY OF ALBERTA

### SHEET LEGEND

- 01 COVER
- 02 GENERAL NOTES
- 03 TEST SET-UP CONFIGURATION
- 04 TEST SET-UP BEAMS SITTING ON ACTUATORS
- 05 SHEAR TAB CONNECTIONS
- 06 DOUBLE ANGLE CONNECTIONS

PRODUCED BY AN AUTODESK EDUCATIONAL PRODUCT

PRODUCED BY AN AUTODESK EDUCATIONAL PRODUCT

**STEEL PACKAGE**

REVISIONS		
DATE	BY	DESCRIPTION
04/25/13	AJ	DRAWN
05/06/13	RD	REVIEWED
07/28/13	AJ	REVIEWED
08/06/13	RD	REVIEWED
08/06/13	AJ	REVIEWED

COVER

DEPARTMENT OF CIVIL AND ENVIRONMENTAL ENGINEERING  
UNIVERSITY OF ALBERTA



DRAWN BY:  
AMR JAMBHI  
CHECKED BY:  
ROBERT G. DRIVER

SHEET NO.  
01 of 06  
SCALE:  
AS SHOWN

1 2 3 4 5 6 7 8 9 10 11 12 13 14 15 16



**GENERAL NOTES**

- UNLESS NOTED OTHERWISE, ALL DIMENSIONS ARE IN MILLIMETERS.
- DRAWING LAYOUTS ARE TO BE PLOTTED ON 11"x17" SHEETS.
- SHOP DRAWINGS SHALL BE CHECKED AND SUBMITTED FOR REVIEW PRIOR TO FABRICATION.
- ALL CIRCULAR BOLT HOLES SHALL BE DRILLED AND SLOTTED HOLES MAY BE PUNCHED.
- PROVIDE ALL BOLTS COMPLETE WITH NUTS AND FLAT WASHERS.
- SUPPLY A COPY OF MILL TEST REPORTS FOR ALL STRUCTURAL STEEL USED.
- ALL PLATE OF SAME THICKNESS SHALL BE CUT FROM ONE PIECE. ALL W-SHAPES AND ANGLES OF SAME SIZE SHALL BE CUT FROM ONE PIECE (EXCEPTION: W530 AND W310 BEAMS).
- PROVIDE THE FOLLOWING FOR MATERIAL TESTING CUT FROM THE SAME PIECE USED FOR SPECIMENS SHOWN IN SHEET 03 TO SHEET 05:
  - 1-PL500x500x6.4
  - 1-PL500x500x5.5
  - 1-L89x89x6.4 (MIN. 1500 LONG)
  - 1-L89x89x5.5 (MIN. 1500 LONG)
  - 1-W250x89 (MIN. 1000 LONG)
- SOME PIECES REQUIRE PAINTING (SP6 SURFACE PREPARATION, PRIMER PLUS SLATE BLUE FINISH COAT), USE NO PAINT UNLESS NOTED OTHERWISE ON DRAWINGS.
- DO NOT SCALE DRAWINGS. IF CLARIFICATION IS REQUIRED, PLEASE CONTACT:
  - AMIR JAMSHIDI
  - TELL: 780-904-9078
  - EMAIL: AJAMSHIDI@UALBERTA.CA
  - ROBERT DRIVER
  - EMAIL: RDRIVER@UALBERTA.CA

**MATERIALS**

- STRUCTURAL STEEL SHALL BE IN ACCORDANCE WITH CSA G40.20-04/G40.21-04 WITH THE FOLLOWING GRADES:  
 ANGLES AND PLATES: GRADE 300W  
 ROLLED W-SECTIONS: GRADE 350W
- UNLESS NOTED OTHERWISE, BOLTS SHALL BE IN ACCORDANCE WITH ASTM A325.
- WELDING SHALL BE IN ACCORDANCE WITH CSA W59-03. WELDING SHALL BE DONE USING MATCHING ELECTRODES.

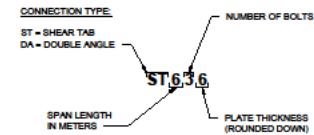
**ABBREVIATIONS**

- @ - AT
- B.S. - BOTH SIDES
- C/C - CENTER TO CENTER
- CJP - COMPLETE JOINT PENETRATION
- CL - CENTER LINE
- CONC. - CONCRETE
- CONT. - CONTINUOUS
- DIA. - DIAMETER
- DWG - DRAWING
- EXIST. - EXISTING
- F/S - FAR SIDE
- ∅ - DIAMETER
- MIN - MINIMUM
- N/S - NEAR SIDE
- PL - PLATE
- QTY. - QUANTITY
- SIM. - SIMILAR
- SYMM - SYMMETRICAL
- T&B - TOP AND BOTTOM
- TYP. - TYPICAL
- U.S. - UNLESS NOTED

**BOLTS SCHEDULE**

BOLT DIA.	BOLT LENGTH	GRADE	QTY.
$\frac{3}{4}$ "	2 $\frac{1}{4}$ "	A325	110
$\frac{7}{8}$ "	2 $\frac{1}{4}$ "	A325	90
$\frac{7}{8}$ "	2 $\frac{1}{4}$ "	A325	20
1"	3 $\frac{1}{4}$ "	A490	70
1"	4"	A490	70

**SPECIMEN DESIGNATION**



REVISIONS		
DATE	BY	DESCRIPTION
04/25/13	AJ	DRAWN
05/06/13	RD	REVIEWED
07/28/13	AJ	REVISED
08/06/13	RD	REVIEWED
08/06/13	AJ	REVISED

**GENERAL NOTES**

DEPARTMENT OF CIVIL AND ENVIRONMENTAL ENGINEERING  
 UNIVERSITY OF ALBERTA

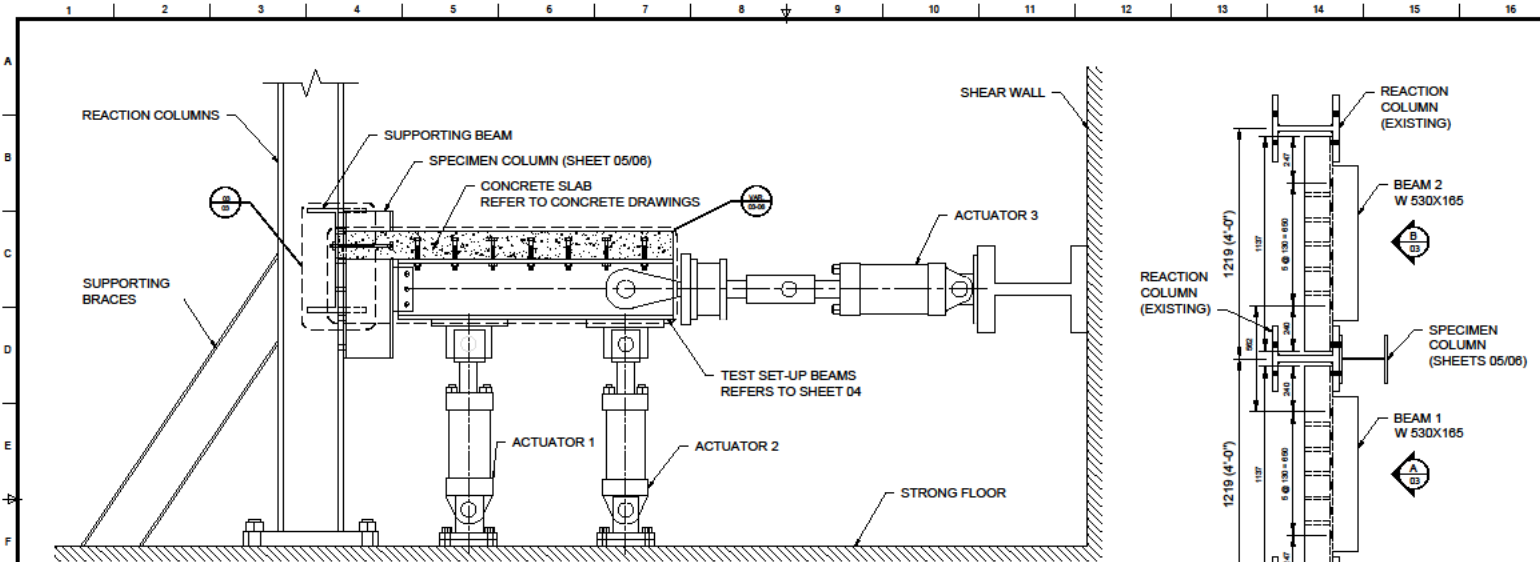


DRAWN BY:  
 AMIR JAMSHIDI

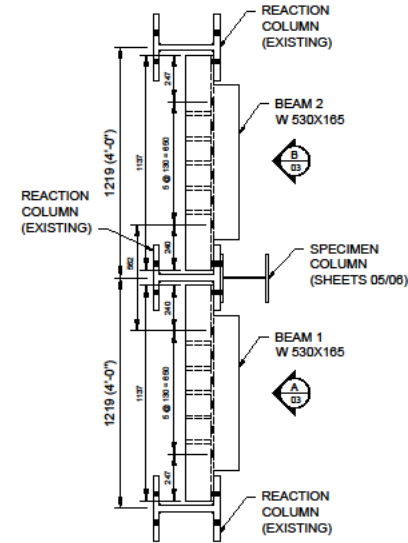
CHECKED BY:  
 ROBERT G. DRIVER

SHEET NO.  
 02 of 06

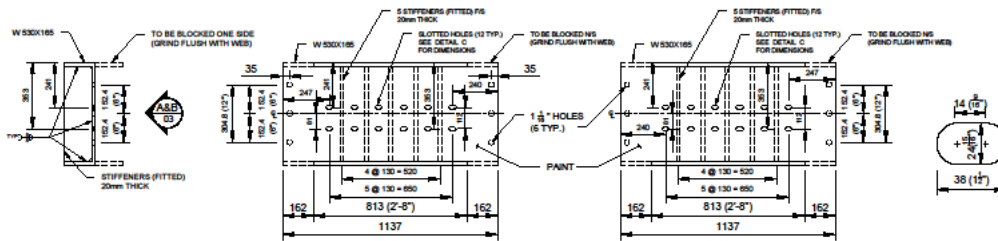
SCALE:  
 AS SHOWN



**01** ELEVATION OF OVERALL TEST SET-UP  
Scale 1:20



**02** PLAN VIEW OF TEST SET-UP  
Scale 1:20



**03** SUPPORTING BEAM  
Scale 1:20

**A** BEAM 1 FRONT VIEW (QTY=1)  
Scale 1:20

**B** BEAM 2 FRONT VIEW (QTY=1)  
Scale 1:20

**C** DETAIL C  
Scale 1:2

REVISIONS		
DATE	BY	DESCRIPTION
04/25/13	AJ	DRAWN
05/06/13	RD	REVIEWED
07/28/13	AJ	REVIEWED
08/06/13	RD	REVIEWED
08/06/13	AJ	REVIEWED

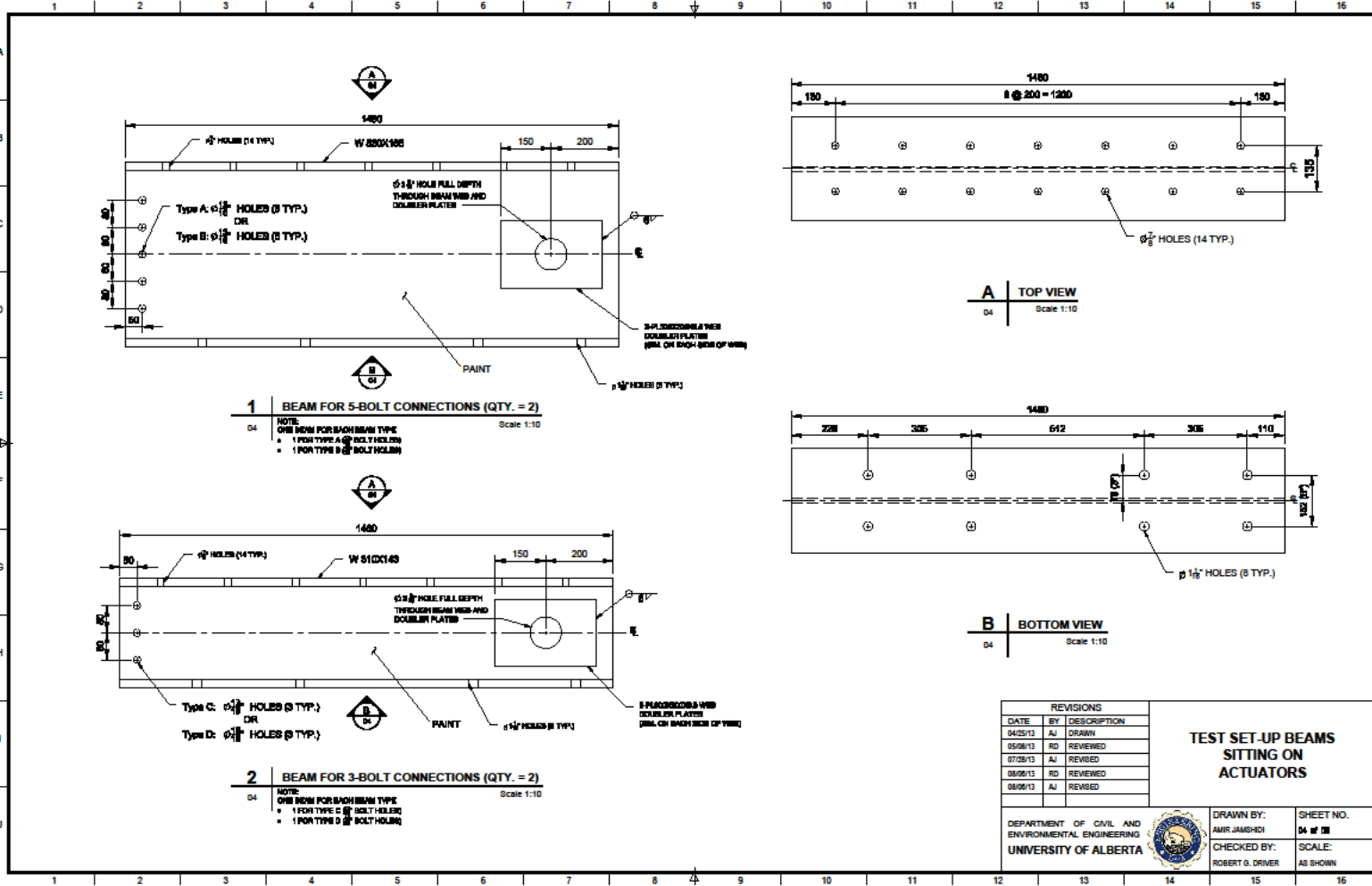
**TEST SET-UP CONFIGURATION**

DEPARTMENT OF CIVIL AND ENVIRONMENTAL ENGINEERING  
UNIVERSITY OF ALBERTA



DRAWN BY:  
AMR JAMSHIDI  
CHECKED BY:  
ROBERT G. DRIVER

SHEET NO.  
1 of 8  
SCALE:  
AS SHOWN



REVISIONS	
DATE	DESCRIPTION
04/25/13	AJ DRAWN
05/06/13	RD REVIEWED
07/28/13	AJ REVIEWED
08/06/13	RD REVIEWED
08/06/13	AJ REVIEWED

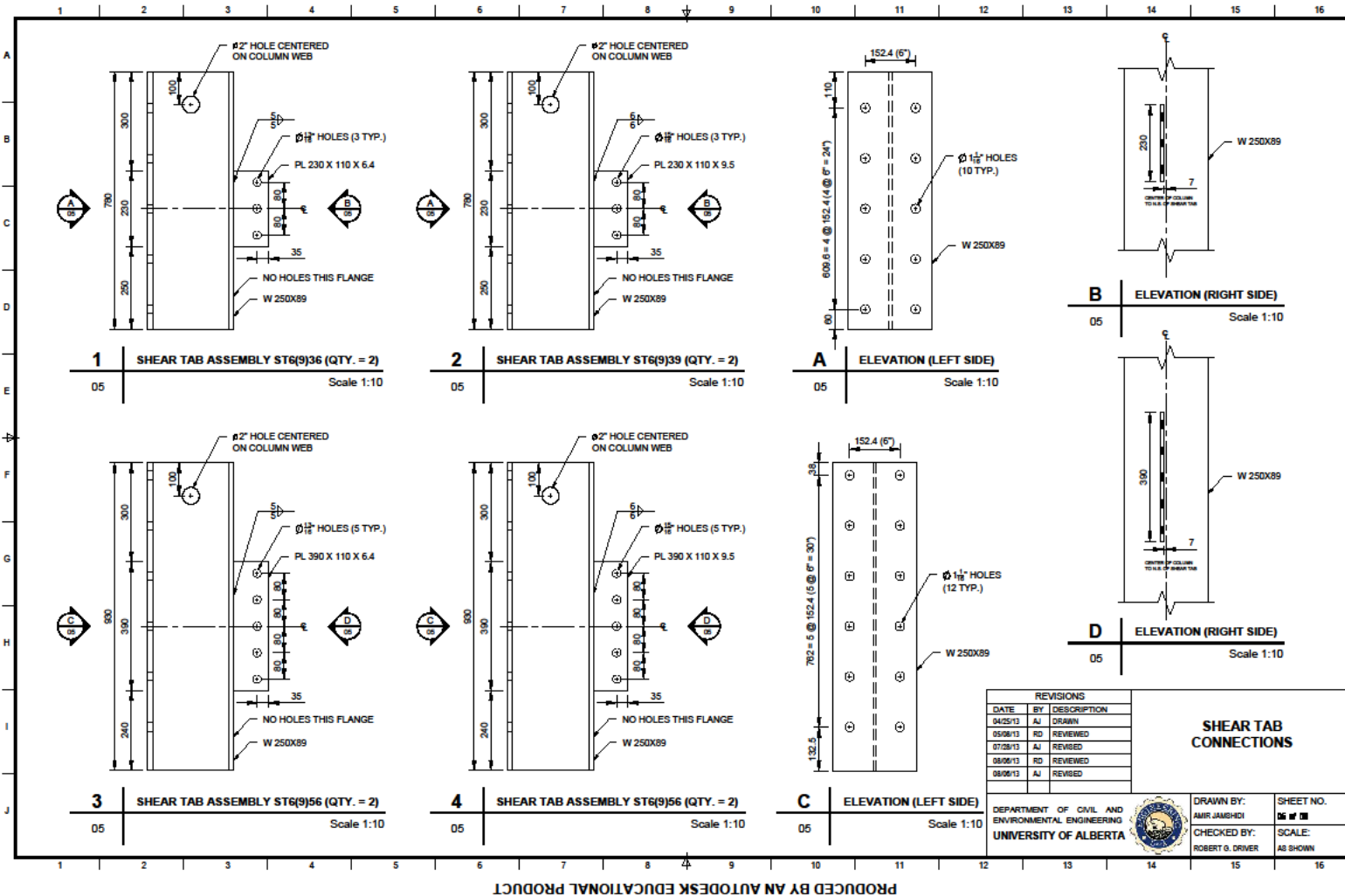
**TEST SET-UP BEAMS  
SITTING ON  
ACTUATORS**

DEPARTMENT OF CIVIL AND ENVIRONMENTAL ENGINEERING  
UNIVERSITY OF ALBERTA



DRAWN BY:  
AMR JAMSHIDI  
CHECKED BY:  
ROBERT G. DRIVER

SHEET NO.  
04 of 08  
SCALE:  
AS SHOWN



REVISIONS		
DATE	BY	DESCRIPTION
04/25/13	AJ	DRAWN
05/06/13	RD	REVIEWED
07/28/13	AJ	REVISED
08/06/13	RD	REVIEWED
08/06/13	AJ	REVISED

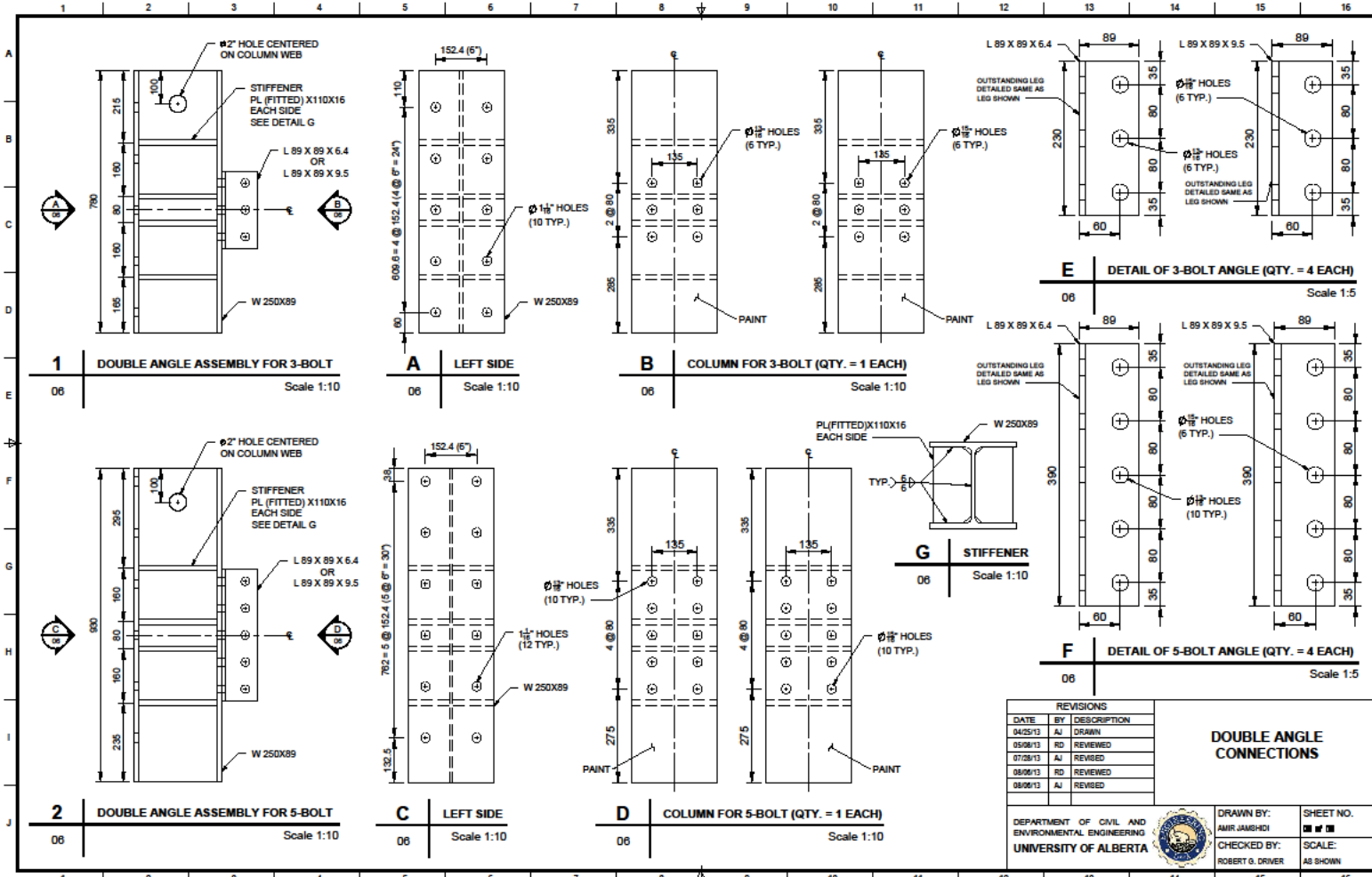
**SHEAR TAB CONNECTIONS**

DEPARTMENT OF CIVIL AND ENVIRONMENTAL ENGINEERING  
UNIVERSITY OF ALBERTA

DRAWN BY: AMR JAMSHIDI  
CHECKED BY: ROBERT G. DRIVER

SHEET NO. **06 of 08**  
SCALE: AS SHOWN





REVISIONS		
DATE	BY	DESCRIPTION
04/25/13	AJ	DRAWN
05/06/13	RD	REVIEWED
07/28/13	AJ	REVIEWED
08/06/13	RD	REVIEWED
08/06/13	AJ	REVIEWED

**DOUBLE ANGLE CONNECTIONS**

DEPARTMENT OF CIVIL AND ENVIRONMENTAL ENGINEERING  
UNIVERSITY OF ALBERTA



DRAWN BY: AMR JAMSHIDI  
CHECKED BY: ROBERT G. DRIVER

SHEET NO. 14 of 14  
SCALE: AS SHOWN

1 2 3 4 5 6 7 8 9 10 11 12 13 14 15 16

A  
B  
C  
D  
E  
F  
G  
H  
I  
J

# PLANS

OF

TEST PROGRAM ON CONNECTIONS  
CONSIDERING CONCRETE SLAB

DEPARTMENT OF CIVIL & ENVIRONMENTAL ENGINEERING

## UNIVERSITY OF ALBERTA

### SHEET LEGEND

- 01 COVER
- 02 GENERAL NOTES
- 03 REINFORCED CONCRETE SLAB
- 04 POSITION OF REINFORCED CONCRETE SLAB ON TEST SET-UP
- 05 DIMENSIONS OF CONCRETE SLABS TO BE USED FOR FORMWORK
- 06 FORMWORKS DIMENSION

### CONCRETE PACKAGE

REVISIONS		
DATE	BY	DESCRIPTION
04/25/13	AJ	DRAWN
05/06/13	RD	REVIEWED
07/28/13	AJ	REVIEWED
08/06/13	RD	REVIEWED
10/30/13	AJ	REVIEWED
10/30/13	AJ	PRINT

COVER

DEPARTMENT OF CIVIL AND ENVIRONMENTAL ENGINEERING  
UNIVERSITY OF ALBERTA



DRAWN BY:  
AMR JAMSHIDI  
CHECKED BY:  
ROBERT G. ORMER

SHEET NO.  
01 of 06  
SCALE:  
AS SHOWN

1 2 3 4 5 6 7 8 9 10 11 12 13 14 15 16

**GENERAL NOTES**

- UNLESS NOTED OTHERWISE, ALL DIMENSIONS ARE IN MILLIMETERS.
- DRAWING LAYOUTS ARE TO BE PLOTTED ON 11"x17" SHEETS.
- SHOP DRAWINGS SHALL BE CHECKED AND SUBMITTED FOR REVIEW PRIOR TO FABRICATION.
- ALL CIRCULAR BOLT HOLES SHALL BE DRILLED AND SLOTTED HOLES MAY BE PUNCHED.
- PROVIDE ALL BOLTS COMPLETE WITH NUTS AND FLAT WASHERS.
- SUPPLY A COPY OF MILL TEST REPORTS FOR ALL STRUCTURAL STEEL AND REBARS USED.
- ALL PLATE OF SAME THICKNESS SHALL BE CUT FROM ONE PIECE. ALL W-SHAPES AND ANGLES OF SAME SIZE SHALL BE CUT FROM ONE PIECE (EXCEPTION: W530 AND W310 BEAMS).
- PROVIDE THE FOLLOWING FOR MATERIAL TESTING CUT FROM THE SAME PIECE USED FOR SPECIMENS SHOWN IN SHEET 03 TO SHEET 09:  
 1-PL500x500x6.4  
 1-PL500x500x9.5  
 1-L89x89x6.4 (MIN. 1500 LONG)  
 1-L89x89x9.5 (MIN. 1500 LONG)  
 1-W250x89 (MIN. 1000 LONG)
- PROVIDE REBARS USED IN CONCRETE SLAB FOR MATERIAL TESTING (MINIMUM 1500mm LONG).
- SOME PIECES REQUIRE PAINTING (SP6 SURFACE PREPARATION, PRIMER PLUS SLATE BLUE FINISH COAT). USE NO PAINT UNLESS NOTED OTHERWISE ON DRAWINGS.
- DO NOT SCALE DRAWINGS. IF CLARIFICATION IS REQUIRED, PLEASE CONTACT:  
 AMIR JAMSHIDI  
 TELL: 780-904-9078  
 EMAIL: AJAMSHIDI@UALBERTA.CA  
 ROBERT DRIVER  
 EMAIL: RDRIVER@UALBERTA.CA

**MATERIALS**

- STRUCTURAL STEEL SHALL BE IN ACCORDANCE WITH CSA G40.20-04/G40.21-04 WITH THE FOLLOWING GRADES:  
 ANGLES AND PLATES: GRADE 300W  
 ROLLED W-SECTIONS: GRADE 350W
- UNLESS NOTED OTHERWISE, BOLTS SHALL BE IN ACCORDANCE WITH ASTM A325.
- WELDING SHALL BE IN ACCORDANCE WITH CSA W59-03. WELDING SHALL BE DONE USING MATCHING ELECTRODES.
- CONCRETE SLAB SHALL HAVE A MINIMUM COMPRESSIVE STRENGTH OF 25 MPa AND MAXIMUM COMPRESSIVE STRENGTH OF 35 MPa AT 28 DAYS.
- REINFORCEMENT FOR THE CONCRETE SLAB SHALL BE 10M FROM GRADE 400 IN ACCORDANCE WITH CAN/CSA G30.18-M92.

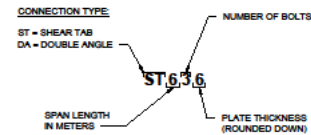
**ABBREVIATIONS**

- @ - AT
- B.S. - BOTH SIDES
- C/C - CENTER TO CENTER
- CJP - COMPLETE JOINT PENETRATION
- CL - CENTER LINE
- CONC. - CONCRETE
- CONT. - CONTINUOUS
- DIA. - DIAMETER
- DWG - DRAWING
- EXIST. - EXISTING
- F/S - FAR SIDE
- ∅ - DIAMETER
- MIN - MINIMUM
- N/S - NEAR SIDE
- PL - PLATE
- QTY. - QUANTITY
- SIM. - SIMILAR
- SYMM - SYMMETRICAL
- T&B - TOP AND BOTTOM
- TYP. - TYPICAL
- U.S. - UNLESS NOTED

**BOLTS SCHEDULE**

BOLT DIA.	BOLT LENGTH	GRADE	QTY.
$\frac{3}{4}$ "	2 $\frac{1}{2}$ "	A325	110
$\frac{7}{8}$ "	2 $\frac{1}{2}$ "	A325	90
$\frac{7}{8}$ "	2 $\frac{1}{2}$ "	A325	20
1"	3 $\frac{1}{2}$ "	A490	70
1"	4"	A490	70

**SPECIMEN DESIGNATION**



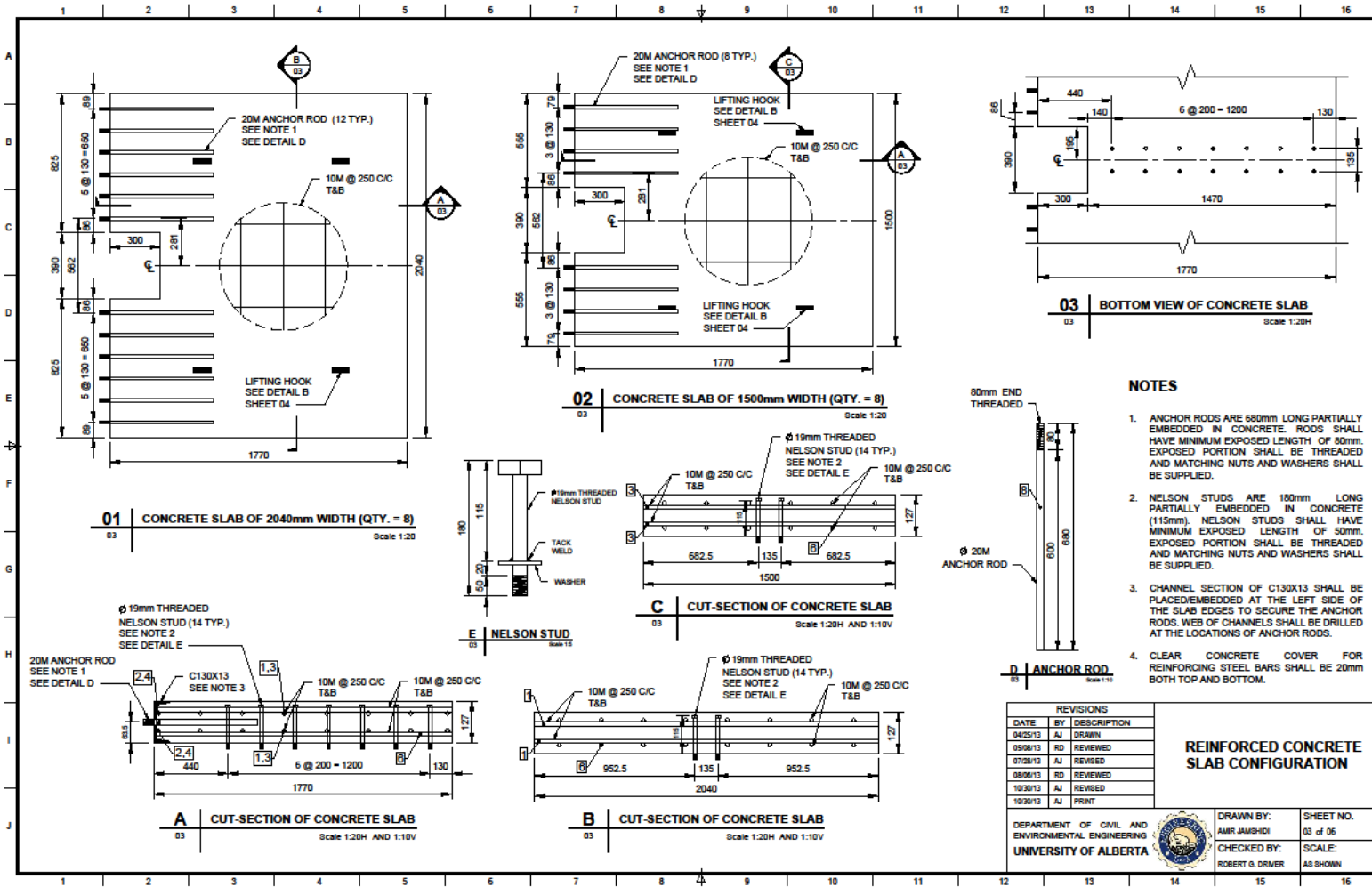
REVISIONS		
DATE	BY	DESCRIPTION
04/25/13	AJ	DRAWN
05/06/13	RD	REVIEWED
07/28/13	AJ	REVISED
08/06/13	RD	REVIEWED
10/30/13	AJ	REVISED
10/30/13	AJ	PRINT

**GENERAL NOTES**

DEPARTMENT OF CIVIL AND ENVIRONMENTAL ENGINEERING  
 UNIVERSITY OF ALBERTA



DRAWN BY:  
 AMR JAMSHIDI  
 SHEET NO.  
 02 of 06  
 CHECKED BY:  
 ROBERT G. DRIVER  
 SCALE:  
 AS SHOWN



**NOTES**

- ANCHOR RODS ARE 680mm LONG PARTIALLY EMBEDDED IN CONCRETE. RODS SHALL HAVE MINIMUM EXPOSED LENGTH OF 80mm. EXPOSED PORTION SHALL BE THREADED AND MATCHING NUTS AND WASHERS SHALL BE SUPPLIED.
- NELSON STUDS ARE 180mm LONG PARTIALLY EMBEDDED IN CONCRETE (115mm). NELSON STUDS SHALL HAVE MINIMUM EXPOSED LENGTH OF 50mm. EXPOSED PORTION SHALL BE THREADED AND MATCHING NUTS AND WASHERS SHALL BE SUPPLIED.
- CHANNEL SECTION OF C130X13 SHALL BE PLACED EMBEDDED AT THE LEFT SIDE OF THE SLAB EDGES TO SECURE THE ANCHOR RODS. WEB OF CHANNELS SHALL BE DRILLED AT THE LOCATIONS OF ANCHOR RODS.
- CLEAR CONCRETE COVER FOR REINFORCING STEEL BARS SHALL BE 20mm BOTH TOP AND BOTTOM.

REVISIONS		
DATE	BY	DESCRIPTION
04/25/13	AJ	DRAWN
05/06/13	RD	REVIEWED
07/28/13	AJ	REVISED
08/06/13	RD	REVIEWED
10/30/13	AJ	REVISED
10/30/13	AJ	PRINT

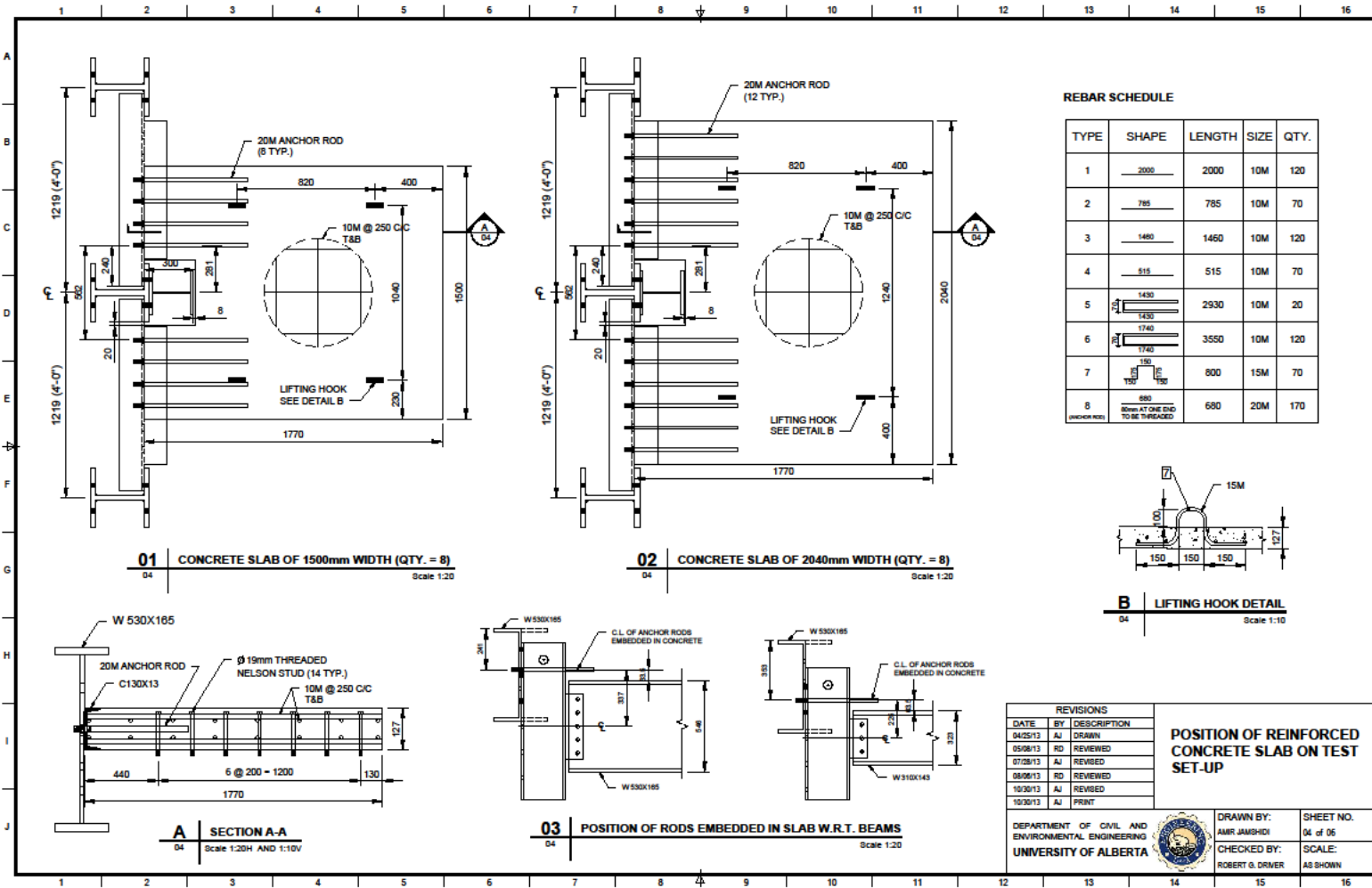
**REINFORCED CONCRETE SLAB CONFIGURATION**

DEPARTMENT OF CIVIL AND ENVIRONMENTAL ENGINEERING  
UNIVERSITY OF ALBERTA

DRAWN BY: AMR JAMSHDI  
CHECKED BY: ROBERT G. ORMER

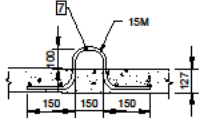
SHEET NO. 03 of 06  
SCALE: AS SHOWN





**REBAR SCHEDULE**

TYPE	SHAPE	LENGTH	SIZE	QTY.
1	2000	2000	10M	120
2	785	785	10M	70
3	1480	1460	10M	120
4	515	515	10M	70
5	1430	2930	10M	20
6	1430 1740	3550	10M	120
7	150	800	15M	70
8	680 80mm AT ONE END TO BE THREADED	680	20M	170



**B** LIFTING HOOK DETAIL  
Scale 1:10

REVISIONS		
DATE	BY	DESCRIPTION
04/25/13	AJ	DRAWN
05/06/13	RD	REVIEWED
07/28/13	AJ	REVIEWED
08/06/13	RD	REVIEWED
10/30/13	AJ	REVIEWED
10/30/13	AJ	PRINT

**POSITION OF REINFORCED CONCRETE SLAB ON TEST SET-UP**

DEPARTMENT OF CIVIL AND ENVIRONMENTAL ENGINEERING  
UNIVERSITY OF ALBERTA

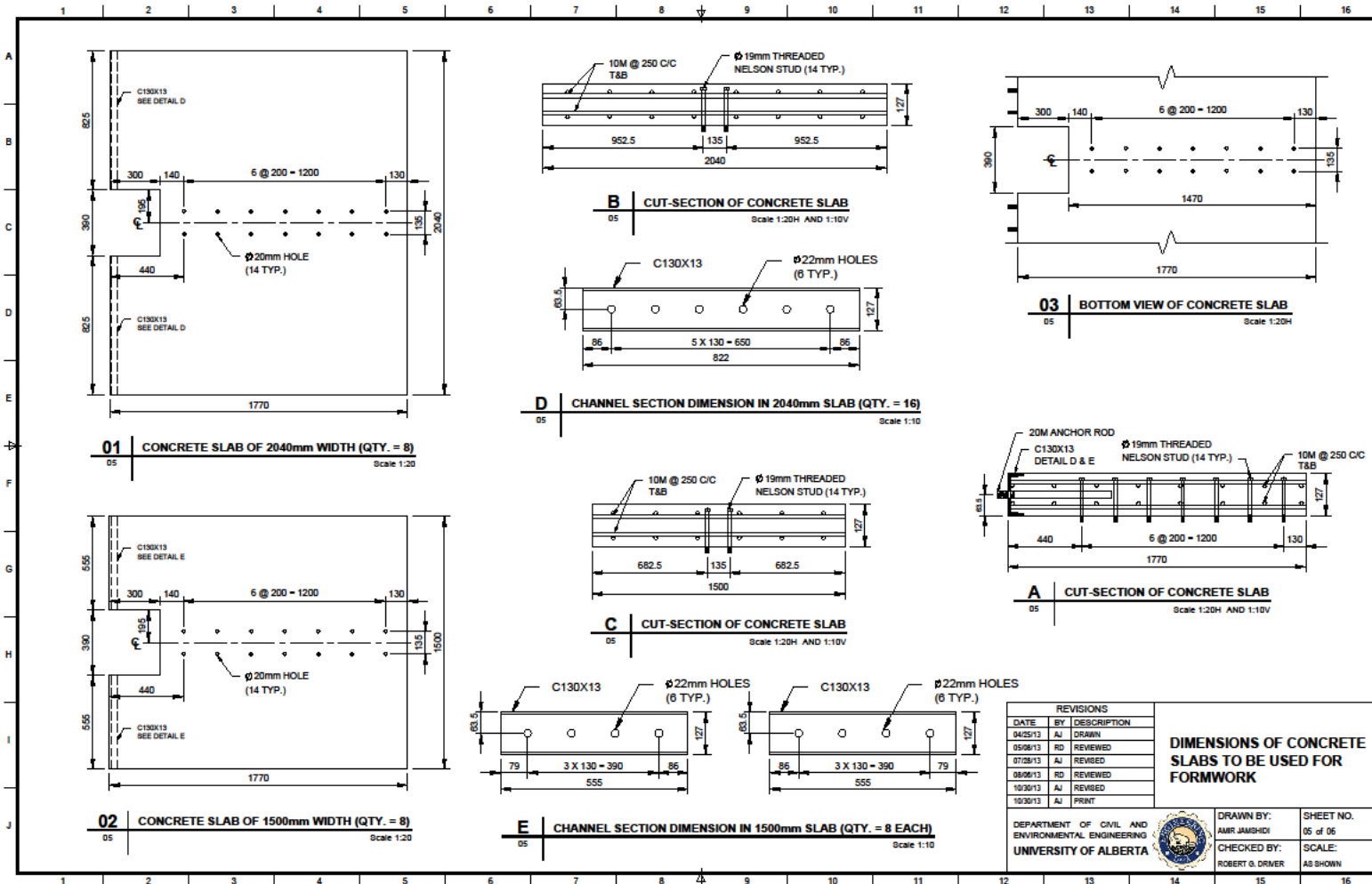


DRAWN BY:  
AMR JAMSHIDI

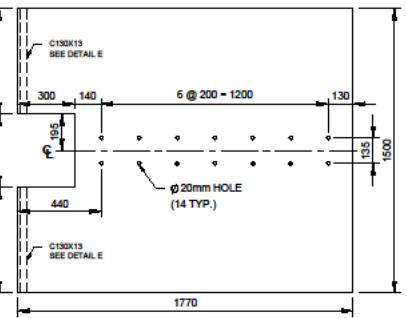
CHECKED BY:  
ROBERT G. ORMER

SHEET NO.  
04 of 06

SCALE:  
AS SHOWN

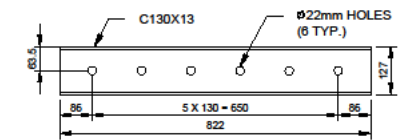


**01** CONCRETE SLAB OF 2040mm WIDTH (QTY. = 8)  
Scale 1:20

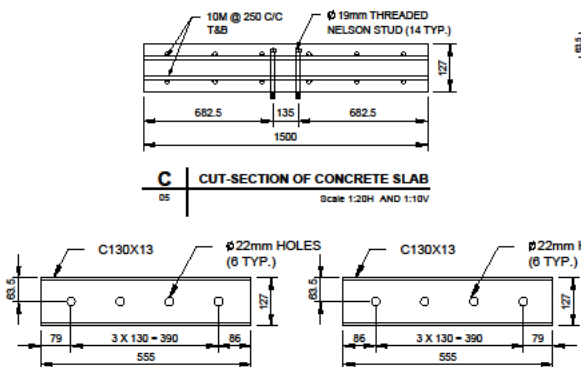


**02** CONCRETE SLAB OF 1500mm WIDTH (QTY. = 8)  
Scale 1:20

**B** CUT-SECTION OF CONCRETE SLAB  
Scale 1:20H AND 1:10V

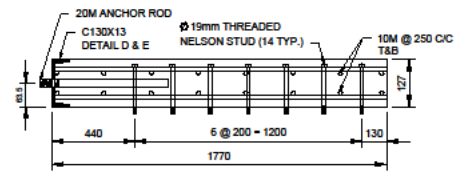


**D** CHANNEL SECTION DIMENSION IN 2040mm SLAB (QTY. = 16)  
Scale 1:10



**E** CHANNEL SECTION DIMENSION IN 1500mm SLAB (QTY. = 8 EACH)  
Scale 1:10

**03** BOTTOM VIEW OF CONCRETE SLAB  
Scale 1:20H



**A** CUT-SECTION OF CONCRETE SLAB  
Scale 1:20H AND 1:10V

REVISIONS		
DATE	BY	DESCRIPTION
04/25/13	AJ	DRAWN
05/06/13	RD	REVIEWED
07/28/13	AJ	REVISED
08/06/13	RD	REVIEWED
10/30/13	AJ	REVISED
10/30/13	AJ	PRINT

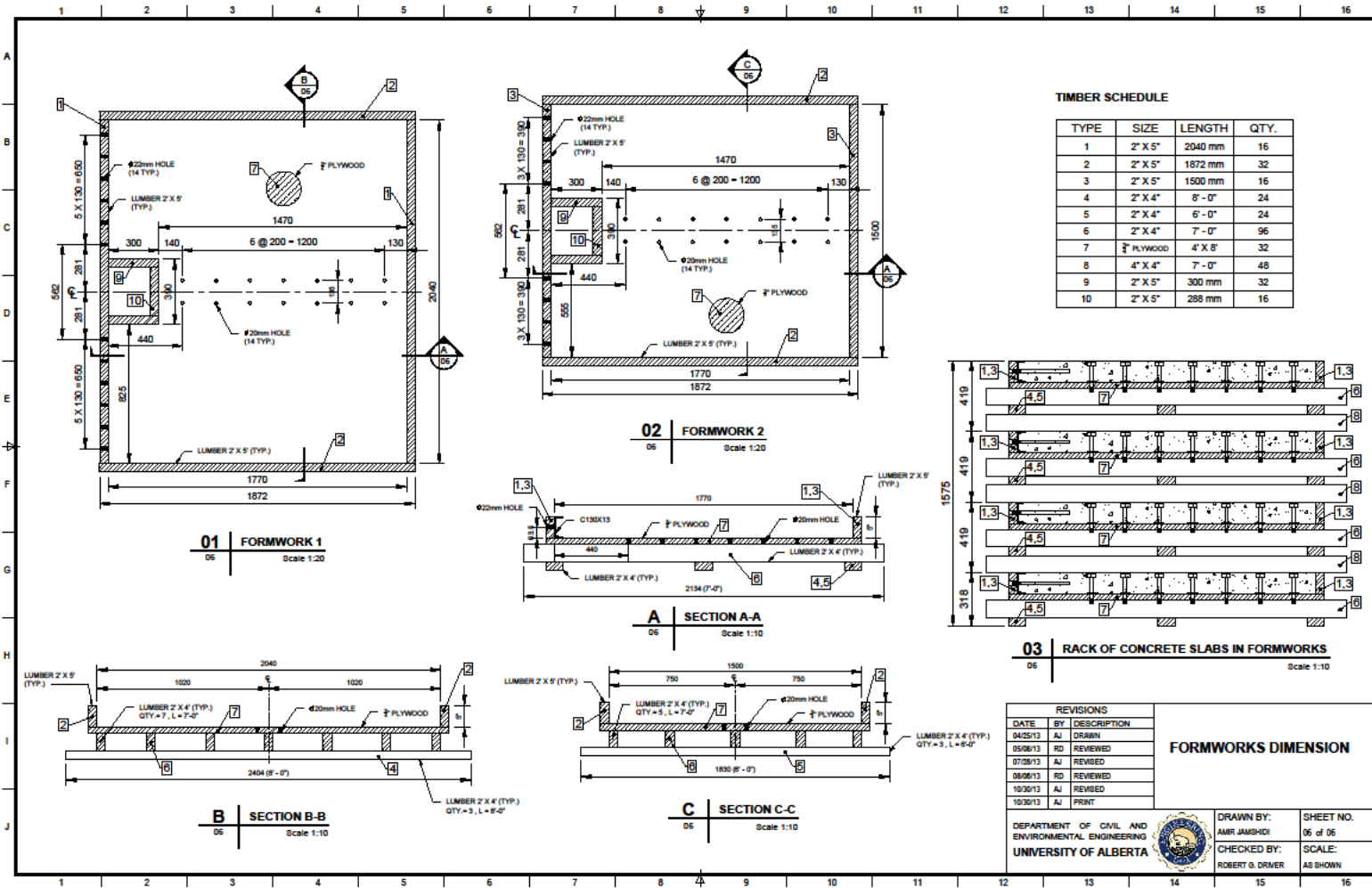
**DIMENSIONS OF CONCRETE SLABS TO BE USED FOR FORMWORK**

DEPARTMENT OF CIVIL AND ENVIRONMENTAL ENGINEERING  
UNIVERSITY OF ALBERTA



DRAWN BY:  
AMR JAMSHIDI  
CHECKED BY:  
ROBERT G. ORMER

SHEET NO.  
05 of 06  
SCALE:  
AS SHOWN



**TIMBER SCHEDULE**

TYPE	SIZE	LENGTH	QTY.
1	2" X 5"	2040 mm	16
2	2" X 5"	1872 mm	32
3	2" X 5"	1500 mm	16
4	2" X 4"	8'-0"	24
5	2" X 4"	6'-0"	24
6	2" X 4"	7'-0"	96
7	PLYWOOD	4' X 8'	32
8	4" X 4"	7'-0"	48
9	2" X 5"	300 mm	32
10	2" X 5"	288 mm	16

REVISIONS		
DATE	BY	DESCRIPTION
04/25/13	AJ	DRAWN
05/06/13	RD	REVIEWED
07/28/13	AJ	REVIEWED
08/06/13	RD	REVIEWED
10/30/13	AJ	REVIEWED
10/30/13	AJ	PRINT

**FORMWORKS DIMENSION**

DEPARTMENT OF CIVIL AND ENVIRONMENTAL ENGINEERING  
UNIVERSITY OF ALBERTA

DRAWN BY:  
AMR JAMSHIDI

CHECKED BY:  
ROBERT G. ORMER

SHEET NO.  
06 of 06

SCALE:  
AS SHOWN

# PLANS

OF

EXPERIMENTAL TEST PROGRAM ON STEEL  
CONNECTIONS CONSIDERING CONCRETE SLAB

DEPARTMENT OF CIVIL AND  
ENVIRONMENTAL ENGINEERING  
**UNIVERSITY OF ALBERTA**

### SHEET LEGEND

- 01 COVER
- 02 GENERAL NOTES
- 03 SHEAR-TAB AND DOUBLE ANGLE CONNECTIONS (THICKNESS OF 9.5mm)

REVISIONS		
DATE	BY	DESCRIPTION
03/18/14	AJ	DRAWN
03/18/14	RD	REVIEWED

COVER

**"REORDERED"**

DEPARTMENT OF CIVIL AND ENVIRONMENTAL ENGINEERING  
UNIVERSITY OF ALBERTA



DRAWN BY:  
AMR JAMHDI  
CHECKED BY:  
ROBERT G. DRIVER

SHEET NO.  
01 of 03  
SCALE:  
AS SHOWN

**GENERAL NOTES**

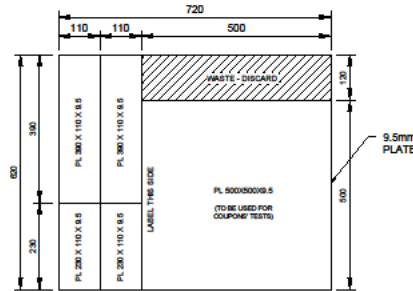
- UNLESS NOTED OTHERWISE, ALL DIMENSIONS ARE IN MILLIMETERS.
- DRAWING LAYOUTS ARE TO BE PLOTTED ON 11"x17" SHEETS.
- SHOP DRAWINGS SHALL BE CHECKED AND SUBMITTED FOR REVIEW PRIOR TO FABRICATION.
- ALL CIRCULAR BOLT HOLES SHALL BE DRILLED AND SLOTTED HOLES MAY BE PUNCHED.
- SUPPLY A COPY OF **MILL TEST REPORTS (MTRS) BEFORE ANY FABRICATIONS** FOR ALL STRUCTURAL STEEL USED.
- ALL PLATE OF SAME THICKNESS SHALL BE CUT FROM ONE PIECE. ALL W-SHAPES AND ANGLES OF SAME SIZE SHALL BE CUT FROM ONE PIECE.
- PROVIDE THE FOLLOWINGS FOR MATERIAL TESTING CUT FROM THE SAME PIECE USED FOR SPECIMENS SHOWN IN SHEET 03:  
 1-PL500x500x9.5 (**CUT-OUT PATTERN IS SHOWN IN DETAIL 1 OF SHEET 02**)  
 1-L89x89x9.5 (MIN. 1000 LONG)  
 1-W250x89 (MIN. 1000 LONG)
- DO NOT SCALE DRAWINGS. IF CLARIFICATION IS REQUIRED, PLEASE CONTACT:

AMIR JAMSHIDI  
 CELL: 780-904-9078  
 EMAIL: AJAMSHIDI@UALBERTA.CA

ROBERT DRIVER  
 EMAIL: RDRIVER@UALBERTA.CA

**MATERIALS**

- STRUCTURAL STEEL SHALL BE GRADE **350W** IN ACCORDANCE WITH CSA G40.20-04/G40.21-04.
- WELDING SHALL BE IN ACCORDANCE WITH CSA W59-03. WELDING SHALL BE DONE USING MATCHING ELECTRODES.



**1** | 9.5mm PLATE CUT-OUT PATTERN  
 02 | Scale 1:10

**ABBREVIATIONS**

- @ - AT
- B.S. - BOTH SIDES
- C/C - CENTER TO CENTER
- CJP - COMPLETE JOINT PENETRATION
- CL - CENTER LINE
- DIA. - DIAMETER
- DRWG - DRAWING
- F.S. - FAR SIDE
- Ø - DIAMETER
- MIN - MINIMUM
- N.S. - NEAR SIDE
- PL - PLATE
- QTY. - QUANTITY
- SYM. - SYMMETRICAL
- TYP. - TYPICAL
- UNO - UNLESS NOTED OTHERWISE

REVISIONS		
DATE	BY	DESCRIPTION
03/18/14	AJ	DRAWN
03/18/14	RD	REVIEWED

**GENERAL NOTES**

DEPARTMENT OF CIVIL AND ENVIRONMENTAL ENGINEERING  
 UNIVERSITY OF ALBERTA

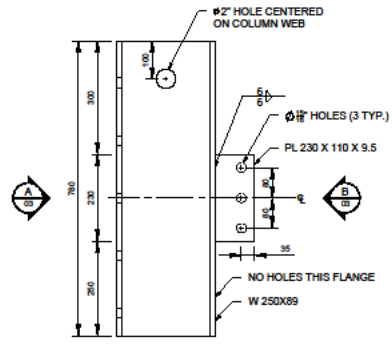


DRAWN BY:  
 AMIR JAMSHIDI

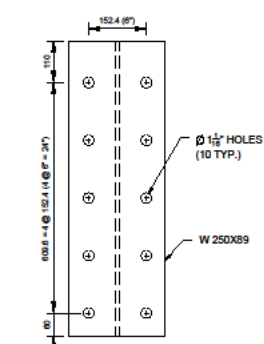
CHECKED BY:  
 ROBERT G. DRIVER

SHEET NO.  
 02 of 03

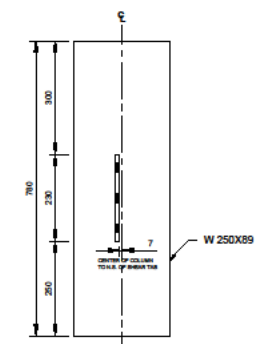
SCALE:  
 AS SHOWN



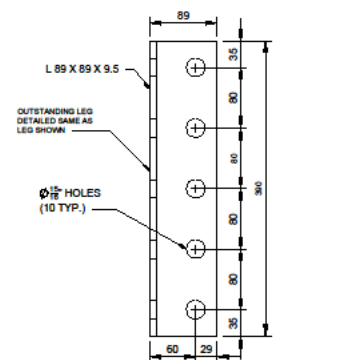
**1 SHEAR-TAB ASSEMBLY - 3 BOLTS (QTY. = 2)**  
Scale 1:10



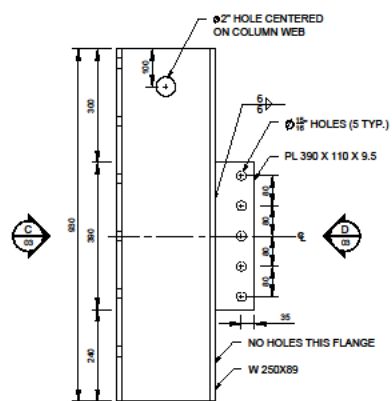
**A ELEVATION (LEFT VIEW)**  
Scale 1:10



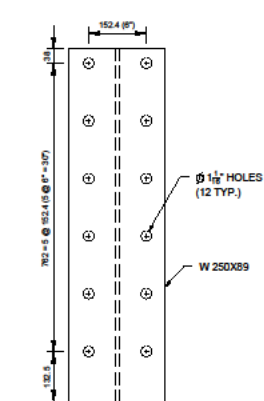
**B ELEVATION (RIGHT VIEW)**  
Scale 1:10



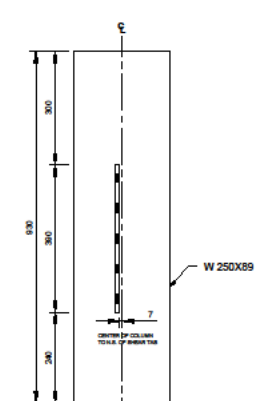
**3 DETAIL OF 5-BOLT ANGLE (QTY. = 4 EACH)**  
Scale 1:5



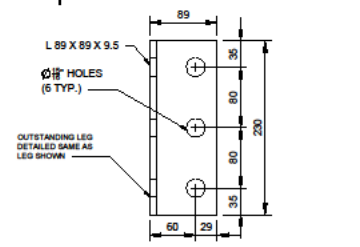
**2 SHEAR-TAB ASSEMBLY - 5 BOLTS (QTY. = 2)**  
Scale 1:10



**C ELEVATION (LEFT VIEW)**  
Scale 1:10



**D ELEVATION (RIGHT VIEW)**  
Scale 1:10



**4 DETAIL OF 3-BOLT ANGLE (QTY. = 4 EACH)**  
Scale 1:5

REVISIONS		
DATE	BY	DESCRIPTION
03/15/14	AJ	DRAWN
03/15/14	RD	REVIEWED

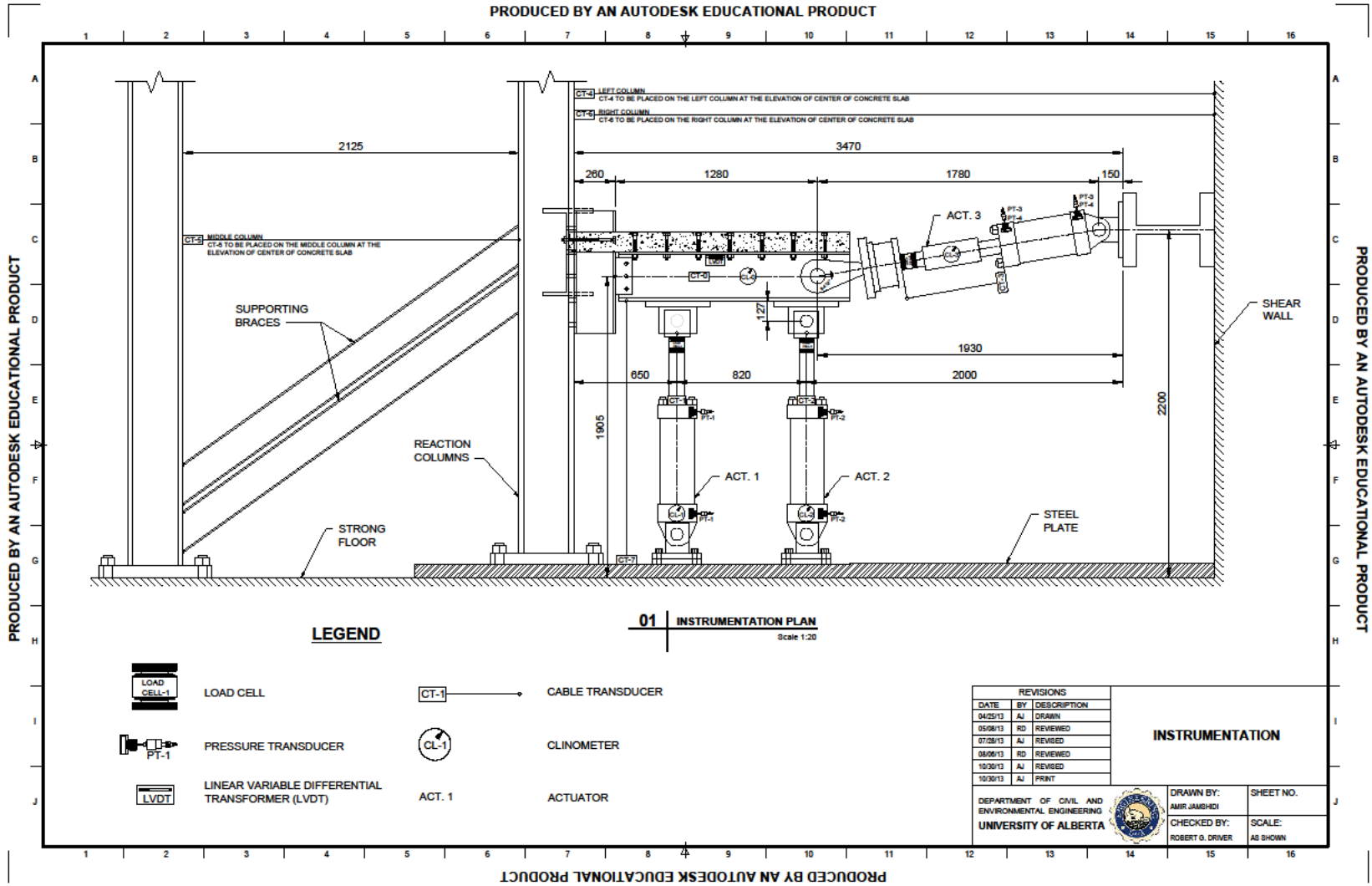
**SHEAR-TAB AND DOUBLE ANGLE CONNECTIONS (THICKNESS OF 9.5mm)**

DEPARTMENT OF CIVIL AND ENVIRONMENTAL ENGINEERING  
UNIVERSITY OF ALBERTA




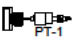
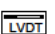
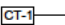

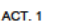
DRAWN BY:  
AMR JAMSHDI  
CHECKED BY:  
ROBERT G. DRIVER

SHEET NO.  
11 of 11  
SCALE:  
AS SHOWN



**LEGEND**

**01 | INSTRUMENTATION PLAN**  
Scale 1:20

-  LOAD CELL
-  PRESSURE TRANSDUCER
-  LINEAR VARIABLE DIFFERENTIAL TRANSFORMER (LVDT)
-  CABLE TRANSDUCER
-  CLINOMETER
-  ACT. 1

REVISIONS		
DATE	BY	DESCRIPTION
04/25/13	AJ	DRAWN
05/06/13	RD	REVIEWED
07/28/13	AJ	REVIEWED
08/06/13	RD	REVIEWED
10/30/13	AJ	REVIEWED
10/30/13	AJ	PRINT

**INSTRUMENTATION**

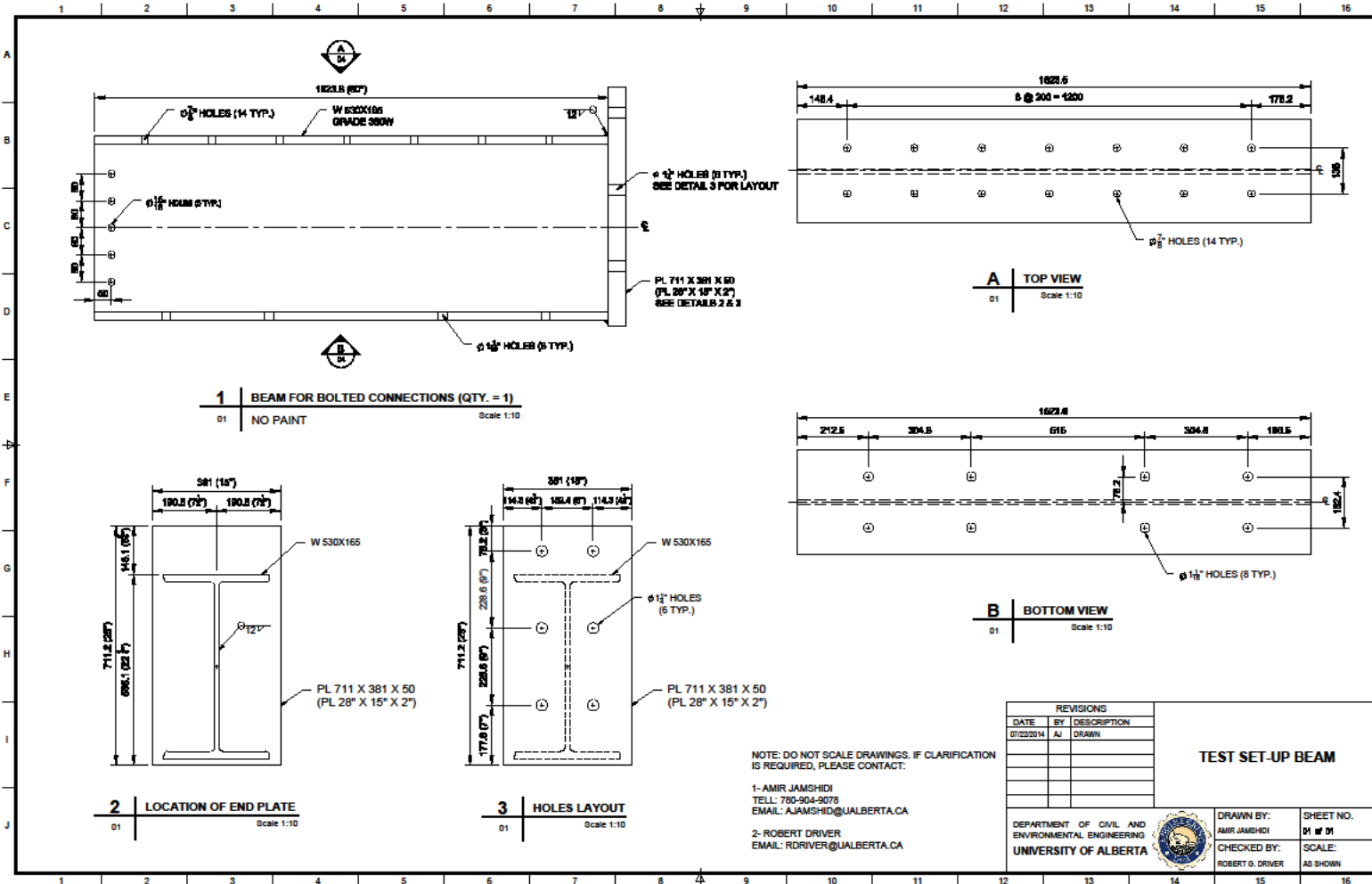
DEPARTMENT OF CIVIL AND ENVIRONMENTAL ENGINEERING  
UNIVERSITY OF ALBERTA

DRAWN BY:  
AMR JAMHDI

CHECKED BY:  
ROBERT G. DRIVER

SHEET NO.

SCALE:  
AS SHOWN

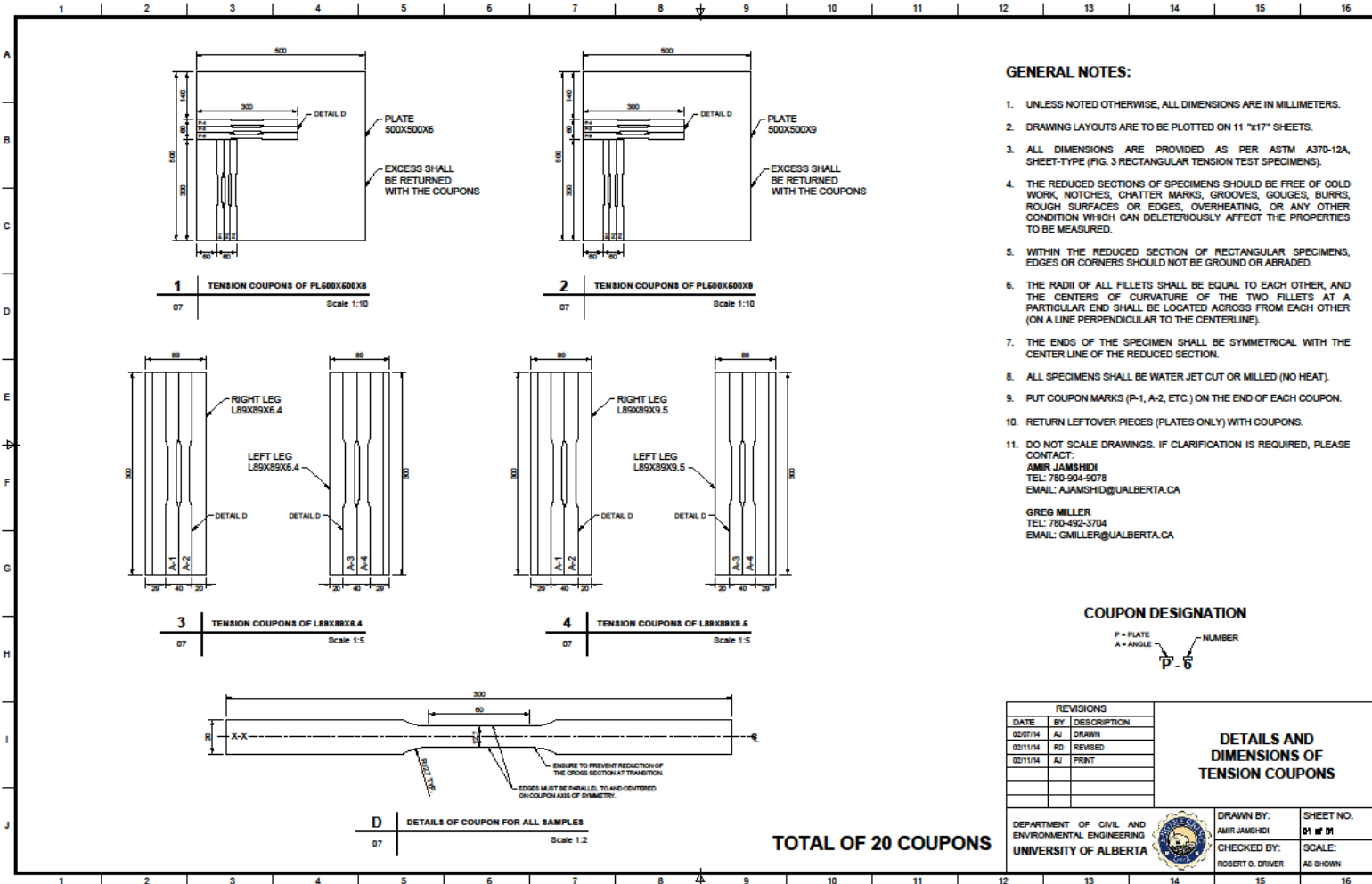


REVISIONS		
DATE	BY	DESCRIPTION
07/23/2014	AJ	DRAWN

**TEST SET-UP BEAM**

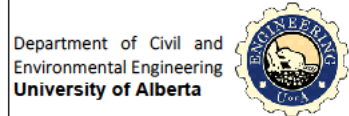
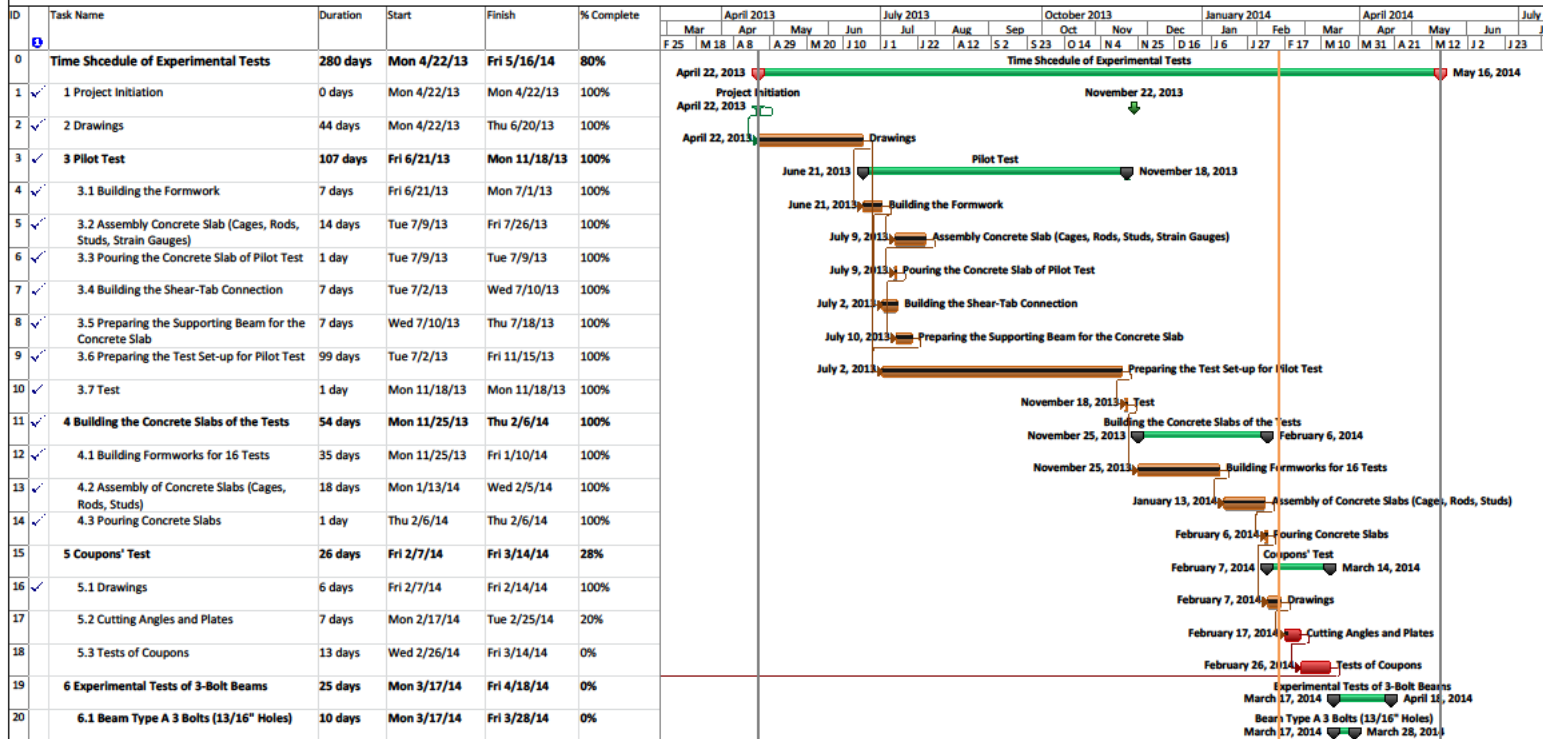
DEPARTMENT OF CIVIL AND ENVIRONMENTAL ENGINEERING UNIVERSITY OF ALBERTA		DRAWN BY: AMIR JAMSHIDI	SHEET NO. 01 of 01
		CHECKED BY: ROBERT G. DRIVER	SCALE: AS SHOWN





### Time Schedule of Experimental Tests

Amir Jamshidi



Task Summary Deadline Progress Critical Path Date  
Milestone Project Summary Critical Task Task Dependency Date



## **APPENDIX C. MATERIAL DATA**

This appendix provides further information regarding the results of the material tests on the plates, concrete slabs, and rebars. The stresses vs. strain curves from the same material are grouped in one graph. Table C-1 through Table C-4 summarises the results of all tension coupon tests of connections' material. Curves for multiple tension coupons of connections extracted from the same specimen are plotted together, shown in Figure C-1 through Figure C-4.

Results of tension tests of rebars are provided in Table C-5 and plotted in Figure C-5. Moreover, results of the concrete cylinder tests are summarised in Table C-6 and Table C-7 and are plotted in Figure C-6 to Figure C-21.

Table C-1: Coupon Test Results of 6 mm Angles

Heat Number: B48445 MTR: GA 621	Coupon	Width	Thick	Initial Area	Final Area	Area Reduction	Initial Gauge	Final Gauge	Elongation	Yield Strength	Tensile Strength	T/Y Ratio	Elastic Modulus	Yield Strain	Yield Strength	Tensile Strength	Elastic Modulus	Yield Strength	Tensile Strength	Elastic Modulus
		mm	mm	mm <sup>2</sup>	mm <sup>2</sup>	%	mm	mm	%	MPa	MPa		MPa	%	MPa	MPa	MPa	MPa	MPa	MPa
	A-1	12.62	6.59	83.1	34.0	59.1%	49.9	65.1	30.6%	335.8	492.8	1.47	195,391	0.17%	346.9	499.7	193,346	346.7	498.9	192,763
	A-2	12.61	6.57	82.9	34.1	58.9%	49.8	65.0	30.4%	358.0	506.7	1.42	191,300	0.19%						
	A-3	12.58	6.60	83.0	33.5	59.6%	49.9	66.6	33.4%	337.4	495.3	1.47	192,662	0.18%	346.5	498.1	192,180			
	A-4	12.60	6.59	82.9	34.5	58.4%	49.9	65.2	30.7%	355.5	500.8	1.41	191,698	0.19%						

Table C-2: Coupon Test Results of 9 mm Angles

Heat Number: SE13101507 MTR: N 1049	Coupon	Width	Thick	Initial Area	Final Area	Area Reduction	Initial Gauge	Final Gauge	Elongation	Yield Strength	Tensile Strength	T/Y Ratio	Elastic Modulus	Yield Strain	Yield Strength	Tensile Strength	Elastic Modulus	Yield Strength	Tensile Strength	Elastic Modulus
		mm	mm	mm <sup>2</sup>	mm <sup>2</sup>	%	mm	mm	%	MPa	MPa		MPa	%	MPa	MPa	MPa	MPa	MPa	MPa
	A-1	12.36	9.77	120.7	45.6	62.2%	49.7	68.2	37.3%	321.5	486.6	1.51	198,703	0.16%	329.4	491.1	197,177	329.3	490.8	195,520
	A-2	12.47	9.62	120.0	47.8	60.2%	50.0	67.1	34.3%	337.3	495.7	1.47	195,651	0.17%						
	A-3	12.45	9.73	121.1	46.3	61.8%	49.9	69.5	39.3%	324.0	487.4	1.50	194,407	0.17%	329.1	490.4	193,862			
	A-4	12.70	9.60	121.9	49.6	59.3%	49.8	67.5	35.7%	334.3	493.4	1.48	193,317	0.17%						

Table C-3: Coupon Test Results of 6 mm Shear Tabs

Heat Number: BIE619	Coupon	Width	Thick	Initial Area	Final Area	Area Reduction	Initial Gauge	Final Gauge	Elongation	Yield Strength	Tensile Strength	T/Y Ratio	Elastic Modulus	Yield Strain	Yield Strength	Tensile Strength	Elastic Modulus	Yield Strength	Tensile Strength	Elastic Modulus	
																					mm
MTR: SAM 166	P-1	12.74	6.26	79.8	24.3	69.5%	50.6	66.2	30.8%	362.4	485.9	1.34	201,299	0.18%							
	P-2	12.67	6.25	79.2	24.0	69.6%	50.2	67.6	34.5%	357.2	484.7	1.36	200,579	0.18%	358.7	482.7	200,627				
	P-3	12.69	6.28	79.7	23.1	71.0%	50.2	67.0	33.4%	356.4	477.6	1.34	200,004	0.18%				355.5	477.8	201,984	
	P-4	12.76	6.33	80.8	21.7	73.1%	50.0	66.8	33.6%	347.4	468.4	1.35	200,767	0.17%							
	P-5	12.69	6.26	79.4	22.5	71.7%	50.2	68.2	35.7%	354.7	476.1	1.34	204,944	0.17%	352.4	472.8	203,340				
	P-6	12.70	6.27	79.7	22.6	71.7%	50.2	67.2	33.8%	355.0	473.9	1.34	204,310	0.17%							

Table C-4: Coupon Test Results of 9 mm Shear Tabs

Heat Number: A3C173	Coupon	Width	Thick	Initial Area	Final Area	Area Reduction	Initial Gauge	Final Gauge	Elongation	Yield Strength	Tensile Strength	T/Y Ratio	Elastic Modulus	Yield Strain	Yield Strength	Tensile Strength	Elastic Modulus	Yield Strength	Tensile Strength	Elastic Modulus	
																					mm
MTR: SAM 224	P-1	12.60	9.45	119.1	40.9	65.6%	50.0	69.9	39.9%	293.2	440.1	1.50	189,106	0.16%							
	P-2	12.60	9.47	119.3	40.1	66.3%	49.9	69.1	38.4%	297.1	438.6	1.48	195,288	0.15%	294.3	439.2	192,873				
	P-3	12.58	9.50	119.4	39.6	66.8%	49.8	69.1	38.8%	292.7	438.9	1.50	194,224	0.15%				300.1	439.5	197,227	
	P-4	12.60	9.43	118.8	47.0	60.4%	50.1	67.9	35.5%	302.4	441.2	1.46	202,919	0.15%							
	P-5	12.60	9.47	119.3	49.8	58.3%	49.8	67.6	35.6%	308.3	437.6	1.42	201,257	0.15%	305.9	439.8	201,581				
	P-6	12.54	9.44	118.3	47.0	60.3%	49.8	68.5	37.4%	306.9	440.5	1.44	200,566	0.15%							

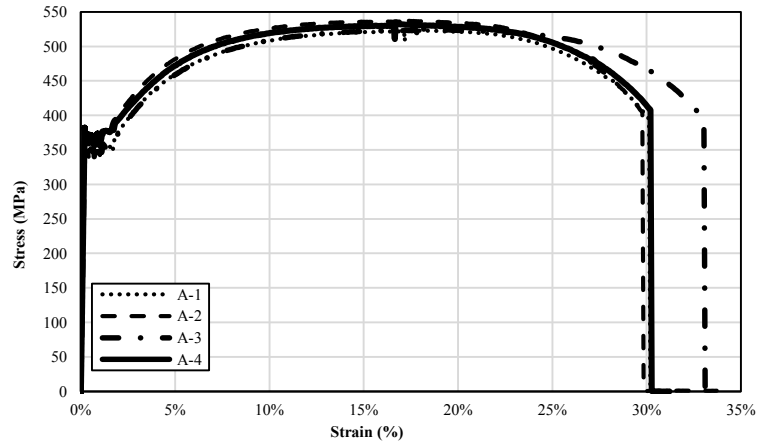


Figure C-1: Stress–Strain Curves of 6 mm Angles

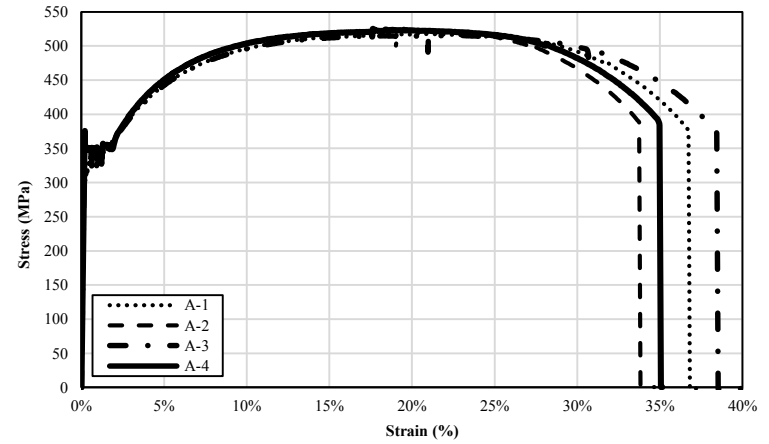


Figure C-2: Stress–Strain Curves of 9 mm Angles

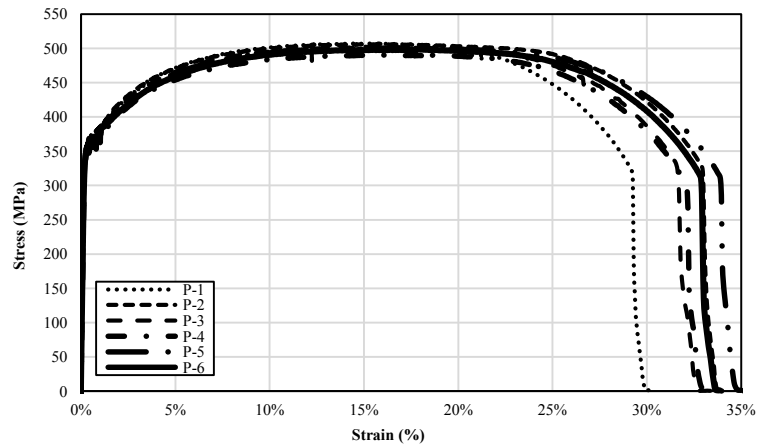


Figure C-3: Stress–Strain Curves of 6 mm Shear Tabs

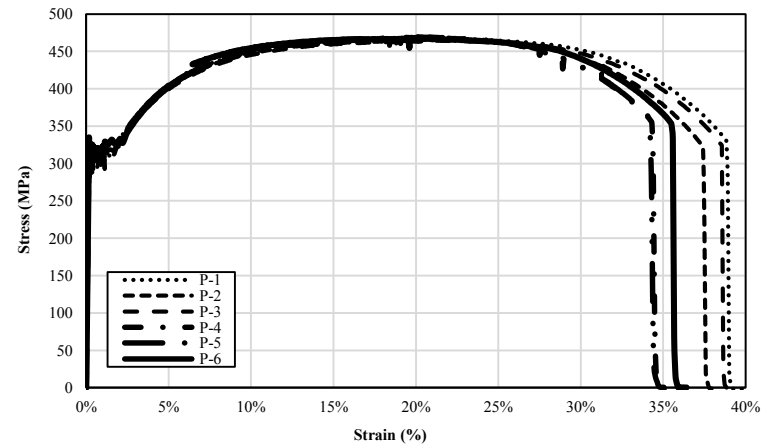


Figure C-4: Stress–Strain Curves of 9 mm Shear Tabs

Table C-5: Rebar Tension Test Results

Rebar	Area	Dia.	Yield Strength	Tensile Strength	Tensile to Yield Ratio	Elastic Modulus	Yield Strain	Fracture Strain	Yield Strength	Tensile Strength	Elastic Modulus	Yield Strength	Tensile Strength	Elastic Modulus
	mm <sup>2</sup>	mm	MPa	MPa	---	MPa	%	%	MPa	MPa	MPa	MPa	MPa	MPa
R-1	95.5	11.03	449.4	654.5	1.46	196,475	0.23%	22.0%	450.6	651.5	198,279	454.3	656.6	192,869
R-2	95.3	11.01	451.8	648.5	1.44	200,083	0.23%	23.0%						
R-3	95.5	11.03	449.0	674.6	1.50	195,275	0.23%	22.9%	452.1	665.1	188,416	454.3	656.6	192,869
R-4	95.5	11.03	455.3	655.5	1.44	181,557	0.25%	20.2%						
R-5	97.5	11.14	459.5	654.2	1.42	192,659	0.24%	24.6%	460.2	653.3	191,913	454.3	656.6	192,869
R-6	97.7	11.15	460.8	652.5	1.42	191,167	0.24%	21.9%						

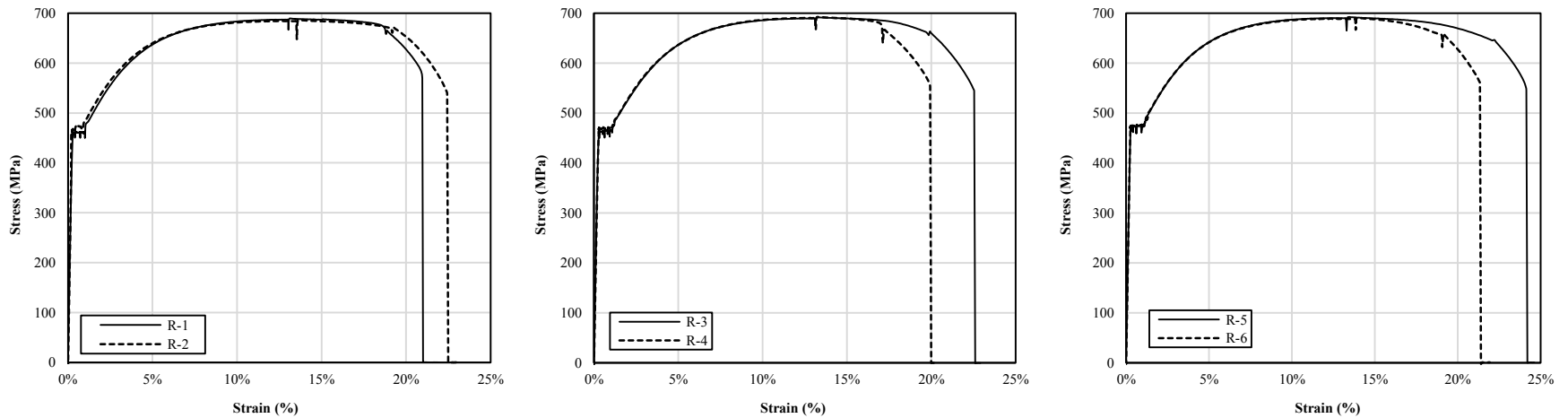


Figure C-5: Stress–Strain Curves of Steel Rebars



Table C-6: Concrete Cylinder Test Results

Cyl.	No.	L <sub>1</sub> mm	L <sub>2</sub> mm	L <sub>3</sub> mm	L <sub>avg</sub> mm	D <sub>1</sub> mm	D <sub>2</sub> mm	D <sub>avg</sub> mm	m gr	A mm <sup>2</sup>	V mLit	g kg/m <sup>3</sup>	f <sub>c</sub> MPa	Strain micro	E <sub>c</sub> MPa	Specimen	Date of Cylinder Test	Casting to Testing (Days)	Hierarchy of Casting	Date of Slab Test
0	1	304.3	304.5	304.8	304.5	151.8	152.7	152.3	12.8	18205	5544	2302	25.8	2502	18,855	28Day	7-Mar-2014	29	0	
	2	304.0	304.0	304.1	304.0	152.2	152.7	152.5	12.8	18256	5551	2299	21.6	1207	23,006					
	3	305.0	304.9	304.8	304.9	152.7	152.2	152.4	12.8	18249	5564	2295	25.3	1867	19,375					
1	1	200.7	200.6	200.6	200.6	101.6	102.8	102.2	3858.6	8205	1646	2344	30.3	2027	21,267	ST36B	25-Jun-2014	139	5	26-Jun-2014
	2	200.1	199.5	200.0	199.9	102.7	102.8	102.8	3878.0	8294	1658	2339	32.0	2214	23,481					
	3	199.2	199.6	199.3	199.4	101.8	102.2	102.0	3834.2	8174	1630	2352	32.9	2307	23,172					
2	1	202.0	202.0	201.9	202.0	102.6	102.5	102.5	3902.8	8256	1668	2340	28.5	2065	23,123	ST59B	8-Oct-2014	244	6	7-Oct-2014
	2	201.9	201.8	201.9	201.9	102.9	102.7	102.8	3898.6	8305	1677	2325	28.6	1953	23,081					
	3	201.1	201.1	201.6	201.3	102.8	102.2	102.5	3868.0	8253	1661	2329	31.7	2194	21,286					
3	1	197.1	196.3	196.3	196.6	102.3	102.3	102.3	3776.4	8219	1616	2337	31.3	2680	19,627	ST56B	25-Sep-2014	231	1	25-Sep-2014
	2	201.1	200.5	200.8	200.8	101.7	102.9	102.3	3855.4	8222	1651	2335	28.4	2007	22,749					
	3	200.6	200.6	200.3	200.5	99.9	99.9	99.9	3673.6	7835	1571	2339	27.1	2044	20,903					
4	1	200.6	200.6	201.0	200.7	103.3	101.4	102.4	3869.4	8228	1652	2343	29.3	2035	22,602	DA56B	5-Sep-2014	211	9	4-Sep-2014
	2	201.7	201.8	201.7	201.7	102.7	102.8	102.7	3894.2	8289	1672	2329	30.3	2182	20,813					
	3	199.9	200.4	199.8	200.0	102.7	101.8	102.2	3870.8	8206	1642	2358	27.8	1741	22,871					
5	1	200.6	200.9	200.6	200.7	101.8	102.7	102.3	3806.8	8211	1648	2310	27.4	2467	20,098	DA36B	25-Aug-2014	200	14	22-Aug-2014
	2	201.2	201.2	201.3	201.2	99.8	100.5	100.2	3646.8	7881	1586	2299	27.6	2450	18,112					
	3	198.4	199.1	198.7	198.7	100.3	103.8	102.1	3764.0	8177	1625	2316	29.1	2571	18,613					
6	1	201.0	200.9	200.9	200.9	102.2	102.6	102.4	3870.4	8239	1655	2338	29.7	2279	20,169	DA39B	14-Oct-2014	250	13	15-Oct-2014
	2	201.5	201.9	201.7	201.7	102.3	101.4	101.8	3859.0	8146	1643	2349	32.3	2416	19,719					
	3	199.3	199.4	199.4	199.4	99.4	100.8	100.1	3659.4	7872	1569	2332	26.9	2256	21,502					
7	1	195.5	195.9	195.5	195.6	100.5	99.9	100.2	3594.0	7889	1543	2329	26.4	1945	22,651	DA59B	27-Oct-2014	263	15	17-Oct-2014
	2	198.6	198.2	198.5	198.5	99.8	100.0	99.9	3639.2	7845	1557	2337	28.8	2470	19,609					
	3	190.6	190.5	190.5	190.5	99.8	101.8	100.8	3544.0	7975	1519	2332	29.3	2144	22,188					
8	1	201.4	201.4	201.3	201.3	102.4	103.0	102.7	3850.4	8277	1666	2310	30.1	2443	20,230	ST39B	3-Oct-2014	239	16	3-Oct-2014
	2	199.7	199.7	199.4	199.6	101.3	98.9	100.1	3664.0	7870	1571	2332	26.1	2287	19,621					
	3	195.1	195.1	195.2	195.1	100.6	99.7	100.1	3576.4	7874	1537	2328	25.9	2169	21,279					

Table C-7: Concrete Cylinder Test Results

Cyl. No.	L <sub>1</sub> mm	L <sub>2</sub> mm	L <sub>3</sub> mm	L <sub>avg</sub> mm	D <sub>1</sub> mm	D <sub>2</sub> mm	D <sub>avg</sub> mm	m gr	A mm <sup>2</sup>	V mLit	g kg/m <sup>3</sup>	f <sub>c</sub> MPa	Strain micro	E <sub>c</sub> MPa	Specimen	Date of Cylinder Test	Casting to Testing (Days)	Hierarchy of Casting	Date of Slab Test	
9	1	202.9	202.4	202.7	202.6	100.8	100.3	100.5	3761.8	7939	1609	2338	28.5	2002	23,120	ST39A	2-Oct-2014	238	3	2-Oct-2014
	2	197.8	197.6	197.7	197.7	103.1	101.0	102.1	3795.6	8180	1617	2347	29.9	2280	22,314					
	3	198.9	198.9	199.0	198.9	101.6	102.8	102.2	3853.2	8205	1632	2361	30.4	2386	21,985					
10	1	195.5	195.5	196.0	195.7	102.0	101.7	101.9	3732.0	8149	1595	2340	31.04	1,988	22,769	DA36A	19-Aug-2014	194	10	20-Aug-2014
	2	199.1	199.0	199.3	199.1	101.7	101.6	101.7	3791.6	8117	1616	2346	30.32	2,142	21,665					
	3	197.4	197.1	197.3	197.3	101.5	102.2	101.8	3756.0	8146	1607	2337	30.35	2,486	18,304					
11	1	197.4	197.3	196.9	197.2	100.5	100.2	100.4	3638.6	7912	1560	2332	28.6	881	27,808	DA56A	29-Aug-2014	204	12	28-Aug-2014
	2	199.7	200.1	199.6	199.8	99.7	100.0	99.9	3672.6	7830	1564	2348	27.2	1926	22,586					
	3	198.8	198.8	198.8	198.8	99.7	100.1	99.9	3662.0	7840	1559	2349	28.8	2159	20,506					
12	1	200.2	199.5	199.6	199.8	101.6	103.2	102.4	3848.4	8238	1646	2339	28.9	2108	23,305	DA39A	16-Oct-2014	252	4	16-Oct-2014
	2	200.4	200.3	200.4	200.4	102.6	102.2	102.4	3839.4	8234	1650	2327	32.4	2519	22,195					
	3	201.6	202.2	201.7	201.8	101.7	103.1	102.4	3895.6	8235	1662	2344	30.5	2045	23,857					
13	1	198.4	198.2	198.8	198.5	102.1	102.3	102.2	3824.8	8199	1627	2350	33.5	2383	21,025	ST36A	18-Jun-2014	132	2	18-Jun-2014
	2	199.2	199.4	199.9	199.5	101.4	102.0	101.7	3813.6	8130	1622	2352	31.1	2055	21,792					
	3	198.5	199.3	198.7	198.8	102.6	102.5	102.6	3864.0	8260	1642	2353	34.1	2370	21,272					
14	1	200.5	200.6	200.5	200.5	101.9	102.2	102.0	3801.6	8176	1640	2319	25.0	2122	20,918	DA59A	28-Oct-2014	264	7	28-Oct-2014
	2	203.1	203.4	203.0	203.2	102.3	102.3	102.3	3857.4	8216	1669	2311	27.6	2182	20,980					
	3	203.4	203.1	203.1	203.2	103.1	101.4	102.3	3839.0	8212	1669	2301	27.1	2484	19,431					
15	1	198.1	198.1	197.7	198.0	102.3	101.6	101.9	3817.0	8160	1615	2363	29.6	2177	22,480	ST59A	10-Oct-2014	246	8	9-Oct-2014
	2	197.6	197.4	197.6	197.5	102.8	102.1	102.5	3820.4	8243	1628	2346	33.2	2343	21,559					
	3	198.6	198.7	198.7	198.7	102.0	102.2	102.1	3822.6	8184	1626	2351	30.0	1847	26,545					
16	1	200.9	200.7	200.2	200.6	102.0	102.3	102.1	3795.6	8192	1643	2310	31.4	2516	21,185	ST56A	10-Sep-2014	216	11	9-Sep-2014
	2	200.2	200.1	200.1	200.1	102.1	101.9	102.0	3772.8	8170	1635	2308	27.0	2015	22,568					
	3	201.8	201.5	201.7	201.7	100.3	100.4	100.4	3669.2	7912	1596	2300	27.0	2091	21,373					

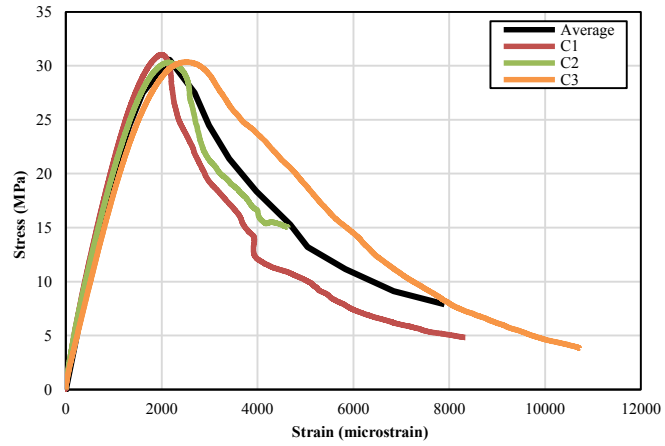


Figure C-6: Stress–Strain Curves of DA36A Slab

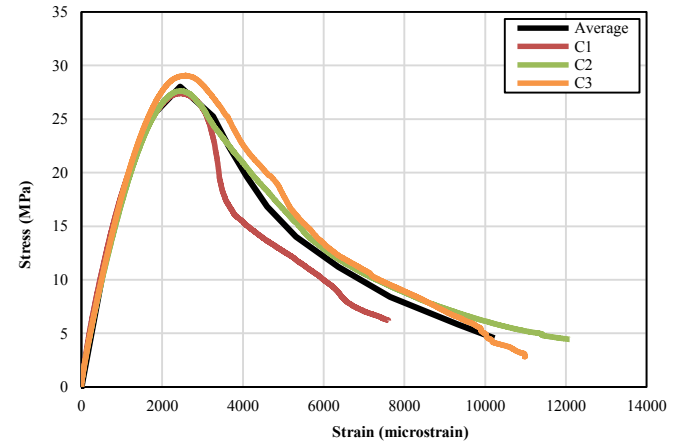


Figure C-7: Stress–Strain Curves of DA36B Slab

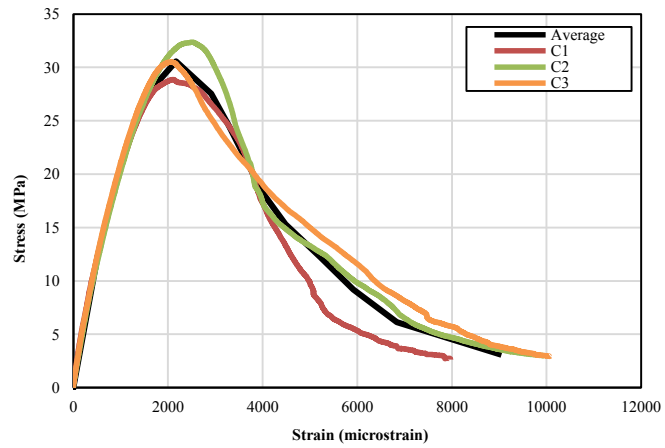


Figure C-8: Stress–Strain Curves of DA39A Slab

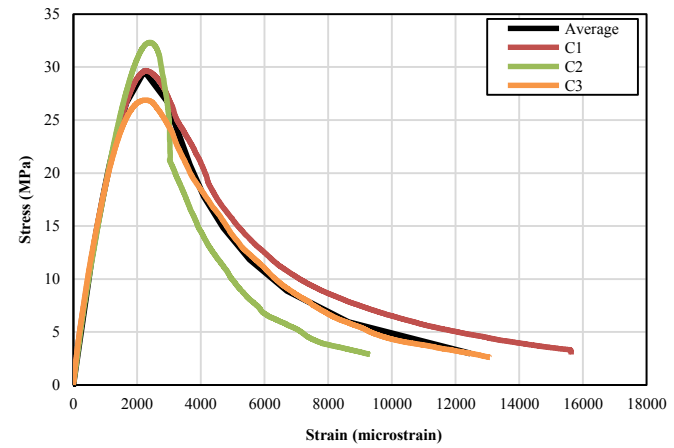


Figure C-9: Stress–Strain Curves of DA39B Slab

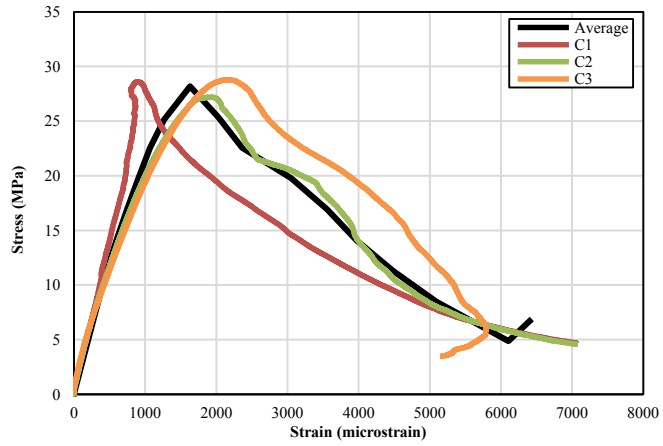


Figure C-10: Stress–Strain Curves of DA56A Slab

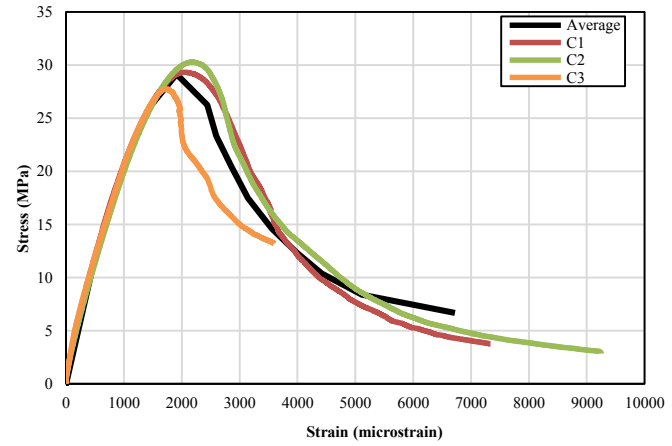


Figure C-11: Stress–Strain Curves of DA56B Slab

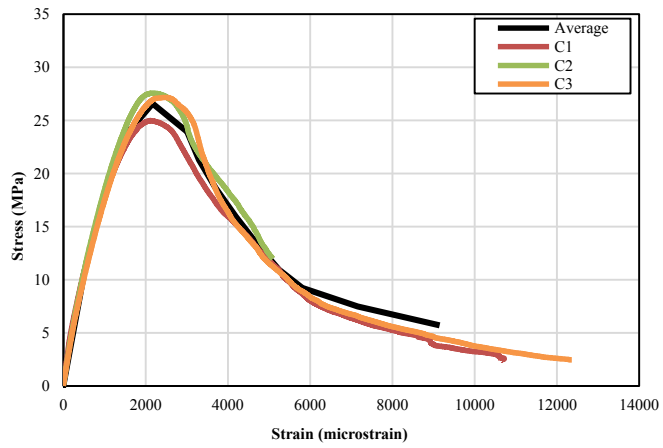


Figure C-12: Stress–Strain Curves of DA59A Slab

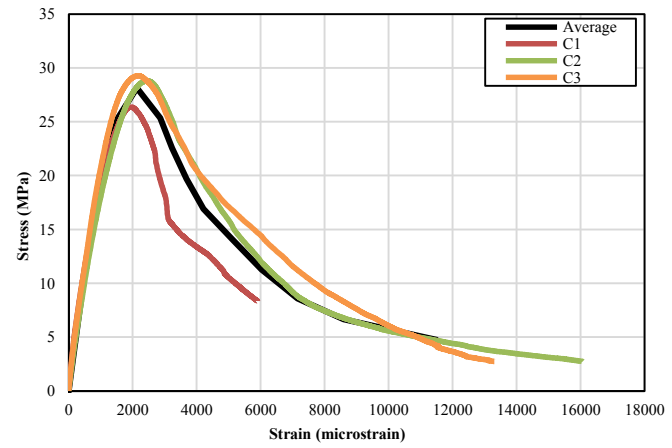


Figure C-13: Stress–Strain Curves of DA59B Slab

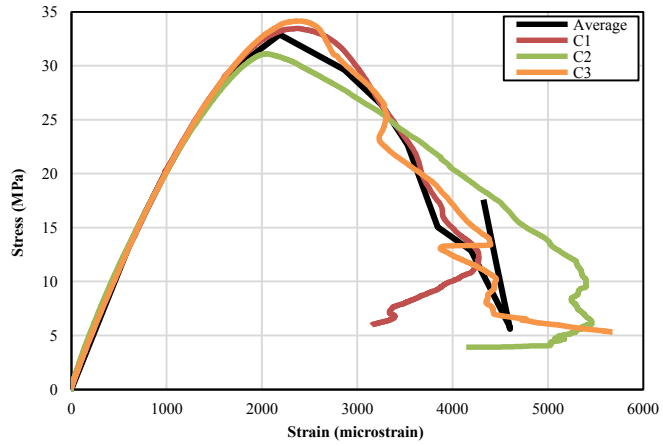


Figure C-14: Stress–Strain Curves of ST36A Slab

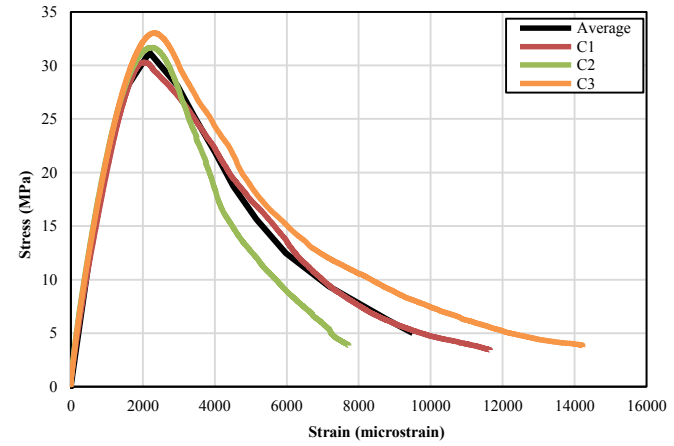


Figure C-15: Stress–Strain Curves of ST36B Slab

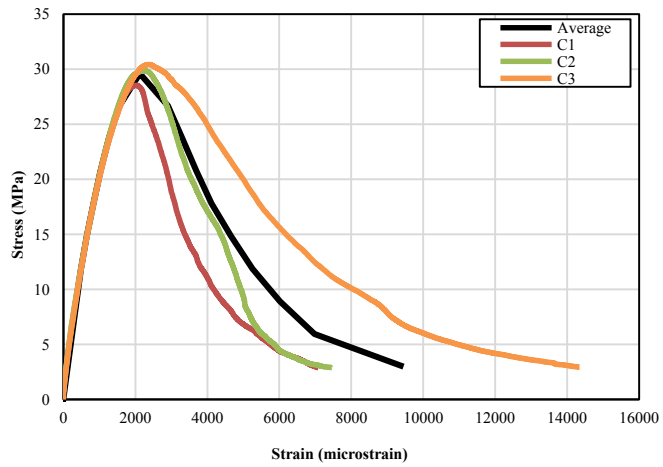


Figure C-16: Stress–Strain Curves of ST39A Slab

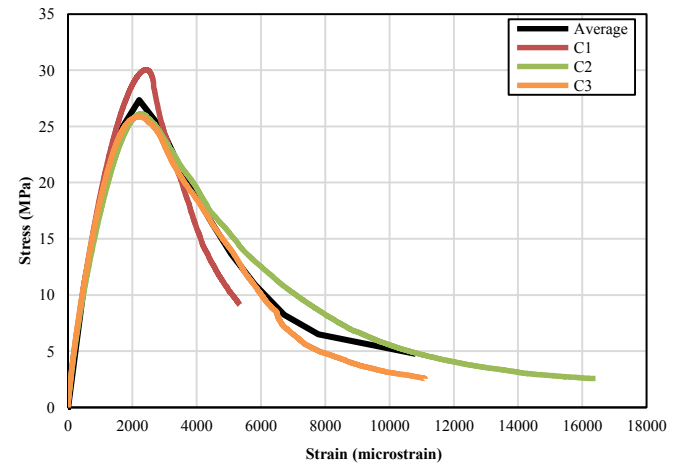


Figure C-17: Stress–Strain Curves of ST39B Slab

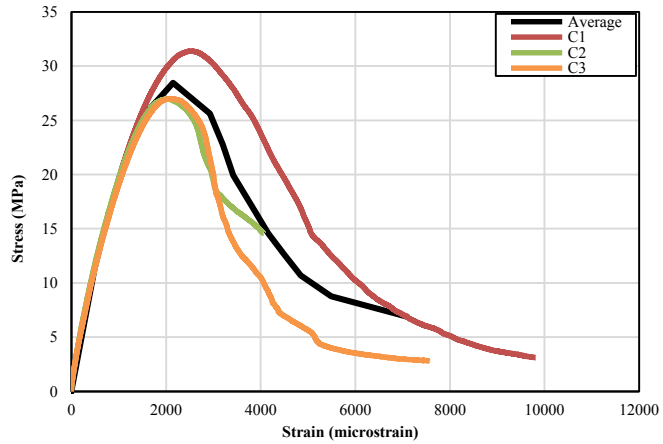


Figure C-18: Stress–Strain Curves of ST56A Slab

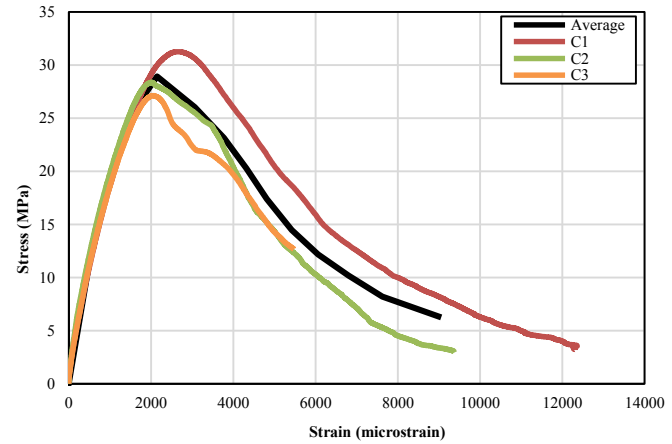


Figure C-19: Stress–Strain Curves of ST56B Slab

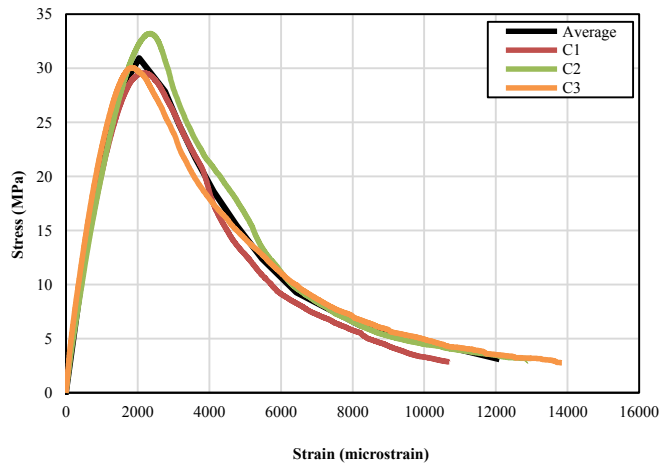


Figure C-20: Stress–Strain Curves of ST59A Slab

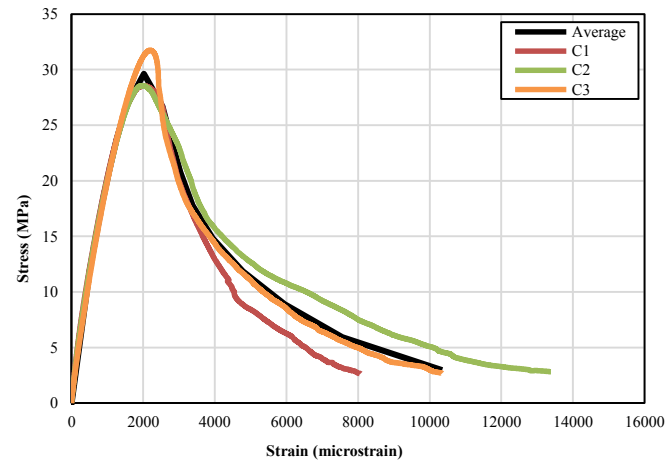


Figure C-21: Stress–Strain Curves of ST59B Slab